szentesi.peter_292_24

MTA DOKTORI PÁLYÁZAT

DOKTORI ÉRTEKEZÉS

Az elemi kalciumfelszabadulási események morfológiája fiziológiás és kóros körülmények között vázizmon

Dr. Szentesi Péter

Debreceni Egyetem Általános Orvostudományi Kar

Élettani Intézet

2025

Tartalomjegyzék

Fejezet **Oldalszám**

1. ÖSSZEFOGLALÁS 4

2. RÖVIDÍTÉSEK JEGYZÉKE 5

3. BEVEZETÉS, IRODALMI ÁTTEKINTÉS 7

3.1 A vázizom felépítése és működése 8

3.2 Az elektromechanikai kapcsolás 10

3.3 A dihidropiridin-receptor felépítése és szabályozása 11

3.4 A rianodin receptor felépítése és szabályozása 11

3.5 Az elemi kalciumfelszabadulási események fajtái és tulajdonságai 14

3.6 Automatikus ECRE kereső algoritmusok 17

4. CÉLKITŰZÉSEK 19

5. ANYAGOK ÉS MÓDSZEREK, MÓDSZERTANI FEJLESZTÉSEK 20

5.1 Vázizomrostok izolálása fluoreszcens kalciumindikátorral végzett konfokális lézerpásztázó mikroszkópos mérések számára 20

5.2 Kalciumkoncentráció változás mérése konfokális lézerpásztázó mikroszkóppal 23

5.3 Az elemi kalciumfelszabadulási események elemzése 25

5.3.1 A stationary wavelet transzformáció 26

5.3.2 Az egydimenziós (line-scan) képek elemzése 27

5.3.3 A kétdimenziós (XY) képek elemzése 29

5.4 Adatelemzés 31

6. EREDMÉNYEK ÉS KÖVETKEZTETÉSEK 32

6.1 Elemi események fiziológiás körülmények között emlősök, kétéltűek és rovarok izomrostjain 32

6.1.1 ECRE-k patkányok harántcsíkolt izmon 32

6.1.2 ECRE-k békák harántcsíkolt izmain 33

6.1.3 ECRE-k egerek harántcsíkolt izmain 35

6.1.4 ECRE-k házi méhek harántcsíkolt izmain 36

6.2 A depolarizáció és különböző kalciumfelszabadulást befolyásoló anyagok hatása az elemi eseményekre 40

6.2.1 Depolarizáció és koffein hatása béka harántcsíkolt izmon 40

6.2.2 A nehézfém-ion kelátor TPEN hatása az ECRE-kre 43

6.2.3 A fenol származék timol hatása az ECRE-kre 45

6.2.4 A benzotiazepin származék K-201 hatása az ECRE-kre 47

6.2.5 Egy skorpió toxin hatása az ECRE-kre 48

6.2.6 A foszfatidilinozitol foszfát hatása az ECRE-kre 50

6.3 Elemi események nem fiziológiás körülmények között 52

6.3.1 ECRE-k szívinfarktuson átesett patkányok harántcsíkolt izmain 52

6.3.2 ECRE-k hiperkoleszterinémiás patkányok harántcsíkolt izmain 53

6.4 Elemi események változása génmódosítás hatására vázizomban 55

6.4.1 A Triadin fehérje szintjének hatása az ECRE-kre tenyésztett harántcsíkolt izomsejtekben 55

6.4.2 ECRE-k a természetes mutációval kialakult hipermuszkuláris egerek harántcsíkolt izomrostjaiban 58

6.4.3 Az embrionális DHPR jelenlétének hatása az ECRE-kre egerek harántcsíkolt izomrostjaiban 60

6.4.4 ECRE-k harántcsíkolt izomrostokban a miotubuláris miopátia egérmodellben 62

6.4.5 ECRE-k harántcsíkolt izomrostokban a centronukleáris miopátia egérmodelljében 67

6.4.6 Az Ankirin1 fehérje szintjének hatása az ECRE-kre egér harántcsíkolt izomrosjaiban 68

7. ÚJ MEGÁLLAPÍTÁSOK 71

8. KÖSZÖNETNYILVÁNÍTÁS 73

9. IRODALOMJEGYZÉK 74

10. APPENDIX 82

11. A FELHASZNÁLT KÖZLEMÉNYEK KÜLÖNLENYOMATAI AZ ELSŐ SZERZŐ NEVE SZERINTI ABC SORRENDBEN 91

1. ÖSSZEFOGLALÁS

A disszertációban összefoglalt kutatások célja az volt, hogy kísérletes módszerekkel tanulmányozzuk a vázizmok elemi kalciumfelszabadulási eseményeit egészséges és kóros körülmények között. Az elemi kalciumfelszabadulási események alapvető tulajdonságainak leírása mellett azt akartuk megérteni, hogy milyen összefüggés van ezek számának vagy alakjának változása és a miopátiát okozó kórfolyamatok súlyossága között. Azt is vizsgáltuk, hogy milyen mechanizmus révén befolyásolják az elemi kalciumfelszabadulási eseményeket az egyes farmakonok vagy a sejtmembrán depolarizációja. Tanulmányoztuk az elemi kalciumfelszabadulási eseményeket génmódosított állatok vázizmaiban is, ahol az elektromechanika kapcsolat egyes kulcsfehérjéinek a kalciumfelszabadulásban betöltött szerepét kívántuk tisztázni.

Minden kutatásunk első lépéseként a vizsgálni kívánt species vázizmának méréseinkre alkalmas preparálását kellett kifejleszteni. Sikeresen megoldottuk egér, patkány és háziméh egyedi egészséges vázizomrostjainak izolálását.

A fentieken kívül kidolgoztunk olyan automatikus esemény-detektáló algoritmusokat, amelyek mind vonalmenti, mind kétdimenziós szkenneléssel mért képeken felhasználói beavatkozás nélkül képesek megtalálni az elemi kalciumfelszabadulási eseményeket. Az így nyert nagymennyiségű mérési adat feldolgozásával voltunk képesek megtalálni az egyes kórfolyamatok vagy környezeti változások hatását az elemi események kialakulására és morfológiájára.

Mivel az elemi kalciumfelszabadulási események kialakulásában az elektromechanikai kapcsolat kulcsfehérjéi aktívan részt vesznek, bármilyen módosulás az eseményben az izom kalciumcsatornáinak megváltozott működésére utal, így ezek a változások közvetve tanulmányozhatók.

A vizsgálatok elvégzéséhez a legmodernebb konfokális mikroszkópiás fluoreszcens módszereket alkalmaztuk. A szupergyors pásztázási technika lehetővé tette, hogy az elemi kalciumfelszabadulási események időbeliségét korábbiakban soha nem látott időbeli felbontásban tanulmányozzuk. Az általunk kapott eredmények hozzájárulhatnak ahhoz, hogy részletesebben megismerjük a vázizmok kalciumhomeosztázisát fiziológiás és kóros körülmények között.

2. RÖVIDÍTÉSEK JEGYZÉKE

Rövidítés	Magyarázat (angol vagy latin nevezéktan)
$[Ca^{2+}]_e$	extracelluláris kalciumkoncentráció
$[Ca^{2+}]_i$	intracelluláris kalciumkoncentráció
CaV1.1	vázizom típusú feszültségérzékeny kalciumcsatorna
CICR	kalcium-indukálta kalciumfelszabadulás (Calcium-Induced Calcium Release)
CLSM	konfokális lézerpásztázó mikroszkóp (Confocal Laser Scanning Microscope)
Cmpt	$Mstn^{Cmpt\text{-}dl1Abc}$ egértörzs
CNM	centronukleáris miopátia (Centronuclear Myopathy)
CoQ_{10}	koenzim Q_{10} (ubiquinon)
CRU	kalciumfelszabadító egység (Calcium Release Unit)
CSQ	kalszekvesztrin
DHPR	dihidropiridin receptor (Dihydropyridine Receptor)
DNM1	dynamin 1
ECC	elektromechanikai kapcsolat (Excitation Contraction Coupling)
ECRE	elemi kalciumfelszabadulási esemény (Elementary Calcium Release Event)
EDL	*musculus extensor digitorum longus*
FDB	*musculus flexor digitorum brevis*
FFT	gyors Fourier transzformáció (Fast Fourier Transform)
FDHM	a *spark*ok időbeli kiterjedése az amplitúdó felénél (Full Duration at Half Maximum, megegyezik az FTHM-el)
FTHM	a *spark*ok időbeli kiterjedése az amplitúdó felénél (Full Time at Half Maximum, megegyezik az FDHM-el)
FWHM	a *spark*ok térbeli szélessége az amplitúdó felénél (Full Width at Half Maximum)
Mstn	miostatin (myostatine)
MTM1	miotubularin (myotubularin) 1
PI(3)P	foszfatidilinozitol 3-foszfát
$PI(3,5)P_2$	foszfatidilinozitol 3,5-biszfoszfát

PI(5)P	foszfatidilinozitol 5-foszfát
PtdInsP	foszfatidilinozitol foszfát
RyR	rianodin receptor (Ryanodine Receptor)
RyR1	vázizom típusú rianodin receptor (Ryanodine Receptor type 1)
SERCA	szarko- endoplazmatikus retikulum Ca^{2+} – ATP-áz (Sarco-Endoplasmatic Reticulum Ca^{2+} – ATPase)
SR	szarkoplazmatikus retikulum (Sarcoplasmic Reticulum)
TGF β	transzformáló növekedési faktor β (Transforming Growth Factor β)
TnC	Troponin-C
TTP	csúcs eléréséhez szükséges idő (Time To Peak)

3. BEVEZETÉS, IRODALMI ÁTTEKINTÉS

Az emberek mindig is szívesen fedezték fel a világuk kis és nagy dolgait. Míg a nagy dolgok kutatására megtalálták a természetes határvonalat az univerzumban, addig a kis dolgok keresésében még nem értek el egy hasonló határt. A biológiai kutatásban az egyre kisebb és kisebb objektumok keresése a kutatás fókuszát először áthelyezte a szervezetről az egyedi szervekre, a szervektől egyetlen sejtre, végül pedig szubcelluláris alkotókra és egyetlen molekulára. Ennek a stratégiának az az erős motivációja, hogy egy rendszer apró részei könnyebben megérthetőek, mint maga a komplex rendszer. Ezt a koncepciót redukcionista megközelítésnek nevezzük. Ez azonban nem mindig volt olyan hasznos, mint amire először számítottunk, elsősorban azért, mert a legkisebb és a legelemibb események összetettségét alul értékeltük. Másodsorban pedig azért, mert a végső cél, hogy a kis darabokból újra összerakjuk a nagy képet, már döbbenetes nehéz feladat.

Az elemi kalciumfelszabadulási események felfedezése és jellemzése, a teljes sejtes jelátviteli eseményekből történő kibontása jó példa arra, hogy a redukcionista megközelítés speciális esetekben mégis működhet.

A kalciumjelátvitel meglepő módon egyszerre egyszerű és összetett abban az értelemben, hogy az egyatomos kalciumion (Ca^{2+}) az ismert legsokoldalúbb biológiai hírvivő. Gyors, tranziens kalciumkoncentráció-változások közvetlenül szabályozzák például az izomösszehúzódást, a sejtmozgást, a hormonszekréciót és az idegi jelátvitelt. Tartós Ca^{2+}-koncentrációemelkedés kulcsszerepet játszik számos biológiai folyamatban a megtermékenyítéstől a génexpresszión át a sejthalálig. Mégis, mivel egy egyatomos kation, a Ca^{2+} csak egy biológiailag releváns formában létezik – amely a katabolikus lebomlás és az anabolikus szintézis egyikén sem megy keresztül – biológiai információkódoló képessége szinte teljes egészében a célfehérjékhez történő kötődéséből és róluk leválásából származik, vagy mint biológiai membránokon keresztüli elektromos áramként jelenik meg. Ez az egyszerűsége a kalciumjelátvitelnek látszólag ellentmond az általa irányított folyamatok tökéletességének és a bonyolultságának. A kalciumion több ezer fehérjét köt össze azáltal, hogy ezek mindegyike egy evolúciósan konzervált Ca^{2+}-kötő alegységet tartalmaz. Ez a tulajdonsága azt a kérdést veti fel, hogy miképpen tudja a Ca^{2+} összehangolni ezeket a molekulákat egy adott sejtben az elképesztően változatos és néha még ellentétes élettani funkciók teljesítésére. Mivel a Ca^{2+} a legjobban

tanulmányozott az összes biológiai hírvivő közül, a róla feltárt eredmények alapvető ismeretekkel szolgálnak az intracelluláris jelátvitel alapelveit illetően.

Az elmúlt három évtizedben élénk kutatás folyt a lokális Ca^{2+}-jelátvitel megismerésére izmokban, idegsejtekben és más ingerelhető és nem ingerelhető sejtekben is. Ez a sok tanulmány megválaszolt már régi dilemmákat és további kérdéseket vetett fel. A diszkrét elemi Ca^{2+}-felszabadulási események felfedezése rávilágított a kalciumjelátviteli rendszer működésének alapelveire és teleológiai betekintést hozott számos szupramolekuláris Ca^{2+}-jelátviteli mechanizmus létezésére különböző típusú sejtekben. Az elemi kalciumesemények elemzéséből kapott ismeretek alapján valóban eljutottunk olyan sokkal bonyolultabb rendszerek jobb megértéshez, mint például az izomsejtek, neuronok, de még egyes nem ingerelhető sejtek is.

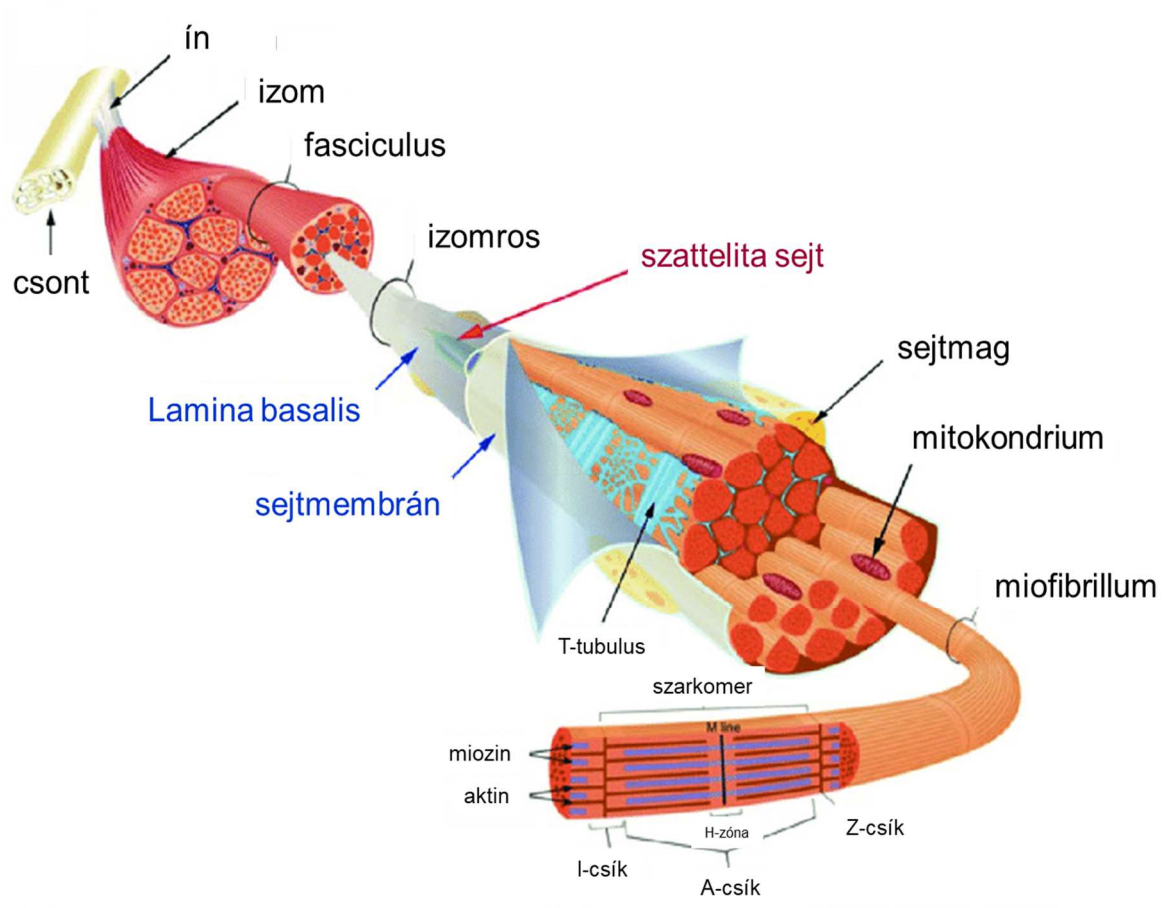
A tisztelt Olvasótól itt kérek elnézést, hogy az értekezésben leggyakrabban elforduló két angol kifejezést nem a magyar megfelelőjeként fogom használni. Az első a „Ca^{2+} *spark*”, amit eredetileg Cheng és munkatársai (1993) használtak a szívizomsejtek belső kalciumraktárából történő spontán Ca^{2+}-felszabadulási események elnevezése, és ma már a lokalizált Ca^{2+}-felszabadulási események általános elnevezéseként használják molekuláris eredetüktől vagy sejttípusuktól függetlenül. A „Ca^{2+} szikrák” fogalom nem honosodott meg hazánkban és a legtöbb magyar kutató is a *spark* elnevezést használja. Ugyan ez érvényes a másik ilyen kifejezésre, a „Ca^{2+} ember”, amit González és munkatársai (2000) vezettek be és úgy definiálták, hogy alacsony intenzitású megnyúlt *spark*. Mivel az „ember” a magyar nyelvben is megtalálható szó, a félreértések elkerülése érdekében a disszertációban mind a *spark*, mind az *ember* szavakat dőlten fogom szedni, ha elemi kalciumfelszabadulásról lesz szó. Továbbá ragozni is fogom ezeket a szavakat, ami néhány Olvasóban megütközést is kiválthat, amiért ezúton szintén elnézést kérek.

3.1 A vázizom felépítése és működése

Gerincesekben a vázizom a mozgás aktív szerve. Alapvető feladata az izületekkel kapcsolódó csontok egymáshoz képest történő elmozdítása. A test fejlődése közben a különálló izomsejtek (mioblasztok) több magvú izomcsövekké (miotubulusok), később henger alakú elágazásmentes izomrostokká alakulnak. Ezeknek a rostoknak a sejtmembránja a szarkolemma, míg a citoplazmája a szarkoplazma. Az izom-összehúzódásban résztvevő kontraktilis elemek

(miofibrillumok) az intracelluláris térben találhatóak. Ezek kétfajta miofilamentumból állnak: az elsősorban aktint tartalmazó vékony, és a főként miozint tartalmazó vastag filamentumokból (Fonyó & Geiszt, 2019; Röchlich, 2006). Az aktin filamentumok a Z-csíkhoz kapcsolódnak és az izomrost két Z-csík közötti szakaszát szarkomernek nevezzük (**1. ábra**).

A miofilamentumokat a szarkoplazmatikus retikulum (SR) membránrendszere veszi körül, amiben az összehúzódáshoz feltétlenül szükséges kalcium tárolódik. Ennek hosszanti elhelyezkedésű része a longitudinális tubulus, míg kiszélesedő vége a terminális ciszterna. Ezek között a felszíni membrán a miofilamentumokra merőlegesen mélyen benyúlik az izomrost belsejébe, létrehozva a T-tubulusokat. Egy T-tubulus és a két oldalán elhelyezkedő terminális ciszternák alkotják a triádot (Fonyó & Geiszt, 2019; Röchlich, 2006; Sorrentino, 2011).



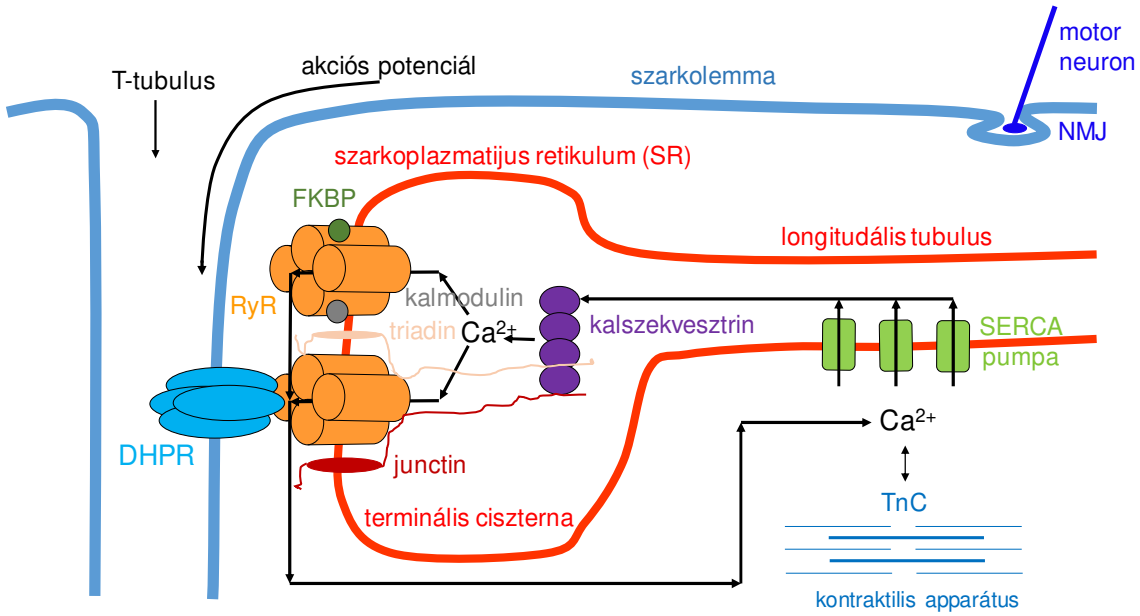
1. ábra. A vázizom felépítése

Módosítva Croissant és mtsai., 2021.

Az izom összehúzódásakor először a Troponin-C (TnC) kalciumot köt, majd a vékony filamentumok becsúsznak a vastag filamentumok közé, tehát az izomrost megrövidül. Ennek molekuláris alapja az, hogy a miozin feje hozzákapcsolódik az aktin filamentumhoz, majd az ezt követő konformáció változás miatt begörbül, így elcsúsztatva az aktin filamentumokat. A kontrakció alatt a miofilamentumok elmozdulásához jelentős mennyiségű szabad Ca^{2+} ionnak kell megjelennie az intracelluláris térben, amelyek az SR-ből szabadulnak ki. Elernyedés során a miozin leválik az aktinról és visszatér eredeti konformációjába. Ezzel párhuzamosan a Tn-C-ről levált Ca^{2+}-t az SR kalciumpumpája (SERCA) visszajuttatja a kalciumraktárba (Cook, 1997; Fonyó & Geiszt, 2019).

3.2 Az elektromechanikai kapcsolás

Vázizomban az elektromechanikai kapcsolás (ECC) során a szarkolemmán érkező elektromos jel (akciós potenciál) több lépésen keresztül alakul át kontrakciós válasszá.



2. ábra. Elektromechanikai kapcsolat (ECC)

***DHPR**: dihidropiridin receptor; **RyR**: rianodin receptor; **TnC**: troponin-C; **FKBP**: FK-506-kötő fehérje; **NMJ**: neuromuszkuláris junkció; **SERCA**: szarko-endoplazmatikus retikulum Ca^{2+} – ATP-áz*

A motorneuronból érkező akciós potenciál végig terjedve a szarkolemmán bejut a T-tubulusokba, ahol aktiválja a vázizom feszültség érzékelőit, a négyes csoportokban (tetrád) elhelyezkedő L-típusú kalciumcsatornákat (dihidropiridin

receptorok, DHPR vagy CaV1.1). Ezek konformáció változása idézi elő az SR terminális ciszternájában található kalciumcsatornák, a rianodin receptorok (RyR) megnyílását és az SR-ben tárolt Ca^{2+} felszabadulását (Franzini-Armstrong & Protasi, 1997) (**2. ábra**). Tehát négy DHPR és egy RyR alkot egy kalciumfelszabadító egységet (Calcium Realease Unit, CRU), ami a két különálló membrán (szarkolemma és SR) találkozásánál jön létre. Fiziológiás körülmények között emlős vázizomrostokban a kontrakcióhoz szükséges kalcium teljes egészében az intracelluláris raktárból (SR) származik, külső, extracelluláris kalcium belépésére nincs szükség (Block et al., 1988; Lytton & Nigam, 1992; Ríos & Stern, 1997).

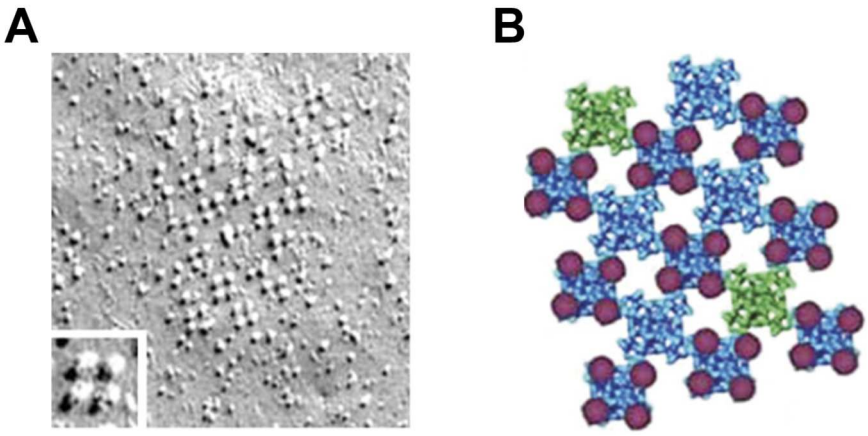
3.3 A dihidropiridin-receptor felépítése és szabályozása

A dihidropiridin-receptor a T-tubulus membránjában elhelyezkedő lassú kinetikájú feszültségfüggő L-típusú Ca^{2+}-csatorna, melynek aktivációs küszöbe kb. -35 mV. Öt polipeptid alegységből áll, melyből az α1-alegység alkotja a csatorna pórusát és a névadó növényi alkaloida dihidropiridin, mint csatorna-gátló, is ide kötődik. Vázizomban az α1-alegység tartalmaz egy citoplazmatikus nyúlványt, ami a sejtmembrán depolarizációjának következtében konformáció-változáson megy keresztül. Ez a konformáció-változás okozza a minden második DHPR tetráddal szoros fizikai közelségben lévő RyR aktivációját (**3. ábra**), aminek hatására elindul az SR-ből a Ca^{2+}-kiáramlás. Ez a kezdeti kalciumkoncentráció-emelkedés a kalcium-indukálta kalciumfelszabadítás révén (CICR) további RyR-kat nyit meg, így az intracelluláris kalciumkoncentráció gyorsan emelkedik (Ríos & Pizarro, 1991).

3.4 A rianodin receptor felépítése és szabályozása

A rianodin receptor a ma ismert legnagyobb molekula tömegű (kb. 2 MDa) homotetramer szerkezetű alacsony szelektivitású kation csatorna, nagy konduktanciával. Vázizomban elsődlegesen Ca^{2+}-csatornaként funkcionál, feladata nagy mennyiségű Ca^{2+} gyors kiengedése az SR-ből. A rianodin receptornak 3 izoformája ismert: a RyR1 legnagyobb számban a vázizomzatban fordul elő, a RyR2 a szívizomban, a RyR3 pedig döntően az agyban, illetőleg az embrionális vázizomban is megtalálható. Ez utóbbi a kifejlett izomból szinte teljesen eltűnik, csak a rekeszizomban és a szemmozgató izomban marad meg minimális mennyiségben az egyedfejlődést követően. A kétéltűek RyR izoformái (RyRα és RyRβ) hasonlóak az emlős RyR1-hez és RyR3-hoz, mind aminosavsorrendjük, mind funkcionális szempontból (Franzini-Armstrong & Protasi, 1997). Az α izoforma szorosan

kapcsolódik a transzverzális (T-) tubulus feszültségérzékelőjéhez, a dihidropiridin receptorokhoz (DHPR-ek) és feszültségvezérelt. A β izoforma nem kapcsolódik



3. ábra. A vázizomrostok Ca^{2+} felszabadító egysége (CRU)

*(**A**) Tetrádokba rendeződött DHPR-ek elektronmikroszkópos képe vázizomban.*

*(**B**) Lila: DHPR tetrádok; zöld és kék: RyR1.* (*Yin és mtsai., 2008)*

DHPR-ekkel, de már az intracelluláris kalciumkoncentráció kismértékű növekedése is megnyithatja (Pouvreau et al., 2007; Rodney & Schneider, 2003). A RyR1 egy nagy intracelluláris és egy kisebb, az SR membránban elhelyezkedő részből áll (Van Petegem, 2012).

Vázizomban a RyR1-k sakktábla-szerűen rendeződnek el: minden RyR1-hez négy másik kapcsolódik a ”sarkoknál”. Csak minden második RyR1 lép kapcsolatba DHPR-rel. A vázizomban a CICR a DHPR kalciumcsatorna közreműködése nélkül jön létre, és a RyR1-n keresztüli kalciumfelszabadulás aktiválja a szomszédos, a DHPR-rel kapcsolatban nem álló RyR1-ket (**3. ábra**).

A RyR1 nyitását fiziológiásan alapvetően maga a kalcium szabályozza: intracellulárisan nM-os koncentráció aktiválja, µM-os koncentráció gátolja (a RyR1 nagy affinitású Ca^{2+}-kötőhelye aktivál, míg alacsony affinitású Ca^{2+}-kötőhelye gátol). Emellett az SR belső Ca^{2+}-koncentrációja is szabályozó szereppel bír: a magas SR Ca^{2+}-koncentráció fokozza a RyR1 nyitvatartási valószínűségét a belső (luminális) oldalán található Ca^{2+}-kötőhely telítettségén keresztül (Csernoch, 1999; Meissner et al., 1986).

Fiziológiásan a magas intracelluláris magnézium-koncentráció (nagyobb, mint 1 mM) gátolja a RyR1 működését. Az egyik elmélet szerint a Mg^{2+} az alacsony affinitású helyért verseng a Ca^{2+}-al és ehhez kötődve a csatorna inaktivációját okozza (Zucchi &

Ronca-Testoni, 1997), míg a másik elmélet szerint a Mg^{2+} kompetitíven gátolja a nagy affinitású, aktiváló Ca^{2+}-kötőhelyet (Jóna et al., 2001).

Az ATP erős RyR1 aktivátor, mely Ca^{2+} hiányában is aktiválja a RyR1-t, Ca^{2+}-al együtt szubmaximális aktivációt okoz. Azonban az ATP hatása nem a csatorna foszforilációján keresztül valósul meg. Származékai is agonisták: az AMP, ADP, cAMP, adenin, adenozin a magnézium hatását csökkentik. Azonban a RyR1 aktivitását foszforilációs úton is lehet szabályozni (Suko et al., 1993). A szimpatikus idegrendszer aktivációja katekolaminok felszabadulásával jár, ami izomban aktiválja a protein kináz-A-t (PKA). A PKA foszforilálja és aktiválja a RyR1-t (Strand et al., 1993), a DHPR-t (Lu et al., 1995), és a SERCA-t (Toyofuku et al., 1993), aminek következtében a szimpatikus aktiváció alatt bekövetkező akciós potenciál által generált Ca^{2+}-tranziens amplitúdója magasabb. A RyR1 defoszforilálásában a protein foszfatáz 2B (kalcineurin) vesz részt.

A receptor névadó agonistája a rianodin, egy mérgező növényi alkaloida, amit a Dél-Amerikai *Ryania speciosa*-ból izoláltak és már régóta rovarirtó szerként használják. Specifikusan nagy affinitással csak a nyitott RyR1-hez kötődik, és nanomoláris koncentrációban félig nyitott állapotban, míg mikromoláris koncentrációban zárt állapotban rögzíti a csatornát. A félig nyitott állapotban rögzített RyR1-n keresztül Ca^{2+} csorog az intracelluláris térbe, melynek következménye a kalciumraktárak kiürülése és masszív izom összehúzódás. A mikromoláris gátlás eredménye paralízis, mind rovarokon, mind emlősökön.

További RyR1 agonisták a 4-kloro-m-krezol, a suramin és a xantin-származékok. Pl. a koffein a receptor Ca^{2+} iránti érzékenységét növeli. Már 5 mmol/l koffein a RyR1 Ca^{2+}-függését a mikromolárisról a pikomoláris tartományba mozdítja el, ezért ekkor már a nyugalmi Ca^{2+}-koncentráció is aktiválhatja a csatornát. A sebészeti altatásokhoz használt halotán is növeli a RyR1 Ca^{2+}-permeabilitását, aminek súlyos következménye van, ha a páciens látensen magában hordozza a RyR1 egy igen súlyos genetikai eredetű izombetegséget, a malignus hipertermiát okozó mutációját (Glahn et al., 2020).

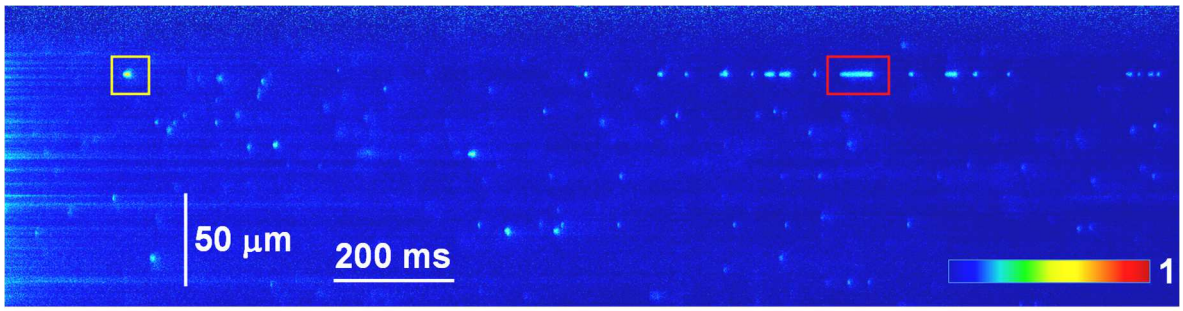
A klinikai gyakorlatban is használt RyR1 antagonista a Dantrolen a malignus hipertermia kezelésére. A gyógyszert 1979-ben vezették be és ezután az altatás okozta műtéti elhalálozások száma nagymértékben csökkent (Glahn et al., 2020). További gátlószerek még a procain, tetracain (lokál anesztetikumok, (Dai et al., 2006))

és a ruténium-vörös (Ma, 1993).

Számos, főleg a csatornához közvetlenül kötődő fehérje szabályozza a rianodin receptort. Ilyen pl. a Kalszekvesztrin (CSQ), ami az SR kalciumtároló fehérjéje; a Triadin, ami egy transzmembrán fehérje a SR-ben, és a CICR-t indítja be; a Junctin, ami az SR-ből történő kalciumfelszabadításban vesz részt (**2. ábra**) (Bers, 2004).

3.5 Az elemi kalciumfelszabadulási események fajtái és tulajdonságai

Az elemi kalciumfelszabadulási esemény (ECRE, Elementary Calcium Release Event) a jelenleg ismert kisebb részekre nem bontható, lokális intracelluláris Ca^{2+}-koncentrációemelkedés: egy rianodin receptor-csoport megnyílásának eredményeként felszabaduló Ca^{2+} mennyisége. A rövid ideig tartó, nagy amplitúdójú, spontán Ca^{2+}-felszabadulási eseményt (*spark*, **4. ábra**) Cheng és mtsai (Cheng et al., 1993) írták le szívizmon 1993-ben. A *spark*ot először a tudományos közösség műterméknek tartotta, de aztán hamar kiderült az izom-élettanban betöltött alapvető szerepe (Tsugorka et al., 1995). Később kétéltűek intakt harántcsíkolt izomrostjain is nagyszámú *spark*ot figyeltek meg (Klein et al., 1996). Emlős intakt vázizomrostokon ellenben a spontán ECRE-k jóval ritkábban fordulnak elő (Shirokova et al., 1998). Az embrionális emlős vázizomrostokon még lehet spontán *spark*ot regisztrálni, ennek oka a RyR1 és RyR3 együttes jelenléte (Conklin et al., 1999). Az izom fejlődése során a



4. ábra. Kalcium *spark*ok és *ember*ek házi méh vázizom roston

A függőleges (y) tengely a rost hossztengelyével párhuzamos fizikai kiterjedés, a vízszintes (x) tengely idő dimenzió. A szkennelés baloldalon indult és a jobboldalon ért véget. A sárga négyzet egy sparkot, míg a piros téglalap egy embert jelöl. Az ábrán egy line-scan háttérflureszcenciára (F_0) normalizált pszeudokolor képe látható. A színskála legmelegebb színe (vörös) a nyugalmi kalciumkoncentrációval (sötétkék, F_0) megegyező nagyságú változást reprezentál.

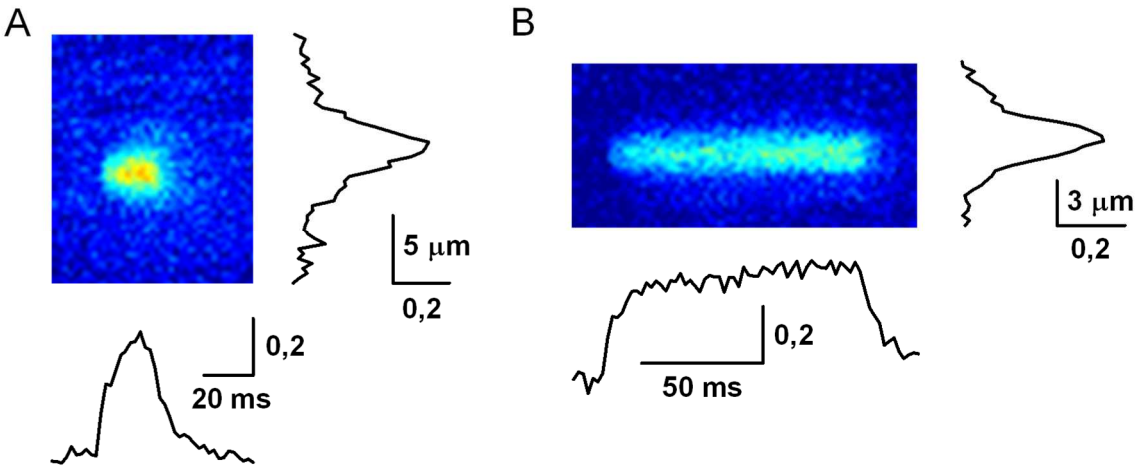
RyR3 eltűnésével a spontán elemi események is egyre ritkábban figyelhetők meg. Mivel a béka vázizomrostjaiban a RyR-nek két olyan izoformája található meg, amelyek hasonlítanak az emlős izom RyR1-re (RyRα) és RyR3-ra (RyRβ) izoformáira, ezzel magyarázhatjuk, hogy rajtuk is nagyszámú *spark* figyelhető meg (Ogawa és mtsai., 2002). Továbbá izomdisztófiában, különösen mechanikai stressz következtében, is megemelkedik a *spark* frekvencia (Kirsch et al., 2001; Zhou et al., 2003, 2006). Vázizmon létezik egy kis amplitúdójú hosszan tartó spontán Ca^{2+}-felszabadulási esemény is (*ember*, **4. ábra**) (González et al., 2000). Az utóbbi 30 évben az elemi események számos típusát írták le és az ezeket összefoglalóan leíró műveket „*spark*ológiának" nevezték le (Cheng & Lederer, 2008; Niggli & Shirokova, 2007).

Az elemi kalciumfelszabadulási esemény csak speciális, nagy térbeli és időbeli felbontású mérési technika mellett rögzíthető és ábrázolható: felfedezését a konfokális mikroszkópia fejlődése tette lehetővé. Ez a mérési módszer kis térfogatban (0,2 x 0,2 x 0,4 μm^3) képes követni fluoreszcencia változásokat. Emellett elengedhetetlen volt olyan fluoreszcens kalciumindikátorok előállítása is, amelyeknek kellően magas a kalciumérzékenysége ahhoz, hogy a kis amplitúdójú Ca^{2+}-koncentrációemelkedés is mérhető fluoreszcencia-intenzitás-változást okozzon.

A jelenleg elfogadott elmélet szerint a számos, térben és időben egyszerre megjelenő *spark* alatt mérhető lokális Ca^{2+}-koncentrációemelkedés összeadódása következtében jön létre a globális intracelluláris Ca^{2+}-tranziens, ami a sejtek extracelluláris ingerekre adott intracelluláris válaszának egyik közös jelátviteli útja. A *spark* megjelenési formája és gyakorisága az együttműködő RyR1-k kapuzási mechanizmusát követi, ezért közvetve a CRU-k működéséről szolgáltat információt.

Mind kétéltűek, mind emlősök vázizmán a leggyakoribb elemi esemény a *spark* (**5A. ábra**). A *spark* a citoszolikus Ca^{2+} -koncentráció időben rövid: általában 10-20 ms ideig tartó; térben erősen lokalizált (2-3 μm) átmeneti emelkedése. Jellemzői a rövid kialakulási idő (Time To Peak vagy Rise Time), az exponenciális lecsengés a csúcs után, és hogy a térbeli kiterjedése Gauss-eloszlást követ (**5A. ábra**). A *spark*ot kb. 20-30 db RyR1 egyszerre történő megnyílásának eredményeként tekintjük, a nyitott csatornák száma egy elemi esemény során állandó. Megszűnésében szerepet játszhat az SR lokális Ca^{2+} kiürülése mellett az emelkedett Ca^{2+}-koncentráció RyR1 csatorna-funkciót gátló hatása. Kétéltűek vázizomrostjain egy *spark* során az SR

terminális ciszternái Ca^{2+}-tartalmának kb. 7%-a szabadul fel (Launikonis et al., 2006).



5. ábra. Az elemi kalciumfelszabadulási események két fő típusa

*(**A**) Spark. (**B**) Ember. A színskála megegyezik a 4. ábrán láthatóval. A képek jobb oldalán az esemény térbeli, míg a kép alatt az időbeli profilja látható.*

Emlős vázizomrostokon az elemi kalciumfelszabadulási események kb. 65%-a *spark*, míg a többi *ember* (**5B. ábra**), vagy a kettő kombinációja. Emlősök esetén az *ember*t tekintjük az abszolút elemi eseménynek, mivel jelenleg egy RyR1 megnyílásának a következményének tartják. Az *ember* térbeli kiterjedése nagyon hasonló a *spark*hoz, azonban időben sokkal hosszabb és amplitúdója kisebb (Csernoch, 2007; González et al., 2000; Kirsch et al., 2001; Klein & Schneider, 2006; Zhou et al., 2003).

Spontán fellépő kalcium *spark*ok ép szívizomsejteken jól megfigyelhetőek, gyakoriságuk (a *spark*ok száma egységnyi időben és térfogatban) viszonylag alacsony. Azonban fiziológiás körülmények között emlősök ép vázizomrostjain nem alakulnak ki ECRE-k. Számos módszert alkalmaztak az események gyakoriságának növelésére: például a megnövelt extracelluláris Ca^{2+}-koncentrációt gyakran használják szívizomsejteken, a felszíni membrán kémiai úton való eltávolítását (nyúzás) egyaránt alkalmazzák szívizomsejteken és vázizomrostokon is. Míg kétéltűek intakt vázizomrostjain és ép szívizomsejteken a depolarizáció *spark*okat generál, addig intakt emlős vázizomban a depolarizáció nem vezet *spark* kialakulásához, hanem *ember*ek figyelhetőek meg.

Fontos hangsúlyozni, hogy egy elfogadható nagyságú esemény gyakoriság döntő fontosságú ezen események elemzése szempontjából, mert a meghatározott

paraméterek függenek a kibocsátási forrás és a konfokális sík relatív helyzetétől. Vagyis ha azt feltételezzük, hogy minden kalcium *spark* azonos nagyságú 3D objektum (a fluoreszcencia növekedése egy adott térfogatban és időintervallumban), a 2D ábrázolásuk (vonalmenti-szkennelés) függ a letapogatási vonal és a kalciumforrás egymáshoz viszonyított helyzetétől. Ezért értelmetlen lenne az események paramétereinek kiszámolása, ha az eseményt véletlenszerűen választanánk ki egy halmazból. Tehát a probléma megoldása, hogy az események paramétereit statisztikai változóknak tekintjük, ami viszont megköveteli a mért adatok nagy számát.

3.6 Automatikus ECRE kereső algoritmusok

A nagyszámú elemi kalciumfelszabadulási esemény konfokális mikroszkópos képeken történő megtalálására már a kezdetektől automatikus felismerési módszereket fejlesztettek ki. A cél az volt, hogy ezek az algoritmusok az egyes elemi események területét észleljék és elkülönítsék a kép zajos hátterétől, majd ezután meghatározzák az események jellemző paramétereit. A legtöbb ilyen módszer kettős küszöbölési algoritmuson alapul (ezt hagyományos módszernek is nevezik) (Cheng et al., 1999). Ennek az algoritmusnak a módosított verzióját több tanulmányban is használták később (Picht et al., 2007; Ríos et al., 2001; Sebille et al., 2005; Zhou et al., 2003). Azonban az eseménymorfológia sokfélesége (pl. emlős vázizomrostokon az *ember*ek és kevert típusú események jelenléte), valamint a mérőrendszerenként változó zajmintázatok miatt sűrűn előforduló megbízhatatlan észlelés miatt, az algoritmus fejlesztésének hangsúlya az interaktív eljárások felé fordult.

Az előbb említett nehézségek leküzdése érdekében kezdték el használni a wavelet-en alapuló módszereket az utóbbi években a képek minőségének javítása és alakzat-felismerés miatt (Von Wegner et al., 2007, 2006). A hagyományos módszer a képeknek csak az amplitúdó - idő összefüggését használta és nem vette figyelembe az amplitúdó - frekvencia kapcsolatot. A wavelet transzformációval a mért jelek időbeli, térbeli és a frekvencia-tartományon belüli elemzése a hagyományos módszerekkel szemben egylépésben hajtható végre. Így a wavelet transzformáció alkalmazásával egy változás a frekvenciaspektrumban az előfordulási idejével egylépésben meghatározható. A wavelet módszert az 1980-as évek közepétől kezdve fejlesztették ki és az orvosi képalkotásban a képek javítására, zajcsökkentésre és tárgyfelismerésre használják (Unser & Aldroubi, 1996). Bár az *„à trous”* („lyukas”) wavelet transzformációnak kiváló képjavító és tárgyfelismerési jellemzői vannak zajos

képeken, ahhoz, hogy teljes mértékben automatikus esemény észlelést biztosítson, az algoritmus paramétereit megfelelően kell beállítani. A teljesen automatikus és felhasználói beavatkozást nem igénylő képfeldolgozó algoritmusok fejlesztése tehát továbbra is napirenden van.

4. CÉLKITŰZÉSEK

Munkánk során az elemi kalciumfelszabadulási események alaptulajdonságait és előfordulásukat befolyásoló tényezőket kívántuk megismerni vázizomrostokon. Tanulmányozni kívántuk az egyes specieseken előforduló ECRE-k hasonlóságát és különbözőségét. Vizsgálni kívántuk, hogy az egyes farmakonok és kórfolyamatok miként módosítják az ECRE-k előfordulásának gyakoriságát és egyes tulajdonságait. Valamint új módszert kívántunk kifejleszteni az ECRE-k automatikus detektálására.

Ezekhez a következő feladatok megvalósítását tűztem ki magam elé célul:

1. A kísérleti modell, a vázizomrostok izolálásának kidolgozása ízeltlábú (házi méh), kétéltű (béka) és emlős (egér, patkány) vázizmaiból. Az optimális mérési protokollok megtalálása.
2. Olyan automatikus ECRE felismerő algoritmus és program kifejlesztése, ami lehetővé teszi vonalmenti és kétdimenziós pásztázással készült konfokális mikroszkópos felvételeken nagyszámú esemény automatikus detektálását és elemzését.
3. Az ECRE-k időbeliségének vizsgálata nagy időbeli felbontású mérésekben.
4. Az ECRE-k változásának tanulmányozása miotóniákban (DNM2, MTM1), hipermuszkularitásban (Cmpt), embrionális DHPR jelenlétében és vázizmokban fiziológiásan jelenlevő fehérjék hiányában (Ank1, Triadin).
5. Az ECRE-k változásának vizsgálata nem vázizom-betegségekben (szívinfarktus, hiperkoleszterinémia).
6. Az ECRE-k változásának megfigyelése depolarizáció és farmakológiai befolyásolás esetén.

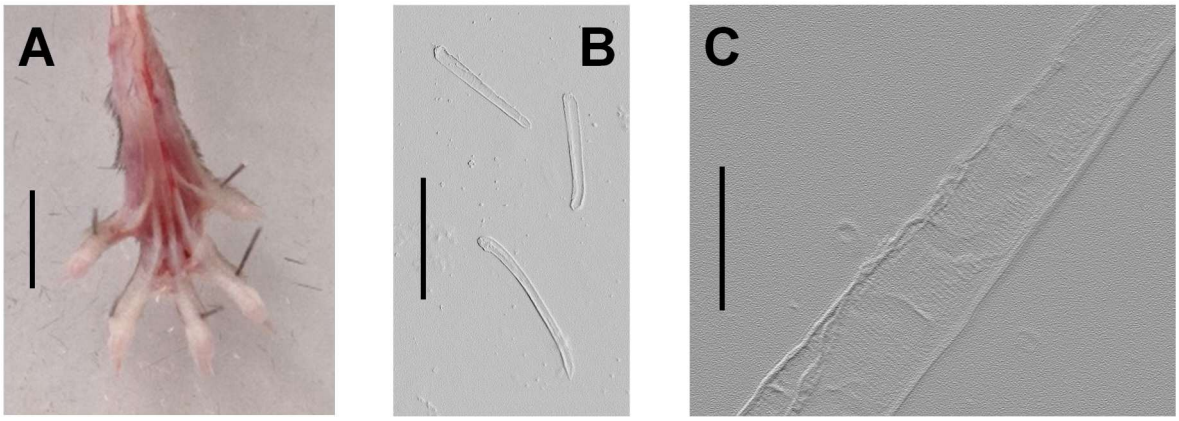
5. ANYAGOK ÉS MÓDSZEREK, MÓDSZERTANI FEJLESZTÉSEK

5.1 Vázizomrostok izolálása fluoreszcens kalciumindikátorral végzett konfokális lézerpásztázó mikroszkópos mérések számára

Az intracelluláris kalciumkoncentráció mérésekhez minden esetben egyedi vázizomrostokat használtunk. Mivel ezeket a méréseket először kétéltűek (békák) izmain végezték, mi is ezzel a preparátummal kezdtük a munkánkat. A preparátumok elkészítésének részletes leírásától itt eltekintek, azokat a fejezet végén sorolom fel. Azonban megemlítek olyan technikai részleteket, amelyeket a közleményekben nem írtunk le. A békákon végzett kísérletek során súlyos problémát okozott, hogy az állatokat ősszel szereztük be halászoktól és nagy beton kádakban tartottuk őket tavaszig. Az állatok fizikai kondíciója idővel egyre romlott és már nem lehetett használható preparátumokat készíteni belőlük. Ekkor támadt az az ötlete Dr. Csernoch László kollégámnak, hogy próbáljuk meg etetni a fogságban levő békákat. Próbálkoztunk tápokkal, apró húsdarabokkal, de sikertelenül. A békák sajnos csak mozgó táplálékot voltak hajlandó elfogyasztani. Ezért az Állatkertből kértünk tenyésztésre tücsköket, amiket ott már sikeresen használtak a terráriumokban tartott kétéltűek és hüllők táplálására. Ezek tenyésztése sem volt egyszerű, de végül elértük, hogy folyamatosan tudtuk etetni békáinkat élő tücskökkel és így meg tudtuk hosszabbítani a kísérletekre alkalmas időintervallumot. Sajnos a békákon végzett kísérleteinket végül be kellett fejeznünk, mert ezek a kétéltűek védetté lettek nyilvánítva Magyarországon.

Emlősökből először patkányból sikerült egyedi sérülésmentes (intakt) vázizomrostot előállítanunk. Mivel a békákból szemészeti ollóval és csipesszel preparáltuk az izomrostokat, először ezzel a módszerrel próbálkoztunk. Hamar rá kellett jönnünk, hogy az emlős vázizom kötőszövetes állománya sokkal erősebb, mint a békáé és nem, vagy csak heroikus munka árán tudunk manuálisan egészséges emlős izomrostot előállítani. Így másokkal párhuzamosan beállítottunk egy enzimatikus emésztési eljárást, amit később sikeresen adaptáltuk egerekre is. Még egy fontos problémát kellett megoldani, ami a vázizom alapvető struktúrájából következett: az izomrostok hossza a legtöbb izomban megegyezik az izom hosszával.

Minél hosszabb egy izom, annál kisebb az esélye, hogy az enzimatikus emésztési eljárás után egészséges egyedi izomrostokat kapunk. Tehát tanulmányoznunk kellett az egér és patkány anatómiáját, hogy megfelelően rövid, de még jól preparálható izmokat találjunk a kísérletek számára. Így esett a választásunk patkány esetében az *extensor digitorum communis*, míg egérnél a *flexor digitorum brevis* izomra (**6. ábra**).

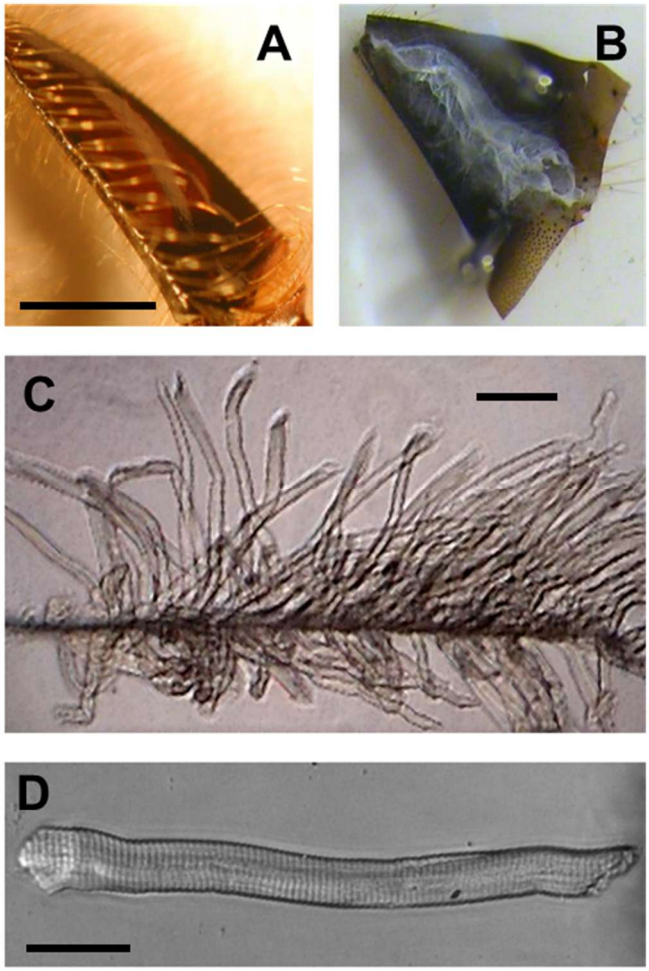


6. ábra. Egér *flexor digitorum brevis* (FDB) izma és rostjai

*(**A**) Az egér lábújmozgató izmai. (**B**) Enzimatikusan izolált egyedi FDB izomrostok. (**C**) Egy FDB izomrost nagy nagyításban, amelyen tisztán látszanak a haránctsíkolatok. Skála: **A**: 5 mm; **B**: 500 μm; **C**: 50 μm.*

Az utolsó, de nem elhanyagolható megoldandó probléma az volt, hogy miképpen juttatjuk az egyedi izomrostokat a mérőkádba úgy, hogy továbbra is sérülésmentesek maradjanak. Ezt végül úgy sikerült megoldanunk, hogy mikropipettával felszippantottuk az izomrostot és finoman beinjektáltuk a mérőkádba.

Az előzőkből következik, hogy a háziméhek izomrostjainak kísérletekre való felhasználása sem volt egyszerű dolog. A békákhoz hasonlóan, a méhek életciklusa is jelentősen változik egy éven belül. Mivel a kísérleteinkhez újszülött, még röpképtelen egyedeket használunk, ezeket csak tavasztól, a kaptárok kinyitásától őszig, azok zárásáig tudtuk begyűjteni. A méhek begyűjtésére méhészekkel vettük fel a kapcsolatot. A tőlük kapott méhek néhány napig életben tarthatók kaptáron kívül is, ha mézzel vagy cukros vízzel tápláljuk őket. A preparálás előtt el kell kábítani őket, amire legalkalmasabb módszer a hibernálás volt. Vagyis néhány percre mélyhűtőbe helyeztük őket. A preparálás első lépése, hogy dekapitáljuk a rovarokat. Azonban ez nem gátolja meg őket abban, hogy akár még percekig is spontán mozgassák a lábaikat, ami ugyancsak nehezíti a preparálást. A *tibia* felnyitására itt is szemészeti



7. ábra. A háziméh harántcsíkolt izomrostjának izolálási lépései

*(**A**, **B**) Metathoracic tibia (3. pár láb) 1-3 napos háziméhből (Apis mellifera). (**C**) Enzimatikus emésztés után a rostköteg. (**D**) Triturálással nyert egyedi intakt izomrost. Skála: **A**, **B**: 1 mm; **C**: 200 µm; **D** 40 µm.*

ollót használunk és ugyancsak enzimatikus emésztéssel szabadítottuk ki az izomrostokat a kötőszövetből (**7. ábra**). Az optimális emésztő oldat megalkotásában segített az emlős izmokon szerzett tapasztalat.

Ahogy azt már korábban említettem, nem mindegy, hogy a mérésekben intakt vagy permeabilizált rostokat használunk. Az intakt rostokba injektálással vagy pipettán keresztül lehet bejuttatni a kalciumérzékeny festékeket. Ha teljesen sérülésmentes sejtmembránnal rendelkező izomrostokon akarunk mérni, akkor pedig a festékek AM (acetoxi-metilészter konjugált) formáját kell használnunk. Az AM formájú festék szabadon átjut a sejtmembránon, majd a sejten belül az acetoxi-metilésztert az intracelluláris észterázok lehasítják a festék molekuláról, szabaddá téve a

kalciumindikátort. A nyúzott rostok használatakor a rostot a mérés során az intracelluláris oldat veszi körül és ebbe helyezzük a kalciumindikátor festéket. Ez teszi lehetővé, hogy szemmel kövessük a felszíni membrán eltávolításának (kilyuggatásának) hatékonyságát. Ha az intakt rostot detergenst (esetünkben szaponint) tartalmazó külső oldatba helyezzük, akkor a kezdő pillanatban a festék csak a roston kívül található meg. Amint a felszíni membrán kezd átjárhatóvá válni, egyre több festék jut a rost belsejébe és végül kialakul az egyensúlyi állapot, azaz a rostot körülvevő oldatban és a rost belsejében ugyan akkora lesz a festékkoncentráció. Ekkor a mérőkádat detergens mentes belső oldatra cseréljük és kezdődhet a mérés.

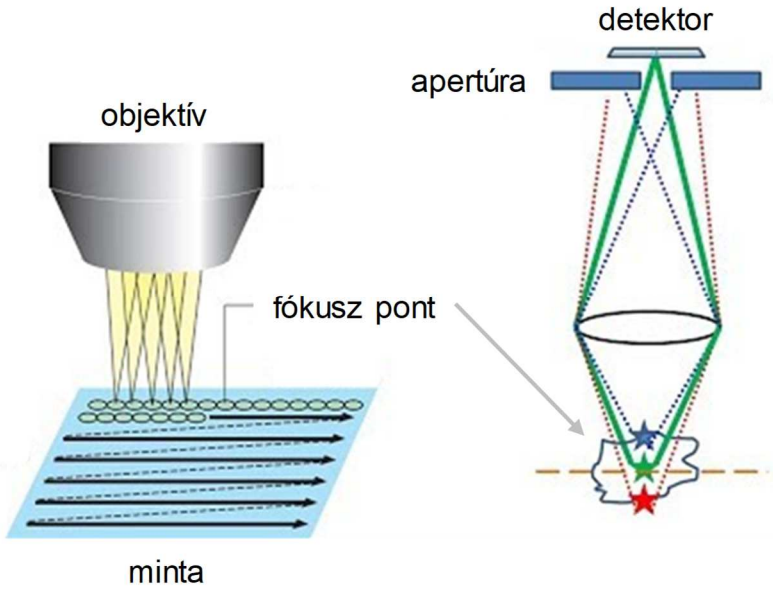
Az általunk használt vázizomrostok preparálásának leírása és a méréseink pontos módszertana részletesen a következő publikációkban található: béka (Cserne Szappanos et al., 2020; Szentesi et al., 2004; Sztretye et al., 2009), patkány (Szentesi et al., 2004; Szigeti et al., 2007), egér (Fodor et al., 2008; Sztretye et al., 2009), háziméh (Collet et al., 2021).

5.2 Kalciumkoncentráció változás mérése konfokális lézerpásztázó mikroszkóppal

A konfokális lézerpásztázó mikroszkóp (CLSM) ki tudja szűrni a fókuszsíkon kívülről származó fényt, így a képek kontrasztosabbak és kevésbé elmosódottak lesznek a hagyományos fluoreszcens mikroszkópok képeihez képest. A módszer segítségével 1-2 µm vastag rétegekről alkothatunk képeket a minta tényleges felszeletelése nélkül (G. Szabó, 2004).

A mikroszkóp felépítésének köszönhetően csak a fókuszsík egy keskeny rétegből kiinduló fotonok jutnak el a detektorra és kerülnek rögzítésre. A mintára fókuszált pásztázó lézersugár által gerjesztett fluoreszcens fény egy objektív lencse gyűjti össze. A konfokális mikroszkópban csak a lencse fókuszában levő kicsiny lyukon, az apertúrán keresztülhaladó fény jut a detektorra (**8. ábra**). Az apertúrán áthaladó fény erőssége legyengül, de a megvilágításként használt lézerfény intenzitása még ekkor is elegendően nagy ahhoz, hogy mérhető jelet kapjunk. A mintának a fókuszmélységén kívül eső rétegeiből kiinduló fény az apertúrán nem jut át, így detektorhoz sem jut el. Tehát a CLSM pontos pásztázó rendszere teszi lehetővé

a tárgy vizsgálni kívánt rétegének egyes pontjaiból jövő információ összegyűjtését.

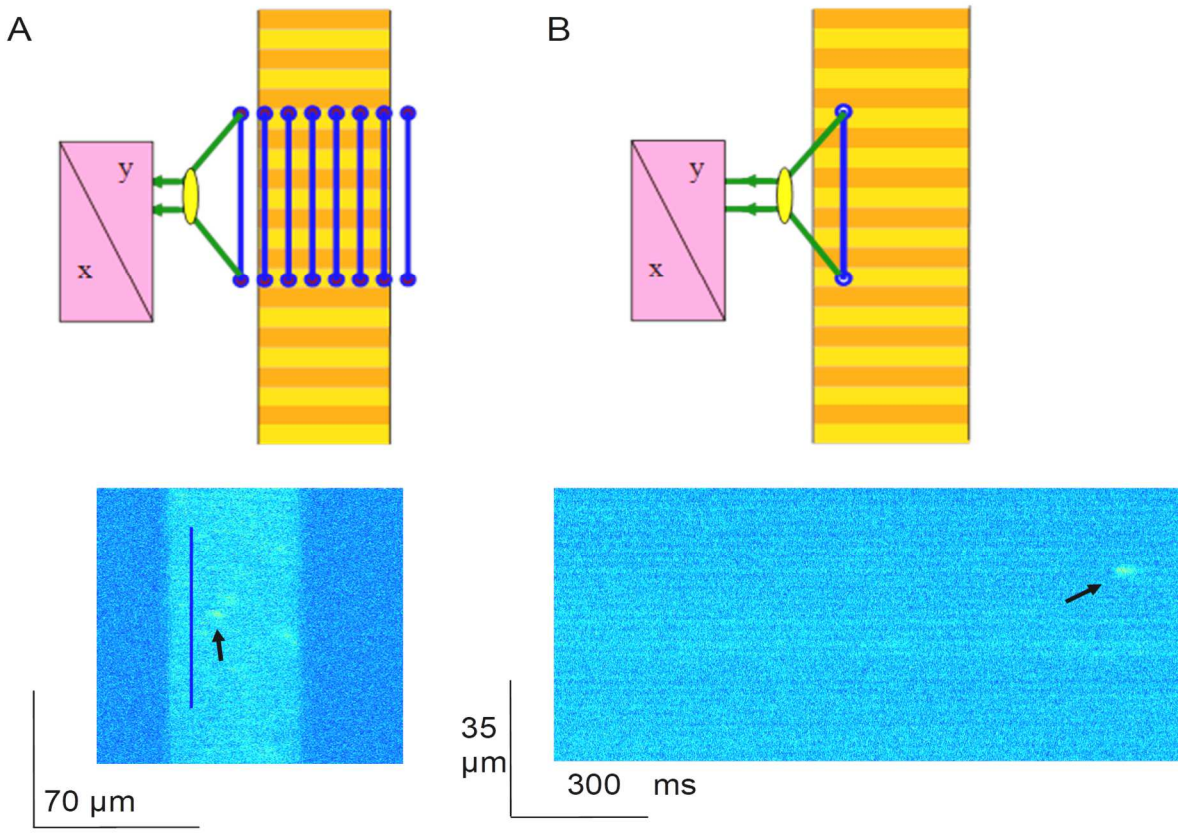


8. ábra. A CLSM felépítése

A fekete nyilak a pásztázás irányát mutatják.

A konfokális mikrószkópia metodikáját svájci tanulmányutam során sajátítottam el Dr. Ernst Niggli laboratóriumában a Berni Egyetem Élettani Intézetében 2002 és 2004 között. Hazatérésem szerencsésen egybeesett a Debreceni Egyetem Élettani Intézetének első konfokális mikroszkópjának beszerzésével.

Az alábbiakban bemutatásra kerülő vizsgálatainkban a 2004-ben beszerzett Zeiss LSM 510 Meta, majd a 2010-ben vásárolt Zeiss LIVE konfokális lézerpásztázó mikroszkópokat (Zeiss, Oberkochen, Németország) használtuk. Míg a META rendszerben pont-szkenner pásztázza a preparátumot, addig LIVE rendszerben egy vonal-szkenner tapogatja le a mérendő tárgyat. Az utóbbi technika segítségével akár 100 szoros sebesség növekedés is elérhető a META rendszerhez képest. Ennek azonban sajnos ára is van. A LIVE rendszerben alkalmazott lézerek nagyobb teljesítményűek, így a mérések során nagyobb mértékben roncsolják a preparátumokat (fototoxicitás). Méréseink során kétfajta pásztázási módot alkalmaztunk (**9. ábra**). Kétdimenziós (XY) képek (**9A. ábra**) rögzítésekor a META rendszerben a lézer a vizsgált tárgyat a **7. ábrán** fekete nyilakkal jelölt útvonalat bejárva világítja meg. A LIVE rendszer ugyanezt a képet a pásztázási vonal mozgatásával tapogatja le, így ennek gyorsasága lehetőséget ad megfelelően nagy sebességű kétdimenziós képsorozatok (filmek) felvételére is. Vonalmenti pásztázás



9. ábra. A CLSM pásztázási módjai

*(**A**) Kétdimenziós pásztázás (XY): a fluoreszcencia intenzitásban bekövetkező változás hely függvényében követhető nyomon. (**B**) Vonalmenti pásztázás (line-scan): a felvett képeken a kiválasztott vizsgált vonal (kék vonal az alsó **A** panelen) mentén az idő függvényében ábrázoljuk a fluoreszcencia intenzitásváltozást. A kép bal szélén van a kezdő (0) időpillanat. A nyilak egy-egy sparkra mutatnak. A narancssárgán csíkozott téglalapok vázizomrostokat ábrázolnak.*

(line-scan, **9B. ábra**) esetén a minta egy kijelölt vonala mentén folyik a lézerpásztázás. Ilyenkor a lézer időben egymás után többször is megvilágítja a preparátum ugyan azt a vonalmenti területét. Ezért ekkor fokozottan kell ügyelni a fototoxicitás minimalizálására.

5.3 Az elemi kalciumfelszabadulási események elemzése

A konfokális mikroszkóppal készült mérési képek feldolgozását legkönnyebben számítógépes eljárásokkal lehet elvégezni a lehető legtöbb részfolyamat automatizálásával. Első lépésben mindig szükséges a kézi kiértékelés, de a nagyszámú mérési eredmény miatt ez gyakorlatilag később elképzelhetetlen. Továbbá

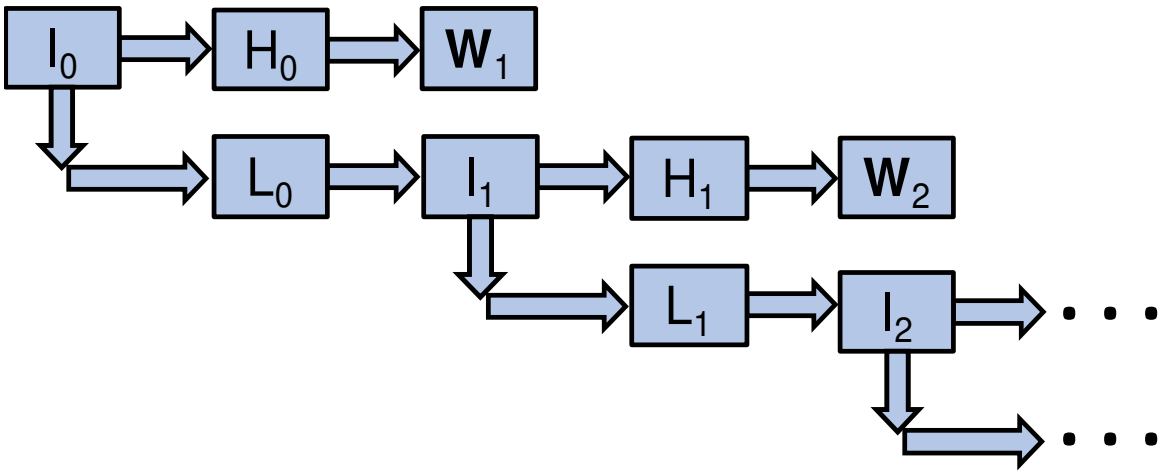
a kalciumfelszabadulási események egyes jellemző paramétereinek meghatározását szintén csak számítógéppel lehet elvégezni. Az elmúlt 25 évben több automatikus kalcium *spark* analizáló programot dolgoztak ki. Néhányan, többek között mi is Waveletet transzformációs módszert használtunk (Prada és mtsai., 2018; Szabó és mtsai., 2010a; Von Wegner és mtsai., 2006). Mások zajküszöbölést (Cheng et al., 1999; Picht et al., 2007), statisztikai elemzést (Bányász et al., 2007), ill. pixelenkénti módszert (Illaste et al., 2019; Tian et al., 2019) alkalmaztak az elemi kalciumfelszabadulási események megtalálására és paramétereik elemzésére.

Az elvégzendő feladathoz szervesen hozzátartozik a mérési körülményekből a képeken keletkező magas zaj kiszűrése, továbbá a konfokális mikroszkóp technikából és a fluoreszcenciára épülő mérési eljárásból kapott képek helyreállítását célzó eljárások alkalmazása. Ezekre a feladatokra olyan speciális eljárásokat hoztak létre, mint a fluorofórokra jellemző fotókioltás korrekció, vagy a konfokális mikroszkóp pont kiterjedés függvény hátasainak figyelembe vétele (Pawley, 2006). A konfokális mikroszkópokban használt érzékelők (pl. fényelektron sokszorozó) jellegzetes zajt okoznak a mért képeken, így ennek eltávolítása is egy mérőrendszer függő feladat. Az elemi események paramétereinek kiszámítására és statisztikai jellemzésükre nincs elérhető nyilvános program. Eddig nem volt a különböző fajta kalciumfelszabadulási eseményekre alkalmazható keresési eljárás sem, amire szükség lenne, mert a kísérletekben megjelenhetnek egyedi alakú események (pl. *ember*).

5.3.1 A stationary wavelet transzformáció

Mielőtt ismertetném a képek analízisének lépéseit, röviden be kell mutatnom a wavelet transzformációt, amit mi mindkét típusú (XY és line-scan) kép elemzéséhez használtunk. Az stationary wavelet transzformáció (SWT), vagy másik nevén *à trous* („lyukas”) wavelet transzformáció a diszkrét wavelet transzformációk egyik fajtája. A bemenő jelet (I_0) a transzformáció különböző összetevőkre bontja, majd egy felüláteresztő szűrő (H_0) adja meg a wavelet-együtthatókat az első szinten (W_1), míg egy aluláteresztő szűrő (L_0) alkalmazása után megkapjuk a bemenő jelet (I_1) a következő transzformációs ciklus számára (**10. ábra**). A bemenő jel (esetünkben egy kép) különböző „részletességi szintekre” való bontását a transzformációs ciklus előre megadott véges számú futtatása után kapjuk meg. Az algoritmus pontos leírása a disszertációban felhasznált egyik cikkben található meg (Szabó és mtsai., 2010). A

legfontosabb függvények kódját az **Appendixben** adom meg.



10. ábra. A stationary wavelet transzformáció folyamatábrája

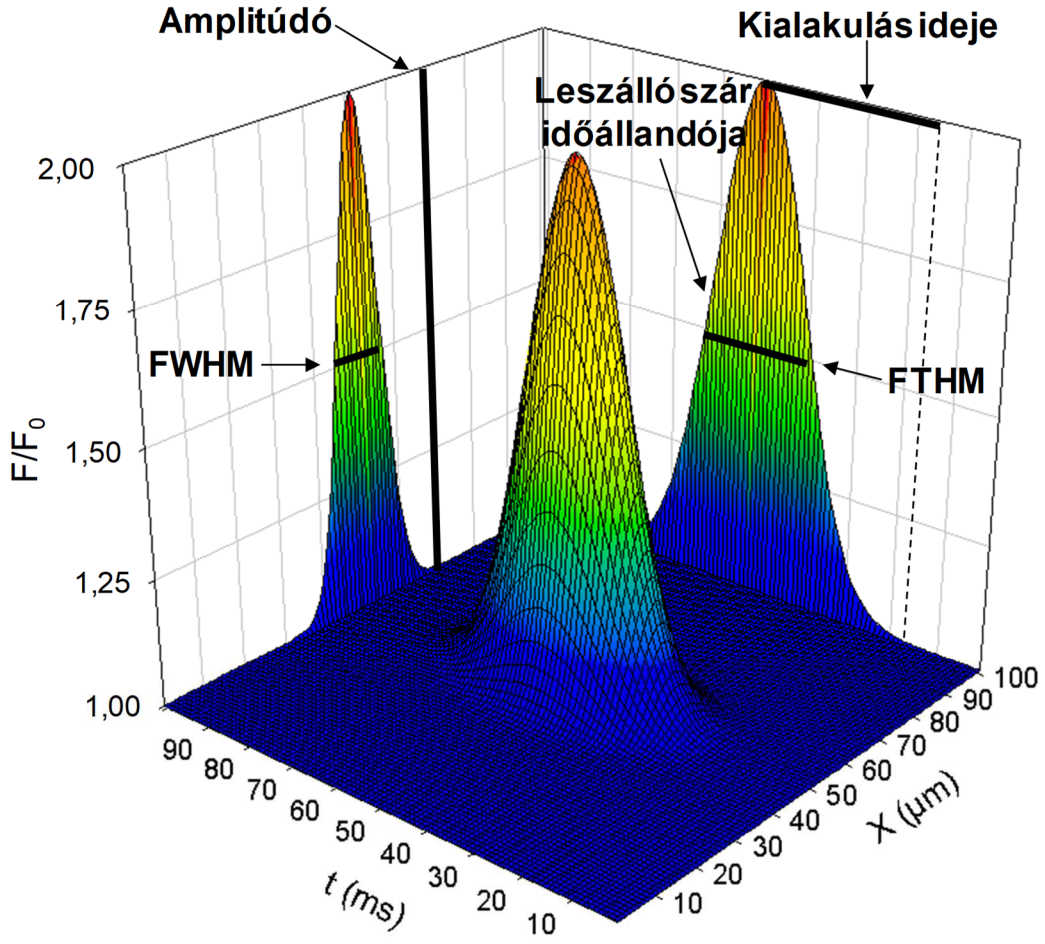
***Ii**: bemenő jel az adott szinten; **Wi**: wavelet koefficiensek az adott szinten; **Hi**: az adott szinten alkalmazott felüláteresztő szűrő; **Li**: az adott szinten alkalmazott aluláteresztő szűrő.*

5.3.2 Az egydimenziós (line-scan) képek elemzése

Line-scan képek (**4.** és **8B. ábra**) esetében a fluoreszcencia intenzitást [F(t)] az eltelt idő (t) függvényeként ábrázoljuk. A mért értékeket a háttérfluoreszcenciára normalizált fluoreszcencia intenzitásként [$F(t)/F_0$] jelenítjük meg. Ezért a disszertáció minden további ábráján a fluoreszcencia értékek dimenzió nélküli valós számként lesznek megadva. Az alapfluoreszcencia intenzitást [F_0] olyan időintervallumban végzett átlagolásával nyertük, ahol a vizsgált időintervallumban nem történt semmilyen intracelluláris Ca^{2+}-koncentrációváltozás. A normalizált képeken ezután wavelet transzformációval zajszűrést végeztünk. A *spark*okat a 2-es és 3-as, míg az *ember*eket a 4-es wavelet szinten tudtuk detektálni.

A **11. ábra** egy teoretikus *spark*ot és a belőle számolható paramétereket mutatja be. Ez a kép egy kicsit eltorzítva ábrázolja egy *spark* időbeli kialakulását majd megszűnését (lásd **5A. ábra**). Valójában nem tudjuk, hogy milyen elméleti függvény írja le egy *spark* időbeliségét, ezért Hollingworth és mtsai. (Hollingworth et al., 2001) alapján a felszálló és a leszálló szárra is exponenciális függvényt illesztettünk. A *spark* térbeli kiterjedését Gauss függvény írja le. Az illesztések után a kapott görbék félérték-szélessége lesz a *spark*okat jellemző félérték-szélesség paramétere: FTHM (időbeli, Full Time at Half Maximum); FWHM (térbeli; Full Width at Half Maximum). Az idő profil

felszálló szárának illesztéséből meghatározható a *spark* csúcsának eléréséhez szükséges idő (Time to Peak), míg a leszálló szár illesztéséből a megszűnésének ideje (Falling Time). A kettő összege fogja megadni a *spark* időbeli hosszát (duration). Végezetül kiszámolható az egy *spark* alatt az SR-ből kiszabadult Ca^{2+} mennyisége (Signal Mass), amelyet szintén Hollingworth és mtsai. (2001) alapján térfogati integrálással határoztunk meg. Így ennek mértékegysége μm^3.



11. ábra. A *spark*ok jellemző paraméterei

***F₀**: háttérfluoreszcencia; **FWHM**: térbeli félérték-szélesség; **FTHM**: időbeli félérték-szélesség.*

Ahogy az az **5. ábrán** jól látható, míg egy *spark* és egy *ember* térbeli profilja nagyon hasonló, addig időbeli profiljuk jelentősen különbözik. Ezért az *ember*ek paramétereinek számolása részben eltér a *spark*oknál leírtaktól. Az *ember*hez három jellemző paramétert rendelünk hozzá: átlagos amplitúdó, térbeli félérték-szélesség

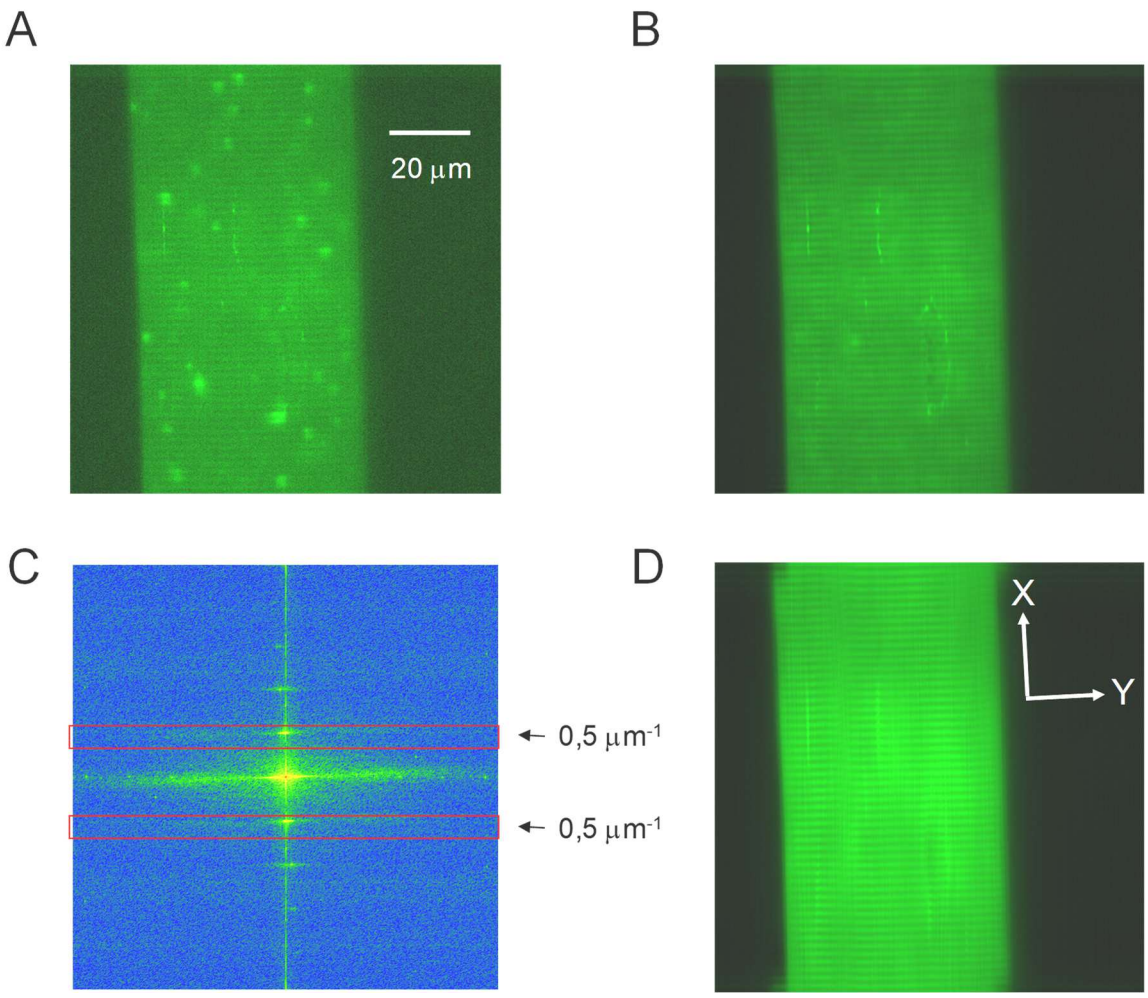
(FWHM), időtartam (duration). Az első kettő számolásához a hosszú *ember*t „egy pontra toljuk össze”. Ehhez az *ember* elején az átlagos amplitúdó 80%-át meghaladó időpontot T1-nek, a végén a 80%-ot már nem meghaladó pontot T2-nek definiálva, átlagoljuk a kép oszlopait a [T1,T2] intervallumon. Az így kapott szinte zajmentes térbeli profilra Gauss függvényt illesztve megkapjuk az FWHM értéket. A T2-T1 értéket pedig az időtartamnak (duration) tekintjük. Mindkét típusú eseményre vonatkozó számolások részletesen megtalálhatóak a disszertáció alapját képező cikkben (Szabó és mtsai., 2010).

5.3.3 A kétdimenziós (XY) képek elemzése

Kétdimenziós szkennelés esetén a képeken általában az izomrost nem fedi le a teljes képet (**12A. ábra**). Ilyenkor a kép egyik vagy mindkét szélén egy sötét sáv látható, ami a rost melletti festéket nem tartalmazó oldat fluoreszcenciája. Valamint a rost képén tisztán látszanak a harántcsíkolatok és néha egyéb strukturális egységek (pl. sejtmag). Tehát az elemzés első lépéseként meg kell határozni a képen a rost által lefedett területet és el kell távolítani a rost strukturális részeit jelentő képpontokat.

A kép elemzésének legelső lépésében a kép minden egyes képpontjára meghatározzuk az adott képpontra érvényes alap fluoreszcencia értéket. Ehhez az adott képponthoz tartozó idősor azon pontjainak átlagos fluoreszcencia-értékét használtuk, melyek az idősor összes pontjának átlaga Mean + NormCri •·SD érték alatt vannak (SD: standard deviáció; NormCri egy konstans, amely a mérőrendszertől és a mérési körülményektől függ, de egy mérési sorozaton belül állandó). Ezután az egyes képpontokhoz tartozó idősorokat az egydimenziós SWT-val komponenseire bontottuk, majd ennek segítségével felüláteresztő szűrést végeztünk. Az F4-es wavelet együtthatóval elosztva az idősor összes adatát kiszűrtük az igen lassú kinetikájú nem elemi kalciumfelszabadulásból származó kalciumszint-változásokat.

Az egyes képpontokhoz tartozó alapvonali fluoreszcencia-értékekből készült nagyon jó jel/zaj arányú képen (**12B. ábra**) meghatároztuk, hogy mely terület tartozik az izomrosthoz. Ezt megkönnyítette, hogy a rosthoz tartozó képpontok fluoreszcenciája jóval magasabb a rajta kívüli kép-pontok fluoreszcenciájától (**12A. ábra**; az intenzitások eloszlása egyértelműen bimodális eloszlást mutatott). A két adathalmaz közötti optimális vágást iteratív módszerrel határoztuk meg, majd az így kapott küszöb feletti egybefüggő területet fogadtuk el a rostnak.



12. ábra. A rost strukturális elemeinek azonosítása

*(**A**) Reprezentatív kétdimenziós (XY) kép egy sparkokat mutató izomrostról. (**B**) Átlagolt jó jel/zaj arányú kép az állandó rost struktúrákkal. (**C**) Gyors Fourier transzformáció utáni frekvencia spektruma a **B** panelen levő képnek. A 0,5 µm^{-1} (és inverzéhez) tartozó csúcs reprezentálja a ~ 2 µm hosszú szarkomereket. (**D**) Az inverz Fourier transzformáció eredménye a szarkomeren kívüli komponensek kitörlése után.*

Végül az izomrost strukturális elemeit a rost hossztengelyének megfelelően elhelyezkedő oszlopok Fourier-transzformációjával határoztuk meg (**12C. ábra**). A kb. 2 µm hosszú szarkomereknek megfelelő Fourier csúcs körüli terület kivételével a többi Fourier együttható értékét kinulláztuk, majd inverz Fourier-transzformációt végeztünk (**12D. ábra**). Az így kapott képen csak a minden képen jelenlevő strukturális elemek maradtak meg, és oszloponkénti lokális maximumkereséssel meghatároztuk a szarkomerek helyét. Ezzel az eljárással az esetlegesen megtörő szarkomerek lefutása

is követhető, így az események félérték-szélesség értékeit meg tudtuk határozni a szarkomerekre merőleges (X) és velük párhuzamos (Y) irányban is.

Az elemi kalciumfelszabadulási események területeinek azonosítása és paramétereik meghatározása előtt nagy hatékonyságú Wavelet zajszűrést végeztünk minden normalizált képen. A *spark*ok elemzése során a már régóta ismert kettős küszöböléses módszer (Cheng et al., 1999) módosított változatát használtuk a területek azonosítására. A módszer részletes leírása a disszertáció alapját képező cikkben megtalálható (Cserne Szappanos et al., 2020). Röviden a *spark*ként azonosított területen belül megkerestük a legmagasabb átlagos fluoreszcenciát mutató 3x3 pixel nagyságú területet, melynek középpontját tekintettük az adott *spark* csúcspontjaként. Az itt mért fluoreszcencia-intenzitás és az alapvonal különbsége adta meg az esemény amplitúdóját. Innen a szarkomerekkel párhuzamos irányban ill. arra merőleges irányban elindulva kerestük meg azokat a pontokat, ahol három egymás melletti pont átlagos intenzitása az amplitúdó értékének fele alatt van. Ezek a pontok lettek az FWHM-X és az FWHM-Y határpontjai. A legközelebbi lokális fluoreszcencia maximumtól való távolság adta meg a *spark* csúcsa és a szarkomer távolságát. Az egymás követő képeken átfedő *spark*ok csúcspontjai közötti távolság adta meg a *spark* elmozdulásának mértékét.

5.4 Adatelemzés

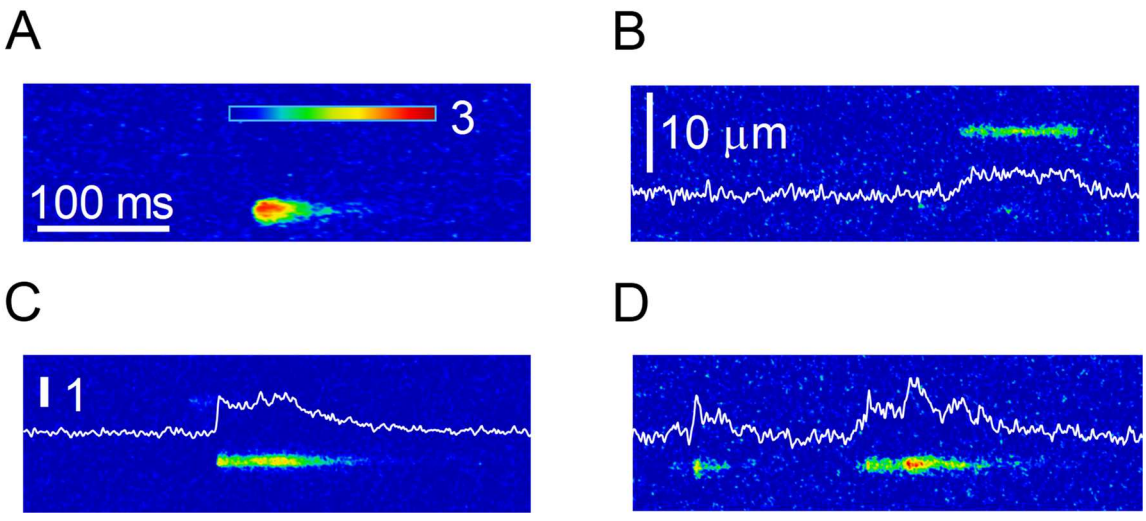
Az adatokat átlag ± standard hiba (SE) alakban adom meg. A szignifikáns különbségek kimutatására Student féle t-próbát alkalmaztunk, miután megvizsgáltuk, hogy az adatsorok normális eloszlásúak-e. A $p<0,05$ szintet fogadtuk el szignifikáns különbségnek. Azokban az esetekben, amikor az adatok nem követték a normál Gauss eloszlást, vagy kettőnél több adatsort kellett összehasonlítani, ANOVA-t használtunk. A különböző körülmények között kapott *spark* (vagy *ember*) paraméterek összehasonlításakor a nagyszámú (sokszor több tízezer) adat megjelenítésére hisztogramos ábrázolást használtunk. Egyes esetekben ezeket is illesztettük egy vagy több Gauss függvény összegével. A különböző függvények illesztésekor minden esetben feljegyeztük az egyes illesztett paraméterek hibáit és az illesztés eredményét csak akkor fogadtuk el, ha ezek elegendően kicsik voltak. Az adatelemzés részletes leírását minden, a disszertációban felhasznált közlemény megfelelő fejezete tartalmazza.

6. EREDMÉNYEK ÉS KÖVETKEZTETÉSEK

6.1 Elemi események fiziológiás körülmények között emlősök, kétéltűek és rovarok izomrostjain

6.1.1 ECRE-k patkányok harántcsíkolt izmon

Patkányok enzimatikusan izolált *extensor digitorum communis* izomrostjain kezdtük az ECRE-k tanulmányozását (Szentesi et al., 2004). Az intakt izomrostokat üvegaljú mérőkádba helyeztük és 0,002% szaponint tartalmazó oldatba tartottuk 2-3 percig, hogy a felszíni membránt átjárhatóvá tegyük. Ezután az oldatot szaponin mentes 100 µM Fluo-3 kalciumérzékeny fluoreszcens festéket tartalmazó belső oldatra cseréltük (összetevők mM-ban: 95 K_2SO_4, 10 HEPES, 1 EGTA, 6 $MgCl_2$, 5 Na_2-ATP, 10 Na-foszfokreatin, 10 glükóz, 0,13 $CaCl_2$, 8% dextrán, 7,2 pH). A line-scan képeket 1,53 ms/vonal sebességgel és 512 pixel/vonal kiterjedéssel (pixel méret 0,142 µm) 63× vízimmerziós objektívvel (1,2 numerikus apertura) mértük egy ZEISS META konfokális lézerpásztázó mikroszkópon. A Fluo-3-t egy Argon ion lézerrel (488 nm) gerjesztettük, az emittált fényt egy felüláteresztő szűrőn (505-570 nm) keresztül mértük és 12 biten digitalizáltuk. A képeket (F[x,t]) háttérfluoreszcenciára normalizáltuk (F_0[x]) és szivárvány színkóddal ábrázoltuk (**13. ábra**). A melegebb színek magasabb $[Ca^{2+}]_i$-t mutatnak. A képek elemzésére az **5.3.2** fejezetben leírt módszert használtuk. Az átlagolásból kihagytuk a 0,2 F/F_0-nál kisebb amplitúdójú eseményeket.



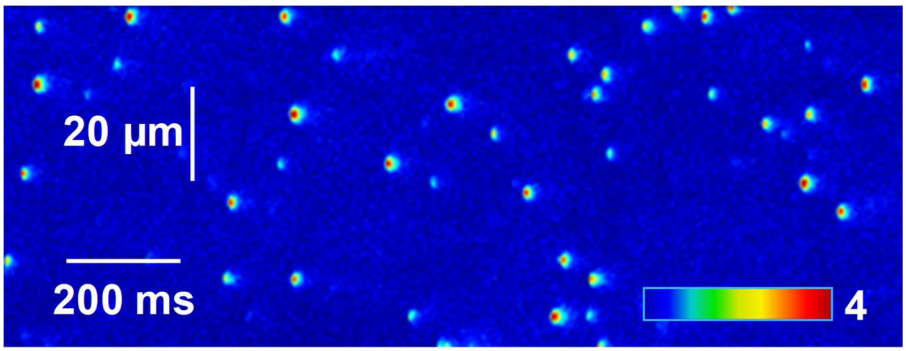
13. ábra. ECRE-k patkányok harántcsíkolt izmán

*Spark (**A**), ember (**B**), spark, amit ember követ (**C**), ember, amit spark követ (**D**).*

A patkány izomrostokon változó morfológiájú kalciumfelszabadulási eseményeket találtunk. A *spark*ok mellett megtalálhatóak voltak a hosszú kis amplitúdójú *ember*ek és ezek együttes előfordulása is (**13. ábra**). Az önálló *spark*ok (1576 esemény) átlagos amplitúdója 0,92±0,01 F/F_0 volt, térbeli félérték-szélességük (FWHM) 1,81±0,03 μm-nek míg hosszuk időben 56±1 ms-nak adódott. Az önálló *ember*ek (454 esemény) átlagos amplitúdója a *spark*októl jóval kisebb volt (0,210±0,004 F/F_0), térbeli kiterjedésük viszont megegyezett a *spark*okéval (FWHM 1,76±0,03 μm) és az átlagos hosszuk jóval nagyobb volt (87±2 ms). Az ECRE-k frekvenciája alacsony (0,059±0,002 1/s/szarkomer) volt és nagyjából 60% volt önálló *spark*, míg a többi az *ember*ek valamelyik formája.

6.1.2 ECRE-k békák harántcsíkolt izmain

Az elemi kalciumfelszabadulási események tanulmányozását békákon folytattuk (Sztretye et al., 2009). Kecskebékák (*Rana esculenta*) *semitendinosus* izmából manuálisan preparált intakt izomrostokat üvegaljú mérőkádba helyeztük. A rostokat 0,004% szaponint tartalmazó oldatba tartottuk 2-3 percig, hogy a felszíni membránt átjárhatóvá tegyük. Ezután az oldatot szaponin mentes 50 μM Fluo-3 kalciumérzékeny fluoreszcens festéket tartalmazó belső oldatra cseréltük (összetevők mM-ban: 140 K-glutamát, 10 HEPES, 1 EGTA, 5,5 $MgCl_2$, 5 Na_2-ATP, 10 Na-foszfokreatin, 10 glükóz, 0,13 $CaCl_2$, 8% dextrán, 7,0 pH). A mérőrendszer, a mérés paraméterei és az adatfeldolgozás megegyeztek a patkányoknál leírtakkal (**6.1.1** fejezet).

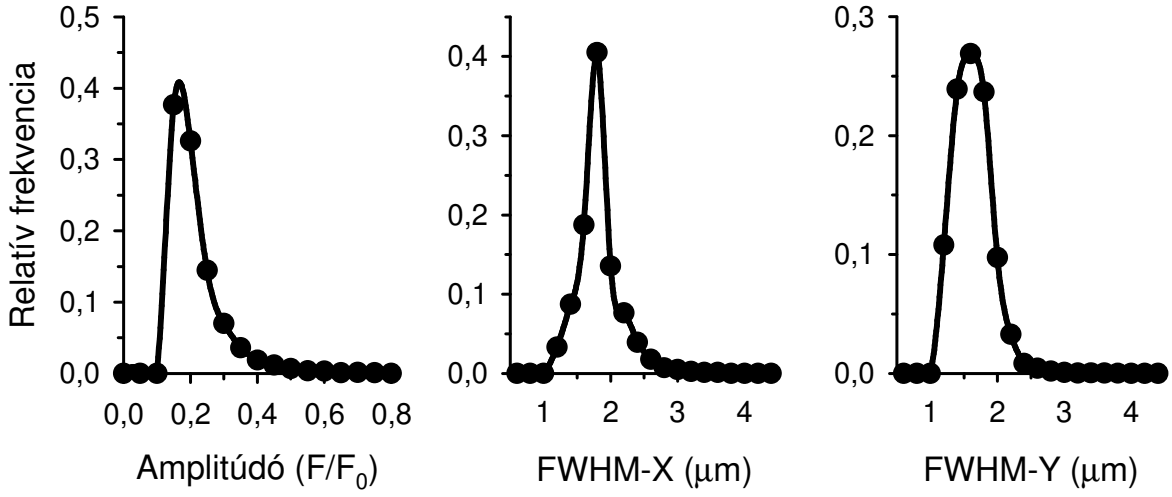


14. ábra. Reprezentatív line-scan kép béka harántcsíkolt izmán

Békák harántcsíkolt izomrostjain lényegesen több *spark*ot találtunk, mint patkány izomrostokon (**14. ábra**). Viszont soha nem láttunk *ember*t kontroll körülmények között. A *spark*ok átlagos amplitúdója a patkányokéhoz hasonló (0,84±0,01 F/F_0), de FWHM-je szélesebb (2,16±0,02 μm), míg hossza rövidebb (34,8±0,3 ms) volt. Az események

frekvenciája 0,19±0,02 1/s/szarkomer volt (1561 esemény), ami nagyjából háromszorosa a patkány izomrostokénak.

A nagysebességű vonal-szkenner ZEISS LIVE konfokális lézerpásztázó mikroszkóp megérkezése után a kísérleteket megismételtük északi leopárd béka (*Rana pipiens*) enzimatikusan izolált intakt *flexor digitorum brevis* izomrostjain (Cserne Szappanos et al., 2020). A rostokat most is üveg aljú mérőkádba helyeztük Ringer oldatba (összetevők mM-ban: 115 NaCl, 2,5 KCl, 1 $MgCl_2$, 1,8 $CaCl_2$, 10 HEPES, 7,0 pH). A mérések megkezdése előtt a rostokat 20 μM Fluo-4 AM-el töltöttük szoba hőmérsékleten 30 percig, amit 20 perc de-észterifikáció követett. A képsorozatokat 30 vagy 60 kép/másodperc sebességgel, 512x512 pixel méretben (106 μm x 106 μm) az előző bekezdésben ismertetett optikai elrendezéssel rögzítettük. A képek elemzésére pedig az **5.3.3** fejezetben leírt módszert használtuk. Az így mért *spark*ok átlagos amplitúdója 0,188±0,001 F/F_0, FWHM-X 1,725±0,005 μm, FWHM-Y 1,508±0,004 μm és frekvenciája 0,19±0,02 1/ms/mm^2 volt (6164 esemény). Az átlagolásból kihagytuk a 0,1 F/F_0-nál kisebb amplitúdójú és az FWHM<1 μm és FWHM>10 μm eseményeket. Ebből a méréssorozatból meg tudtuk állapítani, hogy a *spark*ok aszimmetrikusak és szélesebbek az izomrost hossztengelyével párhuzamosan.



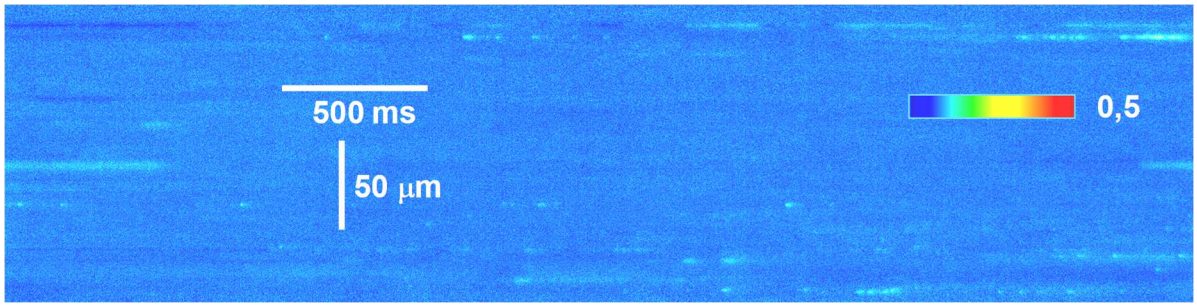
15. ábra. A *spark*ok paramétereinek eloszlása béka harántcsíkolt izmán

A két méréssorozat lényegesen különböző átlagos *spark* amplitúdót adott. Ennek több oka is lehet. Az egyik lényeges eltérést a preparátumban találjuk. Intakt rostokon kisebb *spark*okat kaptunk, mint a permeabilizált, vagyis a felszíni membrántól, így a dihidropiridin receptor kontrolljától felszabadult rianodin receptorokon keresztül kialakuló események esetében. A másik jelentős különbség a mérés metodikájában

rejlik. A LIVE konfokális mikroszkóp rendszer gyorsabb és így több kisebb amplitúdójú eseményt rögzít a képeken. Az XY képeken talált események amplitúdó eloszlása megmutatja, hogy a legtöbb esemény amplitúdója 0,2 F/F_0 körül volt (**15. ábra**). Végezetül a line-scan képek és az XY képsorozatok elemzésére két eltérő módszert használtunk, amelyekben például a minimálisan elfogadott amplitúdó értéke is különbözött. Azonban eredményeink jól egyeznek a hasonló preparátumokon és metodikával mások által mért adatokkal.

6.1.3 ECRE-k egerek harántcsíkolt izmain

Mivel az izombetegségek tanulmányozására egyre több egér modell vált elérhetővé, az elemi kalciumfelszabadulások patkányokra kidolgozott mérési módszerét adaptálnunk kellett erre a speciesre (Bodnár et al., 2014). Egerek *flexor digitorum brevis* izmából enzimatikusan izolált rostokon végeztük az ECRE-k vizsgálatát. Az intakt izomrostokat üvegaljú mérőkádba helyeztük és 0,01% szaponint tartalmazó oldatba tartottuk 1-2 percig, hogy a felszíni membránt átjárhatóvá tegyük. Ezután az oldatot szaponin mentes 50 μM Fluo-3 kalciumérzékeny fluoreszcens festéket tartalmazó belső oldatra cseréltük (összetevők mM-ban: 95 K_2SO_4, 10 HEPES, 1 EGTA, 6 $MgCl_2$, 5 Na_2-ATP, 10 Na-foszfokreatin, 10 glükóz, 0,13 $CaCl_2$, 8% dextrán, 7,2 pH). A mérőrendszer, a mérés paraméterei és az adatfeldolgozás megegyeztek az békáknál leírtakkal (**6.1.1** fejezet).



16. ábra. Reprezentatív line-scan kép egér harántcsíkolt izomrostján

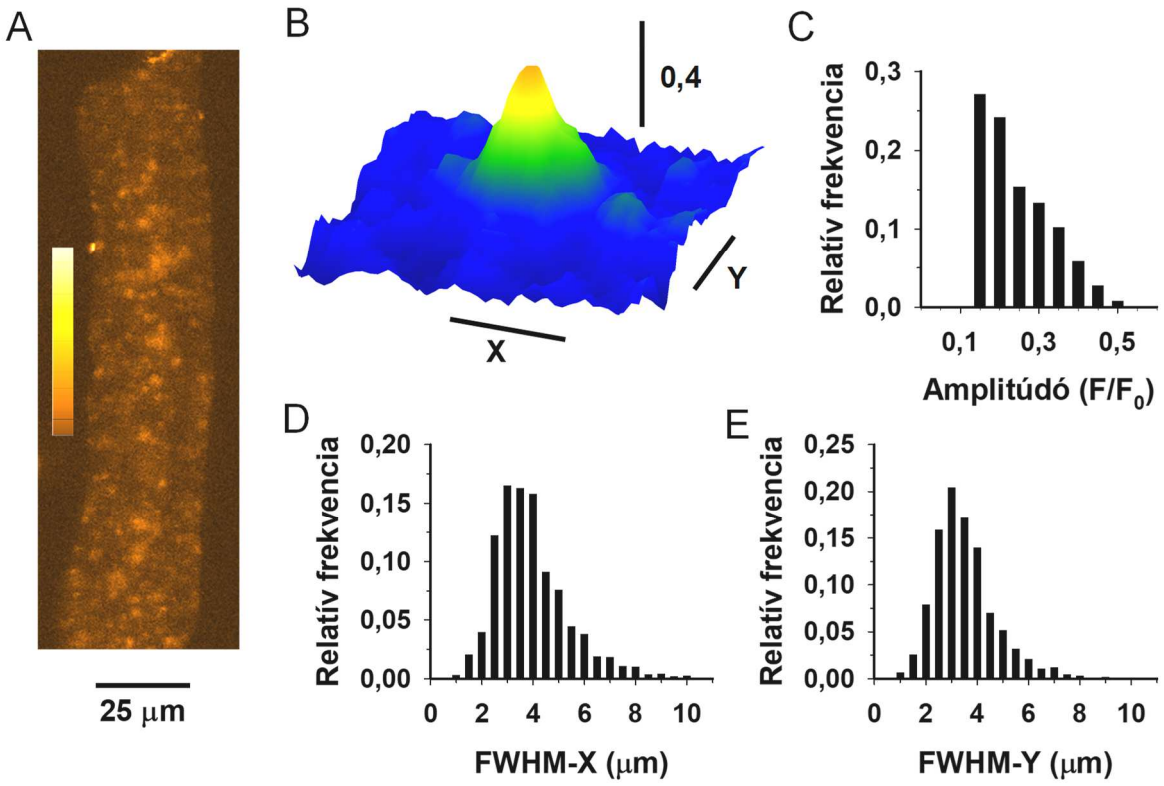
A *spark*ok mellett a patkányokhoz hasonlóan itt is megjelentek az *ember*ek (**16. ábra**). Az egyedül álló *spark*ok átlagos amplitúdója jóval kisebb volt (0,165±0,001 F/F_0), mint a patkányok esetében. A térbeli kiterjedésük (FWHM 1,92±0,01 μm) és hosszuk (40,0±0,3 ms) azonban megegyezett a patkányokban mértekkel. Az önálló *ember*ek átlagos amplitúdója (0,160±0,003 F/F_0) és térbeli kiterjedésük (FWHM 1,85±0,01 μm) a *spark*okhoz hasonló volt. Viszont az átlagos hosszuk (159,4±5,2 ms) több mint duplájának adódott, mint a patkányok esetében. A *spark*ok előfordulásának

frekvenciája 0,48±0,03 Hz, míg az *ember*eké 0,38±0,03 Hz volt.

6.1.4 ECRE-k házi méhek harántcsíkolt izmain

Az elemi kalciumfelszabadulási események mérései során a kétéltűeken és emlősökön felhalmozott tapasztalataink felhasználásával megpróbáltuk ízeltlábúak harántcsíkolt izmainak preparálását is (Collet et al., 2021). A méhek nagyon hatékony beporzó rovarok, ezért kulcsfontosságúak mind a növények biológiai sokféleségének fenntartásában, mind a mezőgazdasági élelmiszertermelésben. A könnyű háziasitásuknak köszönhetően a mézelő méheket régóta használják kutatási modellként különböző területeken, kezdve a sejtfiziológiától az egyének közötti kommunikációig és a szocializációig. Sajnálatos módon a mézelő méhpopulációkban az elmúlt néhány évben világszerte megfigyelt magas mortalitási szint arra késztette a kutatókat, hogy tovább tanulmányozzák ezt az állatmodellt, annak reményében, hogy megértsék a populációcsökkenés eredetét. A mézelő méhek sejtjei értékes modellt kínálnak a kalciumjelátvitel és az intracelluláris kalciumhomeosztázis vizsgálatára rovarokban. A méhek *tibia* izomrostjainak preparálást már az **5.1** fejezetben érintettem, ezért itt csak az ott nem szereplő technikai részleteket említem meg. A harmadik lábpárból származó tibiákat kalciummentes Tyrode-oldatban (összetevők mM-ban: 14 NaCl, 5 KCl, 2 $MgCl_2$, 10 HEPES, 7,2 pH) kimetszettük, hosszirányban felvágtuk és kitűztük. Az így előkészített tibiákat 20 percig 37 °C-os disszociációs oldatban emésztettük (4 enzimet tartalmazó kalciummentes Tyrode: 0,5 mg/ml 1-es típusú kollagenáz, 1,5 mg/ml tripszin, 1,5 mg/ml papain és 1 mg/ml pronáz). Miután kalciummentes Tyrode oldatban lemostuk az enzimeket normál (2 mM $CaCl_2$) Tyrode-ban pipettával triturálva az izomból egyedi intakt izomrostokat nyertünk, amelyeket üveg aljú mérőkádba helyeztünk. A rostokat 30 percig 5 µM Fluo-8-AM sejtmembrán permeábilis festékkel töltöttük szobahőmérsékleten. A feltöltött sejteket Zeiss LSM 5 LIVE lézerpásztázó konfokális mikroszkóppal vizsgáltuk, amely Plan-Neofluar 40× olajimmerziós objektívvel volt felszerelve (NA=1,3). A Fluo-8-at egy 488 nm-es argon lézerrel gerjesztettük, és a kibocsátott fluoreszcens fényt felüláteresztő szűrőn (505-570 nm) mértük és 12 biten digitalizáltuk. A spontán aktivitást mutató rostokon 512×512 pixel (XY) képsorozatokat rögzítettük, 1 Hz-en. A pixel mérete 0,328 µm, a megvilágításának ideje pedig 1 ms volt. A line-scan képeket 1 vagy 2 ms/sor sebességgel készítettük, és a pixelméret itt is 0,328 µm volt. Az ECRE-k kimutatása és elemzése megegyezett az békáknál leírtakkal (**6.1.1** fejezet).

A spontán aktív izomrostokon mért XY képsorozatokon klasszikus *spark*okat találtunk (**17AB. ábra**). A 25 db roston detektált 4898 db esemény analízise alapján az átlagos amplitúdó elég alacsony (0,220±0,001 F/F_0) volt a békákon tapasztaltakhoz



17. ábra. *Spark*ok és paramétereik házi méh harántcsíkolt izmán

*30 db (30 s) háttér fluoreszcenciára normalizált XY kép összege (**A**). Reprezentatív spark (**B**). Amplitúdó (**C**), FWHM-X (**D**, rostra merőleges) és FWHM-Y (**E**, rosttal párhuzamos) hisztogramok. A B panelen a kalibrációs vonalak 5 μm hosszúak.*

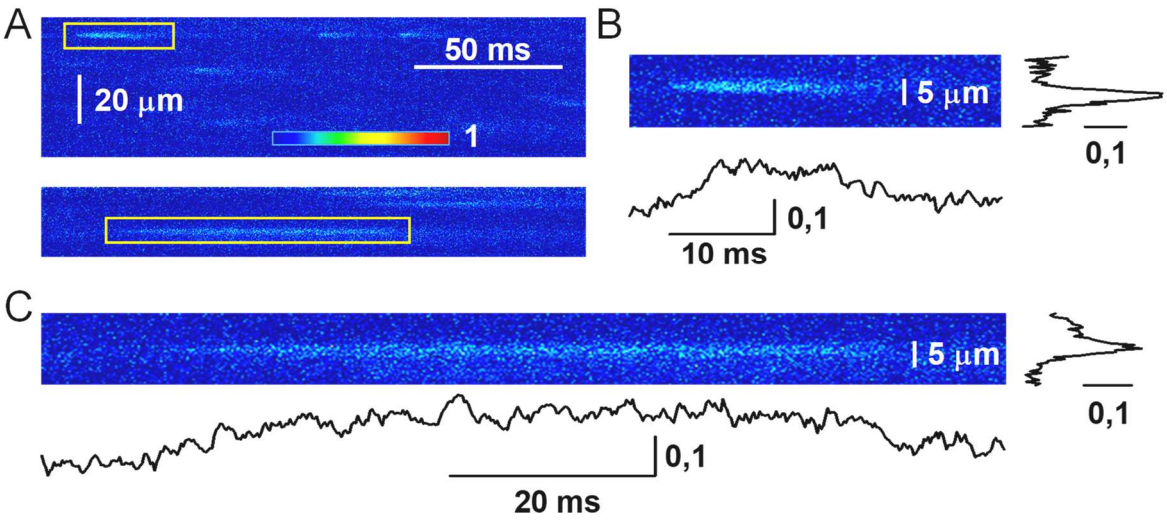
képest. Azonban néhány *spark* esetében az amplitúdó elérte a 0,5 F/F_0 értéket (**17C. ábra**). Az események átlagos frekvenciája nagyon nagy volt (**17A. ábra**, 1696±367 Hz/mm^2). A rostra merőleges átlagos szélesség (FWHM-X, 3,73±0,02 μm) és a rosttal párhuzamos átlagos szélesség (FWHM-Y, 3,30±0,02 μm) nagyobbnak adódott a béka és emlős izomrostokon megszokott értéknél (**17DE. ábra**). Találtunk néhány eseményt, amely nagy területre terjedt ki (FWHM>10 μm, **17DE. ábra**). A *spark*ok alakja nem volt tökéletes kör, az átlagos FWHM-X/FWHM-Y hányados szignifikánsan nagyobb volt, mint 1 (1,22±0,01; $p<0,001$). Kiszámoltuk az események alatt felszabadult Ca^{2+} mennyiségét (Signal Mass, SM) is, amelynek átlagos értéke 14,52±0,29 μm^3 volt.

Az események morfológiájának részletes analízise céljából line-scan méréseket is végeztünk 22 db aktív izomroston (**3.5 fejezet 4. ábra**). Az emlős izomrostokon látottakhoz hasonlóan, találtunk *spark*okat és *ember*eket is (**3.5 fejezet 5. ábra**). Ezek aránya nagyjából 2:1 volt (**1. táblázat**). Míg a kétfajta esemény átlagos amplitúdója azonosnak adódott, az *ember*ek lassabban alakultak ki és térben szélesebbek voltak, mint a *spark*ok, így az átlagos Signal Mass is nagyobb volt esetükben (**1. táblázat**).

1. táblázat: ECRE-k paraméterei line-scan mérésekből

	Spark n=2244	***Ember*** n=1094
Amplitúdó (F/F_0)	0,185±0,001	0,186±0,002
TTP (ms)	10,45±0,11	27,02±0,41***
FWHM (µm)	2,65±0,02	3,18±0,04***
FTHM (ms)	25,52±0,16	56,95±0,58***
Signal Mass (μm^3)	6,00±0,20	10,29±0,41***
Frekvencia (1/mm/s)	174,0±14,4	63,1±6,6***

*** szignifikáns eltérést mutat a *spark*ok értékeitől ($p<0,001$).



18. ábra. *Spark* és *ember* nagy időbeli felbontású line-scan mérésben

*(**A**) Reprezentatív normalizált line-scan kép nagyon gyors szkenneléssel (0,2 ms/vonal) regisztrálva. Kinagyított spark (**B**) és ember (**C**) időbeli és térbeli profiljával.*

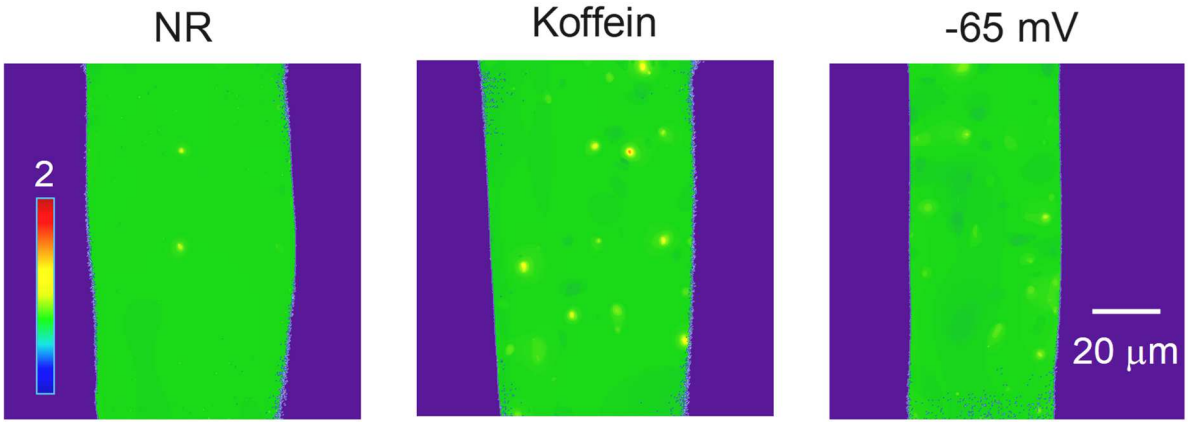
Az események kinetikáját tovább vizsgáltuk nagyon gyors line-scan mérésekben. A **18. ábrán** jól látszik, hogy a *spark* gyorsabban alakul ki, mint az *ember*, azonban az

események megszűnése időben hasonló. Összegzés képpen megállapíthatjuk, hogy a méhek lábából izolált harántcsíkolt izomrostokon a gerincesek izomrostjain mért ECRE-khez hasonló spontán *spark*ok és *ember*ek alakulnak ki. Így feltehetjük, hogy méhekben is ezek az elektromechanikai kapcsolat alap kalciumfelszabadulási eseményei (Collet et al., 2021).

6.2 A depolarizáció és különböző kalciumfelszabadulást befolyásoló anyagok hatása az elemi eseményekre

6.2.1 Depolarizáció és koffein hatása béka harántcsíkolt izmon

A kétéltűek vázizomrostjain a *spark*ok egyaránt lehetnek feszültségfüggő és feszültségtől független, ligandum által aktivált kalciumfelszabadulási események. Azonban, az hogy ezek tulajdonságai és eredetük hasonlóságokat mutat-e, még mindig vita tárgyát képezi. Ennek tisztázására megemelt KCl tartalmú oldatokat használtunk a nyugalmi membránpotenciál kismértékű depolarizációjára és a dihidropiridin receptorok aktiválására, míg koffeint a rianodin receptorok (RyR) megnyitására békák intakt izomrostjain (Cserne Szappanos et al., 2020). Mindkét kezelés növelte a *spark*ok előfordulásának gyakoriságát és megváltoztatta azok morfológiáját (**19. ábra**).



19. ábra. Normalizált (F/F_0) XY kép béka harántcsíkolt izmán

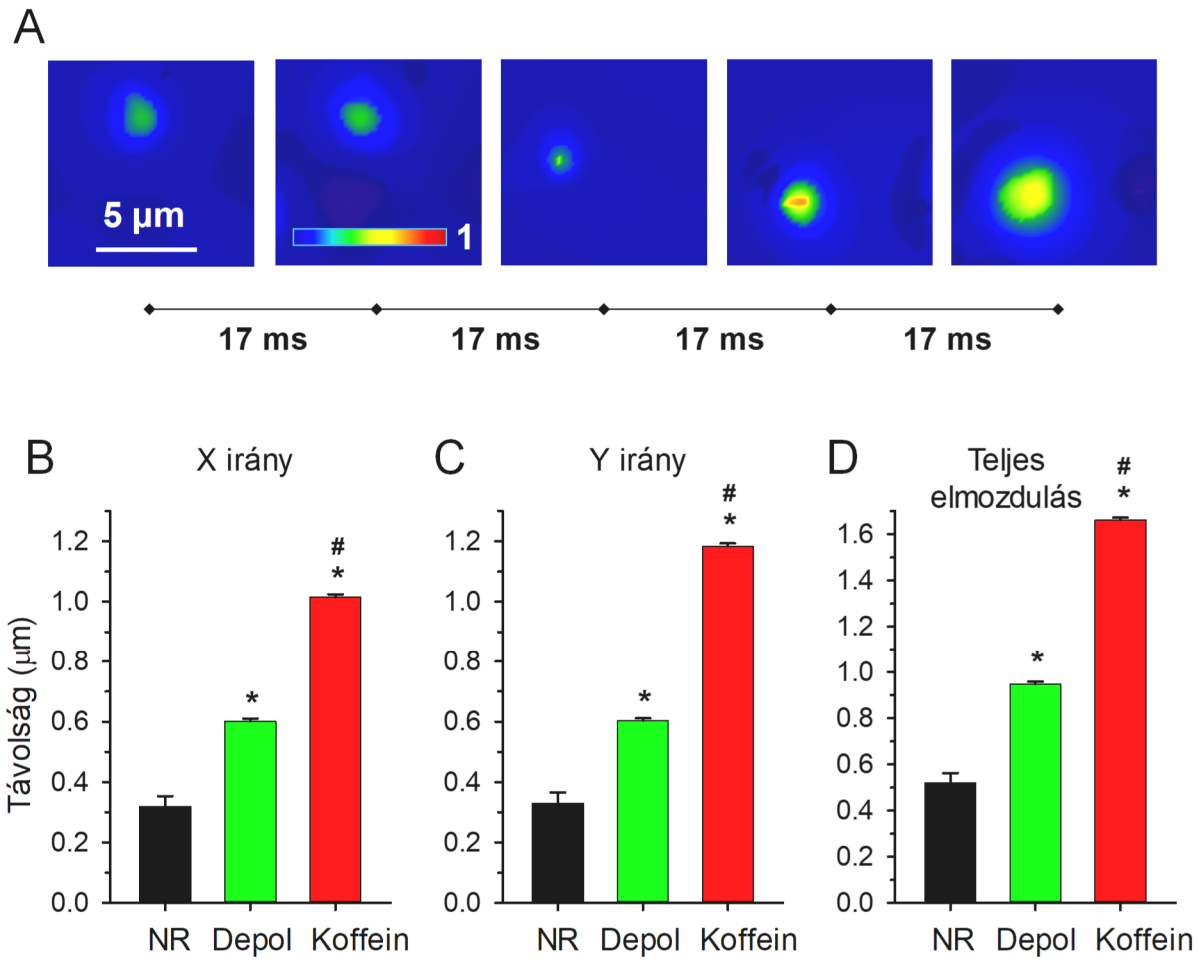
Normál Ringer (NR), 1 mM koffein jelenlétében, -65 mV-ra depolarizáló oldatban. A skálák minden panelre vonatkoznak.

A *spark*ok amplitúdója és a teljes szélességük a maximum felénél szignifikánsan nagyobb volt a koffeinkezelés után, mint a depolarizált sejteken (**2. táblázat**). A depolarizáció mellett alkalmazott koffein kezelés tovább növelte az események számát, de a többi paraméter értékét már nem változtatta meg lényegesen a depolarizáció nélküli koffeinadagoláshoz képest. A depolarizált rostokon észlelt *spark*ok nagyjából 10%-a és a koffeinnel aktivált *spark*ok egyharmada tovaterjedő volt (több egymást követő mérési képen is megjelent). A *spark*ok vándorlása – amit az egymást követő képeken a középpontjuk elmozdulásaként határoztunk meg – lényegesen hosszabb volt az egymást követő képkockák között koffeinkezelés után, mint depolarizáció hatására (**20. ábra**).

2. táblázat. *Spark*ok paraméterei különböző körülmények között

	NR (-90 mV)	-65 mV	Koffein
Rostok száma	106	47	21
***Spark*ok száma**	6164	43326	24942
Frekvencia (1/ms/mm^2)	1,47±0,30	37,15±4,35*	91,54±21,36*#
Amplitúdó (F/F_0)	0,188±0,001	0,164±0,001*	0,259±0,001*#
FWHM-X (μm)	1,725±0,005	1,917±0,003*	2,342±0,005*#
FWHM-Y (μm)	1,508±0,004	1,676±0,002*	2,081±0,005*#
SM (μm^3)	1,024±0,009	1,335±0,007*	4,354±0,034*#

* szignifikáns eltérést mutat normál Ringer-től (NR), # szignifikáns eltérést mutat -65 mV-tól ($p<0,001$).

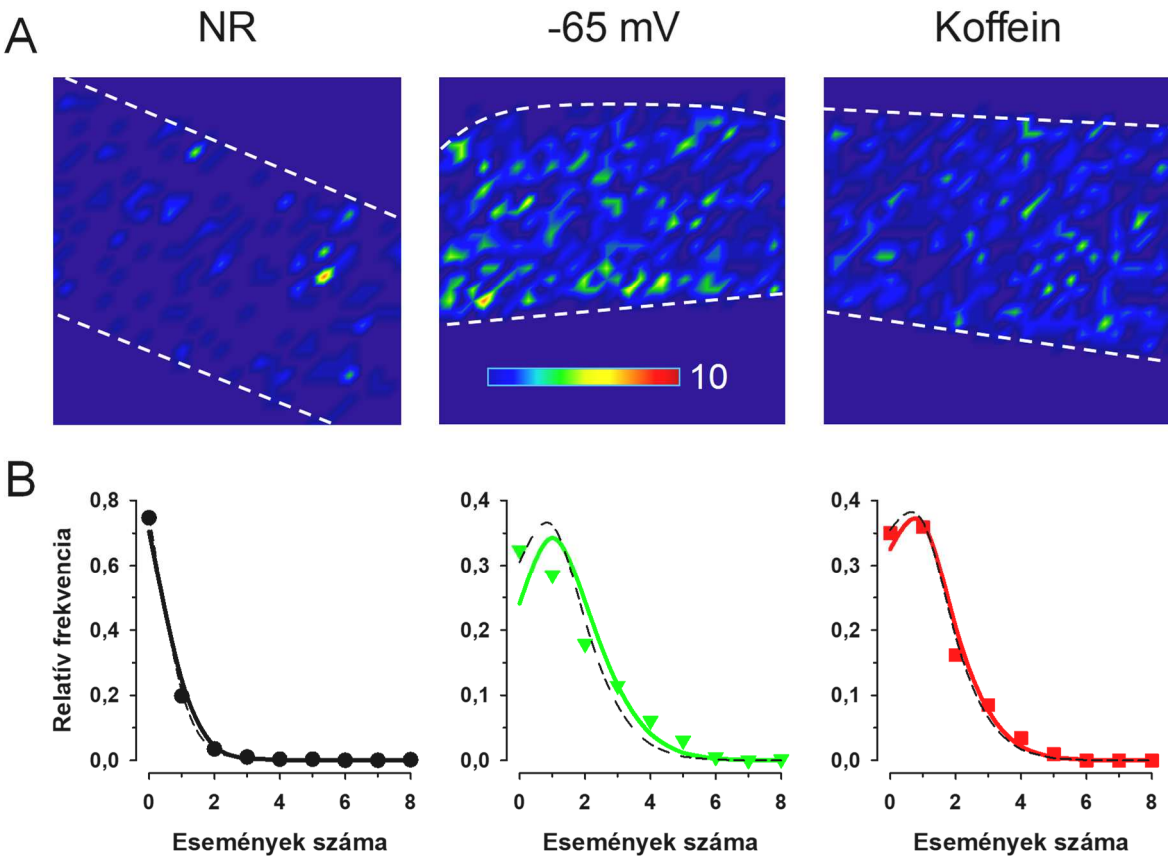


20. ábra. Tovaterjedő *spark*ok és az általuk megtett út

*(**A**) Egy reprezentatív tovaterjedő spark öt egymást követő képen. A szarkomerekre merőleges (**B**) és velük párhuzamos (**C**), és teljes (**D**) elmozdulás.*

** szignifikáns eltérést mutat NR-től, # szignifikáns eltérést mutat -65 mV-tól ($p<0,001$).*

A depolarizált vagy koffeinnel kezelt rostokon az XY mérésekben megjelenő nagyszámú spark lehetővé tette, hogy megvizsgáljuk, az események megjelenésének helye hogyan oszlik meg az egyes rostokban. Ahogy az a **21A. ábrán** látható (-65 mV-ra depolarizálva és koffein jelenlétében), ha sok esemény alakul ki egy izomroston, akkor azok egyenletesen eloszlanak a vizsgált területen. Ennek az állításnak a bizonyítására az egységnyi területen kialakult események számát megillesztettük a független eseményrendszert leíró Poisson-eloszlás függvényével (**21B. ábra**). Mindhárom vizsgálati csoportban tökéletes illesztést kaptunk a mérési adatokra.



21. ábra. A *spark*ok kialakulási helyének eloszlása a rostokban

*(**A**) A sparkok darabszáma 16 x 16 pixel nagyságú területeken 60 darab egymást követő XY képből kiszámolva. A színskála a sparkok számát 0 darabtól (sötétkék) 10 darabig (piros) mutatja. Szaggatott vonal jelöli a rost szélét. (**B**) A különböző számú sparkot tartalmazó területek eloszlása. A szaggatott vonal az átlagos spark számmal megegyező λ állandójú Poisson eloszlást mutatja. A folyamatos vonal pedig a mérési pontokra illesztett Poisson eloszlás.*

Eredményeink arra utalnak, hogy a békák vázizmában található kétféle rianodin receptor, a DHPR-ek által szabályozott junkcionális és a feszültség független parajunkcionális RyR-ek, egymástól függetlenül aktiválódnak, alternatív módokon, de fennállhat az együttműködés lehetősége (CICR) a szomszédos kalciumcsatornák között. Valamint a *spark*ok egyenletesen oszlanak el anélkül, hogy frekventált területek alakulnának ki a vázizomrostokban (Cserne Szappanos et al., 2020).

6.2.2 A nehézfém-ion kelátor TPEN hatása az ECRE-kre

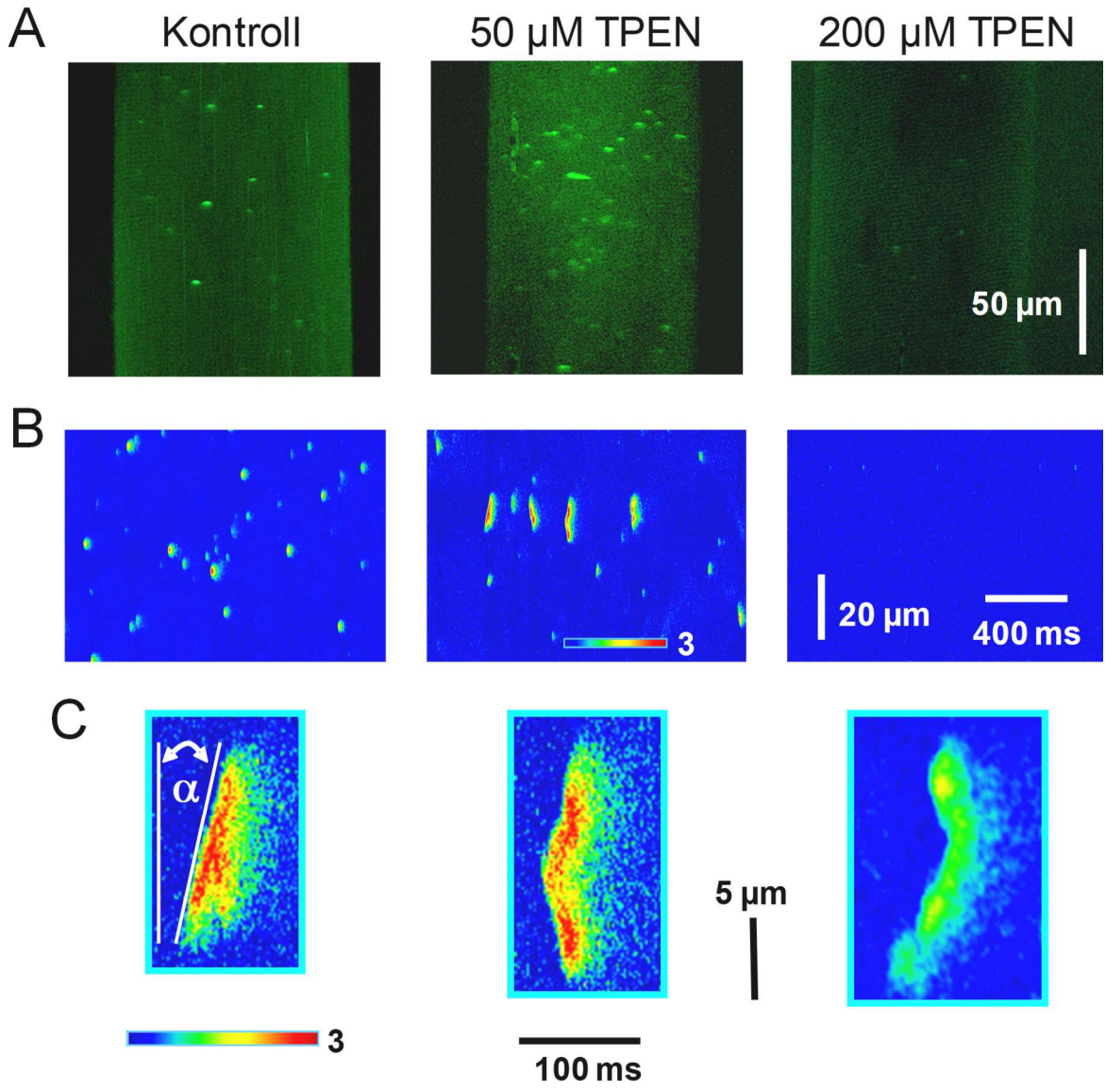
Az előző bekezdésben már említettem, hogy bizonyos körülmények között a *spark*ok keletkezési helyükről tovaterjedhetnek. Ennek részletes vizsgálatára egy kalciumkelátort, a TPEN-t használtuk (Sztretye et al., 2009). A TPEN (N,N,N,N-tetrakisz(2-piridil-metil)-etilén-diamin) egy membránpermeábilis nehézfém-ion kelátképző, amelynek a Ca^{2+}-ra vonatkozó disszociációs állandója hasonló az intracelluláris raktárak kalciumkoncentrációjához. Korábban az intracelluláris nehézfémek és az SR szabad Ca^{2+}-koncentráció modulátoraként használták anélkül, hogy befolyásolná a nanomoláris tartományba eső citoszolikus $[Ca^{2+}]$-t. Szívizmon már bizonyítottuk, hogy a TPEN a pufferelő képességétől függetlenül módosítja a harántcsíkolt izom Ca^{2+}-homeosztázisát (Jung et al., 2007). Lipid kettős rétegben negatív potenciálokon és alacsony $[Ca^{2+}]_i$ mellett a TPEN növelte a RyR nyitvatartási valószínűségét, míg pozitív potenciáloknál gátolta a csatorna aktivitását.

3. táblázat. *Spark*ok jellemző paraméterei TPEN kezelés után

Patkány	n	Amplitúdó (F/F_0)	FWHM (µm)	Hossz (ms)	Frekvencia (1/ms/szarkomer)
Kontroll	574	0,80±0,01	1,52±0,03	41,84±0,63	32±5
50 µM TPEN	159	0,43±0,01*	1,54±0,05	34,81±1,06*	31±14
500 µM TPEN	197	0,32±0,01*	1,09±0,03*	36,68±0,98*	21±26
Béka					
Kontroll	4365	0,92±0,005	2,12±0,01	41,3±0,2	230±50
50 µM TPEN	9885	0,78±0,003*	2,41±0,01*	42,3±0,2*	330±20**
200 µM TPEN	286	0,65±0,03*	1,74±0,04*	30,3±0,8*	90±20**

* és ** szignifikáns különbség a kontrolltól ($p<0,05$ és $p<0,01$)

Békák permeabilizált vázizomrostjain 50 µM TPEN növelte a *spark*ok számát és tovaterjedő eseményeket okozott 273±7 µm/s átlagos terjedési sebességgel (**22. ábra**). Ez az aktiváló hatás azonban patkány vázizomrostokon nem volt megfigyelhető. Az amúgy is alacsony frekvenciával megjelenő *spark*okat a TPEN tovább ritkította emlős izomrostokon (**3. táblázat**).



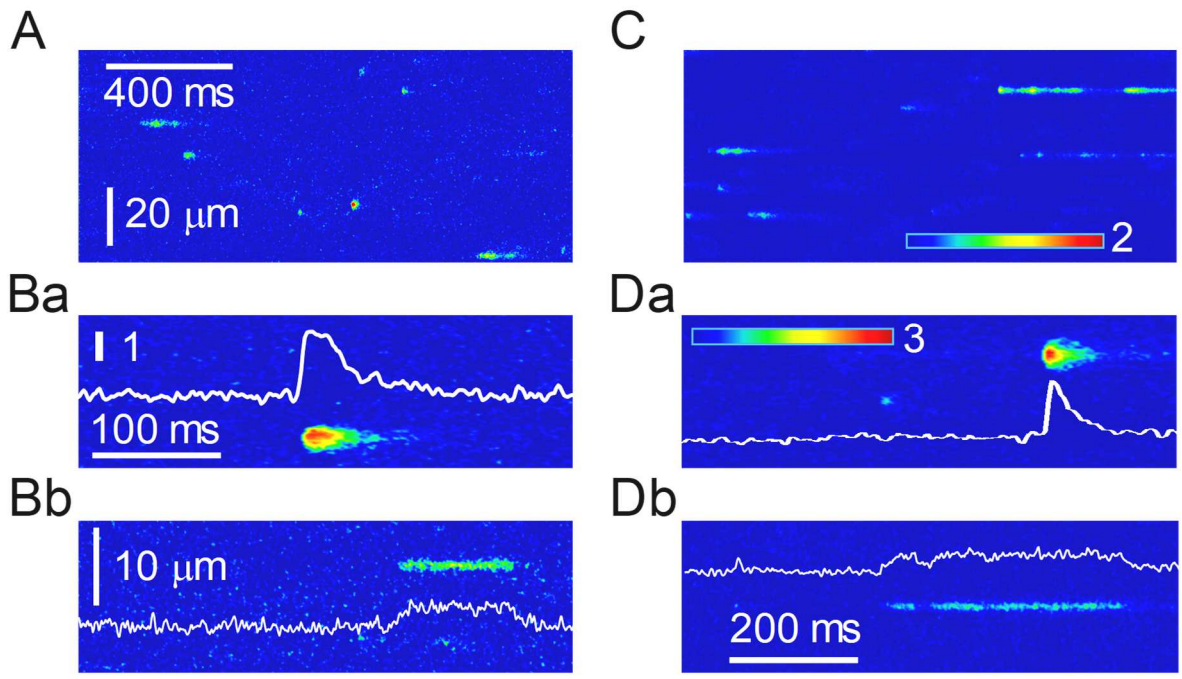
22. ábra. TPEN hatása a *spark*okra béka vázizomrostokban

*Reprezentatív kétdimenziós (**A**) és line-scan (**B**) képek 0, 50 és 200 µM TPEN jelenlétében. (**C**) A tovaterjedő sparkok három jellemző alakja: egyirányú (bal szélső), egy pontból induló kétirányú (középső), két pontból egy irányba terjedő (jobb szélső). A hullámfront szögét (a baloldali képen α) használtuk a terjedés sebességének becsléséhez, ami ennél az eseménynél 299 µm/s-nak adódott.*

A tovaterjedő *spark*ok megjelenése békák vázizomrostjain bizonyítja, hogy a CICR működik kétéltűek vázizmaiban. Ez a megfigyelésünk tovább erősíti azt a feltételezést, hogy a CICR kialakulásának feltétele a békák izmaiban megtalálható, nem feszültség-vezérelt (parajunkcionális) RyR-ek jelenléte. A *spark*ok általunk kiszámolt terjedési sebessége pedig jó becslést ad a kalcium diffúziós sebességére a citoszólban és jól egyezik Zhou és mtsai. (Zhou et al., 2005) által becsült 100-250 μm/s értékkel (Sztretye et al., 2009).

6.2.3 A fenol származék timol hatása az ECRE-kre

Érdekes módon, a TPEN-nel folytatott kísérleteinkben soha nem találtunk *embert* a kalciumfelszabadulási események között patkány izomrostokon. Ezzel szemben, amikor a fenol származék timollal kezeltük az emlős izomrostokat, nagyszámú alacsony amplitúdójú hosszú eseményt láttunk (Szentesi et al., 2004). Erre a szerre azért esett a választásunk, mert a folyékony halotán altatószer stabilizáló szere és a



23. ábra. Timol hatása az ECRE-kre patkány vázizomrostokban

*Reprezentatív line-scan képek 0 (**A, Ba, Bb**) és 30 μM Timol (**C, Da, Db**) jelenlétében. Az idő- és kiterjedés skála az **A** és **B** panelen azonos. Az idő- és kiterjedés skála a **Ba** és **Bb** panelen azonos. Az időskála a **Da** és **Db** panelan azonos, míg a kiterjedés skála ezeken megegyezik a **Bb** paneléval. Az **A** panel fluoreszcencia intenzitás skálája megegyezik a **C** panelével, míg a **Ba**, **Bb** és **Db** panelé a **Da** panelével.*

malignus hipertermiás betegek altatása közben szerepet játszhat a műtétek alatt tapasztalt kórkép kialakításában. Mivel a timolról is kimutattuk, hogy a lipid kettősrétegbe ültetett RyR1-t aktiválja, ezért megvizsgáltuk hatását a permeabilizált emlős vázizomrostokon kialakuló elemi kalciumfelszabadulási eseményekre.

Kontroll körülmények között az elemi események mintegy 63% volt *spark*, míg a maradék események vagy tisztán *ember*, vagy a két esemény típus keverékeként jelentek meg (**23. ábra**). Timol alig változtatta meg az események frekvenciáját (58,7±2,0 1/ms/szarkomer-ről 65,4±1,6 1/ms/szarkomer-re), de csökkentette amplitúdójukat és megnövelte a hosszukat (**4. táblázat**). Timol jelenlétében nagyon hosszan tartó eseményeket is regisztráltunk (**23Db. ábra**). Ezek valószínűleg a csatorna kapuzásának a szer okozta azon változásának a következményei, amit a lipid kettősrétegben végzett kísérletek során hosszan tartó csatorna-nyitásoknak láttunk. Az a tény, hogy ilyenkor a kalciumfelszabadulási események majdnem állandó fluoreszcencia változást és lényegében azonos térbeli szélességet mutattak az egész esemény alatt, azt jelenti, hogy a felszabaduló kalcium a diffúzióval és a kalcium kötőhelyekhez való kötődésével elérte egyensúlyi állapotát. Ezek az eredmények közvetlen kísérleti bizonyítékot szolgáltatnak arra vonatkozóan, hogy egyetlen rianodin csatorna megnyílása *ember*t eredményez, nem pedig *spark*ot emlősök vázizomrostjában. Továbbá a különböző típusú események alatt felszabadult kalcium mennyiségéből az is megbecsülhető volt, hogy kb. 30 csatorna egyidejű megnyílása hoz létre egy átlagos *spark*ot (Szentesi et al., 2004).

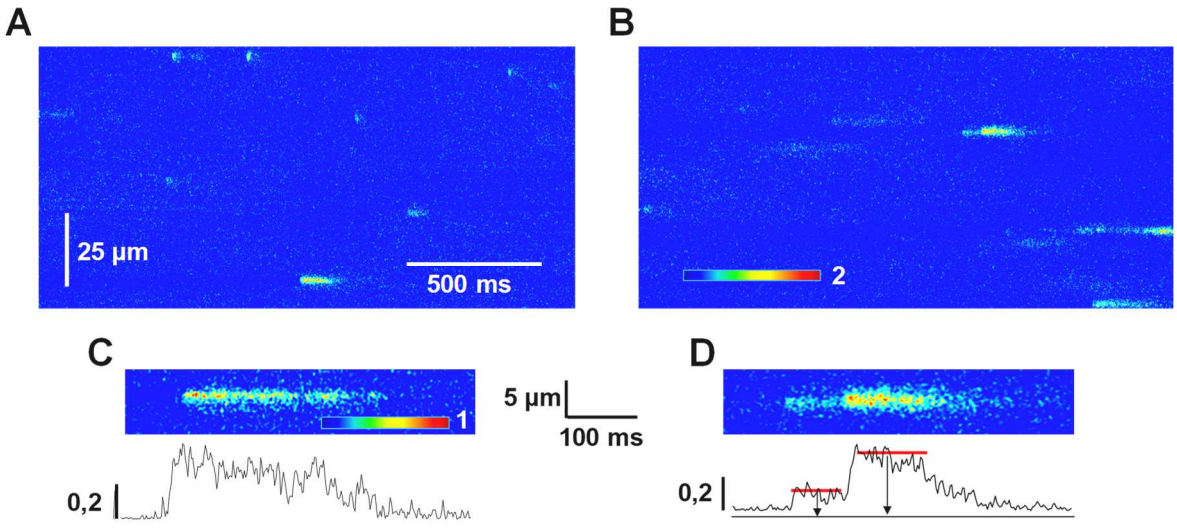
4. táblázat. **Timol hatása az ECRE-k paramétereire**

	Kontroll		**30 µM timol**	
	Spark (n=1576)	***Ember*** (n=454)	***Spark*** (n=1605)	***Ember*** (n=873)
Amplitúdó (F/F_0)	0,92±0,01	0,21±0,01	0,70±0,01*	0,17±0,01*
FWHM (µm)	1,81±0,03	1,76±0,03	1,74±0,01*	1,77±0,02
TTP (ms)	9,4±0,1	-	9,6±0,1	-
Hossz (ms)	56±1	87±2	79±1*	102±2*

* szignifikáns különbség a kontrolltól ($p<0,05$). *Ember*eknél az átlagos amplitúdót adjuk meg.

6.2.4 A benzotiazepin származék K-201 hatása az ECRE-kre

A timolhoz hasonlóan, a klinikai gyakorlatban használt számos vegyületről írták már le, hogy befolyásolja az intracelluláris [Ca^{2+}]-t. Ezek közül mi az antiaritmiás hatású benzotiazepin származék K-201 hatásait vizsgáltuk a RyR1-re (Almassy et al., 2008). A lipid kettős rétegekbe ültetett csatornán a K-201 két szubkonduktancia állapotot hozott létre pozitív potenciáloknál, míg negatív potenciáloknál ez nem volt



24. ábra. K-201 hatása az ECRE-kre patkány vázizomrostokban

*Reprezentatív line-scan képek 0 (**A**) és 1 µM K-201 (**B**) jelenlétében. Reprezentatív ember időbeli profiljával 0 (**C**) és 1 µM K-201 (**D**) jelenlétében. A **D** panelen az ember line-scan alatti időprofilján jól látszik a két piros vonallal jelölt szubkonduktancia szint. Az idő- és kiterjedés skála valamint a fluoreszcencia intenzitás skála az **A** és **B** panelen azonos. A **C** és **D** panel idő- és kiterjedés skálája a két panel között látható. A **D** panel fluoreszcencia intenzitás skálája megegyezik a **C** paneléval.*

megfigyelhető. A K-201 megváltoztatta az elemi kalciumfelszabadulási események gyakoriságát emlős vázizomrostokban: a *spark*ok frekvenciája lecsökkent, míg az *ember*eké nőtt (**5. táblázat**). Továbbá különböző amplitúdójú illetve lépcsős *ember*ek jelentek meg a szer hozzáadása után a RyR1 szubkonduktancia állapotainak megfelelően (**24. ábra**), amelyek nem voltak figyelhetők kontroll körülmények között.

1 µM K-201 szignifikánsan csökkentette a *spark*ok amplitúdóját (**5. táblázat**), ami arra utal, hogy az eseményhez hozzájáruló csatornák átlagos száma jelentősen csökkent. Az ismert, hogy az ECRE nincs jelen ép emlős rostokon, ezért az aktiválódó

csatornák számának csökkenése úgy is értelmezhető, mint a szernek a csatornát stabilizáló hatása. Mivel a szerről kimutattuk azt, hogy a SERCA-ra is hat, az ECRE-k számára és morfológiájára gyakorolt hatását nem tekinthetjük csak a RyR1-re kifejtett hatásnak. A kísérletsorozat zárásaként megvizsgáltuk a szert postinfarktusos patkányok vázizomrostjain is és a kontroll állatokhoz hasonló eredményeket kaptunk (Almassy et al., 2008).

5. táblázat. **K-201 hatása az ECRE-k paramétereire**

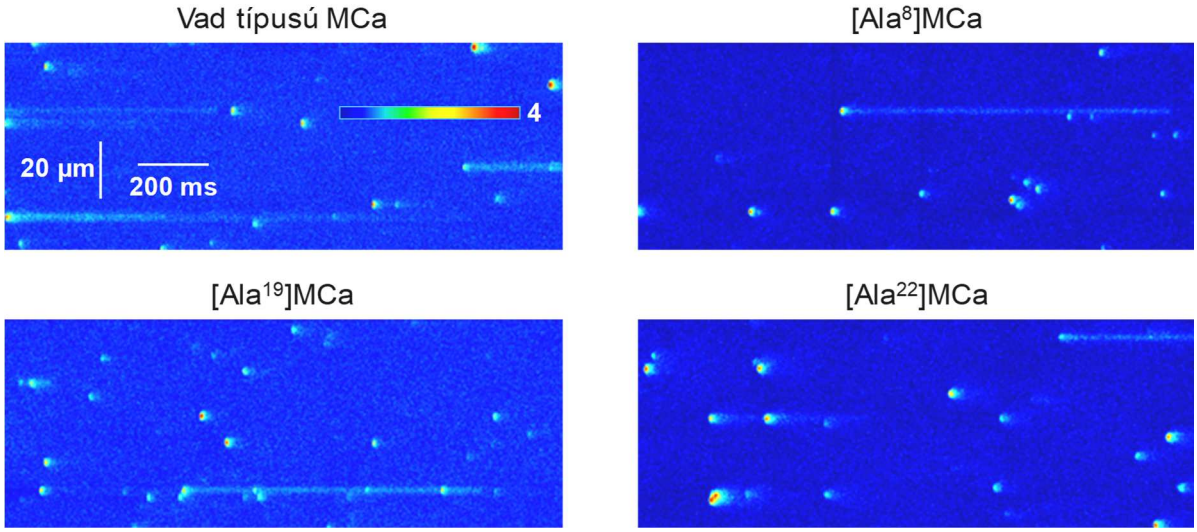
	Kontroll		**1 µM K-201**	
	Spark (n=2182)	***Ember*** (n=564)	***Spark*** (n=798)	***Ember*** (n=1050)
Frekvencia (1/ms/szarkomer)	39±1	11±1	23±1*	23±1*
Amplitúdó (F/F_0)	0,78±0,01	0,21±0,01	0,63±0,01*	0,23±0,01
FWHM (µm)	1,64±0,01	1,86±0,02	1,68±0,02	1,95±0,04
Hossz (ms)	34,6±0,4	87,9±0,4	35,6±0,6	88,6±2,1

* szignifikáns különbség a kontrolltól ($p<0,05$). *Ember*eknél az átlagos amplitúdót adjuk meg.

6.2.5 Egy skorpió toxin hatása az ECRE-kre

Az ECRE-k farmakológiai befolyásolhatóságának vizsgálatát egy skorpió toxinnal folytattuk (Lukács et al., 2008). A *Scorpio maurus palmatus* toxinjából izolált 33 aminosavból álló Maurokalcin (MCa) fehérje azért került az izomkutatók érdeklődésének középpontjába, mert aminosav szekvenciája nagyon hasonlít a dihidropiridin receptor azon részéhez, amivel a rianodin receptorhoz kötődik.

Munkánk során patkányok és békák vázizomrostjain vizsgáltuk a toxin kalciumfelszabadulásra kifejtett hatásait. A MCa (50 nM) adagolásának kezdetén, akut hatásként fokozódott a csatorna megnyílás, ami az elemi események megnövekedett számában mutatkozott meg (**25. ábra**). A *spark*ok átlagos amplitúdója a kontroll 0,86+0,01 F/F_0-ról (n=1576) 0,46+0,01 F/F_0-ra (n=1821) csökkent MCa hatására, mert a toxin egy csökkentett vezetőképességű, bár tartósan meglévő csatornaállapotot hozott létre a RyR1-on, miközben az FWHM változatlan maradt (kontroll: 1,84+0,03 µm; MCa adagolás után: 1,84+0,02 µm). A toxin hosszan tartó alkalmazása az izomrostokon olyan ritkán kialakuló, de hosszantartó (301+12 ms, n=102)



25. ábra. MCa és mutánsainak hatása a spontán ECRE-kre békák izomrostjain

Reprezentatív line-scan képek 50 nM toxin jelenlétében. A bal felső panelen levő skálák minden panelre vonatkoznak. [Ala^{8}]MCa, [Ala^{19}]MCa, [Ala^{22}]MCa a 8-, 19- és 22-es aminosav Alaninra való mutációval létrejött toxint jelöli.

kalciumfelszabadulási eseményeket hozott létre, amelyek egyáltalán nem voltak megtalálhatóak kontroll körülmények között (**25. ábra**). Egy korábbi kutatás felhívta a figyelmet a MCa 24. pozíciója körüli aminosavakra, mint lehetséges kölcsönhatási helyekre a peptid RyR1-hez kötődése során (Estève et al., 2003). Ezért megvizsgáltuk e pozíció és tőle távolabbi aminosavak Alaninra történő cseréjének hatását a toxin aktivitására. Az [Ala^{24}]MCa mutáns még a magas 500 nM-os koncentrációban sem befolyásolta az elemi Ca^{2+}-felszabadulási eseményeket és nem alakultak ki *ember*ek sem. Ahogy távolodott a mutáció a 24. aminosavtól, egyre több *ember* alakult ki (**25. ábra**).

6. táblázat. A mutáció helyének hatása az *ember*ek hosszára

MCa fajtája	**Vad típus** (n=258)	**[Ala^{8}]MCa** (n=65)	**[Ala^{19}]MCa** (n=267)	**[Ala^{22}]MCa** (n=86)
Hossz (ms)	628,1±26,9	532,6±47,6	515,1±21,6*	312,3±34,2*

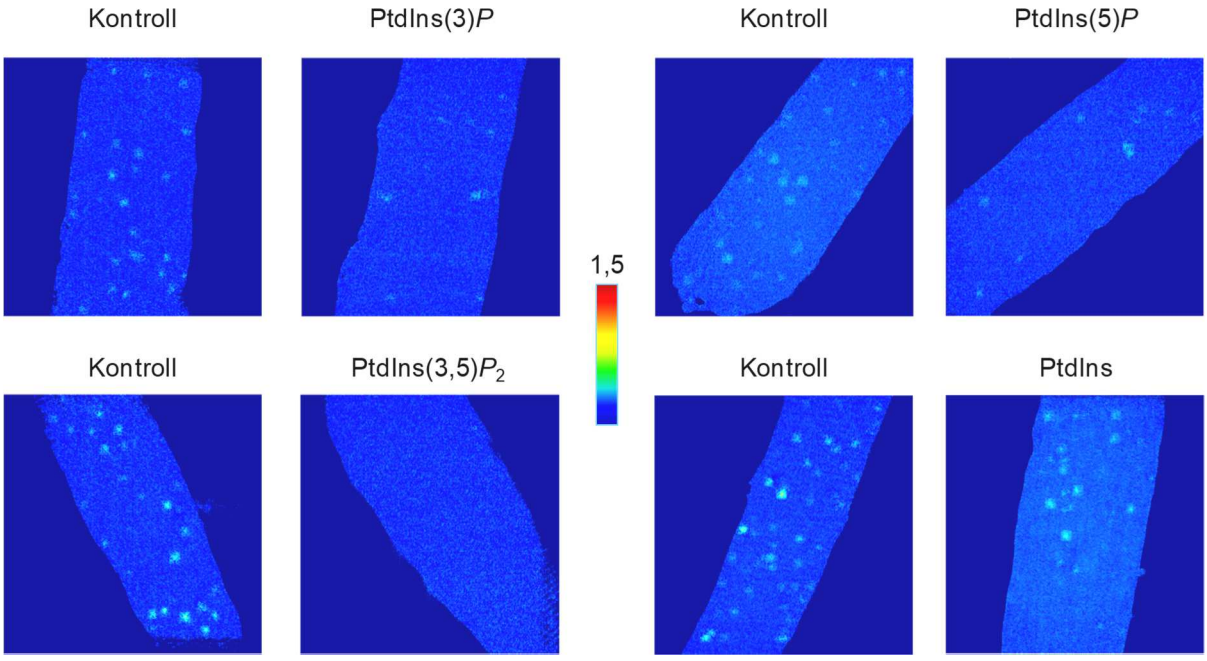
* szignifikáns különbség a vad típustól ($p<0,05$).

Ezek az eredmények azt bizonyítják, hogy a Maurocalcin aktiválja RyR1-t, így fokozza a Ca^{2+}-felszabadulást a belső kalciumraktárból. Aminosavcserével módosítható a toxin hatékonysága: például az [Ala^{24}]MCa mutánsnak a receptorkötődésben szerepet játszó fehérjeszakasza annyira megváltozik, hogy a

toxin elveszíti a RyR1 aktiválásához szükséges képességét. Azonban ha a mutáció helye távolodik a 24. aminosavtól, a toxin hatása egyre jobban megközelíti a vad típusú peptidét (**6. táblázat**) (Lukács et al., 2008).

6.2.6 A foszfatidilinozitol foszfát hatása az ECRE-kre

Eddig bemutatott vizsgálatainkban exogén szerek hatását tanulmányoztuk az ECRE-kre. Azonban néhány kórfolyamat hatására egyes endogén ligandok szintje is változhat és hatással lehet az $[Ca^{2+}]_i$-ra, így az elemi kalciumfelszabadulási eseményekre is. Egy súlyos genetikai izombetegségben, az X-kapcsolt miotubuláris miopátiában a MTM1-t (miotubularin) kódoló gén mutációit írták le (Bolis et al., 2007). A foszfatidilinozitol foszfát (PtdInsP) foszfatázok szubsztrátjai vagy hidrolizált termékei az MTM1-nek. Így az egyik kézenfekvő magyarázat az ECC hibás működésére, a MTM1 PtdInsP-foszfatáz aktivitás megváltozása lehet. Ezt Shen és mtsai. (Shen et al., 2009) eredményei is alátámasztják, akik egy másik PtdInsP-foszfatáz (MTMR14) elvesztésével magyarázták az izom intracelluláris Ca^{2+}-homeosztázisának változását.



26. ábra. PtdInsP-k hatása a spontán ECRE-kre egerek permeabilizált izomrostjain

Reprezentatív ECRE aktivitás összegezve 200 db egymást követő konfokális képen kontroll oldatban és a megadott PtdInsP jelenlétében. Minden kép 84×84 µm méretű. A panelek közötti fluoreszcencia intenzitás skála mindegyik képre vonatkozik.

Ezért megvizsgáltuk, hogy a PtdInsP-k fiziológiás körülmények között részt vesznek-e a $[Ca^{2+}]_i$ és ECC szabályozásában egészséges izomban (González Rodríguez et al., 2014).

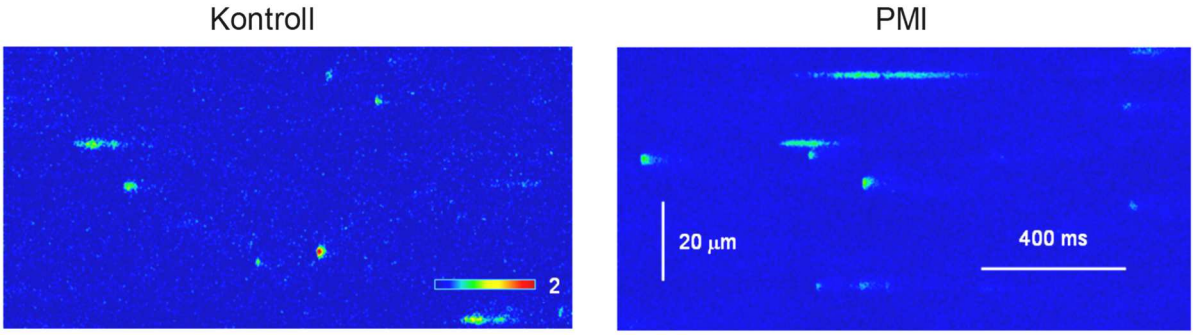
Permeabilizált egér vázizomrostokon jelentősen csökkent az észlelt ECRE-k száma PtdIns(3,5)P_2, PtdIns(3)P és PtdIns(5)P jelenlétében és a legnagyobb hatást a PtdIns(3,5)P_2 esetén találtuk (**26. ábra**). Az átlagos ECRE amplitúdó enyhén, de szignifikánsan megnövekedett PtdIns(5)P jelenlétében, míg az FWHM mind az x, mind az y irányban ~10%-kal csökkent PtdIns(3,5)P_2 jelenlétében. Összességében a tesztelt PtdInsP-k csak kismértékben befolyásolták az ECRE-k amplitúdóját és térbeli tulajdonságaikat, miközben jelentősen csökkentették az események előfordulását. Az eredmények alátámasztják azt a lehetőséget, hogy az MTM1 szubsztrátok kóros felhalmozódása csökkentheti a rianodin receptoron keresztüli Ca^{2+}-felszabadulást, ezáltal hozzájárulhatnak a csökkent izomműködés kialakulásához (González Rodríguez et al., 2014).

6.3 Elemi események nem fiziológiás körülmények között

6.3.1 ECRE-k szívinfarktuson átesett patkányok harántcsíkolt izmain

Sajnos vannak olyan nem vázizmokat érintő kórfolyamatok, amelyek közvetve kihatnak az izmok működésére és így megváltoztathatják annak kalciumhomeosztázisát is. Ezek közül mi először a szívinfarktus vázizomra kifejtett hatásait vizsgáltuk egy patkány modellben. Ez az egyik legsúlyosabb kórkép a szív- és érrendszeri betegségek között halálozási szempontból. A felnőtt lakosságban a szívinfarktus okozza a halálesetek 20%-át. Krónikus szívelégtelenségben a vázizmok olyan gyengesége alakul ki, amely nem a keringési funkciók zavarához kapcsolódik, hanem maguknak a vázizomrostoknak az elváltozásához. Ennek tanulmányozására baloldali koronária szűkítésen átesett patkányokat használtunk 24 héttel a beavatkozást követően (Szigeti et al., 2007).

Az infarktuson átesett (PostMyocardial Infarction: PMI) állatok vázizomrostjaiban az elemi kalciumfelszabadulási események morfológiája megváltozott, az *ember*ek relatív aránya megnőtt (**27. ábra**). A *spark*ok kisebb amplitúdójúak voltak és a csúcs eléréséhez szükséges idő meghosszabbodott, vagyis lassabban alakultak ki. Továbbá az egy *spark* alatt kiáramlott Ca^{2+} mennyisége (Signal Mass, SM) lecsökkent a PMI állatokban (**7. táblázat**).



27. ábra. Szívinfarktus hatása a spontán ECRE-kre patkányok permeabilizált izomrostjain

Reprezentatív line-scan képek kontroll és infarktuson átesett (PMI) patkányok vázizomrostjain. A skálák mindkét panelre vonatkoznak.

7. táblázat. A szívinfarktus hatása az ECRE-k paramétereire

	Spark		***Ember***	
	Kontroll (n=1284)	**PMI** (n=937)	**Kontroll** (n=454)	**PMI** (n=765)
Amplitúdó (F/F_0)	0,81±0,01	0,48±0,01**	0,21±0,004	0,17±0,003*
TTP (ms)	12,4±0,2	14,6±0,3*	-	-
FWHM (μm)	1,72±0,02	1,66±0,02*	1,78±0,02	1,81±0,02
Hossz (ms)	34,6±0,4	35,6±0,6	87,9±0,4	88,6±2,1
SM (μm^3)	2,59±0,24	1,42±0,25**	-	-

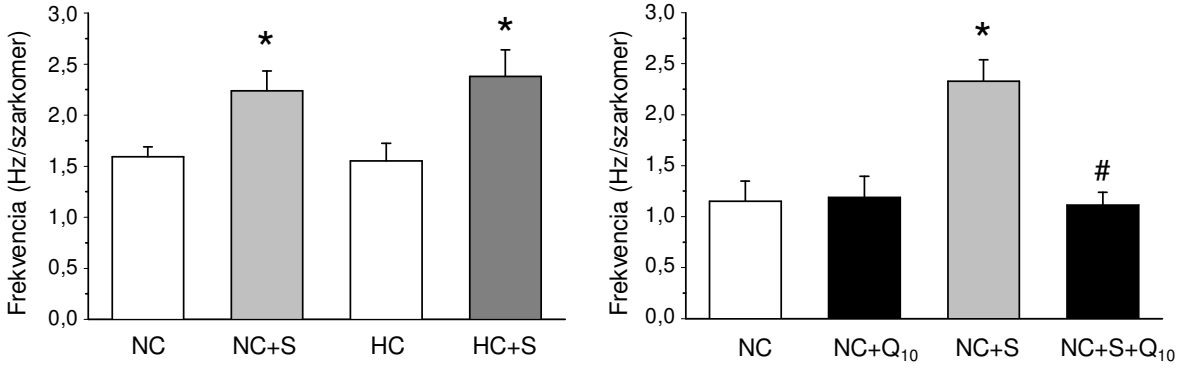
* és ** szignifikáns különbség a kontrolltól ($p<0,05$, $p<0,01$). *Ember*eknél az átlagos amplitúdót adjuk meg.

Ezek a megfigyelések azt mutatják, hogy egy kalciumfelszabadulási esemény során megnyíló csatornák száma lecsökkent, és a RyR1 működése megváltozott, így a kalciumfelszabadulás kisebb vázizomban szívinfarktus után. Eredményeink magyarázatot adnak a károsodott vázizomműködésre a PMI állatokban (Szigeti et al., 2007).

6.3.2 ECRE-k hiperkoleszterinémiás patkányok harántcsíkolt izmain

Egy másik népbetegség, a hiperkoleszterinémia és a kezelésére használt statinok vázizmokra kifejtett hatását is vizsgáltuk szintén egy állatmodellben (Vincze et al., 2015). A magas vér koleszterinszint, az elhízás és az érelmeszesedés sok embert érintő egészségügyi probléma. Elősegítik az olyan szív- és érrendszeri betegségeket, mint a koszorúér-szűkület, szívizom ischaemia vagy az infarktus és a stroke. Világszerte a statinok a legelterjedtebb és leghatékonyabb gyógyszerek a koleszterinszint csökkentésére. A szérum koleszterin-szintet akár 50%-al képesek csökkenteni. A statin-kezelés jótékony hatásai mellett számos mellékhatással is jár, leggyakrabban a különféle izmokat érintők fordulnak elő (10%). A rabdomiolízis a statin-terápia legsúlyosabb és potenciálisan életveszélyes mellékhatása. Ez az izomszövet akut károsodása, ami során a sérült izomsejtek egyes alkotói (pl. kreatin kináz, mioglobin, K^+) a keringésbe jutnak. Ezt az állapotot modellező állatkísérletben tanulmányoztuk az ECRE-k előfordulását és paramétereinek változását a hiperkoleszterenémia és a statin kezelés hatására. A vizsgálatainkat kiegészítettük a koenzim Q_{10} (ubiquinon, CoQ_{10}) szerepének tisztásával, mivel a statinok gátolják a CoQ_{10} szintézisét is. A statin-miopátiás betegeken történő CoQ_{10} alkalmazásról szóló tanulmányok eddig nem tudták egyértelműen bizonyítani a terápia jótékony hatását.

Kísérleteink során a fluvastatint és/vagy a koenzim Q_{10}-et krónikusan adtuk normokoleszterolémiás vagy hiperkoleszterolémiás patkányoknak, és a kalciumhomeosztázis módosulásait vizsgáltuk. Míg a hiperkoleszterolémia nem változtatta meg a *spark*ok előfordulásának gyakoriságát, a fluvastatin növelte azt mind a normokoleszterinémiás mind a hiperkoleszterinémiás patkányok izomrostjain (**28. ábra**).



28. ábra. A statin és Q_{10} kezelés hatása a *spark*ok frekvenciájára patkányok permeabilizált izomrostjain

*NC: normokoleszterinémiás; HC: hiperkoleszterinémiás; +S: statinnal kezelt; +Q_{10}: Q_{10}-zel kezelt. *: szignifikáns különbség a statinnal nem kezelt csoporthoz képest (p<0,05). #: szignifikáns különbség a Q_{10}-zel nem kezelt csoporthoz képest (p<0,05*

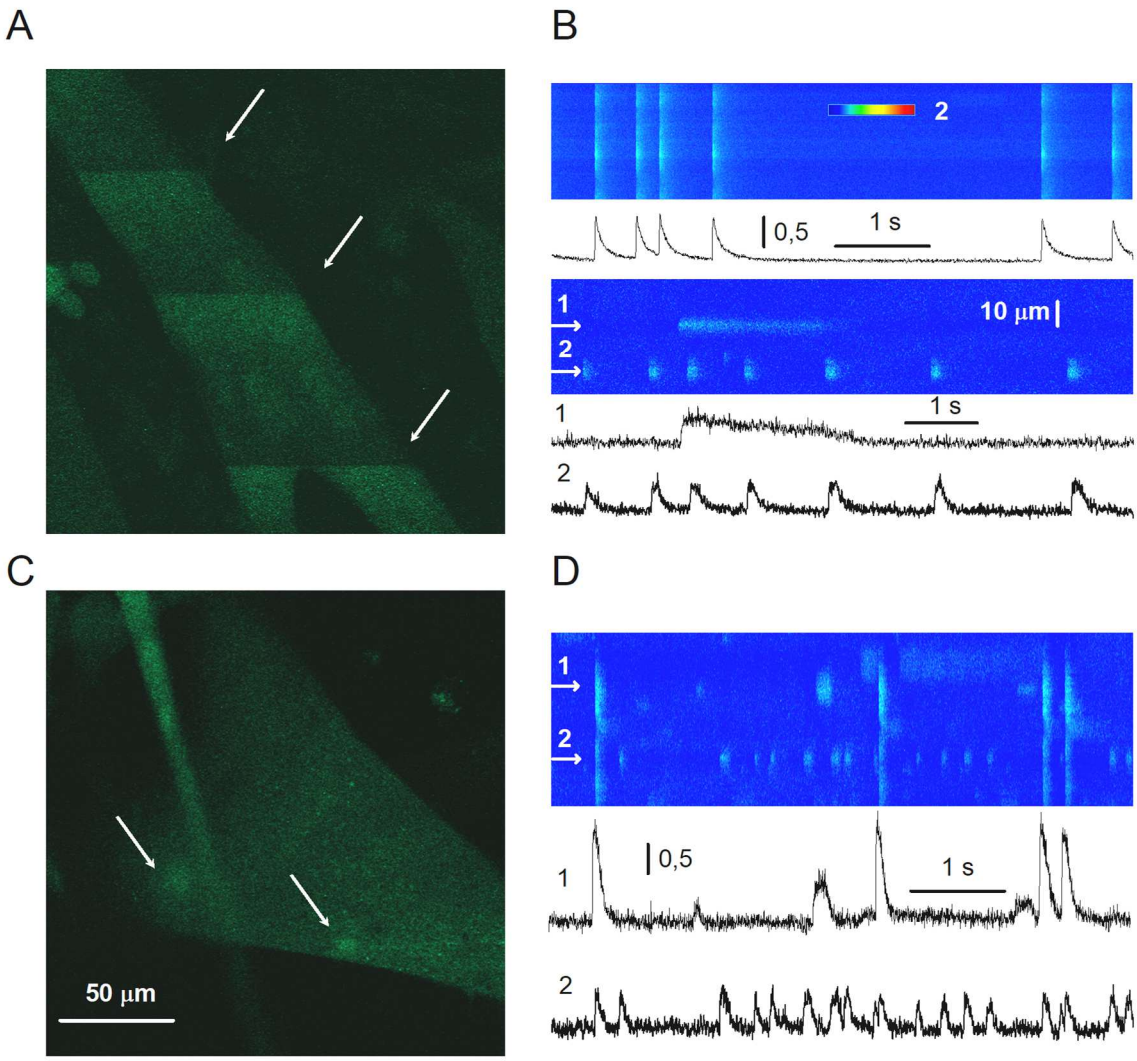
Azonban a koenzim Q_{10} kezelés jelentősen csökkentette a spontán kalciumfelszabadulási események gyakoriságát (**28. ábra**), de nem befolyásolta amplitúdójukat és térbeli kiterjedésüket a fluvastatinnal kezelt patkányok izomrostjaiban. Viszont nem változtatta meg a *spark*ok frekvenciáját normokoleszterinémiás állatok vázizmában (**28. ábra**). Ez azt jelzi, hogy a koenzim Q_{10} kezelés megakadályozta a *spark*ok frekvenciájának fluvastatin hatására történő növekedését anélkül, hogy jelentősebb hatása lett volna az egy esemény során felszabaduló kalcium mennyiségre. Összefoglalva, azt találtuk, hogy a fluvastatin, függetlenül a vér koleszterinszintjétől, következetesen és kifejezetten növelte a kalcium *spark*ok gyakoriságát a vázizomrostokban, amely hatás talán megelőzhető a koenzim Q_{10} étrendbe történő hozzáadásával.

Eredményeink alátámasztják az intracelluláris Ca^{2+}-koncentráció szerepét a statin kezelés által kiváltott miopátiában és egy lehetséges utat mutatnak a koenzim Q_{10} használatára a betegek vázizomtüneteinek enyhítésére (Vincze et al., 2015).

6.4 Elemi események változása génmódosítás hatására vázizomban

6.4.1 A Triadin fehérje szintjének hatása az ECRE-kre tenyésztett harántcsíkolt izomsejtekben

A génmódosítás technika megjelenésekor és a genetikailag módosított állatok széleskörű elterjedése előtt sejttenyészeteken folytak a kutatások. Mi is végeztünk ilyen jellegű vizsgálatokat immortalizált vázizom eredetű sejtvonalon (C2C12) és



29. ábra. Spontán Ca^{2+} tranziensek és ECRE-k patkány primér miotubulusokon

*Reprezentatív XY (**A**, **C**) és line-scan (**B**, **D**) képek kontroll (**A**, **B**) és shRNS-el csökkentett Triadint expresszáló (**C**, **D**) miotubulusokon. Az XY képeken a nyilak a spontán eseményekre mutatnak. A line-scan képeken a számozott nyilakkal jelölt vonalak mentén számolt intenzitásváltozás látható a képek alatt.*

frissen izolált vázizom sejtekből indított tenyészeten (primer sejtkultúra). Ezekben az izomsejtekben végzett kísérletekben a vizsgálatok célja a Triadin nevű fehérje szerepének tisztázása volt (Fodor et al., 2008).

A Triadin, az SR membránban található fehérje (Caswell et al., 1991), egy rövid N-terminális része van a citoszolban és egy hosszú C-terminális az SR lumen belsejében (Marty et al., 1995). 95 kDa-os izoformája (Trisk95) a vázizomban az SR terminális ciszternái junkciós membránjában helyezkedik el (Marty et al., 1995) és a vizsgálatok alapján kötődik mind a kalszekvesztrinhez (CSQ), mind a RyR1-hez (Caswell et al., 1999). Ő lehet a CSQ és a RyR1 közötti kapcsoló molekula, amely segítségével a kalszekvesztrin a kalciumcsatornát szabályozza (Beard et al., 2002).

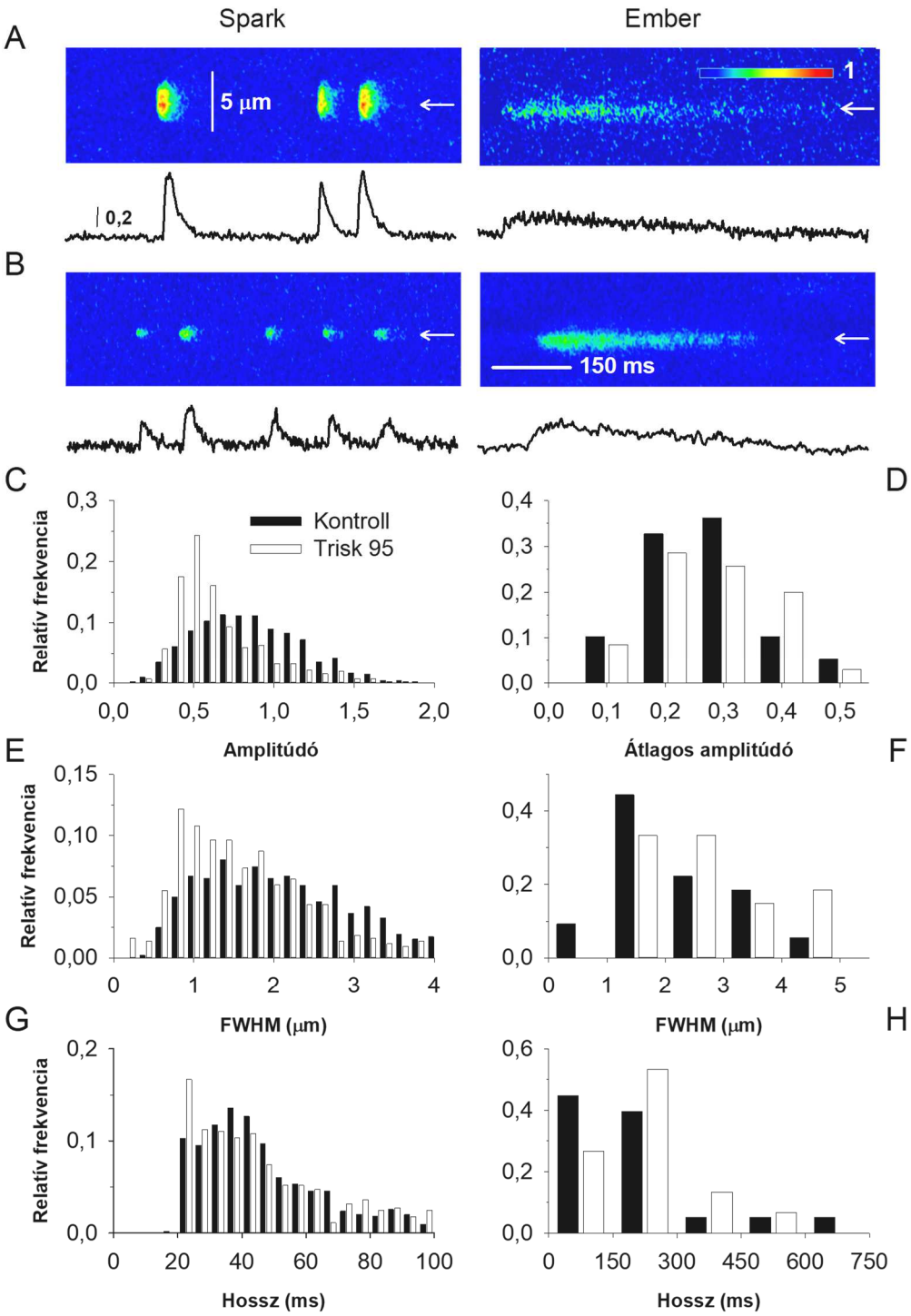
Először shRNS technikával csökkentettük a Triadin szintjét majd transzfekcióval túltermeltettük a fehérjét (overexpresszáltuk) a miotubulusokban.

A kontroll miotubulusokon spontán kalciumtranzienseket lehetett megfigyelni mind XY (**29A. ábra**) mind line-scan képeken (**29B. ábra**). Azonban ECRE-k csak elvétve voltak megtalálhatóak, bár ritkán *spark*okat és *ember*eket is megfigyelhettünk (**29B. ábra alsó kép**). A Triadin expressziójának csökkentése drámaian megnövelte az ECRE-k előfordulását a miotubulusokon mind XY (**29C. ábra**), mind line-scan mérésekben (**29D. ábra**). Kalciumtranziensek továbbra is megjelentek hasonló frekvenciával (0,99±0,16 Hz), mint a kontroll (1,01±0,22 Hz) sejtekben. Azonban a tranziensek amplitúdója több mint kétszeresére nőtt (0,62±0,05 F/F_0-ról 1,39±0,08 F/F_0-ra) a transzfektált sejtekben. A *spark*ok és *ember*ek amplitúdójában hasonló emelkedést találtunk (**8. táblázat**) és számuk is nőtt, addig az események hosszában nem volt lényeges különbség (**8. táblázat**).

8. táblázat. ECRE-k paraméterei Triadin shRNS-el kezelt miotubulusokon

	Spark		***Ember***	
	Kontroll (n=143)	**Triadin shRNS** (n=649)	**Kontroll** (n=23)	**Triadin shRNS** (n=117)
Amplitúdó (F/F_0)	0,49±0,03	0,89±0,04**	0,27±0,05	0,49±0,03**
Hossz (ms)	39,7±4,3	44,0±2,5	229±33	198±13

** szignifikáns különbség a kontrolltól ($p<0,01$). *Ember*eknél az átlagos amplitúdót adjuk meg.



30. ábra. A Triadin overexpresszió hatása az ECRE-kre C2C12 miotubulusokon

*Reprezentatív line-scan képek kontroll (**A**) és Triadint overexpresszáló (**B**) miotubulusokon. Sparkok (**C**, **E**, **G**) és emberek (**D**, **F**, **H**) paramétereinek eloszlásai. Az A és B panelen a line-scan képek alatti vonalas ábrák a képeken nyíllal jelölt sorokból számolódottak.*

A Triadin túltermeltetése a sejtekben az előzőekben bemutatotthoz képest ellentétes hatást gyakorolt a kalciumfelszabadulási eseményekre. A C2C12 sejtekben is találtunk *spark*okat és *ember*eket is úgy, mint a primér vázizomsejteken (**30. ábra**). Míg a fehérje túltermeltetése csökkentette a *spark*ok amplitúdóját (0,81±0,01 F/F_0-ról 0,59±0,01 F/F_0-ra, $p<0,001$; **30CD. ábra**), addig az események többi paraméterén nem változtatott jelentősen (**30E-H. ábra**).

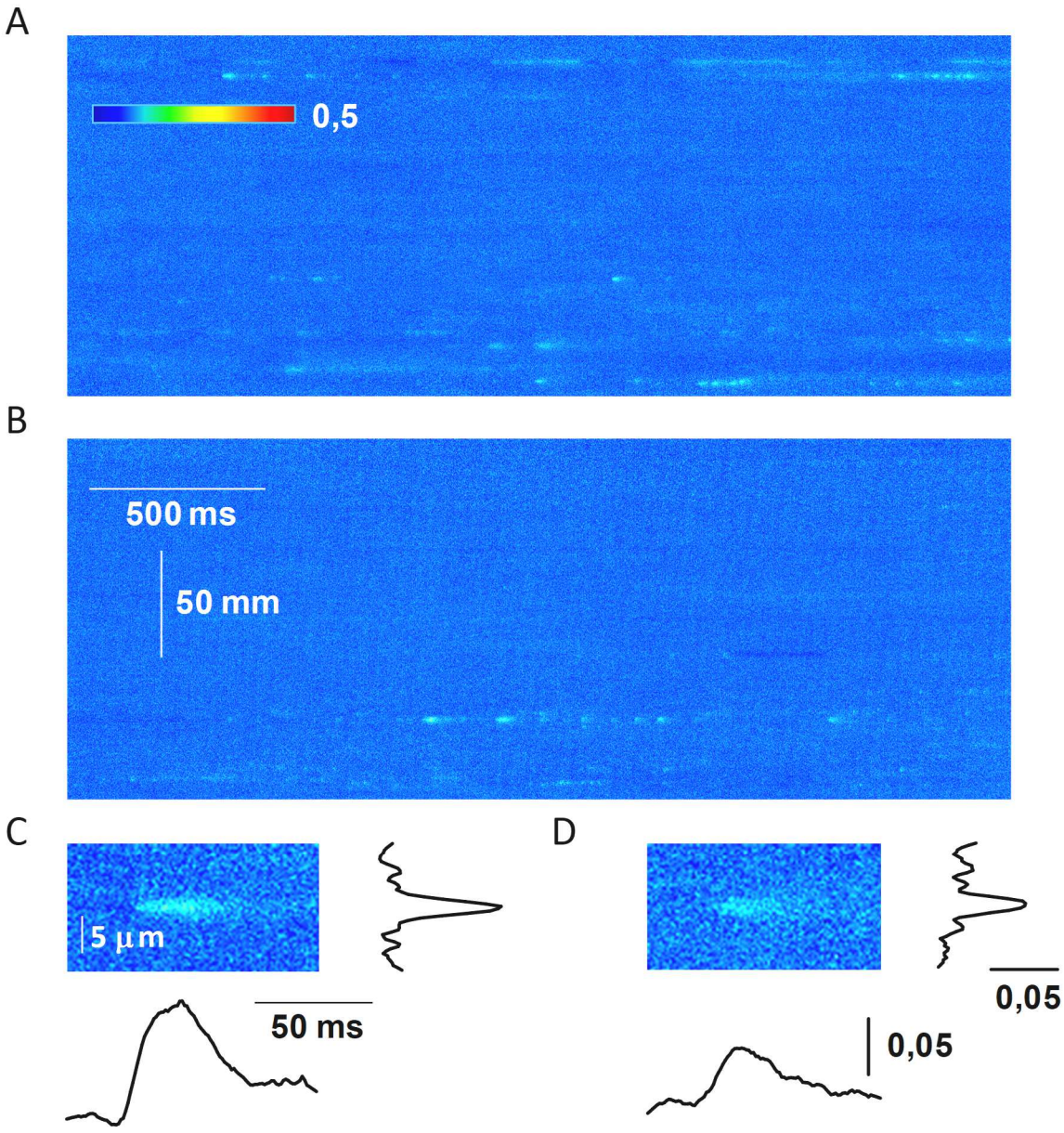
Hasonló eredményeket kaptunk Triadint overexpresszáló primér patkány miotubulusokon is. Mivel a fehérje túlzott expressziója csökkentette az SR-ből a kalciumfelszabadulást és a Triadin transzlációjának gátlása növelte a kalciumfelszabadulási események frekvenciáját és amplitúdóját, így megfigyeléseink egyértelműen alátámasztják azt az elképzelést, hogy a Triadin a RyR1 nyitásának negatív szabályozója lehet (Fodor et al., 2008).

6.4.2 ECRE-k a természetes mutációval kialakult hipermuszkuláris egerek harántcsíkolt izomrostjaiban

Sejttenyészetek után egy természetes mutációval kialakuló túlzott izomtömeget mutató (hipermuszkuláris, miosztatin hiányos) egértörzzsel folytattuk az elemi események vizsgálatát (Bodnár et al., 2014). A miosztatin (Mstn) egy extracelluláris citokin és a transzformáló növekedési faktor-béta (TGF-β) szupercsaládba tartozik. A széleskörűen elfogadott nézet szerint nagyon fontos negatívan szabályozó szerepet tölt be a vázizom növekedésében (McPherron et al., 1997). Mstn hiányos egereket (Cmpt mutáció) összehasonlítva a kontroll állatokkal, jelentős izomtömeg növekedést és zsírszövet csökkenést találtak (Hamrick et al., 2006). Azonban a várakozásokkal ellentétben, a megnövekedett izomtömeg nem jár nagyobb fizikai teljesítménnyel (Amthor et al., 2007). Hasonló változások megtalálhatóak a Mstn természetes mutációját hordozó szarvasmarhák, kutyák, juhok és emberek esetében is (Clop et al., 2006; Grobet et al., 1997; Mcpherron & Lee, 1997; Mosher et al., 2007).

Hogy tisztázzuk a Cmpt egerekben megfigyelt gyengébb fizikai teljesítmény okát, megvizsgáltuk ezen állatok vázizomrostjainak kalciumhomeosztázisát. Mivel a KCl-al és depolarizációval kiváltott kalciumtranziensek amplitúdója is kisebb volt a Cmpt vázizomrostokban, elemi kalciumfeszabadulási eseményeket mértünk enzimatikusan izolált FDB rostokon. Habár a Cmpt vázizomrostokon is találtunk spontán elemi eseményeket (**31. ábra**), a jellemző paramétereik jelentősen eltértek a kontroll

állatokhoz képest (**9. táblázat**).



31. ábra. ECRE-k kontroll és Cmpt egerek vázizomrostjain

Reprezentatív line-scan képek kontroll (A) és Cmpt FDB rostokról. Reprezentatív spark térbeli és időbeli lefolyása kontroll (C) és Cmpt állatban (D).

A Cmpt rostokon mért *spark*ok átlagos amplitúdója szignifikánsan kisebb volt a kontroll rostokon mértekhez képest (**9. táblázat**). Továbbá nagyobb számban találtunk rajtuk gyorsan kialakuló *spark*okat a kontrollhoz képest, vagyis a csúcs eléréséhez szükséges idő (TTP) átlagos értéke szignifikánsan csökkent (**9. táblázat**). Az átlagos FWHM a Cmpt mutáció hatására szignifikánsan lecsökkent (**9. táblázat**). Továbbá a *spark*ok frekvenciája szignifikánsan kisebb volt a Cmpt állatokból izolált izomrostokon

a kontroll állatokhoz képest (**9. táblázat**).

9. táblázat. *Spark*ok paraméterei Cmpt mutációt hordozó egerek vázizomrostjaiban

	Kontroll	**Cmpt**
Amplitúdó (F/F_0)	0,165±0,001	1,154±0,002***
FWHM (μm)	1,92±0,01	1,87±0,01**
TTP (ms)	34,7±0,9	24,3±0,8**
Frekvencia (Hz)	33,0±2,7	6,2±0,5***

** és *** szignifikáns különbség a kontrolltól ($p<0,01$, $p<0,001$).

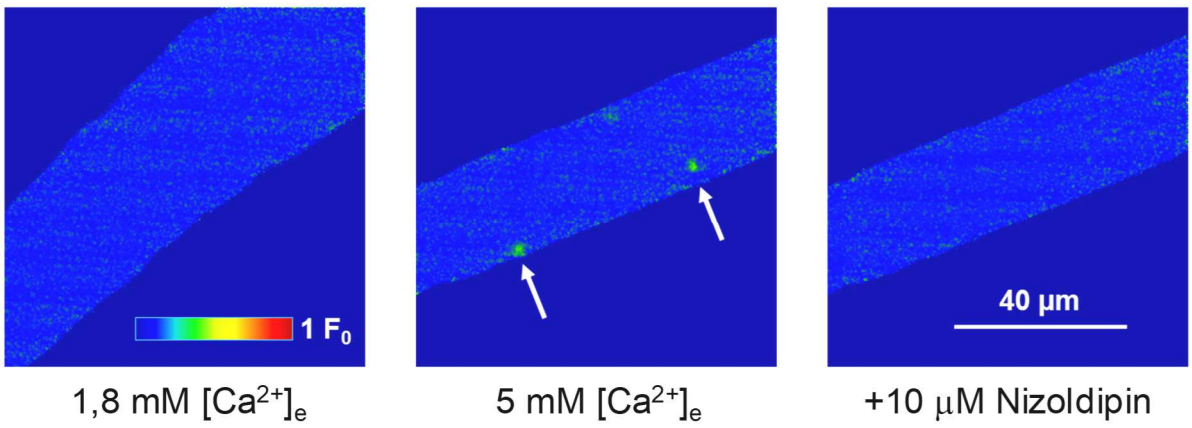
A Cmpt izomrostokon talált kevesebb ECRE és az eseményenként felszabaduló kalcium csökkent mennyisége megmagyarázzák, hogy miért kisebbek a globális kalciumtranziensek a mutáns állatokban. Ezek az eredmények azt sugallják, hogy a Cmpt fenotípust kísérő változások (pl. a csökkent izomerő) részben a kalcium felszabadulási folyamatok redukált működésének a következménye. Ennek pedig a legvalószínűbb magyarázata az SR kalciumtartalmának csökkenése lehet (Bodnár et al., 2014).

6.4.3 Az embrionális DHPR jelenlétének hatása az ECRE-kre egerek harántcsíkolt izomrostjaiban

A **3.3** fejezetben már említés rekerült, hogy harántcsíkolt izomban a feszültségfüggő kalciumcsatornák (DHPR vagy CaV1.1) és a RyR1 fizikailag egymással összekapcsolódnak, így a CaV1.1 feszültségfüggő aktiválása közvetlenül megnyithatja a RyR1-t. A kifejlett izomban többségében jelen levő CaV1.1a variánson keresztül folyó áram kicsi és lassan aktiválódik, csak nagy és hosszú membrándepolarizáció esetén mérhető, így fiziológiás körülmények között nem játszik szerepet a kalciumfelszabadulás elindításában. Érdekes módon emlősökben a vázizomzat érése során a depolarizáció függő kalciumbeáramlás folyamatosan csökken CaV1.1a variáns mennyiségének növekedése által. A magzati izmokban még a CaV1.1e csatornaváltozat van többségben, amelyen mérhető nagyságú kalcium áram folyik keresztül, és ez részt vesz az SR-ből történő kalciumfelszabadulás aktiválásában (Tuluc et al., 2009). A születés után az izmokban a CaV1.1e variáns szinte teljesen kicserélődik a felnőtt, rosszul vezető CaV1.1a variánsra (Flucher & Tuluc, 2011). Megfigyelték 1-es típusú miotóniás disztrófiás (DM1) betegekben, hogy az embrionális kalciumvezető CaV1.1e variáns rendellenes expressziójának nagysága

korrelál az izomgyengeségük mértékével (Tang et al., 2012). Mivel osztrák kollaborációs partnerünknek sikerült előállítani egy genetikailag módosított egér törzset, amelyben a CaV1.1e csatorna felnőtt izomban is jelen van, lehetőségünk volt tanulmányozni ezeken az állatokon a kalciumfelszabadulást harántcsíkolt izomrostokban (Sultana et al., 2016).

Nyugalmi állapotban fiziológiás extracelluláris kalciumkoncentráció (1,8 mM) jelenlétében nem alakultak ki *spark*ok sem a kontroll, sem a CaV1.1e csatornát expresszáló egerekből származó izomrostokon (**32. ábra**). Azonban ha megemeltük az extracelluláris kalciumkoncentrációt csak a CaV1.1e csatornát tartalmazó izomrostokon jelentek meg *spark*ok (**32. ábra**), melyek átlagos amplitúdója 0,140±0,001 F/F_0 és frekvenciája 0,724±0,211 1/ms/mm volt. Amikor az L-típusú kalciumcsatorna blokkoló Nizoldipint hozzáadtuk a mérőkádban levő oldathoz, a *spark*ok eltűntek (**32. ábra**). Ezek a megfigyelések igazolják, hogy a *spark*ok kialakulásához, vagyis a kalcium kiáramlásához az SR-ből a RyR1-en keresztül, szükséges a CaV1.1e csatornán beáramló külső kalcium. Kísérleteink azt a korábbi megfigyelést is megmagyarázzák, hogy a fejlődő izomsejtekben ahol még jelen van a CaV1.1e csatorna, miért alakulnak ki *spark*ok, míg kifejlett izomrostokon ahol már csak a CaV1.1a csatorna expresszálódik, miért nem találhatóak meg (Sultana et al., 2016).

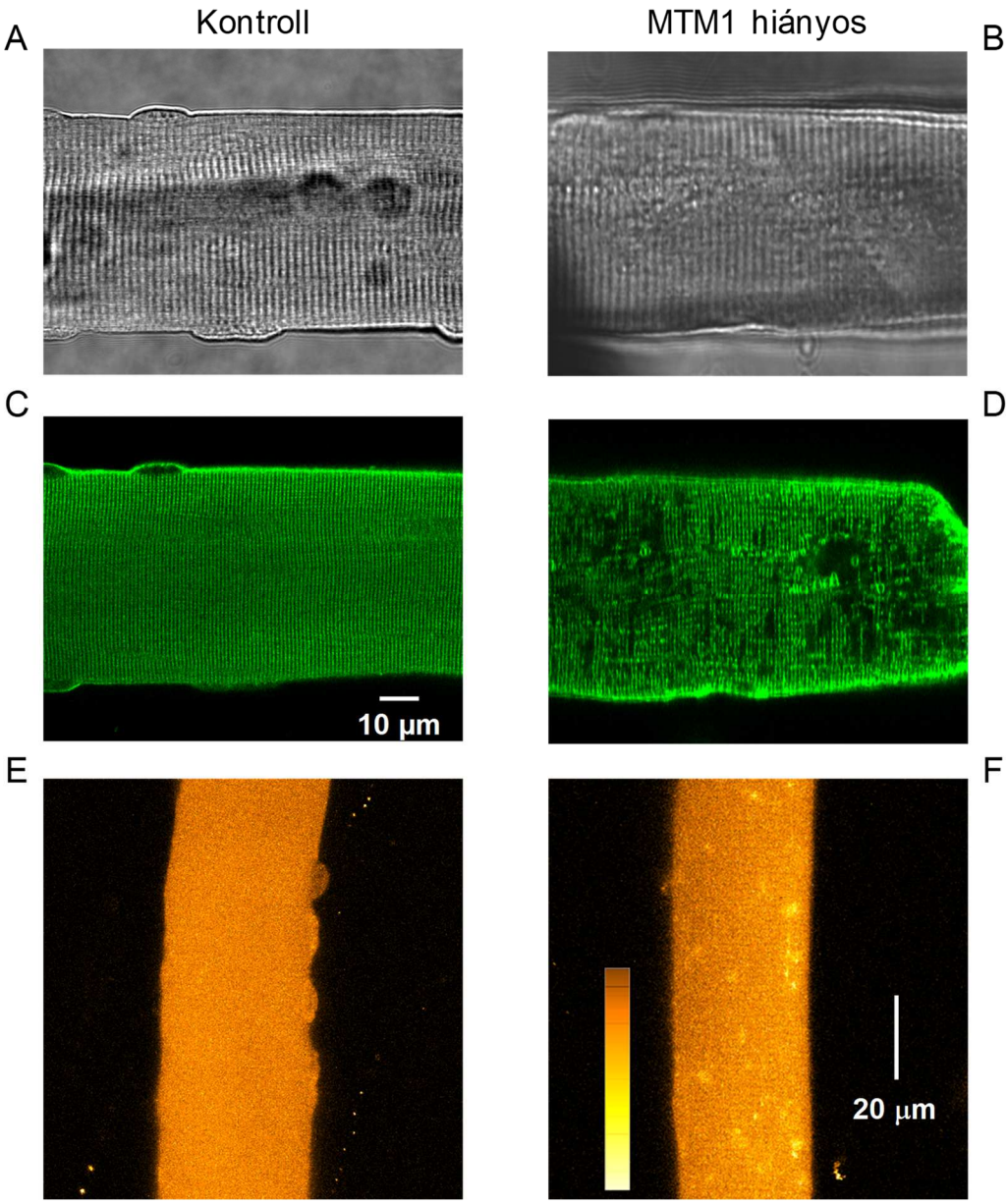


32. ábra. *Spark*ok CaV1.1e csatornát expresszáló izomrostokon

Reprezentatív XY konfokális képek nyugalomban levő CaV1.1e FDB izomrostokon normál (1,8 mM) és megemelt (5 mM) extracelluláris kalciumkoncentráció mellett. Sparkok (fehér nyilak) csak 5 mM kalciumban jelentek meg és 10 µM Nizoldipin blokkolta a kialakulásukat.

6.4.4 ECRE-k harántcsíkolt izomrostokban a miotubuláris miopátia egérmodellben

Az elektromechanikai kapcsolat tökéletlenül működik miotubuláris miopátiában, amely betegségben a PtdInsP foszfatáz miotubularint (MTM1) kódoló gén mutálódik (lásd 6.2.6 fejezet) (Laporte et al., 1996). Ezt az MTM1-hiányos egér segítségével



33. ábra. *Spark*ok MTM1 mutáns izomrostokon

*Reprezentatív XY konfokális képek nyugalomban levő FDB izomrostokról áteső fényben (**A**, **B**) és a T-tubulusokat di-8-Anepps fluoreszcens festékkel megjelölve (**C**, **D**). Fluo-4 kalcium érzékeny festékkel feltöltött izomrostok (**E**, **F**). Jól látszanak a sérült T-tubulusok (**D**) és a sparkok (**F**) az MTM1 hiányos izomrostokon.*

állapították meg, amely modell jól reprodukálja az emberi miotubuláris miopátia fő jellemzőit (Buj-Bello et al., 2002): MTM1 hiányában az izomrostokban a triádok (az a régió, ahol egy T-tubulus két junkcionális SR terminális ciszternával néz szembe) száma lecsökken, megszakad a T-tubulus hálózat (**33D. ábra**) és csökken a CaV1.1 és RYR1 mennyisége is (Al-Qusairi et al., 2009). Funkcionális szinten a feszültség által aktivált SR-ből történő kalciumfelszabadulás amplitúdója csökken, késleltetett aktivációs kinetikát és szubcelluláris egyenetlenséget mutat (Al-Qusairi et al., 2009; Kutchukian et al., 2016).

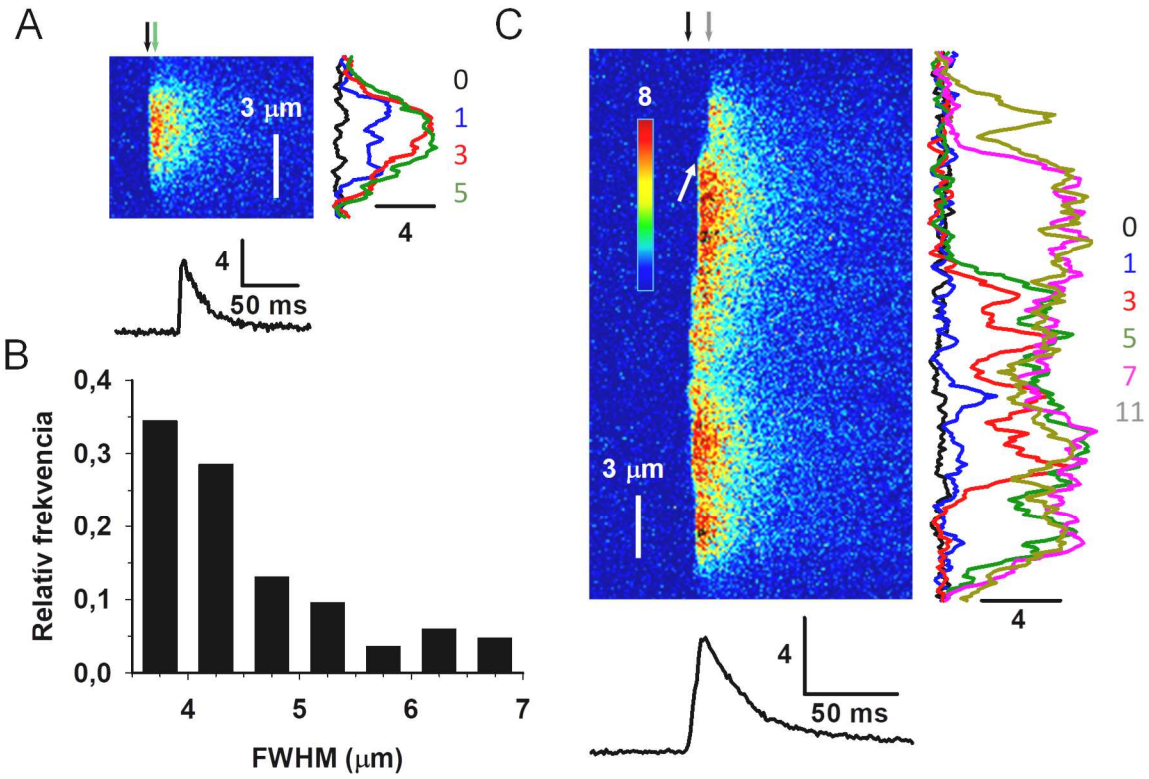
Ezen előzmények alapján úgy gondoltuk, hogy érdemes megvizsgálni az elemi kalciumfelszabadulási eseményeket az MTM1 hiányos izomrostokon (Kutchukian et al., 2019). A kontroll preparátumokkal ellentétben (**33A-C. ábra**), a mutáns rostokon jelentős mennyiségű *spark*ot detektáltunk nyugalmi állapotban (**33E-F. ábra**). Míg a 43 db kontroll izomroston csak 34 db *spark*ot tudtunk regisztrálni, addig 51 db MTM1 hiányos FDB-n 1008 db elemi eseményt találtunk. Érdekes módon a *spark*ok átlagos amplitúdója nem változott meg a mutáns izomrostokban, de a rosttal párhuzamos térbeli kiterjedésük jelentősen megnőtt (**10. táblázat**).

10. táblázat. *Spark*ok paraméterei kontroll és MTM1 hiányos vázizomrostokban

	Kontroll	**MTM1 hiányos**
Amplitúdó (F/F_0)	1,01±0,06	1,04±0,02
FWHM rosttal párhuzamosan (μm)	1,71±0,08	2,15±0,02***
FWHM rostra merőlegesen (μm)	1,67±0,07	1,78±0,02
Frekvencia (Hz/mm^2)	11,9±5,0	336,7±53,4***

*** szignifikáns különbség a kontrolltól ($p<0,001$).

A *spark*ok térbeli kiszélesedését megvizsgáltuk line-scan kísérletekben is. Meglepő módon az MTM1 hiányos rostok szokatlanul nagy amplitúdójú és térbeli szélességű masszív Ca^{2+}-felszabadulási eseményeket produkáltak. Ezek az összes ECRE nagyjából 5%-át tették ki. Egy példát a **34A. ábrán** mutatok be. Ez az esemény 4 F/F_0-nál nagyobb amplitúdóval és megközelítően 4 μm FWHM-el rendelkezik. Ilyen széles események létezése csak úgy magyarázható ha egyidőben jelentős számú RyR1 aktiválódik. Kiszámoltuk, hogy a 3,5 μm-nél nagyobb FWHM-el rendelkező események mintegy 20%-ának 5 μm-nél is nagyobb a térbeli szélessége (**34B. ábra**). Az egyik ilyen gigantikus szélességű esemény látható a **34C. ábrán**, amely esetében

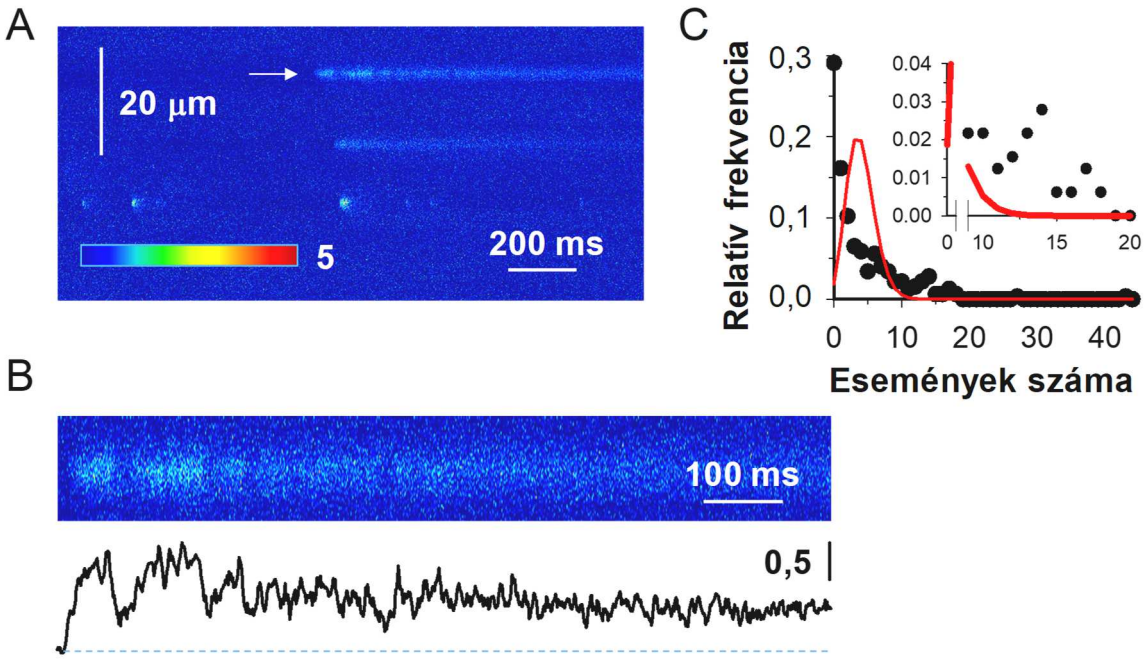


34. ábra. Szokatlanul széles események MTM1 mutáns izomrostokon

*(**A**) Egy széles és nagy amplitúdójú kalcium spark. A térbeli kiterjedés a line-scan mellett az 1., 3. és 5. szkenneléskor. (**B**) A 3,5 µm-nél szélesebb események FWHM-jének eloszlása (n=55). (**C**) Szomszédos RyR1 egységeket aktiváló kalciumfelszabadulási esemény. A térbeli kiterjedés a line-scan mellett az 1., 3., 5., 7. és 11. szkenneléskor. Jól láthatóan nagyobb ugrásokkal szélesedik az esemény idővel.*

az idő előre haladtával újabb és újabb rostszakaszokon aktiválódnak a RyR1-ek. Ez és a hasonló események elemzése lehetővé tette, hogy meghatározzuk a szomszédos kalciumfelszabadulási csatornák feltehetően CICR általi aktiválódásának sebességét. A **34C ábrán** látható esemény esetében ez 170 µm/s-nak, míg további 6 hasonló eseményből kiszámolva átlagosan 228±47 µm/s-nak adódott. Ez a terjedési sebesség közel van ahhoz (273±7 µm/s,) amit a békák harántcsíkolt izmain kaptunk TPEN jelenlétében (**6.2.2. fejezet**). Ezek az eredmények azt bizonyítják, hogy a RyR1-ek egy junkcionális egységben molekuláris kapcsolatokon keresztül aktiválódnak, míg a szomszédos junkcionális egységek aktiválódását a CICR mechanizmus közvetíti.

Az MTM1 hiányos izomrostokon végzett kísérleteink során még egy érdekes megfigyelést tettünk. A kalciumfelszabadulási események az izomrostok kitüntetett részein fordulnak elő, mivel a térbeli eloszlásuk nem illeszkedik az egymástól független eseményeket leíró Poisson-eloszlásra (**35. ábra,** vesd össze **21. ábra**). Ezt azzal tudjuk magyarázni, hogy az események valószínűleg a rost sérült T-tubulussal rendelkező helyein alakulnak ki.

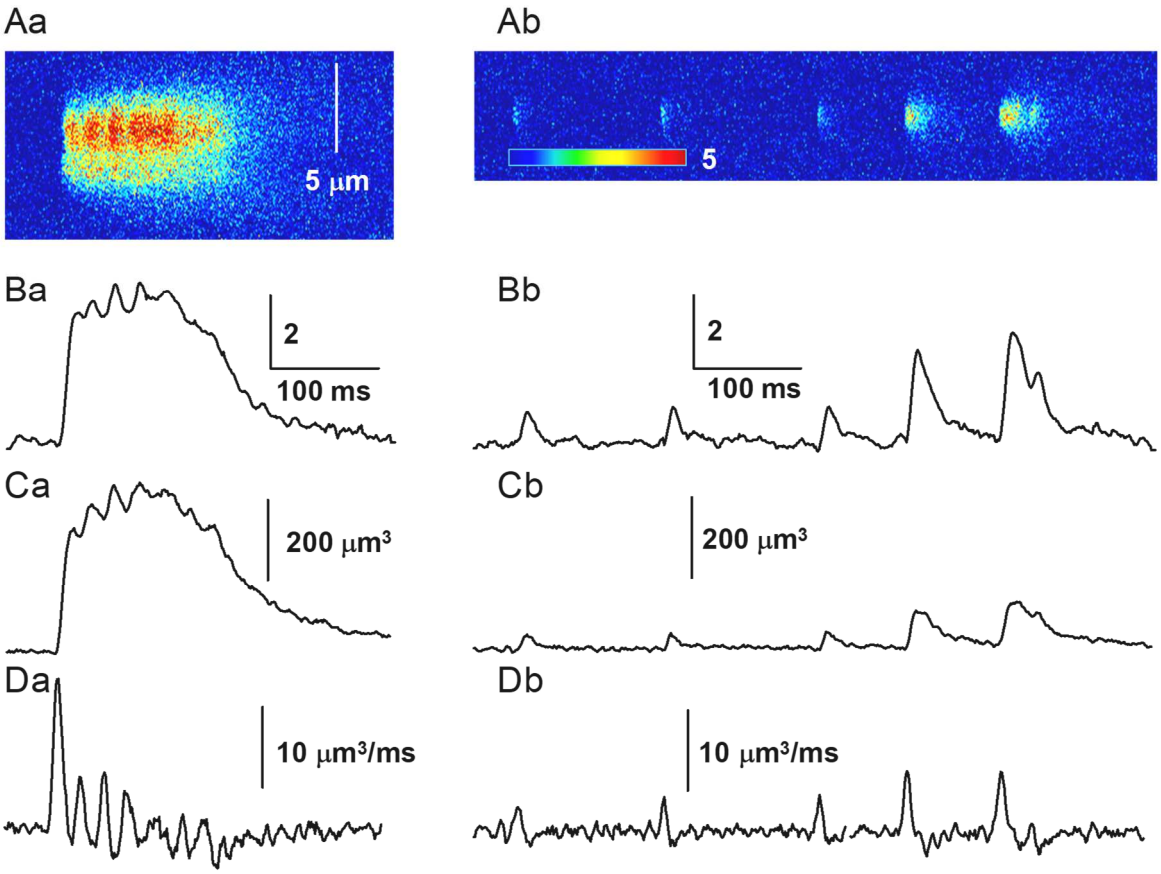


35. ábra. Egy helyen ismételten kialakuló események MTM1 mutáns izomrostokon

*Reprezentatív line-scan ismételten aktiválódó kalciumcsatornákkal (**A**). Az A panelen nyíllal jelölt esemény kinagyítva időbeli profiljával. (**B**) A különböző számú kalcium felszabadulási eseményt tartalmazó line-scan képek számának eloszlása (**C**). A folyamatos piros vonal az egymástól függetlenül kialakuló események eloszlásának megfelelő λ=3,99 állandójú Poisson eloszlást mutatja. A betét koordináta rendszerben kinagyítva látható, hogy jelentős számú képen találtunk nagyszámú eseményt.*

Az ismételten kialakuló eseményeket nagy időbeli felbontású mérésekben is megvizsgáltuk. A **36. ábrán** bemutatjuk a SR-ből történő kalcium felszabadulás időbeli lefutását egy lépcsőzetesen kialakuló *spark* (bal oldali panelek) és a rost egy helyén ismételten kialakuló *spark* sorozat esetében (jobb oldali panelek). A kalcium

mennyiségének (Signal Mass) időbeli lefutása térfogati integrálással határoztunk meg az amplitúdók és FWHM-k időbeli lefutásából (Hollingworth et al., 2001) (**36C. ábra**). A **36D. ábra** az SM idő szerinti deriváltját mutatja (d(SM)/dt), vagyis az SR kalciumfelszabadulási fluxus időbeli lefutását reprezentálja. Ez jól közelíti a globális kalciumfelszabadulás sebességének görbéjét, amely egy kezdeti csúccsal majd egy hosszan megmaradó alacsonyabb fenntartott értékkel rendelkezik (**36Da. ábra**). Ez összhangban van azzal az állítással, hogy ha a kalciumfelszabadulás hosszabb ideig fennmarad, akkor az RYR1 kalciumfüggő inaktiválása helyi szinten történik.



36. ábra. A kalciumfelszabadulás sebessége MTM1 mutáns izomrostokon

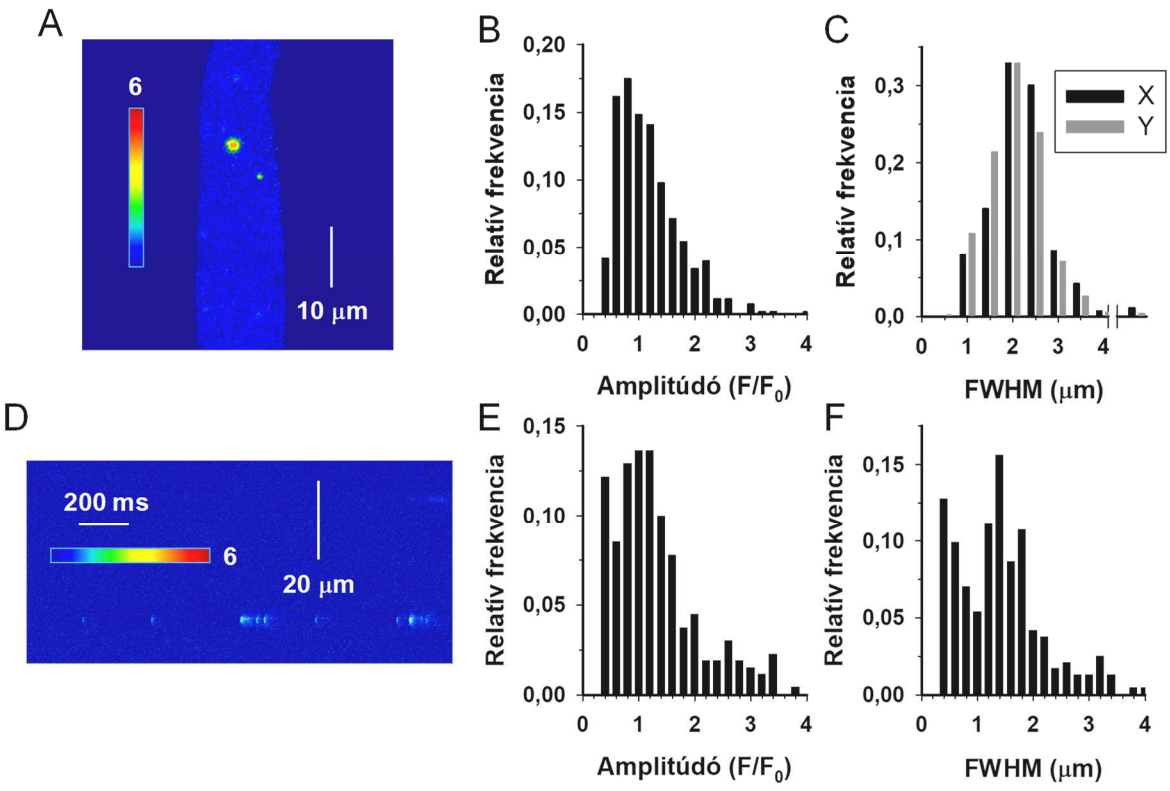
*Lépcsőzetesen (**Aa**) és ismételten kialakuló spark (**Ab**). Az A panelen levő események időbeli profiljai. (**Ba**, **Bb**) A felszabaduló kalcium mennyiségének (Signal Mass, SM) időbeli lefutása (**Ca**, **Cb**). A kalciumfelszabadulás sebessége (dSM/dt) (**Da**, **Db**).*

Eredményeink szerint az MTM1 gén hiányában a T-tubuláris rendszerben kialakuló változások a RyR1-k kóros aktiválódását eredményezik, ami magyarázhatja, hogy miért csökken az SR-ből történő kalciumfelszabadulás és a mutációt hordozó egerekben valamint a betegekben az izomerő (Kutchukian et al., 2019).

6.4.5 ECRE-k harántcsíkolt izomrostokban a centronukleáris miopátia egérmodelljében

Centronukleáris miopátiák az öröklött izombetegségek csoportjába tartoznak. A betegség kezdete (életkor) és az izomgyengeség súlyossága és progressziója szempontjából heterogén jellemzőt mutat, de minden beteg izommintájában megtalálható a sejtmagok központi elhelyezkedése az izomrostokban. A betegség előidézésében szerepet játszó legismertebb mutációk a miotubulint (MTM1) (Laporte et al., 1996) és a dinamin 2-t (DNM2) (Bitoun et al., 2005) érintik. Ennek a betegségnek is létrehozták a DNM2-t mutációt hordozó egérmodelljét (Durieux et al., 2010), amit módunkban volt használni (Kutchukian et al., 2017). A mutáns egerek reprodukálják az emberi betegség fő tüneteit: az állatokban fokozatosan izomgyengeség, majd 2 hónapos koruk után izomsorvadás alakul ki a mitokondriumok elváltozásával kísérve.

Az MTM1 hiányos egereken látottakhoz hasonló eredményeket kaptunk a DNM2



37. ábra. ECRE-k DNM2 mutáns izomrostokon

*Reprezentatív XY (**A**) és line-scan (**D**) képek DNM2 mutáns FDB izomroston nyugalomban. Amplitúdó (**B**, **E**) és FWHM (**C**, **F**) eloszlások az XY (**B**, **C**) és line-scan (**E**, **F**) képekből számolva.*

mutációját hordozó állatokon: nagyszámú spontán elemi kalciumfelszabadulási esemény jelent meg a nyugalomban levő FDB rostokon (**37AD. ábra**). Az MTM1 mutációval ellentétben ezek az események teljesen szimmetrikusak voltak térben (**37C. ábra**, **11 táblázat**) és elenyésző számban találtunk köztük 3,5 μm-nél szélesebb *spark*okat. Viszont a *spark*ok minden jellemző paramétere szignifikánsan nagyobb volt a kontrol eseményeken találtakhoz viszonyítva (**11. táblázat**). A DNM2 mutáns egerek vázizomrostjain nyugalomban talált jelentős számú ECRE és a depolarizációval kiváltott kalcium tranziensek csökkent amplitúdója is azt bizonyítja, hogy ezekben az állatokban megváltozik az ECC működése, ami magyarázhatja a genetikailag módosított egerekben és a betegekben is a gyengébb izomműködést (Kutchukian et al., 2017).

11. táblázat: *Spark*ok paraméterei kontroll és DNM2 mutáns FDB izomrostokban

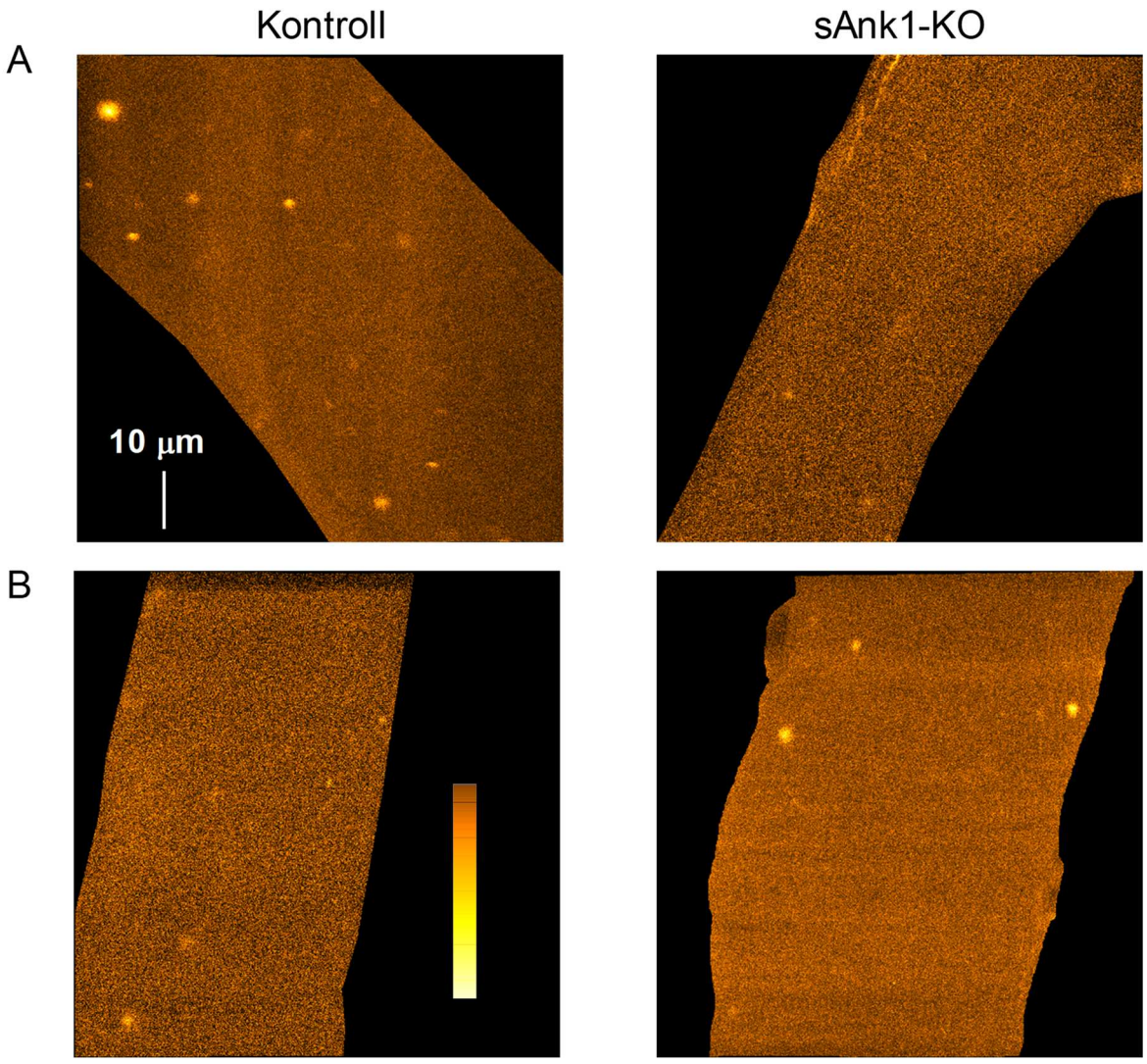
	Kontroll	**DNM2 mutáns**
Amplitúdó (F/F_0)	0,75±0,06	1,07±0,02***
FWHM rosttal párhuzamosan (μm)	1,20±0,06	1,94±0,03***
FWHM rostra merőlegesen (μm)	1,09±0,07	1,79±0,03***
Frekvencia ($1/s/mm^2$)	15,0±6,2	153,1±34,4***

*** szignifikáns különbség a kontrolltól ($p<0,001$).

6.4.6 Az Ankirin1 fehérje szintjének hatása az ECRE-kre egér harántcsíkolt izomrosjaiban

Az SR megfelelő elhelyezkedése a miofibrillumok körül és a T-tubulusokkal való közvetlen kapcsolat (triád, **1. ábra**) elengedhetetlen az izomösszehúzódás hatékony szabályozásához. Az ankyrinek azon speciális kapcsoló fehérjék családjába tartoznak, amelyek részt vesznek membrándomének összeszervezésében (Bennett & Healy, 2009). Az Ank1 gén kódolja a kis molekula tömegű (20–25 kDa) izomspecifikus sAnk1 izoformák expresszióját. A sAnk1 hiányos egerekben kimutatták, hogy a fehérje hiánya az SR mennyiségének valamint a RyR1 és SERCA fehérjeszintjének jelentős csökkenését eredményezi (Giacomello et al., 2015). Ezek alapján feltételeztük, hogy a felsorolt változások hatással lehetnek az ECRE-k kialakulására és paramétereire a mutáns vázizomrostokban (Pierantozzi et al., 2019).

Spontán kalciumfelszabadulási eseményeket mértünk fiatal (4 hónapos) és idős (10 hónapos) kontroll és sAnk1 hiányos (sAnk1-KO) egerek szaponinnal kezelt FDB izomrostjain (**38. ábra**). A képek analíziséből kiderült, hogy a *spark*ok frekvenciája csökkent a fiatal sAnk1-KO egerekben a hasonló életkorú kontroll egerekhez képest (**12. táblázat**). Az ECRE-k gyakorisága csökkent a 10 hónapos kontroll egerek rostjaiban is a fiatal kontroll állatok FDB rostjaihoz képest, de a frekvencia már nem csökkent tovább az idős sAnk1-KO állatokban (**12. táblázat**). A *spark*ok minden paramétere és a felszabadult kalcium mennyisége (Signal Mass: SM) is szignifikánsan csökkent mindkét életkorban a sAnk1-KO állatok vázizomrostjaiban (**12. táblázat**).



38. ábra. ECRE-k kontroll és sAnk1 hiányos izomrostokon

Reprezentatív XY képek szaponinnal kezelt fiatal (A) és idős (B) FDB izomroston. A képek 120 db mérési kép összeadásából készültek.

12. táblázat. ECRE-k paraméterei kontroll és sAnk1-KO izomrostokban

	4 hónapos		10 hónapos	
	Kontroll (3 egér) (43 rost)	**sAnk1-KO (9 egér) (87 rost)**	**Kontroll (3 egér) (79 rost)**	**sAnk1-KO (4 egér) (105 rost)**
***Spark*ok száma**	1084	1231	1063	1646
Amplitúdó (F/F_0)	0,216±0,005	0,158±0,003***	0,205±0,006	0,171±0,003***,##
FWHM-X (µm)	2,239±0,023	2,048±0,020***	2,312±0,025#	1,972±0,020***,##
FWHM-Y (µm)	1,968±0,020	1,784±0,017***	1,991±0,022	1,761±0,017***
SM (μm^3)	3,195±0,130	1,852±0,090***	2,909±0,124	1,996±0,088***
Frekvencia ($1/s/mm^2$)	65,8±13,8	28,8±8,6*	35,0±5,7#	39,1±6,9

* és *** szignifikáns különbség a kontrolltól ($p<0,05$ és $p<0,001$). # és ## szignifikáns különbség a fiatal azonos genetikai hátterű állatoktól ($p<0,05$ és $p<0,01$).

Ezek az adatok azt mutatják, hogy vagy az SR-ből felszabadítható Ca^{2+} mennyisége csökken vagy a kalciumcsatornák nyitása károsodott, vagy mindkettő jelenség egyszerre okozhatja a *spark*ok paramétereiben talált változásokat fiatal sAnk1-KO egerekben. A Ca^{2+}-homeosztázisban megfigyelt különbség kevésbé nyilvánvaló idős állatokban, mivel az életkor előre haladtával a Ca^{2+}-felszabadulás eleve csökken a vázizomrostokban. Ez arra utal, hogy a fiatal sAnk1-KO izomrostokban a kalciumháztartásban kialakult változások már nem módosulnak idővel és a vad típusú öreg egerekben találhatókhoz hasonló szintet érnek el (Pierantozzi et al., 2019).

7. ÚJ MEGÁLLAPÍTÁSOK

Kísérleteinkben minden esetben a spontán módon kialakuló elemi kalciumfelszabadulási eseményeket (ECRE) vizsgáltuk különböző preparátumokon és eltérő körülmények között.

1. Kidolgoztuk az egyedi vázizomrostok enzimatikus preparálásának módszerét békákból, patkányokból, egerekből és házi méhekből. Megvalósítottuk az ECRE-k optimális mérési eljárását egyedi vázizomrostokon konfokális lézerpásztázó mikroszkópon. Leírtuk az ECRE-k jellemző paramétereit mindegyik preparátumon.
2. Kifejlesztettünk két wavelet alapú automatikus ECRE felismerő programot, amelyek lehetővé teszik egyrészt vonal-menti (line-scan), másrészt kétdimenziós (XY) pásztázással készült konfokális mikroszkópos felvételeken nagyszámú esemény automatikus detektálását és elemzését.
3. Megmutattuk, hogy békák harántcsíkolt izomrostjaiban a kisfokú depolarizáció és a koffeinnel való kezelés különböző hatásmechanizmussal, de emeli a *spark*ok frekvenciáját és amplitúdóját. Egészséges izomrostban a *spark*ok egyenletesen oszlanak el, nincsenek kitüntetett helyek az elemi kalciumfelszabadulási események szempontjából. A tovaterjedő események 273±7 μm/s átlagos terjedési sebességgel mozognak.
4. Emlősök vázizomrostjain bebizonyítottuk, hogy egyetlen rianodin csatorna megnyílása *ember*t eredményez, nem pedig *spark*ot. A különböző típusú események alatt felszabadult kalcium mennyiségéből megbecsültük, hogy kb. 30 RyR csatorna egyidejű megnyílása hoz létre egy átlagos *spark*ot. A különböző amplitúdójú *spark*ok illetve lépcsős *ember*ek megjelenésével bebizonyítottuk, hogy a RyR1-nek szubkonduktancia állapotai vannak.
5. A humán miopátiák egérmodelljeiben megállapítottuk, hogy az MTM1 gén hiányában a T-tubuláris rendszerben kialakuló változások a RyR1-k abnormális aktiválódását eredményezik, ami megmagyarázza az SR-ből történő kalciumfelszabadulás csökkenését és a betegekben az izomerő hanyatlását. A sérült belső struktúrájú izomrostokon a *spark*ok kialakulásának helyei nem egyenletesen oszlanak meg, a T-tubulusok hiányában a RyR1

könnyebben megnyílnak. A DNM2 gén mutációja pedig jelentős számú ECRE kialakulását eredményezi a nyugalomban levő vázizomrostokon, ami szintén megmagyarázhatja a betegekben a csökkent vázizomműködést. A humán betegségre jellemző PtdInsP-k kóros felhalmozódásáról megmutattuk, hogy csökkenti a rianodin receptoron keresztüli Ca^{2+}-felszabadulást.

6. A vázizmokat közvetlenül nem érintő két kórfolyamatot vizsgálva kimutattuk, hogy az infarktuson átesett patkányok vázizomrostjain az *ember*ek relatív aránya megnőtt, a *spark*ok amplitúdójúak kisebb lett, lassabban alakultak ki és az egy *spark* alatt kiáramlott Ca^{2+} mennyisége lecsökkent. Ez megmagyarázhatja a károsodott vázizomműködést szívinfarktus után. Bebizonyítottuk, hogy amíg a hiperkoleszterinémia patkányokban nem változtatja meg a *spark*ok frekvenciáját, addig a fluvastatin függetlenül a vér koleszterinszintjétől, növeli a *spark*ok gyakoriságát a vázizomrostokban, így okozva izomgyengeséget, amely hatás megelőzhető a koenzim Q_{10} étrendbe történő alkalmazásával.

7. A vázizmokat érintő genetikai mutációk vizsgálata során egerek vázizmaiban azt találtuk, hogy a miosztatin gén károsodása után csökken az ECRE-k száma és kisebb az eseményenként felszabaduló kalcium mennyisége. Megmutattuk, hogy magas extracelluláris Ca^{2+}-koncentráció jelenlétében az embrionális CaV1.1e kalciumcsatornát tartalmazó vázizomrostokon nyugalomban *spark*ok alakulnak ki. Az SR normális elhelyezkedését biztosító Ankirin1 fehérje hiányában pedig kevesebb és kisebb amplitúdójú *spark*ot találtunk. Vagyis minden vizsgált mutáció az SR-ből felszabadítható Ca^{2+} mennyiségét csökkenti vagy a kalciumcsatornák nyitását akadályozza, ami gyengült izomműködéséhez vezet.

8. KÖSZÖNETNYILVÁNÍTÁS

Ezúton szeretném megköszönni korábbi és jelenlegi intézetigazgatómnak, Prof. Dr. Kovács Lászlónak és Prof. Dr. Csernoch Lászlónak, hogy annak idején bizalmat szavaztak egy matematikusnak és vették a fáradtságot, hogy élettanászt faragjanak belőlem. Köszönöm, hogy bevezettek az izmok működésének rejtelmeibe és rávezettek egy olyan tudományterületre, ahol kamatoztatni tudtam korábbi egyetemi tanulmányaimat. Hálával tartozom számos hazai és külföldi társszerzőmnek, akik nélkül nem jutottam volna el pályafutásomnak erre a pontjára. Külön köszönettel tartozom Dr. Szabó Lászlónak és Dr. Vincze Jánosnak a képanalizáló programok kifejlesztéséért. Szeretném megköszönni Őri Rózának, hogy a kísérletek elvégzésében a kezdetektől fogva technikai segítséget nyújtott. Végül szeretném családomnak, szüleimnek és feleségemnek is megköszönni a munkám során kapott önzetlen támogatásukat.

9. IRODALOMJEGYZÉK

Al-Qusairi, L., Weiss, N., Toussaint, A., Berbey, C., Messaddeq, N., Kretz, C., Sanoudou, D., Beggs, A. H., Allard, B., Mandel, J. L., Laporte, J., Jacquemond, V., & Buj-Bello, A. (2009). T-tubule disorganization and defective excitation-contraction coupling in muscle fibers lacking myotubularin lipid phosphatase. *Proceedings of the National Academy of Sciences of the United States of America*, *106*(44), 18763–18768. https://doi.org/10.1073/pnas.0900705106

Almassy, J., Sztretye, M., Lukacs, B., Dienes, B., Szabo, L., Szentesi, P., Vassort, G., Csernoch, L., & Jona, I. (2008). Effects of K-201 on the calcium pump and calcium release channel of rat skeletal muscle. *Pflugers Archiv European Journal of Physiology*, *457*(1), 171–183. https://doi.org/10.1007/s00424-008-0504-7

Amthor, H., Macharia, R., Navarrete, R., Schuelke, M., Brown, S. C., Otto, A., Voit, T., Muntoni, F., Vrbó va, G., Partridge, T., Zammit, P., Bunger, L., & Patel, K. (2007). Lack of myostatin results in excessive muscle growth but impaired force generation. *Proceedings of the National Academy of Sciences of the United States of America*. www.pnas.org/cgi/content/full/

Bányász, T., Chen-Izu, Y., Balke, C. W., & Izu, L. T. (2007). A new approach to the detection and statistical classification of Ca 2+ sparks. *Biophysical Journal*, *92*(12), 4458–4465. https://doi.org/10.1529/biophysj.106.103069

Beard, N. A., Sakowska, M. M., Dulhunty, A. F., & Laver, D. R. (2002). Calsequestrin is an inhibitor of skeletal muscle ryanodine receptor calcium release channels. *Biophysical Journal*, *82*(1), 310–320. https://doi.org/10.1016/S0006-3495(02)75396-4

Bennett, V., & Healy, J. (2009). Membrane Domains Based on Ankyrin and Spectrin Associated with Cell–Cell Interactions. *Cold Spring Harbour Perspective in Biol Ogy*, *1*, 1–17.

Bers, D. M. (2004). Macromolecular complexes regulating cardiac ryanodine receptor function. *Journal of Molecular and Cellular Cardiology*, *37*(2), 417–429. https://doi.org/10.1016/j.yjmcc.2004.05.026

Bitoun, M., Maugenre, S., Jeannet, P. Y., Lacène, E., Ferrer, X., Laforêt, P., Martin, J. J., Laporte, J., Lochmüller, H., Beggs, A. H., Fardeau, M., Eymard, B., Romero, N. B., & Guicheney, P. (2005). Mutations in dynamin 2 cause dominant centronuclear myopathy. *Nature Genetics*, *37*(11), 1207–1209. https://doi.org/10.1038/ng1657

Block, B., Imagawa, T., Campbell, K., & Franzini-Armstrong, C. (1988). Structural evidence for direct interaction between the molecular components of the transverse tubule/sarcoplasmic reticulum junction in skeletal muscle. *Journal of Cell Biology*, *107*, 2587–2600.

Bodnár, D., Geyer, N., Ruzsnavszky, O., Oláh, T., Hegyi, B., Sztretye, M., Fodor, J., Dienes, B., Balogh, Á., Papp, Z., Szabó, L., Müller, G., Csernoch, L., & Szentesi, P. (2014). Hypermuscular mice with mutation in the myostatin gene display altered calcium signalling. *Journal of Physiology*, *592*(6), 1353–1365. https://doi.org/10.1113/jphysiol.2013.261958

Bolis, A., Zordan, P., Coviello, S., & Bolino, A. (2007). Myotubularin-related (MTMR) phospholipid phosphatase proteins in the peripheral nervous system. *Molecular Neurobiology*, *35*(3), 308–316. https://doi.org/10.1007/s12035-007-0031-0

Buj-Bello, A., Laugel, V., Messaddeq, N., Zahreddine, H., Laporte, J., Pellissier, J. F., & Mandel, J. L. (2002). The lipid phosphatase myotubularin is essential for skeletal muscle maintenance but not for myogenesis in mice. *Proceedings of the National Academy of Sciences of the United States of America*, *99*(23), 15060–15065. https://doi.org/10.1073/pnas.212498399

Caswell, A. H., Brandt, N. R., Brunschwig, J. P., & Purkerson, S. (1991). Localization and partial characterization of the oligomeric disulfide-linked molecular weight 95,000 protein (triadin) which binds the ryanodine and dihydropyridine receptors in skeletal muscle triadic vesicles. *Biochemistry*, *30*(30), 7507–7513. https://doi.org/10.1021/bi00244a020

Caswell, A. H., Motoike, H. K., Fan, H., & Brandt, N. R. (1999). Location of Ryanodine Receptor Binding Site on Skeletal Muscle Triadin. *Biochemistry*, *38*(1), 90–97. https://doi.org/10.1021/bi981306+

Cheng, H., & Lederer, W. J. (2008). Calcium sparks. *Physiological Reviews*, *88*(4), 1491–1545. https://doi.org/10.1152/physrev.00030.2007

Cheng, H., Lederer, W. J., & Cannell, M. B. (1993). Calcium Sparks : Elementary Events Underlying Excitation-Contraction Coupling in Heart Muscle. *Science*, *262*(5134), 740–744. 10.1126/science.8235594

Cheng, H., Song, L. S., Shirokova, N., González, A., Lakatta, E. G., Ríos, E., & Stern, M. D. (1999). Amplitude distribution of calcium sparks in confocal images: Theory and studies with an automatic detection method. *Biophysical Journal*, *76*(2), 606–617. https://doi.org/10.1016/S0006-3495(99)77229-2

Clop, A., Marcq, F., Takeda, H., Pirottin, D., Tordoir, X., & Bibe, B. (2006). A mutation creating a potential illegitimate microRNA target site in the myostatin gene affects muscularity in sheep. *Nature Genetics*, *38*, 813–818.

Collet, C., Charreton, M., Szabo, L., Takacs, M., Csernoch, L., & Szentesi, P. (2021). Elementary calcium release events in the skeletal muscle cells of the honey bee Apis mellifera. *Scientific Reports*, *11*(1). https://doi.org/10.1038/s41598-021-96028-w

Conklin, M. W., Barone, V., Sorrentino, V., & Coronado, R. (1999). Contribution of ryanodine receptor type 3 to Ca2+ sparks in embryonic mouse skeletal muscle. *Biophysical Journal*, *77*(3), 1394–1403. https://doi.org/10.1016/S0006-3495(99)76988-2

Cook, R. (1997). Actomyosin interaction in striated muscle. *Physiology Review*, *77*, 671–697.

Cserne Szappanos, H., Vincze, J., Bodnár, D., Dienes, B., Schneider, M. F., Csernoch, L., & Szentesi, P. (2020). High Time Resolution Analysis of Voltage-Dependent and Voltage-Independent Calcium Sparks in Frog Skeletal Muscle Fibers. *Frontiers in Physiology*, *11*. https://doi.org/10.3389/fphys.2020.599822

Csernoch, L. (1999). Regulation of the ryanodine receptor calcium release channel of the sarcoplasmic reticulum in skeletal muscle. *Acta Physiologica Hungarica*, *86*(2), 77–97.

Csernoch, L. (2007). Sparks and embers of skeletal muscle: The exciting events of contractile activation. *Pflugers Archiv European Journal of Physiology*, *454*(6), 869–878. https://doi.org/10.1007/s00424-007-0244-0

Dai, J. M., Kuo, K. H., Leo, J. M., Van Breemen, C., & Lee, C. H. (2006). Mechanism of ACh-induced asynchronous calcium waves and tonic contraction in porcine tracheal muscle bundle. *American Journal of Physiology - Lung Cellular and Molecular Physiology*, *290*(3), 459–469. https://doi.org/10.1152/ajplung.00092.2005

Durieux, A. C., Vignaud, A., Prudhon, B., Viou, M. T., Beuvin, M., Vassilopoulos, S., Fraysse, B., Ferry, A., Lainé, J., Romero, N. B., Guicheney, P., & Bitoun, M. (2010). A centronuclear myopathy-dynamin 2 mutation impairs skeletal muscle structure and function in mice. *Human Molecular Genetics*, *19*(24), 4820–4836. https://doi.org/10.1093/hmg/ddq413

Estève, E., Smida-Rezgui, S., Sarkozi, S., Szegedi, C., Regaya, I., Chen, L., Altafaj, X., Rochat, H., Allen, P., Pessah, I. N., Marty, I., Sabatier, J. M., Jona, I., De Waard, M., & Ronjat, M. (2003). Critical amino acid residues determine the binding affinity and the Ca 2+ release efficacy of maurocalcine in skeletal muscle cells. *Journal of Biological Chemistry*, *278*(39), 37822–37831. https://doi.org/10.1074/jbc.M305798200

Flucher, B. E., & Tuluc, P. (2011). A new L-type calcium channel isoform required for normal patterning of the developing neuromuscular junction. *Channels*, *5*(6). https://doi.org/10.4161/chan.5.6.17951

Fodor, J., Gönczi, M., Sztretye, M., Dienes, B., Oláh, T., Szabó, L., Csoma, E., Szentesi, P., Szigeti, G. P., Marty, I., & Csernoch, L. (2008). Altered expression of triadin 95 causes parallel changes in localized Ca2+ release events and global Ca2+ signals in skeletal muscle cells in culture. *Journal of Physiology*, *586*(23), 5803–5818. https://doi.org/10.1113/jphysiol.2008.160457

Fonyó, A., & Geiszt, M. (Eds.). (2019). *Az orvosi élettan tankönyve* (8th ed.). Medicina. https://www.medicina-kiado.hu/kiadvanyaink/szak-es-tankonyvek/elettan/az-orvosi-elettan-tankonyve-8-kiadas/

Franzini-Armstrong, C., & Protasi, F. (1997). Ryanodine receptors of striated muscles: a complex channel capable of multiple interactions. *Physiological Reviews*, *77*(3), 699–729. https://doi.org/10.1152/physrev.1997.77.3.699

Giacomello, E., Quarta, M., Paolini, C., Squecco, R., Fusco, P., Toniolo, L., Blaauw, B., Formoso, L., Rossi, D., Birkenmeier, C., Peters, L. L., Francini, F., Protasi, F., Reggiani, C., & Sorrentino, V. (2015). Deletion of small ankyrin 1 (SANK1) isoforms results in structural and functional alterations in aging skeletal muscle fibers. *American Journal of Physiology - Cell Physiology*, *308*(2), C123–C138. https://doi.org/10.1152/ajpcell.00090.2014

Glahn, K. P. E., Bendixen, D., Girard, T., Hopkins, P. M., Johannsen, S., Rüffert, H., Snoeck, M. M., & Urwyler, A. (2020). Availability of dantrolene for the management of malignant hyperthermia crises: European Malignant Hyperthermia Group guidelines. *British Journal of Anaesthesia*, *125*(2), 133–140. https://doi.org/10.1016/j.bja.2020.04.089

González, A., Kirsch, W. G., Shirokova, N., Pizarro, G., Stern, M. D., & Ríos, E. (2000). The spark and its ember: Separately gated local components of Ca2+ release in skeletal muscle. *Journal of General Physiology*, *115*(2), 139–157. https://doi.org/10.1085/jgp.115.2.139

González Rodríguez, E., Lefebvre, R., Bodnár, D., Legrand, C., Szentesi, P., Vincze, J., Poulard, K., Bertrand-Michel, J., Csernoch, L., Buj-Bello, A., & Jacquemond, V. (2014). Phosphoinositide substrates of myotubularin affect voltage-activated Ca2+ release in skeletal muscle. *Pflugers Archiv European Journal of Physiology*, *466*(5), 973–985. https://doi.org/10.1007/s00424-013-1346-5

Grobet, L., Martin, L. J., Poncelet, D., Pirottin, D., Brouwers, B., & Riquet, J. (1997). A deletion in the bovine myostatin gene causes the doublemuscle phenotype in cattle. *Nature Genetics*, *17*, 71–74.

Hamrick, M. W. W., Pennington, C., Webb, C. N. N., & Isales, C. M. M. (2006). Resistance to body fat gain in 'double-muscled' mice fed a high-fat diet. *International Journal of Obesity*, *30*(5), 868–870. https://doi.org/10.1038/sj.ijo.0803200

Hollingworth, S., Peet, J., Chandler, W. K., & Baylor, S. M. (2001). Calcium sparks in intact skeletal muscle fibers of the frog. *Journal of General Physiology*, *118*(6), 653–678. https://doi.org/10.1085/jgp.118.6.653

Illaste, A., Wullschleger, M., Fernandez-Tenorio, M., Niggli, E., & Egger, M. (2019). Automatic Detection and Classification of Ca2+ Release Events in Line- and Frame-Scan Images. *Biophysical Journal*, *116*(3), 383–394. https://doi.org/10.1016/j.bpj.2018.12.013

Jóna, I., Szegedi, C., Sárközi, S., Szentesi, P., Csernoch, L., & Kovács, L. (2001). Altered inhibition of the rat skeletal ryanodine receptor/calcium release channel by magnesium in the presence of ATP. *Pflugers Archiv European Journal of Physiology*, *441*(6), 729–738. https://doi.org/10.1007/s004240000484

Jung, C., Zima, A. V., Szentesi, P., Jona, I., Blatter, L. A., & Niggli, E. (2007). Ca2+ release from the sarcoplasmic reticulum activated by the low affinity Ca2+ chelator TPEN in ventricular myocytes. *Cell Calcium*, *41*(2), 187–194. https://doi.org/10.1016/j.ceca.2006.06.009

Kirsch, W. G., Uttenweiler, D., & Fink, R. H. A. (2001). Spark- and ember-like elementary Ca2+ release events in skinned fibres of adult mammalian skeletal muscle. *Journal of Physiology*, *537*(2), 379–389. https://doi.org/10.1111/j.1469-7793.2001.00379.x

Klein, M. G., Cheng, H., Santana, L. F., Jiang, Y. H., Lederer, W. J., & Schneider, M. F. (1996). Two mechanisms of quantized calcium release in skeletal muscle. *Nature*, *379*(6564), 455–458. https://doi.org/10.1038/379455a0

Klein, M. G., & Schneider, M. F. (2006). Ca2+ sparks in skeletal muscle. *Progress in Biophysics and Molecular Biology*, *92*(3), 308–332. https://doi.org/10.1016/j.pbiomolbio.2005.05.016

Kutchukian, C., Scrudato, M. Lo, Tourneur, Y., Poulard, K., Vignaud, A., Berthier, C., Allard, B., Lawlor, M. W., Buj-Bello, A., Jacquemond, V., & Kunkel, L. M. (2016). Phosphatidylinositol 3-Kinase Inhibition restores Ca2+ release defects and prolongs survival in myotubularin-deficient mice. *Proceedings of the National Academy of Sciences of the United States of America*, *113*(50), 14432–14437. https://doi.org/10.1073/pnas.1604099113

Kutchukian, C., Szentesi, P., Allard, B., Buj-Bello, A., Csernoch, L., & Jacquemond, V. (2019). Ca 2+ -induced sarcoplasmic reticulum Ca 2+ release in myotubularin-deficient muscle fibers. *Cell Calcium*, *80*, 91–100. https://doi.org/10.1016/j.ceca.2019.04.004

Kutchukian, C., Szentesi, P., Allard, B., Trochet, D., Beuvin, M., Berthier, C., Tourneur, Y., Guicheney, P., Csernoch, L., Bitoun, M., & Jacquemond, V. (2017). Impaired excitation–contraction coupling in muscle fibres from the dynamin2R465W mouse model of centronuclear myopathy. *Journal of Physiology*, *595*(24), 7369–7382. https://doi.org/10.1113/JP274990

Laporte, J., Hu, L. J., Kretz, C., Mandel, J. L., Kioschis, P., Coy, J. F., Klauck, S. M., & A. Poustka, N. D. (1996). A gene mutated in X-linked myotubular myopathy defines a new putative tyrosine phosphatase family conserved in yeast. *Nature Genetics*, *13*, 175–182.

Launikonis, B. S., Zhou, J., Royer, L., Shannon, T. R., Brum, G., & Ríos, E. (2006). Depletion 'skraps' and dynamic buffering inside the cellular calcium store. *Proceedings of the National Academy of Sciences of the United States of America*, *103*(8), 2982–2987. https://doi.org/10.1073/pnas.0511252103

Lu, X., Xu, L., & Meissner, G. (1995). Phosphorylation of dihydropyridine receptor II-III loop peptide regulates skeletal muscle calcium release channel function: Evidence for an essential role of the β-OH group of Ser687. *Journal of Biological Chemistry*, *270*(31), 18459–18464. https://doi.org/10.1074/jbc.270.31.18459

Lukács, B., Sztretye, M., Almássy, J., Sárközi, S., Dienes, B., Mabrouk, K., Simut, C., Szabó, L., Szentesi, P., De Waard, M., Ronjat, M., Jóna, I., & Csernoch, L. (2008). Charged surface area of maurocalcine determines its interaction with the skeletal ryanodine receptor. *Biophysical Journal*, *95*(7), 3497–3509. https://doi.org/10.1529/biophysj.107.120840

Lytton, J., & Nigam, S. (1992). Intracellular calcium: molecules and pools. *Current Opinion Cell Biology*, *4*(2), 220–226.

Ma, J. (1993). Block by Ruthenium Red of the Ryanodine-activated Calcium Release Channel of Skeletal Muscle. *Journal of General Physiology*, *102*, 1031–1056. http://rupress.org/jgp/article-pdf/102/6/1031/1767746/1031.pdf

Marty, I., Robert, M., Ronjat, M., Bally, I., Arlaud, G., & Villaz, M. (1995). Localization of the N-terminal and C-terminal ends of triadin with respect to the sarcoplasmic reticulum membrane of rabbit skeletal muscle. *Biochemical Journal*, *307*(3), 769–774. https://doi.org/10.1042/bj3070769

McPherron, A. C., Lawlert, A. M., & Lee, S.-J. (1997). Regulation of skeletal muscle mass in mice by a new TGF-fl superfamily member. *Nature*, *387*, 83–90.

Mcpherron, A. C., & Lee, S.-J. (1997). Double muscling in cattle due to mutations in the myostatin gene. In *Genetics Communicated by Daniel Nathans* (Vol. 94). www.pnas.org.

Meissner, G., Darling, E., & Eveleth, J. (1986). Kinetics of rapid Ca2+ release by sarcoplasmic reticulum. Effects of Ca2+, Mg2+, and adenine nucleotides. *Biochemistry*, *25*(1), 236–244.

Mosher, D. S., Quignon, P., Bustamante, C. D., Sutter, N. B., Mellersh, C. S., Parker, H. G., & Ostrander, E. A. (2007). A mutation in the myostatin gene increases muscle mass and enhances racing performance in heterozygote dogs. *PLoS Genetics*, *3*(5), 779–786. https://doi.org/10.1371/journal.pgen.0030079

Niggli, E., & Shirokova, N. (2007). A guide to sparkology: The taxonomy of elementary cellular Ca2+ signaling events. *Cell Calcium*, *42*(4–5), 379–387. https://doi.org/10.1016/j.ceca.2007.02.010

Ogawa, Y.; Murayama, T. . K., & N. (2002). Ryanodine receptor isoforms of non-mammalian skeletal muscle. *Frontiers in Bioscience*, *7*, d1184–d1194.

Pawley, J. B. (2006). *Handbook of biological confocal microscopy*. Springer Velag.

Picht, E., Zima, A. V., Blatter, L. A., & Bers, D. M. (2007). SparkMaster: Automated calcium spark analysis with ImageJ. *American Journal of Physiology - Cell Physiology*, *293*(3), 1073–1081. https://doi.org/10.1152/ajpcell.00586.2006

Pierantozzi, E., Szentesi, P., Al-Gaadi, D., Oláh, T., Dienes, B., Sztretye, M., Rossi, D., Sorrentino, V., & Csernoch, L. (2019). Calcium homeostasis is modified in skeletal muscle fibers of small ankyrin1 knockout mice. *International Journal of Molecular Sciences*, *20*(13). https://doi.org/10.3390/ijms20133361

Pouvreau, S., Royer, L., Yi, J., Brum, G., Meissner, G., Ríos, E., & Zhou, J. (2007). Ca2+ sparks operated by membrane depolarization require isoform 3 ryanodine receptor channels in skeletal muscle. *Proceedings of the National Academy of Sciences of the United States of America*, *104*(12), 5235–5240. https://doi.org/10.1073/pnas.0700748104

Prada, J., Sasi, M., Martin, C., Jablonka, S., Dandekar, T., & Blum, R. (2018). An open source tool for automatic spatiotemporal assessment of calcium transients and local 'signal-close-to-noise' activity in calcium imaging data. In *PLoS Computational Biology* (Vol. 14, Issue 3). https://doi.org/10.1371/journal.pcbi.1006054

Ríos, E., & Pizarro, G. (1991). Voltage sensor of excitation–contraction coupling in skeletal muscle. *Physiological Reviews*, *71*, 849–908.

Ríos, E., Shirokova, N., Kirsch, W. G., Pizarro, G., Stern, M. D., Cheng, H., & González, A. (2001). A preferred amplitude of calcium sparks in skeletal muscle. *Biophysical Journal*, *80*(1), 169–183. https://doi.org/10.1016/S0006-3495(01)76005-5

Ríos, E., & Stern, M. D. (1997). Calcium in close quarters: microdomain feedback in excitation-contraction coupling and other cell biological phenomena. *Annual Rewiev of Physiology*, *26*, 47–82.

Röchlich, P. (2006). *Szövettan*. Semmelweis Kiadó.

Rodney, G. G., & Schneider, M. F. (2003). Calmodulin modulates initiation but not termination of spontaneous Ca2+ sparks in frog skeletal muscle. *Biophysical Journal*, *85*(2), 921–932. https://doi.org/10.1016/S0006-3495(03)74531-7

Sebille, S., Cantereau, A., Vandebrouck, C., Balghi, H., Constantin, B., Raymond, G., & Cognard, C. (2005). Calcium sparks in muscle cells: Interactive procedures for automatic detection and measurements on line-scan confocal images series. *Computer Methods and Programs in Biomedicine*, *77*(1), 57–70. https://doi.org/10.1016/j.cmpb.2004.06.004

Shen, J., Yu, W. M., Brotto, M., Scherman, J. A., Guo, C., Stoddard, C., Nosek, T. M., Valdivia, H. H., & Qu, C. K. (2009). Deficiency of MIP/MTMR14 phosphatase induces a muscle disorder by disrupting Ca2+ homeostasis. *Nature Cell Biology*, *11*, 769–776.

Shirokova, N., García, J., & Ríos, E. (1998). Local calcium release in mammalian skeletal muscle. *Journal of Physiology*, *512*(2), 377–384. https://doi.org/10.1111/j.1469-7793.1998.377be.x

Sorrentino, V. (2011). Sarcoplasmic reticulum: Structural determinants and protein dynamics. *International Journal of Biochemistry and Cell Biology*, *43*(8), 1075–1078. https://doi.org/10.1016/j.biocel.2011.04.004

Strand, M. A., Louis, C. F., & Mickelson, J. R. (1993). Phosphorylation of the porcine skeletal and cardiac muscle sarcoplasmic reticulum ryanodine receptor. *BBA - Molecular Cell Research*, *1175*(3), 319–326. https://doi.org/10.1016/0167-4889(93)90224-D

Suko, J., Maurer-Fogy, I., Plank, B., Bertel, O., Wyskovsky, W., Hohenegger, M., & Hellmann, G. (1993). Phosphorylation of serine 2843 in ryanodine receptor-calcium release channel of skeletal muscle by cAMP-, cGMP- and CaM-dependent protein kinase. *Biochimica et Biophysica Acta - Molecular Cell Research - Molecular Cell Research*, *1175*(2), 193–206. https://doi.org/10.1016/0167-4889(93)90023-I

Sultana, N., Dienes, B., Benedetti, A., Tuluc, P., Szentesi, P., Sztretye, M., Rainer, J., Hess, M. W., Schwarzer, C., Obermair, G. J., Csernoch, L., & Flucher, B. E. (2016). Restricting calcium currents is required for correct fiber type specification in skeletal muscle. *Development (Cambridge)*, *143*(9), 1547–1559. https://doi.org/10.1242/dev.129676

Szabó, G. (Ed.). (2004). *Sejtbiológia*. Medicina.

Szabó, L. Z., Vincze, J., Csernoch, L., & Szentesi, P. (2010). Improved spark and ember detection using stationary wavelet transforms. *Journal of Theoretical Biology*, *264*(4), 1279–1292. https://doi.org/10.1016/j.jtbi.2010.04.005

Szentesi, P., Szappanos, H., Szegedi, C., Gönczi, M., Jona, I., Cseri, J., Kovács, L., & Csernoch, L. (2004). Altered Elementary Calcium Release Events and Enhanced Calcium Release by Thymol in Rat Skeletal Muscle. *Biophysical Journal*, *86*, 1436–1253.

Szigeti, G. P., Almássy, J., Sztretye, M., Dienes, B., Szabó, L., Szentesi, P., Vassort, G., Sárközi, S., Csernoch, L., & Jóna, I. (2007). Alterations in the calcium homeostasis of skeletal muscle from postmyocardial infarcted rats. *Pflugers Archiv European Journal of Physiology*, *455*(3), 541–553. https://doi.org/10.1007/s00424-007-0298-z

Sztretye, M., Almássy, J., Deli, T., Szentesi, P., Jung, C., Dienes, B., Simut, C. A., Niggli, E., Jona, I., & Csernoch, L. (2009). Altered sarcoplasmic reticulum calcium transport in the presence of the heavy metal chelator TPEN. *Cell Calcium*, *46*(5–6), 347–355. https://doi.org/10.1016/j.ceca.2009.10.002

Tang, Z. Z., Yarotskyy, V., Wei, L., Sobczak, K., Nakamori, M., Eichinger, K., Moxley, R. T., Dirksen, R. T., & Thornton, C. A. (2012). Muscle weakness in myotonic dystrophy associated with misregulated splicing and altered gating of Ca v1.1 calcium channel. *Human Molecular Genetics*, *21*(6), 1312–1324. https://doi.org/10.1093/hmg/ddr568

Tian, Q., Schröder, L., Schwarz, Y., Flockerzi, A., Kaestner, L., Zeug, A., Bruns, D., & Lipp, P. (2019). Large scale, unbiased analysis of elementary calcium signaling events in cardiac myocytes. *Journal of Molecular and Cellular Cardiology*, *135*(July), 79–89. https://doi.org/10.1016/j.yjmcc.2019.08.004

Toyofuku, T., Kurzydlowski, K., Tada, M., & MacLennan, D. H. (1993). Identification of regions in the Ca2+-ATPase of sarcoplasmic reticulum that affect functional association with phospholamban. *Journal of Biological Chemistry*, *268*(4), 2809–2815. https://doi.org/10.1016/s0021-9258(18)53845-x

Tsugorka, A., Ríos, E., & Blatter, L. A. (1995). Imaging elementary events of calcium release in skeletal muscle cells. *Science*, *269*(5231), 1723–1726. https://doi.org/10.1126/science.7569901

Tuluc, P., Molenda, N., Schlick, B., Obermair, G. J., Flucher, B. E., & Jurkat-Rott, K. (2009). A Cav1.1 Ca2+ channel splice variant with high conductance and voltage-sensitivity alters EC coupling in developing skeletal muscle. *Biophysical Journal*, *96*(1), 35–44. https://doi.org/10.1016/j.bpj.2008.09.027

Unser, M., & Aldroubi, A. (1996). A review of wavelets in biomedical applications. *Proceedings of the IEEE*, *84*(4), 626–638.

Van Petegem, F. (2012). Ryanodine receptors: Structure and function. *Journal of Biological Chemistry*, *287*(38), 31624–31632. https://doi.org/10.1074/jbc.R112.349068

Vincze, J., Jenes, Á., Füzi, M., Almássy, J., Németh, R., Szigeti, G., Dienes, B., Gaál, Z., Szentesi, P., Jóna, I., Kertai, P., Paragh, G., & Csernoch, L. (2015). Effects of fluvastatin and coenzyme Q10 on skeletal muscle in normo- and hypercholesterolaemic rats. *Journal of Muscle Research and Cell Motility*, *36*(3), 263–274. https://doi.org/10.1007/s10974-015-9413-5

Von Wegner, F., Both, M., Fink, R. H. A., & Friedrich, O. (2007). Fast XYT imaging of elementary calcium release events in muscle with multifocal multiphoton microscopy and wavelet denoising and detection. *IEEE Transactions on Medical Imaging*, *26*(7), 925–934. https://doi.org/10.1109/TMI.2007.895471

Von Wegner, F. V., Both, M., & Fink, R. H. A. (2006). Automated detection of elementary calcium release events using the à trous wavelet transform. *Biophysical Journal*, *90*(6), 2151–2163. https://doi.org/10.1529/biophysj.105.069930

Zhou, J., Brum, G., González, A., Launikonis, B. S., Stern, M. D., & Ríos, E. (2003). Ca2+ sparks and embers of mammalian muscle. Properties of the sources. *Journal of General Physiology*, *122*(1), 95–114. https://doi.org/10.1085/jgp.200308796

Zhou, J., Brum, G., González, A., Launikonis, B. S., Stern, M. D., & Ríos, E. (2005). Concerted vs. sequential. Two activation patterns of vast arrays of intracellular ca2+ channels in muscle. *Journal of General Physiology*, *126*(4), 301–309. https://doi.org/10.1085/jgp.200509353

Zhou, J., Yi, J., Royer, L., Launikonis, B. S., González, A., García, J., & Ríos, E. (2006). A probable role of dihydropyridine receptors in repression of Ca 2+ sparks demonstrated in cultured mammalian muscle. *American Journal of Physiology - Cell Physiology*, *290*(2). https://doi.org/10.1152/ajpcell.00592.2004

Zucchi, R., & Ronca-Testoni, S. (1997). The sarcoplasmic reticulum Ca2+ channel/ryanodine receptor: Modulation by endogenous effectors, drugs and disease states. *Pharmacological Reviews*, *49*(1), 1–50.

10. APPENDIX

A spark kereső és analizáló program fontosabb függvényei Matlab m kódban:

1 dimenziós wavelet analízis

```
function [p, w] = atrous1 (x, levels)
%1D a trous transform
%input:
% B: convolution kernel
% x: is a column vector with data
% levels: wavelet levels to calculate
%returns:
% w(:,i) wavelet coefficients i=1..levels
% p(:,i) reziduum, i=1..levels

B=[ 1  4  6  4  1  ] ./ 16; % spline of order 3 kernel
p=[];
w=[];

[ m, n ] =size(x);

%check if circular convolution is possible
z=length(upsample(B, 2.^(levels-1) ));

if z > n  |  m~=1
    error('x is small sized or not a column vector');
end

for i = 1:levels
    if i==1
        B1=B;
    else
        zs=2.^(i-1);
        B1 = upsample(B,2.^(i-1));
        B1=B1(1:end-(zs-1)); %eliminate 0-s from the end
    end

    if i==1
        a=imfilter_plus_1D(x,B1);
    else
        a=imfilter_plus_1D(p(:,i-1)',B1);
    end
    p(:,i) = a';

    if i==1
       w(:,i) = x' - p(:,i);
    else
       w(:,i) = p(:,i-1) - p(:,i);
    end
end
return
```

```
function res1=imfilter_plus_1D (x,B)
%convolve circular x with B
%input:
% x: column vector
% B: column vector
%returns:
% res1: convolved x

L=length(x);
LB=length(B);

res = imfilter (x,B,'circular','conv','full');
halfr=fix(LB/2) +1;
res1 = res ( halfr : L+halfr-1);
return
```

2 dimenziós wavelet analízis

```
function [p,w] = atrous2 (x,L)
%2D a trous transform
%input:
% x: 2D array with data
% levels: wavelet levels to calculate
%returns:
% w(:,i) 2D wavelet coefficients for i=1..levels
% p(:,i) reziduum, i=1..levels

%B: convolution kernel
B=[  1/256, 1/64, 3/128, 1/64, 1/256 ; ...
        1/64 , 1/16, 3/32, 1/16, 1/64 ; ...
        3/128, 3/32, 9/64, 3/32, 3/128; ...
        1/64 , 1/16, 3/32, 1/16, 1/64 ; ...
        1/256, 1/64, 3/128, 1/64, 1/256     ];
[ro, co]=size(x);
p=zeros(ro,co,L);
w=p;

for i = 1:L
    if i==1
        B1 = a_trous(B,i);
        a=imfilter_plus(x,B1);
        p(:,:,i) = a;
        w(:,:,i) = x - p(:,:,i);
    else
        B1 = a_trous(B,i);
        a=imfilter_plus(p(:,:,i-1),B1);
        p(:,:,i) = a;
        w(:,:,i) = p(:,:,i-1) - p(:,:,i);
    end
end
return
```

```
function B2 = a_trous(B,L)
%calculate level L of the a trous transform
%input:
% B: convolution kernel
% L: level
%returns:
% B2: kernel for the Lth level
zs=2^(L-1);
B1=upsample(B,zs);
B2=upsample(B1',zs);
r = size(B2,1);
h=zs-1;  % number of holes
B2=B2(1:end-h, 1:end-h);
return

function res1 = imfilter_plus ( p, B )
%calculate the transform
%input:
% p: data
% B: kernel for the Lth level
%returns:
% res1: transformed data
[ r c ] = size(B);       % assume r == c
[ rows cols ] = size(p);
res = imfilter(p(:,:),B,'circular','conv','full');
halfr=fix((r-1)/2)+1;
halfc=halfr;
res1 = res( halfr : rows+halfr-1, halfc : cols+halfc-1);
return
```

2 dimenziós wavelet detektálás

```
function [B1 ,spark_rc, labels] =
             wavelet_detect
(img,sigma,tau,L,detect_from,detect_to)
%detects calcium events with the a trous transform
%input params
% img: denoised image
% sigma: estimated standard deviation of the noise
% tau: adjustable threshold
% L: vavelet levels
% detect from & to: wavelet levels used for detection
% some parameters read from configuration data with
getswconfig()
%returns
% B1: mask with spark areas in image
% spark_rc: cell array with detected sparks positional
parameters
% labels: color mask with spark areas, label colors

%size of events to be descarded
```

```
DROPSMALL=getswconfig('SPARKMETA.dropsmall');
%distance for 2 events to be merged
MERGE=getswconfig('SPARKMETA.merge');

%calculate wavelet transorms for L levels
[r,w]=atrous2(img,L);

%threshold for each plane
sWGNj = calc_thresh (img, L) .* sigma .* tau ;
[m n]=size(img);

%calculate the multiresolution support
M=zeros(m,n,L);
for j=1:L
    wc = w(:,:,j);
    ma = wc >= sWGNj(j);
    M(:,:,j) = ma;
end

%detection

AND_OR = 0;  % 0 use OR, 1 use AND when creating mask from MRS
             % common use is 0

BAND = ones(m,n);
B = zeros(m,n);
for j=detect_from:detect_to
    BAND = B & M(:,:,j);
    B = B | M(:,:,j);
end

%no tests, normal flow - detection ends here
if ~getswconfig('TEST_W')
    %drop small areas if 'SPARKMETA.dropsmall' difers from 0
    if DROPSMALL
       [B1, spark_rc, labels] = wavelet_dropsmall (B,
DROPSMALL, 8);
       lsrc=length(spark_rc);
       if length(spark_rc) > getswconfig('spark_limit')
            disp('Event count exceeds limit.')
            return
       end
    else
        B1=B;
    end

    %if USE_MERGE
    if MERGE
        %between centroids
        %ms between and and start of BoundingBox
        [B1, spark_rc, labels ] = mergeareas4 (B1, MERGE);
```

```
    end

%run single spark test
else
    %check mask for all levels
    for j=detect_from:detect_to
       [B1, spark_rc, labels]= get_sparkrc (M(:,:,j),
DROPSMALL, 8);
       if ~isempty(spark_rc)
         x = spark_rc{1};
         % r1 r2 c1 c2
         disp(
             sprintf('Mask position level %d: %d %d %d %d', j,
x )
             );
          [ a, b ] = mask_size (M(:,:,j));
        else
         disp( sprintf ( 'Mask position level %d: no mask',
j ));
        end
    end

    %calculate spark positional parameters
    %mask: row1, row2, col1, col2
    [B1, spark_rc, labels]= get_sparkrc (B, DROPSMALL, 8);
end
return
```

Normalizált kép kiszámítása

```
function  Fp = wavelet_deltaFpF (F, B)
%deltaF/F filter
%input
% F: original image, pixel values in double format
% B: mask with pixels above considered threshold on 0,
%    pixels under threshold (background) on 1
%output:
% Fp: normalized image

%J=> t direction , I=> x direction
J=rows(F);
I=cols(F);

P  = zeros (1,J); % t time direction vector
Q  = zeros (1,I); % space direction vector
Fr = zeros (1,I); %

Fp = F ; %start with original values

%mean of background pixel values for each i vector (space
direction)
for i = 1:I;
```

```
    %number of pixels on 1 in the i'th column
    pixels = length(find (B(:,i)==1));
    if pixels==0
        Fr(i) = sum ( Fp(:,i) ) ./ J;
    else
        Fr(i) = sum ( Fp(:,i) .* B(:,i) ) ./  pixels;
    end
end;

%calculate normalized image, divide pixels by Fr(i)
for i=1:I
    j=1:1:J;
    ix=find(Fr==0);
    if ~isempty(ix)
        non_z_ix=find(Fr~=0);
        Fr_nz=Fr(non_z_ix);
        Fr(ix)=mean(Fr_nz);
    end
    Fp(j,i) = Fp(j,i) ./  Fr(i) ;
    end;

if any(isnan(Fp(:)))
    error('wavelet_deltaFpF: Fp contains NaN-s');
end
return
```

Zajszűrés

```
function [dn_img, sigma] =
denoise_starck( img, r, w, L, delta, EPSILON)
%input
% img: normalized or original image
% r: residuals
% w: wavelet scales
% L: wavelet levels used
% delta: threshold level
% EPSILON: difference to stop when calculating sigma
%returns:
% dn_img: denoised image
% sigma: standard deviation of the noise


%calculate thresh array sWGN
sWGN = calc_thresh (img, L); % sigma in wavelet levels of a
standard
                             % normal distribution

%calculate initial sigma

[m,n]=size(img);
```

```
%img1 pixels > 3 sigma excluded
[img1, mask] = sigmafilter (img, 2.5); % pixels above 3 sigma
are set to 0

img2=img1(find(img1~=0));
sigma = std (img2(:));  %init sigma of pixels below 2.7 sigma
%this is a rough approximation

ksigmas = ksigma ( img );
disp(sprintf('k-sigma estimated %.2f',ksigmas));

maxdoit=20;             %limit: stop after  20 cycles if no
result
doit=maxdoit;
%calculate a beter approximation of sigma
while doit > 0
    M=zeros(m,n,L);  %multiresolution support
    for j=1:L
        sj= 3 .* sWGN(j) .* sigma;
        wc = w(:,:,j);
        ma = wc < sj;
        M(:,:,j) = ~ma; %points above threshold
    end

    %vizualise multiresolution support
    S=zeros(m,n);
    for j=1:L
        ma=M(:,:,j);
        S = S  +  ma * 2 ^ j;
    end
    %end visualisation

    mask = S ~= 0;  %all pixels above threshold
    N = ( img - r(:,:,L) ) .*  ~mask;   %extract background

    %eliminate zeros
    N=N(find(N ~= 0));
    sigma1=std(N(:));
    eps=abs(sigma-sigma1) / (sigma+0.00000001);
    sigma=sigma1;
    doit=doit-1;
    if eps < EPSILON
        break
    end
    if doit < 0
        disp('denoise_starck: can''t find sigma for noise');
    end
    if sigma == NaN
        error('panic: sigma is NaN');
    end
end
```

```
% see Starck and Murtagh 1998,  Automatic noise ...
sigma = sigma ./ 0.974;

disp(sprintf('sigma for noise %.2f detected with %d
iterations',sigma,maxdoit-doit));

%use selected threshold type
if getswconfig('soft_thresh')
    disp('Soft thresh');
    for j=1:L
        sj= delta * sWGN(j) * sigma ;%* (L-j)/L;
        absw=abs(w(:,:,j));
        w(:,:,j) = (absw-sj) .* sign(w(:,:,j)) .* (absw > sj);
    end

elseif getswconfig('hard_thresh')        %threshold wj at
delta * sigmaj
    disp('Hard thresh');
    for j=1:L
        sj= delta * sWGN(j) * sigma ;%* (L-j)/L;
        ma = abs(w(:,:,j)) > sj;
        w(:,:,j) = ma .* w(:,:,j) ;
    end
elseif getswconfig('affine_thresh')
    disp('Affine thresh');
    for j=1:L
        T = delta * sWGN(j) * sigma ;%* (L-j)/L;
        ex=abs(w(:,:,j)) < T/2 ;  % ex=1 excluded pixels
        uc=abs(w(:,:,j)) > T ;    % uc=1 where they remain
unchanged
        %T/2 negative values.
        minush= w(:,:,j) >= -T   &  w(:,:,j) <= -T/2;
        %T/2 positive values
        plush = w(:,:,j) <=  T   &  w(:,:,j) >=  T/2;
        res = w(:,:,j) .* uc;   % unchanged
        res = res + (w(:,:,j) .* 2 + T ) .* minush;
        res = res + (w(:,:,j) .* 2 - T ).* plush ;
        w(:,:,j) = res;
    end
elseif getswconfig('universal_thresh')
    disp('Universal thresh');
    Npixels=m.*n;
    for j=1:L
        sj= sWGN(j) .* sqrt(2.*log10(Npixels)) .* sigma;
        ma = w(:,:,j) > sj;
        w(:,:,j) = ma .* w(:,:,j) ;
    end
    z=1;
else
    error('wavelet threshold radio buttons?');
end
```

```
dn_img = iatrous2_denoise(r,w); %rebuild image , but  drop
plane 1
return
```

A kiugró pixelek kiszűrése

```
function [img1 , plist]= wspike ( img )
%input:
% img: normalized image
%returns:
% img1: spike filtered image
% plist: list of spike locations

f=[0.125 0.125 0.125; 0.125 0 0.125; 0.125 0.125 0.125];
imf=filter2(f,img);  %filtered mean

HAT=getswconfig('HAT'); %parameter for tuning the threshold
level
                        %values between 3.5 and 4.5

[p,w]=atrous2(img,2);
plist={};
p1=w(:,:,1); p2=w(:,:,2);

xr=p1+p2;  %high frequency

sigma=std2(xr);
m=mean2(xr);

B = abs(xr-m) > HAT.*sigma;

%discard connected regions
B1 = imfilter(B,[1/9 1/9 1/9; 1/9 1/9 1/9; 1/9 1/9 1/9 ]);
B2=B1>=0.3332;

B = B.*~B2;

c=length(find(B~=0));
disp ( [ num2str(c) ' spikes removed' ] );
img1 = img.*~B   + imf.*B;   % places of spikes

[r,c]=find(B==1);
for kk=1:length(r)
   plist{kk}=[r(kk), c(kk)];
end
return
```

Pflugers Arch - Eur J Physiol
DOI 10.1007/s00424-008-0504-7

szentesi.peter_292_24

MUSCLE PHYSIOLOGY

Effects of K-201 on the calcium pump and calcium release channel of rat skeletal muscle

Janos Almassy · Monika Sztretye · Balazs Lukacs · Beatrix Dienes · Laszlo Szabo · Peter Szentesi · Guy Vassort · Laszlo Csernoch · Istvan Jona

Received: 28 December 2007 / Revised: 14 March 2008 / Accepted: 21 March 2008
© Springer-Verlag 2008

Abstract The benzothiazepine derivative K-201 has been suggested as a potential therapeutic agent due to its antiarrhythmogenic action. To understand how the drug alters calcium release from the sarcoplasmic reticulum (SR), we investigated its effects on the SR calcium channel and calcium pump by single channel electrophysiology, whole-cell confocal microscopy, and ATPase activity measurements on control and post-myocardial infarcted (PMI) rat skeletal muscle. In bilayers, K-201 induced two subconductance states corresponding to ~24% (S_1) and ~13% (S_2) of the maximum conductance. Dependence of event frequency and of time spent in S_1 and S_2 on the drug concentration was biphasic both in control and in PMI rats, with a maximum at 50 μM. At this concentration, the channel spends 26±4% and 24±4%, respectively, of the total time in these subconductance states at positive potentials, while no subconductances are observed at negative potentials. K-201 altered the frequency of elementary calcium release events: spark frequency decreased from 0.039±0.001 to 0.023±0.001 s^{-1} sarcomere^{-1}, while the frequency of embers increased from 0.011±0.001 to 0.023±0.001 s^{-1} sarcomere^{-1}. Embers with different amplitude levels were observed after the addition of the drug. K-201 inhibited the Ca^{2+} ATPase characterized by $IC_{50,contr}$=119±21 μM and $n_{Hill,contr}$=1.84±0.48 for control and $IC_{50,PMI}$=122±18 μM and $n_{Hill,PMI}$=1.97±0.24 for PMI animals. These results suggest that although K-201 would increase the appearance of subconductance states, the overall calcium release is reduced by the drug. In addition, the effect of K-201 is identical on calcium release channels from control and PMI rats.

Keywords Calcium spark · Ryanodine receptor · Single channel · JTV519 · Sarcoplasmic reticulum

J. Almassy · M. Sztretye · B. Lukacs · B. Dienes · L. Szabo · P. Szentesi · L. Csernoch · I. Jona
Department of Physiology, University of Debrecen, Debrecen, Hungary

L. Szabo
Department of Electrical Engineering, Sapientia Hungarian University of Transilvania, Tirgu Mures, Transylvania, Romania

G. Vassort
INSERM U-637, Physiopathologie Cardiovasculaire, Université Montpellier 1, Montpellier, France

I. Jona (✉)
Department of Physiology, Medical School, University of Debrecen, Debrecen, Hungary
e-mail: jonai@phys.dote.hu

Introduction

Altered intracellular calcium handling, including anomalous calcium release from the sarcoplasmic reticulum (SR), altered calcium reuptake, and SR calcium load, is associated with decreased muscle contractility in heart failure, which is one of the most frequent causes of death [22]. A large number of drugs have been aimed at the correction of the disabled calcium transport between the different cellular compartments and between the extra- and intracellular spaces [2]. Despite all efforts, there is a lack of therapeutic agents which specially act on the particular cellular components—molecules—which are directly responsible for the different abnormalities. Another problem generally associated with the presently known drugs is their interference with other cellular processes.

A benzothiazepine derivative, K-201 (4[3(1-(4-benzyl) piperidinyl)propionyl]-7-methoxy-2,2,4,5-tetrahydro-1,4-benzothiazepine), was described to have suppressive effects against sudden cardiac cell death caused by myofibrillar overcontraction [9]. The drug has been reported to have a very strong antiarrhythmic effect by reversing atrial fibrillation in a canine sterile pericarditis model [16]. It has also been reported that the drug exhibits significant potential for improving myocardial relaxation during ischemia, accompanied by the inhibition of the decrease in the cellular ATP level [13]. The involvement of FKBP 12.6 (FK-506 binding protein, calstabin2) suggested the importance of the calcium handling system in these cardioprotective effects [31, 32]. This idea was reinforced by the stabilization of calcium microwave-induced unbalanced calcium cycling [3].

Other observations suggest that K-201 might have some effects independent from strengthening the interaction between the ryanodine receptor (RyR) and calstabin. K-201 not only affects type 1 (RyR1) and type 2 (RyR2) receptors, but it also alters the gating properties of the sarcolemmal voltage sensor (dihydropyridine receptor, DHPR), increasing the peak Ca^{2+} flux by 22% at 1 μM and by 60% at 3 μM concentration [15]. Thus, the cardioprotection consists of several components, including the RyR, the FKBP 12.6, the voltage sensor of the sarcolemma and the calcium pump of the SR [7, 30]. In a familiar polymorphic ventricular tachycardia, the involvement of a leaky RyR was reported, which is due to its hyperphosphorylated FKBP 12.6. The gating of these leaky RyR2 channels could be partially restored by the use of K-201 [18]. Furthermore, diminished skeletal muscle function that developed after ischemia could be partially reversed by the strengthening of the SR calcium handling abilities by the administration of K-201 [12, 30].

Annexin V could also be a specific target for K-201 as indicated by the crystallization of the annexin V–K-201 complex [10]. K-201 inhibited the annexin V-dependent calcium flux in an artificial vesicle system, pointing out that K-201 inhibits different types of calcium channels [11]. Kawabata [13] interpreted the reported cardioprotective effect of K-201 as a consequence of its inhibition of the nitric oxide synthase. Besides its several positive effects on the heart, K-201 also has a natriuretic effect and enhances the glomerular filtration rate [21].

Little is known, however, how K-201 directly affects RyR1 function and whether calcium release channels from post-myocardial infarcted rats (PMI) would respond differently to the drug. In this study, we thus investigated the effect of K-201 on the isolated skeletal type ryanodine receptor using control and PMI rats, confocal calcium imaging of skeletal muscle fibers, and the effect of the drug on the calcium reuptake system.

Materials and methods

Animal model

Male Wistar rats were subjected to coronary artery ligation to produce PMI, and sham-operated animals served as controls [29]. In brief, rats (180–220 g) were anesthetized (pentobarbital, 60 mg/kg) and ventilated. After left-median thoracotomy, the left anterior coronary artery was occluded with a 7–0 silk suture at the most proximal position. Sham-operated animals were subjected to the same surgical operation without any ligation of the coronary artery. PMI rats were used ~24 weeks after surgery and were arbitrarily selected according to the visible level of remodeling estimated by the size (at least 50%) of the fibrotic area on the left ventricle. No difference was observed between control and PMI animals in muscle mass.

Heavy SR vesicle preparation

Heavy SR (HSR) vesicles—containing sealed vesicles formed from membrane fragments of the terminal cisternae of the SR—were isolated from rat skeletal muscle according to Lai and Meissner [17] with slight modifications [8]. After a homogenization in 100 mM NaCl, 20 mM ethylene glycol tetraacetic acid (EGTA), 20 mM Na-(4-(2-hydroxyethyl)-1-piperazineethanesulfonic acid) (HEPES), pH=7.5, first crude microsomes were collected by centrifugation at 40,000×*g*. After removing the actomyosin contamination by solubilization in 600 mM KCl, the microsome fraction was collected at 109,000×*g*. The pellet was resuspended and loaded onto a 20–45% linear sucrose gradient. HSR vesicles were extracted from the 36–38% region of the continuous sucrose gradient, collected by centrifugation and resuspended in 0.4 M sucrose, 10 mM K-PIPES, pH=7.0. Vesicles were immediately used for RyR1 purification or aliquoted and rapidly frozen in LN_2 and stored at −78°C for further use. Light SR (LSR) vesicles were collected from the 30–32% region of the continuous sucrose gradient, collected by centrifugation and resuspended in 250 mM KCl, 20 mM K-PIPES, pH=7.4, aliquoted and rapidly frozen in liquid nitrogen, then stored at −78°C for further use. Protein concentration was measured by the Biuret method.

RyR1 reconstitution and single-channel recording

Measurements of channel activity were carried out using purified RyR1 incorporated into planar lipid bilayers. RyR1 was purified from rat SR vesicles as previously described [28]. The bilayers were formed using phosphatidylethanolamine, phosphatidylserine, and L-phosphatidylcholine in a ratio of 5:4:1 dissolved in *n*-decane up to the final lipid concentration of 20 mg/ml. Bilayers were formed across a

szentesi.peter_292_24

200- or 250-μm diameter aperture of a Delrin cap using a symmetrical buffer solution (250 mM KCl, 100 μM K_2H_2EGTA, 150 μM $CaCl_2$, 20 mM PIPES, pH 7.2). A small aliquot of purified RyR1 was added into the chamber which was defined as the *cis* (cytoplasmic) side, whereas the other chamber was labeled as the *trans* (luminal) side and was kept on ground potential. To ensure the orientation of the incorporated RyR1, we tested the effect of Ca^{2+} on both sides. After successful incorporation of the RyR1 channel, free calcium concentration in the *cis* chamber was adjusted to 238 nM by the addition of EGTA. Electrical signals were filtered at 1 kHz through an eight-pole low-pass Bessel filter and digitized at 3 kHz using Axopatch 200 and pCLAMP 6.03 (Axon Instruments, Union City, CA, USA). Total recording time in each experiment was 10–20 min for each experimental condition tested. After changing conditions, at least 5 min were allowed for equilibration, which appeared to be enough to reach the new equilibrium of the parameters. Single-channel measurements were carried out at 22±1°C. The free Ca^{2+} concentration was calculated using the computer program and affinity constants published by Fabiato [4]. Open probabilities were calculated using the common 50% criteria with a medial dead zone of ±2.5%. Current amplitude distribution—from the all-point histograms—was analyzed using Origin (Microcal Software, Northampton, MA, USA). Partial open probabilities of the S_1 (P_{S1}) and of the S_2 substate (P_{S2}) were calculated using the amplitudes of the all point histograms, such as the ratio of the amplitude of S_1 to the sum of the amplitudes of the four possible states (open + S_1 + S_2 + closed, called as "total" in the figures). The expression "physiological" current direction is used when the cations (Ca^{2+} or K^+) move as the calcium ions move during calcium release (from the SR), while "reverse" direction denotes when cations move in the opposite direction.

Calcium flux of HSR vesicles

HSR vesicles were actively loaded with calcium, and the calcium efflux was determined by measuring the extravesicular calcium concentration using a Fluoromax spectrofluorometer (Jobin-Yvon, New Jersey, USA) modified for absorption measurements by monitoring the transmittance at 710 and 790 nm and calculating the corrected absorbance change ($A_{710}-A_{790}$), as described earlier [23]. In brief, vesicles were suspended in the cuvette (final volume 2 ml) in a medium containing 92.5 mM KCl, 1 mM $MgCl_2$, 180 μM APIII, 54 μM $CaCl_2$, 18.5 mM K-MOPS up to a final protein concentration of 260 μg/ml. Vesicles were actively loaded with calcium in the cuvette by the addition of 1 mM ATP followed by the addition of the appropriate amount of $CaCl_2$. The K-201 was added to see whether there is an increase of the calcium leak. Calcium efflux was calculated from the time segment between 10 and 70 s after the addition of K-201 by fitting a straight line to the trace. At the end of the experiment, 300 μM thymol were applied to check the calcium load. Measurements were carried out at 37°C with continuous stirring using a special magnetic stirrer having a mixing time of 0.2–0.5 s.

Determination of ATPase activity

ATPase activity was determined at 37°C by a coupled enzyme assay in a medium containing 100 mM KCl, 20 mM Tris–HCl, 5 mM $MgCl_2$, 5 mM ATP, 0.42 mM phosphoenolpyruvate, 0.001 mM calcimycin (A23187, a Ca^{2+} ionophore), 0.2 mM NADH, 7.5 U/ml pyruvate kinase, and 18 U/ml lactate dehydrogenase (pH 7.5). Total hydrolytic activity was measured as the decrease of optical density at the NADH absorbance wavelength (340 nm) and expressed in micromoles of inorganic phosphate per milligrams of protein per minute, abbreviated as A.U. Total hydrolytic activity of the LSR vesicles ranged from 6.12 to 6.86 A.U., while Ca^{2+}-dependent ATPase activity was identified as the portion of total hydrolytic activity inhibited by 5 μM thapsigargin (Szentesi et al.) [27]. Relative ATPase activity was calculated to reduce the differences of "maximal activity" between the different preparations. The drug was added to the preparation 5 min before starting measurements of enzyme activity. The assay was performed in the presence of Ca^{2+}, and EGTA mixtures producing estimated free Ca^{2+} concentration (2 μM) were found to induce maximum SERCA activation. The K-201 dependence of the enzymatic activity was fitted using the Hill equation: $y = V_{max} * \left(1 - x^n / \left(IC_{50}^n + x^n\right)\right)$, where y is the normalized inhibition of the hydrolytic activity at the given K-201 concentration (x), IC_{50} is the half effective inhibitory concentration, and n is the Hill coefficient.

Isolation of single fibers

Single skeletal muscle fibers from the *extensor digitorum communis* muscles, muscles consisting mostly of fast 2A type fibers, of rats were isolated enzymatically as described previously [26]. Rats of either sex were anaesthetized and killed by cervical dislocation after the protocol approved by the institutional Animal Care Committee. Individual fibers were dissociated from the muscle using collagenase treatment. The selected fiber was transferred to the recording chamber, and the surface membrane was permeabilized with a relaxing solution (125 mM potassium glutamate, 10 mM HEPES, 1 mM EGTA, 5 mM $MgCl_2$, 5 mM Na_2–ATP, 10 mM sodium phosphocreatine, 10 mM glucose, 0.13 mM $CaCl_2$ and 8% dextran, 0.05 mM Fluo-3) containing 0.002% saponin. This solution was then changed to a potassium–glutamate- or K_2SO_4-based inter-

nal solution (mM: 95 K_2SO_4, 10 HEPES, 1 EGTA, 6 $MgCl_2$, 5 Na_2–ATP, 10 sodium phosphocreatine, 10 glucose, 0.26 $CaCl_2$, 0.1 Fluo-4, and 8% dextran). The pH of the solutions was adjusted to 7.2. K-201 was added from 20 mM stock solution in 1 μM final concentration.

Measurement of elementary calcium release events

Fibers were imaged with an LSM 510 META laser scanning confocal microscope (Zeiss, Oberkochen, Germany) as reported previously [27]. Line-scan images of fluorescence ($F(x,t)$) were taken at 1.54 ms line^{-1} and 512 pixels line^{-1} (pixel size 0.142 μm) parallel to the fiber axis. Fluo-4 was excited at 488 nm (argon ion laser), and emitted light was collected through a band-pass filter and digitized at 12 bit. Elementary calcium-release events were captured using an automatic computer detection method as described in our previous reports [25, 27]. Briefly, the program identified elementary events as regions with fluorescence above a relative threshold, calculated from the noise in the images, and having amplitudes greater than 0.2 $\Delta F/F_0$ units. The eventless portion of the image was used to calculate baseline fluorescence ($F_0(x)$). The program also determined the amplitude (A, as $\Delta F/F_0$), spatial half-width measured at the time of the peak (full width at half-maximum; FWHM), duration, and rise time for sparks and sparks with embers, and average amplitude, duration, and FWHM for lone embers. FWHM was calculated by fitting a Gaussian function to the spatial distribution obtained by averaging three lines at the peak for sparks or by all lines except the first and last 10 ms of the event for lone embers.

Chemicals

Protease inhibitors were obtained from Boeringer (Mannheim, Germany), Fluo-3 and Fluo-4 were purchased from Molecular Probes (Eugene, OR, USA), while all other chemicals, unless otherwise specified, were from Sigma (St. Louis, MO, USA). K-201 was supplied by AETAS Pharma, Tokyo, Japan as a powder, and stock solutions of 20 mM were prepared in the same buffer, which were used in the given experiment.

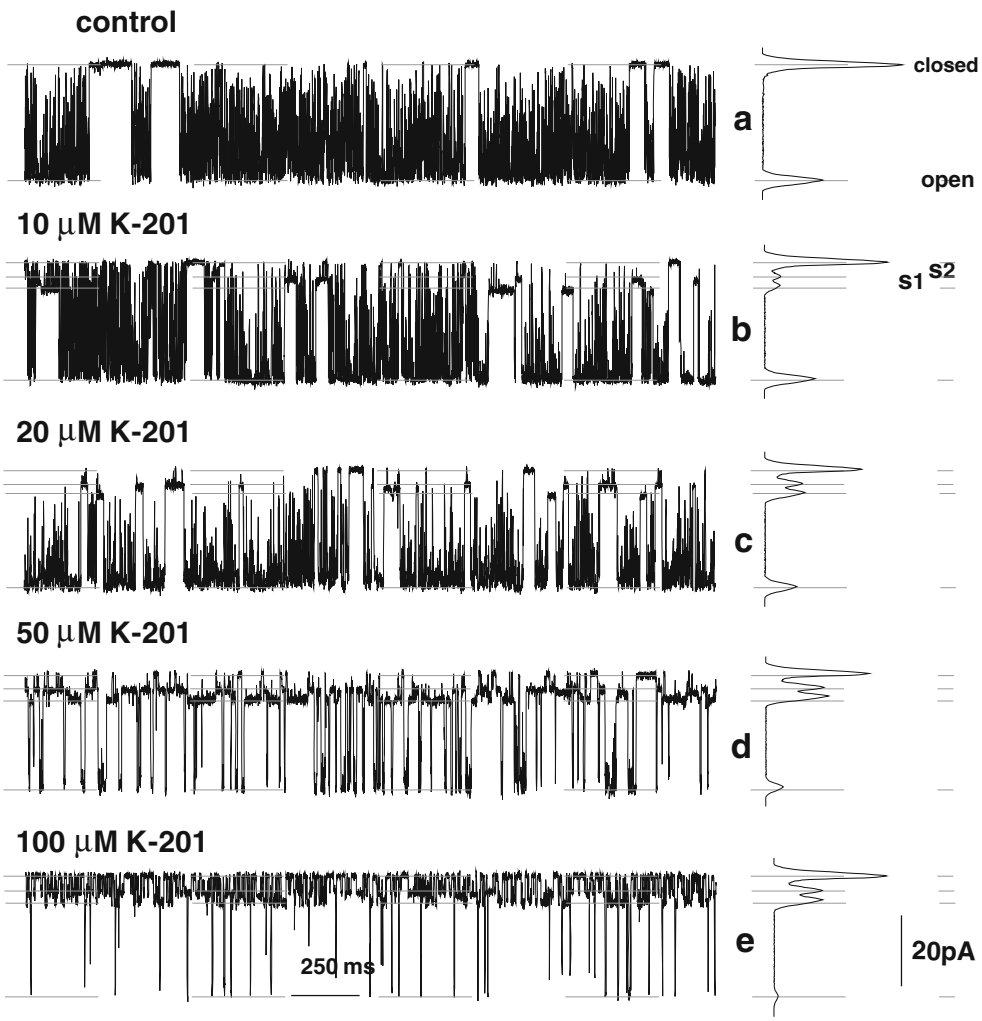


Fig. 1 K-201 induces subconductance states of the control RyR1. Solubilized Ryanodine receptor of control rats was incorporated into a lipid bilayer, and the channel current was recorded under voltage clamp condition using 64 mV as the holding potential. The charge carrier was 250 mM KCl with a symmetrical free calcium concentration of 50 (M. Channel openings are represented by downward deflections. The open, the closed and the subconductance states of the channel are marked on the *right side of the current traces*, with the all-point histograms for all recordings made at the given concentration of K-201. Current trace in the absence of the drug (**a**, control), and in the presence of 1 μM K-201 (**b**) exhibiting two subconductance states (S1, S2). Current trace in the presence of 10 μM K-201 (**c**), 20 μM K-201 (**d**), 50 μM K-201 (**e**), and 100 μM K-201 (**f**)

szentesi.peter_292_24

Statistics

All values were expressed as mean±SE of mean of *n* data. For testing significant differences between control and K-201 data, the Microsoft Office Excels' built-in *t* test for two samples assuming equal variance statistical test was used at 0.05 confidence level. To find the coefficients (parameters) of the independent variable(s) that give the "best fit" between the equation and the data, built-in functions and methods of SigmaPlot (SPSS, Chicago, IL, USA) were used that apply the Marquardt–Levenberg algorithm. The results of the fits are present as the parameters±error of the fit.

Results

Effect of K-201 on channel gating

The effect of K-201 on channel gating was tested using solubilized RyR1 from control rats incorporated into planar lipid bilayer (Fig. 1 trace a). At 10 μM, the drug drastically changed the channel gating. Under normal conditions, RyR1 channel exhibits two states (open and closed); after the addition of 10 μM K-201 to the bath, the channel changes its gating mode, showing two subconductance states denoted as S_1 and S_2 (Fig. 1, trace b) in addition to the open and closed states. In this concentration range, this change is accompanied by a decreased probability of both the open and the closed states. Increasing the drug concentration, the probability of the S_1 and the S_2 states increased at the expense of both the open and the closed states up to 50 μM K-201 concentration (Fig. 1, traces c and d). Note that at this concentration, compared to the control case, the relative reduction of the open state was much more pronounced than that of the closed state. With any further increase in K-201 concentration, the probability of the S_1 and the S_2 states decreased again (Fig. 1, trace e), and also, the open state became less and less favorable for the RyR1, so the overall open probability of the channel substantially decreased.

RyR1 isolated from PMI rats were used for bilayer experiments exactly as RyR1 isolated from sham-operated

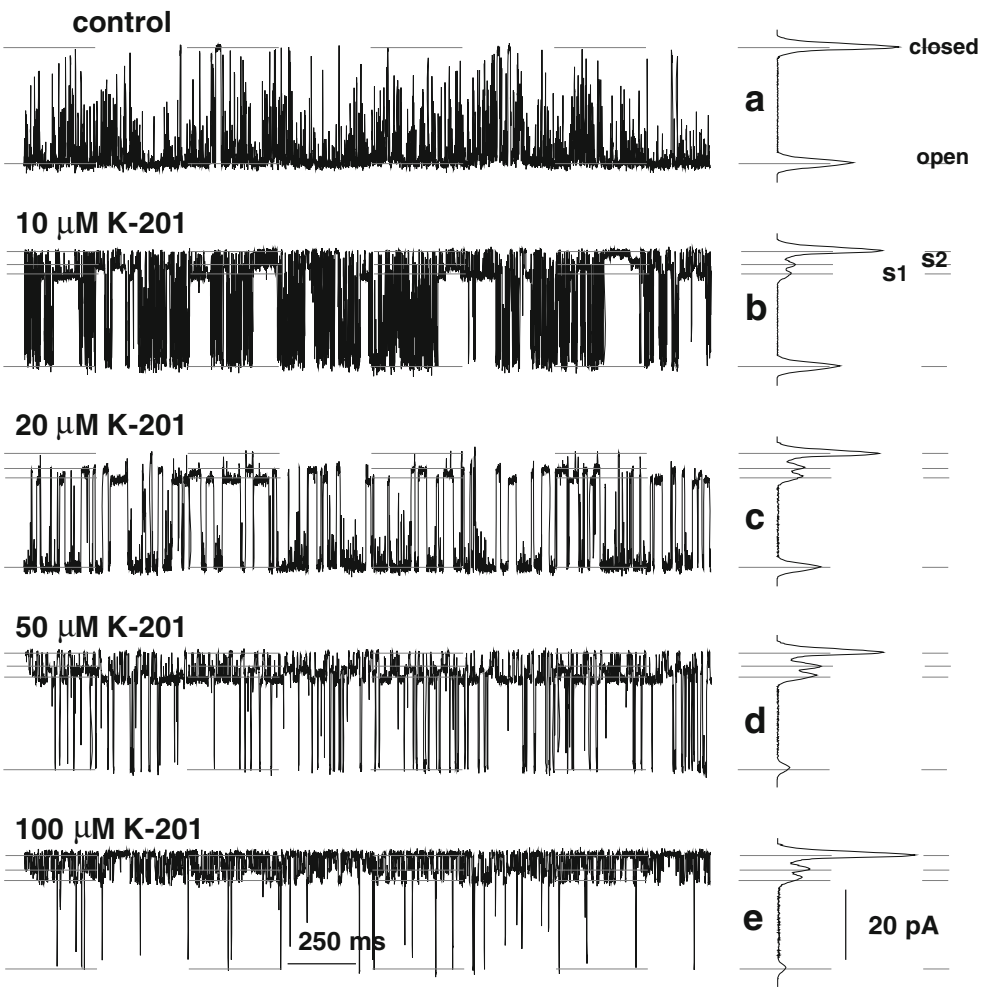


Fig. 2 K-201 induces subconductance states of the PMI rat RyR1. Solubilized Ryanodine receptor of PMI rats was incorporated into a lipid bilayer, and the channel current was recorded under voltage clamp condition using identical conditions and procedures as for Fig. 1. Current traces shown in the absence (**a**) and in the presence of 1 μM (**b**), 10 μM (**c**), 20 μM (**d**), 50 μM (**e**), and 100 μM K-201 (**f**)

(control) rats. Apart from the higher starting Po at the given free calcium concentration (see also [28]), these experiments revealed no difference between control and PMI channels, showing very similar subconductance states (Fig. 2). Plotting the open probability of the channel using the common 50%±2.5% dead zone as a function of K-201 concentration exhibits a decrease of the open state probability. This inhibition is characterized by a half inhibitory constant of IC_{50}=25.1±2.7 μM and n_{Hill}=1.74±0.28 Hill coefficient (fitting correlation of R^2=0.99) for the control (Fig. 3a) and IC_{50}=22.0±1.0 μM and n_{Hill}=1.98±0.17 Hill coefficient (R^2=0.996) for the PMI channels (Fig. 3b). These data reveal that both the control and the PMI RyR1 have two binding sites for K-201, and the half inhibitory concentration values are almost identical. The decrease of the probability of the full open event is due to the induction of the S_1 and S_2 subconductance states at the expense of the open events up to about 50 μM K-201 concentration as shown by the histograms in Figs. 1 and 2.

Analyzing the concentration dependence of the probability of the S_1 (Fig. 4a) and of the S_2 (Fig. 4b) substates using control and PMI channels show a biphasic character. The probability of the S_1 subconductance state increases with increasing K-201 concentration up to 50 μM K-201—reaching about 0.259±0.053 in the control channel and 0.196±0.041 in the case of the PMI channel. Further increases in drug concentration resulted in a decrease of the S_1 partial probability down to 0.02±0.006 at 300 μM K-201 for control and also for PMI channels. Statistical analysis shows that the corresponding partial probabilities

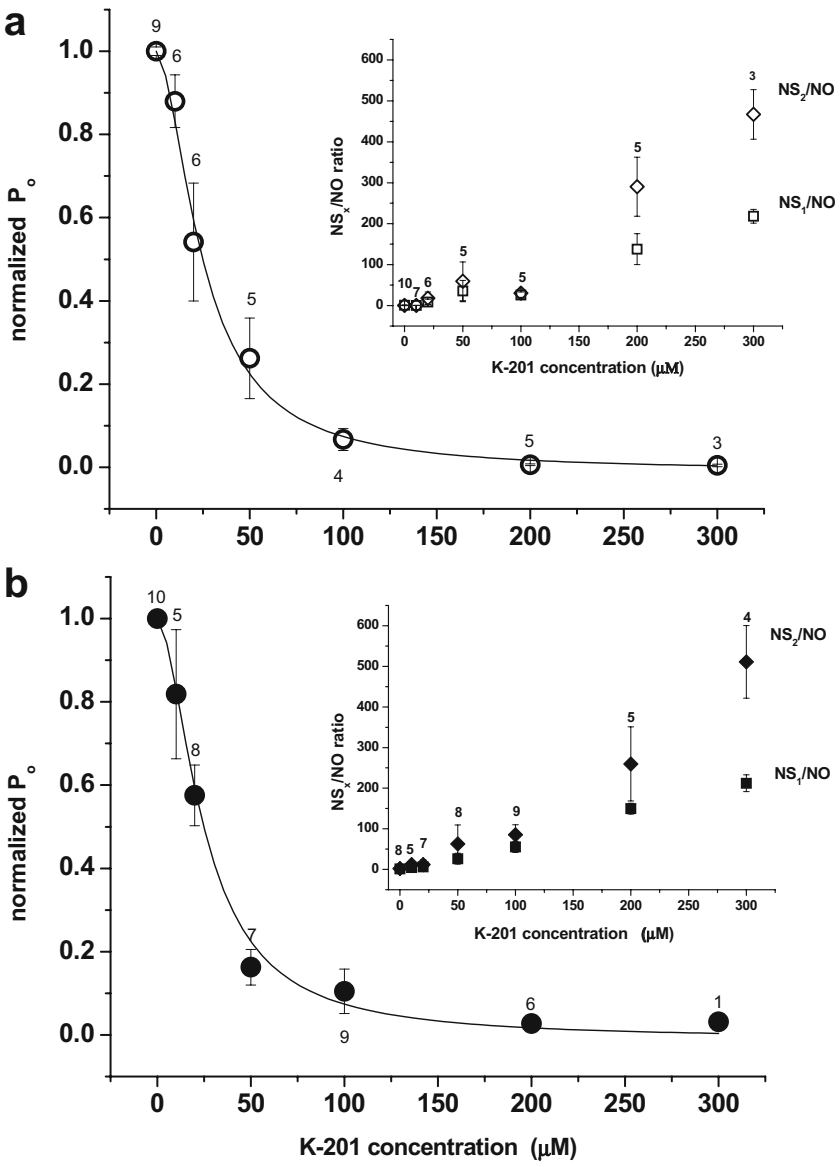


Fig. 3 Dose–response curve of the K-201. Current traces obtained at different K-201 concentrations were analyzed as described in the "Materials and methods" section using the common 50%±2.5% criteria. *Open symbols* represent the control data, while *filled symbols* represent the PMI data. **a** (for the control) and **b** (for the PMI channel) show the decrease of the classical open probability as a function of K-201 concentration. The *insets* show the K-201 dependence of the ratio of the partial probability of the S1 to the full open state for the control animal (*upper panel*: S1: *empty squares*, S2: *empty diamonds*) and for the PMI animal (*lower panel*: S1: *filled squares*, S2: *filled diamonds*). Number of bilayers used for a given concentration is shown *above each symbol*

szentesi.peter_292_24

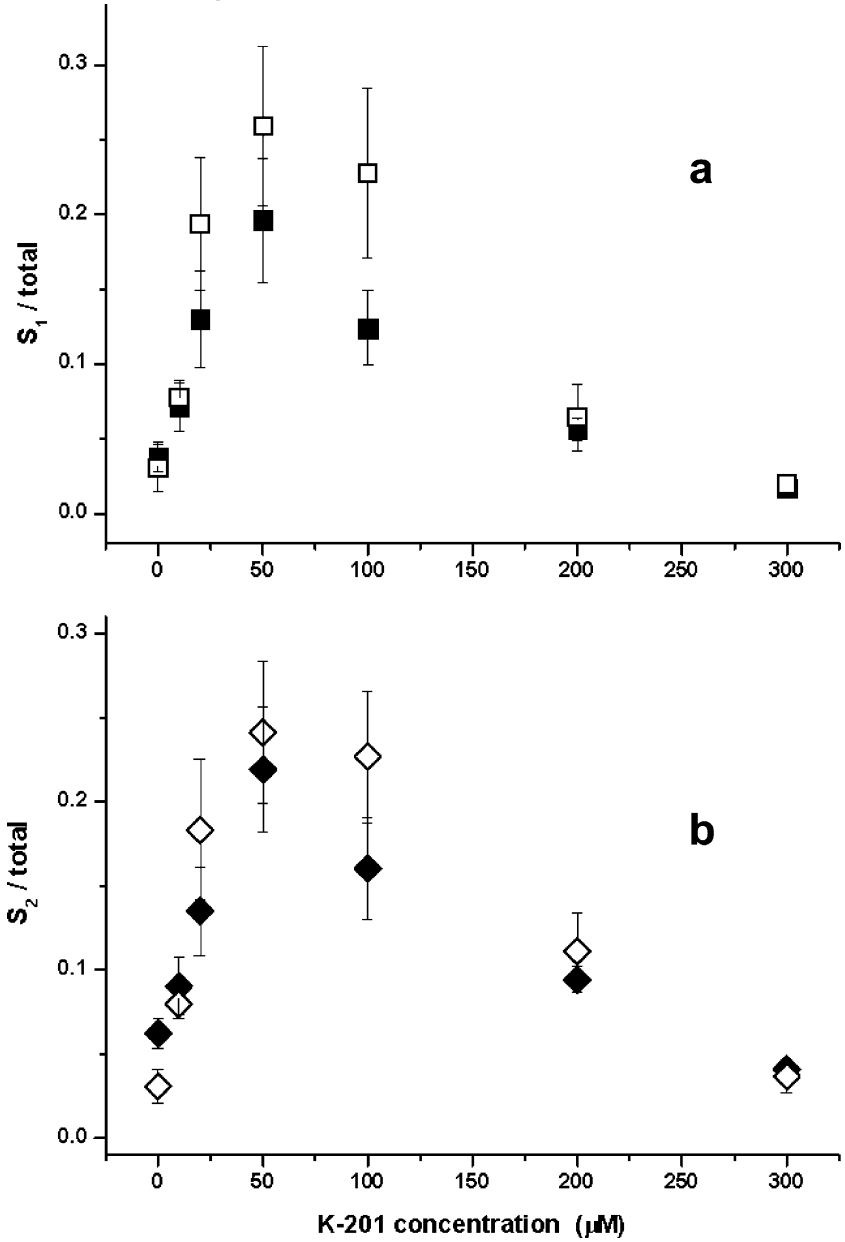


Fig. 4 Effect of K-201 on the probability of the substates in control and in PMI channels. Current traces obtained at different K-201 concentrations were analyzed as described in the "Materials and methods" section to calculate the partial probabilities of the S1 (control: *empty squares*, PMI: *filled squares*) and of the S2 (control: *empty diamonds*, PMI: *filled diamonds*) subconductance states. *Open symbols* represent the control animal, while *filled symbols* represent the PMI data. The *upper panel* shows the probability of the S1, while the *lower panel* shows the S2 substate at different K-201 concentrations. Probabilities of the given state were calculated from 10-min long intervals for each bilayer evaluated. Same experiments as in Fig. 3

do not differ for S_1 and S_2 when comparing PMI to control rats. The overall concentration dependence of the probabilities of S_1 and S_2 substates shows similar characteristics. As it is demonstrated by the insets in Fig. 3, the two substates are generated at the expense of the open state.

Calcium-release experiments were carried out to verify the single channel data measuring the initial rate of release from actively loaded SR vesicles (Fig. 5). Calcium release was evoked by the addition of 10 μM K-201. This K-201 concentration was chosen because it introduces the (S_1 and S_2) substates while decreasing only slightly the common (50%±2.5% criteria) open probability. These initial release data reckon that the S_1 and S_2 subconductance states seen on the bilayer records are indeed calcium-conducting conformations, i.e., the calcium release channel is able to transport calcium ions in these substates.

Effect of K-201 on the SR Ca^{2+} pump

Effect of K-201 was investigated on the SR calcium pump using the coupled enzyme assay as described in the "Materials and methods" section. Dose–response curves were determined and analyzed for control (Fig. 6a) and for PMI rats (Fig. 6b) using light SR vesicles. Data analysis revealed a half inhibitory K-201 concentration $IC_{50\ contr}$= 118.5±20.9 μM for the control and $IC_{50\ PMI}$=121.5± 17.5 μM for the PMI group, while the Hill constants were $n_{i\ contr}$=1.84±0.48 and $n_{i\ PMI}$=1.97±0.24. The differences

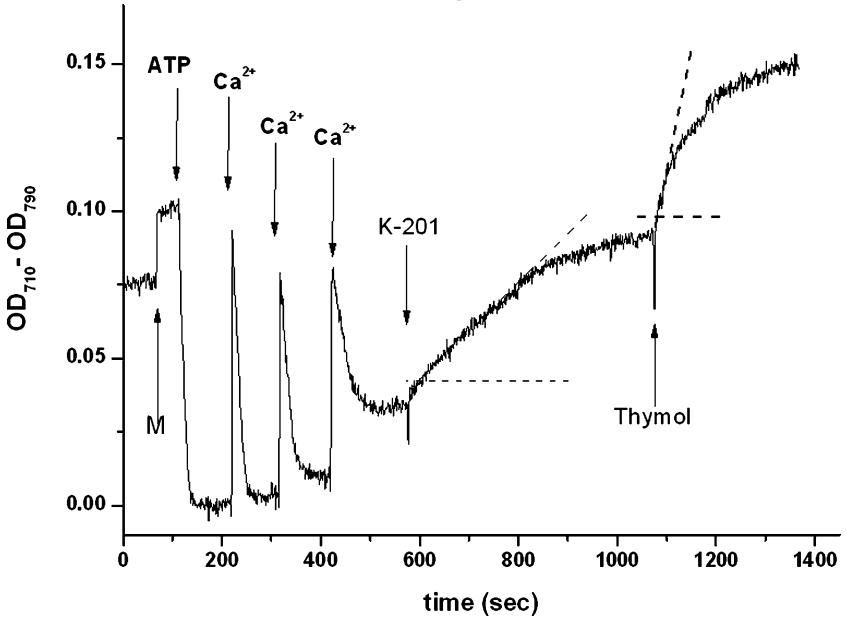


Fig. 5 K-201 evokes calcium release from HSR vesicles. Vesicles were actively loaded with calcium and extravesicular calcium concentration measured using APIII as described in the "Materials and methods" section. First, HSR vesicles were added (*M*) followed by the addition of ATP (*ATP*) and calcium (Ca^{2+}). After successive loading, the extravesicular Ca^{2+} concentration stabilized because of the balance of calcium uptake by the ATPase and of the Ca^{2+} leak. After the addition of 10 μM K-201, the release rate of the calcium has markedly increased (*fitted with solid line*) due to the induction of conducting substates by K-201. After reaching the new equilibrium, Thymol was added to release (*fitted with dashed line*) all the calcium previously taken up. Fitted line to the analogous curve has shown which were used to estimate the initial rate of release after the additions. Fitting stated at the intersection of the *horizontal* (baseline) and the *fitted line*

between the data from control and PMI rats are statistically not significant ($p>0.4$).

K-201 modifies calcium release event properties in permeabilized fibers

It was shown previously that K-201 can improve skeletal muscle fatigue by increasing the binding of calstabin-1 to RyR1 [31]. To explore the effects of the drug in more detail, fibers from rat skeletal muscle were permeabilized and loaded with Fluo-4. Fibers held in sulfate-based internal solution had stable background fluorescence and showed spontaneous elementary calcium release events (ECRE; Fig. 7a) in accordance with previous observations [14, 25, 33]. Both sparks and embers were readily observable in the absence and in the presence of K-201. A total of 2,182 vs. 798 sparks and 564 vs. 1,050 embers from 16 vs. 10 fibers (11 vs. 4 animals) were analyzed under control conditions and in the presence of K-201, respectively, and their characteristic parameters are presented in Table 1. Shortly after the addition of 1 μM K-201 (2–10 min), the frequency of sparks decreased, while the frequency of embers increased considerably (Fig. 7b). The ratio of embers to sparks increased from 26% to 132% showing that K-201 caused more long openings. As shown by the inset to Fig. 7b, the drug was capable of inducing the characteristic subconductance state (S_2) on isolated RyR1 even in this low concentration.

The parameters of ECRE were altered by the drug as demonstrated in Fig. 8. The distribution of event amplitudes, measured 2–10 min after the addition of K-201, was shifted to the left in the case of sparks (Fig. 8a). On the other hand, the drug did not modify the average amplitude of embers (Fig. 8b). K-201 reduced the mean amplitude of sparks by 20%, while it increased the mean amplitude of embers by about 10% (Table 1; with the latter not being statistically significant). Unlike event amplitude, the spatial spread (FWHM) remained unaltered by K-201 for both sparks and embers (Fig. 8c,d).

Examining the embers measured in the presence of K-201 (Fig. 9d) revealed resolvable levels within embers that were not seen under control conditions (Fig. 9b). These levels were identified as steady fluorescence within the event that lasted at least 25 ms. In the images presented in Fig. 9, the levels corresponded to 0.12 and 0.40 as expressed in values of $\Delta F/F_0$. From the 1,050 events recorded in the presence of K-201, there were 21 (2%) identified as having such multiple levels. Overall, the amplitude of the lower level was, on average, 40.4±2.2% of that of the greater. Although this value is higher than that found for the larger subconductance state in single channel measurements (see e.g. Fig. 1 or Fig. 7b), the observation is

szentesi.peter_292_24

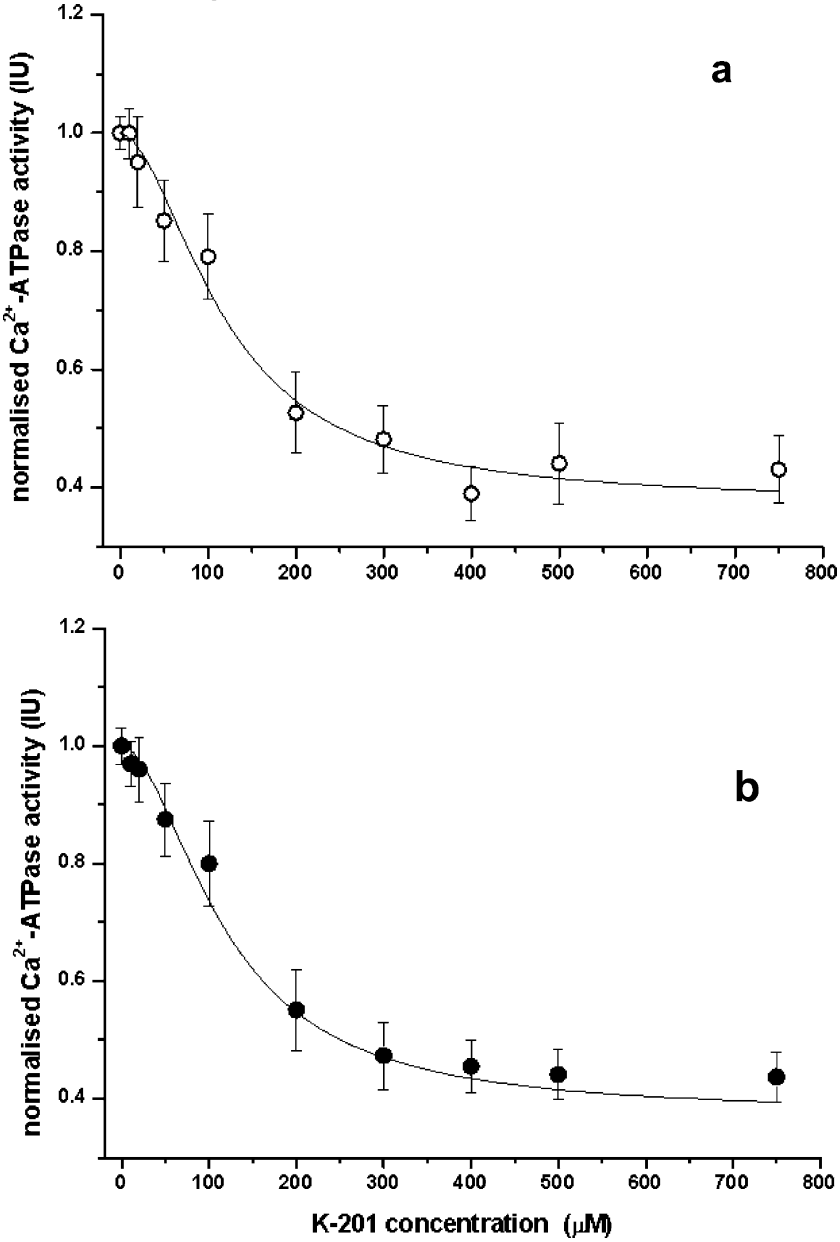


Fig. 6 K-201 inhibits the Ca^{2+}–ATPase activity of LSR vesicles. LSR vesicles were prepared and hydrolytic activity was determined as described in the "Materials and methods". To reduce differences of the preparations, activity values normalized for the activity obtained in the absence of the drug. Dose–response curve of K-201 shown for the control animal (**a**) and for the PMI animal (**b**). Experimental data were fitted using the Hill equation and *continuous lines* show the results of the best fit

clearly in line with the possibility that K-201 would induce the appearance of such states not only under isolated but under intact conditions as well.

Discussion

The 1,4 benzothiazepine derivative K-201 demonstrates cardioprotective [9, 12] and antiarrhythmic [16, 19] effects. These have, at least partially, been attributed to the suppression of SR calcium efflux [e.g., 20] associated with RyR stabilization through calstabin [30–32]. Although the interaction of K-201 and the cardiac isoform of RyR has been described, its effect on RyR1 and the consequent alterations in skeletal muscle function remain elusive. Here, we demonstrate that K-201 induces characteristic subconductance states in RyR1 and alters the elementary events of SR calcium release by reducing the frequency of sparks and increasing the occurrence of embers. These changes result in a decreased open probability of RyR with increasing K-201 concentration, with an apparent K_d around 25 μM, if the open probability is defined in the usual way. Interestingly, RyR1 prepared from PMI rats behaves indistinguishably from control channels with respect to its K-201 sensitivity. In addition, the drug, at higher concentrations, inhibits the reuptake of calcium into the SR.

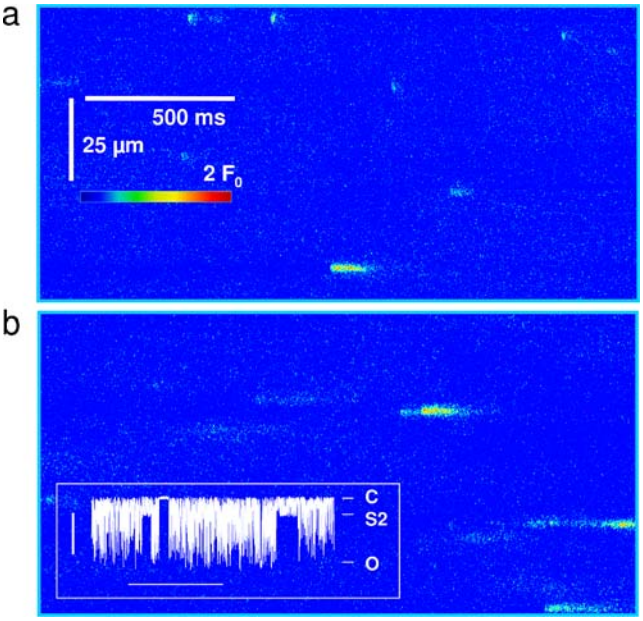


Fig. 7 Effect of K-201 on the calcium-release events Confocal line-scan images of single Saponin permeabilized fibers loaded with the calcium-sensitive fluorescent probe Fluo-4 under control conditions (**a**) and in the presence of 1 μM K-201 (**b**). Images were normalized for baseline fluorescence (F/F0) and are presented in artificial color. Note the more frequent occurrence of short events (sparks) in control, while the presence of long events in the presence of K-201. *Inset* in (**b**) shows a typical single channel record measured at 1 μM K-201 demonstrating the characteristic subconductance state. Vertical calibration is 20 pA, horizontal calibration is 500 ms

Subconductance states of RyR1 in the presence of K-201

To understand whether the effects of K-201 on RyR1 could also be interpreted as decreasing the activity of leaky channels, similar to that in cardiac failure [15, 19, 32], one must consider the properties of the subconductance states induced by the drug. These states—with an approximate conductance of 13% and 24% of the fully open state—are clearly different from those induced either by ryanodine or the removal of calstabin-1 (FKBP 12). Not only are the conductances of these states different from those mentioned above, but their appearance is voltage dependent, namely, they are not seen at negative voltages. Although this voltage dependence might seem to be a peculiarity, its importance is pivotal to interpret the results for in vivo conditions. If the membrane potential of the SR is negative enough, the subconductance states are not present, and the drug acts clearly as a stabilizer. If these states, on the other hand, are generated under in vivo conditions, the drug induces an extra, albeit small leak from the SR.

It is not without precedent [1] that the action of a substance depends on the direction of the membrane potential, i.e., on the direction of the movement of the charge carrier. These characteristics—a special kind of rectification—is essentially identical if the current is elicited by a voltage difference or by a concentration gradient. Although transient changes in membrane potential might be associated with the opening of RyR1 during the course of EC-coupling at the terminal cisternea of the SR and to a much lesser extent at the longitudinal part of the SR during the reuptake of the calcium, it is widely accepted that the SR has no permanent membrane potential. Unfortunately, the exact membrane voltage where the subconductance states appear cannot be determined using the bilayer technique due to the noise on the records in the −25 and +25 mV voltage range, rendering the physiological interpretation difficult. However, two independent observations seem to favor the presence of these substates at or around 0 mV SR membrane potential. First, calcium flux data demonstrated an increased calcium efflux from SR vesicles upon the addition of K-201 (Fig. 5). Second, embers, the elementary calcium release events associated with the opening of a single RyR1, showed resolvable levels within a single event (Fig. 9). Although neither observation is conclusive, taken together, they indicate that the subconductance states are indeed present on calcium release channels in their native environment.

Elementary calcium release events in the presence of K-201

Original reports have indicated that K-201 would stabilize leaky cardiac RyR [15, 20, 32], while the measurements presented here favor the hypothesis that the drug would, at low concentrations, partially activate the isolated skeletal-type calcium release channel by inducing subconductance

Table 1 Characteristic properties of ECRE in control and in K-201 treated fibers

	Spark		Ember	
	Control n=2182	K-201 n=798	Control n=564	K-201 n=1050
Amplitude[a]	0.78±0.01	0.63±0.01*	0.21±0.01	0.23±0.01
Frequency (s^{-1} sarcomere^{-1})	0.039±0.001	0.023±0.001*	0.011±0.001	0.023±0.001*
FWHM (μm)	1.64±0.01	1.68±0.02	1.86±0.02	1.95±0.04
Duration (ms)	34.6±0.4	35.6±0.6	87.9±0.4	88.6±2.1

[a] For embers, the average amplitude is given.
*Significant difference (p<0.05) compared to control

szentesi.peter_292_24

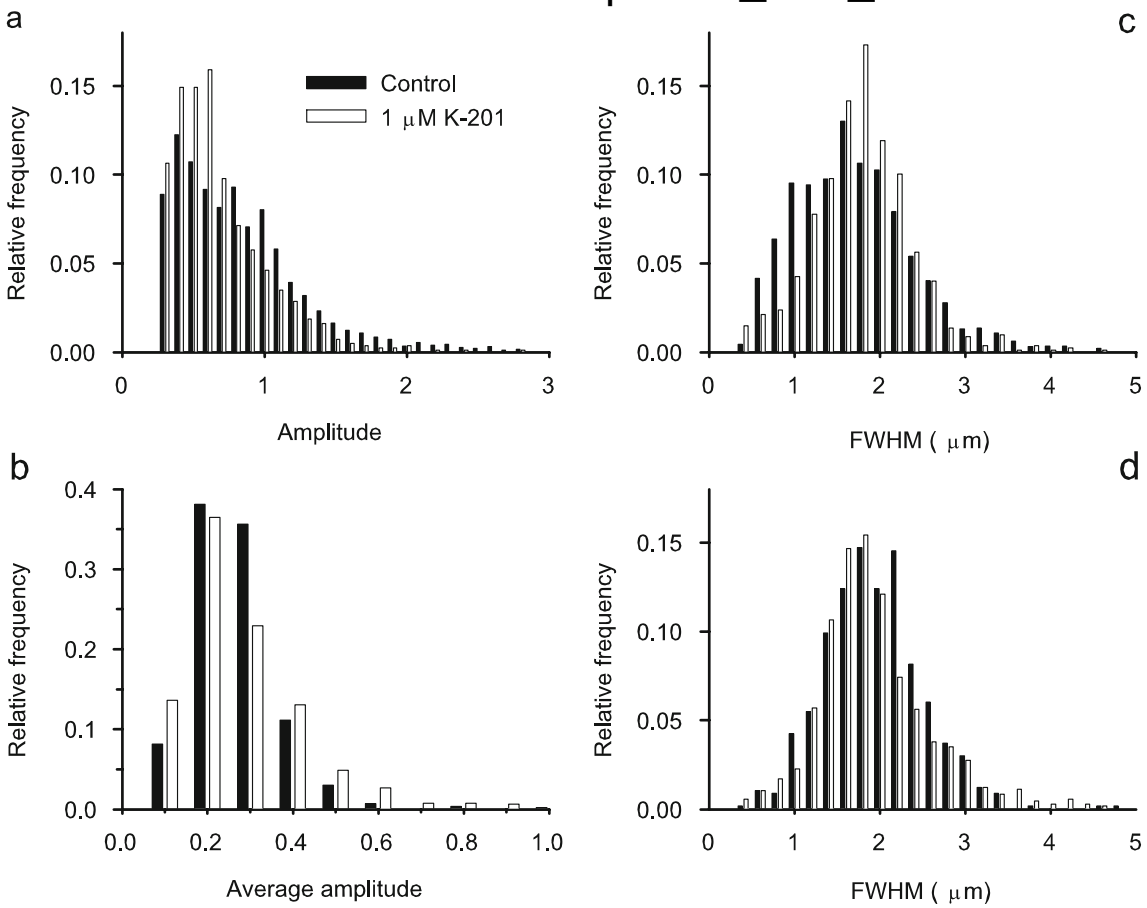


Fig. 8 Parameters of sparks and embers The distribution of events amplitudes (**a**), average amplitude (**b**), and FWHM (**c** and **d**) were calculated for sparks (**a** and **c**) and for embers (**b** and **d**) under control conditions and in the presence of K-201. Note that while the spatial spread of the events was not significantly modified by the drug, K-201 shifted the amplitude histogram of sparks to the left indicative of an increase in the number of events with smaller amplitude, while in case of embers, there is a shift to the right to greater values

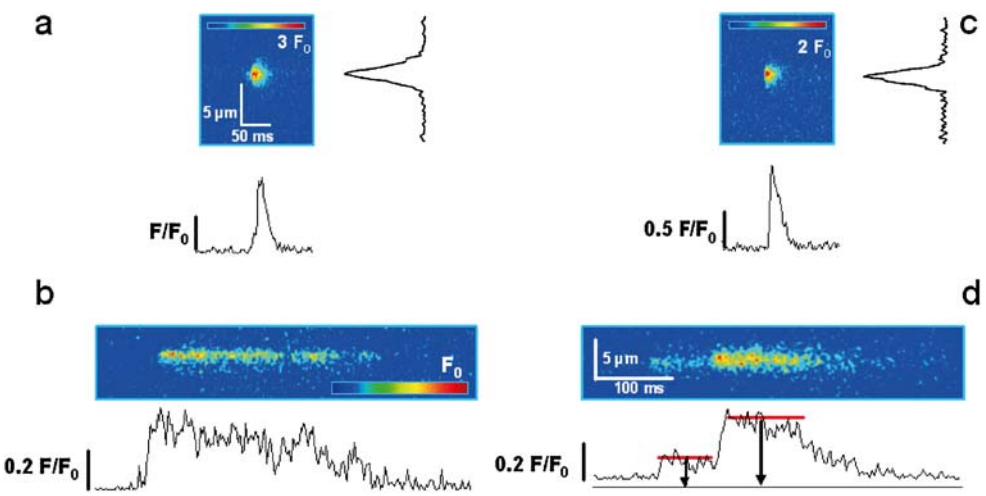


Fig. 9 Representative sparks and embers pseudo-colored line-scan images in control condition (*left panels*) and in the presence of K-201 (*right panels*). The same scanning direction and image correction was applied as in Fig. 7. Note the embers with subconductance states in the presence of K-201. The traces below the images show the average of five neighboring lines at the middle of the event. The straight lines represent linear fits to the steps of the traces

states. The observations made in this study, with respect to the calcium-release events, might explain these apparently distinct effects.

Although ECRE on isolated rat skeletal muscle fibers were present with essentially unaltered overall frequency after the addition of 1 μM K-201, the drug had characteristic effects on their morphology. This manifested in a reduction of the relative contribution of sparks and a large increase in the relative contribution of embers to the total number of events. In addition, the amplitude of the sparks was also reduced. These observations suggest that the average number of channels contributing to an event considerably decreased. Although the drug was shown to alter SR calcium uptake and thus could modify the calcium content of the SR, this is unlikely to explain the above observations due to the two orders of magnitude difference in concentrations (1 μM for the confocal measurements and 120 μM for the IC_{50} value). As ECRE are not present on intact mammalian fibers [14, 24, 25], the reduction in the number of contributing channels could be interpreted as a stabilizing effect of the drug. On the other hand, embers showed stepwise changes in fluorescence, not observed under control conditions, which could correspond to the subconductance states seen with isolated channels. The relatively low frequency of occurrence of these subconductance states in ECRE compared to the bilayer experiments could readily be accounted for by the lower concentration of the drug used in the former experiments and the membrane potential of the SR (see above). Finally, a higher concentration of the drug (10 μM) increased the frequency of ECRE in amphibians, again in line with the observations from isolated channels (data not shown).

It should be stressed, however, that the observations on ECRE were obtained using a concentration, 1 μM, which is identical to those used in other studies where K-201 on heart failure was investigated [31]. These studies indicated that K-201 would exert its effects via increasing the association of calstabin-2 (FKBP 12.6) to RyR2 [19, 31], which in turn would reduce the amplitude of calcium sparks [5] similarly as seen in this study. While we cannot exclude the possibility that this stabilizing effect was partially, or fully, responsible for the alterations seen here, it seems unlikely due to the fact that the skeletal isoform calstabin-1 (FKBP 12) is strongly and stably bound to the skeletal RyR. On the other hand, a recent report suggested that K-201 could have calstabin-2-independent effects on RyR [6] providing additional support to our interpretation in which the effects of the drug on ECRE in mammalian skeletal muscle are not mediated through an altered association of calstabin-1. Furthermore, as K-201 inhibits the SR calcium pump (i.e., lowers the reuptake of calcium into the SR), it might also contribute to the overall effects of the drug on striated muscle.

Acknowledgements The authors are grateful for the technical assistance of Ms R. Őri and Ms. É. Sági. The work was supported by grants from the Hungarian Scientific Research Fund OTKA (T049151, T61442, NK61412) and by INSERM.

References

1. Altafaj X, France J, Almassy J, Jona I, Rossi D, Sorrentino V, Mabrouk K, De Waard M, Ronjat M (2007) Maurocalcine interacts with cardiac ryanodine receptor without inducing channel modification. Biochem J 406:309–315
2. Aronow WS (2006) Epidemiology, pathophysiology, prognosis, and treatment of systolic and diastolic heart failure. Cardiol Rev 14:108–124
3. Boyden PA, Dun W, Barbhaiya C, Ter Keurs HE (2004) 2APB- and JTV519(K201)-sensitive micro Ca^{2+} waves in arrhythmogenic Purkinje cells that survive in infarcted canine heart. Heart Rhythm 1:18–26
4. Fabiato A (1988) Computer programs for calculating total from specified free or free from specified total ionic concentrations in aqueous solutions containing multiple metals and ligands. Methods Enzymol 157:378–417
5. Gómez AM, Schuster I, Fauconnier J, Prestle J, Hasenfuss G, Richard S (2004) FKBP12.6 overexpression decreases Ca^{2+} spark amplitude but enhances [Ca^{2+}] transient in rat cardiac myocytes. Am J Phys 287:H1987–H1993
6. Hunt DJ, Jones PP, Wang R, Chen W, Bolstad J, Chen K, Shimoni Y, Chen SR (2007) K201(JTV519) suppresses spontaneous Ca^{2+} release and [^{3}H]ryanodine binding to RyR2 irrespective of FKBP12.6 association. Biochem J 404:431–438
7. Inagaki K, Kihara Y, Izumi T, Sasayama S (2000) The cardioprotective effects of a new 1,4-benzothiazepine derivative, JTV519, on ischemia/reperfusion-induced Ca^{2+} overload in isolated rat hearts. Cardiovasc Drugs Ther 14:489–495
8. Jona I, Szegedi C, Sarkozi S, Szentesi P, Csernoch L, Kovacs L (2001) Altered inhibition of the rat skeletal ryanodine receptor/calcium release channel by magnesium in the presence of ATP. Pflügers Arch - Eur J Physiol 441:729–738
9. Kaneko N (1994) New 1,4-Benzothiazepine derivative, K201, demonstrates cardioprotective effects against sudden cardiac cell death and intracellular calcium blocking action. Drug Dev Res 33:429–438
10. Kaneko N, Ago H, Matsuda R, Inagaki E, Miyano M (1997a) Chrystal structure of annexin V with its ligand K-201 as a calcium channel activity inhibitor. J Mol Biol 274:16–20
11. Kaneko N, Matsuda R, Toda M, Shimamoto K (1997b) Inhibition of annexin V-dependent Ca^{2+} movement in large unilamellar vesicles by K201, a new 1,4-benzothiazepine derivative. Biochim Biophys Acta 1330:1–7
12. Kawabata H, Ryomoto T, Ishikawa K (2000) Effect of a novel cardioprotective agent, JTV-519, on metabolism, contraction and relaxation in the ischemia-reperfused rabbit heart. Jpn Circ J 64:772–776
13. Kawabata H, Nakawaga K, Ishikawa K (2002) A novel cardioprotective agent, JTV-519, is abolished by nitric oxide synthase inhibitor on myocardial metabolism in ischemia-reperfused rabbit hearts. Hypertens Res 25:303–309
14. Kirsch WG, Uttenweiler D, Fink RH (2001) Spark- and ember-like elementary Ca^{2+} release events in skinned fibres of adult mammalian skeletal muscle. J Physiol 537:379–389
15. Kohno M, Yano M, Kobayashi S, Doi M, Oda T, Tokuhisa T, Okuda S, Ohkusa T, Kohno M, Matsuzaki M (2003) A new cardioprotective agent, JTV519, improves defective channel

szentesi.peter_292_24

gating of ryanodine receptor in heart failure. Am J Physiol Heart Circ Physiol 284:H1035–H1042
16. Kumagai K, Nakashima H, Gondo N, Saku K (2003) Antiarrhythmic effects of JTV-519, a novel cardioprotective drug, on atrial fibrillation/flutter in a canine sterile pericarditis model. J Cardiovasc Electrophysiol 14:880–884
17. Lai FA, Meissner G (1990) Structure of the calcium release channel of skeletal muscle sarcoplasmic reticulum and its regulation by calcium. Adv Exp Med Biol 269:73–77
18. Lehnart SE, Wehrens XH, Laitinen PJ, Reiken SR, Deng SX, Cheng Z, Landry DW, Kontula K, Swan H, Marks AR (2004) Sudden death in familial polymorphic ventricular tachycardia associated with calcium release channel (ryanodine receptor) leak. Circulation 109:3208–3214
19. Lehnart SE, Terrenoire C, Reiken SR, Wehrens XH, Song LS, Song LS, Tillman EJ, Mancarella S, Coromilas J, Lederer WJ, Kass RS, Marks AR (2006) Stabilization of cardiac ryanodine receptor prevents intracellular calcium leak and arrhythmias. PNAS 103:7906–7910
20. Lehnart SE (2007) Novel targets for treating heart and muscle disease-stabilizing ryanodine receptors and preventing intracellular calcium leak. Curr Opin Pharmacol 7:225–232
21. Lisy O, Burnett JC Jr (2006) New cardioprotective agent K201 is natriuretic and glomerular filtration rate enhancing. Circulation 113:246–251
22. Pitt GS, Dun W, Boyden PA (2006) Remodelled cardiac calcium channels. J Moll Cell Cardiol 43:373–388
23. Sarkozi S, Szentesi P, Jona I, Csernoch L (1996) Effects of cardiac glycosides on excitation-contraction coupling in frog skeletal muscle fibres. J Physiol 495:611–626
24. Shirokova N, Garcia J, Rios E (1998) Local calcium release in mammalian skeletal muscle. J Physiol 512:377–384
25. Szappanos H, Smida-Rezgui S, Cseri J, Simut C, Sabatier JM, De Waard M, Kovacs L, Csernoch L, Ronjat M (2005) Differential effects of maurocalcine on Ca^{2+} release events and depolarization-induced Ca^{2+} release in rat skeletal muscle. J Physiol 565:843–853
26. Szentesi P, Jacquemond V, Kovacs L, Csernoch L (1997) Intramembrane charge movement and sarcoplasmic calcium release in enzymatically isolated mammalian skeletal muscle fibers. J Physiol 505:371–384
27. Szentesi P, Szappanos H, Szegedi C, Gonczi M, Jona I, Cseri J, Kovacs L, Csernoch L (2004) Altered elementary calcium release events and enhanced calcium release by thymol in rat skeletal muscle. Biophys J 86:1436–1453
28. Szigeti GP, Almassy J, Sztretye M, Dienes B, Szabo L, Szentesi P, Vassort G, Sarkozi S, Csernoch L, Jona I (2007) Alterations in the calcium homeostasis of skeletal muscle from postmyocardial infarcted rats. Pflugers Arch 455:541–553
29. Ward CW, Reiken S, Marks AR, Marty I, Vassort G, Lacampagne A (2003) Defects in ryanodine receptor calcium release in skeletal muscle from post-myocardial infarct rats. FASEB J 17:1517–1519
30. Werhens XH, Lehnart SE, Reiken SR, Deng SX, Vest JA, Cervantes D, Coromilas J, Landry DW, Marks AR (2004) Protection from cardiac arrhythmia through ryanodine receptor-stabilizing protein calstabin2. Science 304:292–296
31. Wehrens XH, Lehnart SE, Reiken SR, van der Nagel R, Morales R, Sun J, Cheng Z, Deng SX, de Windt LJ, Landry DW, Marks AR (2005) Enhancing calstabin binding to ryanodine receptors improves cardiac and skeletal muscle function in heart failure. PNAS 102:9607–9612
32. Yano M, Kobayasi S, Kohno M, Doi M, Tokuhisa T, Okuda S, Suetsugu M, Hisaoka T, Obayashi M, Okhusa T, Kohno M, Matsuzaki M (2003) FKBP12.6-mediated stabilization of calcium-release channel (ryanodine receptor) as a novel therapeutic strategy against heart failure. Circulation 107:477–484
33. Zhou J, Brum G, Gonzalez A, Launikonis BS, Stern MD, Rios E (2003) Ca^{2+} sparks and embers of mammalian muscles. Properties of the sources. J Gen Physiol 122:195–114

The Journal of Physiology

Hypermuscular mice with mutation in the myostatin gene display altered calcium signalling

Dóra Bodnár[1], Nikolett Geyer[1], Olga Ruzsnavszky[1], Tamás Oláh[1], Bence Hegyi[1], Mónika Sztretye[1], János Fodor[1], Beatrix Dienes[1], Ágnes Balogh[2], Zoltán Papp[2], László Szabó[3], Géza Müller[1], László Csernoch[1] and Péter Szentesi[1]

[1]*Department of Physiology, Medical and Health Science Centre, University of Debrecen, Debrecen, Hungary*
[2]*Department of Cardiology, Medical and Health Science Centre, University of Debrecen, Debrecen, Hungary*
[3]*Department of Electrical Engineering, Sapientia Hungarian University of Transylvania, Târgu Mureş, Romania*

Key points

- Hypermuscularity associated with naturally occurring mutations in the myostatin gene as found in *Compact* mice results in increased muscle mass but reduced specific force.
- The calcium sensitivity of the contractile apparatus as assessed on chemically skinned skeletal muscle fibres under isometric conditions is not altered in these animals.
- While the resting calcium concentration remains unaffected, depolarization-evoked increases in intracellular calcium concentration are suppressed.
- Spontaneous calcium release events from sarcoplasmic reticulum are also decreased in frequency, amplitude and spatial spread.
- Our results suggest that mutations in the myostatin gene are accompanied by alterations in excitation contraction coupling, which manifest as a reduction in sarcoplasmic calcium release.

Abstract Myostatin, a member of the transforming growth factor β family, is a potent negative regulator of skeletal muscle growth, as myostatin-deficient mice show a great increase in muscle mass. Yet the physical performance of these animals is reduced. As an explanation for this, alterations in the steps in excitation–contraction coupling were hypothesized and tested for in mice with the 12 bp deletion in the propeptide region of the myostatin precursor ($Mstn^{Cmpt\text{-}dl1Abc}$ or *Cmpt*). In voluntary wheel running, control C57BL/6 mice performed better than the mutant animals in both maximal speed and total distance covered. Despite the previously described lower specific force of *Cmpt* animals, the p_{Ca}–force relationship, determined on chemically permeabilized fibre segments, did not show any significant difference between the two mouse strains. While resting intracellular Ca^{2+} concentration ($[Ca^{2+}]_i$) measured on single intact flexor digitorum brevis (FDB) muscle fibres using Fura-2 AM was similar to control (72.0 ± 1.7 *vs.* 78.1 ± 2.9 nM, $n = 38$ and 45), the amplitude of KCl-evoked calcium transients was smaller (360 ± 49 *vs.* 222 ± 45 nM, $n = 22$) in the mutant strain. Similar results were obtained using tetanic stimulation and Rhod-2 AM, which gave calcium transients that were smaller (2.42 ± 0.11 *vs.* 2.06 ± 0.10 $\Delta F/F_0$, $n = 14$ and 13, respectively) on *Cmpt* mice. Sarcoplasmic reticulum (SR) calcium release flux calculated from these transients showed a reduced peak (23.7 ± 3.0 *vs.* 15.8 ± 2.1 mMs^{-1}) and steady level (5.7 ± 0.7 *vs.* 3.7 ± 0.5 mM s^{-1}) with no change in the peak-to-steady ratio. The amplitude and spatial spread of calcium release events detected on permeabilized FDB fibres were also significantly smaller in mutant mice. These results suggest that reduced SR calcium release underlies the reduced muscle force in *Cmpt* animals.

© 2014 The Authors. The Journal of Physiology © 2014 The Physiological Society
DOI: 10.1113/jphysiol.2013.261958

Downloaded from J Physiol (jp.physoc.org) at Imperial College London Library on September 3, 2014

(Received 5 September 2013; accepted after revision 16 January 2014; first published online 20 January 2014)
Corresponding author P. Szentesi: Department of Physiology, Faculty of Medicine, Medical and Health Science Centre, University of Debrecen, PO Box 22, H-4012 Debrecen, Hungary. Email: szentesi.peter@med.unideb.hu

Abbreviations ECC, excitation–contraction coupling; EDL, extensor digitorum longus; FDB, flexor digitorum brevis; FWHM, full width at half maximum; RyR, ryanodine receptor; SR, sarcoplasmic reticulum; T-tubular, transverse-tubular

Introduction

Myostatin – originally named growth and differentiation factor-8 (GDF-8) – a member of the transforming growth factor β (TGF-β) superfamily, has emerged as a potent negative regulator of skeletal muscle growth (McPherron *et al.* 1997). It plays a key role in skeletal muscle homeostasis and has been well described since its discovery. During embryogenesis, myostatin is exclusively expressed in skeletal muscle to control the differentiation and proliferation of myoblasts (Langley *et al.* 2002). It mediates the cell signalling cascade through activin receptors in the muscle, which interfere with the activity and expression of myoblast determination protein (MyoD; Langley *et al.* 2002). Recently, myostatin has also been shown to inhibit Akt, a kinase that regulates muscle growth (Bodine *et al.* 2001; Lai *et al.* 2004), in part through the activation of protein synthesis (e.g. Elkina *et al.* 2011).

Myostatin was first identified when null-mutant knock-out mice exhibited a huge increase in skeletal muscle mass due to hypertrophy and hyperplasia (McPherron *et al.* 1997). Mutations causing hypermuscularity in the double-muscled Belgian Blue and Piedmontese cattle breeds were described in the myostatin gene (Kambadur *et al.* 1997). Similarly, whippet dogs with excessive muscle growth were found to have a heterozygous naturally occurring mutation (Mosher *et al.* 2007).

Hypermuscular mice were also found by several groups in selection studies examining the genetic basis of protein accretion (Varga *et al.* 1997; Bünger *et al.* 2001). These include the so-called 'Compact' mice (Varga *et al.* 1997), in which sequencing of the myostatin gene revealed a 12 bp deletion – and thus the name $Mstn^{Cmpt\text{-}dl1Abc}$ (Szabo *et al.* 1998) – in the propeptide region of the myostatin precursor. In homozygous *Cmpt*/*Cmpt* mutants, mature myostatin is active (Szabó *et al.* 1998), enabling genes modifying the expression of myostatin or modulating downstream signalling to have a significant influence on the hypermuscular phenotype (Varga *et al.* 2003).

Amthor *et al.* (2007) showed that despite the larger muscle mass relative to age-matched wild-types, there was no increase in maximal tetanic force generation, but rather that when expressed as a function of muscle size (specific force) extensor digitorum longus (EDL) muscles of myostatin knock-out ($Mstn^{-/-}$) and *Cmpt* mice were weaker than wild-type muscles. In addition, muscles from $Mstn^{-/-}$ animals had a marked increase in the number of type IIb fibres as compared to wild-type controls. They suggested that with myostatin deficiency, decreased force production is accompanied by a loss of oxidative characteristics of skeletal muscle.

On the other hand, while alterations in fibre type and oxidative characteristics of the muscles in *Cmpt* mice could explain a reduction in overall endurance, they fail to explain why specific force is decreased in these animals. Therefore, modifications in one or more of the events leading to shortening – i.e. in excitation–contraction coupling (ECC) – could be the underlying reason for the alterations in muscle force of *Cmpt* mice. Nevertheless, the steps in ECC have not yet been investigated in these animals.

In skeletal muscle ECC begins when depolarization of the transverse (T-)tubular membrane initiates the release of calcium from its intracellular store, the sarcoplasmic reticulum (SR), via specialized Ca^{2+} release channels known as ryanodine receptors (RyR; e.g. Franzini & Protasi, 1997). RyR activation is achieved by the depolarization-evoked conformational change of the dihydropyridine receptors (DHPRs) localized in the T-tubular membrane (e.g. Rios & Pizarro, 1991; Lamb, 2002). Calcium ions then bind to the regulatory sites on troponin-C to initiate a conformational change, which in turn enables the binding of myosin to actin and, ultimately, results in muscle contraction.

To understand the apparent discrepancy between increased muscle mass and reduced specific force reported in the literature for *Cmpt* mice, we hypothesized that ECC is also modified in these animals. To this end, we give an in-depth investigation of muscle function by comparing the physical endurance of control and *Cmpt* mutant mice as well as changes of ECC. For the latter, intracellular calcium concentration measurements were conducted using electrical stimulation or prolonged depolarization of enzymatically isolated fibres loaded with fluorescent calcium indicators while the contractile activation was studied on chemically skinned fibre segments. We demonstrate that reduced SR Ca^{2+} release underlies the suppression of specific force. Part of this work was presented to the European Muscle Society (Jenes *et al.* 2012).

© 2014 The Authors. The Journal of Physiology © 2014 The Physiological Society

Downloaded from J Physiol (jp.physoc.org) at Imperial College London Library on September 3, 2014

Methods

Animal care

Animal experiments conformed to the guidelines of the European Community (86/609/EEC). The experimental protocol was approved by the institutional Animal Care Committee of the University of Debrecen (22/2011/DE MAB). The mice were housed in plastic cages with mesh covers, and fed with pelleted mouse chow and water *ad libitum*. Room illumination was an automated cycle of 12 h light and 12 h dark, and room temperature was maintained within the range 22–25°C. When necessary mice were killed by cervical dislocation.

Mating and genotyping of *Cmpt* mice

The *Cmpt* mice (see Supplementary Fig. S1*A* top, S1*B*) originated from G.M.'s lab (Varga *et al.* 2003). To monitor the *Cmpt* mutation, heterozygous mice were obtained by mating wild-type C57BL/6 ($Mstn^{+/+}$; control; Fig. S1*A* bottom, S1*C*) and *Cmpt* mice. Tail-tip biopsy was performed for genotyping (see Fig. S2).

In vivo experiments

Voluntary activity wheel measurement. Twelve- to 16-week-old *Cmpt* ($n = 8$) and C57BL/6 ($n = 8$) mice were singly housed in a cage with a mouse running wheel (Campden Instruments Ltd, Loughborough, UK). Wheels were interfaced to a computer and revolutions were recorded at 20 min intervals, continuously for 14 days. The average and maximal speed, and the distance and duration of running were calculated for individual mice and then averaged by strains.

Forepaw grip test. Twelve- to 16-week-old *Cmpt* ($n = 5$) and C57BL/6 ($n = 11$) mice were held perpendicular to the bar connected to a capacitive force transducer, so that they did not reach at an angle during the trials. The hind limbs were not allowed to touch any surfaces. When the unrestrained forepaw was brought into contact with the bar of the grip test meter, the animals reliably grasped the bar, and the animal was then gently pulled away from the device. The grip test meter then measured the maximal force before the animal released the bar. We allowed the mouse to grip the bar fully. Force responses were digitized at 2 kHz and stored via an online connected computer.

In vitro experiments

Isolation of single skeletal muscle fibres. Experiments were carried out on skeletal muscle fibres from the flexor digitorum brevis (FDB), EDL and soleus muscles of the mice. Single muscle fibres were enzymatically dissociated in calcium-free modified Tyrode's solution (in mM: 137 NaCl, 5.4 KCl, 0.5 $MgCl_2$, 11.8 Hepes, pH 7.4) containing 0.2% Type I collagenase (Sigma, St Louis, MO, USA) at 37°C for 50–55 min (Csernoch *et al.* 2008).

To release single fibres muscles were triturated gently in modified Tyrode's solution supplemented with 1.8 mM $CaCl_2$. The fibres were then mounted on laminin-coated cover slip floors of culture dishes and kept at 4°C until use.

Resting membrane potential measurement

FDB muscle fibres were superfused with oxygenized Tyrode's solution (in mM: 137 NaCl, 5.4 KCl, 0.5 $MgCl_2$, 1.8 $CaCl_2$, 11.8 Hepes-NaOH, 1 g l^{-1} glucose, pH 7.4) at room temperature (22°C). Only cells with an intact surface membrane and clear cross striations were used. Membrane potentials were recorded using 3 M KCl filled sharp glass microelectrodes having tip resistances between 30 and 40 MΩ. The electrodes were connected to the input of a Multiclamp-700A amplifier (Axon Instruments, Foster City, CA, USA) under current clamp conditions. Membrane potentials were digitized at 100 kHz using a Digidata 1322 A/D card (Axon Instruments) under software control (pClamp 9.2, Axon Instruments, Foster City, CA, USA) and stored for later analysis.

Ca^{2+} sensitivity of the contractile proteins

Ca^{2+}-dependent active isometric force and its Ca^{2+} sensitivity, and Ca^{2+}-independent passive force of permeabilized EDL and soleus muscle fibres were determined by a mechanical measuring system at 15°C as previously described (Papp *et al.* 2002; for additional details see Supplementary Material). Briefly, Ca^{2+} contractures were evoked by transferring the fibres from Ca^{2+}-free relaxing solution (in mM: 37.34 KCl, 10 BES, 6.24 $MgCl_2$, 7 EGTA, 6.99 Na_2ATP and 15 sodium creatinin-phosphate, pH 7.2) to activating solutions (relaxing solution supplemented with Ca) of gradually increasing $[Ca^{2+}]$. During single Ca^{2+} contractures, when the force reached the maximal value, a quick release–re-stretch manoeuvre was performed in the activating solution. As a result of this intervention, the force dropped from peak level to zero, allowing determination of the total force level (F_{total}), and then started to redevelop. Force redevelopment was fitted to a single exponential function to estimate the rate constant of force redevelopment (k_{tr}). The fibre was then returned to the relaxing solution, where a shortening to 80% of the original preparation length was performed to assess the passive force level ($F_{passive}$). The active isometric force (F_{active}) was calculated by subtracting $F_{passive}$ from F_{total}. F_{active} and $F_{passive}$ were normalized for

© 2014 The Authors. The Journal of Physiology © 2014 The Physiological Society

Downloaded from J Physiol (jp.physoc.org) at Imperial College London Library on September 3, 2014

the fibre cross-sectional area calculated from the width and height of the fibres. Isometric force values were normalized for the maximal Ca^{2+}-activated active force, and Ca^{2+}–force relationships were plotted to determine the Ca^{2+} sensitivity of isometric force production.

The relationship between force and p_{Ca} was fitted with a modified Hill equation:

$$F_{Ca} = F_{max}([Ca^{2+}]^{nH}/(pCa_{50}^{nH} + [Ca^{2+}]^{nH})) + F_{min}, \quad (1)$$

where F_{Ca} is the steady-state force, F_{max} is the steady isometric force at saturating Ca^{2+} concentration ($p_{Ca} = 4.75$), the Hill coefficient (nH) is a measure of the steepness of the relationship, p_{Ca50} is the midpoint of the relationship and F_{min} is defined as the isometric force recorded at $p_{Ca} = 9$.

Table 1. Grip-strength test data

	Control ($n = 11$)	*Cmpt* ($n = 5$)[#]
Body weight (g)	20.7 ± 0.7	56.0 ± 3.3***
Absolute force (mN)	71.1 ± 1.4	126.7 ± 4.0***
Force normalized to body weight (mN g^{-1})	3.48 ± 0.07	2.36 ± 0.09***

***Significant difference at $P < 0.001$ as compared to control.
[#]Numbers in parentheses denote the number of animals.

Table 2. Distance and speed in voluntary wheel running

	Control ($n = 8$)	*Cmpt* ($n = 8$)[#]
Distance (m day^{-1})	7145 ± 553	3387 ± 283**
Average speed (m min^{-1})	13.3 ± 1.0	9.6 ± 0.8**
Maximal speed (m min^{-1})	23.1 ± 1.0	18.6 ± 1.0**
Duration (min day^{-1})	544 ± 31	356 ± 25**

**Significant difference at $P < 0.01$ as compared to control.
[#]Numbers in parentheses denote the number of animals.

Whole-cell intracellular Ca^{2+} concentration measurement

Changes in intracellular Ca^{2+} concentration ($[Ca^{2+}]_i$) were monitored using Fura-2 as described previously (Fodor *et al.* 2008; for additional details see Supplementary Material). Briefly, isolated FDB fibres were mounted on laminin-coated cover slips and loaded with 5 μM Fura-2 AM for 60 min. Ca^{2+} transients were evoked by KCl depolarization. $[Ca^{2+}]_i$ was calculated from the ratio of measured fluorescence intensities (F_{340}/F_{380}) using an *in vivo* calibration as described in our earlier report (Fodor *et al.* 2008).

Detection of the changes in $[Ca^{2+}]_i$ using confocal microscopy

Individual action potentials were evoked by applying supra-threshold 2 ms square pulses (S88 Stimulator, Grass Technologies, Warwick, RI, USA) through a pair of platinum electrodes placed close to the fibre. Tetanic depolarizations were initiated using trains of supra-threshold 2 ms square pulses with a frequency of 100 Hz within the train. Each train lasted for 500 ms. Depolarization-evoked calcium transients were measured at 22°C using a confocal laser scanning microscope system (Zeiss 5 Live, Oberkochen, Germany) after loading the fibres with 20 μM Rhod-2 AM for 15 min at room temperature. Line-scan images (512 pixels per line) were used to monitor the fluorescence intensity changes at 1 ms per line and using a 40× water immersion objective. Rhod-2 was excited with a helium–neon ion laser at 543 nm, and emission was detected with a 550 nm long pass filter. To obtain the time course of Rhod-2 fluorescence change (F_{rhod}), corresponding data points (usually 10–15) in the line-scan images were averaged in the spatial domain. Resting fluorescence was determined as the average fluorescence before the depolarization. Changes in $[Ca^{2+}]_i$ were then calculated using the formula

$$[Ca^{2+}]_i = Kd_{rhod} \cdot (F_{rhod} - F_{rhod,min})/(F_{rhod,max} - F_{rhod}) \quad (2)$$

where $F_{rhod,max}$ and $F_{rhod,min}$ were determined in our laboratory, while other parameters ($k_{off,rhod}$ and $k_{on,rhod}$, backward and forward rate constants for the calcium-dye reaction, respectively, with $Kd_{rhod} = k_{off,rhod}/k_{on,rhod}$) for Rhod-2 were taken from Escobar *et al.* (1997).

Detection of calcium release events

After enzymatic dissociation, FDB fibres were permeabilized using 0.01% saponin for a few seconds. Spontaneous calcium release events were visualized by 50 μM Fluo-3 using a confocal laser scanning microscope (Zeiss 5 META, Oberkochen, Germany) at 22°C (as described by Lukacs *et al.* 2008; for additional details see Supplementary Material).

Images containing spontaneous calcium release events were analysed using an automatic event detection program (Szentesi *et al.* 2004; Szabo *et al.* 2010), which calculated the amplitude ($\Delta F/F_0$), full width at half maximum (FWHM), rise time and duration of the identified events.

© 2014 The Authors. The Journal of Physiology © 2014 The Physiological Society

Downloaded from J Physiol (jp.physoc.org) at Imperial College London Library on September 3, 2014

Table 3. Calcium sensitivity of isometric force

	Control		*Cmpt*	
	EDL ($n = 8$)	Soleus ($n = 8$)	EDL ($n = 7$)	Soleus ($n = 8$)[#]
Cross section (μm^2)	1887 ± 343	1714 ± 235	2602 ± 380	3303 ± 386*
T_{active} (kN m^{-2})	26.14 ± 5.06	26.87 ± 3.98	25.25 ± 4.01	21.89 ± 2.18
$T_{passive}$ (kN m^{-2})	2.24 ± 0.58	2.07 ± 0.48	2.15 ± 0.47	2.86 ± 0.37
k_t (s^{-1})	3.43 ± 0.39	1.98 ± 0.21	6.15 ± 0.65**	1.84 ± 0.40
p_{Ca50}	5.73 ± 0.02	5.73 ± 0.04	5.77 ± 0.03	5.78 ± 0.05
nH	3.21 ± 0.19	3.12 ± 0.29	3.15 ± 0.16	2.75 ± 0.20

**Significant difference at $P < 0.01$ as compared to control.
[#]Numbers in parentheses denote the number of fibres from four control and four *Cmpt* animals.
$T_{passive}$: passive isometric tension; T_{active}: active isometric tension; k_{tr}: rate constant of force redevelopment; p_{Ca50}: midpoint of the force-calcium relationship; nH: Hill coefficient

Calculation of calcium release from the SR

The Ca^{2+} release flux (R_{rel}) was defined as the sum of Ca^{2+} fluxes entering the myoplasmic space and that transported back into the calcium storage organelle:

$$R_{rel} = d[Ca]_T/dt = d(Ca_{total} + Ca_{transp})/dt, \quad (3)$$

where Ca_{total} is the total Ca^{2+} in the myoplasm, and Ca_{transp} is the amount of Ca^{2+} transported by the removal processes. Ca_{total} was estimated as the sum of free Ca^{2+} (Ca_{free}) and the amount of Ca^{2+} bound to intracellular binding sites such as dye (Ca_{dye}), troponin-C (Ca_{tropC}), parvalbumin (Ca_{parv}) and pump (Ca_{pump}):

$$Ca_{total} = Ca_{free} + (Ca_{dye} + Ca_{tropC} + Ca_{parv} + Ca_{pump}), \quad (4)$$

In eqn (3) Ca_{transp} is the calcium quantity carried by Ca^{2+} removal mechanisms (pumps), which was considered proportional to the relative saturation of the pumps ($[Ca_{pump}]/[pump]$). The proportionality factor is the maximum speed of Ca^{2+} removal (PV_{max}):

$$Ca_{transp} = PV_{max} \cdot ([Ca_{pump}]/[pump]), \quad (5)$$

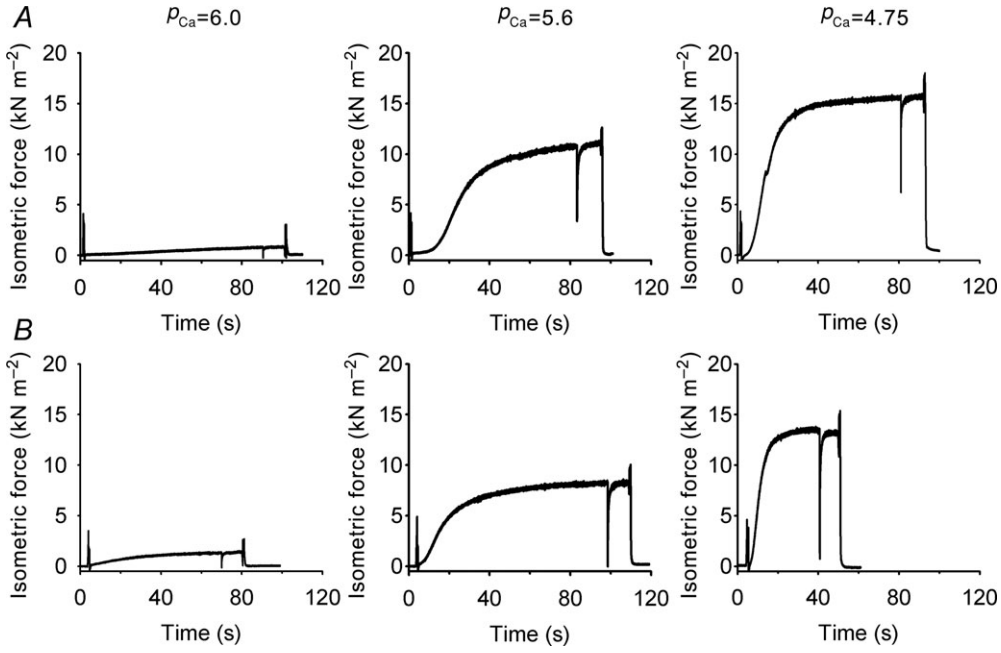


Figure 1. Time course of isometric force on skinned muscle fibres
Isometric force was measured on chemically skinned (0.5% Triton-X 100) fibre segments isolated from the EDL muscle of control (*A*) and of *Cmpt* (*B*) mice at three different calcium concentrations ($p_{Ca} = 6.0$, 5.6 and 4.75). Fibres were rapidly transferred from a relaxing solution ($p_{Ca} = 9$) to the test solutions and the time-course of force development was recorded. In all cases a rapid release and re-stretch manoeuvre was also performed. Experimental conditions: fibre cross section area 1764 and 2074 μm^2 in control and *Cmpt* mice, respectively; temperature 15°C.

© 2014 The Authors. The Journal of Physiology © 2014 The Physiological Society

Downloaded from J Physiol (jp.physoc.org) at Imperial College London Library on September 3, 2014

Removal parameters were taken from the literature (Schuhmeier *et al.* 2003; Jacquemond 2012) and used as described in our earlier reports (Csernoch *et al.* 1990; Szappanos *et al.* 2004).

Chemicals and statistical analysis

Chemicals, unless otherwise stated, were purchased from Sigma and were of analytical grade. Pooled data were expressed as mean ± standard error of the mean (SEM). The differences between control and *Cmpt* animals were assessed using one-way analysis of variance (ANOVA) and all pair-wise multiple comparison procedures (Student–Newman–Keuls method). An *F*-test was used to test the significance and $P < 0.05$ was considered to indicate a statistically significant difference.

Results

In vivo experiments

Cmpt mice displayed great hypermuscularity and their weight was more than twice that of control animals (see Fig. S1, Table 1). To check the *in vivo* muscle performance of the adult animals, 12–16-week-old mice were used from both groups in grip tests. As expected, based on the increased muscle mass, *Cmpt* mice performed significantly better than the wild-type animals in these tests. That is, the maximal force that they could produce was significantly greater than that of control animals. However, after normalization to body weight – to compensate for the increased muscle mass – wild-type mice displayed significantly greater relative force as compared to the *Cmpt* animals (Table 1).

Experiments with the voluntary wheel gave similar results. Control mice performed significantly better given both the average and maximal speed and the total distance covered. In addition, they spent more time in the wheel than *Cmpt* mice (Table 2). Overall, these experiments clearly indicated that although *Cmpt* mice were larger and stronger, their strength was less than would be expected from the increase in muscle mass. To clarify the mechanisms underlying this, the steps in ECC were investigated in detail.

In vitro experiments

Resting membrane potential. To exclude the possibility that the electrical properties of the cell membrane were substantially altered, the resting membrane potential of FDB muscle fibres from four control and three *Cmpt* animals was determined. Although average resting membrane potential was slightly depolarized in *Cmpt* animals (-77.8 ± 0.2 mV, $n = 18$) as compared to control mice (-79.2 ± 0.3 mV, $n = 13$), we do not consider this difference to be physiologically relevant.

Calcium sensitivity of the contractile system. As the next step, the possible alterations in the contractile machinery were studied in both *Cmpt* and control mice. Force development during isometric contractions was measured in 31 fibre segments (segment length 80.7 ± 5.1 μm) dissected from soleus and EDL fibres of four wild-type and four *Cmpt* mice. Figure 1 displays six

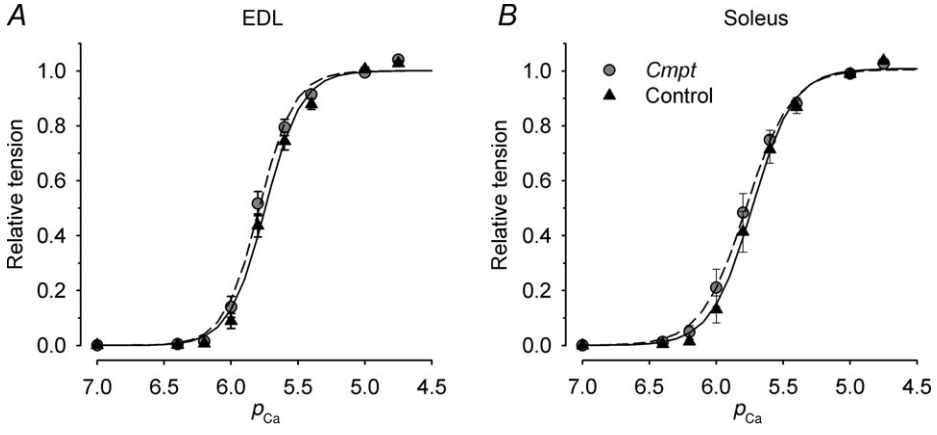


Figure 2. Calcium concentration dependence of isometric force
Maximal steady isometric force was determined for EDL (*A*) and soleus (*B*) muscles in control (black triangles) and in *Cmpt* mice (grey circles) at different calcium concentrations. These values were then normalized to those measured at $p_{Ca} = 4.75$, averaged over the individual fibres and plotted as a function of the calcium concentration of the activating solution. The lines indicate the Hill curves (eqn (1)) fitted to the data points (continuous line, control; dashed line, *Cmpt*). Parameters used to generate the fitted curves were: for EDL, nH = 3.21 and 3.32, $p_{Ca50} = 5.74$ and 5.79; for soleus, nH = 2.82 and 2.59, $p_{Ca50} = 5.73$ and 5.78 in control and *Cmpt*, respectively.

© 2014 The Authors. The Journal of Physiology © 2014 The Physiological Society

Downloaded from J Physiol (jp.physoc.org) at Imperial College London Library on September 3, 2014

representative isometric contractions at low ($p_{Ca} = 6.0$), intermediate ($p_{Ca} = 5.6$) and saturating ($p_{Ca} = 4.75$) calcium concentrations. Table 3 presents the average maximal active and passive isometric tension (T_{active} and $T_{passive}$, respectively), which were obtained by normalizing the force values to the cross section of the fibre segments. There was no significant difference in these values between wild-type and *Cmpt* animals.

To gain further insight into the effects of the *Cmpt* mutation on force generation, the Ca^{2+} sensitivities of the isometric force on EDL and soleus muscles of control and *Cmpt* mice were compared (Fig. 2). After fitting eqn (1) to the data points, no significant difference was observed in p_{Ca50} or nH between the two groups of animals (Table 3). These results clearly suggest that the contractile machinery, including its calcium sensitivity, is not altered in the *Cmpt* strain.

Changes in $[Ca^{2+}]_i$ in *Cmpt* mice. Since the calcium sensitivity of the contractile proteins were similar in both groups of animals, the possible effects of the *Cmpt* mutation on calcium homeostasis was examined in isolated, single FDB skeletal muscle fibres of both types of mice. Twelve- to 16-week-old wild-type and *Cmpt* mice were used for functional experiments. Figure 3*A* presents calcium transients measured on these fibres evoked by depolarization using 120 mM KCl in the presence of a normal (1.8 mM) extracellular calcium concentration. The pooled data to confirm that the *Cmpt* mutation had little, if any, effects on the resting $[Ca^{2+}]_i$ (Fig. 3*B*), suggesting that the calcium leak from and the extrusion into the extracellular environment was unaffected under these conditions. On the other hand, depolarization-evoked calcium transients were almost 50% higher in control than in *Cmpt* fibres (Fig. 3*C*).

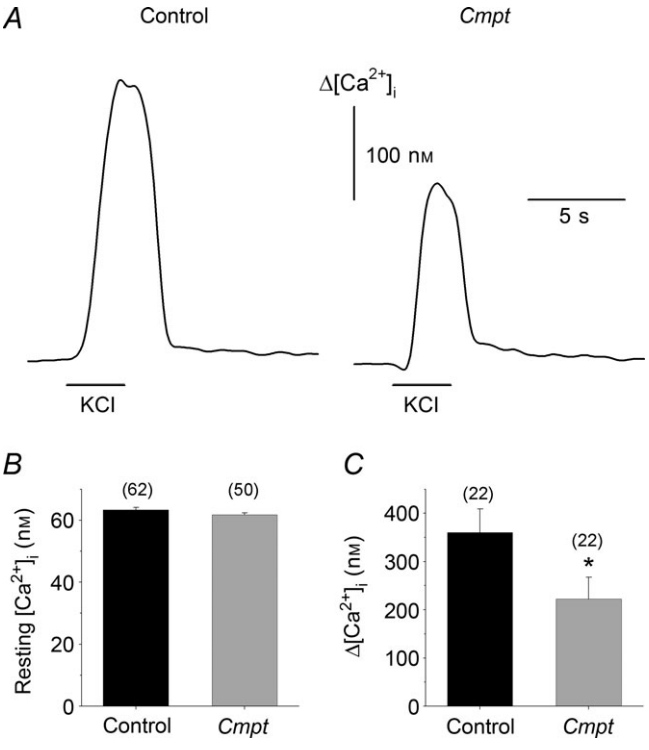


Figure 3. $[Ca^{2+}]_i$ at rest and during KCl-evoked depolarisations
A, depolarization-evoked changes in intracellular calcium concentration on intact fibres isolated from the FDB muscles of control (left) and of *Cmpt* (right) mice. Depolarization was achieved by the local perfusion of 120 mM KCl for 3 s as indicated by the horizontal lines below the transients. *B*, pooled data from three control and three *Cmpt* animals. Averaged values of resting $[Ca^{2+}]_i$ (*B*) and $\Delta[Ca^{2+}]_i$ (*C*). Numbers in parentheses are the number of fibres investigated. *Significant ($P < 0.05$) difference from control. Measurements were carried out at 22°C.

Action potential-evoked calcium transients in FDB fibres. Field stimulation-induced global calcium transients were also measured on FDB fibres. These calcium transients were visualized using laser scanning confocal microscopy in the line-scan mode. Figure 4 displays representative fluorescence intensity changes during single pulses (panels A and B) and during trains (panels C and D) of depolarizations. Note that the spatial profile of the transients was homogenous in both strains (see expanded images in Fig. 4*A–D*), indicating a normal propagation of the depolarization in the T-tubular system.

To analyse the calcium transients, the line-scans were normalized and 10–15 points of the images in the space domain were averaged. Figure 5 presents representative fluorescence transients after normalization using single (top panel) and train (bottom panel) stimulation from control (left) and *Cmpt* (right) mice. Analysis of these transients revealed that the average amplitudes of the calcium transients in *Cmpt* fibres were almost identical during the single stimulation (2.37 ± 0.12 F/F_0, $n = 25$ in control; 2.50 ± 0.15 F/F_0, $n = 26$ in *Cmpt*, $P > 0.4$) but significantly reduced during the train stimulation as compared to controls (Table 4).

During the measurements either six or three calcium transients were recorded for single or train stimulations, respectively. There was no significant decrease in the amplitude of the consecutive transients either in the single (Fig. 5*E*) or in the train (Fig. 5*F*) depolarizations in either animal group.

To further analyse calcium release from the SR, first the normalized fluorescence values of the train depolarisations were transformed to calcium concentration (eqn (2)), and then the total amount of calcium released ($[Ca]_T$) and the calcium release flux (R_{rel}) through the RyRs was calculated (eqns (3)–(5)). It is clear from Fig. 6 that the change in $[Ca^{2+}]_i$ (top panel) as well as the total calcium released into the myoplasm (middle panel), and the corresponding calcium release flux (bottom panel) were reduced in *Cmpt*

© 2014 The Authors. The Journal of Physiology © 2014 The Physiological Society

Downloaded from J Physiol (jp.physoc.org) at Imperial College London Library on September 3, 2014

mice. R_{rel} reached its peak 9 ms after the onset of the depolarization and was significantly smaller in the *Cmpt* strain (Table 4). Furthermore, a significant difference was observed in the maintained steady level of R_{rel}. On the other hand, the ratio of peak-to-steady level and the time constant of the inactivation remained unchanged, i.e. they were essentially identical in the two animal groups. The amount of released calcium showed roughly a 30% decrease (Table 4) in the mutant animals. The data presented in Figs 4–6 and in Table 4 clearly demonstrate that depolarization-evoked calcium release from the SR was significantly reduced in *Cmpt* mice.

Elementary calcium release events in *Cmpt* fibres. To understand the reasons underlying the suppressed SR calcium release, localized calcium release events were measured in control and in *Cmpt* fibres using high speed laser scanning confocal microscopy. The fibres displayed calcium sparks (calcium release events with large amplitude and short duration) and embers (events with small amplitude and long duration) (Fig. 7*A*). Note that the number of calcium sparks was far greater than that of embers. Although fibres from *Cmpt* mice generated calcium sparks and embers as for control cells (Fig. 7*B*), the characteristic parameters of these events were altered. Plotting the amplitude histograms of sparks (Fig. 8*A*) revealed that the *Cmpt* mutation was associated with an increase in the relative frequency of calcium sparks with smaller amplitudes. Pooled data show that on average the amplitude of the calcium sparks was significantly higher in control fibres than in *Cmpt* cells (0.165 ± 0.001 *vs.* 0.154 ± 0.002, respectively; $P < 0.001$). Similarly, we observed a relatively higher amount of faster evolving sparks in *Cmpt* than in control mice (Fig. 8*B*), the average rise time showed a significant (30%, $P < 0.01$) reduction (from 34.7 ± 0.9 to 24.3 ± 0.8 ms in control and *Cmpt* mice, respectively). Although the overall shape of FWHM histograms remained unaffected in *Cmpt* animals, the distribution was slightly shifted to the left (Fig. 8*C*). That is, the *Cmpt* mutation decreased the average FWHM significantly ($P < 0.01$) from the control 1.92 ± 0.01 to 1.87 ± 0.01 μm. The distribution of event duration was also altered by the mutation (Fig. 8*D*), showing a relatively high frequency of shorter events in *Cmpt*

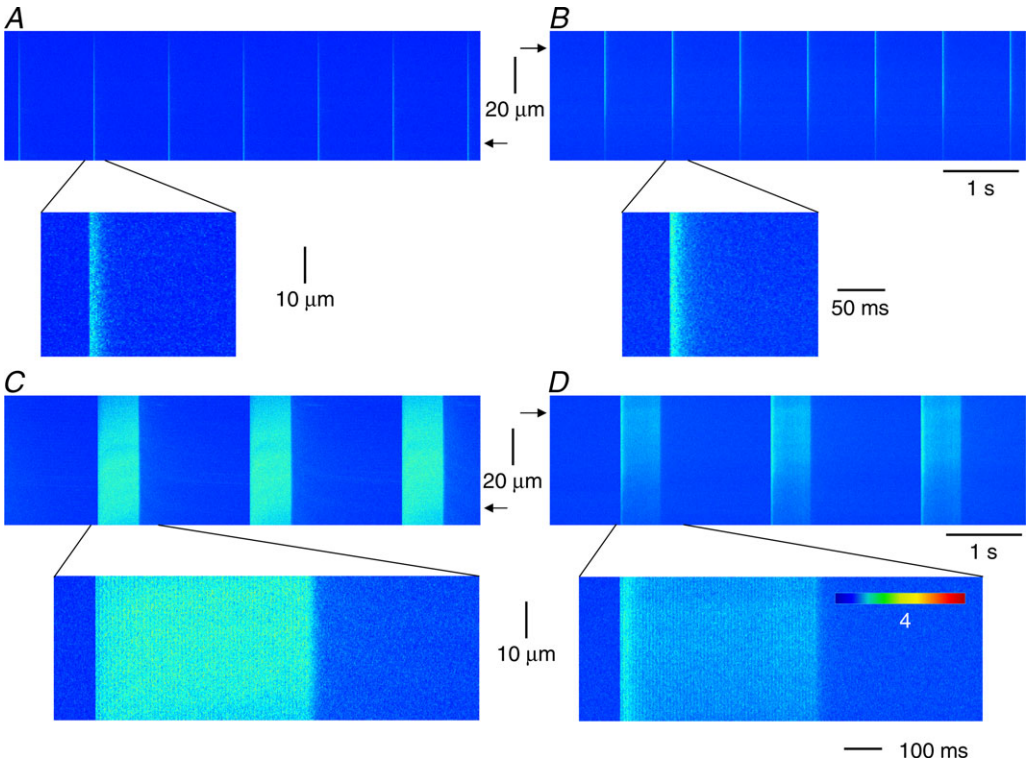


Figure 4. Field stimulation-evoked fluorescence changes in FDB fibres
Intact fibres isolated from the FDB muscles were loaded with the calcium-sensitive fluorescent dye Rhod-2. Suprathreshold pulses were used to initiate action potentials, and the accompanying changes in Rhod-2 fluorescence were detected on a confocal microscope in the line-scan mode. Images of fluorescence intensity changes as evoked by single (*A* and *B*) and trains (*C* and *D*) of depolarizations in control (*A* and *C*) and in *Cmpt* (*B* and *D*) mice. Expanded images in all panels demonstrate the homogenous activation of the fibres. Arrows indicate the spatial point where the time courses presented in Fig. 5 were determined. Acquisition parameters: 4096 × 512 pixels, 1.53 ms line^{-1}, 0.14 μm pixel^{-1}; temperature 22°C.

© 2014 The Authors. The Journal of Physiology © 2014 The Physiological Society

Downloaded from J Physiol (jp.physoc.org) at Imperial College London Library on September 3, 2014

szentesi.peter_292_24

mice. In addition, and in accordance with the above, the frequency of the spontaneous calcium release events was also significantly ($P < 0.001$) reduced in fibres from *Cmpt* mice (6.2 ± 0.5 Hz) as compared to the control group (33.0 ± 2.7 Hz).

Discussion

Myostatin knock-out as well as *Cmpt* mice – despite their increased muscle weight – were found to have reduced specific force as compared to control animals (Amthor *et al.* 2007). Despite the fact that changes in fibre composition and consequently altered metabolic status of the muscles from these mice have been reported (e.g. Girgenrath *et al.* 2005), a clear explanation for the altered contractile function is not yet available. Here, on the one hand, we complement the observations previously made *in vivo* and, on the other, provide evidence that alterations in calcium signalling but not in the activation of the contractile machinery underlie the reduced force production.

Table 4. Parameters of the depolarization-evoked calcium transients and of the corresponding calcium release flux

	Control ($n = 14$)	*Cmpt* ($n = 13$)[#]
$\Delta F/F_0$	2.42 ± 0.03	2.07 ± 0.10*
$\Delta[Ca^{2+}]_T$ (mM)	3.06 ± 0.39	2.08 ± 0.23*
R_{rel} peak (μM ms^{-1})	23.7 ± 3.0	15.8 ± 2.1*
R_{rel} steady level (μM ms^{-1})	5.7 ± 0.7	3.7 ± 0.5*
R_{rel} peak/steady level	4.3 ± 0.4	4.6 ± 0.6
Time to peak of R_{rel} (ms)	8.9 ± 0.3	8.9 ± 0.2
Tau of inactivation (ms)	6.7 ± 0.9	8.8 ± 1.3

*Significant difference at $P < 0.05$ as compared to control.
[#]Numbers in parentheses denote the number of fibres from three control and three *Cmpt* animals.
$\Delta F/F_0$: amplitude of calcium transient; $[Ca^{2+}]_T$: amount of calcium released from the SR; R_{rel}: Ca^{2+} release flux

Our results from *in vivo* measurements are in agreement with those published earlier for both $Mstn^{-/-}$ (Amthor *et al.* 2007; Savage & McPherron, 2010) and *Cmpt* mice (Amthor *et al.* 2007) showing a reduced physical performance, as *Cmpt* animals were less agile in voluntary

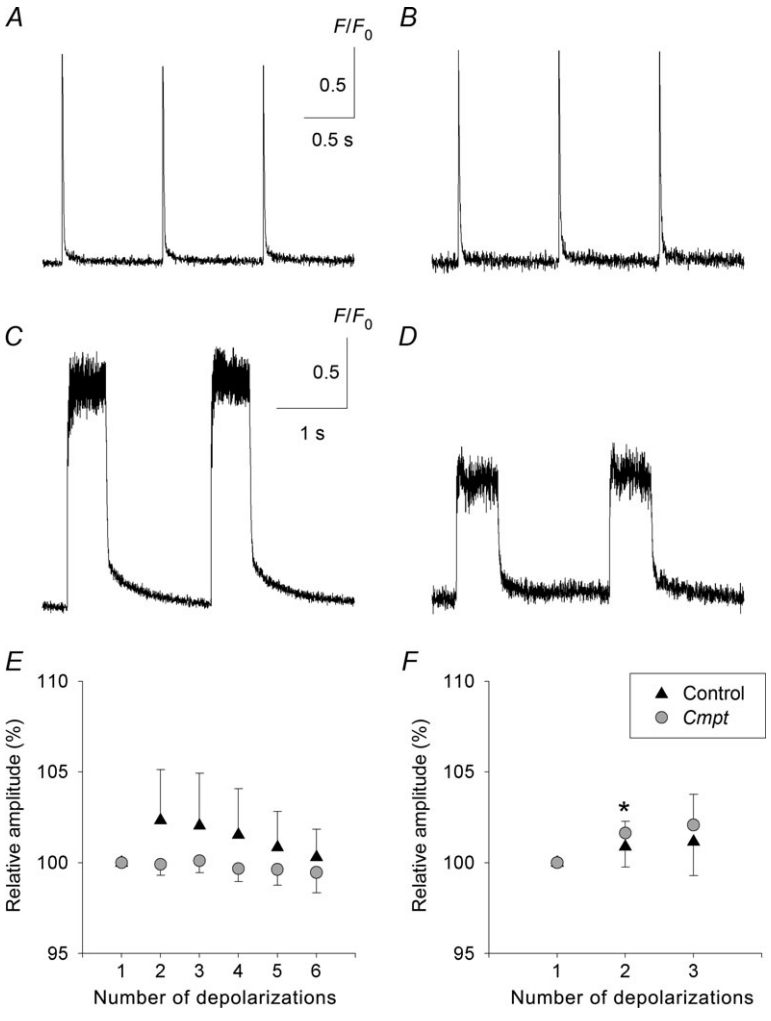


Figure 5. Time course of fluorescence changes in FDB fibres during the depolarisations
The traces (*A–D*) are spatially averaged time courses of Rhod-2 fluorescence of the line-scans in Fig. 4*A–D*, respectively, after normalizing to baseline fluorescence (F/F_0). The average was calculated from 10 consecutive lines of the line-scans at the arrows in Fig. 4. Background was calculated from data points before the depolarization. Average of consecutive peaks of fluorescence intensities normalized to the first peak during the single (*E*) and train (*F*) depolarizations. Pooled data from three control (14 fibres) and three *Cmpt* (13 fibres) animals. *Significant ($P < 0.05$) difference from the first peak.

© 2014 The Authors. The Journal of Physiology © 2014 The Physiological Society

Downloaded from J Physiol (jp.physoc.org) at Imperial College London Library on September 3, 2014

wheel running. Furthermore, the observation that the normalized force – force normalized to body weight – was reduced in the grip-strength tests in *Cmpt* mice is consistent with the idea that the increased muscle mass was not accompanied by a parallel and proportional increase in overall force. Although it is likely that alterations in cardiovascular and/or respiratory functions also contributed to the reduced physical performance in the activity wheel for these animals, based on previous reports as well as on our own findings mentioned above, changes in the events that couple electrical excitation to contraction are also part of the pathology.

Based on the previously reported changes in fibre metabolism associated with the myostatin mutation, including shifts in the oxidative state of the muscle (Girgenrath *et al.* 2005; Baan *et al.* 2013) as well as a large increase in the ATP cost of contraction (Giannesini *et al.* 2013), it was tempting to assume that an altered acto-myosin interaction would be responsible for the reduced specific force since the former can be accompanied by modifications in myosin expression. In contrast to this expectation we were unable to demonstrate any modification in the p_{Ca} dependence of force production as studied in chemically skinned fibre segments. Neither fast nor slow muscles displayed any change in their p_{Ca}–tension curves. In addition, the maximal attainable tension was also similar in control and *Cmpt* animals.

On the other hand, action potential-evoked calcium transients were significantly reduced in mutant as compared to control animals. This reduction in the increase in $[Ca^{2+}]_i$ during a train of action potentials that is the physiological stimulus during *in vivo* contractions – taken together with the unaltered p_{Ca}–tension relationship – readily explains the reduced overall tension. Note, however, that the reduction in $[Ca^{2+}]_i$ and the consequently anticipated reduced force, based on the

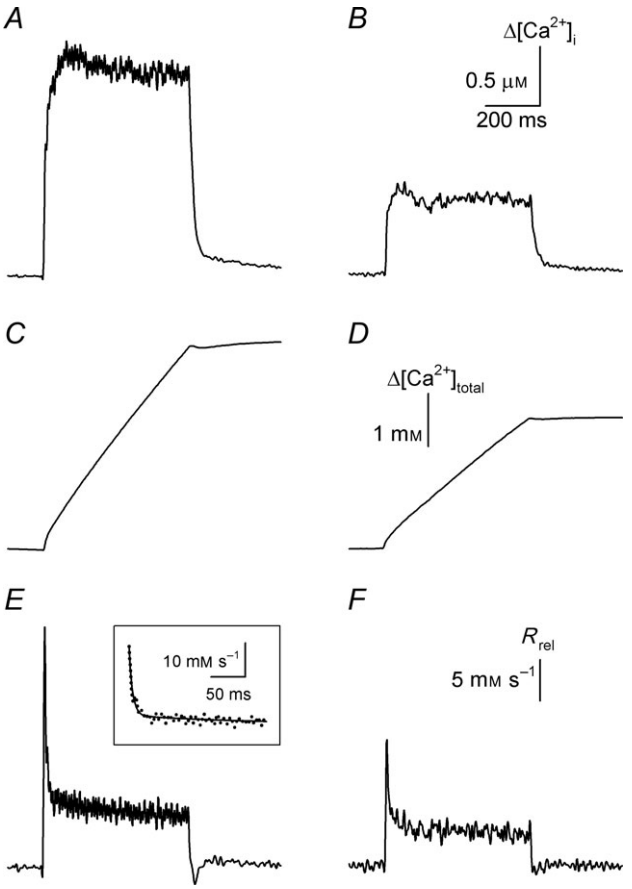


Figure 6. Depolarization-evoked changes in $[Ca^{2+}]_i$ and the corresponding calcium release flux
A and *B*, changes in intracellular calcium concentration calculated from the first transient shown in Fig. 5*C* and *D*, respectively, using eqn (2). *C* and *D*, the amount of calcium released ($[Ca^{2+}]_T$; eqn (3)) from the SR as determined from the transients shown in *A* and *B*. To calculate $[Ca^{2+}]_T$ a removal model – with the following parameters: [dye] = 20 μM, $k_{off,rhod}$ = 130 s^{-1}, $k_{on,rhod}$ = 82 μM^{-1} s^{-1}, [parvalbumin] = 2 mM, Kd_{pump} = 1 μM, $[Ca^{2+}]_{rest}$ = 70 nM – was fitted to the declining phase of the transients following the depolarization (see Methods). *E* and *F*, the corresponding calcium release flux (FL) through the RyRs. The inset in *E* shows an enlarged portion of FL and the fitted exponential (τ = 5.1 ms), which was used to determine the time constant of inactivation.

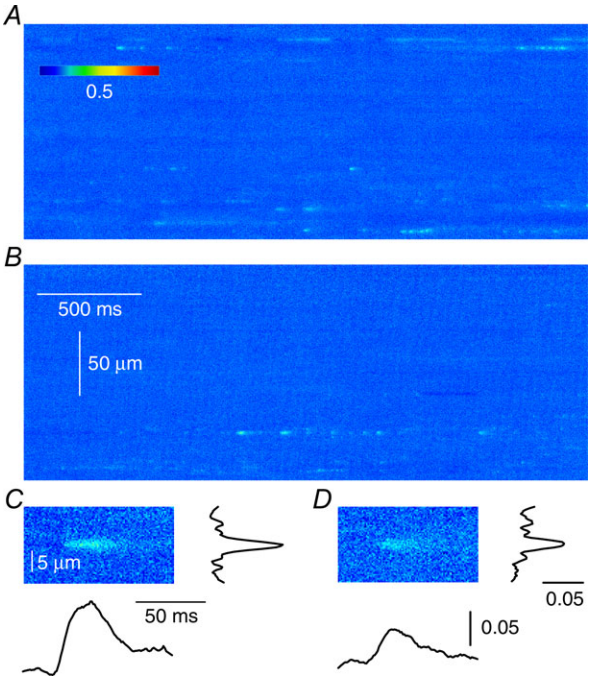


Figure 7. Spontaneous Ca^{2+} release events in FDB fibres
A and *B*, line-scan images from fibres of FDB muscles taken from control (*A*) and from *Cmpt* (*B*) mice. Enzymatically isolated fibres were permeabilized with a brief exposure to 0.01% Saponin and loaded with Fluo-3. *C* and *D*, representative sparks with their spatial profiles and time courses detected in control (*C*) and in *Cmpt* (*D*) mice. Spatial and temporal profiles were calculated from the average of five consecutive rows or columns at the maximum of the event. Acquisition parameters: 4096 × 512 pixels, 1 ms $line^{-1}$, 0.33 μm $pixel^{-1}$; temperature 22°C.

© 2014 The Authors. The Journal of Physiology © 2014 The Physiological Society

Downloaded from J Physiol (jp.physoc.org) at Imperial College London Library on September 3, 2014

measured p_{Ca}–tension relationship, was proportionally less than the increase in muscle diameter (2.35 ± 0.19 *vs.* 6.93 ± 0.32 mm^2 in the control ($n = 13$) and *Cmpt* ($n = 19$) strains, respectively, for EDL, $P < 0.001$) not accounting fully for the observed greater strength in grip tests.

SR calcium release flux was determined from the global calcium transients and a 33% reduction was observed in both the peak and the maintained steady flux. Since the peak-to-steady ratio was unaltered in *Cmpt* mice, i.e. the waveform of the SR calcium release flux was essentially the same in the mutant and the control animals, the kinetics of activation and inactivation of the calcium release channels was probably not affected. This was further strengthened by the findings that the time-to-peak of SR calcium release flux as well as the rate constant of inactivation, calculated by fitting an exponential function to the declining phase, were essentially unchanged. Note at this point that a slight (but statistically not significant) increase in the time constant was indeed observed, which is in line with previous reports that a reduced SR calcium release would initiate a slower inactivation (see e.g. Sárközi *et al.* 1996). Furthermore, in accordance with the above, a clear reduction in the amount of calcium released from the SR during a train of action potentials was also detected.

These observations leave three possibilities, or their combination, to explain the reported findings. First, there is a reduction in SR calcium content; second, there is a reduction in RyR permeability/conductance; and third, the number of activated RyRs is reduced. It should be stressed, however, that the magnitude of these modifications should not be too extensive or changes in the kinetics of inactivation would accompany the reduced SR calcium release. Indeed, the reduction in SR calcium release flux observed here was within these limits and was comparable to earlier studies in which the effect of SR depletion on the SR calcium release waveform was investigated (Klein *et al.* 1988). Reduced RyR permeability or SR calcium content could be the result of an altered metabolic state of the muscle since the redox sensitivity of RyRs has been demonstrated in a number of publications (e.g. Liu *et al.* 1994; Bull *et al.* 2007; Petrotchenko *et al.* 2011). These reports concluded that reducing conditions transform the channel to a low-open probability state, while oxidative conditions transform it to a high-open probability state (Marengo *et al.* 1998). Therefore, shifts in the redox state of the myoplasm from the control to more reducing would result in a reduced activation, while shifts to a more oxidative state would result in an increased resting SR leak and a consequent reduction in SR calcium content (e.g. Oba *et al.* 2002), both in line with the observations seen here. To determine whether the RyR channels *per se* were affected in the mutant strain, direct measurements of the channel activity would be needed. At present, there are no data available in the literature on RyRs isolated from *Cmpt* or Mstn$^{-/-}$ mice. Here we attempted to gain insight into channel function using Saponin-skinned fibres and determining the characteristics of calcium release events. Although

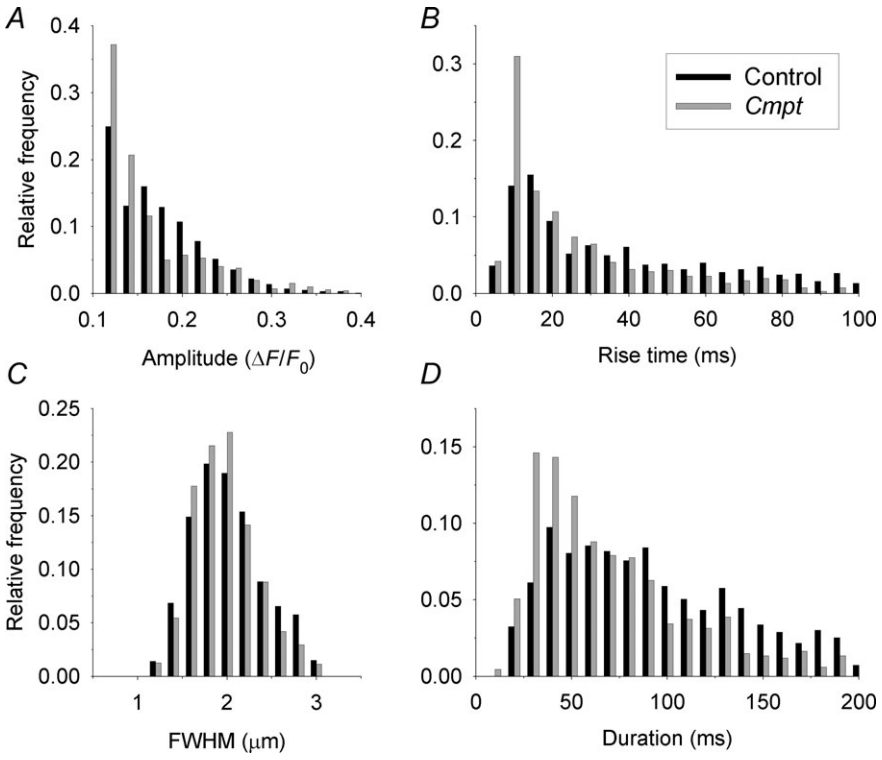


Figure 8. Distribution histograms of calcium release event parameters
Amplitude (*A*), rise time (*B*), FWHM (*C*) and duration (*D*) histograms of calcium release events from control (black bars, eight animals) and from *Cmpt* (grey bars, six animals) mice. Events were identified in the line-scan images with an automated detection routine based on wavelet transformation (see Methods). Values of the selected parameters were binned and plotted as relative frequencies to present their distributions. Events with amplitudes smaller than 0.1 $\Delta F/F_0$ and with FWHM smaller than 0.3 μm were not included in the analysis.

© 2014 The Authors. The Journal of Physiology © 2014 The Physiological Society

Downloaded from J Physiol (jp.physoc.org) at Imperial College London Library on September 3, 2014

these events should be regarded with caution since they do not appear with appreciable frequency in non-skinned fibres, their study appear the only way to tackle channel behaviour in the native environment (Klein & Schneider 2006). Due to the above mentioned clear limitations, only the simplest properties were investigated in detail in this study. It is clear from the results that calcium release events occur with a lower frequency in *Cmpt* animals than they do in control mice (Fig. 7). In addition, these events have a smaller amplitude and FWHM than their control counterparts. These observations are consistent with the idea that channels open less readily and release less calcium once they are opened in the mutant as compared to control mice. Although we cannot exclude the possibility that fibres from *Cmpt* animals respond differently to Saponin treatment, it is more likely that the observed changes are indeed due to alterations in calcium release. This is strengthened by the fact that the observed changes in the parameters of the calcium release events are clearly in line with the alterations seen for global calcium transients in intact fibres. In particular, the reduced number of events and the amount of calcium released per event would readily explain why global calcium transients were smaller in the mutant animals. These findings would then suggest that the alterations that explain the *Cmpt* phenotype – with regard to the reduced force – reside, at least in part, in the calcium release process.

Considering the above, the most likely explanation for the reduced calcium release is a reduction in SR content. This would then influence the release process through at least two routes. The activation of RyRs depends on the calcium concentration inside the SR, namely a lower intraluminar calcium concentration results in a lower activation level of the channels (Laver, 2005). In addition, due to the lower SR calcium, the current through the channels is also reduced. These effects combined would then explain the lower frequency as well as the lower amplitude of the calcium release events and, finally, the reduced calcium transients. Although, at present, we have no clear explanation for how the mutation leads to the reduction in SR calcium content, all the data are consistent with the idea that the reduced specific force of these mice is the consequence of this alteration.

References

Amthor H, Macharia R, Navarrete R, Schuelke M, Brown SC, Otto A, Voit T, Muntoni F, Vrbóva G, Partridge T, Zammit P, Bunger L & Patel K (2007). Lack of myostatin results in excessive muscle growth but impaired force generation. *Proc Natl Acad Sci U S A* **104**, 1835–1840.

Baán JA, Kocsis T, Keller-Pintér A, Müller G, Zádor E, Dux L & Mendler L (2013). The compact mutation of myostatin causes a glycolytic shift in the phenotype of fast skeletal muscles. *J Histochem Cytochem* **61**, 889–900.

Bodine SC, Stitt TN, Gonzalez M, Kline WO, Stover GL, Bauerlein R, Zlotchenko E, Scrimgeour A, Lawrence JC, Glass DJ & Yancopoulos GD (2001). Akt/mTOR pathway is a crucial regulator of skeletal muscle hypertrophy and can prevent muscle atrophy *in vivo*. *Nat Cell Biol* **3**, 1014–1019.

Bull R, Finkelstein JP, Humeres A, Behrens MI & Hidalgo C (2007). Effects of ATP, Mg^{2+}, and redox agents on the Ca^{2+} dependence of RyR channels from rat brain cortex. *Am J Physiol Cell Physiol* **293**, C162–C171.

Bünger L, Laidlaw AH, Bulfield G, Eisen EJ, Medrano JF, Bradford GE, Prichner F, Renne U, Schlote W & Hill WG (2001). Inbred lines of mice derived from long-term on growth selected lines: unique resources for mapping growth genes. *Mamm Genome* **12**, 678–686.

Csernoch L, Kovács L, Nilius B & Szücs G (1990). Caffeine and the myoplasmic calcium removal mechanisms in cut frog skeletal muscle fibres. *Gen Physiol Biophys* **9**, 251–266.

Csernoch L, Pouvreau S, Ronjat M & Jacquemond V (2008). Voltage-activated elementary calcium release events in isolated mouse skeletal muscle fibers. *J Membr Biol* **226**, 43–55.

Elkina Y, von Haehling S, Anker SD & Springer J (2011). The role of myostatin in muscle wasting: an overview. *J Cachexia Sarcopenia Muscle* **2**, 143–151.

Escobar AL, Velez P, Kim AM, Cifuentes F, Fill M & Vergara JL (1997). Kinetic properties of DM-nitrophen and calcium indicators: rapid transient response to flash photolysis. *Pflugers Arch* **434**, 615–631.

Fodor J, Gönczi M, Sztretye M, Dienes B, Oláh T, Szabó L, Csoma E, Szentesi P, Szigeti GP, Marty I & Csernoch L (2008). Altered expression of triadin 95 causes parallel changes in localized Ca^{2+} release events and global Ca^{2+} signals in skeletal muscle cells in culture. *J Physiol* **586**, 5803–5818.

Franzini-Armstrong C & Protasi F (1997). Ryanodine receptors of striated muscles: a complex channel capable of multiple interactions. *Physiol Rev* **77**, 699–729.

Giannesini B, Vilmen C, Amthor H, Bernard M & Bendahan D (2013). Lack of myostatin impairs mechanical performance and ATP cost of contraction in exercising mouse gastrocnemius muscle *in vivo*. *Am J Physiol Endocrinol Metab* **305**, E33–E40.

Girgenrath S, Song K & Whittemore LA (2005). Loss of myostatin expression alters fiber-type distribution and expression of myosin heavy chain isoforms in slow- and fast-type skeletal muscle. *Muscle Nerve* **31**, 34–40.

Jacquemond V (2012). Waveless mammalian muscle. *J Physiol* **590**, 1783.

Jenes A, Bodnár D, Ruzsnavszky O, Geyer N, Dienes B, Balogh A, Papp Z, Szentesi P & Csernoch L (2012). Modified EC coupling in myostatin deficient ($MSTN^{-/-}$) mice. *J Muscle Res Cell Motil* **33**, 242–243.

Kambadur R, Sharma M, Smith TP & Bass JJ (1997). Mutations in myostatin (GDF8) in double-muscled Belgian Blue and Piedmontese cattle. *Genome Res* **7**, 910–916.

Klein MG, Simon BJ, Szucs G & Schneider MF (1988). Simultaneous recording of calcium transients in skeletal muscle using high- and low-affinity calcium indicators. *Biophys J* **53**, 971–988.

© 2014 The Authors. The Journal of Physiology © 2014 The Physiological Society

Downloaded from J Physiol (jp.physoc.org) at Imperial College London Library on September 3, 2014

szentesi.peter_292_24

Klein MG & Schneider MF (2006). Ca^{2+} *sparks* in skeletal muscle. *Progr Biophys Mol Biol* **92**, 308–332.

Lai KV, Gonzalez M, Poueymirou WT, Kline WO, Na E, Zlotchenko E, Stitt TN, Economides AN, Yancopoulos GD & Glass DJ (2004). Conditional activation of Akt in adult skeletal muscle induces rapid hypertrophy. *Mol Cell Biol* **24**, 9295–9304.

Lamb G (2002). Voltage-sensor control of Ca^{2+} release in skeletal muscle: insights from skinned fibers. *Front Biosci* **7**, 834–842.

Langley B, Thomas M, Bishop A, Sharma M, Gilmour S & Kambadur R (2002). Myostatin inhibits myoblast differentiation by down-regulating MyoD expression. *J Biol Chem* **277**, 49831–49840.

Laver DR (2005). Coupled calcium release channels and their regulation by luminal and cytosolic ions. *Eur Biophys J* **34**, 359–368.

Liu G, Abramson JJ, Zable AC & Pessah IN (1994). Direct evidence for the existence and functional role of hyperreactive sulfhydryls on the ryanodine receptor-triadin complex selectively labeled by the coumarin maleimide 7-diethylamino-3-(4′-maleimidylphenyl)-4-methylcoumarin. *Mol Pharmacol* **45**, 189–200.

Lukács B, Sztretye M, Almássy J, Sárközi S, Dienes B, Mabrouk K, Simut C, Szabó L, Szentesi P, De Waard M, Ronjat M, Jóna I & Csernoch L (2008). Charged surface area of maurocalcine determines its interaction with the skeletal ryanodine receptor. *Biophys J* **95**, 3497–3509.

Marengo JJ, Hidalgo C & Bull R (1998). Sulfhydryl oxidation modifies the calcium dependence of ryanodine-sensitive calcium channels of excitable cells. *Biophys J* **74**, 1263–1277.

McPherron AC, Lawler AM & Lee SJ (1997). Regulation of skeletal muscle mass in mice by a new TGF-β superfamily member. *Nature* **387**, 83–90.

Mosher DS, Quignon P, Bustamante CD, Sutter NB, Mellersh CS, Parker HG & Ostrander EA (2007). A mutation in the myostatin gene increases muscle mass and enhances racing performance in heterozygote dogs. *PLoS Genet* **3**, e79.

Oba T, Murayama T & Ogawa Y (2002). Redox states of type 1 ryanodine receptor alter Ca^{2+} release channel response to modulators. *Am J Physiol Cell Physiol* **282**, C684–C692.

Papp Z, Szabo A, Barends JP & Stienen GJM (2002). The mechanism of the force enhancement by Mg-ADP under simulated ischaemic conditions in rat cardiac myocytes. *J Physiol* **543**, 177–189.

Petrotchenko EV, Yamaguchi N, Pasek DA, Borchers CH & Meissner G (2011). Mass spectrometric analysis and mutagenesis predict involvement of multiple cysteines in redox regulation of the skeletal muscle ryanodine receptor ion channel complex. *Res Rep Biol* **2011**, 13–21.

Ríos E & Pizarro G (1991). Voltage sensor of excitation–contraction coupling in skeletal muscle. *Physiol Rev* **71**, 849–908.

Savage KJ & McPherron AC (2010). Endurance exercise training in myostatin null mice. *Muscle Nerve* **42**, 355–362.

Sárközi S, Szentesi P, Jona I & Csernoch L (1996). Effects of cardiac glycosides on excitation–contraction coupling in frog skeletal muscle fibres. *J Physiol* **495**, 611–626.

Schuhmeier RP, Dietze B, Ursu D, Lehmann-Horn F & Melzer W (2003). Voltage-activated calcium signals in myotubes loaded with high concentrations of EGTA. *Biophys J* **84**, 1065–1078.

Szabó G, Dallmann G, Müller G, Patthy L, Soller M & Varga L (1998). A deletion in the myostatin gene causes the compact (*Cmpt*) hypermuscular mutation in mice. *Mamm Genome* **9**, 671–672.

Szabó LZ, Vincze J, Csernoch L & Szentesi P (2010). Improved spark and ember detection using stationary wavelet transforms. *J Theor Biol* **264**, 1279–1292.

Szappanos H, Cseri J, Deli T, Kovács L & Csernoch L (2004). Determination of depolarisation- and agonist-evoked calcium fluxes on skeletal muscle cells in primary culture. *J Biochem Biophys Methods* **59**, 89–101.

Szentesi P, Szappanos H, Szegedi C, Gönczi M, Jona I, Cseri J, Kovács L & Csernoch L (2004). Altered elementary calcium release events and enhanced calcium release by thymol in rat skeletal muscle. *Biophys J* **86**, 1436–1453.

Varga L, Szabó G, Darvasi A, Müller G, Sass M & Soller M (1997). Inheritance and mapping of *Compact* (*Cmpt*), a new mutation causing hypermuscularity in mice. *Genetics* **147**, 755–764.

Varga L, Müller G, Szabó G, Pinke O, Korom E, Kovács B, Patthy L & Soller M (2003). Mapping modifiers affecting muscularity of the myostatin mutant ($Mstn^{Cmpt\text{-}dl1Abc}$) compact mouse. *Genetics* **165**, 257–267.

Additional information

Competing interests

None.

Author contributions

D.B., N.G., O.R., T.O., B.H, M.Sz., J.F., B.D., Á.B., L.Sz. and P.Sz. performed experiments, and collected, analysed and interpreted data. Z.P., G.M., L.Cs. and P.Sz. designed and supervised the study, analysed and interpreted data and wrote the paper. This work is part of the PhD thesis of D.B. under the supervision of P.Sz. All authors approved the final version of the manuscript. All experiments were performed at the University of Debrecen.

Funding

This work was supported by grants from the Hungarian Scientific Research Found (OTKA NN-107765), from the Hungarian Ministry of Human Resources (TÁMOP-4.2.1/B-09/1/KONV-2010-0007, TÁMOP-4.2.2/B-10/1-2010-0024 and TÁMOP-4.2.2.A-11/1/KONV-2012-0025). This paper was supported by the János Bólyai Research Scholarship of the Hungarian Academy of Sciences to J.F. and the Bridging Fund of UD Faculty of Medicine.

Acknowledgements

None declared.

© 2014 The Authors. The Journal of Physiology © 2014 The Physiological Society

Downloaded from J Physiol (jp.physoc.org) at Imperial College London Library on September 3, 2014

szentesi.peter_292_24

scientific reports

Check for updates

OPEN

Elementary calcium release events in the skeletal muscle cells of the honey bee *Apis mellifera*

Claude Collet[1]✉, Mercédès Charreton[1], Laszlo Szabo[2], Marianna Takacs[3], Laszlo Csernoch[4] & Peter Szentesi[4]

Calcium sparks are involved in major physiological and pathological processes in vertebrate muscles but have never been characterized in invertebrates. Here, dynamic confocal imaging on intact skeletal muscle cells isolated enzymatically from the adult honey bee legs allowed the first spatio-temporal characterization of subcellular calcium release events (CREs) in an insect species. The frequency of CREs, measured in x–y time lapse series, was higher than frequencies usually described in vertebrates. Honey bee CREs had a larger spatial spread at half maximum than their vertebrate counterparts and a slightly ellipsoidal shape, two characteristics that may be related to ultrastructural features specific to invertebrate cells. In line-scan experiments, the histogram of CREs' duration followed a bimodal distribution, supporting the existence of both sparks and embers. Unlike in vertebrates, embers and sparks had similar amplitudes, a difference that could be related to genomic differences and/or excitation–contraction coupling specificities in honey bee skeletal muscle fibres. The first characterization of CREs from an arthropod which shows strong genomic, ultrastructural and physiological differences with vertebrates may help in improving the research field of sparkology and more generally the knowledge in invertebrates cell Ca^{2+} homeostasis, eventually leading to a better understanding of their roles and regulations in muscles but also the myotoxicity of new insecticides targeting ryanodine receptors.

Bees are very efficient pollinator insects, and are thus crucial both for plant biodiversity maintenance and agricultural food production. Amongst bees, owing to their easy domestication, honey bees have long been used as a research model in various fields, ranging from cell physiology to inter-individual communication and sociability[1,2]. Moreover, the high levels of mortality in honey bee's populations observed worldwide in the last few years prompted researchers to further study this model with the hope of understanding origins of this decline. Honeybee cells provide valuable models to study calcium signalling and intracellular calcium homeostasis in insects[3–11]. Calcium is an essential intracellular second messenger which plays pivotal roles in neuromuscular cellular processes such as signal transduction and modulation in motor or sensory neurons, contraction in cardiac, smooth, and skeletal muscle cells. More generally, Ca^{2+} plays a major role in development/maturation, cell shape modulation and migration, cell division, cell-membrane repair, hormonal secretion, and gene expression in virtually all cell types. In the honey bee, macroscopic intracellular Ca^{2+} variations have been recorded with Ca^{2+}-imaging techniques in neurons from central brain structures such as mushroom bodies[3,4] or antennal lobes[7,8]. Recently, Ca^{2+} was also monitored in peripheral sensory neurons from the antennae, i.e. the 'nose' of honeybees[10]. Global Ca^{2+} fluctuations were also studied in photoreceptor cells from the honey bee compound eye[11]. Finally, cytoplasmic Ca^{2+} transients (i.e. transient Ca^{2+} increases that can be elicited by a stimulation) and excitation–contraction coupling have been described in bee skeletal muscle cells as well, using fluorescent dyes and electrophysiological techniques[5,6]. Recently, studying intracellular Ca^{2+} signalling in bees and pollinators gained renewed interest because new classes of insecticides targeting several molecular players involved in Ca^{2+} homeostasis have been launched on the pesticides market and are now widely used in agriculture. Notably, most recent diamide type insecticides such as flubendiamide and chlorantraniliprole induce detrimental effects in

[1]UR406 Bees and Environment, French National Institute For Agriculture, Food and Environment, INRAE, 84914 Avignon, France. [2]Department of Electrical Engineering, Sapientia Hungarian University of Transylvania, Tîrgu Mureş, Romania. [3]Department of Animal Science, Faculty of Agricultural and Food Sciences and Environmental Management, University of Debrecen, Debrecen, Hungary. [4]Department of Physiology, Medical Faculty, University of Debrecen, Debrecen, Hungary. ✉email: claude.collet@inrae.fr

szentesi.peter_292_24

honey bees by anarchically mobilizing Ca^{2+} from intracellular stores through Ca^{2+} release channels in neurons from the antenna and in skeletal muscle cells from the leg[9,10].

A major molecular player in Ca^{2+} signalling is undoubtedly the ryanodine receptor. The molecular identity of this receptor was unravelled thanks to the botanical alkaloid ryanodine, present in root extracts of the plant species *Ryana*, which was used in the 50's as a natural insecticide (now withdrawn owing its's toxicity towards environment). Ryanodine receptors are huge macromolecular complexes functioning as ion channels to provide a route for Ca^{2+} to be massively transferred on demand from intracellular storage organelles (sarco and endoplasmic reticulums) to the cytoplasmic compartment[12,13]. Increasing the intracellular cytoplasmic Ca^{2+} concentration ($[Ca^{2+}]_i$) from submicromolar to tenths of micromolar ranges thus allows Ca^{2+} to play its multiple regulatory roles[14,15]. At rest, $[Ca^{2+}]_i$ is tightly regulated and maintained at around 100 nM to avoid the toxicity of sustained Ca^{2+} increases and this low resting $[Ca^{2+}]_i$ provides both a wide dynamic range and a high signal-to-noise ratio. Optical and electrophysiological techniques evolved and allowed characterizing cytoplasmic Ca^{2+} fluctuations with continuously increased acuity along with recent years. Nowadays, laser-scanning confocal microscopes allow detecting optically subcellular cytoplasmic Ca^{2+} fluctuations in the µm spatial and in the ms temporal ranges with the help of fast and high-affinity Ca^{2+} dyes (Ca^{2+} indicators). These localized fluctuations are believed to originate from the release of Ca^{2+} by one or a cluster of several ryanodine receptors and in striated muscles, they are considered as the unitary bricks of voltage-induced global Ca^{2+} release[16]. Localized elevation in $[Ca^{2+}]_i$ can also fuse to initiate propagating macroscopic Ca^{2+} waves and have specific cytosolic localizations such as the perinuclear space where they can modulate nuclear Ca^{2+} independently of the bulk cytosolic Ca^{2+}[17]. So far, local fluctuations in $[Ca^{2+}]_i$ have been studied only in muscle cells from vertebrate species. First discovered in cardiac myocytes[18], and originally termed Ca^{2+} sparks, similar signalling events were identified later in smooth muscle cells, skeletal muscle fibres, neurons and oocytes. The role and regulation of mechanisms of these spatially localized fluctuations are however elusive and remain to be fully identified with a rather unique research field dedicated to their study: 'sparkology'[16,17]. This research field is essential as these signals are frequently altered in genetic diseases linked to mutations in the ryanodine receptor genes (ryanodinopathies). Even under physiological conditions, it soon turned out that localized Ca^{2+} fluctuations had many temporal patterns, not only an archetypal steep increase (~ 5 ms) and a fast mono-exponential decrease, and new terms emerged to better describe this signals diversity e.g. embers, macrosparks, compound sparks, bursts, sparklets…[19]. A more general term is now used to depict these $[Ca^{2+}]_i$ fluctuations : elementary Ca^{2+} release events (CREs).

While CREs have been identified in many tissues from several vertebrate species (rat, mouse, frog and fish), to our knowledge, they have never been identified in an invertebrate tissue. Here, using honey bee as a model, we describe for the first time elementary CREs in an insect species and compare their spatiotemporal characteristics in the light of interspecific physiological and ultrastructural cellular differences. Part of this work was presented to the Biophysical Society[20].

Material and methods

Isolation of leg muscle cells. Muscle fibres were prepared from young adult domestic honey bees (*Apis mellifera*), as described earlier[5], with slight modifications. Newborn bees were collected outdoor, directly on a frame of a hive and used during the following 4 days. Bees were chilled (~ 4 °C) until lethargic immobility and then killed by decapitation. Tibias from the third pair of legs were dissected in a Tyrode's solution without calcium (in mM: NaCl 140, KCl 5, $MgCl_2$ 2, HEPES 10, pH 7.2), cut longitudinally and pinned open. Tibias were bathed 20 min in a dissociation solution at 37 °C (Tyrode's solution without calcium containing four enzymes: collagenase type 1, trypsin, papain, and pronase at concentrations 0.5, 1.5, 1.5 and 1 mg/ml, respectively). After rinsed in Tyrode's solution without calcium and normal Tyrode (2 mM $CaCl_2$), muscle masses were triturated with a pipette and dispersed in the central well of a clean glass bottom dish (MatTek Corp., Ashland, MA, USA). Cell were loaded for 30 min with the cell permeant dye Fluo-8-AM (5 µM).

Measurement of Ca^{2+} release events (CREs) in intact bee muscle fibres. Fluo-8-AM loaded cells were kept in normal Tyrode's solution and observed with a laser scanning confocal microscope Zeiss LSM 5 LIVE (Zeiss, Oberkochen, Germany) equipped with a Plan-Neofluar 40 × oil immersion objective (NA = 1.3). Fluo-8 was excited with the 488 nm wavelength of an argon laser and the emitted fluorescent light was measured through a band-pass filter (505–570 nm) and digitized at 12 bit. First the fibres were examined by eye and the fibres showing spontaneous activity were recorded with series of 512 × 512 (*XYT*) images, captured at 1 Hz. The pixel size was 0.328 µm and the pixel dwell time was 1 ms. CRE detection and analysis were performed using methods and algorithms previously described[21,22]. In brief, the region of the fibre and the background was defined on the first image of each series. The averaged background fluorescence was subtracted from each pixel of all images in one series. Ca^{2+} release events were detected by the stationary wavelet method. The filtering was made by soft thresholding wavelet detection. Finally the amplitude and full width at half maximum (FWHM) of the sparks were calculated. Two FWHM values were determined: perpendicular to (X) and parallel (Y) with the Z-lines. To detect the Z-lines the frequency spectrum in each line of all images was calculated using fast Fourier transform. To remove the Z-lines from the images, inverse FFT of the frequency components corresponding to sarcomeres was used. Bleaching correction was performed on all images by calculating the change in fluorescence intensity of each pixel in time. Finally images were normalized using stationary wavelet transform. The event frequency was determined by counting the number of events on all images from a series. Events that appeared on consecutive images at the same location were counted as a single event. To get the frequency the number of events was normalized to fibre area and duration of recording. To assess the amount of Ca^{2+} released during a CRE, the Signal Mass (SM) was calculated as described earlier[23]. To estimate FWHM in the z direction (i.e. the optical axis) in two-dimensional measurements, the average of the two FWHMs in the focal plane (x

szentesi.peter_292_24

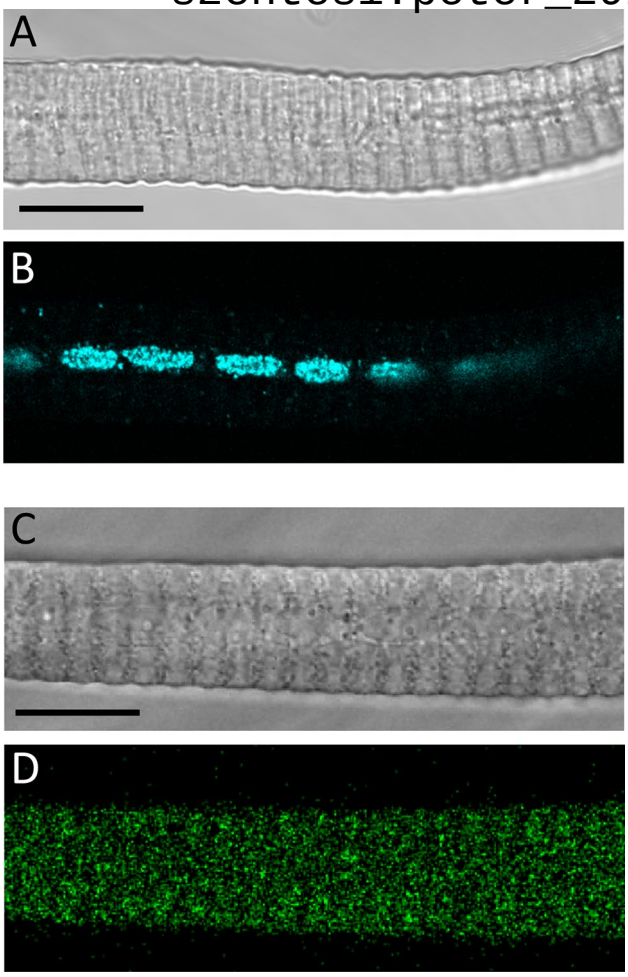


Figure 1. General structure of bee muscle fibres. (**A**) Transmitted light for a honey bee tibia muscle fibre (mean sarcomere length 4,9 µm). (**B**) Confocal longitudinal section through the fluorescent central row of nuclei labelled with Hoechst stain (same fibre as in A). (**C**) Transmitted light for a Fluo-8 stained fibre (mean sarcomere length 4,4 µm). (**D**) Confocal fluorescence image of the fibre shown in C. Scale bars = 20 µm.

and y directions) was used. Figure 1 and Supplementary Video 1 were made under the ImageJ software (v1.52a, Rasband, W.S. ImageJ, U.S. National Institutes of Health, Bethesda, Maryland, USA, https/imagej.nih.gov/ij/, 1997–2018).

Line-scan images (*XT*) were taken at 1 or 2 ms/line and the pixel size was 0.328 µm. In some cases 0.2 ms/line was used to study the temporal properties of CREs in high time resolution. The length of the line was variable and depended on the actual fibre width. The images (F[x,t]) were normalized to baseline fluorescence (F_0[x]). Line-scan images containing spontaneous calcium release events were analysed using an automatic event detection program[21], which calculated the amplitude ($\Delta F/F_0$), rise time, full width at half maximum (FWHM), and full duration at half maximum (FDHM) of the identified events. An event was identified as an ember if it had a clear plateau and was longer than 40 ms in time. Otherwise, it was considered as a spark. Events with an amplitude smaller than 0.1 $\Delta F/F_0$ units were excluded from the analysis. All measurements were carried out at room temperature (22–23 °C).

Depolarization-evoked Ca^{2+} transients measurements. Ca^{2+} transients were elicited on CRE free (silent) intact fibres with field stimulation and recorded in line-scan mode. Two platinum electrodes were placed adjacent to the fibres and 50 ms long depolarizations with amplitude ranging between 40 and 80 V were used to evoke Ca^{2+} transients (S88 Stimulator, Grass Technologies, Warwick, RI, USA). Whole-cell Ca^{2+} transients were recorded in patch-clamp experiment as described earlier[5].

Nuclei staining. Fibres were stained with Hoechst 33258 (5 µg/ml) in Tyrode during 30 min. After being loaded, fibres were rinsed twice in Tyrode's solution and nuclei were visualized under a Zeiss LSM710 confocal inverted microscope with a 63 × 1.42 NA objective (Zeiss, Oberkochen, Germany).

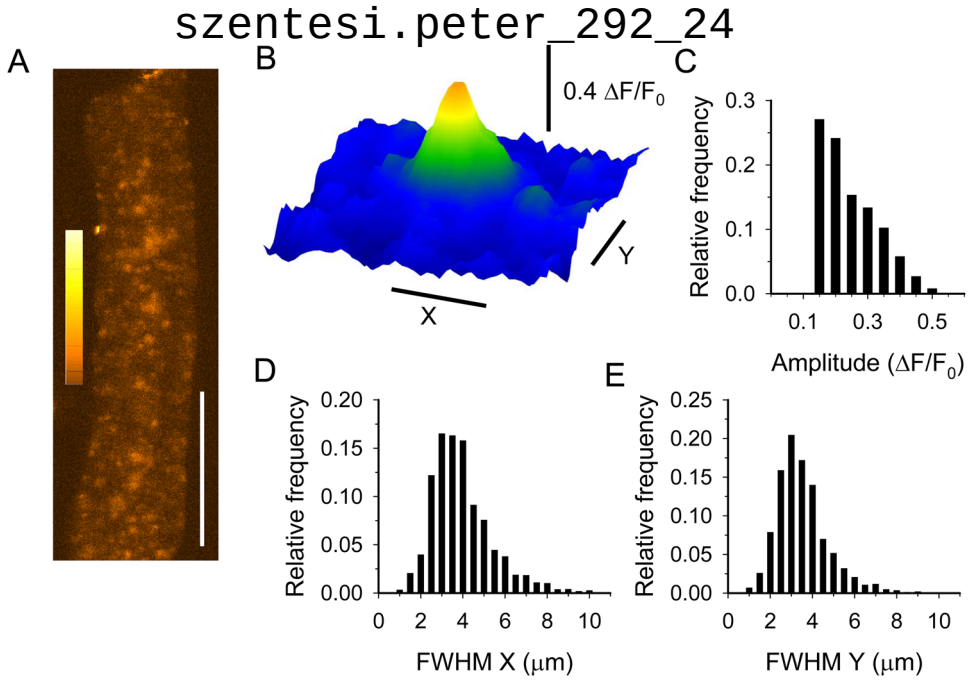


Figure 2. Spontaneous elementary calcium release events in two dimensional (XY) experiments. (**A**) Sum of 30 background corrected images of a Fluo-8 loaded fibre representing 30 s. (**B**) A representative spark. Histograms of parameters of calcium sparks: amplitude (**C**), FWHM perpendicular (D) and parallel (E) to the fibre axis. Calibration on panel A is 50 μm. Calibrations on panel B are 5 μm.

Resting membrane potential measurement. Single muscle fibres were superfused with normal Tyrode's at room temperature (24 °C). Membrane potentials were recorded using 3 M KCl filled sharp glass microelectrodes with tip resistances ranging between 30 and 40 MΩ only in cells with intact surface membrane and clear cross striations. The electrodes were connected to the input of a Multiclamp-700A amplifier (Axon Instruments, Foster City, CA, USA) under current-clamp conditions. Membrane potentials were digitized at 100 kHz using Digidata 1322 A/D card (Axon Instruments) under software control (pClamp 9.2, Axon Instruments, Foster City, CA, USA) and stored for later analysis.

Statistical analysis. Pooled data were expressed as mean ± standard error (SE) of the mean. The differences were assessed using one-way analysis of variance (ANOVA) and all pairwise multiple comparison procedures (Student–Newman–Keuls method). A p-value of less than 0.05 was considered statistically significant. Graphpad Prism 6.0 software (GraphPad software, San Diego, USA) was used for statistical analysis and non-linear regression.

Results

Honey bee intact skeletal muscle fibres isolated from the legs present a nice sarcomere striation under light microscope and the nuclei are located in the centre of the fibres[5] instead of right underneath the sarcolemma as in other adult organisms like amphibians and mammals (Fig. 1A, B, Hoechst staining). The axial row of nuclei give them a so-called 'tubular' appearance in histological transverse sections. The sarcomere pattern in healthy muscle fibres used in this study showed a period of ~ 4 μm, indicating a relaxed status for the contractile machinery. Their membrane potential, measured with sharp microelectrodes (-58.0 ± 6.9 mV, n = 3) was consistent with measurements made in other insect species[24] and in enzymatically-isolated mammalian muscle fibres that are polarized around -60 mV[25–27]. An extensive t-tubular organization has been demonstrated earlier in these non-flight muscle fibres, as well as functional Ca^{2+} and K^+ ionic channels and excitation–contraction coupling[5,28]. Here, examining Fluo-8-loaded leg fibres in confocal fluorescence (Fig. 1C, D) revealed that around one fifth of fibres produced spontaneous calcium release events when bathed in a physiological extracellular solution (Tyrode's solution).

In spontaneously active fibres, localized calcium release events appeared randomly in time and space (Supplementary video 1, Fig. 2A). The events appearing in *XYT* image sequences showed classical spark shape (Fig. 2B). The analysis of a number (4898) of CREs revealed that their average amplitude is quite small (0.220 ± 0.001 $\Delta F/F_0$), but some higher amplitude events (up to 0.6 $\Delta F/F_0$) were observed as well (Fig. 2C). This amplitude can be compared to ~ 1–2 $\Delta F/F_0$ global Ca^{2+} transients we observed during field stimulations (Supplementary Fig. S1) and previously measured under voltage-clamp in bee muscle cells loaded with Fluo-3[5]. The average frequency of CREs was high (1696 ± 367 Hz/mm^2, n = 25 fibres). The CREs were wide in space since both FWHMs (X and Y) were greater than 3 μm in average (3.73 ± 0.02, and 3.30 ± 0.02 μm, respectively). The probability histograms of FWHMs (Fig. 2D and E) show that some events had a broad size (> 10 μm). The shape of honey bee CREs in space were not completely circular. The average ratio of FWHMs (X/Y) were significantly greater than 1

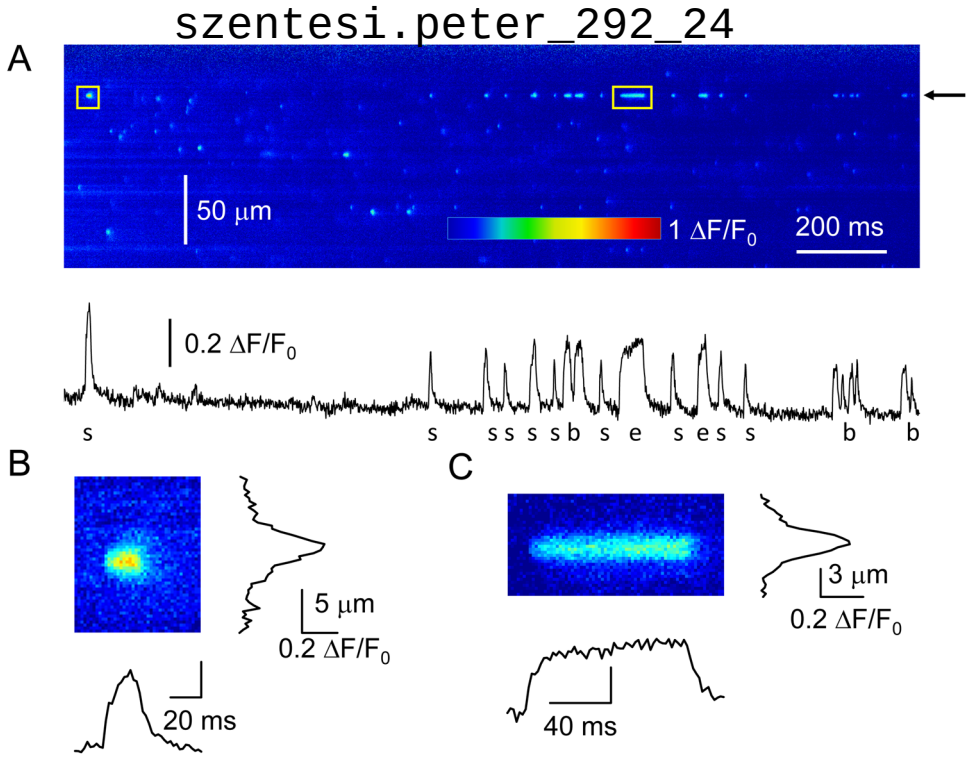


Figure 3. Sparks and embers on line-scan image. (**A**) Representative background corrected line-scan image measured with 2 ms/line scanning speed. The trace below the image was calculated by averaging 5 lines at the position marked by the arrow. Enlarged image of a spark (**B**) and an ember (**C**) with its spatial and time profile. The positions of the events are marked with yellow rectangular in panel A.

(22 fibres)	Amplitude ($\Delta F/F_0$)	Rise time (ms)	FWHM (μm)	FDHM (ms)	Signal mass (μm^3)	Frequency (mm^{-1} s^{-1})
All events (3338)	0.185 ± 0.001	15.88 ± 0.20	2.82 ± 0.02	35.82 ± 0.34	7.41 ± 0.19	265.1 ± 15.0
Sparks (2244)	0.185 ± 0.001	10.45 ± 0.11	2.65 ± 0.02	25.52 ± 0.16	6.00 ± 0.20	174.0 ± 14.4
Embers (1094)	0.186 ± 0.002	27.02 ± 0.41***	3.18 ± 0.04***	56.95 ± 0.58***	10.29 ± 0.41***	63.1 ± 6.6***

Table 1. Characteristics of honey bee elementary calcium release events detected in line-scan (*XT*) experiments. Events with less than 0.1 amplitude were discarded. All events with greater than 40 ms duration were classified as ember. The numbers in parenthesis are the number of event analysed. ***Denotes significant differences from spark, $p < 0.001$. FWHM – full width at half maximum, FDHM – full duration at half maximum.

(1.22 ± 0.01; $p < 0.001$). The signal mass (SM), calculated to estimate the amount of Ca^{2+} released during a CRE, was 14.52 ± 0.29 μm^3 on average.

To study elementary CREs in more details, we performed line-scan experiments. Figure 3A shows a representative background-corrected line-scan image in pseudo colour. This fibre was very active, and several sparks (Fig. 3B) and long lasting embers (Fig. 3C) were observed in this record. Most CREs appeared randomly in space and time. However, there were some frequently firing sites which generated more than one event in the same place. The trace calculated from Fig. 3A at the position marked by an arrow, shows a representative example of this phenomenon. The time profile of the active calcium release unit demonstrates that the spontaneous event originating from the same place can be a spark, an ember, or a burst[29].

First, the spatiotemporal parameters of CREs were calculated supposing a homogeneous population (Table 1, Fig. 4). However, as it is clearly visible in Fig. 3 there are some long lasting events, called traditionally embers[30]. The histogram of duration of all CREs was indeed well fitted by the sum of two Gaussian functions (Fig. 4D). The peak position of the first Gaussian was found at 25.5 ± 0.5 ms, while the second function peaked at 44.3 ± 3.9 ms. The intersection of the two Gaussian functions was at around 40 ms and this value was thus chosen as the threshold of duration to distinguish a spark from an ember (see Table 4, column entitled "Threshold duration of embers"). All CREs with a duration longer than 40 ms were categorized as embers.

Based on this classification we found that 67% of the events were sparks, with a high frequency (Table 1). The average amplitude of sparks was 0.185 ± 0.001 $\Delta F/F_0$, but the histogram of amplitudes shows some events with higher amplitudes up to 0.4 $\Delta F/F_0$ (Fig. 5A). The average FWHM of sparks was found to be 2.65 ± 0.02 μm,

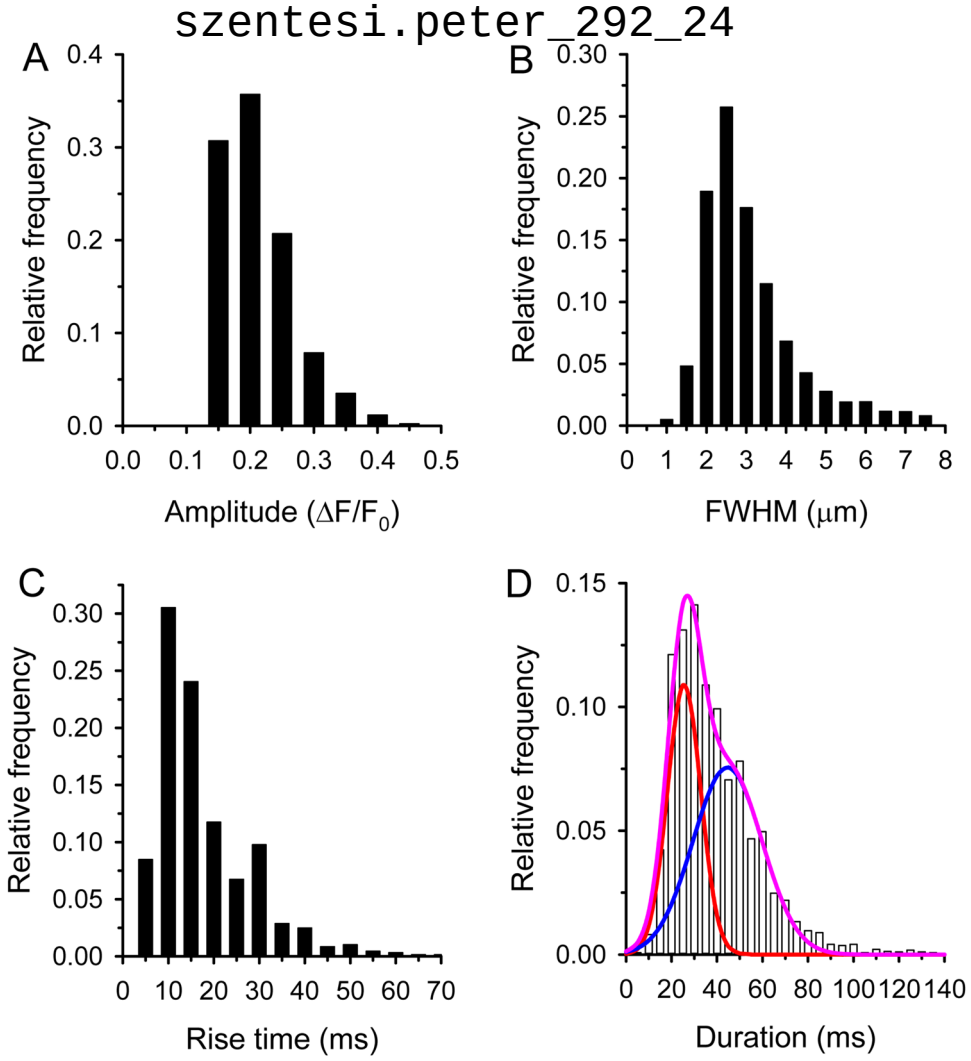


Figure 4. Parameters of calcium release events. Histogram of amplitudes (**A**), FWHMs (**B**), rise times (**C**), and durations (**D**). The number of calcium release events was 3338. The parameters of Gaussian fits in panel D are 0.109 and 0.076 for the amplitude and 25.54 and 44.26 s for the mean to spark (red) and embers (blue), respectively. Pink line represents the sum of the two (red and blue) Gaussian functions.

interestingly we found some very wide sparks with a FWHM greater than 7 μm (Fig. 5B). The distribution of rise times clearly shows that the majority of sparks developed in less than 15 ms (Fig. 5C). The average duration was identical with the first peak position of the theoretical Gaussian function (25.52 ± 0.16 ms). The histogram of duration did not show the classical bell shaped curve since the upper limit was chosen arbitrarily (Fig. 5D).

We classified 33% of events as embers with significantly lower frequency than sparks (Table 1). Their average amplitude was identical to that of sparks (0.186 ± 0.002 $\Delta F/F_0$; $p > 0.6$). The maximum of ember amplitude was 0.5 $\Delta F/F_0$ (Fig. 6A). The average FWHM was significantly larger than for sparks (Table 1), likely because calcium had more time to diffuse during embers (Fig. 6B). The average rise time was also significantly longer than for sparks (Table 1) showing that the development of embers is a slower process (Fig. 6C). The average duration was somewhat bigger than the second peak position of the theoretical Gaussian function (56.95 ± 0.56 ms). We found some very long events and more than 5% of the embers were longer than 100 ms (Fig. 6D).

High speed confocal scanning was used to study in more details the time profile of CREs (Fig. 7A). This speed (200 μs/line) allowed us to explore the rising and the falling phases of the events. We could confirm our observation that the amplitude of sparks and embers are roughly the same in honey bee muscle. Furthermore if one compares the time profile of a spark (Fig. 7B) to that of an ember (Fig. 7C), it is clear that embers need more time to reach their peak.

Discussion

In the honey bee leg skeletal muscle, excitation–contraction coupling relies on a calcium entry through plasma membrane voltage-gated calcium channels, which activates ryanodine receptors to release more Ca^{2+} from intracellular stores[5,6]. Whereas macroscopic calcium signalling has been studied in invertebrate species, subcellular calcium release events such as Ca^{2+} sparks have never been described in detail. Our work may help understanding

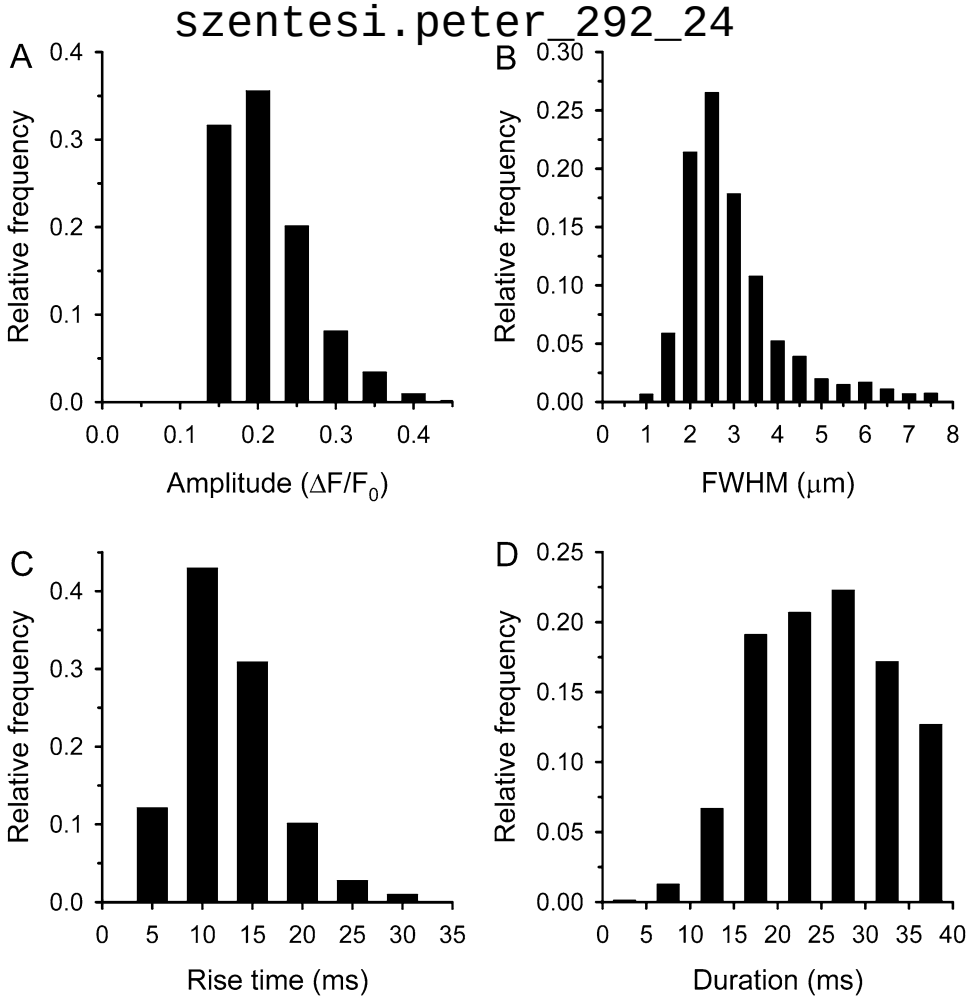


Figure 5. Parameters of calcium sparks. Histogram of amplitudes (**A**), FWHMs (**B**), rise times (**C**), and durations (**D**). The number of sparks was 2244.

the role and regulation of these events, since interspecific comparisons often lead unravelling cellular phenomena. Data collected in the present study were compared to all available data on CREs recorded in intact freshly isolated skeletal muscle fibres and in intact cell-cultured myotubes, gathered in Tables 2–4. In our comparison, 'intact' refers to the integrity of the plasma-membrane, without any attempt at manipulating the intracellular cytoplasmic composition and with physiological extracellular solutions bathing the cells. In honey bee fibres, both sparks (i.e. CREs of short duration) and embers which are CREs of long duration first characterized in adult frog muscle cells[30], were recorded. Similar short- or long-lasting events have been characterized, for instance in adult mammalian fibres subjected to surface membrane skinning[31] or in intact foetal mammalians muscle fibres[32]. Embers were seen in intact mouse fibres challenged with depolarization[33]. By comparison, embers are more difficult to detect spontaneously in frog muscle fibres unless pharmacological manipulations were applied[16].

A major difference lies in the spatial spreading of CREs from adult bees, which are clearly wider than CREs from adult intact vertebrate muscle fibres (FWHM, Tables 2–4). First, it could be related to the fact that sarcomeres are almost twice as long in bee leg muscle fibres 4.2 ± 0.1 μm[6], as compared as vertebrate ones (~ 2–2.5 μm). Secondly, insect myofibrils are radially oriented around a central row of nuclei, (an arrangement which is not seen in adult vertebrate muscle fibres), giving a so-called 'tubular' morphology to the fibres. Accordingly, insect tubular muscle fibres have relatively straight t-tubules arranged in radial symmetry from the surface membrane to central nuclei in order to convey action potentials throughout the fibre volume[34]. This spatial configuration may lead to less restricted diffusion along long portions of straight T-tubules. The average ratio of FWHMs (X/Y) honey bee CREs was greater than 1 (1.23 ± 0.01), which indicates that ellipsoidal sparks diffuse slightly more freely in the X direction (along the long axis of the fibre) than in the Y direction (along T-tubules). Elongated sparks were detected in frog skeletal muscle as well[22,35] and CREs non-circularity has been previously attributed to a 'channelled diffusion' due to tubes of mitochondria[17], but this hypothesis remains to be explored in bee fibres. Thirdly, an interesting feature is that bee T-tubules are running at the junction of A and I bands, like in mammalian skeletal muscle fibres, so that two T-tubules run per sarcomere[5], increasing the chance to recruit release sites for large CREs. Fourthly, electron microscopy and rotary shadowing techniques showed that RyR disposition in invertebrate muscle differ from their disposition in vertebrates[36], an arrangement that may favour wider CREs in honey bees. Finally, ultrastructural differences were also identified in the invertebrate

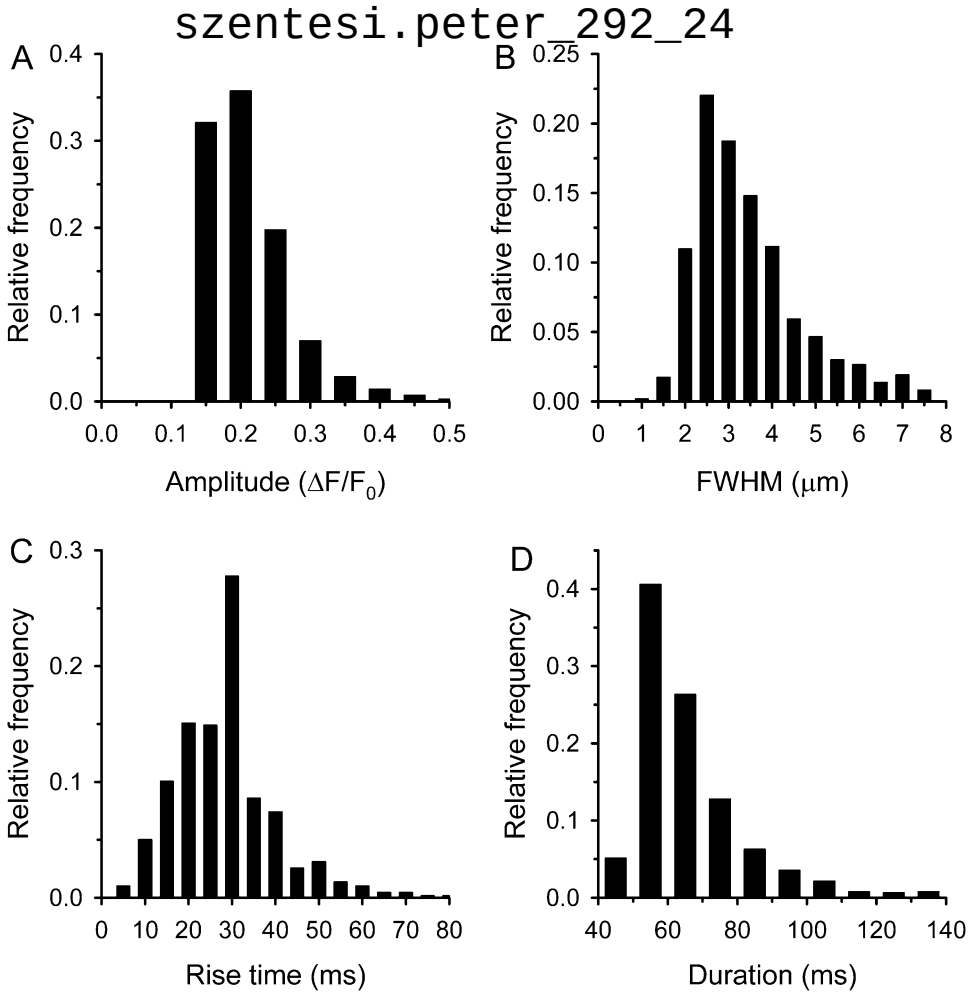


Figure 6. Parameters of calcium embers. Histogram of amplitudes (**A**), FWHMs (**B**), rise times (**C**), and durations (**D**). The number of embers was 1094.

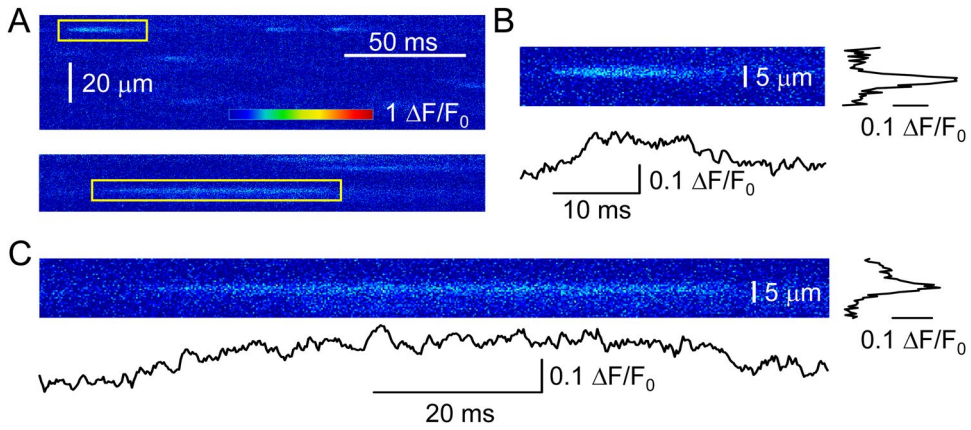


Figure 7. Events on line-scan images at fast scan speed (0.2 ms/line). (**A**) Normalized line-scan images showing sparks (top) and an ember (bottom). Enlarged image of a spark (**B**) and an ember (**C**) with its spatial and time profile. The positions of the events are marked with yellow rectangular in panel A.

couplons, i.e. the functional arrangement of RyRs and voltage-gated calcium channels from the plasma membrane (DHPRs, for dihydropyridine receptors), and previous studies underlined that this architecture was reminiscent of the cardiac striated muscle[37]. Accordingly, other ultrastructural similarities can be pointed out in between bee skeletal and vertebrate cardiac muscles, such as the presence of dyads in both tissues instead of the triads observed in vertebrate skeletal muscles[5]. Besides structural and ultrastructural differences, that clearly settle the

szentesi.peter_292_24

Type of intact cells	Organism	Age (days after birth)	Sarcomere (µm)	Dye	Ext. Sol	$[Ca^{2+}]_{ext}$ (mM)	Frame rate (image/s)	Incidence (% cells)	Frequency (events/s/mm²)	Amplitude ($\Delta F/F_0$)	FWHM or EDHM (µm)	Signal mass (µm³)	Reference
Adult tibia fibres	Honey bee	1-4	~4	Fluo-8-AM	Tyrode	2	1	<20%	1696 ± 367	0.220 ± 0.001	3.73 ± 0.02 (X) 3.30 ± 0.02 (Y) 3.30 ± 0.02 (Y)	14.52 ± 0.29	This study
Adult FDB fibres	Frog	–	~2	Fluo-4-AM	Ringer	1.8	30 and 60	~20%#	1470 ± 300	0.188 ± 0.001	1.73 ± 0.01 (x) 1.51 ± 0.01 (y)	1.02 ± 0.01	Cserne-Szappanos 2020
Adult FDB fibres	Mouse	>90	–	Fluo-3-AM	Krebs	2	1.2	<5%	–	–	–	–	Conklin 1999
Adult fibres*	Mouse	1	–	Fluo-4-AM	Ringer	1.8	1	–	~80 (EDL) ~55 (D)	~0.9 (EDL) ~0.9 (D)	1.56 ± 0.04 (EDL) ~1.6 (D)	2.17 ± 0.20 (EDL) ~2.0 (D)	Chun 2003*
Adult fibres *	Mouse	7	–	Fluo-4-AM	Ringer	1.8	1	–	~5 (EDL) ~25 (D)	~0.9 (EDL) ~0.7 (D)	~1.25 (EDL) ~1.32 (D)	~1.2 (EDL) ~0.8 (D)	Chun 2003*
Adult fibres *	Mouse	14	–	Fluo-4-AM	Ringer	1.8	1	–	~7 (EDL) ~5 (D)	~1 (EDL) 0.65 ± 0.05 (D)	1.10 ± 0.05 (EDL) ~1.3 (D)	0.66 ± 0.12 (EDL) 0.80 ± 0.25 (D)	Chun 2003*
Adult interossei fibres	Mouse	–	–	Fluo-4AM	Ringer	2	0.9	–	15.1 ± 1.2	–	–	–	Teichmann 2008
Foetal intercostal fibres	Mouse	3 days before birth	–	Fluo-3-AM	Krebs	2	1.2	<20%	–	–	–	–	Conklin 1999
Foetal diaphragm fibres	Mouse	3 days before birth	–	Fluo-4AM	Ringer	1.8	1	~20%	~80	1.24 ± 0.02	~1.67 (D)	3.79 ± 0.22 (D)	Chun 2003*

Table 2. Interspecific comparison of calcium sparks' parameters measured in two dimensional (XY) experiments made in intact cells. In this table studies are ordered according to i) the developmental stage (from adult to foetal stages) and ii) the species (Honey bee, Frog and Mouse). All cells were freshly isolated muscle fibres. *Chun values are from adult P1, P7 and P14 diaphragm (D) and EDL muscle. Foetal diaphragm is from E18, I.e. 3 days before birth. #Personal communication. Data marked with ~ is approximated from figures. All data depicted at room temperature. FDB – flexor digitorum brevis; EDL – extensor digitorum longus; D-diaphragm; AM – acetoxymethyl ester; FWHM – full width at half maximum; EDHM – equivalent diameter at half maximum.

conditions for broad CREs in insect muscle fibres, genomic differences could favour it as well. Homology data on RyR sequences suggest that invertebrates and vertebrates show important genomic differences. First, insects have only one *ryr* gene whereas amphibians have two (*ryr* α also named ryr 1, and *ryr* β also named *ryr* 3) and mammalians have three[38,39]. Two isoforms are actually expressed in vertebrate skeletal muscles (*ryr* 1 and *ryr* 3 in mammalians and amphibians), since the *ryr* 2 gene is expressed in cardiac mammalian muscle only. After the 'honey bee genome sequencing consortium' made available the honey bee (*Apis mellifera*) genome sequence[40], the predicted amino acid sequence for the *Apis mellifera* RyR protein (*Am*RyR) has been obtained from an annotated genomic sequence NC_037639.1 (Gene 408680 on chromosome LG2) using traditional gene prediction methods (GNOMON, supported by EST evidence). Like in other species, predicted *Am*RyR protein isoforms (X1 to X9) contain ~5000 amino acids. According to BLAST tools (NCBI database), the homology degree of the honey bee *Am*RyR with vertebrate RyRs is around 45%. Such a difference may well settle the basis for strong differences into the protein functions and regulations leading to morphological differences in bee CREs as compared to other species. In zebrafish skeletal muscle cells, two RyR isoforms have been shown to be essential to achieve normal sparks production[41]. The second frog RyR isoform may also be related to high spark production in this species[42]. In foetal mammalian muscles, the two isoforms of RyR (1 and 3) are expressed and it was suggested that they both contribute to generate sparks[43]. Conversely, at the mature adult stage, most intact mammalian skeletal fibres (which no longer express RyR3) require specific conditions to fire sparks and at a relatively low frequency. Our data show that a single *ryr* gene allows the production of a high CREs frequency with wide spatial spread in intact insect fibres.

Functional differences could also lead to the specific shape properties of bees CREs. In the honeybee muscle, as in other invertebrates, excitation–contraction coupling relies on i) Ca^{2+} entry through the plasmalemmal membrane via voltage-gated channels and ii) on a calcium induced calcium release (CICR) mechanism[5,44]. CICR is thus a crucial mechanism in the skeletal muscle from bees and other insects (which are devoid of TTX-sensitive voltage-gated channels) where voltage-gated calcium currents activate quickly to achieve a rapid action potential overshoot[6,45,46]. The role of CICR in excitation–contraction coupling implies that honey bee RyRs must be highly sensitive to Ca^{2+}, a feature that favours broad CREs. CICR has been shown in frog muscle fibres as well

szentesi.peter_292_24

Type of intact cells	Organism	Age (days)	Sarcomere (µm)	Dye	Ext. Sol	$[Ca^{2+}]_{ext}$ (mM)	Speed of recording (line/ms)	Frequency (events/ /s/ mm)	Sparks amplitude ($\Delta F/F_0$)	FWHM (µm)	FDHM or FTHM (ms)	Rise time (ms)	Signal mass (μm^3)	Depolarization-induced macroscopic Ca^{2+}transient ($\Delta F/F_0$)	Reference
Adult tibia fibres	Honey bee	1-4	~4	Fluo-8-AM	Tyrode	2	1	174.0 ± 14.4	0.185 ± 0.001	2.65 ± 0.02	25.52 ± 0.16	10.45 ± 0.11	6.00 ± 0.20	1.5 ± 0.16	This study
Adult iliofibularis and semitendinosus fibres	Frog	–	~3 ‡	Fluo-3 (injected)	Ringer	1.8	2.048	23 ± 9	0.92 ± 0.02	0.95 ± 0.04	5.66 ± 0.23	0–100% rise time 3.49 ± 0.15	1.28 ± 0.17	18.6 ± 0.9	Hollingworth 2001
Adult FDB fibres	Mouse	> 90	–	Fluo-3-AM	Krebs	2	2.05	< 20	0.9 ± 0.3	2.0 ± 0.5	40.3 ± 35	16.4 ± 14	–	–	Conklin 1999
Adult fibres	Mouse	1	–	Fluo-4-AM	Ringer	1.8	2	–	0.7 ± 0.1 (EDL) 0.8 ± 0.1 (D)	1.5 ± 0.1 (EDL) 0.7 ± 0.2 (D)	13.2 ± 0.7 (EDL) 10.5 ± 1.1 (D)	8.9 ± 0.7 (EDL) 8.0 ± 1.2 (D)	–	–	Chun 2003*
Adult fibres	Mouse	7	–	Fluo-4-AM	Ringer	1.8	2	–	0.6 ± 0.1 (EDL) 0.7 ± 0.1 (D)	1.7 ± 0.1 (EDL) 1.6 ± 0.2 (D)	12.6 ± 0.9 (EDL) 11.3 ± 1.1 (D)	7.3 ± 0.7 (EDL) 6.1 ± 0.6 (D)	–	–	Chun 2003*
Adult fibres	Mouse	14	–	Fluo-4-AM	Ringer	1.8	2	–	1.5 ± 0.5 (EDL) 0.5 ± 0.1 (D)	1.6 ± 0.2 (EDL) 1.5 ± 0.1 (D)	13.5 ± 1.6 (EDL) 11.2 ± 0.9 (D)	9.3 ± 1.4 (EDL) 7.6 ± 1.3 (D)	–	–	Chun 2003*
Foetal fibres	Mouse	3 days before birth	–	Fluo-3-AM	Krebs	2	2.05	< 20	1.6 ± 0.6	3.5 ± 1.1	84.5 ± 46	42.8 ± 24	–	–	Conklin 1999
Foetal fibres	Mouse	3 days before birth	–	Fluo-4-AM	Ringer	1.8	2	–	0.9 ± 0.1	1.9 ± 0.1	13.9 ± 0.4	Rise(10–90%) 7.6 ± 0.3	–	–	Chun 2003*
Larval tail fibres	Zebrafish	3 days post-fertilization	~1.5	Fluo-4-AM	Ringer with 0.3 mM Caffeine	2	–	~44	~0.8	~1.3	~5.2	~4	~3	–	Perni 2015
Primary myotubes culture	Mouse	–	–	Fluo-3-AM	TEA-$MeSO_3$	2	2	–	0.94 ± 0.05	2.1 ± 0.3	11.8 ± 1.6	–	–	–	Shirokova 1998
Primary myotubes culture	Rat	~5 days in vitro	–	Fluo-4-AM	Tyrode	1.8	1.54	3.2 ± 1.9	0.49 ± 0.03	1.67 ± 0.16	39.7 ± 4.3	15.4 ± 2.2	–	0.62 ± 0.05	Fodor 2008
C2C12 cell line myotubes	Mouse	3–6 days in vitro	–	Fluo-3-AM	Ringer	10	0.02–007	0.3	~300 nM	–	–	–	–	–	Gyorke 1996
C2C12 cell line myotubes	Mouse	> 5 days in vitro	–	Fluo-4-AM	Tyrode	2	0.8	16	0.49 ± 0.01	3.8 ± 0.08	92.8 ± 8.7	55.9 ± 4.2	–	~2.5	Altomare 2013$

Table 3. Interspecific comparison of calcium sparks' and depolarization-evoked transients' parameters measured in line-scan (XT) experiments performed in intact cells. In this table studies are ordered according to i) the developmental stage (from adult to foetal/larval stages) and ii) the species (Honey bee, Frog, Mouse, Rat, Zebrafish). All preparations were freshly isolated muscle fibres except the last four where the cells were in cell culture. *Chun values are from P1, P7, and P14 EDL muscle and from foetal (3 days before birth) diaphragm, rise time was calculated between 10–90% of the peak amplitude. ‡sarcomere stretched to ~3 µm. $parameters of CREs originate from sparks and embers together. Data marked with ~ is approximated from figures. All data depicted at room temperature except Perni et al. 2015 (18 °C). Hollingworth et al. 2001 cooled the fibres to 17–20 °C. All studies were from intact cells bathed in a physiological solution (Ringer, Krebs or Tyrode), except for Perni et al. 2015 (caffeine added) and Shirokova et al. 1998 (150 TEA-$MeSO_3$) [57]. FDB – flexor digitorum brevis; EDL – extensor digitorum longus; D- diaphragm; AM – acetoxymethyl ester; FWHM – full width at half maximum; FDHM – full duration at half maximum; FTHM – full time at half maximum.

(with a crucial role attributed to the second RyR isoform) but it plays a null or minor role in rat fibres[47]. Despite a demonstrated CICR in frog, CREs from frog fibres are narrower than CREs from mammalian fibres, both in intact cells (Table 3) or in permeabilized fibres[48]. In the two vertebrate species, CREs width is narrower than in bees, which is clearly in agreement with a more important role for CICR in insects. In half of adult bee leg muscle fibres, a low-voltage-activated (LVA) current has been identified in addition to the nifedipine-sensitive high-voltage activated (HVA) current[5,49]. Both HVA- and LVA- calcium currents exists in mammalian fibres as well, but the density of the later gradually decreases postnatally to eventually disappear after 2–3 weeks of age[50]. Whereas DHPRs responsible for the HVA- (L-type) current are involved in triggering and/or repressing sparks in immature and adult mammalian muscle fibres[27,32], pharmacological proofs indicate that the LVA- (T-type) calcium channel doesn't modulate sparks frequency[32]. A role for the LVA- current in the genesis or regulation of honey bee CREs thus remains to be studied.

Amplitude of honey bee sparks measured in *XYT* experiments appeared smaller than in almost all other intact preparations (Table 2, 3). This parameter is however highly subjected to the experimental set-up performances, imaging analysis and thresholding strategies, as illustrated in *XT* experiments from frog, where amplitude can vary by a factor 5 (Table 3). Namely, using the traditional threshold-based sparks detection method, the former study of sparks in intact frog fibres described an average amplitude of ~1 $\Delta F/F_0$[23], whereas a recent publication using the wavelet detection method described an average amplitude of ~0.2 $\Delta F/F_0$[22]. The difference may be in part attributed to the more efficient detection of CREs of low amplitude with the wavelet method, but other factors may be involved because the maximal amplitudes detected in the later publication reached ~0.85 $\Delta F/F_0$[22]. Interestingly, in intact muscle fibres from a mouse model of myopathy (*mdx*), a similar analysis strategy ('à trous implementation of the two-dimensional undecimated discrete wavelet transform') led to the detection of CREs up to 1.3 $\Delta F/F_0$, with a half cumulative frequency value (CF_{50}) of 0.53[51]. The apparently low amplitude of honey

szentesi.peter_292_24

Type of intact cells	Organism	Age (days)	Sarcomere (µm)	Dye	Ext. Sol	$[Ca^{2+}]_{ext}$ (mM)	Speed of recording (line/ms)	Threshold for duration of embers (ms)	Frequency (events/ /s/ mm)	Amplitude ($\Delta F/F_0$)	FWHM (µm)	Duration (ms)	Rise time (ms)	Signal mass (μm^{n3})	Reference
Adult tibia fibres	Honey bee	1–4	~4	Fluo-8 AM	Tyrode	2	1	40	63.1 ± 6.6	0.186 ± 0.002	3.18 ± 0.04	56.95 ± 0.58	27.02 ± 0.41	10.29 ± 0.41	This study
Adult FDB fibres	Mouse	1–14	–	Fluo-4 AM	Ringer	1.8	2	30	~4% of CREs ǂ	–	–	–	–	–	Chun 2003*
Primary myo-tubes culture	Rat	~5 days in vitro	–	Fluo-4 AM	Tyrode	1.8	1.54	60	2.4 ± 1.4	0.27 ± 0.05	-	229 ± 33	–	–	Fodor 2008
C2C12 cell line myo-tubes	Mouse	>5 days in vitro	–	Fluo-4 AM	Tyrode	2	0.8	50	53.4% of CREs ǂ	–	–	–	–	–	Altomare 2013

Table 4. Interspecific comparison of calcium embers' parameters measured in line-scan (XT) experiments performed in intact cells. In this table studies are ordered according to i) the developmental stage and ii) the species (Honey bee, Frog, Mouse, Rat). Preparations were freshly isolated muscle fibres or cell culture. *Chun values are from EDL and diaphragm muscles. Rise time was calculated between 10–90% of the peak amplitude. ǂThe embers frequency was given as a percentage of total CRE in these studies. Data marked with ~ is approximated from figures. All data depicted at room temperature. FDB – flexor digitorum brevis; AM – acetoxymethyl ester; FWHM – full width at half maximum.

bee sparks as compared to canonical sparks may thus be more related to species specificities and/or experimental conditions than to the detection method we used. Another striking difference between bees and vertebrates is that in bees, embers had almost the same amplitude as sparks, whereas embers are usually smaller than sparks in mammals, as shown in non-intact preparations[16,31]. This finding implies the idea that in bee muscle during a CRE, the same number of RyRs open and only the duration of their opening vary stochastically. The amplitude of sparks from honey bee is ~ eightfold smaller than the amplitude of voltage-gated global Ca^{2+} transients (Table 3), a result consistent with the idea that sparks are the unitary building blocks of macroscopic calcium release. This ratio is in the same range in intact frog fibres (in *Rana pipiens* fibres, sparks are ~ 20 smaller than voltage-activated macroscopic transients[23]). In intact mouse primary myotubes and in the C2C12 mouse cell line, sparks are 1.4 and ~ fivefold smaller than macroscopic transients, respectively[52,53]. To the best of our knowledge, no study relates both sparks amplitude and macroscopic transients in intact non voltage-clamped mouse fibres. A ratio of ~ 6 can however be calculated from macroscopic Ca^{2+} transients recorded under similar conditions as those depicted in Table 3 for fibres of the mouse FDB muscle[54].

Honey bee sparks had similar kinetics properties as other species. Most features of honey bee embers were reminiscent to other species ones as well. Previous studies classified the embers using their durations (Table 4). Although there was no clear border between the duration of sparks and embers in bee muscle (see Fig. 4D), the distribution of the probability histogram of bee CREs duration was nevertheless successfully fitted by a bimodal Gaussian function, according to a previously described methodology[55] and the value 40 ms was retained as the threshold for ember detection. Importantly, the amplitude could not be used as the second separator parameter since CREs in bee fibres are more homogeneous in amplitude than in mammalian muscles where the amplitude of embers is much smaller than that of the sparks.

To our knowledge, few studies depict incidence of sparks in intact skeletal muscle (i.e. the percentage of fibres where such events can be detected). CREs were seen in < 20% of adult honey bee intact fibres. By comparison, the incidence of spontaneous CREs was less than 5% of intact adult mouse fibres whereas it was more elevated in embryonic fibres[43]. A comparison of sparks frequency collected in *XT* line-scan experiments in intact cells shows that in honey bee, frequency is four fold to 600 fold higher than in any other mature or immature cells from frog, mouse, rat or zebrafish (Table 3, *XT*). In *XYT* images series from adult bees' fibres, the frequency is one or two orders of magnitude higher as compared to intact cells from adult or immature mammalian cells (20–300 fold higher, Table 2). For instance, in mouse cells the frequency of CREs in *XYT* has been described to be between 5 and 80 Hz/mm^2 only (Table 2, *XYT*). Interestingly, the *XYT* frequency observed in bees is almost identical to what was reported in intact adult frog muscle recently[22]. Again, these differences in CREs frequency among species may thus be a consequence of the relative incidence that CICR has in excitation–contraction coupling or to ultrastructural differences discussed before. It is important to point out that frequency similarities between bees and frogs are not only related to the analysis strategy, because a similar procedure used in mouse fibres led to a 100 fold lower frequency[51]. Finally, the proportion of embers as compared to the total number of CREs in *XT* experiments shows that honey bee embers are much more frequent than in adult or foetal mouse cells (33% in honey bee vs 4% in mouse) and either higher or identical in myotubes from rat and mouse respectively (Table 4).

In honey bee fibres, CREs appear most of the time in a stochastic manner and rarely at a given triad. However, a repetitive mode of activation was observed in specific hot spots. This second mode, previously termed *rep*-mode, has been identified when voltage-clamped vertebrate fibres (cut fibres mounted in a Vaseline gap chamber) were stimulated by a low-amplitude depolarization[56]. This activity mode can also happen in chronically depolarized frog fibre right after a brief repolarization protocol. Such an activity was seen in intact adult mouse fibres as well[43] and in embryonic and postnatal mouse fibres, where 29% of all events location had reoccurring Ca^{2+} release events[32]. A pharmacological manipulation with caffeine is also increasing the appearance of the repetitive CREs in intact frog fibres[22]. However, whereas CREs in rep-mode were short in duration in frog fibres, bee hot spots led to CREs with various kinetics ranging from sparks to burst and embers.

szentesi.peter_292_24

In addition to provide the first interspecific comparison of sparks between vertebrates and invertebrates, the present study sets the basis for a future comparison of sparks in other invertebrates, where these subcellular localized Ca^{2+} signals have not been described yet. We have overcome the difficulty of isolating single fibres from insects (firmly attached to the insect exoskeleton through tonofilaments), and this methodological advancement will allow an in-depth characterization of sparks in insects in general. Our methods could in particular be transposed to common insect models used either in fundamental research (fruit flies, cockroaches, grasshoppers) or models of interest in agronomy (aphids, moths, bugs, etc.). This study would be of particular interest to characterize the interspecific difference in susceptibility to new insecticides targeting RyRs, the phthalic acid diamides and anthranilic diamides. Diamides are highly efficient to control a variety of pests. They are widely used to kill a number of insect species, including lepidopterans (moths), hemipterans (aphids), dipterans (flies) and so on. Their major mode of action is to interfere with normal function of ryanodine receptors. They have been designed to ensure a favourable vertebrate selectivity ratio, that is to say: being more toxic to invertebrates than to vertebrates. However, insects exposed to these compounds, whether they are considered either as pests or beneficial insects, show strong symptoms of intoxication (from sublethal effects to mortality). For instance, we have shown that sublethal doses of chlorantraniliprole were highly deleterious to honey bees that encounter long lasting locomotor deficits lasting for several days, leading to high susceptibility to other threats[9]. Higher doses kill the bees quickly. Insect ryanodine receptors are quite divergent from those of vertebrates (~45% a.a. identity), but RyRs from insect species from all orders show a strong molecular proximity (~80%). The honeybee RyR (XP_006569098.1) shows 83, 80, 79 and 78% amino acid identity with RyRs from the beetle *Tribolium castaneum* (NP_001308588.1), the moth *Plutella xylostella* (XP_037970554.1), the aphid *Myzus Persicae* (XP_022160123.1) and the fly *Drosophila melanogaster* (NP_476991.1), respectively. Although fruit flies *D. melanogaster* are considered as models, the intracellular homeostasis in insect tubular muscle fibres has so far not been studied thoroughly owing to the difficulty of isolating muscle fibres from the cuticle, which is a prerequisite for calcium imaging. The honey bee fibres provide a suitable model in this context and the dissociation procedure we developed here to study sparks will be helpful in many instances.

Conclusion

In addition to the characterization of localized Ca^{2+}-release events of the honey bee, a detailed comparison of their major specificities as compared with their vertebrate counterparts has been carried out. The successful isolation of insect muscle fibres and the thorough characterization of subcellular Ca^{2+} signalling in the honey bee muscle paves the way for further in vitro studies, which are clearly needed to elucidate the origins of the established differential toxicity of the RyR-targeting diamides insecticides between vertebrates and invertebrates. Furthermore, while a so-called 'vertebrate selectivity toxicological ratio' already exists for diamides, no protective selectivity ratio has been established yet for useful insects. Pest insects and non-pest insects share a high degree of homology in their RyR and a comparative study of Ca^{2+} sparks among insects may help to better characterize the toxicity of diamides, which constitute a threat to useful insects such as pollinators.

Data availability

The datasets generated and analysed during the current study are available on reasonable request.

Received: 19 March 2021; Accepted: 4 August 2021
Published online: 18 August 2021

References

1. Galizia, G., Eisenhardt, D. & Giurfa, M. *Honeybee Neurobiology and Behavior* (Springer, 2012).
2. Winston, M. L. *The Biology of the Honey Bee*. (Harvard University Press, 1991).
3. Bicker, G. Transmitter-induced calcium signalling in cultured neurons of the insect brain. *J. Neurosci. Methods* **69**, 33–41 (1996).
4. Szyszka, P., Galkin, A. & Menzel, R. Associative and non-associative plasticity in kenyon cells of the honeybee mushroom body. *Frontiers in Systems Neuroscience* **2**. https://doi.org/10.3389/neuro.06.003.2008 (2008).
5. Collet, C. Excitation-contraction coupling in skeletal muscle fibers from adult domestic honeybee. *Pflugers Arch* **458**, 601–612. https://doi.org/10.1007/s00424-009-0642-6 (2009).
6. Collet, C. & Belzunces, L. Excitable properties of adult skeletal muscle fibres from the honeybee Apis mellifera. *J. Exp. Biol.* **210**, 454–464. https://doi.org/10.1242/jeb.02667 (2007).
7. Deisig, N., Giurfa, M., Lachnit, H. & Sandoz, J. C. Neural representation of olfactory mixtures in the honeybee antennal lobe. *Eur. J. Neurosci.* **24**, 1161–1174 (2006).
8. Galizia, C. G., Kuttner, A., Joerges, J. & Menzel, R. Odour representation in honeybee olfactory glomeruli shows slow temporal dynamics: an optical recording study using a voltage-sensitive dye. *J. Insect Physiol.* **46**, 877–886 (2000).
9. Kadala, A., Charreton, M., Charnet, P. & Collet, C. Honey bees long-lasting locomotor deficits after exposure to the diamide chlorantraniliprole are accompanied by brain and muscular calcium channels alterations. *Sci. Rep.* **9**, 2153. https://doi.org/10.1038/s41598-019-39193-3 (2019).
10. Kadala, A., Charreton, M. & Collet, C. Flubendiamide, the first phthalic acid diamide insecticide, impairs neuronal calcium signalling in the honey bee's antennae. *J. Insect. Physiol.* 104086. https://doi.org/10.1016/j.jinsphys.2020.104086 (2020).
11. Walz, B., Baumann, O., Zimmermann, B. & Ciriacy-Wantrup, E. V. Caffeine- and ryanodine-sensitive Ca^{2+}-induced Ca^{2+} release from the endoplasmic reticulum in honeybee photoreceptors. *J. Gen. Physiol.* **105**, 537–567 (1995).
12. Meissner, G. & Lu, X. Dihydropyridine receptor-ryanodine receptor interactions in skeletal muscle excitation-contraction coupling. *Biosci. Rep.* **15**, 399–408. https://doi.org/10.1007/bf01788371 (1995).
13. Collet, C. & Jacquemond, V. Sustained release of calcium elicited by membrane depolarization in ryanodine-injected mouse skeletal muscle fibers. *Biophys. J .* **82**, 1509–1523. https://doi.org/10.1016/S0006-3495(02)75504-5 (2002).
14. Carafoli, E. & Krebs, J. Why calcium? How calcium became the best communicator. *J. Biol. Chem.* **291**, 20849–20857. https://doi.org/10.1074/jbc.R116.735894 (2016).
15. Collet, C. in *Toxicologie chez l'abeille domestique* (eds C. Collet, Sandoz J.C., & P. Charnet) (CNRS Editions, in press, 2021).

szentesi.peter_292_24

16. Csernoch, L. Sparks and embers of skeletal muscle: the exciting events of contractile activation. *Pflügers Arch. Eur. J. Physiol.* **454**, 869–878. https://doi.org/10.1007/s00424-007-0244-0 (2007).
17. Cheng, H. & Lederer, W. J. Calcium sparks. *Physiol. Rev.* **88**, 1491–1545. https://doi.org/10.1152/physrev.00030.2007 (2008).
18. Cheng, H., Lederer, W. & Cannell, M. Calcium sparks: elementary events underlying excitation-contraction coupling in heart muscle. *Science* **262**, 740–744. https://doi.org/10.1126/science.8235594 (1993).
19. Niggli, E. & Shirokova, N. A guide to sparkology: the taxonomy of elementary cellular Ca2+ signaling events. *Cell Calcium* **42**, 379–387. https://doi.org/10.1016/j.ceca.2007.02.010 (2007).
20. Collet, C. *et al.* Subcellular calcium events and calcium waves in leg skeletal muscle fibers isolated from the honey bee Apis mellifera. *Biophys. J .* **114**, 289a. https://doi.org/10.1016/j.bpj.2017.11.1655 (2018).
21. Szabó, L. Z., Vincze, J., Csernoch, L. & Szentesi, P. Improved spark and ember detection using stationary wavelet transforms. *J. Theor. Biol.* **264**, 1279–1292. https://doi.org/10.1016/j.jtbi.2010.04.005 (2010).
22. Cserne Szappanos, H. *et al.* High Time Resolution Analysis of Voltage-Dependent and Voltage-Independent Calcium Sparks in Frog Skeletal Muscle Fibers. *Frontiers in Physiology* **11**, https://doi.org/10.3389/fphys.2020.599822 (2020).
23. Hollingworth, S., Peet, J., Chandler, W. K. & Baylor, S. M. Calcium sparks in intact skeletal muscle fibers of the frog. *J. Gen. Physiol.* **118**, 653–678. https://doi.org/10.1085/jgp.118.6.653 (2001).
24. Wareham, A. C., Duncan, C. J. & Bowler, K. The resting potential of cockroach muscle membrane. *Comp. Biochem. Physiol. A Physiol.* **48**, 765–797. https://doi.org/10.1016/0300-9629(74)90619-7 (1974).
25. Bekoff, A. & Betz, W. Properties of isolated adult rat muscle fibres maintained in tissue culture. *J. Physiol.* **271**, 537–547. https://doi.org/10.1113/jphysiol.1977.sp012013 (1977).
26. Allard, B., Bernengo, J. C., Rougier, O. & Jacquemond, V. Intracellular Ca2+ changes and Ca2+-activated K+ channel activation induced by acetylcholine at the endplate of mouse skeletal muscle fibres. *J. Physiol.* **494**, 337–349. https://doi.org/10.1113/jphysiol.1996.sp021496 (1996).
27. Pickering, J. D., White, E., Duke, A. M. & Steele, D. S. DHPR activation underlies SR Ca2+ release induced by osmotic stress in isolated rat skeletal muscle fibers. *J. Gen. Physiol.* **133**, 511–524. https://doi.org/10.1085/jgp.200910191 (2009).
28. Baumann, O. Distribution of ryanodine receptor Ca2+ channels in insect photoreceptor cells. *J. Compar. Neurol.* **421**, 347–361. https://doi.org/10.1002/(SICI)1096-9861(20000605)421:3%3c347::AID-CNE4%3e3.0.CO;2-Z (2000).
29. Parker, I. & Gil Wier, W. Variability in frequency and characteristics of Ca2+ sparks at different release sites in rat ventricular myocytes. *J. Physiol.* **505**, 337–344. https://doi.org/10.1111/j.1469-7793.1997.337bb.x (1997).
30. González, A. *et al.* The spark and its ember: separately gated local components of Ca2+ release in skeletal muscle. *J. Gen. Physiol.* **115**, 139–158. https://doi.org/10.1085/jgp.115.2.139 (2000).
31. Kirsch, W. G., Uttenweiler, D. & Fink, R. H. Spark- and ember-like elementary Ca2+ release events in skinned fibres of adult mammalian skeletal muscle. *J. Physiol.* **537**, 379–389. https://doi.org/10.1111/j.1469-7793.2001.00379.x (2001).
32. Chun, L. G., Ward, C. W. & Schneider, M. F. Ca2+ sparks are initiated by Ca2+ entry in embryonic mouse skeletal muscle and decrease in frequency postnatally. *Am. J. Physiol. Cell Physiol.* **285**, C686-697. https://doi.org/10.1152/ajpcell.00072.2003 (2003).
33. Csernoch, L., Pouvreau, S., Ronjat, M. & Jacquemond, V. Voltage-activated elementary calcium release events in isolated mouse skeletal muscle fibers. *J. Membr. Biol.* **226**, 43. https://doi.org/10.1007/s00232-008-9138-0 (2008).
34. Gilai, A. Electromechanical coupling in tubular muscle fibers. II. Resistance and capacitance of one transverse tubule. *J. Gen. Physiol.* **67**, 343–367. https://doi.org/10.1085/jgp.67.3.343 (1976).
35. Brum, G., Gonzalez, A., Rengifo, J., Shirokova, N. & Rios, E. Fast imaging in two dimensions resolves extensive sources of Ca2+ sparks in frog skeletal muscle. *J. Physiol.* **528**, 419–433. https://doi.org/10.1111/j.1469-7793.2000.00419.x (2000).
36. Loesser, K. E., Castellani, L. & Franzini-Armstrong, C. Dispositions of junctional feet in muscles of invertebrates. *J. Muscle Res. Cell Motil.* **13**, 161–173. https://doi.org/10.1007/BF01874153 (1992).
37. Takekura, H. & Franzini-Armstrong, C. The structure of Ca2+ release units in arthropod body muscle indicates an indirect mechanism for excitation-contraction coupling. *Biophys. J .* **83**, 2742–2753. https://doi.org/10.1016/S0006-3495(02)75284-3 (2002).
38. Xu, X., Bhat, M. B., Nishi, M., Takeshima, H. & Ma, J. Molecular Cloning of cDNA encoding a drosophila ryanodine receptor and functional studies of the carboxyl-terminal calcium release channel. *Biophys. J .* **78**, 1270–1281. https://doi.org/10.1016/S0006-3495(00)76683-5 (2000).
39. Troczka, B. J., Richardson, E., Homem, R. A. & Davies, T. G. E. An analysis of variability in genome organisation of intracellular calcium release channels across insect orders. *Gene* **670**, 70–86. https://doi.org/10.1016/j.gene.2018.05.075 (2018).
40. Weinstock, G. M., Robinson, G. E. & Consortium, T. H. G. S. Insights into social insects from the genome of the honeybee Apis mellifera. *Nature* **443**, 931–949. https://doi.org/10.1038/nature05260 (2006).
41. Perni, S. *et al.* Structural and functional properties of ryanodine receptor type 3 in zebrafish tail muscle. *J. Gen. Physiol.* **145**, 253. https://doi.org/10.1085/jgp.20141130302112015c (2015).
42. Felder, E. & Franzini-Armstrong, C. Type 3 ryanodine receptors of skeletal muscle are segregated in a parajunctional position. *Proc. Natl. Acad. Sci. USA* **99**, 1695–1700. https://doi.org/10.1073/pnas.032657599 (2002).
43. Conklin, M. W., Barone, V., Sorrentino, V. & Coronado, R. Contribution of ryanodine receptor type 3 to Ca(2+) sparks in embryonic mouse skeletal muscle. *Biophys J.* **77**, 1394–1403. https://doi.org/10.1016/S0006-3495(99)76988-2 (1999).
44. Gyorke, S. & Palade, P. Calcium-induced calcium release in crayfish skeletal muscle. *J. Physiol.* **457**, 195–210. https://doi.org/10.1113/jphysiol.1992.sp019373 (1992).
45. Ashcroft, F. M. & Stanfield, P. R. Calcium and potassium currents in muscle fibres of an insect (*Carausius morosus*). *J. Physiol.* **323**, 93–115 (1982).
46. Gielow, M. L., Gu, G. G. & Singh, S. Resolution and pharmacological analysis of the voltage-dependent calcium channels of Drosophila larval muscles. *J. Neurosci.* **15**, 6085–6093 (1995).
47. Rios, E. & Zhou, J. Control of dual isoforms of Ca2+ release channels in muscle. *Biol. Res.* **37**, 583–591 (2004).
48. Zhou, J. *et al.* Ca2+ Sparks and embers of mammalian muscle. Properties of the sources. *J. Gen. Physiol.* **122**, 95–114. https://doi.org/10.1085/jgp.200308796 (2003).
49. Rousset, M. *et al.* Honeybee locomotion is impaired by Am-CaV3 low voltage-activated Ca2+ channel antagonist. *Sci. Rep.* **7**, 41782. https://doi.org/10.1038/srep41782 (2017).
50. Beam, K. G. & Knudson, C. M. Effect of postnatal development on calcium currents and slow charge movement in mammalian skeletal muscle. *J. Gen. Physiol.* **91**, 799–815. https://doi.org/10.1085/jgp.91.6.799 (1988).
51. Teichmann, M. D. H. *et al.* Inhibitory control over Ca2+ Sparks via mechanosensitive channels is disrupted in dystrophin deficient muscle but restored by mini-dystrophin expression. *PLoS ONE* **3**, e3644. https://doi.org/10.1371/journal.pone.0003644 (2008).
52. Fodor, J. *et al.* Altered expression of triadin 95 causes parallel changes in localized Ca2+ release events and global Ca2+ signals in skeletal muscle cells in culture. *J. Physiol.* **586**, 5803–5818. https://doi.org/10.1113/jphysiol.2008.160457 (2008).
53. Altomare, C. *et al.* Altered functional differentiation of mesoangioblasts in a genetic myopathy. *J. Cell Mol. Med.* **17**, 419–428. https://doi.org/10.1111/jcmm.12023 (2013).
54. Caputo, C. & Bolaños, P. Fluo-3 signals associated with potassium contractures in single amphibian muscle fibres. *J. Physiol.* **481**, 119–128. https://doi.org/10.1113/jphysiol.1994.sp020423 (1994).
55. Rueda, A., Fernández-Velasco, M., Benitah, J.-P. & Gómez, A. M. Abnormal Ca2+ Spark/STOC coupling in cerebral artery smooth muscle cells of obese Type 2 diabetic mice. *PLoS ONE* **8**, e53321. https://doi.org/10.1371/journal.pone.0053321 (2013).

szentesi.peter_292_24

56. Klein, M. G., Lacampagne, A. & Schneider, M. F. A repetitive mode of activation of discrete Ca2+ release events (Ca2+ sparks) in frog skeletal muscle fibres. *J. Physiol.* **515**(Pt 2), 391–411. https://doi.org/10.1111/j.1469-7793.1999.391ac.x (1999).
57. Shirokova, N., García, J. & Ríos, E. Local calcium release in mammalian skeletal muscle. *J. Physiol.* **512**, 377–384. https://doi.org/10.1111/j.1469-7793.1998.377be.x (1998).

Acknowledgements

The authors thank Ms. R. Ori for her excellent technical assistance, Dr A. Aouacheria for observations of nuclei under a confocal microscope and Dr C. Dienes for his help in the resting membrane potential measurements. The research was supported by Grants from the French National Research Agency (ANR-13-BSV7-0010 and ANR-20-CE34-0017), the Ministry of Europe and Foreign Affairs (PHC Balaton 2019 #41908SC), the Hungarian Research Fund (2018-2.1.13-TÉT-FR-2018-00005) and by the Thematic Excellence Programme (TKP2020-IKA-04) which has been implemented with the support provided from the National Research, Development and Innovation Fund of Hungary, financed under the 2020-4.1.1-TKP2020 funding scheme.

Author contributions

Conceived and designed the experiments: C.C., P.S. Performed the experiments: C.C., P.S. Analysed the data: C.C., P.S. Contributed reagents/materials/analysis tools: L.S., M.T., M.C. Wrote the paper: C.C., P.S., L.C.

Competing interests

The authors declare no competing interests.

Additional information

Supplementary Information The online version contains supplementary material available at https://doi.org/10.1038/s41598-021-96028-w.

Correspondence and requests for materials should be addressed to C.C.

Reprints and permissions information is available at www.nature.com/reprints.

Publisher's note Springer Nature remains neutral with regard to jurisdictional claims in published maps and institutional affiliations.

Open Access This article is licensed under a Creative Commons Attribution 4.0 International License, which permits use, sharing, adaptation, distribution and reproduction in any medium or format, as long as you give appropriate credit to the original author(s) and the source, provide a link to the Creative Commons licence, and indicate if changes were made. The images or other third party material in this article are included in the article's Creative Commons licence, unless indicated otherwise in a credit line to the material. If material is not included in the article's Creative Commons licence and your intended use is not permitted by statutory regulation or exceeds the permitted use, you will need to obtain permission directly from the copyright holder. To view a copy of this licence, visit http://creativecommons.org/licenses/by/4.0/.

© The Author(s) 2021

frontiers in Physiology

szentesi.peter_292_24

ORIGINAL RESEARCH
published: 15 December 2020
doi: 10.3389/fphys.2020.599822

High Time Resolution Analysis of Voltage-Dependent and Voltage-Independent Calcium Sparks in Frog Skeletal Muscle Fibers

*Henrietta Cserne Szappanos[1,2], János Vincze[2], Dóra Bodnár[2], Beatrix Dienes[2], Martin F. Schneider[1], László Csernoch[2] and Péter Szentesi[2]**

[1] Department of Biochemistry and Molecular Biology, School of Medicine, University of Maryland, Baltimore, Baltimore, MD, United States, [2] Department of Physiology, Faculty of Medicine, University of Debrecen, Debrecen, Hungary

OPEN ACCESS

Edited by:
Heinrich Brinkmeier, Universitätsmedizin Greifswald, Germany

Reviewed by:
Isabelle Marty, Institut National de la Santé et de la Recherche Médicale (INSERM), France
Gustavo Brum, Universidad de la República, Uruguay

***Correspondence:**
Péter Szentesi
szentesi.peter@med.unideb.hu

Specialty section:
This article was submitted to Striated Muscle Physiology, a section of the journal Frontiers in Physiology

Received: 28 August 2020
Accepted: 25 November 2020
Published: 15 December 2020

Citation:
Cserne Szappanos H, Vincze J, Bodnár D, Dienes B, Schneider MF, Csernoch L and Szentesi P (2020) High Time Resolution Analysis of Voltage-Dependent and Voltage-Independent Calcium Sparks in Frog Skeletal Muscle Fibers. Front. Physiol. 11:599822. doi: 10.3389/fphys.2020.599822

In amphibian skeletal muscle calcium (Ca^{2+}) sparks occur both as voltage-dependent and voltage-independent ligand-activated release events. However, whether their properties and their origin show similarities are still in debate. Elevated K^+, constant Cl^- content solutions were used to initiate small depolarizations of the resting membrane potential to activate dihydropyridine receptors (DHPR) and caffeine to open ryanodine receptors (RyR) on intact fibers. The properties of Ca^{2+} sparks observed under control conditions were compared to those measured on depolarized cells and those after caffeine treatment. Calcium sparks were recorded on intact frog skeletal muscle fibers using high time resolution confocal microscopy (x-y scan: 30 Hz). Sparks were elicited by 1 mmol/l caffeine or subthreshold depolarization to different membrane potentials. Both treatments increased the frequency of sparks and altered their morphology. Images were analyzed by custom-made computer programs. Both the amplitude (in $\Delta F/F_0$; 0.259 ± 0.001 vs. 0.164 ± 0.001; n = 24942 and 43326, respectively; mean ± SE, $p < 0.001$) and the full width at half maximum (FWHM, in μm; parallel with fiber axis: 2.34 ± 0.01 vs. 1.92 ± 0.01, $p < 0.001$; perpendicular to fiber axis: 2.08 ± 0.01 vs. 1.68 ± 0.01, $p < 0.001$) of sparks was significantly greater after caffeine treatment than on depolarized cells. 9.8% of the sparks detected on depolarized fibers and about one third of the caffeine activated sparks (29.7%) overlapped with another one on the previous frame on x-y scans. Centre of overlapping sparks travelled significantly longer distances between consecutive frames after caffeine treatment then after depolarization (in μm; 1.66 ± 0.01 vs. 0.95 ± 0.01, $p < 0.001$). Our results suggest that the two types of ryanodine receptors, the junctional RyRs controlled by DHPRs and the parajunctional RyRs are activated independently, using alternate ways, with the possibility of cooperation between neighboring release channels.

Keywords: skeletal muscle, frog, excitation-contraction coupling, ryanodine receptor, calcium-induced calcium release, membrane depolarization, calcium spark, caffeine

INTRODUCTION

Calcium ion is a ubiquitous second messenger in many intracellular signaling pathways, but it also regulates highly specialized cellular processes such as contraction in muscle cells. Ca^{2+} sparks are the openings of a local cluster of ryanodine receptors (RyR) which are the Ca^{2+}-release channels of the sarcoplasmic reticulum (SR; Wang et al., 2004). Sparks in amphibians are elementary events igniting global Ca^{2+} release during depolarization (Klein et al., 1997). Thus, the study of Ca^{2+} sparks provides useful information about the Ca^{2+} release process itself and the gating kinetics of RyR Ca^{2+} release channels.

Elementary calcium release events were first found in cardiac myocytes (Cheng et al., 1993), then in many other cell types as smooth (Nelson et al., 1995) and skeletal muscle (Tsugorka et al., 1995; Klein and Schneider, 2006). Morphology and frequency of calcium release events in various cell types, or from different species show marked alterations. One of the possible explanations could be the difference in the expression pattern of calcium release channels. In non-mammalian and embryonic mammalian skeletal muscle fibers two RyR isoforms coexist in almost equal amounts in contrast to fibers from adult mammals where the RyR1 isoform predominates (Sutko and Airey, 1996; Ogawa et al., 1999; Felder and Franzini-Armstrong, 2002). Interestingly mammalian skeletal muscle express the RyR3 isoform embryonically and certain muscles in adult, like diaphragm and soleus, and lower levels in abdominal muscles and tibialis anterior (Ogawa et al., 1999). The frog RyR isoforms (RyRα and RyRβ) are similar to mammalian RyR1 and RyR3, both in terms of their amino acid sequence and functional properties (Franzini-Armstrong and Protasi, 1997).

The α isoform is closely associated with the voltage sensor dihydropyridine receptors (DHPRs) located in the transverse (T-) tubule, and is voltage controlled. The β isoform is not connected with DHPRs, but even a small increase in intracellular calcium concentration can open it (Rodney and Schneider, 2003; Zhou et al., 2004; Pouvreau et al., 2007). The response to caffeine reportedly varies depending on animal species, muscle type, and age, with characteristically higher sensitivity and responsiveness reported on frog muscles than mammalian muscles which do not express RyR3 or just very low level (Ogawa et al., 1999; Rossi et al., 2001, Kashiyama et al., 2010).

Electron microscopic studies showed highly organized pattern of RYR receptors, called 'feet' on the SR membrane oriented toward the DHPR receptors in the T-tubule. Muscles expressing RyRβ/3 have additional clusters in the SR membrane. These are segregated from junctional RyRα/1s and are located in a parajunctional position (Felder and Franzini-Armstrong, 2002). This observation led to the hypothesis of two different mechanisms of RyR activation: a voltage-controlled intracellular calcium release through the RYRα/1s and the voltage-independent or calcium induced calcium release (CICR) pathway via the opening of RyRβ/3s (Rios and Pizarro, 1988; Franzini-Armstrong, 2004).

Previously, frog skeletal muscle Ca^{2+} sparks were shown to occur both in a voltage-dependent and voltage-independent, ligand-activated manner. Voltage-dependent sparks can be evoked experimentally by a subthreshold depolarization of a skeletal muscle fiber, and the frequency of Ca^{2+} sparks increases steeply with increasing depolarization (Klein et al., 1996). Voltage dependent activation of SR Ca^{2+} release in skeletal muscle is regulated by intramembrane voltage sensors, the dihydropyridine receptors (Franzini-Armstrong, 2004) in the transverse tubule membrane. The voltage dependence of intramembrane charge movement indicates that changes in membrane potential lead to the redistribution of these voltage sensors between intramembrane locations according to the Boltzmann relationship (Schneider and Ward, 2002). Voltage-independent sparks were ignited by endogenous ligands of RyRs via Ca^{2+}-induced Ca^{2+} release mechanisms (Klein et al., 1996). Caffeine was used to activate RyRs and increase the frequency of the calcium release events on skeletal muscle fibers (Brum et al., 2000; Gonzalez et al., 2000a,b). In these studies increased frequency, higher amplitude and eccentricity was distinctive to the caffeine induced events.

Skeletal muscle fibers expressing both RyR isotype show a higher incidence of spontaneous calcium release events, than fibers missing the RyRβ/3 isotype. It was also found that spontaneous sparks remain visible in fully depolarized (voltage clamped to 0 mV) frog fiber, or blocking DHPRs (nifedipine, Klein et al., 1996, Cd^{2+}/La^{3+} Perez et al., 2003). Although these applications could abolish the calcium movement through the voltage sensor DHPR, it was also demonstrated, that non-conducting DHPRs remain functional as voltage sensor for conformational EC coupling (Dayal et al., 2017).

Previous studies have also demonstrated that a chemical or mechanical skinning procedure results in a partial destabilization of the coupling between the DHPR–RyR that leads to the appearance of calcium release events (Kirsch et al., 2001; Zhou et al., 2003; Szappanos et al., 2005). Isaeva et al. (2005) found that the contents of the cytosol of skinned fibers were washed out and the number of the calcium release events changed consequently. Hollingworth et al. (2001) concluded in their studies that properties of spontaneous and voltage-activated sparks were similar in intact muscle fibers. They controlled membrane potential by using extracellular Ringer's solutions with different potassium ion concentrations like as used in this study with some modification (see in "Materials and Methods").

In our previous experiments using voltage clamped cut frog skeletal muscle fibers (Klein et al., 1996) we concluded that the amplitude of spontaneous sparks measured at the holding potential (–90 mV) was much smaller than that of voltage-dependent sparks during small depolarizations. Distribution of the amplitude of voltage-dependent sparks could be fitted by the sum of Gaussian functions with means being multiples of the unitary amplitude of the spontaneous sparks.

To re-examine the difference between voltage-dependent and independent sparks, as well as to characterize the voltage dependence of spark frequency, we have reinvestigated the properties of Ca^{2+} sparks performing a high time resolution analysis. To this end a Zeiss LSM 5 Live laser scanning confocal microscope system was used, with a maximum data acquisition

szentesi.peter_292_24

speed up to 15.4 μs/line to record sparks in intact fibers isolated from frog toe muscle.

We found significant differences in the amplitude of the voltage-dependent and -independent sparks. Their spatial and temporal properties were different, similarly to the results of our previous experiments performed on cut fibers.

The novelty in our experiments are the high resolution data acquisition and the analysis. Using the high speed confocal microscopic technique with about 50 times faster acquisition rates at high resolution allowed us to study the spatial and temporal characteristics of sparks with minimal photo-toxicity. Part of this work was presented to the Biophysical Society (Vincze et al., 2013, 2014).

MATERIALS AND METHODS

Fiber Preparation and Solutions

Frogs (*Rana pipiens*) were placed into crushed ice-water slurry for 30 min then killed by decapitation followed by spinal cord destruction according to protocols approved by the University of Maryland Institutional Animal Care and Use Committee. Toe muscles (*flexor digitorum brevis*) were removed, and individual muscle fibers were enzymatically isolated (8 mg/ml neutral dispase II, 1.3 mg/ml collagenase A, at 37°C, 1 h), in nominally calcium-free Ringer solution (in mM: 115 NaCl, 2.5 KCl, 1 $MgCl_2$, 10 HEPES, pH 7.0). The separated, intact fibers were plated on extracellular matrix covered, glass bottom dishes, in Ringer solution containing 1.8 mM $CaCl_2$. Before each experiments the cells were incubated with 20 μM Fluo-4 AM at room temperature for 30 min, followed by 20 min de-esterification.

To initiate voltage activated sparks in intact fibers we used high concentration potassium ion (K^+) containing extracellular solutions (**Table 1**). Stepwise solution change with increased K^+ content allowed us to reach small depolarizations between -70 and -60 mV while avoiding transient intracellular calcium level increase and subsequent contractions. The Goldman-Hodgkin-Katz equation was used to estimate the actual membrane potential in each K^+ containing solutions. Methane sulfonic acid was used to keep the concentration of Cl^- constant in all solutions and so the ionic strength and the osmolality of the depolarization solutions.

Caffeine in 1 mM concentration was used to increase the appearance of sparks.

Individual fibers were monitored and fibers with increased overall fluorescence or physical deformities following laser exposure or solution change were not used for spark recording. The basic spontaneous activity was also recorded for 10 and 5 fibers before introducing small depolarizations, or 1 mM caffeine, respectively. All measures were taken to avoid photo damage or photo bleaching therefore subsequent images were taken on the same fiber after repositioning. To avoid movement artifacts no local perfusion was used during recordings. This is demonstrated by combining all images in a time-series to show that structural elements did not move (**Supplementary Figures 1C,D** and **Supplementary Video 1**).

TABLE 1 | Composition of the external solution to induce different depolarizations.

In mM	Ringer (−90 mV)	−70 mV	−65 mV	−60 mV
NaCl	115	115	115	115
KCl	2.5	0	0	0
$CaCl_2$	1.8	1.8	1.8	1.8
$MgCl_2$	1	1	1	1
Hepes	10	10	10	10
K methane sulfonate	–	10.2	13.8	18.1

High Speed Recording and Analysis of Ca^{2+} Sparks in Intact Fiber

The fibers were imaged using a Zeiss LSM 5 LIVE laser scanning confocal microscope (Zeiss, Oberkochen, Germany). Instead of imaging the specimen pixel by pixel, it scans along a whole line at the same time, obtaining high temporal resolution image at high acquisition speed. Two dimensional (x-y) image series were taken with speed of 30 or 60 frame per second (FPS), the pixel (line) acquisition time was 47.4 and 15.4 μs. The 512 × 512 pixel image corresponds to 106 μm × 106 μm image size in our experimental setting (pinhole 17 μm, objective: 63X water, NA: 1.2). Fluo-4 was excited with an Argon ion laser (at 488 nm), emitted light was collected through a beam-path filter and digitized at 12 bit. The images were normalized to events excluded baseline fluorescence (F_0).

Identification of Cell Structure and Calcium Sparks on x-y Images

The x-y image sequences containing spontaneous elementary calcium release events (**Figure 1A**) were evaluated using a homemade computer program developed in Borland Delphi (Borland Software Co., Austin, TX, United States). The program allows full automatic analysis of the sequence of images without human intervention.

As the first step in image analysis, the baseline fluorescence value for each pixel of the image was determined. To obtain this value, the average fluorescence value of the points in the time domain for a given pixel that are below $Mean + NormCri \cdot \sigma$ values for all pixel was calculated, where Mean and σ correspond to the average and standard deviation of the fluorescence values of a given pixel in the time domain, respectively. The optimal value of *NormCri* was 1.1. As a next step, the components of the time series belonging to each pixel was determined by the single-dimensional stationary wavelet transformation (Szabo et al., 2010) and then a high pass filtering was applied. Finally, the changes in calcium levels with very slow kinetics not caused by spark formation was removed by dividing all the data of the time-series with the value of the 4th wavelet level (see Szabo et al., 2010, **Figure 1**).

The area belonging to the cell was determined from an image with good signal-to-noise ratio created from the baseline fluorescence values for each pixel (**Figure 1B**). The fluorescence of the cell-associated pixels was much higher than the fluorescence of the extracellular image points; the distribution of intensity was distinctly bimodal. The optimal cut between the

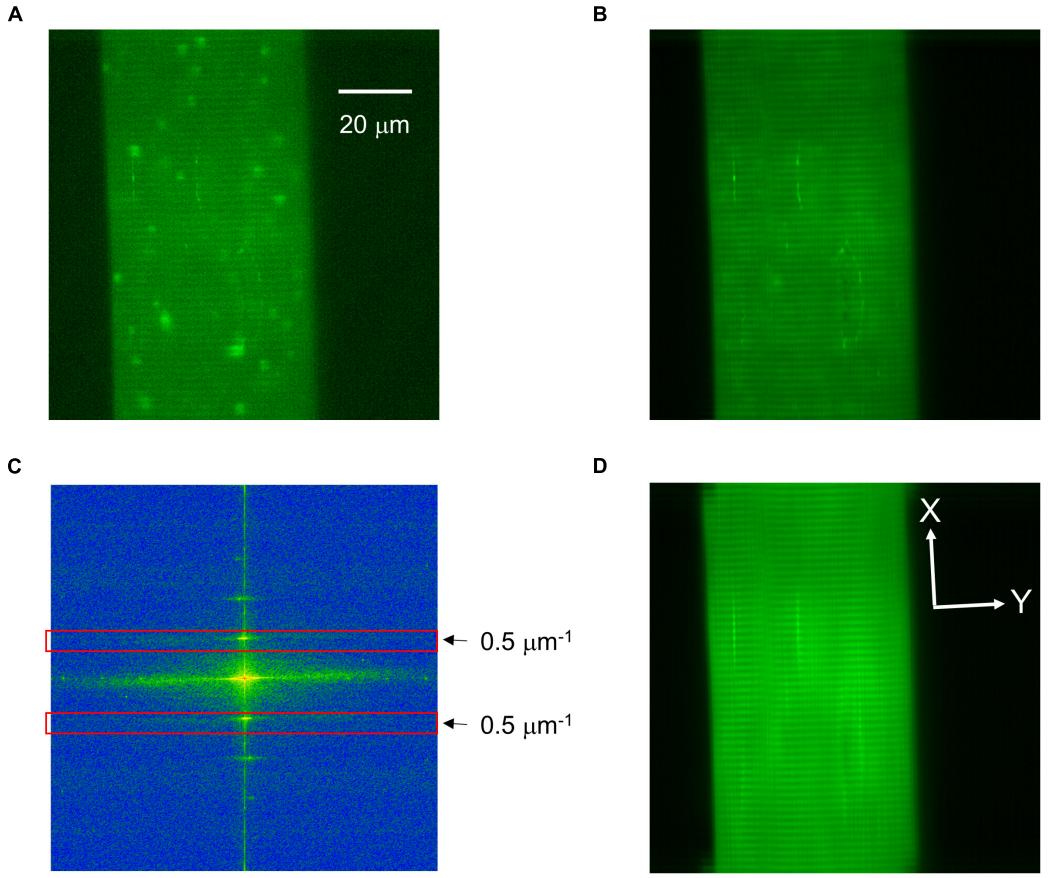


FIGURE 1 | Identification of the cell structure in a representative x-y image. **(A)** An original x-y image of an intact frog skeletal muscle fiber loaded with Fluo-4 displaying calcium release events. **(B)** The picture of the basic fluorescence values of each pixel showing good signal-to-noise ratio for static image elements, such as Z-lines. **(C)** Fast Fourier transform showing the frequency spectrum of the image in panel **(B)**. At 0.5 μm^{-1} (and at its inverse, red rectangles) the sharp band corresponding to one sarcomere is clearly visible. **(D)** The result of the inverse Fourier transformation, where the Z-lines are excellently traceable. White lines perpendicular (X) and parallel (Y) to the Z-lines determine the directions of FWHMs. Scale of panels **(B,D)** is identical to that in panel **(A)**.

two sets of pixels was determined with iterative method, then the area above the threshold was defined as the cell.

After the removal of all variable elements (i.e., calcium sparks) from the image series Z-lines became even more pronounced with some other constant features being present. The structural elements of the cell were determined by the Fourier transform of longitudinally oriented cell areas (**Figure 1C**). The values observed at 0.5 μm^{-1} corresponded to the expected (approximately 2 μm) sarcomere length. Except this peak and the center area of the frequency components all other coefficients were set to zero and an inverse Fourier transformation was performed. In the resulting picture only the components corresponding to the structural elements remained (**Figure 1D**). The Z-lines were determined by searching for the local maximum at columns. With this method the incidentally breaking Z-lines could have also been followed and the parameters of the events could be determined in directions perpendicular (X) and parallel (Y) to the Z-lines (**Figure 1D**).

The efficiency of Z-line identification was tested with images containing artificially created fiber structures. The inclination angle of fibers was determined from the orientation of Z-lines and was compared to the pre-defined creation angle. The developed method gave back almost identical inclination angles (**Supplementary Figure 2**).

Before identifying the ROIs and defining their parameters, high-efficiency Wavelet noise filtering (δ = 3; Szabo et al., 2010) was performed on each normalized image. To identify ROIs corresponding to elemental calcium release events a modified double-threshold method (Cheng et al., 1999) was used in the analysis (**Figure 2**). Contiguous areas with values over *Mean* + *LoCri*·σ that contained at least one pixel with a value greater than *Mean* + *HiCri*·σ were identified as events. The optimal value of *LoCri* and *HiCri* in our case was 1.7 and 2.8, respectively.

To test the method a spark free x-y image with sarcomeric structure and some higher intensity areas throughout the experiment, was merged with artificial Gaussian sparks with different amplitudes (**Supplementary Figure 3A**). Sparks were added to the image by convolving the function producing two-dimensional Gaussian curves with the image containing

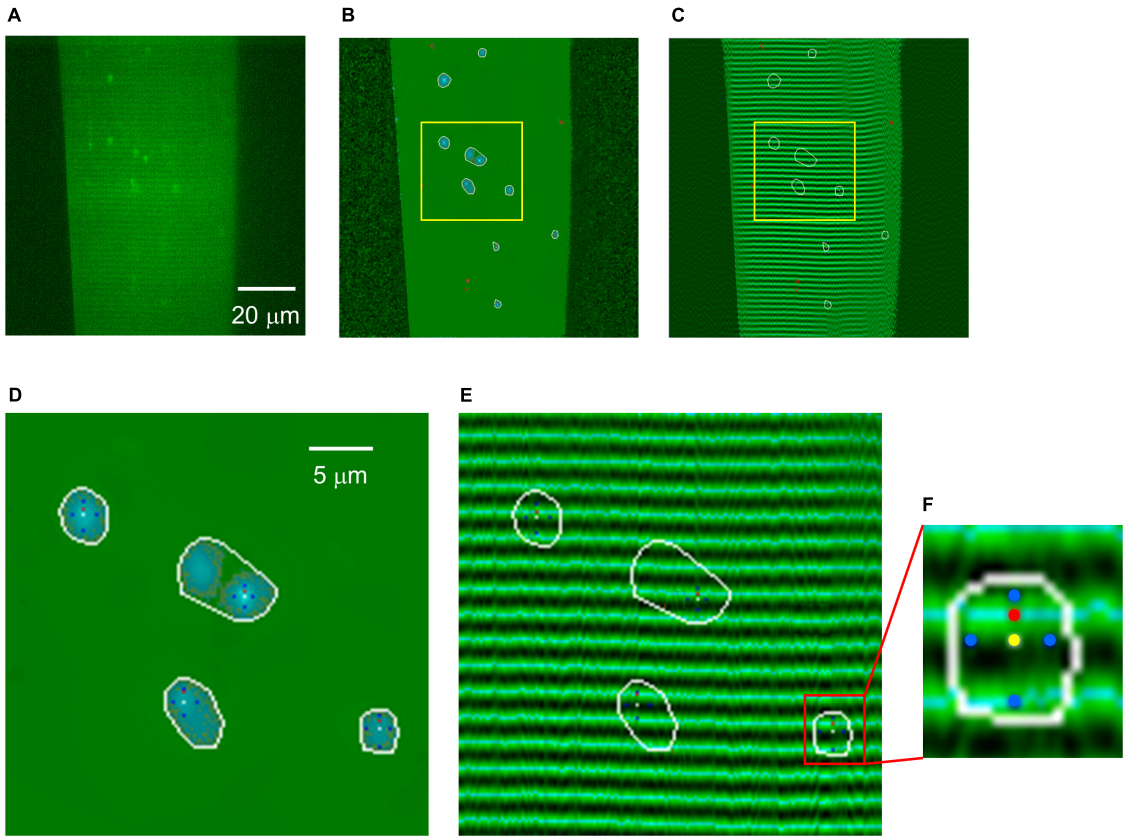


FIGURE 2 | Generation of structure-free normalized image for spark identification and localization. **(A)** Original x-y image. **(B)** F/F_0 image to show that the structure was removed and only the sparks are visible. **(C)** Fiber structure superimposed with areas of sparks. **(D)** Part of the image in **(B)** showing four events at high magnification. White curves encircle the areas corresponding to the identified events. Yellow dots present the position of the maxima, while the four blue dots in each event show the orientation of the two axis (perpendicular and parallel to the Z-lines) within the spark. Red pixels represent the position of the fluorescence maximum of Fluo-4, and thus the distance between yellow and red pixels was used to calculate the distance of the center of the spark from the nearest Z-line. **(E)** Same area as in panel **(B)** enlarged from panel **(C)** showing the superimposed Z-lines. The dark bands mark the triads at the Z-lines. **(F)** A spark enlarged from panel **(E)** showing the location of color dots described above. Light blue lines show the fluorescence maximum (i.e., the middle of a sarcomere).

no sparks at random locations (minimal distance of sparks was 4 μm). Number of sparks per frame (30) and spatial parameters corresponded to the averages found under control conditions (Full-width at half maximum in the X direction, FWHM-X = 1.74 μm; Full-width at half maximum in the Y direction, FWHM-Y = 1.52 μm). The amplitude ranged between 0.15 and 0.6. The sensitivity of the wavelet based detection method was proven, all events with amplitude higher than 0.2 were identified (**Supplementary Figure 3B**). Events with amplitude of 0.2 were captured with around 0.6 sensitivity while events with smaller amplitude were lost. The positive predicted curve (**Supplementary Figure 3C**) was, however, very sharp, all events with amplitude higher than 0.15 were identified correctly. According to these findings events with amplitude less than 0.15 were excluded from all further evaluation. Due to the large number of sparks in x-y images analyzed, small sparks not found due to the chosen thresholds did not cause any significant drop in the analysis and considered as out of focus events.

Within all identified ROI a 3 × 3 area with the highest average amplitude was determined and the center was defined as the center of the event (**Figure 2D**). The difference between the fluorescence intensity of this point and the baseline was used to calculate the amplitude of the spark. The program also considered this point as focal point in the direction parallel and perpendicular to the Z-lines. Where the average intensity of three points reached half of the amplitude value of the spark, the program identified these points as the boundaries of FWHM-X and FWHM-Y. The distance for each event from the nearest Z-line was assessed by calculating the difference of the estimated half sarcomere length and the distance from the nearest fluorescence maximum (**Figure 2E**). The position of the center of the spark was identified on each consecutive image and was used to calculate the movement of the spark, if present, in the X and Y directions.

The effects of the amplitude on the other parameters of the spark were also tested. Images (n = 40) containing artificial sparks with different amplitudes (n = 30) were evaluated and the amplitude and FWHM in both directions were calculated. The program slightly under estimated the original amplitudes (**Supplementary Figure 4A**). Calculated FWHMs at

szentesi.peter_292_24

both directions were the most accurate at 0.25 amplitude. At smaller amplitudes both FWHMs were under estimated, while at higher amplitudes they were overestimated (**Supplementary Figures 4B,C**). We also tested the effects of the orientation of fiber in the image on FWHMs. By limiting the ROI to the central part of the events, the FWHM values (**Supplementary Figure 5**) and eccentricity of sparks (**Supplementary Figure 6B**; see below) were not affected by fiber orientation.

Ca^{2+} spark frequency was calculated from the number of sparks during the recording period divided by the area of the fiber and the duration of the acquisition (number of sparks per area per time) at each conditions.

Signal mass (SM) was calculated as follows:

$$SM = 1.206 \times (FWHM - X) \times (FWHM - Y) \times \left(\frac{(FWHM - X)}{2} + \frac{(FWHM - Y)}{2}\right), \quad (1)$$

where Amp is the amplitude, while FWHM-X and FWHM-Y have their usual meaning (Hollingworth et al., 2001). The spark was assumed to be a spherical 3D object with different X, Y and Z diameters. The diameter in the Z direction was estimated as the average of the X and Y diameter.

To assess the shape of the recorded spark a modified eccentricity value was calculated defined as:

$$E = 1 - \left(\frac{FWHM - Y}{FWHM - X}\right)^2, \quad (2)$$

Note that this is different from the classical definition of eccentricity for an ellipsis (see **Supplementary Figure 6**) to account for the case when FWHM-Y is greater than FWHM-X.

Chemicals and Statistical Analysis

Chemicals, unless otherwise stated, were purchased from Sigma (St. Louis, CA, United States) and were of analytical grade.

Pooled data were expressed as mean ± standard error (SE) of the mean. The differences between control and treatments was assessed using one-way analysis of variance (ANOVA) and all pair wise multiple comparison procedures (Student-Newman-Keuls Method). F test was used to test the significance and a p value of less than 0.05 was considered statistically significant.

RESULTS

Event Frequency and Parameters of Sparks in Different Conditions

Both caffeine treatment and depolarization increased the frequency, the amplitude, the spatial dimensions, and the signal mass of sparks in frog skeletal muscle fibers (**Table 2** and **Figures 3**, **4**). Using incremental depolarization steps, the highest frequency was found at -60 mV (**Table 2**). In the presence of 1 mM caffeine sparks occurred at higher frequency. Depolarization and caffeine treatment together led to even more sparks (**Table 2**). Simultaneously applied depolarization and caffeine gave the highest frequency at -65 mV. However, at this voltage both the amplitude, the spatial spread, and the signal mass were significantly reduced. This was likely due to the fact that the depolarization induced a partial inactivation of the voltage sensors (e.g., Huang, 1996) and the large frequency of sparks induced a partial depletion of calcium in the SR thus 1./greater depolarizations in the presence of caffeine were not explored in detail and 2./except for **Table 2** the data for caffeine treatment at -65 mV were not combined with the other data and are presented in **Supplementary Figures 7–9**.

Calcium sparks detected on frog fibers were not symmetric in the spatial domain, their FWHM was smaller in the Y then in the X direction. Average FWHM in both directions was increasing with increased depolarization and further increased when caffeine was added (**Table 2**). The distribution histograms of spark parameters clearly demonstrate that both depolarization and caffeine increased the frequency of the larger sparks (**Figures 4B–D**), the effect was more pronounced for the latter. Since both depolarization and caffeine treatment elicit sparks with larger spatial widths, the calculated signal mass was also higher under these conditions (**Table 2**).

Representative images are shown for the three treatment groups in **Figure 5A** that display the cumulated number of sparks recorded in every 16 × 16 pixel regions of the fiber. Under control conditions only few active positions existed while during depolarization and in the presence of caffeine the events seemed to appear more equally spread along the fiber. The distribution of spark numbers among dedicated regions (16 × 16 pixel mesh) was compared to the Poisson distribution for all three treatments (**Figure 5B**). Since the theoretical Poisson functions calculated with the λ equal to the average of the event number was almost identical to the Poisson functions fitted to the measured values, our result suggests that both depolarization and caffeine treatment increased the frequency of the events evenly along the fiber without creating spatial clusters or 'hot spots' identified by concentrated activity specific to each conditions (**Figure 5A**).

Based on the spatial cluster analysis we hypothesized that sparks were randomly distributed within the cell, therefore the distance distribution of the center-to-center for each spark pair would follow a linear function. **Figure 6** presents the distances between all spark pairs on each frame for all images recorded. Only distances where one of the sparks was in the center of the respective fiber were considered in order to compensate for the finite size of the fiber. Furthermore, distances that were less than the radius of the given fiber were calculated. It should also be noted that events with centers closer than two FWHM could not be separated by the automated detection method (as their "contiguous areas" overlap and thus they are detected as a single, but large event; see Methods) thus only those sparks were considered where the centers were at least 15, 17, and 20 pixels (control, depolarization and caffeine, respectively) apart. Concentric squares (grid distance) were used instead of circles so as not to have any bias because of the grid pattern of pixels. Under control conditions (**Figure 6A**), on depolarized fibers (**Figure 6B**) and even in the presence of caffeine (**Figure 6C**) the data follow

TABLE 2 | Parameters of sparks in different conditions.

	0 mM Caffeine				1 mM Caffeine		
	NR	**−70 mV**	**−65 mV**	**−60 mV**	**NR**	**−70 mV**	**−65 mV**
Number of fibers	106	64	47	33	21	8	7
Number of events[§]	6164	55312	43326	21410	24942	16029	12391
Frequency (1/ms/mm^2)	1.47 ± 0.30	24.10 ± 3.80$^{*\#}$	37.15 ± 4.35*	38.15 ± 8.25*	91.54 ± 21.36$^{*\#}$	115.28 ± 40.34$^{*\#}$	147.77 ± 60.40$^{*\#}$
Amplitude (F/F_0)	0.188 ± 0.001	0.171 ± 0.001$^{*\#}$	0.164 ± 0.001*	0.173 ± 0.001$^{*\#}$	0.259 ± 0.001$^{*\#}$	0.305 ± 0.001$^{*\#}$	0.176 ± 0.001$^{*\#}$
FWHM-X (μm)	1.725 ± 0.005	1.836 ± 0.002$^{*\#}$	1.917 ± 0.003*	2.089 ± 0.004$^{*\#}$	2.342 ± 0.005$^{*\#}$	2.482 ± 0.005$^{*\#}$	2.150 ± 0.006$^{*\#}$
FWHM-Y (μm)	1.508 ± 0.004	1.587 ± 0.001$^{*\#}$	1.676 ± 0.002*	1.776 ± 0.004$^{*\#}$	2.081 ± 0.005$^{*\#}$	2.270 ± 0.006$^{*\#}$	1.845 ± 0.005$^{*\#}$
SM (μm^3)	1.024 ± 0.009	1.138 ± 0.004$^{*\#}$	1.335 ± 0.007*	1.776 ± 0.004$^{*\#}$	4.354 ± 0.034$^{*\#}$	6.464 ± 0.062$^{*\#}$	2.085 ± 0.021$^{*\#}$

[§]*All events with amplitude less than 0.1 and FWHM less than 1 and greater than 10 μm were discarded.*
**denotes significant difference from NR at $p < 0.001$.*
#denotes significant difference from −65 mV without caffeine treatment at $p < 0.001$.

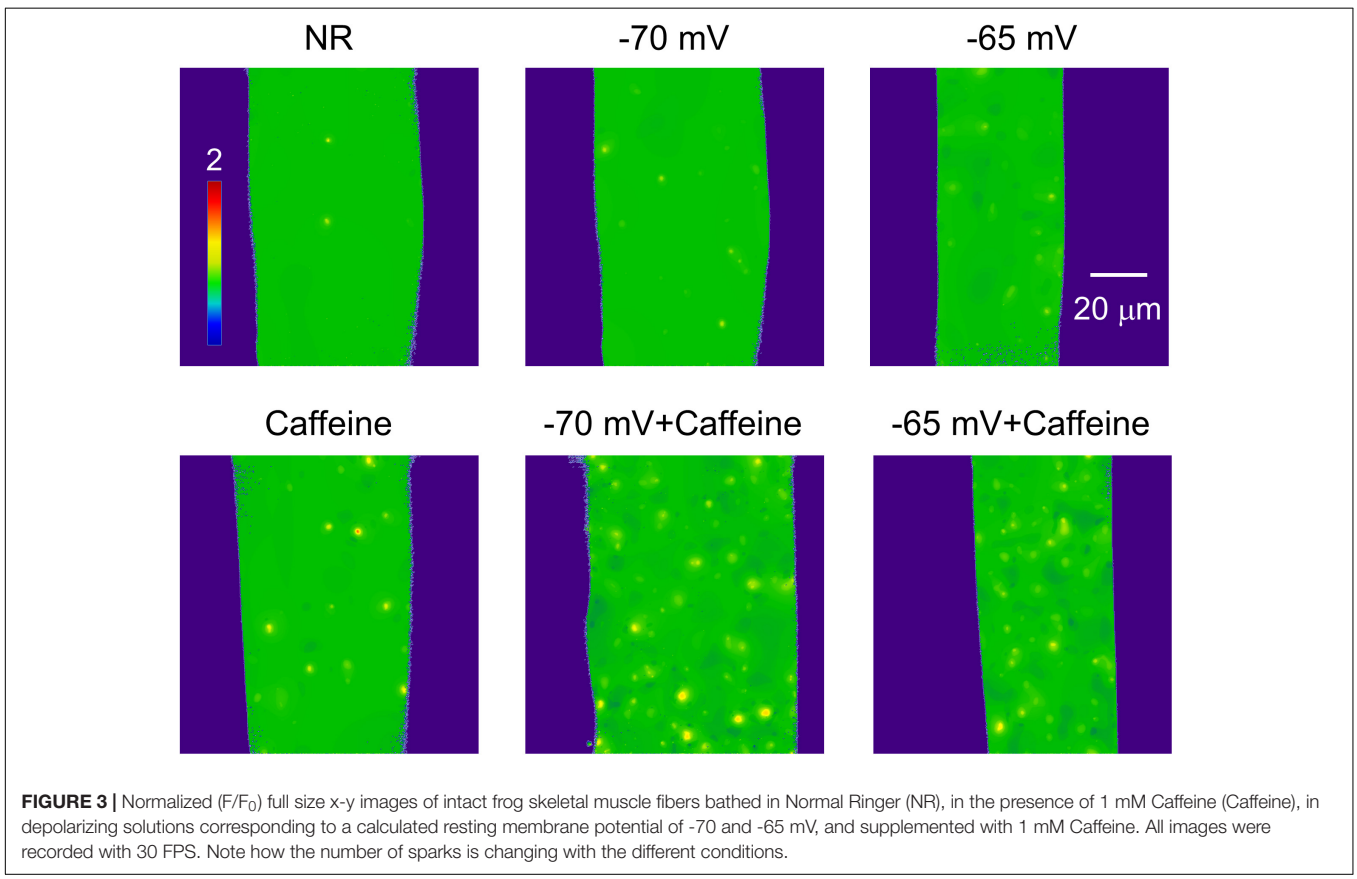


FIGURE 3 | Normalized (F/F_0) full size x-y images of intact frog skeletal muscle fibers bathed in Normal Ringer (NR), in the presence of 1 mM Caffeine (Caffeine), in depolarizing solutions corresponding to a calculated resting membrane potential of -70 and -65 mV, and supplemented with 1 mM Caffeine. All images were recorded with 30 FPS. Note how the number of sparks is changing with the different conditions.

a close to linear function, as demonstrated by the superimposed dashed lines, confirming the random distribution of the events.

Relative Position of Sparks to Z-Lines and Other Events

The determination of fiber structure during the analysis of images allowed us to examine the positions of sparks relative to the Z-lines. **Figure 7A** shows the position and orientation of Z-lines with superimposed sparks (the outlines of sparks are marked with white curves in the enlarged images). The histogram in **Figure 7B** presents the distribution of the distances of the position of the pixel with the highest intensity for each spark from the nearest Z-line. Under control conditions the average distance was calculated to be 0.311 ± 0.003 μm, which was increased significantly either by depolarization (0.401 ± 0.001 μm) or caffeine (0.391 ± 0.002 μm) treatment (**Figure 7C**).

Spatial Morphology of Sparks

To address the spatial orientation of sparks relative to the Z-lines FWHM-X and FWH-Y were measured under all experimental conditions and the modified eccentricity was calculated. As demonstrated in **Figure 8A**, the modified eccentricity showed

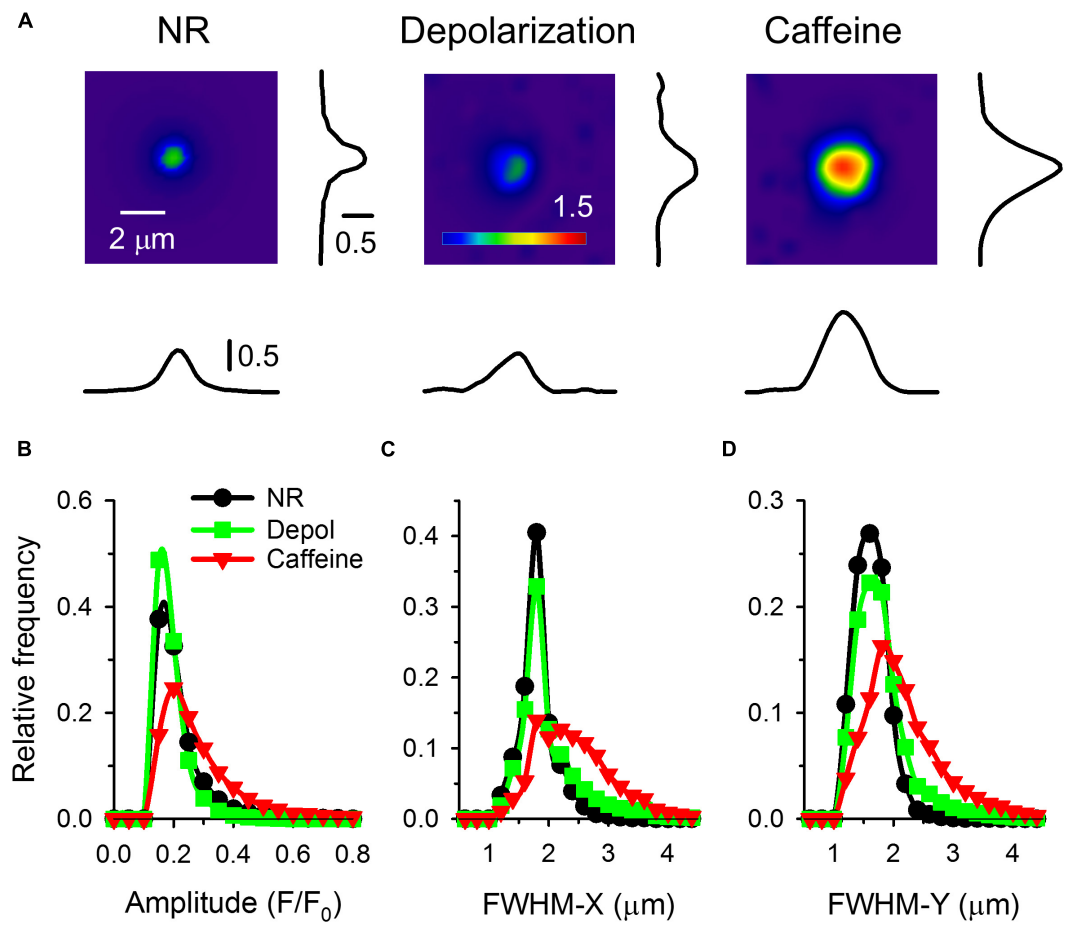


FIGURE 4 | (A) Individual sparks on a larger scale. All images were recorded with 30 FPS. Next to the spark the spatial profile of F/F_0 in X & Y direction (parallel and perpendicular to fiber axis) are presented. Panels **(B–D)** present the distribution histograms for the amplitude **(B)**, FWHM-X **(C)**, and FWHM-Y **(D)** under control conditions (black circles), on fibers depolarized to a calculated value of -65 mV (green squares), and in the presence of 1 mM caffeine (red triangles). Note how both depolarization and caffeine has shifted the distribution the higher values, especially visible in case of FWHM-X and FWHM-Y in the presence of caffeine from 2.5 μm to 4 μm.

an asymmetric distribution both under control conditions, on depolarized fibers, and in the presence of caffeine, indicating that FWHM-X was greater than FWHM-Y for most of the events detected. It is also clear from the histogram that the modified eccentricity was most frequent found between 0.30 and 0.42. This value is significantly greater than that expected to be introduced by scanning (see **Supplementary Figure 6**). Furthermore, larger modified eccentricity values appeared with greater frequency in depolarized as well as in caffeine treated cells. This is reflected in the mean values of modified eccentricity, as this mean was significantly greater for both the depolarized condition and the caffeine treatment (**Figure 8B**). Importantly, the asymmetric shape of the events suggests that either the source is extended or the diffusion is faster in the X direction, or both.

Travelling Sparks

Most sparks were visible only in one frame even when detected with high speed confocal microscopy. For sparks that were present in more than one consecutive frames (**Figure 9A**; **Supplementary Video 2**, **3**), the distance traveled by the center of the spark between two frames was calculated (**Figures 9B–D**). Note that a traveling spark indicates the presence of calcium-induced opening of RyR(s) that didn't get activated first at the beginning of the event.

While under control conditions only 1.5% of events appeared in two consecutive images, the probability was higher in depolarized fibers (9.8%) and even higher after caffeine treatment (29.7%). Sparks traveled significantly longer distances after caffeine treatment (1.66 ± 0.01 μm, n = 7416) than in depolarized fibers (0.95 ± 0.01 μm, n = 4247) which, nonetheless, was still significantly longer than under control conditions (0.52 ± 0.01 μm, n = 94; **Figure 9D**). While under control conditions and during depolarization the distance traveled by the events was the same in X and Y directions, in the caffeine-treated cells sparks traveled significantly longer distances especially in the Y direction ($p < 0.001$; **Figures 9B,C**). These results indicate that depolarization and caffeine treatment "primed" the release sites for subsequent activation by calcium.

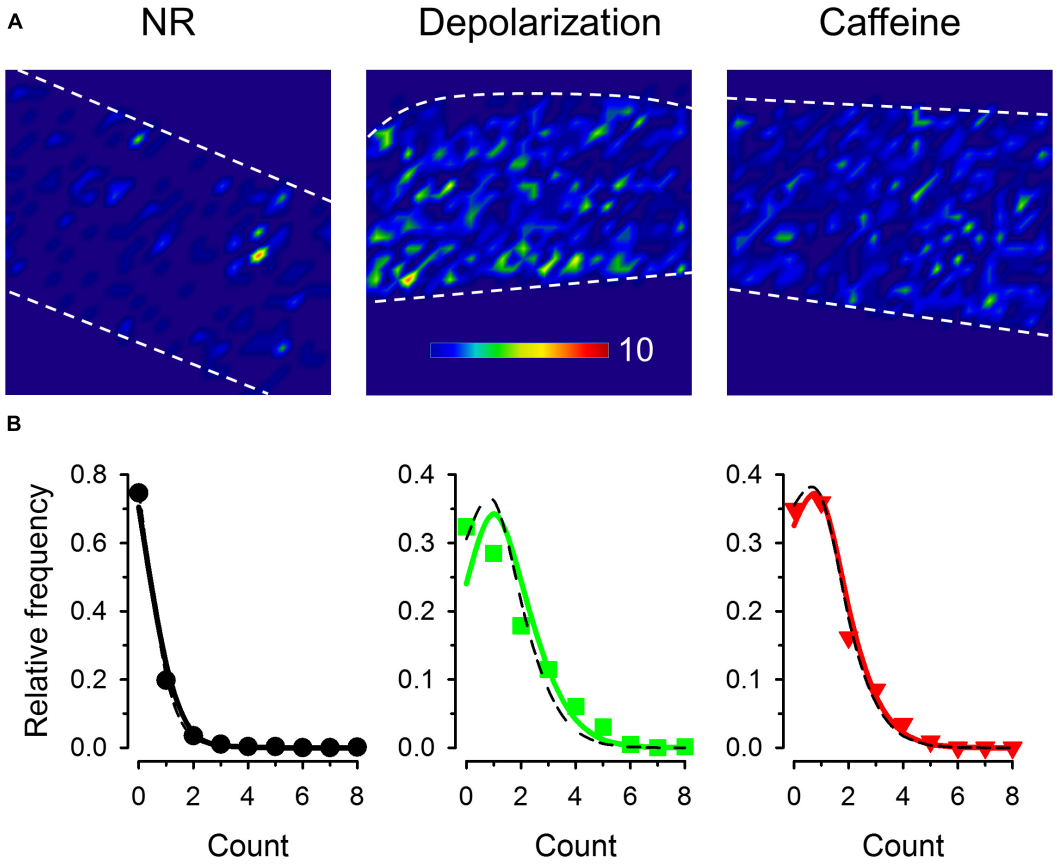


FIGURE 5 | Identifying positions of spark occurrence in images. **(A)** Mesh plot of frequencies of spark occurrence (i.e., the number of sparks in the given region) in a 16 × 16 pixel voxels (generated from 60 consecutive images). All images were recorded with 30 FPS. **(B)** Frequency distribution of regions with different number of sparks. Solid line superimposed is the fitted Poisson distribution, while dashed black curves show the Poisson distribution generated with λ being equal to the average event numbers. The values for λ used to generate the dashed curves were 0.349, 1.42, and 1.12 while those obtained from the fits were 0.281, 1.19, and 1.04 for control conditions, for depolarized fibers, and in the presence of caffeine, respectively.

DISCUSSION

In the past 15 years several automatic Ca^{2+} spark analyzer programs were developed. Some of them used Wavelet transformation methods (von Wegner et al., 2006; Szabo et al., 2010, Prada et al., 2018). Others employed noise thresholding (Picht et al., 2007), statistical analysis (Bányász et al., 2007), or pixel-by-pixel method (Illaste et al., 2019; Tian et al., 2019) to capture and analyze local calcium events.

In this study we showed that our Wavelet based automatic analysis method was suitable to reveal the spatial and temporal characteristics of calcium sparks detected via high-speed confocal microscopy. The program not only captured the calcium release events but was capable of identifying constant cell structures, like Z-lines, and calculate the distance between these structures and the detected sparks. Furthermore, it could calculate the distance between sparks and follow the movement of events appearing in consecutive images. These new features allowed us to describe the behavior of localized elementary calcium release more precisely, perform high throughput data analysis. It also gave us the opportunity to raise hypotheses on the role of the two types of RyRs present in frog skeletal muscle.

RyRα and RyRβ are present in nearly equal amounts in frog skeletal muscle, and are homologs of RyR1 and RyR3 of mammalian muscles (Ogawa et al., 2002). The depolarization-induced Ca^{2+} release is believed to be mediated by RyRα because of its similarity to RyR1 (Oyamada et al., 1994) and its location adjacent to DHPRs. While calcium-induced calcium release works with both types of RyRs in frog skeletal muscle, its activity on RyRα may have 20-fold lower than that on RyRβ (Murayama and Ogawa, 2001). From this, one can hypothesize that the two isoforms of RyR may have distinct roles in calcium release. We successfully showed that sparks detected on depolarized or caffeine treated frog muscle fibers have distinct spatiotemporal parameters and amplitude distribution in our experiments.

We found that sparks appeared at a higher frequency in both depolarized and caffeine treated fibers as compared to control. Importantly, although both the depolarization and caffeine increased both the signal mass of the sparks – i.e., the amount of calcium released during the event – and their frequency, this was not always the case when applied together. At greater

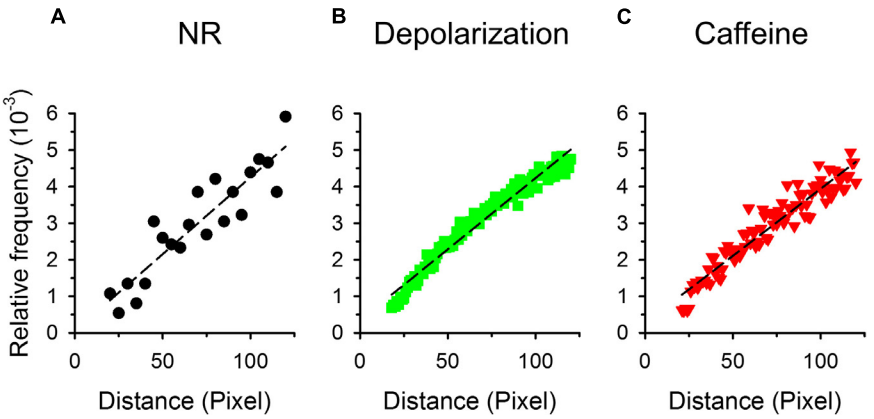


FIGURE 6 | Distribution of the distances between the centers of two sparks. For each spark concentric squares were constructed around the center of the selected spark. The number of sparks with centers falling onto the side of the given square were then counted. The relative frequency of these neighboring sparks are presented for control conditions **(A)**, for depolarized **(B)**, and caffeine-treated fibers **(C)**. Note that in this representation the number of pixels increases linearly with the length of the side of the square, thus if sparks appear randomly a linearly increasing distribution is expected. To avoid the problem of bringing pixels from outside of the fiber into the counting 1./only those sparks were selected that lay close to the center of the fiber and 2./the side of the square was restricted to being less the 120 pixels (appr. 25 μm). Thus in the panels **(A–C)** the ordinate is in pixels. Dashed lines represent least-squares fits of a straight line to the data points in each graph with R^2 being 0.829, 0.964, and 0.918, for panels **(A–C)**, respectively.

depolarizations albeit the frequency was further increased, the signal mass, due to a drop in both the amplitude and the spatial spread, decreased dramatically. This can be reconciled if one assumes that the large number of events leads to a partial depletion of calcium in the terminal cisternae of the SR. Indeed, if the rate of calcium release exceeds the uptake rate of the SR calcium pump one expects a depletion of calcium in the SR. However, in this case the cytosolic calcium concentration should increase as the released but not reuptake calcium should appear in the intracellular space. Although Fluo-4 is not suitable to allow a precise calculation of the exact calcium concentration, the overall increase in fluorescence seen at greater depolarizations supports this idea.

The analysis of FWHM on depolarized fibers treated with caffeine (**Supplementary Figure 7**) suggests that the two interventions exerted their effect independent of one another. We also observed widening of the spatial spread and shifting of the center of the spark further away from the Z-line (**Figure 7C** and **Supplementary Figure 9A**). In this framework under control conditions a small group of RyRα-s open under a strict control of DHPRs and depolarization recruits additional RyRα-s. The calcium thus released can then albeit to a small extent activate additional release channels via CICR. The addition of caffeine primes the release channels to the activating calcium making CICR more probable. As RyRβ-s are more sensitive to caffeine than RyRα (see e.g., Murayama and Ogawa, 2001; Kashiyama et al., 2010) calcium sparks in the presence of caffeine are likely to be generated more by RyRβ than by RyRα. This is reflected in our finding that sparks in the presence of caffeine appear with greater amplitude and frequency (**Table 2**). RyR-deficient myotubes expressing RyRα have uniform and sustained calcium release, whereas cells expressing RyRβ have regenerative Ca^{2+} release events (waves and oscillations; Kashiyama et al., 2010). Examining the distribution of amplitudes and FWHMs of the sparks revealed that under control conditions the spontaneously generated calcium sparks were initiated predominantly by RyRα since the distribution of their parameters was similar to those on depolarized fibers (**Figures 4B–D**). An important finding of our study was that the signal mass of sparks (representing the amount of calcium released) was only slightly increased by depolarization, but multiplied after caffeine treatment (**Table 2**).

The high number of events allowed us to statistically analyze the appearance of sparks macroscopically in a fiber. One important finding was that there were no "hot spots" where more sparks would develop than at other places in intact frog skeletal muscle fibers. The appearance of sparks in the whole fiber followed the Poison distribution in all cases examined (**Figure 5**). Similar results were found by Klein et al. (1996) during depolarization in also frog muscle fibers. This suggests that the events arose following a random process independently from depolarization and the presence of caffeine. The microscopic analysis of event position lead to the same conclusion. Interspark distances are close to linearly distributed on depolarized or caffeine treated muscle fibers indicating that sparks form independently from one another (**Figure 6**). Nevertheless, a slight deviation from this linearity can be observed at short distances on depolarized fibers and in the presence of caffeine. It was hypothesed by Stern et al. (2013) that calcium release from one couplon could influence its neighbors in several ways: (1) SR calcium can travel to other couplons by diffusion within the SR lumen; (2) cytosolic calcium can diffuse to activate or influence RyRs; and (3) SR calcium can be increased by SERCA uptake following the diffusion in the cytosol.

Calcium sparks were asymmetric and wider in the direction parallel to the axis of the muscle fibers. The events exhibited some eccentricity (**Figure 8**, **Supplementary Figures 6**, **9**B) comparable to that what was reported for the RyR cluster shape in cardiac myocytes (Galice et al., 2018). This behavior of sparks

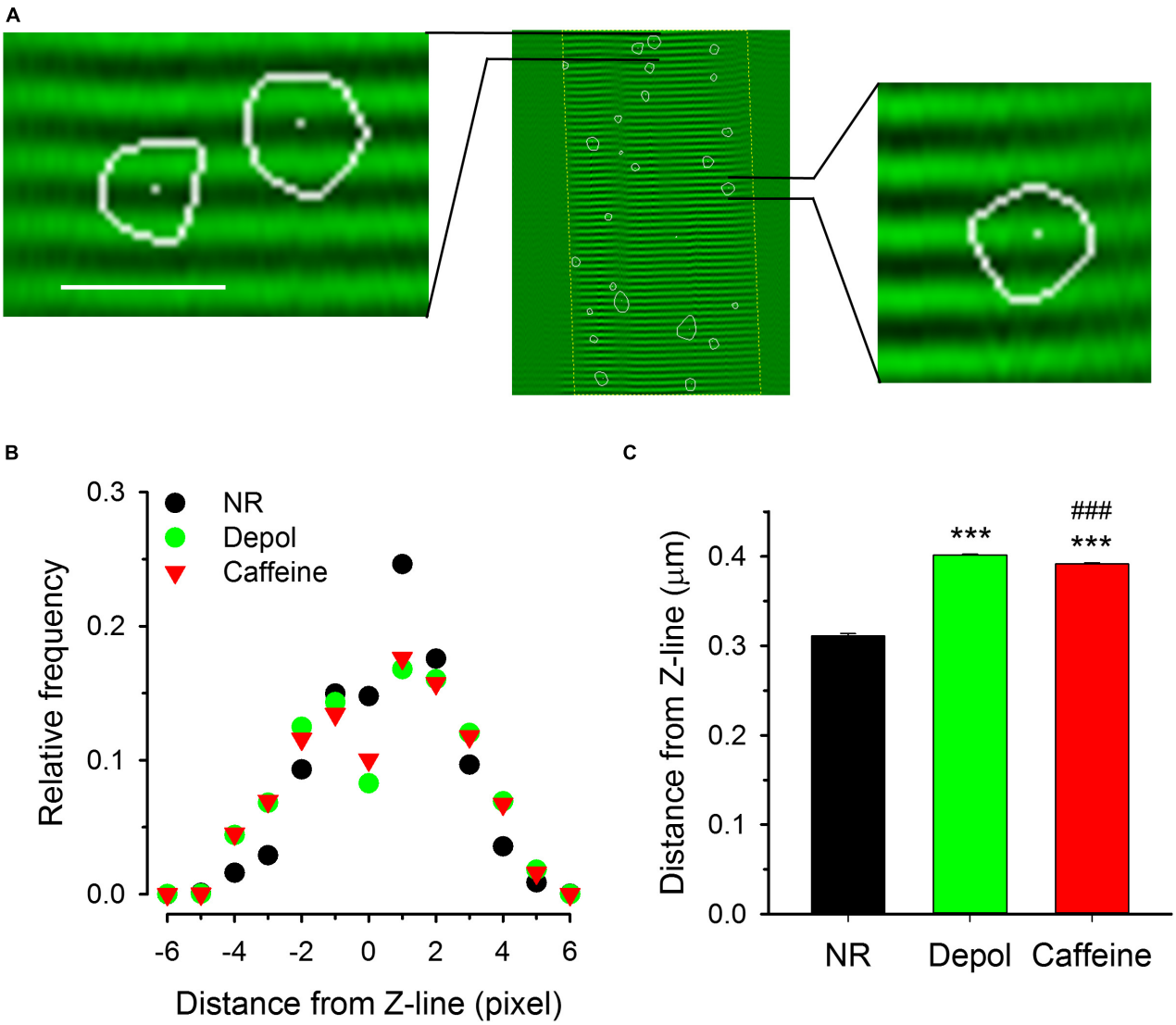


FIGURE 7 | Localization of spark centers relative to the Z-line. **(A)** Two samples from an image showing the fiber structure superimposed with sparks (indicated by the areas encircled by the white lines). White dots present the position of the center of the sparks. **(B)** Distribution histograms of the distance between center of sparks and the nearest Z-line for control conditions (NR, black circles), on depolarized fibers (green squares), and in the presence of caffeine (red triangles). Note that the distributions are essentially symmetric to the Z-line. **(C)** Mean distances of spark centers under the three conditions. Both the depolarization and the presence of caffeine shifted the center of the spark to positions further away from the Z-line as compared to the control conditions. Scale in panel A corresponds to 40 μm for the middle image and 4.3 μm for the enlarged images on left and right side. The middle image was recorded with 30 FPS. Here and in subsequent figures *** denotes significant difference versus NR at $p < 0.001$, ### denotes significant difference vs. Depol at $p < 0.001$.

was independent of the depolarization and caffeine treatment suggesting the idea that the size of RyR cluster creating a sparks was greater than in control but similar in the two investigated conditions. We have to underline that the difference between the FWHM values in the X and in the Y direction did not result from the non-instantaneous scanning of the frame (**Supplementary Figure 6A**). Taking the value for the speed of Ca^{2+} diffusion in the cytosol (0.73 μm/ms; Donahue and Abercrombie, 1987) and the speed of scanning (3.19 μm/ms, calculated as 106 μm/512/0.065 ms from 65 μs/line, 512 lines/frame, 106 μm/frame scanning parameters) one can conclude that the speed of diffusion is around one quarter of the scanning. This would result in a deformed spot of release (see **Supplementary Figure 6A**) and contribute to the eccentricity of events. The theoretical eccentricity calculated from the two speeds (diffusion divided by scanning) was 0.23 in our case. Eccentricity, however, did not take the orientation of the spark relative to that of the fiber into account. We have, thus introduced a modified eccentricity to keep this spatial information. From the calculations the eccentricity introduced by the scanning and represented by the value of the modified eccentricity was much smaller than those observed under either condition (see **Supplementary Figure 5**).

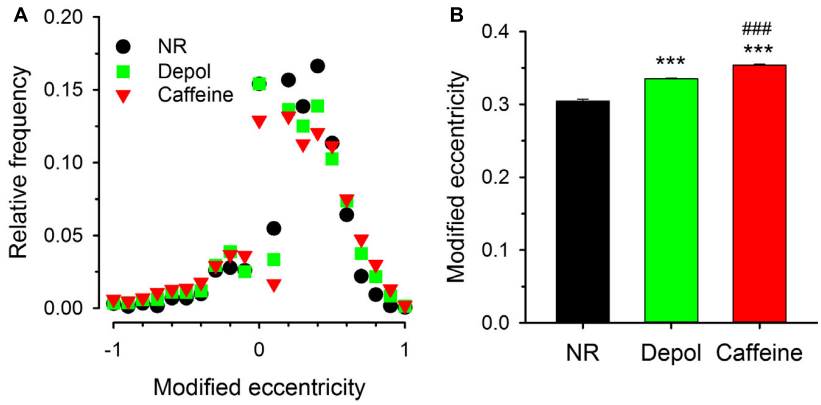


FIGURE 8 | Modified eccentricity of the sparks **(A)**. Distribution of the modified eccentricity calculated using Eqn. 2 for control conditions (NR, black circles), for depolarized fibers (green squares), and in the presence of caffeine (red triangles). Note that albeit negative values were present, the distribution is not symmetric, it is shifted toward positive values indicating that FWHM-X was, in most cases, greater than FWHM-Y. **(B)** Average modified eccentricity for the three experimental conditions calculated using only the positive values from panel **(A)**. Note that both the depolarization and caffeine treatment increased the modified eccentricity, and, furthermore, its value was far greater even under control conditions than what is expected from the skewing introduced by the scanning.

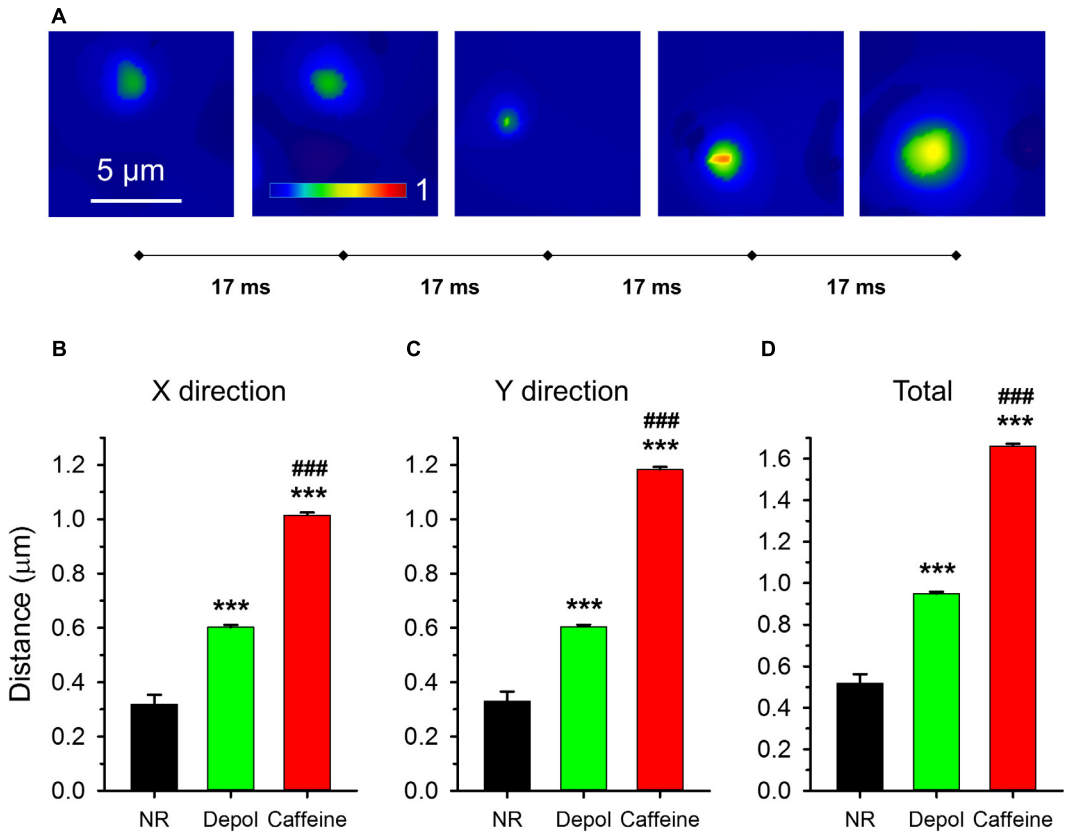


FIGURE 9 | Traveling events on consecutive x-y images. **(A)** Five consecutive F/F_0 images with the traveling sparks identified. The sampling rate was 17 ms/image (60 FPS). **(B–D)** Averages of distances traveled. **(B,C)** report distances in X and Y direction, respectively, while panel **(D)** presents the total distance traveled. The numbers of events analyzed are presented in **Table 2**.

This indicates that either the source was extended or the diffusion was not homogenous in all directions, or both. Furthermore, as both the depolarization and caffeine increased the value of modified eccentricity and neither is likely to alter the diffusion of calcium in the cytosol, one must conclude that they affected the size of the source. This is substantiated by the finding that

szentesi.peter_292_24

both interventions increased the signal mass, i.e., the amount of calcium released, in an event.

The detailed examination of consecutive images provided that only a minority (1.5%) of sparks could "travel" from their origin by around half μm under control conditions. Depolarization doubled and caffeine tripled this distance in average (**Figure 9D**) and the number of traveling sparks increased dramatically in both cases (∼10% and ∼30% of all events, respectively). Similar observation was obtained after the application of the special calcium chelator TPEN (Sztretye et al., 2009). All these interventions, depolarization and caffeine in this report and TPEN in that of Sztretye et al. (2009) have one feature in common. Namely, they prime RyRs for oncoming activating stimuli, in our case the calcium that diffuses from a neighboring release site. The observation that caffeine promoted longer distances of traveling than the depolarization did argue in favor of the hypothesis that the latter involved RyRs located further away from the original release site.

CONCLUSION

In this study we have analyzed a vast number of calcium sparks from intact frog skeletal muscles under control condition, during subthreshold depolarizations and in the presence of caffeine. We have introduced a method that enabled us to obtain spatial information of spark morphology and location relative to the orientation of the fiber axis and the Z-line. Understanding the role of CICR in the generation of spontaneous calcium sparks could help in revealing the mechanisms underlying the appearance of such events under pathological conditions and during regeneration in mammalian skeletal muscle. Furthermore, the role RyRα and RyRβ play in the generation of spontaneous calcium sparks should shed light on the interaction of RyR1 and RyR3 in those mammalian muscle fibers where RyR3 is expressed in greater amounts.

DATA AVAILABILITY STATEMENT

The raw data supporting the conclusions of this article will be made available by the authors, without undue reservation.

ETHICS STATEMENT

The animal study was reviewed and approved by University of Maryland Institutional Animal Care and Use Committee.

AUTHOR CONTRIBUTIONS

HC and MS designed the experiments. HC participated in the confocal microscopy spark experiments. JV wrote the image analyzer program. BD, HC, LC, and PS wrote the manuscript. DB, JV, and PS did the statistical analysis and prepared the figures. All authors contributed to discussion, and reviewed/edited the manuscript.

FUNDING

This work was supported by NIH grant 5R01NS023346 to MS. This work was supported by grant from the Hungarian National Research, Development and Innovation Office (EFOP-3.6.2-16-2017-0006 and GINOP-2.3.2-15-2016-00044). The project is co-financed by the European Union and the European Regional Development Fund.

SUPPLEMENTARY MATERIAL

The Supplementary Material for this article can be found online at: https://www.frontiersin.org/articles/10.3389/fphys.2020.599822/full#supplementary-material

REFERENCES

Bányász, T., Chen-Izu, Y., Balke, C. W., and Izu, L. T. (2007). A new approach to the detection and statistical classification of $Ca2^{+}$ sparks. *Biophys*. J. 92 4458–4465. doi: 10.1529/biophysj.106.103069

Brum, G., Gonzalez, A., Rengifo, J., Shirokova, N., and Rios, E. (2000). Fast imaging in two dimensions resolves extensive sources of Ca2+ sparks in frog skeletal muscle. *J. Physiol.* 528, 419–433. doi: 10.1111/j.1469-7793.2000.00419.x

Cheng, H., Lederer, W. J., and Cannell, M. B. (1993). Calcium sparks: elementary events underlying excitation-contraction coupling in heart muscle. *Science* 262, 740–744. doi: 10.1126/science.8235594

Cheng, H., Song, L. S., Shirokova, N., González, A., Lakatta, E. G., Ríos, E., et al. (1999). Amplitude distribution of calcium sparks in confocal images: theory and studies with an automatic detection method. *Biophys. J.* 76, 606–617. doi: 10.1016/S0006-3495(99)77229-2

Dayal, A., Schrötter, K., Pan, Y., Föhr, K., Melzer, W., and Grabner, M. (2017). The Ca2+ influx through the mammalian skeletal muscle dihydropyridine receptor is irrelevant for muscle performance. *Nat. Comm.* 8:475. doi: 10.1038/s41467-017-00629-x

Donahue, B. S., and Abercrombie, R. F. (1987). Free diffusion coefficient of ionic calcium in cytoplasm. *Cell Calcium* 8, 437–448. doi: 10.1016/0143-4160(87)90027-3

Felder, E., and Franzini-Armstrong, C. (2002). Type 3 ryanodine receptors of skeletal muscle are segregated in a parajunctional position. *Proc. Natl. Acad. Sci. U.S.A.* 99, 1695–1700. doi: 10.1073/pnas.032657599

Franzini-Armstrong, C. (2004). Functional implications of RyR-dHPR relationships in skeletal and cardiac muscles. *Biol. Res.* 37, 507–512. doi: 10.4067/s0716-97602004000400003

Franzini-Armstrong, C., and Protasi, F. (1997). Ryanodine receptors of striated muscles: a complex channel capable of multiple interactions. *Physiol. Rev.* 77, 699–729. doi: 10.1152/physrev.1997.77.3.699

Galice, S., Xie, Y., Yang, Y., Sato, D., and Bers, D. M. (2018). Size matters: ryanodine receptor cluster size affects arrhythmogenic sarcoplasmic reticulum calcium release. *Heart Assoc.* 7:e008724. doi: 10.1161/JAHA.118.008724

Gonzalez, A., Kirsch, W. G., Shirokova, N., Pizarro, G., Brum, G., Pessah, I. N., et al. (2000a). Involvement of multiple intracellular release channels in calcium sparks of skeletal muscle. *PNAS* 97, 4380–4385. doi: 10.1073/pnas.070056497

Gonzalez, A., Kirsch, W. G., Shirokova, N., Pizarro, G., Stern, M. D., and Rios, E. (2000b). The spark and its ember: separately gated local components of Ca2+

szentesi.peter_292_24

release in skeletal muscle. *J. Gen. Physiol.* 115, 139–157. doi: 10.1085/jgp.115.2.139

Hollingworth, S., Peet, J., Chandler, W. K., and Baylor, S. M. (2001). Calcium sparks in intact skeletal muscle fibers of the frog. *J. Gen. Physiol.* 118, 653–678. doi: 10.1085/jgp.118.6.653

Huang, C. L. (1996). Kinetic isoforms of intramembrane charge in intact amphibian striated muscle. *J. Gen. Physiol.* 107, 515–534. doi: 10.1085/jgp.107.4.515

Illaste, A., Wullschleger, M., Fernandez-Tenorio, M., Niggli, E., and Egger, M. (2019). Automatic detection and classification of Ca2+ release events in line- and frame-scan images. *Biophys. J.* 116, 383–394. doi: 10.1016/j.bpj.2018.12.013

Isaeva, E. V., Shkryl, V. M., and Shirokova, N. (2005). Mitochondrial redox state and Ca2+ sparks in permeabilized mammalian skeletal muscle. *J. Physiol.* 565, 855–872. doi: 10.1113/jphysiol.2005.086280

Kashiyama, T., Murayama, T., Suzuki, E., Allen, P. D., and Ogawa, Y. (2010). Frog alpha- and beta-ryanodine receptors provide distinct intracellular Ca2+ signals in a myogenic cell line. *PLoS One* 5:e11526. doi: 10.1371/journal.pone.0011526

Kirsch, W. G., Uttenweiler, D., and Fink, R. H. (2001). Spark- and ember-like elementary Ca2+ release events in skinned fibres of adult mammalian skeletal muscle. *J. Physiol.* 537, 379–389. doi: 10.1111/j.1469-7793.2001.00379.x

Klein, M. G., Cheng, H., Santana, L. F., Jiang, Y. H., Lederer, W. J., and Schneider, M. F. (1996). Two mechanisms of quantized calcium release in skeletal muscle. *Nature* 379, 455–458. doi: 10.1038/379455a0

Klein, M. G., Lacampagne, A., and Schneider, M. F. (1997). Voltage dependence of the pattern and frequency of discrete Ca2+ release events after brief repriming in frog skeletal muscle. *Proc. Natl. Acad. Sci. U.S.A.* 94, 11061–11066. doi: 10.1073/pnas.94.20.11061

Klein, M. G., and Schneider, M. F. (2006). Ca2+ sparks in skeletal muscle. *Prog. Biophys. Mol. Biol.* 92, 308–332. doi: 10.1016/j.pbiomolbio.2005.05.016

Murayama, T., and Ogawa, Y. (2001). Selectively suppressed Ca2+-induced Ca2+ release activity of alpha-ryanodine receptor (alpha-RyR) in frog skeletal muscle sarcoplasmic reticulum: potential distinct modes in Ca2+ release between alpha-and beta-RyR. *J. Biol. Chem.* 276, 2953–2960. doi: 10.1074/jbc.M005809200

Nelson, M. T., Cheng, H., Rubart, M., Santana, L. F., Bonev, A. D., Knot, H. J., et al. (1995). Relaxation of arterial smooth muscle by calcium sparks. *Science* 270, 633–637. doi: 10.1126/science.270.5236.633

Ogawa, Y., Kurebayashi, N., and Murayama, T. (1999). Ryanodine receptor isoforms in excitation-contraction coupling. *Adv. Biophys.* 36, 27–64. doi: 10.1016/s0065-227x(99)80004-5

Ogawa, Y., Murayama, T., and Kurebayashi, N. (2002). Ryanodine receptor isoforms of non-Mammalian skeletal muscle. *Front. Biosci.* 7, d1184–d1194.

Oyamada, H., Murayama, T., Takagi, T., Iino, M., Iwabe, N., Miyata, T., et al. (1994). Primary structure and distribution of ryanodine-binding protein isoforms of the bullfrog skeletal muscle. *J. Biol. Chem.* 269, 17206–17214.

Perez, C. F., Voss, A., Pessah, I. N., and Allen, P. D. (2003). RyR1/RyR3 Chimeras Reveal that multiple domains of RyR1 are involved in skeletal-type E-C coupling. *Biophys. J.* 84, 2655–2663.

Picht, E., Zima, A. V., Blatter, L. A., and Bers, D. M. (2007). SparkMaster: automated calcium spark analysis with ImageJ. *Am. J. Physiol. Cell Physiol.* 293, C1073–C1081. doi: 10.1152/ajpcell.00586.2006

Pouvreau, S., Royer, L., Yi, J., Brum, G., Meissner, G., Ríos, E., et al. (2007). Ca2+ sparks operated by membrane depolarization require isoform 3 ryanodine receptor channels in skeletal muscle. *Proc. Natl. Acad. Sci. U.S.A.* 104, 5235–5240. doi: 10.1073/pnas.0700748104

Prada, J., Sasi, M., Martin, C., Jablonka, S., Dandekar, T., and Blum, R. (2018). An open source tool for automatic spatiotemporal assessment of calcium transients and local 'signal-close-to-noise' activity in calcium imaging data. *PLoS Comput. Biol.* 14:e1006054. doi: 10.1371/journal.pcbi.1006054

Rios, E., and Pizarro, G. (1988). Voltage sensors and calcium channels of excitation-contraction coupling. *Physiology* 6, 223–227.

Rodney, G. G., and Schneider, M. F. (2003). Calmodulin modulates initiation but not termination of spontaneous Ca2+ sparks in frog skeletal muscle. *Biophys. J.* 85, 921–932. doi: 10.1016/S0006-3495(03)74531-7

Rossi, R., Bottinelli, R., Sorrentino, V., and Reggiani, C. (2001). Response to caffeine and ryanodine receptor isoforms in mouse skeletal muscles. *Am. J. Physiol. Cell Physiol.* 281, C585–C594.

Schneider, M. F., and Ward, C. W. (2002). Initiation and termination of calcium sparks in skeletal muscle. *Front. Biosci.* 7, d1212–d1222.

Stern, M. D., Ríos, E., and Maltsev, V. A. (2013). Life and death of a cardiac calcium spark. *J. Gen. Physiol.* 142, 257–274. doi: 10.1085/jgp.201311034

Sutko, J. L., and Airey, J. A. (1996). Ryanodine receptor Ca2+ release channels: does diversity in form equal diversity in function? *Physiol. Rev.* 76, 1027–1071. doi: 10.1152/physrev.1996.76.4.1027

Szabo, L. Z., Vincze, J., Csernoch, L., and Szentesi, P. (2010). Improved spark and ember detection using stationary wavelet transforms. *J. Theor. Biol.* 264, 1279–1292. doi: 10.1016/j.jtbi.2010.04.005

Szappanos, H., Smida-Rezgui, S., Cseri, J., Simut, C., Sabatier, J.-M., De Waard, M., et al. (2005). Differential effects of maurocalcine on Ca2+ release events and depolarization-induced Ca2+ release in rat skeletal muscle. *J. Physiol.* 565, 843–853. doi: 10.1113/jphysiol.2005.086074

Sztretye, M., Almássy, J., Deli, T., Szentesi, P., Jung, C., Dienes, B., et al. (2009). Altered sarcoplasmic reticulum calcium transport in the presence of the heavy metal chelator TPEN. *Cell Calcium* 46, 347–355. doi: 10.1016/j.ceca.2009.10.002

Tian, Q., Schröder, L., Schwarz, Y., Flockerzi, A., Kaestner, L., Zeug, A., et al. (2019). Large scale, unbiased analysis of elementary calcium signaling events in cardiac myocytes. *J. Mol. Cell Cardiol.* 135, 79–89. doi: 10.1016/j.yjmcc.2019.08.004

Tsugorka, A., Rios, E., and Blatter, L. A. (1995). Imaging elementary events of calcium release in skeletal muscle cells. *Science* 269, 1723–1726. doi: 10.1126/science.7569901

Vincze, J., Szabo, L. Z., Dienes, B., Szentesi, P., and Csernoch, L. (2013). Efficient automatic analysis of high-speed confocal images containing localized calcium release events. *Biophys. J.* 104:437a.

Vincze, J., Szabo, L. Z., Dienes, B., Szentesi, P., and Csernoch, L. (2014). Increased accuracy of calcium spark parameter detection using high-speed confocal microscopy. *Biophys. J.* 106:532a.

von Wegner, F., Both, M., and Fink, R. H. (2006). Automated detection of elementary calcium release events using the á trous wavelet transform. *Biophys. J.* 90, 2151–2163. doi: 10.1529/biophysj.105.069930

Wang, S. Q., Stern, M. D., Rios, E., and Cheng, H. (2004). The quantal nature of Ca2+ sparks and in situ operation of the ryanodine receptor array in cardiac cells. *Proc. Natl. Acad. Sci. U.S.A.* 101, 3979–3984. doi: 10.1073/pnas.0306157101

Zhou, J., Brum, G., Gonzalez, A., Launikonis, B. S., Stern, M. D., and Ríos, E. (2003). Ca2+ sparks and embers of mammalian muscle. Properties of the sources. *J. Gen. Physiol.* 122, 95–114. doi: 10.1085/jgp.200308796

Zhou, J., Launikonis, B. S., Rios, E., and Brum, G. (2004). Regulation of Ca2+ sparks by Ca2+ and Mg2+ in mammalian and amphibian muscle. An RyR isoform-specific role in excitation-contraction coupling? *J. Gen. Physiol.* 124, 409–428. doi: 10.1085/jgp.200409105

Conflict of Interest: The authors declare that the research was conducted in the absence of any commercial or financial relationships that could be construed as a potential conflict of interest.

Copyright © 2020 Cserne Szappanos, Vincze, Bodnár, Dienes, Schneider, Csernoch and Szentesi. This is an open-access article distributed under the terms of the Creative Commons Attribution License (CC BY). The use, distribution or reproduction in other forums is permitted, provided the original author(s) and the copyright owner(s) are credited and that the original publication in this journal is cited, in accordance with accepted academic practice. No use, distribution or reproduction is permitted which does not comply with these terms.

The Journal of Physiology

Altered expression of triadin 95 causes parallel changes in localized Ca^{2+} release events and global Ca^{2+} signals in skeletal muscle cells in culture

János Fodor[1], Monika Gönczi [1], Monika Sztretye[1], Beatrix Dienes[1], Tamás Oláh[1], László Szabó[1,2], Eszter Csoma[3], Péter Szentesi[1], Gyula P. Szigeti[1], Isabelle Marty[4] and László Csernoch[1]

[1]*Department of Physiology, Research Centre for Molecular Medicine, Medical and Health Science Centre, University of Debrecen, Debrecen, Hungary*
[2]*Department of Electrical Engineering, Sapientia Hungarian University of Transylvania, Targu Mures, Romania*
[3]*Department of Microbiology, Research Centre for Molecular Medicine, Medical and Health Science Centre, University of Debrecen, Debrecen, Hungary*
[4]*Inserm U836, Grenoble Institut des Neurosciences; Université Joseph Fourier, Grenoble, France*

The 95 kDa triadin (Trisk 95), an integral protein of the sarcoplasmic reticular membrane in skeletal muscle, interacts with both the ryanodine receptor (RyR) and calsequestrin. While its role in the regulation of calcium homeostasis has been extensively studied, data are not available on whether the overexpression or the interference with the expression of Trisk 95 would affect calcium sparks the localized events of calcium release (LCRE). In the present study LCRE and calcium transients were studied using laser scanning confocal microscopy on C2C12 cells and on primary cultures of skeletal muscle. Liposome- or adenovirus-mediated Trisk 95 overexpression and shRNA interference with triadin translation were used to modify the level of the protein. Stable overexpression in C2C12 cells significantly decreased the amplitude and frequency of calcium sparks, and the frequency of embers. In line with these observations, depolarization-evoked calcium transients were also suppressed. Similarly, adenoviral transfection of Trisk 95 into cultured mouse skeletal muscle cells significantly decreased both the frequency and amplitude of spontaneous global calcium transients. Inhibition of endogenous triadin expression by RNA interference caused opposite effects. Primary cultures of rat skeletal muscle cells expressing endogenous Trisk 95 readily generated spontaneous calcium transients but rarely produced calcium sparks. Their transfection with specific shRNA sequence significantly reduced the triadin-specific immunoreactivity. Functional experiments on these cells revealed that while caffeine-evoked calcium transients were reduced, LCRE appeared with higher frequency. These results suggest that Trisk 95 negatively regulates RyR function by suppressing localized calcium release events and global calcium signals in cultured muscle cells.

(Received 24 July 2008; accepted after revision 2 October 2008; first published online 9 October 2008)
Corresponding author L. Csernoch: Department of Physiology, University of Debrecen, P.O. Box 22, Hungary H-4012. Email: csl@phys.dote.hu

In skeletal muscle shortening is initiated by the increase in intracellular calcium concentration ($[Ca^{2+}]_i$) following the depolarization of the surface and transverse (T-) tubular membranes. Calcium ions are released from the sarcoplasmic reticulum (SR), a specialized intracellular calcium store, through ryanodine receptor (RyR) calcium channels. The depolarization is conveyed to the opening of RyR via a direct mechanical link to the dihydropyridine receptor (DHPR) of the T-tubular membrane.

The opening of a single or a group of calcium release channels gives rise to localized calcium release events (LCRE) termed calcium sparks (Tsugorka *et al.* 1995; Klein *et al.* 1996) and embers (Gonzalez *et al.* 2000). Although these events have been studied in detail and their characteristics described in both adult (Kirsch *et al.* 2001) and embryonic skeletal muscle (Chun *et al.* 2003) certain properties of LCRE remain unclear. Specifically, the termination of the inherent positive feed-back from calcium-induced calcium release involved in these events, has not been resolved completely (see e.g. Szentesi *et al.* 2004; Miller *et al.* 2005).

In addition, while calcium sparks are readily observable in skeletal muscle fibres from amphibians and in mammalian skeletal muscle cells in culture, skeletal muscle fibres from adult mammals lack these events (e.g. Shirokova *et al.* 1998). The observation that mammalian

© 2008 The Authors. Journal compilation © 2008 The Physiological Society DOI: 10.1113/jphysiol.2008.160457

Downloaded from J Physiol (jp.physoc.org) at unknown institution on July 2, 2009

fibres with disrupted surface and T-tubular membranes, achieved with a mild treatment with saponin, readily produce calcium sparks (Kirsch *et al.* 2001; Zhou *et al.* 2003) led to the suggestion that a structural element is involved in the suppression of these events under physiological conditions. This was strengthened by the finding that calcium sparks are restrained to areas without T-tubules in cultured muscle cells (Zhou *et al.* 2006).

Triadin, an integral membrane protein of the SR (Brandt *et al.* 1990; Caswell *et al.* 1991), has a short N-terminal part in the cytosol and a long C-terminal inside the lumen of the SR (Marty *et al.* 1995). Its 95 kDa skeletal isoform (Trisk 95) has been localized to the junctional membrane of the terminal cisternae in the SR (Marty *et al.* 1995) and suggested to bind to both calsequestrin (CSQ) and to RyR (Knudson *et al.* 1993; Caswell *et al.* 1999; Kobayashi *et al.* 2000). As a link between CSQ and RyR it could be the molecule that conveys the control associated with calsequestrin to the calcium release channel (Beard *et al.* 2002).

Recent evidence has, however, both questioned and strengthened the role of triadin in excitation–contraction (E-C) coupling. The lack of an obvious phenotype and the absence of contractile dysfunction in triadin knock-out mice led to the suggestion that triadins are not essential for E-C coupling (Shen *et al.* 2007). Nevertheless, RyRs with altered C-terminal luminal sequences, which interfered with Trisk 95 binding, gave rise to reduced SR calcium release in response to both depolarization and RyR agonists (Goonasekera *et al.* 2007) indicating that triadin binding is crucial for normal RyR function.

Here we demonstrate that altered expression of Trisk 95 results in a parallel modification in both the calcium transients and the localized calcium release events. Overexpression of the protein resulted in a decreased calcium release from the SR and in the reduction of both the frequency and amplitude of calcium sparks. Interference with the translation of the protein, on the other hand, increased the frequency and amplitude of these localized events of calcium release. Our observations clearly support the idea that triadin plays an important role as a negative regulator of RyR opening.

Some aspects of this work were presented to the Biophysical Society (Csernoch *et al.* 2007).

Methods

Cell cultures and transfection

C2C12 skeletal muscle cells were cultured in Dulbecco's modified Eagle's medium (DMEM) supplemented with 10% fetal bovine serum (FBS), 50 U ml^{-1} penicillin, and 50 μg ml^{-1} streptomycin and were incubated at 37°C in a humidified incubator with 5% CO_2–95% O_2 as described in our earlier studies (Deli *et al.* 2007). Full length coding sequence of Trisk 95 was ligated into the *Eco*R1 restriction site of pcDNA 3.1 expression vector (Marty *et al.* 2000). Transfection was performed in Opti-MEM reduced serum content medium using Lipofectamine 2000 reagent (Invitrogen, Carlsbad, CA, USA) for 2.5 h at 37°C. Cells were allowed to express the introduced genes for 48 h in growth medium then were selected in DMEM containing 1000 μg ml^{-1} geneticin. After 14–18 days, single colonies were isolated and experiments were carried out on pools of transfected cells. Differentiation of transfected cells was induced at 80% confluency by changing the culture medium for DMEM supplemented with 5% horse serum (HS), 2% FBS and penicillin–streptomycin. The efficiency of Trisk 95 overexpression was monitored by immunostaining, using specific Trisk 95-antibody labelling the C-terminus of the protein (Marty *et al.* 2000). Functional experiments were carried out on 5- to 7-day-old differentiated myotubes.

Primary cultures of skeletal muscle cells were obtained from 1-day-old mice or 5- to 10-day-old rats as described earlier (Szappanos *et al.* 2004). Animals were killed following approved protocols (14/2004.DE MAB and 15/2004.DE MAB) of the Animal Care Committee of the University of Debrecen. They were anaesthetized by ether and killed with cervical dislocation. Skeletal muscle was collected from the hindlimbs, put in Hank's solution (Sigma Chemical Co., St Louis, MO, USA) and then cut into small pieces. The muscle tissue was dissociated at 37°C using 0.75 mg ml^{-1} collagenase type I, 1.5 mg ml^{-1} trypsin in a calcium/magnesium free phosphate buffer. The enzymatic reaction was inhibited with the addition of 10% HS. After filtration through a multilayer nylon membrane, the cells were collected by centrifugation at 150 g for 10 min and seeded onto coverslips in a proliferation medium (Ham's F12 medium supplemented with 15% FBS and penicillin–streptomycin). On the third day of culturing the medium was changed to DMEM supplemented with 5% HS to allow differentiation of the myotubes. In this system adenoviral transfection was used to modify triadin expression. Two types of adenovirus were used (both from Gene Vector Production Network, at Genethon III; Évry, France): a control virus (rAdV5-DsRed) with the cDNA of the red fluorescent protein and the test containing the full-length sequence of skeletal muscle Trisk 95 (rAdV5-Trisk 95-ires-DsRed). All the transgenes were controlled by the CMV promoter. After 48 h proliferation, cells were incubated with the viruses for 10 h in Ham's F12 medium without serum (the cell nucleus to virus ratio was 1 : 40), and then differentiation was induced by changing the medium. Control cells were infected with the control virus (rAdV5-DsRed), and Trisk 95 overexpressing myotubes consisted of cells infected with rAdV-Trisk 95-ires-DsRed. Confocal microscopy studies were performed after 55–60 h of infection/differentiation.

© 2008 The Authors. Journal compilation © 2008 The Physiological Society

Downloaded from J Physiol (jp.physoc.org) at unknown institution on July 2, 2009

The presence of Trisk 95 was determined by immunostaining at different differentiation stages (2, 3, 4 days in differentiation medium). The RNA interference technique was applied in order to reduce endogenous Trisk 95 expression. The shRNA was engineered by RNAi Construct Builder (Genscript, Piscataway, NJ, USA) and produced by SigmaGenosys. The chosen shRNA cassette sequence besides the sense (5′GGCAAAGATGTAAAGCCTAAA) and antisense (5′TTTAGGCTTTACATCTTTGCC) region contains a loop and termination sequence resulting in a hairpin siRNA. Blast filtering ensured that this sequence has homology only with Trisk 95 and not with any other known gene. Scrambled shRNA was used to demonstrate that the target specific shRNS did not induce a non-specific effect on gene expression. The shRNA transfection was carried out after 30–36 h of differentiation with application of Lipofectamine 2000 reagent during 2.5 h in Opti-MEM transfection medium at 37°C, 5% CO_2. Immunostaining was performed after 3–4 days of differentiation in order to monitor the efficiency of RNA interference. Calcium imaging studies were also performed at this stage using a confocal microscope.

Immunostaining

Immunolabelling was performed the same way on C2C12 cells and on primary cultures. Cultured cells were washed with ice-cold phosphate-buffered saline (PBS; 0.02 M NaH_2PO_4, 0.1 M NaCl), fixed with 4% paraformaldehyde for 15 min, permeabilized with 0.1% Triton X-100 in PBS for 10 min and blocked with 1% BSA diluted in PBS (blocking solution) for 30 min at room temperature. The cells were then incubated with the anti-Trisk 95 primary antibody (dilution was 1 : 500 in blocking solution; the primary rabbit antibody was directed against the C-terminus of Trisk 95, the specific epitope corresponds to amino acids 673–687 of Trisk 95) for 2 h at room temperature and with fluorescein labelled anti-rabbit secondary antibody for 1 h at RT. Vectashield mounting medium with DAPI (Vector Laboratories, Burlingame, CA, USA) was used to make the nuclei visible. Images were obtained using fluorescence and confocal microscopy. Fluorescence intensities were calculated from regions of interest (10 on each cell) of fluorescent images with Image pro Plus software (Media Cybernetics Inc., Bethesda, MD, USA).

Whole cell calcium measurement

Changes in $[Ca^{2+}]_i$ were measured using the calcium sensitive fluorescent dye Fura-2 as reported earlier (Szappanos *et al.* 2004). Myotubes were incubated with Fura-2-AM (10 μM) for 1 h (37°C, 5% CO_2) in DMEM supplemented with 10% FBS and neostigmin to inhibit choline-esterase. C2C12 myotubes were then placed on the stage of an inverted fluorescence microscope. Measurements were performed in normal Tyrode solution (in mM: 137 NaCl, 5.4 KCl, 0.5 $MgCl_2$, 1.8 $CaCl_2$, 11.8 Hepes, 1 g l^{-1} glucose, pH 7.4) or calcium-free Tyrode solution. To obtain a calcium-free Tyrode solution, no $CaCl_2$ was added in the presence of 5 mM EGTA. In the depolarizing solution 120 mM NaCl was exchanged for KCl. Caffeine was prepared as a stock solution in Tyrode buffer and used at a final concentration up to 30 mM. Excitation wavelength was alternated between 340 and 380 nm by a dual wavelength monochromator (Deltascan, Photon Technology International, New Brunswick, NJ, USA), while the emission was monitored at 510 nm using a photomultiplier. $[Ca^{2+}]_i$ was calculated from the ratio of fluorescence intensities ($R = F_{340}/F_{380}$) using an *in vivo* calibration ($R_{min} = 0.2045$, $R_{max} = 8.315$, $K_d\beta = 1183$).

Confocal measurements

Localized calcium release events were monitored with the LSM 510 META confocal laser scanning microscope (Zeiss, Oberkochen, Germany) as described earlier (Szentesi *et al.* 2004). In brief, C2C12 myotubes were treated with a modified relaxing solution (in mM: 125 potassium glutamate, 10 Hepes, 1 EGTA, 5 $MgCl_2$, 5 Na-ATP, 10 sodium phosphocreatine, 10 glucose, 0.13 $CaCl_2$ and 8% dextran) containing 0.002% saponin for 2–3 min. Permeabilization of the surface membrane was monitored by the addition of 50 μM Fluo-3 into the solution and imaging the fibre. This solution was then exchanged with an internal medium (in mM: 125 potassium glutamate, 10 Hepes, 1 EGTA, 5 $MgCl_2$, 5 Na-ATP, 10 sodium phosphocreatin, 10 glucose, 0.13 $CaCl_2$, 0.1 Fluo-3 and 8% dextran).

Myotubes from primary cultures were incubated with 10 μM Fluo-4-AM for 1 h at 37°C. Calcium imaging was performed in normal Tyrode solution. Two dimensional (x–y) and line-scan images were used to monitor the fluorescence intensity. Line-scan images were recorded at 1.54 ms per line and 512 pixels per line using a 63× water immersion objective. Fluo-3 or -4 was excited with an argon ion laser. Images were analysed using an automatic event detection program (Szentesi *et al.* 2004), which calculated the amplitude ($\Delta F/F_0$), full width at half-maximum (FWHM), rise time and duration of the identified events. Events longer than 40 pixels (60 ms) and displaying steady fluorescence were considered as 'embers'; otherwise they were taken as 'sparks' or 'sparks with embers'. Note that rise time was calculated only for sparks, while only average amplitude was obtained for embers (Szentesi *et al.* 2004).

© 2008 The Authors. Journal compilation © 2008 The Physiological Society

Downloaded from J Physiol (jp.physoc.org) at unknown institution on July 2, 2009

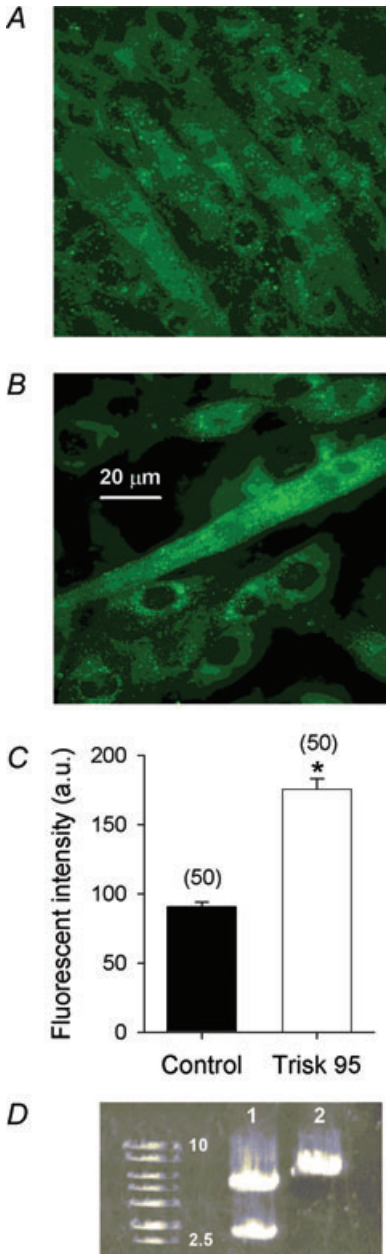


Figure 1. Overexpression of Trisk 95 in C2C12 cells
Either the pcDNA3.1 vector alone or that encoding for Trisk 95 was transfected into C2C12 cells and clones stably overexpressing the protein were selected. The presence and the amount of the protein were visualized using a triadin specific antibody. *A*, endogenous triadin 95 expression in C2C12 myotubes stably transfected with the pcDNA3.1 vector. *B*, c2C12 clones stably overexpressing Trisk 95. Vertical scale is 20 μm for the two images. *C*, pooled data of triadin expression in control and transfected cells determined by comparing the fluorescence intensities of identical areas. Asterisk marks significant difference as compared to control. Numbers in parentheses give the number of cells examined. *D*, ethidium bromide stained agarose gel showing the cDNA for Trisk 95 and the pcDNA3.1 vector before (lane 1) and after (lane 2) cloning. Left calibration shows 1 kb DNA ladder.

Statistical evaluation

Data are displayed as means ± S.E.M. To assess the significance of the differences, Student's *t* test or for very asymmetric distributions the non-parametric Mann–Whitney test (SPSS statistical software for Windows, SPSS Inc., Chicago, IL, USA) was used. A difference was regarded as significant when $P < 0.05$.

Results

Calcium transients in triadin overexpressing C2C12 cells

The effect of triadin 95 overexpression was examined in a mouse skeletal muscle cell line. Endogenous expression of this regulatory protein could be demonstrated in C2C12 myotubes (Fig. 1*A*). Trisk 95 protein synthesis has been amplified using a pCDNA3.1 plasmid-vector system. The successful ligation of the plasmid vector and triadin 95 cDNA was checked prior to transfection using agarose gel electrophoresis (Fig. 1*D*). The stable overexpression of the protein in the selected clones was confirmed with immunocytochemistry at the myotube stage (Fig. 1*B*). Quantitative analysis of the fluorescence intensities revealed a significant ($P < 0.01$) 94% over-expression of the protein as compared to C2C12 cells transfected with the empty pCDNA3.1 plasmid vector (Fig. 1*C*).

Control and Trisk 95-transfected, differentiated (5–7 days old) C2C12 myotubes were used for functional experiments. First we examined whether the protein overexpression alters the calcium homeostasis of the myotubes. The resting intracellular calcium concentration was similar ($P > 0.2$) in both groups (77.4 ± 5.2 nM, $n = 48$ in control and 71.3 ± 4.8 nM, $n = 54$ in Trisk 95 overexpressing cells). The presence of functional ryanodine receptors and the presence of releasable calcium in the SR were investigated using 15 mM caffeine (Fig. 2*A*). No significant difference was observed in the amplitude of caffeine-induced transient elevation of $[Ca^{2+}]_i$ between control and Trisk 95 overexpressing myotubes (142 ± 10 nM, $n = 41$ and 123 ± 11 nM, $n = 44$, respectively). Calcium transients could also be evoked by depolarization using 120 mM KCl both in normal (extracellular calcium concentration 1.8 mM; Fig. 2*B*) and in a Ca^{2+}-free bathing solution (Fig. 2*C*). In the presence of extracellular calcium the amplitude of KCl-induced calcium transients were similar in control and in triadin overexpressing myotubes (168 ± 10 nM, $n = 48$ and 200 ± 31 nM, $n = 54$, respectively). In contrast, the amplitude of the KCl-induced calcium transients in Ca^{2+}-free solution was significantly reduced in Trisk 95 overexpressing myotubes (98 ± 10 nM, $n = 42$) as compared to control cells (170 ± 14 nM, $n = 29$).

© 2008 The Authors. Journal compilation © 2008 The Physiological Society

Downloaded from J Physiol (jp.physoc.org) at unknown institution on July 2, 2009

Figure 2*D* plots pooled data to confirm that triadin overexpression had little, if any, effects on the caffeine-evoked calcium transients suggesting that the calcium content of the SR was unaffected under these conditions. On the other hand, depolarization-evoked calcium transients in the absence of external calcium, that is when calcium release from the SR was the sole source of the calcium ions appearing in the myoplasm, were significantly reduced in Trisk 95 overexpressing cells as observed previously on rat primary skeletal muscle cell culture (Rezgui *et al.* 2005).

Localized calcium release events in triadin overexpressing C2C12 cells

To understand the underlying reasons for the suppressed SR calcium release, localized calcium release events were examined in control and in triadin overexpressing cells using laser scanning confocal microscopy. Control myotubes readily displayed both calcium sparks (calcium release events with large amplitude and short duration; Fig. 3*A*, left panel) and embers (events with small amplitude and long duration; Fig. 3*A*, right panel).

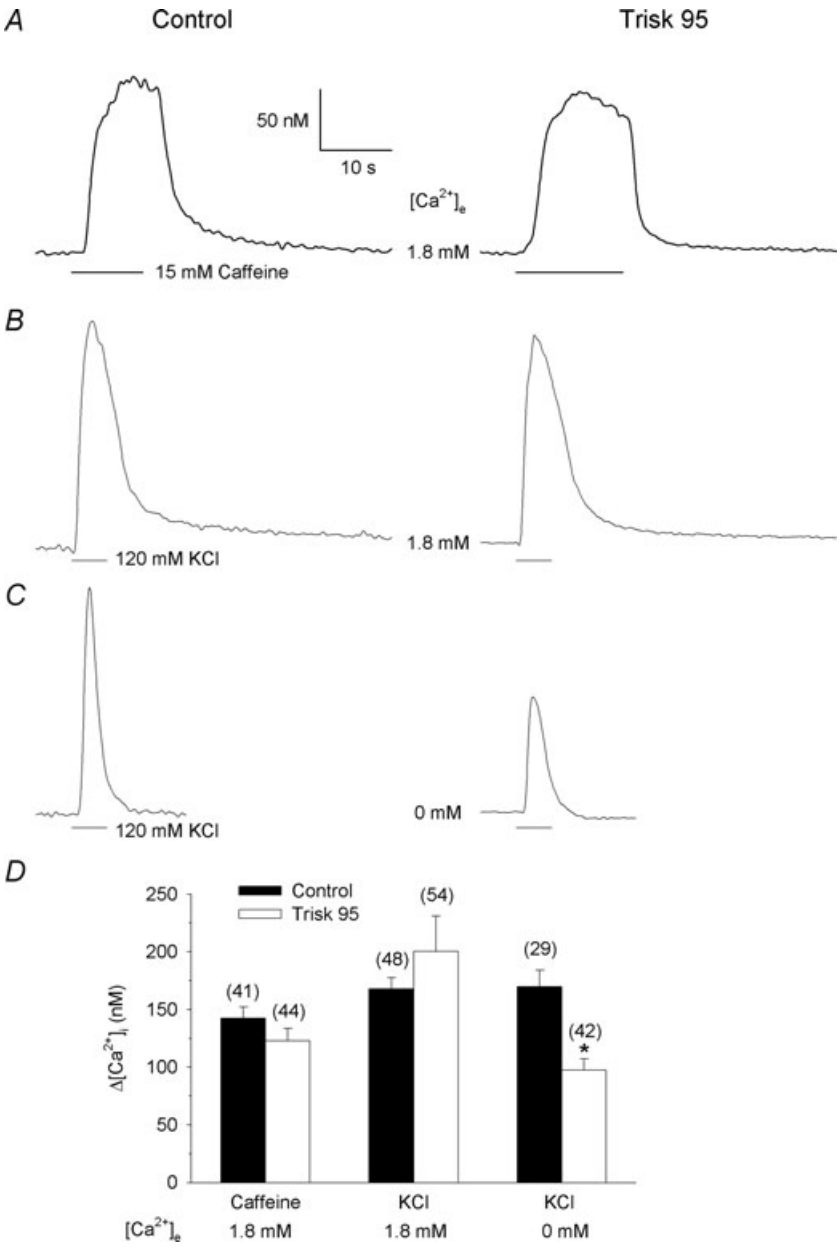


Figure 2. Whole cell Ca^{2+} transients in control and in Trisk 95 overexpressing myotubes
A–C, representative Ca^{2+} transients evoked by the addition of either caffeine (15 mM; *A*) or KCl (120 mM; *B* and *C*) detected using Fura-2 in control (left column) and in triadin-overexpressing (right column) cells. KCl-evoked calcium transients were measured both in the presence (*B*) and in the absence of external calcium (*C*). *D*, pooled data for the amplitude of the calcium transients ($\Delta[Ca^{2+}]_i$). Numbers in parentheses give the number of cells, while the asterisk denotes statistically significant difference as compared to control.

© 2008 The Authors. Journal compilation © 2008 The Physiological Society

Downloaded from J Physiol (jp.physoc.org) at unknown institution on July 2, 2009

It should be noted, however, that the number of calcium sparks was far greater than that of embers. Although, myotubes following the transfection with the triadin-plasmid generated calcium sparks and embers as control cells did (Fig. 3*B*), the characteristic parameters of these events were altered. Plotting the amplitude histograms of LCRE (Fig. 3*C* and *D*) revealed that triadin overexpression increased the relative frequency of

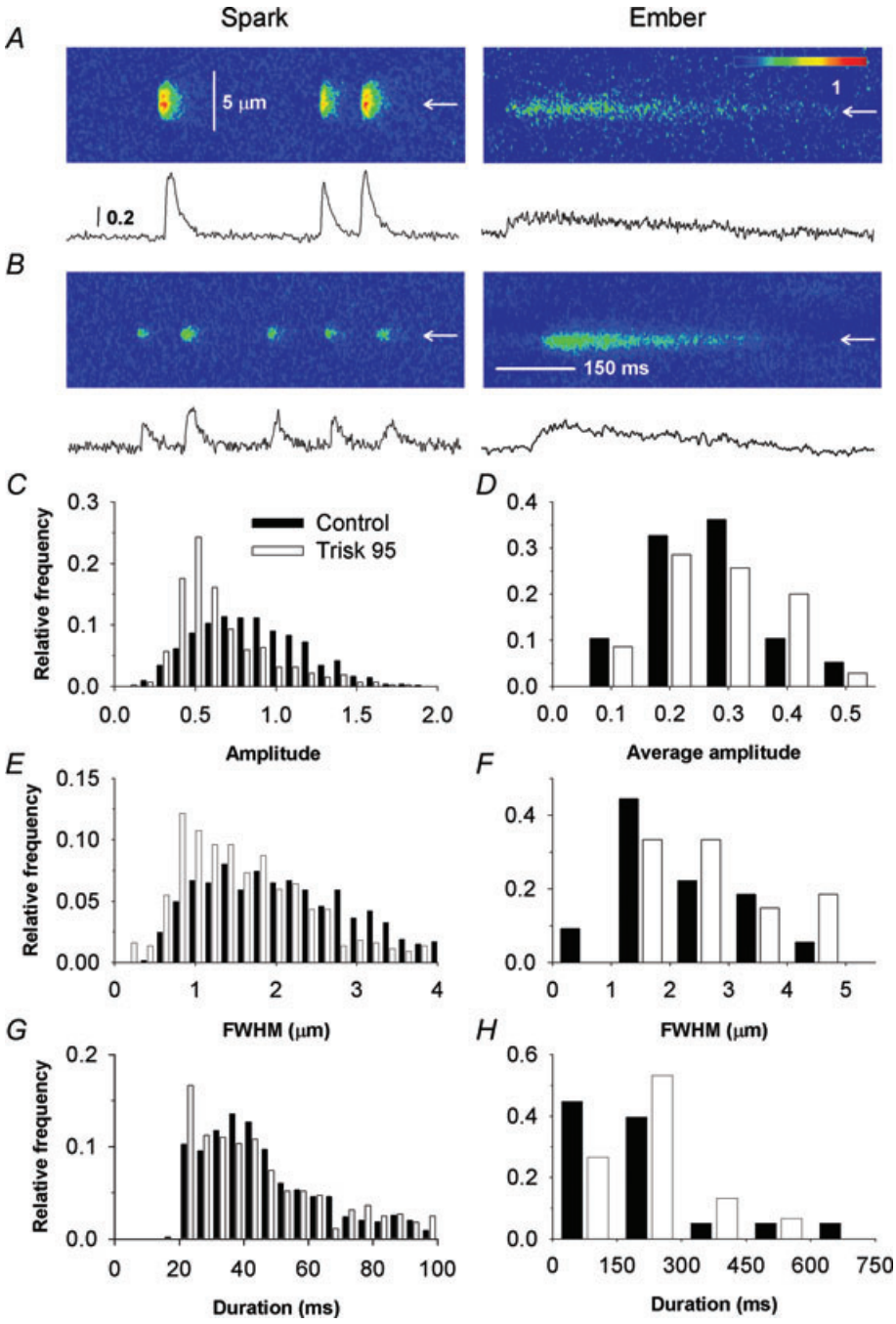


Figure 3. Localized Ca^{2+} release events in control and in Trisk 95 overexpressing myotubes
A, line-scan images and time courses of events detected under control conditions. Note the two distinct subtypes, the classical Ca^{2+} sparks (left panel) and one with small amplitude (referred to as embers; right panel). *B*, both types of events were detected in Trisk 95 overexpressing myotubes with different parameters as compared to control. Note especially the altered morphology of Ca^{2+} sparks. Time courses were calculated from the lines marked by arrows on the line-scan images. Vertical scale represents 5 μm, horizontal scale represents 150 ms for all images. *C* and *D*, amplitude histograms of Ca^{2+} sparks (*C*) and embers (*D*) from control and from triadin-overexpressing myotubes. *E* and *F*, histograms of FWHM presented as that in panels *C* and *D* for Ca^{2+} sparks (*E*) and embers (*F*). *G* and *H*, histograms of event duration presented as that in panels *C* and *D* for Ca^{2+} sparks (*G*) and embers (*H*).

© 2008 The Authors. Journal compilation © 2008 The Physiological Society

Downloaded from J Physiol (jp.physoc.org) at unknown institution on July 2, 2009

calcium sparks with small amplitudes while the relative frequency of calcium sparks with large amplitudes were reduced as compared to control myotubes (Fig. 3*C*). The distribution of the average amplitude of embers, on the other hand, was not altered in triadin overexpressing C2C12 cells (Fig. 3*D*). Similarly, the histograms of FWHM demonstrate that the overexpression of triadin shifted the distribution to the left for sparks (Fig. 3*E*), whereas that of the embers remained unaffected (Fig. 3*F*). The distribution of event duration, on the other hand, was altered neither for sparks (Fig. 3*G*) nor for embers (Fig. 3*H*) by the overexpression of Trisk 95.

In accordance with the above, pooled data show that on average the amplitude of the calcium sparks was significantly smaller in triadin overexpressing myotubes than in control cells (0.59 ± 0.01 *versus* 0.81 ± 0.01; $P < 0.001$), while the average amplitude for the embers was only slightly affected in Trisk 95 overexpressing myotubes (0.22 ± 0.01 *versus* 0.26 ± 0.02; $P > 0.07$). While we could not observe any significant difference between the duration (47.1 ± 0.9 *versus* 51.1 ± 1.8 ms for sparks and 215 ± 21 *versus* 224 ± 21 ms for embers in control and triadin overexpressing cells, respectively; $P > 0.3$) or rise time (14.1 ± 0.4 *versus* 15.7 ± 0.6 ms; $P > 0.1$) of events in the two groups, FWHM for calcium sparks, but not for embers, was significantly smaller in triadin transfected myotubes ($1.26 \pm 0.07\ \mu$m; $P < 0.01$) than in control cells ($1.86 \pm 0.06\ \mu$m). In addition, the frequency of the spontaneous calcium release events was also significantly ($P < 0.05$) reduced in Trisk 95 overexpressing myotubes (1.04 ± 0.14 Hz for sparks and 0.09 ± 0.04 Hz for embers) as compared to the control group (1.85 ± 0.21 Hz for sparks and 0.19 ± 0.02 for embers).

Triadin overexpression in mouse skeletal muscle cells in primary culture

The overexpression of triadin in primary cultured skeletal muscle cells of mice was carried out using an adenoviral transfection. Differentiated myotubes were infected either with the virus encoding only the DsRed label (control, Fig. 4*A*) or with the virus containing both the Trisk 95 and DsRed cDNA (Fig. 4*B*). Experiments were carried out on six control and four Trisk 95 overexpressing differentiated myotubes. Both control and triadin overexpressing myotubes generated calcium transients (Fig. 4*C* and *D*, respectively), probably triggered by spontaneous action potentials as tests on some cells showed that they could be blocked by $0.3\ \mu$M tetrodotoxin (see online Supplemental Material). These calcium transients were visualized using laser scanning confocal microscopy in the line-scan mode. The analysis of these images revealed that both the amplitude and the frequency of the calcium transients in triadin overexpressing myotubes were significantly reduced (0.56 ± 0.03 and 0.26 ± 0.01 Hz, respectively, $n = 71$; $P < 0.02$ and 0.001, respectively; Fig. 4*D*) as compared to controls (0.68 ± 0.02 and 0.75 ± 0.04 Hz, respectively, $n = 169$; Fig. 4*C*).

Calcium transients were also elicited using external electrical stimulation as shown in Fig. 4*E* and *F*. These transients, as expected, did not differ substantially in their amplitude and kinetics from their spontaneous counterparts. The observations also confirmed the significant ($P < 0.05$) reduction in the amplitude following the overexpression of Trisk 95, from a control value of 0.64 ± 0.09 ($n = 17$, four cells) to 0.46 ± 0.05 ($n = 45$, nine cells).

Inhibition of endogenous triadin expression using specific shRNAs in rat primary cultured skeletal muscle cells

In contrast to the measurements on triadin overexpression, to study the effects of reduced Trisk 95 expression a system where the frequency of LCRE is relatively low under control conditions – rat myotubes in primary culture (see Fig. 7) – was selected. Immunocytochemical analysis at different stages of culturing revealed that endogenous expression of triadin 95 in these cells started from the third day after switching to differentiating medium. When large, multinucleated myotubes were formed (Fig. 5*B*), usually on the third day of culture, the distribution of triadin displayed a characteristic dotted pattern (Fig. 5*C*). Differentiating myotubes were transfected with Rhodamine-red labelled Trisk 95 specific shRNA using a liposome-induced transfection protocol. Two days after transfection the shRNA positive cells were easily identified by their red fluorescence (Fig. 5*A*). However, red fluorescence was not homogeneous within the myotubes, rather, brighter and darker areas were clearly distinguishable. Importantly, areas where intense red fluorescence was observed showed suppressed triadin expression as assessed by their less intense labelling for Trisk 95 (Fig. 5*C*). This correlation, although to various degrees, was present in all cultures ($n = 6$) examined (Fig. 5*E*).

In some experiments we utilized this observation by comparing data measured in cells (subcellular areas) with intense red fluorescence, assumed to have suppressed Trisk 95 expression, to those obtained from cells with low red fluorescence. This gave, in addition to the measurements with scrambled shRNA, a possibility to obtain 'endogenous' controls.

Calcium transients in cultured rat skeletal muscle cells with suppressed triadin expression

As a first step global calcium transients were measured on shRNA transfected cells. Addition of 30 mM caffeine

© 2008 The Authors. Journal compilation © 2008 The Physiological Society

Downloaded from J Physiol (jp.physoc.org) at unknown institution on July 2, 2009

to the bathing medium induced a transient elevation in $[Ca^{2+}]_i$ both on control myotubes and on myotubes with suppressed Trisk 95 expression (Fig. 6*A*). The latter transients were always smaller than those in control suggestive of a reduced SR calcium content. This was confirmed by the pooled data for the amplitude of the caffeine-induced calcium transients demonstrating a clear and significant reduction following the transfection with the shRNA (Fig. 6*C*). In line with this observation, the resting $[Ca^{2+}]_i$ was found to be increased in myotubes with reduced Trisk 95 expression if held in a calcium free extracellular solution (64.9 ± 3.3 *versus* 85.7 ± 6.9 nM; $n = 15$ and 12; control myotubes and myotubes with reduced triadin expression, respectively). In addition, depolarization, induced by the addition of 120 mM KCl in the absence of external calcium, could

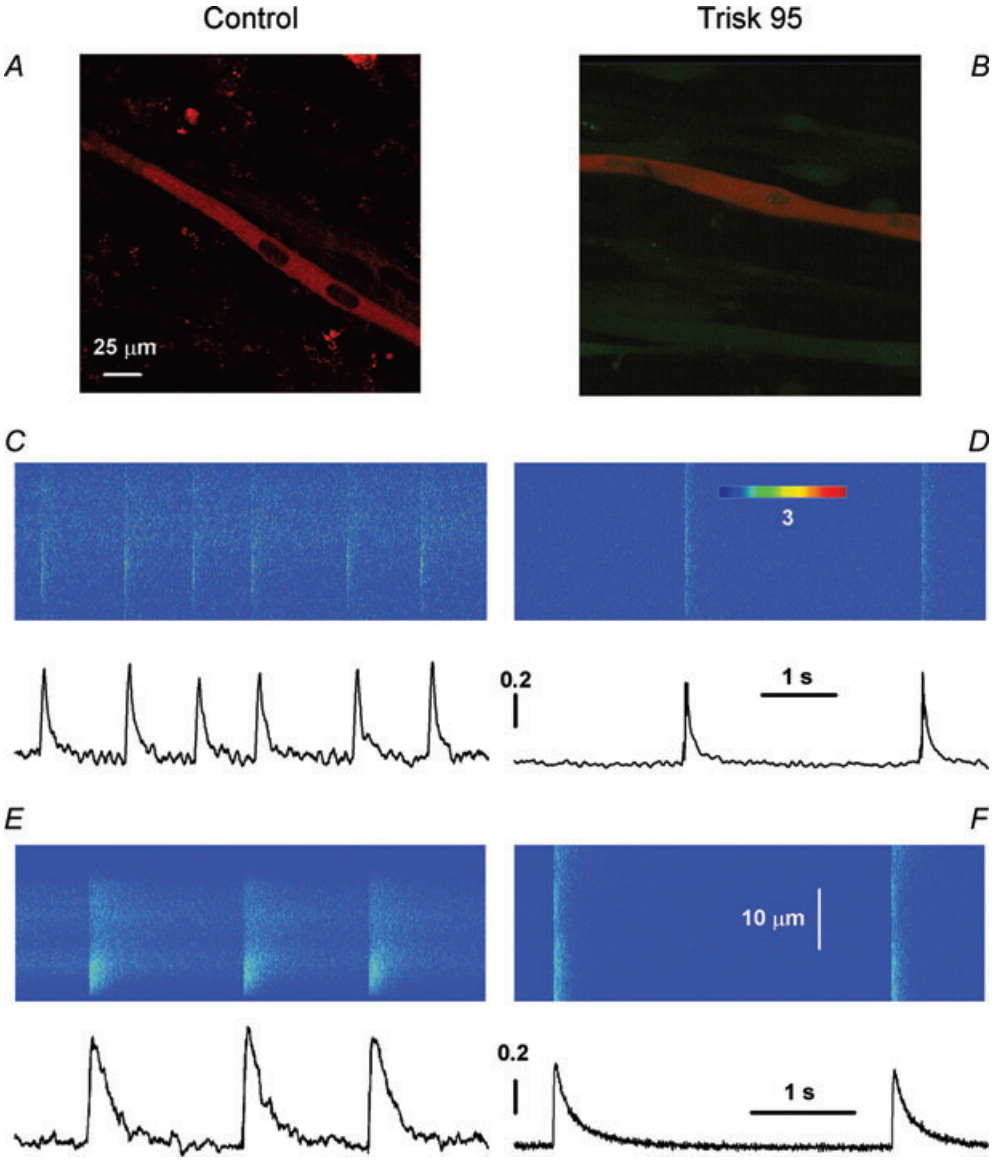


Figure 4. Spontaneous Ca^{2+} transients in mouse myotubes infected with an adenovirus vector encoding either DsRed only or Trisk 95 and DsRed
A and *B*, images of infected myotubes were visualized by their red fluorescence. Scaling bar represents 25 μm for both images in panels *A* and *B*. Green fluorescence is from Fluo-3. *C* and *D*, line-scan images of spontaneous Ca^{2+} transients detected in control (expressing DsRed only; *C*) and in Trisk 95 overexpressing myotubes (*D*). The traces below the images are spatially averaged time courses of Fluo-3 fluorescence normalized to baseline fluorescence (F/F_0). Note the difference in time scales for the control and the triadin-overexpressing myotube. *E* and *F*, line-scan images of electrically evoked Ca^{2+} transients measured on control (*E*) and on Trisk 95 overexpressing myotubes (*F*). The traces below the images were generated as in *C* and *D*. Vertical scaling bar represents 15 μm for all images in panels *C*–*F*.

© 2008 The Authors. Journal compilation © 2008 The Physiological Society

Downloaded from J Physiol (jp.physoc.org) at unknown institution on July 2, 2009

szentesi.peter_292_24

readily induce calcium release from the SR (Fig. 6*B*) clearly demonstrating that the reduced triadin expression did not interfere with the normal E-C coupling. However, in contrast to what was seen for triadin overexpressing cells, myotubes with reduced Trisk 95 expression had, in spite of the reduced SR calcium content, identical KCl-evoked calcium transients to those measured in control cells (Fig. 6*C*).

Calcium release events in cells with suppressed Trisk 95 expression

The results obtained from the global changes in $[Ca^{2+}]_i$ suggested that suppressed triadin expression might have the opposite effect to that seen with Trisk 95 overexpression. To test this hypothesis spontaneous calcium transients and localized calcium release events were recorded using laser scanning confocal microscopy. Control myotubes readily produced spontaneous calcium transients visible both in *x–y* (Fig. 7*A*) and in line-scan images (Fig. 7*B*). These transients had an average amplitude of 0.62 ± 0.05 ($n = 553$ on 23 myotubes) and appeared with an average frequency of 1.01 ± 0.22 Hz. On the other hand, LCRE were scarce on these cells. A large fraction of images (225 out of 279), as the one presented in Fig. 7*B* (upper image), were devoid of such events. Although both sparks and embers were occasionally observed (see e.g. Fig. 7*B*, lower image) their numbers were low; altogether 143 sparks and 23

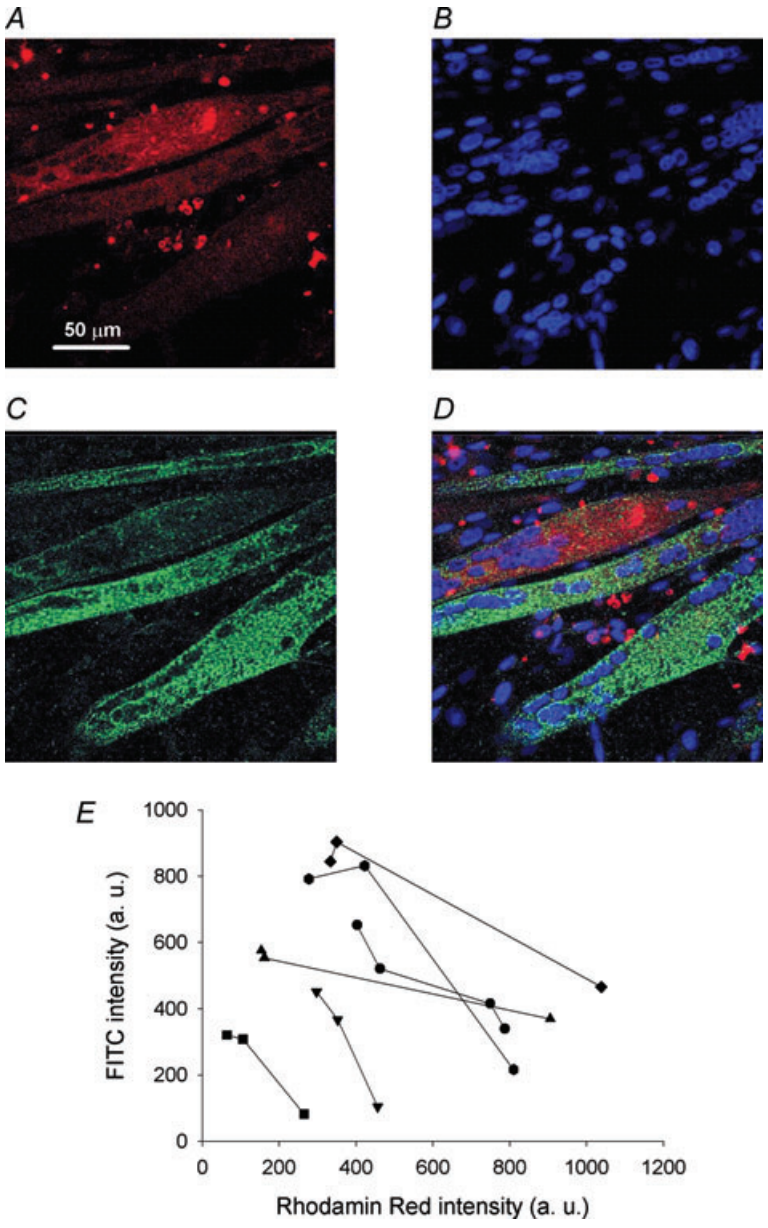


Figure 5. Suppressed Trisk 95 expression in rat primary myotubes transfected with a rhodamine red labelled shRNA
A, transfected myotubes are visualized by their red fluorescence. *B*, cell nuclei stained with DAPI. Note the large number of nuclei in the differentiated myotubes. *C*, triadin expression visualized by immunocytochemistry using a Trisk 95 primary and an anti-rabbit secondary antibody labelled with FITC. *D*, overlay image of those presented in panels *A*–*C*. Note the characteristic dotted pattern of Trisk 95 labelling in non-transfected cells as compared to the suppressed expression in the transfected myotube. Horizontal scaling bar is 50 μm for all images. *E*, effectiveness of the suppression of triadin expression. The intensity of Trisk 95 associated green fluorescence (FITC) was correlated with the shRNA associated red fluorescence (rhodamine) of the same area. Altogether 6 cultures and 19 areas were analysed; different symbols denote different cultures.

© 2008 The Authors. Journal compilation © 2008 The Physiological Society

Downloaded from J Physiol (jp.physoc.org) at unknown institution on July 2, 2009

embers (in 54 images) were detected. This accounts for an average frequency of $0.0032 \pm 0.0019\ s^{-1}\ \mu m^{-1}$ and $0.0024 \pm 0.0014\ s^{-1}\ \mu m^{-1}$, respectively.

The suppression of triadin expression in these myotubes had dramatic effects on the appearance of LCRE. Ca^{2+} sparks and embers became readily observable in both x–y (Fig. 7*C*) and in line-scan images ($n = 649$ and 117 for sparks and embers, respectively, from 5 myotubes, 218 out of 385 images; Fig. 7*D*). Not only LCRE but spontaneous calcium transients were also present on these cells as visible in the image in Fig. 7*D*. They appeared with approximately the same frequency (0.99 ± 0.16 Hz; $n = 888$ on 20 myotubes) but with a larger amplitude (1.39 ± 0.08; $P < 0.01$) than those in control (see above).

Not only was the frequency of LCRE altered in myotubes with suppressed Trisk 95 expression but their characteristic parameters were also changed. Figure 8*A* and *B* present two typical Ca^{2+} sparks measured in a control and in a triadin-suppressed myotube, respectively. These events were selected to represent the top 10% of events with respect to their amplitude. As evidenced from these two sparks and from the amplitude histograms presented in Fig. 8*C*, the proportion of Ca^{2+} sparks with large amplitude was increased in myotubes with suppressed Trisk 95 expression. As a result, the average amplitude of all sparks was significantly increased, from 0.49 ± 0.03 in control to 0.89 ± 0.04 ($P < 0.01$) in these cells. Not only the amplitude of sparks, but the average amplitude of embers was also increased, from 0.27 ± 0.05 to 0.49 ± 0.03 ($P < 0.01$; Fig. 8*D*). This was mainly due to the appearance of events with amplitudes greater than 0.6, hardly ever observed on control myotubes and never on adult fibres. On the other hand, neither the average duration of embers (229 ± 33 *versus* 198 ± 13 ms in control and in

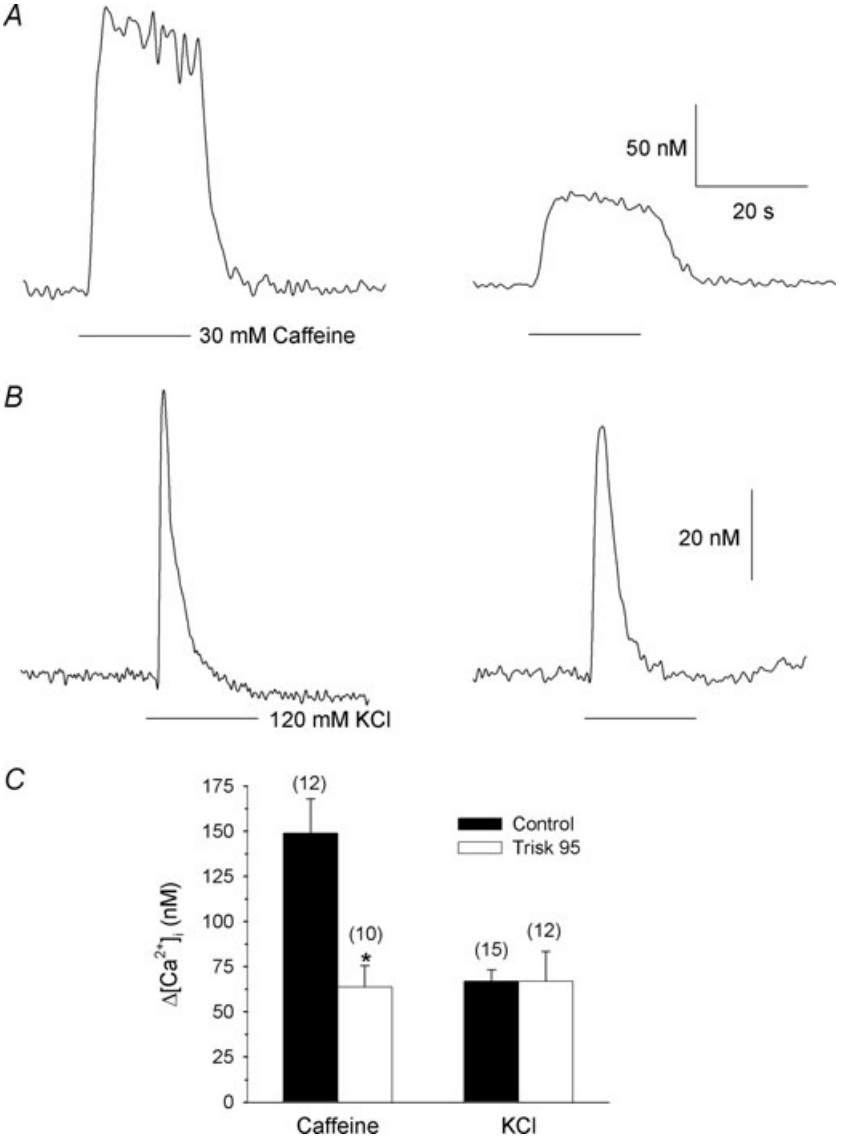


Figure 6. Calcium transients from control myotubes and from cells transfected with Trisk 95 specific shRNA
A and *B*, representative calcium transients evoked by either caffeine (30 mM; *A*) or by KCl-evoked depolarization (120 mM; *B*). Cells were kept in normal (*A*) or Ca^{2+}-free Tyrode solution (*B*) during the measurement. *C*, pooled data for $\Delta[Ca^{2+}]_i$. Note that control represents cells (subcellular areas) where Trisk 95 specific shRNA-associated red fluorescence was weak as compared to other cells of the same culture or cells from cultures treated with scrambled shRNA sequence. Asterisk marks significant difference as compared to control while the numbers in parentheses give the number of cells investigated.

© 2008 The Authors. Journal compilation © 2008 The Physiological Society

Downloaded from J Physiol (jp.physoc.org) at unknown institution on July 2, 2009

szentesi.peter_292_24

shRNA treated myotubes, respectively; see also Fig. 8*F*) nor that of sparks (39.7 ± 4.3 *versus* 44.0 ± 2.5 ms) was altered significantly ($P > 0.3$ and 0.07, respectively). In contrast, the spatial spread (from 1.67 ± 0.16 to 1.38 ± 0.07; $P < 0.02$) was reduced, while the rise time (from 15.4 ± 2.2 to 22.0 ± 2.9 ms; $P < 0.01$) of Ca^{2+} sparks was increased in myotubes with suppressed triadin expression.

Discussion

Triadin, an integral SR membrane protein, has previously been shown to interact with both the calcium release channel and calsequestrin, the low affinity calcium binding protein of the SR lumen. They seem to form a tri-, or maybe a tetra-molecular complex which also includes junctin (Beard *et al.* 2002; Györke *et al.* 2004; Wei *et al.* 2006). This close association suggests that triadin could influence RyR function. Indeed, triadin overexpression was shown to suppress calcium transients in cultured rat myotubes (Rezgui *et al.* 2005). However, no information is available on whether triadin overexpression might affect the localized calcium release events alterations in which are likely to reflect modifications in RyR function. Furthermore, data on the effects of transiently suppressed triadin expression on the calcium transients or on LCRE are also missing.

Here we demonstrate that both the increase and the decrease in Trisk 95 expression will affect the calcium transients and the localized calcium release events in cultured skeletal muscle cells. These effects, as expected, are opposite, demonstrating a clear and specific role of triadin in regulating RyR function. When overexpressed triadin reduced the amplitude of spontaneous and

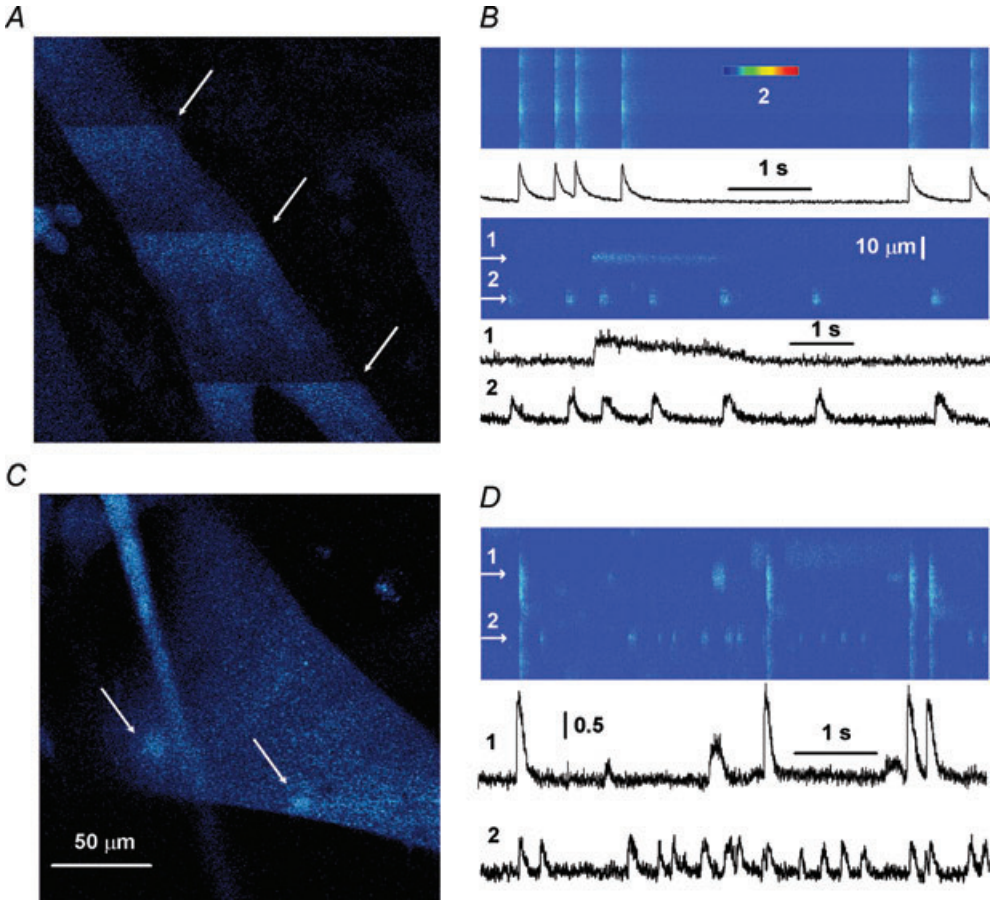


Figure 7. Spontaneous Ca^{2+} transients and Ca^{2+} release events in rat primary myotubes
A, an *x*–*y* image of a control myotube loaded with Fluo-3 displaying spontaneous Ca^{2+} transients (arrows). *B*, line-scan images of rat primary myotubes generating spontaneous Ca^{2+} transients. The traces below the images are spatially averaged time courses of Fluo-3 fluorescence from either the entire image (upper image) or from the lines marked by arrows. Note the absence of localized events on the upper image. *C*, *x*–*y* image of shRNA transfected myotubes. Note the localized Ca^{2+} release events marked by arrows. *D*, line-scan image of rat primary myotubes with suppressed Trisk 95 expression generating spontaneous Ca^{2+} release events. Traces below the images were generated as those in panel *B*. Note the large number of events. Vertical calibrations are the same for the images and for all traces in *B* and *D*.

© 2008 The Authors. Journal compilation © 2008 The Physiological Society

Downloaded from J Physiol (jp.physoc.org) at unknown institution on July 2, 2009

depolarization-evoked calcium transients and suppressed the appearance of LCRE by reducing their number and size. The interference with its expression, on the other hand, increased the amplitude of the calcium transient and of LCRE together with increasing the number of the latter. Since increased expression of triadin was accompanied by suppression, while decreased expression was followed by an augmentation of calcium release, we propose that triadin *in situ* is exerting a tonic negative effect on the opening of RyR.

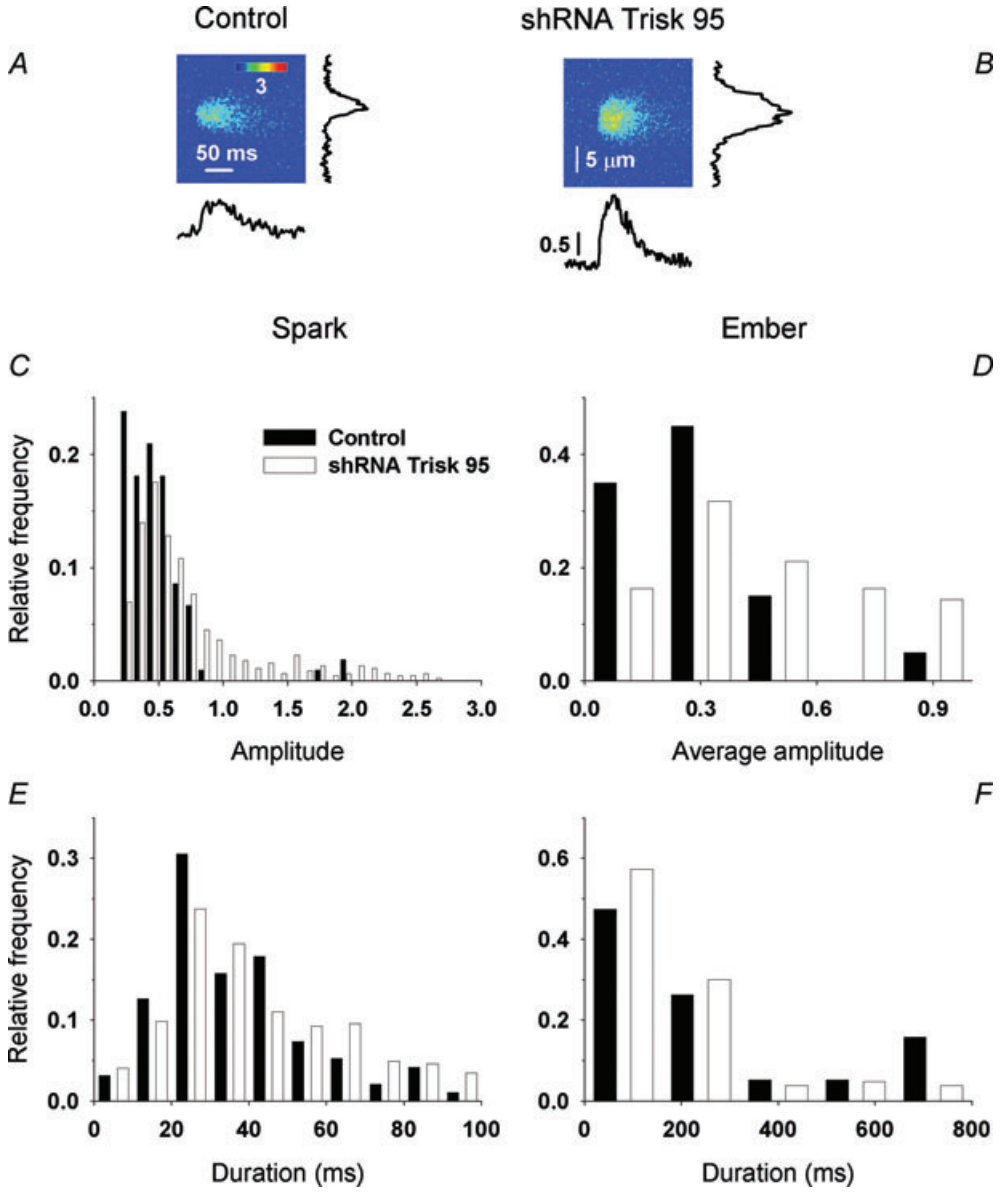


Figure 8. Parameters of Ca^{2+} sparks from control rat primary myotubes and from myotubes with suppressed Trisk 95 expression
A and *B*, typical Ca^{2+} sparks from a control myotube (*A*) and from a cell with suppressed triadin expression (*B*). Traces below and next to the images give the time course and the spatial distribution of fluorescence, respectively, measured at the position of the peak. Horizontal and vertical calibrations correspond to both images and to all four traces in *A* and *B*. *C*, amplitude histogram of Ca^{2+} sparks from control myotubes and from myotubes with suppressed triadin expression. Note the larger scatter for the control data due to the relatively low number of events (143 *versus* 649; control and Trisk 95 suppressed, respectively). *D*, histogram of the average amplitude of embers generated as in panel *C*. Note the significant contribution from events with large average amplitude in Trisk 95 suppressed myotubes. *E* and *F*, histograms of event duration presented as that in panels *C* and *D* for Ca^{2+} sparks (*E*) and embers (*F*).

© 2008 The Authors. Journal compilation © 2008 The Physiological Society

Downloaded from J Physiol (jp.physoc.org) at unknown institution on July 2, 2009

Calcium transients in myotubes with altered triadin expression

The changes in whole-cell calcium transients following altered Trisk 95 expression, whether evoked by KCl-induced depolarization or by spontaneously occurring or electrically evoked action potentials, are clearly in line with the hypothesis that triadin serves as a tonic negative regulator of RyR function. Data reported here as well as those published earlier (Rezgui *et al.* 2005; Csernoch *et al.* 2007) established that Trisk 95 overexpression suppresses the depolarization-evoked calcium transients. It should be noted, however, that calcium transients in the presence of external calcium were only suppressed if evoked by action potentials (Fig. 4) and not if the addition of 120 mM KCl was used (Fig. 2*D*) to initiate calcium release. This apparent contradiction can be resolved with either of the two following possibilities. One might assume that external calcium influx gives a large contribution to the global change in $[Ca^{2+}]_i$ only if the depolarization is long enough. Although this seems as an intriguing possibility as L-type calcium current is activating slowly in skeletal myotubes (e.g. O'Connell & Dirksen, 2000), simple calculations show that the amount of calcium that enters into the myoplasm through these channels is not enough to explain the above phenomenon (Szappanos *et al.* 2004). The other and definitely more likely possibility is that the calcium entering through the L-type channels serves as a trigger for the activation of RyR (calcium-induced calcium release) and thus overrides the inhibition exerted by the overexpressed triadin. This would also explain why action potential-evoked transients are suppressed under these conditions, since the action potential is too short to allow substantial influx of external calcium.

It should also be noted that in case of action potential-evoked calcium transients the alteration in calcium release could result from the modification of the action potential itself. While there is evidence that links Trisk 95 to surface membrane channels (see below), none exists that would suggest an interaction between triadin and either the sodium or potassium channels responsible for the generation of the action potential in skeletal muscle.

Recently calcium transients from muscles with reduced triadin expression were derived from triadin knock-out animals (Shen *et al.* 2007). In these mice both the higher – 95 and 60 kDa – and lower molecular weight triadins – 35–40 kDa – were absent. While exhibiting no clear phenotype, the animals were characterized by an elevated resting intracellular Ca^{2+} concentration while reduced SR calcium content and calcium transients in response to caffeine or K^+-induced depolarization. In addition, reduced expression of certain junctional proteins, junctin, junctophilin-1 and CSQ, with no clear alteration in the expression of type 1 RyR (RyR1) was observed in adult fast twitch muscles. Interestingly, no alteration in the expression of junctin or CSQ was detected in myotubes.

Our results – from cells transfected with the appropriate shRNA and thus with reduced Trisk 95 expression – showing an increased resting $[Ca^{2+}]_i$ and reduced response to caffeine are essentially identical to those of Shen *et al.* (2007). Similar reduction in agonist-induced SR calcium release was reported for cells, where the interaction of RyR and triadin was interfered with (Goonasekera *et al.* 2007). On the other hand, we found identical calcium transients for KCl-evoked depolarization in control cells and in cells with reduced triadin expression (Fig. 6). This was observed in spite of the reduced caffeine response indicative of a reduced SR calcium content for the latter cells. This finding is, nevertheless, in line with the results obtained here both with the parameters of LCRE on these cells (see below) and with the data with Trisk 95 overexpression. To explain the apparent discrepancy one might consider the fact that in the reports of Shen *et al.* (2007) and Goonasekera *et al.* (2007) the RyR–triadin interaction is completely disrupted while in our experiments it is only reduced. One could then assume that the depletion of Ca^{2+} in the SR in our experiments where the Trisk 95 expression is not completely eliminated is less than that in the report of Shen *et al.* (2007). This would explain how the increased activation of RyR – due to the partial absence of triadin – could compensate for the reduced SR content.

Interestingly not only the amplitude of the spontaneous calcium transients but also their frequency was altered by altered triadin expression; reduced expression increased while increased expression reduced the frequency. We have no clear explanation at the moment whether triadin expression would alter membrane excitability, although several reports link triadin to surface membrane channels. Early reports suggested that triadin might bind to the DHPR itself and serve as a bridge between the SR and the T-tubular membranes (Caswell *et al.* 1991). This, however, has later been questioned based on the topology – short, only 46 amino acids long, intracellular segment – of triadin (Groh *et al.* 1999). In addition, recent reports linked triadin expression to store-operated calcium influx (Vassilopoulos *et al.* 2007), and the functional interaction between TRPC channels and RyR was connected to triadin expression (Lee *et al.* 2006).

Localized calcium release events with altered triadin expression

To our knowledge no previous reports have investigated whether Trisk 95 overexpression or the inhibition of its translation would affect the localized events of calcium release to assess the *in situ* effects of triadin on RyR. However, the addition of triadin to RyRs reconstituted into planar lipid bilayers resulted in a decrease of channel open

© 2008 The Authors. Journal compilation © 2008 The Physiological Society

Downloaded from J Physiol (jp.physoc.org) at unknown institution on July 2, 2009

probability (Groh *et al.* 1999). Similarly, triadin inhibited [^{3}H]ryanodine binding to heavy SR vesicles (Guo & Campbell, 1995). These observations clearly suggested that triadin would suppress the calcium release channel function in line with the data on whole-cell calcium transients.

These assumptions were clearly confirmed by our findings that suppressed Trisk 95 expression was accompanied by an increase while the overexpression of triadin was followed by a reduction in the frequency of LCRE. Not only were the number of events altered, their amplitude and spatial parameters were also affected together with the modified expression of Trisk 95. In triadin overexpressing cells sparks were smaller, both the amplitude and FWHM, indicating that the number of channels involved in the generation of an event was reduced in these cells. In line with this assumption, and with the observation that SR calcium load was not affected, the characteristic parameters of embers were essentially identical with those in control cells. On the other hand, suppression of Trisk 95 increased not only the frequency but also the amplitude of the sparks in line with more channels opening during an event. Interestingly, embers with average amplitudes greater than 0.6 were readily observed in myotubes with reduced triadin expression. These events suggest that either the conductance of the channel or the SR calcium load is increased or more than a single channel was opened during the event. While all above possibilities, or their combination could explain the observations, the most likely scenario is the change in the number of channels since mutations interfering with triadin binding had no effect on single channel conductance in planar lipid bilayers (Goonasekera *et al.* 2007) and we saw a reduction in SR load in whole-cell calcium measurements (Fig. 6).

Recently the importance of type 3 RyR (RyR3) as well as that of the inositol trisphosphate receptor (IP_3R) in the generation of LCRE has been documented (Pouvreau *et al.* 2007 and Balghi *et al.* 2006, respectively). This raises the possibility that the observations presented in this study could correspond to interactions of Trisk 95 with either RyR3 or IP_3R and not the type 1 or skeletal isoform of RyR, thus explaining some of the differences between the results seen here and with knock-out animals (Shen *et al.* 2007; see above). While the involvement of IP_3R in the generation of LCRE seems established in mouse myotubes lacking dystrophin, they were reported to be less important if a mini-dystrophin is expressed in these cells (Balghi *et al.* 2006). Although not conclusive, it is likely that the involvement of IP_3R would be even smaller in cells expressing normal amounts of dystrophin. In addition, the localization of Trisk 95 and IP_3R seem to be distinct. The distribution of the 95 kDa isoform of triadin shows a clear dotted pattern (see e.g. Fig. 5) and the protein is confined to the junctional region. In contrast, IP_3R shows a more diffuse distribution and seems to colocalize with the 32 kDa isoform member of the triadin family (Vassilopoulos *et al.* 2007). Although RyR3 is found in the triadic junction and could therefore interact with Trisk 95 no such protein–protein interaction has been described so far. One cannot, however, exclude the possibility that the overexpression of triadin could result in the appearance of the protein at locations other than those where it is physiologically present. This could, at least partially, explain why calcium release events and calcium transients are suppressed if Trisk 95 is overexpressed. It could not, however, account for the opposite effects seen with shRNA since it is unlikely the triadin would appear at altered locations if its expression is reduced.

Finally, it should be considered whether interfering with the expression of Trisk 95 altered the expression levels of other key proteins, e.g. RyR and CSQ, of excitation–contraction coupling thus resulting in the modification of calcium release. We have therefore checked the expression level of these two proteins in our cultures and found no significant alteration in their expression (in line with the report of Shen *et al.* 2007; see also Supplemental Material). This is in line with the report of Perez *et al.* (2005) who found that the overexpression of neither RyR1 nor RyR3 influenced the expression of triadin.

Taken together our data clearly establish that Trisk 95 regulates LCRE in cultured skeletal myotubes by exerting a tonic negative effect. Although these localized events have only been indirectly linked to normal E-C coupling in adult mammalian skeletal muscle (see e.g. Csernoch, 2007) the channels involved in their generation are most likely to be the same as those activated by membrane depolarization, suggestive of a role for Trisk 95 in regulating calcium release channel function *in situ*.

References

Balghi H, Sebille S, Mondin L, Cantereau A, Constantin B, Raymond G & Cognard C (2006). Mini-dystrophin expression down-regulates IP_3-mediated calcium release events in resting dystrophin-deficient muscle cells. *J Gen Physiol* **128**, 219–230.

Beard NA, Sakowska MM, Dulhunty AF & Laver DR (2002). Calsequestrin is an inhibitor of skeletal muscle ryanodine receptor calcium release channels. *Biophys J* **82**, 310–320.

Brandt NR, Caswell AH, Wen SR & Talvenheimo JA (1990). Molecular interactions of the junctional foot protein and dihydropyridine receptor in skeletal muscle triads. *J Membr Biol* **113**, 237–251.

Caswell AH, Brandt NR, Brunschwig JP & Purkerson S (1991). Localization and partial characterization of the oligomeric disulfide-linked molecular weight 95,000 protein (triadin) which binds the ryanodine and dihydropyridine receptors in skeletal muscle triadic vesicles. *Biochemistry* **30**, 7507–7513.

© 2008 The Authors. Journal compilation © 2008 The Physiological Society

Downloaded from J Physiol (jp.physoc.org) at unknown institution on July 2, 2009

Caswell AH, Motoike HK, Fan H & Brandt NR (1999). Location of ryanodine receptor binding site on skeletal muscle triadin. *Biochemistry* **38**, 90–97.

Chun LG, Ward CW & Schneider MF (2003). Ca^{2+} sparks are initiated by Ca^{2+} entry in embryonic mouse skeletal muscle and decrease in frequency postnatally. *Am J Physiol Cell Physiol* **285**, C686–C697.

Csernoch L (2007). Sparks and embers of skeletal muscle: the exciting events of contractile activation. *Pflugers Arch* **454**, 869–878.

Csernoch L, Fodor J, Fehér M, Dienes B, Deli T, Szentesi P, Szabó L & Marty I (2007). Suppressed SR calcium release and modified elementary calcium release events in Triadin-overexpressing cultured myotubes. *Biophys J* **92** (Suppl.), 79a.

Deli T, Szappanos H, Szigeti GP, Cseri J, Kovács L & Csernoch L (2007). Contribution from P2X and P2Y purinoreceptors to ATP-evoked changes in intracellular calcium concentration on cultured myotubes. *Pflugers Arch* **453**, 519–529.

Gonzalez A, Kirsch WG, Shirokova N, Pizarro G, Stern MD & Rios E (2000). The sparks and its ember: separately gated local components of Ca^{2+} release in skeletal muscle. *J Gen Physiol* **115**, 139–157.

Goonasekera SA, Beard NA, Groom L, Kimura T, Lyfenko AD, Rosenfeld A, Marty I, Dulhunty AF & Dirksen RT (2007). Triadin binding to the C-terminal luminal loop of the ryanodine receptor is important for skeletal muscle excitation contraction coupling. *J Gen Physiol* **130**, 365–378.

Groh S, Marty I, Ottolia M, Prestipino G, Chapel A, Villaz M & Ronjat M (1999). Functional interaction of the cytoplasmic domain of triadin with the skeletal ryanodine receptor. *J Biol Chem* **274**, 12278–12283.

Guo W & Campbell KP (1995). Association of triadin with the ryanodine receptor and calsequestrin in the lumen of the sarcoplasmic reticulum. *J Biol Chem* **270**, 9027–9030.

Györke I, Hester N, Jones LR & Györke S (2004). The role of calsequestrin, triadin, and junctin in conferring cardiac ryanodine receptor responsiveness to luminal calcium. *Biophys J* **86**, 2121–2128.

Kirsch WG, Uttenweiler D & Fink RH (2001). Spark- and ember-like elementary Ca^{2+} release events in skinned fibres of adult mammalian skeletal muscle. *J Physiol* **537**, 379–389.

Klein MG, Cheng H, Santana LF, Jang YH, Lederer WJ & Schneider MF (1996). Two mechanisms of quantized calcium release in skeletal muscle. *Nature* **379**, 455–458.

Knudson CM, Stang KK, Moomaw CR, Slaughter CA & Campbell KP (1993). Primary structure and topological analysis of a skeletal muscle-specific junctional sarcoplasmic reticulum glycoprotein (triadin). *J Biol Chem* **268**, 12646–12654.

Kobayashi YM, Alseikhan BA & Jones LR (2000). Localization and characterization of the calsequestrin-binding domain of triadin 1. Evidence for a charged β-strand in mediating the protein–protein interaction. *J Biol Chem* **275**, 17639–17646.

Lee EH, Cherednichenko G, Pessah IN & Allen PD (2006). Functional coupling between TRPC3 and RyR1 regulates the expressions of key triadic proteins. *J Biol Chem* **281**, 10042–10048.

Marty I, Robert M, Ronjat M, Bally I, Arlaud G & Villaz M (1995). Localization of the N-terminal and C-terminal ends of triadin with respect to the sarcoplasmic reticulum membrane of rabbit skeletal muscle. *Biochem J* **307**, 769–774.

Marty I, Thevenon D, Scotto C, Groh S, Sainnier S, Robert M, Grunwald D & Villaz M (2000). Cloning and characterization of a new isoform of skeletal muscle triadin. *J Biol Chem* **275**, 8206–8212.

Miller SL, Currie S, Loughrey CM, Kettlewell S, Seidler T, Reynolds DF, Hasenfuss G & Smith GL (2005). Effects of calsequestrin over-expression on excitation-contraction coupling in isolated rabbit cardiomyocytes. *Cardiovasc Res* **67**, 667–677.

O'Connell KM & Dirksen RT (2000). Prolonged depolarization promotes fast gating kinetics of L-type Ca^{2+} channels in mouse skeletal myotubes. *J Physiol* **529**, 647–659.

Perez CF, López JR & Allen PD (2005). Expression levels of RyR1 and RyR3 control resting free Ca^{2+} in skeletal muscle. *Am J Physiol Cell Physiol* **288**, C640–C649.

Pouvreau S, Royer L, Yi J, Brum G, Meissner G, Ríos E & Zhou J (2007). Ca^{2+} sparks operated by membrane depolarization require isoform 3 ryanodine receptor channels in skeletal muscle. *Proc Natl Acad Sci U S A* **104**, 5235–5240.

Rezgui SS, Vassilopoulos S, Brocard J, Platel JC, Bouron A, Arnoult C, Oddoux S, Garcia L, De Waard M & Marty I (2005). Triadin (Trisk 95) overexpression blocks excitation-contraction coupling in rat skeletal myotubes. *J Biol Chem* **280**, 39302–39308.

Shen X, Franzini-Armstrong C, Lopez JR, Jones LR, Kobayashi YM, Wang Y, Kerrick WG, Caswell AH, Potter JD, Miller T, Allen PD & Perez CF (2007). Triadins modulate intracellular Ca^{2+} homeostasis but are not essential for excitation-contraction coupling in skeletal muscle. *J Biol Chem* **282**, 37864–37874.

Shirokova N, Garcia J & Rios E (1998). Local calcium release in mammalian skeletal muscle. *J Physiol* **512**, 377–384.

Szappanos H, Cseri J, Deli T, Kovács L & Csernoch L (2004). Determination of depolarisation- and agonist-evoked calcium fluxes on skeletal muscle cells in primary culture. *J Biochem Biophys Methods* **59**, 89–101.

Szentesi P, Szappanos H, Szegedi C, Gönczi M, Jona I, Cseri J, Kovács L & Csernoch L (2004). Altered elementary calcium release events and enhanced calcium release by thymol in rat skeletal muscle. *Biophys J* **86**, 1436–1453.

Tsugorka A, Ríos E & Blatter LA (1995). Imaging elementary events of calcium release in skeletal muscle cells. *Science* **269**, 1723–1726.

Vassilopoulos S, Brocard J, Garcia L, Marty I & Bouron A (2007). Retrograde regulation of store-operated calcium channels by the ryanodine receptor-associated protein triadin 95 in rat skeletal myotubes. *Cell Calcium* **41**, 179–185.

Wei L, Varsányi M, Dulhunty AF & Beard NA (2006). The conformation of calsequestrin determines its ability to regulate skeletal ryanodine receptors. *Biophys J* **91**, 1288–1301.

Zhou J, Brum G, Gonzalez A, Launikonis BS, Stern MD & Rios E (2003). Ca^{2+} sparks and embers of mammalian muscle. Properties of the sources. *J Gen Physiol* **122**, 95–114.

© 2008 The Authors. Journal compilation © 2008 The Physiological Society

Downloaded from J Physiol (jp.physoc.org) at unknown institution on July 2, 2009

Zhou J, Yi J, Royer L, Launikonis BS, Gonzalez A, Garcia J & Rios E (2006). A probable role of dihydropyridine receptors in repression of Ca^{2+} sparks demonstrated in cultured mammalian muscle. *Am J Physiol Cell Physiol* **290**, C539–C553.

Acknowledgements

The authors wish to thank R. Öri for the excellent technical assistance. This work was supported by grants from the Hungarian Science Fund (OTKA T049151, NK61412), and from Association Française contre les Myopathies (AFM) to I.M. MG was a recipient of an OTKA postdoctoral fellowship.

© 2008 The Authors. Journal compilation © 2008 The Physiological Society

Downloaded from J Physiol (jp.physoc.org) at unknown institution on July 2, 2009

Pflugers Arch - Eur J Physiol
DOI 10.1007/s00424-013-1346-5

szentesi.peter_292_24

MUSCLE PHYSIOLOGY

Phosphoinositide substrates of myotubularin affect voltage-activated Ca^{2+} release in skeletal muscle

Estela González Rodríguez · Romain Lefebvre · Dóra Bodnár · Claude Legrand · Peter Szentesi · János Vincze · Karine Poulard · Justine Bertrand-Michel · Laszlo Csernoch · Anna Buj-Bello · Vincent Jacquemond

Received: 23 May 2013 / Revised: 29 August 2013 / Accepted: 29 August 2013
© Springer-Verlag Berlin Heidelberg 2013

Abstract Skeletal muscle excitation–contraction (E–C) coupling is altered in several models of phosphatidylinositol phosphate (PtdIns*P*) phosphatase deficiency and ryanodine receptor activity measured in vitro was reported to be affected by certain PtdIns*P*s, thus prompting investigation of the physiological role of PtdIns*P*s in E–C coupling. We measured intracellular Ca^{2+} transients in voltage-clamped mouse muscle fibres microinjected with a solution containing a PtdIns*P* substrate (PtdIns(3,5)P_2 or PtdIns(3)*P*) or product (PtdIns(5)*P* or PtdIns) of the myotubularin phosphatase MTM1. No significant change was observed in the presence of either PtdIns(5)*P* or PtdIns but peak SR Ca^{2+} release was depressed by ~30% and 50% in fibres injected with PtdIns(3,5)P_2 and PtdIns(3)*P*, respectively, with no concurrent alteration in the membrane current signals associated with the DHPR function as well as in the voltage dependence of Ca^{2+} release inactivation. In permeabilized muscle fibres, the frequency of spontaneous Ca^{2+} release events was depressed in the presence of the three tested phosphorylated forms of PtdIns*P* with PtdIns(3,5)P_2 being the most effective, leading to an almost complete disappearance of Ca^{2+} release events. Results support the possibility that pathological accumulation of MTM1 substrates may acutely depress ryanodine receptor-mediated Ca^{2+} release. Overexpression of a mCherry-tagged form of MTM1 in muscle fibres revealed a striated pattern consistent with the triadic area. Ca^{2+} release remained although unaffected by MTM1 overexpression and was also unaffected by the PtdIns-3-kinase inhibitor LY2940002, suggesting that the 3-phosphorylated PtdIns lipids active on voltage-activated Ca^{2+} release are inherently maintained at a low level, inefficient on Ca^{2+} release in normal conditions.

Keywords Calcium homeostasis · Excitation–contraction coupling · Ryanodine receptor · Sarcoplasmic reticulum Ca^{2+} release · Phosphatidylinositol phosphate

Electronic supplementary material The online version of this article (doi:10.1007/s00424-013-1346-5) contains supplementary material, which is available to authorized users.

E. González Rodríguez
Departamento de Fisiología, Genética y Microbiología, Universidad de Alicante, Alicante, Spain

R. Lefebvre · C. Legrand · V. Jacquemond (✉)
Centre de Génétique et de Physiologie Moléculaire et Cellulaire, Université Lyon 1, UMR CNRS 5534, Bât. Raphaël Dubois, 43 boulevard du 11 novembre 1918, F69622, Villeurbanne, France
e-mail: vincent.jacquemond@univ-lyon1.fr

D. Bodnár · P. Szentesi · J. Vincze · L. Csernoch
Department of Physiology, University of Debrecen, Debrecen, Hungary

K. Poulard · A. Buj-Bello
Department of Research and Development, Généthon, INSERM, Evry, France

J. Bertrand-Michel
Lipidomic Core Facility, Metatoul Platform, INSERM U1048, Université de Toulouse, Université Paul Sabatier, Toulouse, France

Introduction

The function of phosphoinositides had for a long time remained limited to the possible role of phosphatidylinositol 4,5-bisphosphate (PtdIns(4,5)P_2) as a substrate of phospholipase C to produce inositol-trisphosphate (Ins(1,4,5)P_3) and diacylglycerol. The last decade has seen a remarkable expansion of the concept so as to now include the role of PtdIns*P*s phosphorylated in the 3-OH position, which control a wide array of cellular functions including membrane trafficking, cytoskeleton remodeling, protein docking, and membrane transport (for review, see [12]), and numerous studies have also

Published online: 11 September 2013

revealed the fundamental role of PtdIns*P*s in regulating ion channel activity (for reviews, see [25, 35]).

Skeletal muscle cells contract in response to depolarizing changes of their plasma membrane voltage: action potentials fired at the end-plate of the muscle fibres propagate throughout the transversal (t-) tubule system: coupling between membrane depolarization and contraction occurs within the triad regions where one t-tubule faces two terminal cisternae of sarcoplasmic reticulum (SR). There, depolarization changes the conformation of the dihydropyridine receptor (DHPR, the Cav1.1 protein, the voltage-sensing component of the system) which opens up the SR calcium release channel (type 1 ryanodine receptor, RyR1) through protein–protein conformational coupling. Upon membrane repolarization, RyR1 channels close, and muscle relaxation occurs due to cytosolic Ca^{2+} extrusion driven by the SR Ca^{2+} pump.

This basic functional scheme is either known or presumed to be controlled, regulated or modulated by a wide array of accessory proteins and messenger molecules (for review, see [22]). The possible role of PtdIns*P*s in the regulation of Ca^{2+} homeostasis and excitation–contraction (E–C) coupling in muscle remained elusive until recent years. Indeed, if one excludes the controversies related to the possible role of the Ins(1,4,5)P_3 pathway (e.g., [16]), only very few studies in the 1990s suggested that PtdIns(4,5)P_2 could affect the SR Ca^{2+} release process [6, 20, 29]. However, recent data from transgenic models of PtdIns*P*-phosphatase deficiency, specifically MTM1 (myotubularin) and parent proteins ("myotubularin and myopathy related" phosphatases [MTMRs]; see [3]) provided completely unanticipated insights into the field: in humans, more than 200 mutations of the gene encoding MTM1 are associated with X-linked myotubular myopathy (see [23]), characterized by very severe muscle weakness and consequent fatal outcome, often within weeks following birth [30]. The link between MTM1 deficiency and muscle weakness remained obscure until muscle fibres from MTM1-deficient mice were shown to suffer from a critically defective E–C coupling process [1]. Concurring data from a MTM1-deficient zebrafish model were provided by Dowling et al. [14]. In mouse, MTM1-deficient muscle fibres yield defects in the internal membrane system structure and organization, reduced levels of DHPR and RyR1 and a strong decrease in the amplitude of voltage-activated cytosolic Ca^{2+} signals. This functional alteration is certainly the direct cause of muscle weakness in the affected patients. Results by Al-Qusairi et al. [1] also demonstrated that SR Ca^{2+} content and cytosolic Ca^{2+} removal capabilities are unaltered in MTM1-deficient muscle fibres. At the functional level, the disease status thus appears to specifically affect the SR Ca^{2+} release process.

The internal membrane architecture defects may contribute to this alteration but are likely not the sole explanations: inner structure alterations are common features of several types of muscle disorders and are already observed in young MTM1-deficient mice which have limited defects in muscle function [1]. Furthermore, MTMR14 deficiency in zebrafish is also associated with defective E–C coupling, but without the inner-membrane-systems architecture defects observed in absence of MTM1 [13]. The reduction in the level of RyR1 would also, intuitively, be expected to play a role in muscle weakness, but actually the question of how much of the normal RyR1 content is necessary to sustain E–C coupling in muscle is far from clearly established. It is important to point out in this respect that several human muscle diseases due to *RYR1* mutations have been shown to be associated with a more severe reduction in RyR1 than observed under the conditions of MTM1 deficiency; the fact that severe RyR1 reduction in these cases was associated with a much lesser impact on muscle function and life expectancy [27, 37–39] seems to indicate that this may not be the critical issue determining the severity of myotubular myopathy.

One obvious possibility is that the E–C coupling defect results from altered PtdIns*P*s metabolism due to the loss of MTM1 PtdIns*P*-phosphatase activity. It is supported by results from Shen et al. [34] showing that loss of another PtdIns*P*-phosphatase (MTMR14) is responsible for alterations of intracellular Ca^{2+} homeostasis in muscle, attributable to defective regulation of RyR1 channel activity by PtdIns*P*s. Recent data also indicate that muscle weakness associated with aging may be due to altered Ca^{2+} homeostasis because of a reduced level of MTMR14 [33]. This trend of data thus tends to suggest a role for PtdIns*P*s in the regulation of skeletal muscle Ca^{2+} homeostasis and E–C coupling under normal conditions and a role for alteration of this regulation in certain muscle diseases. We looked here for a direct evidence that PtdIns*P*s are physiologically involved in the regulation of Ca^{2+} and E–C coupling in normal muscle. We demonstrate that MTM1 main PtdIns*P* substrates inhibit the function of E–C coupling while maneuvers intended to reduce the level of these 3-OH phosphorylated PtdIns have no effect.

Materials and methods

All experiments and procedures were in accordance with the guidelines of the local animal ethics committee of University Lyon 1 and University of Debrecen, of the French Ministry of Agriculture (87/848) and of the European Community (86/609/EEC).

In vivo transfection

An expression plasmid encoding wild-type mouse MTM1 fused N-terminally to mCherry was constructed using the pmCherry-C1 vector (Clontech, Mountain View, CA, USA). Swiss OF1 male mice that were 1–2 months old were used. Transfection was performed in the *flexor digitorum brevis*

szentesi.peter_292_24

(*fdb*) and interosseus muscles of the animals. Details of the procedure used for in vivo electroporation are given in Electronic supplementary material. Experimental observations and measurements were carried out 7–10 days later.

Preparation of isolated muscle fibres

Single fibres were isolated from the *fdb* and interosseus muscles from mouse using a previously described procedure [18]. In brief, mice were killed by cervical dislocation before removal of the muscles. Muscles were treated with collagenase (Sigma, type 1) for 60 min at 37°C. Single fibres were then obtained by triturating the muscles within the experimental chamber. They were dispersed on the glass bottom of a 50-mm-wide culture μ-dish (Biovalley, Marne la Vallée, France). For intracellular Ca^{2+} measurements under voltage-clamp conditions, fibres were first partially insulated with silicone grease as described previously [18]; in brief, fibres were embedded within silicone so that only a portion of the fibre extremity was left out of the silicone. Under these conditions, fibres remained well maintained on the bottom of the chamber and this allowed whole-cell voltage clamp to be achieved on the silicone-free extremity of the fibre. Once partially embedded within silicone, indo-1 or fluo-4 was introduced into the myoplasm through local pressure micro-injection with a micropipette containing 1 mM of the dye. Indo-1 was dissolved in the standard intracellular-like solution (see Solutions) whereas fluo-4 was dissolved in a solution containing 100 mM EGTA and 40 mM $CaCl_2$. Details regarding the use of EGTA are given in the Electronic supplementary material. Microinjection was always performed within the silicone-embedded part of the fibre, away from the silicone-free end portion under study. Following diffusion and equilibration within the cytoplasm, this was believed to achieve a final cytoplasmic concentration or indo-1 or fluo-4 within the 100 μM range and of EGTA within the 10 mM range, respectively (for details concerning micro-injections, see [10]). Experiments were usually performed on fibres from the *fdb* muscle; only when testing the effect of MTM1 overexpression were a few control and MTM1-positive fibres from interosseus muscles used. For all experimental situations, control fibres (either untreated with the tested reagent or non-expressing the tested transfected gene) were always from the same muscles as the tested fibres. All experiments were performed at room temperature (20–22°C).

Electrophysiology

An RK-400 patch-clamp amplifier (Bio-Logic, Claix, France) was used in whole-cell voltage-clamp configuration. Fibres were bathed in the TEA-containing extracellular solution (see Solutions). Command voltage pulse generation was achieved with an analog–digital converter (Digidata 1440A; Axon Instruments, Foster City, CA, USA) controlled by pClamp 9 software (Axon Instruments). Voltage-clamp was performed with a microelectrode filled with the intracellular-like solution (see Solutions). The tip of the microelectrode was inserted through the silicone, within the insulated part of the fibre. Analog compensation was systematically used to decrease the effective series resistance. Membrane depolarizing steps were applied from a holding command potential of −80 mV, unless otherwise specified. Removal of the linear leak and capacitive components of the current changes elicited by a depolarizing pulse was achieved as previously described [8, 32]. Details of the procedures used for membrane current analysis are given in the Electronic supplementary material.

Fluorescence measurements in voltage-clamped fibres

Indo-1 fluorescence was measured on an inverted Nikon Diaphot epifluorescence microscope equipped with a commercial optical system allowing the simultaneous detection of fluorescence at 405 nm (F405) and 485 nm (F485) by two photomultipliers (IonOptix, Milton, MA, USA), upon 360 nm excitation. Background fluorescence at both emission wavelengths was measured next to each fibre tested and was then subtracted from all measurements.

Confocal fluorescence measurements were done using a Zeiss LSM 5 Exciter confocal microscope equipped with a × 63 oil immersion objective (numerical aperture 1.4). Fluo-4 excitation was provided by the 488 nm line of an argon laser and a 505- to 600-nm band-pass filter was used on the detection channel. For detection of mCherry fluorescence the excitation was from the 543-nm line of a HeNe laser and fluorescence was collected above 560 nm. Intracellular $[Ca^{2+}]$-related fluorescence changes were imaged by using the line-scan mode of the system with the line parallel to the longitudinal fibre axis. The majority of images were taken with a scanning frequency of 1.15 ms per line. Image processing and analysis was performed using Image/J (NIH, USA) and Microcal Origin (Microcal Software Inc., Northampton, MA, USA).

$[Ca^{2+}]$ and Ca^{2+} release calculation in intact fibres

For indo-1 fluorescence signals, the standard ratio method was used with the parameters: $R=F_{405}/F_{485}$, with R_{min}, R_{max}, K_D and β having their usual definitions. Results were either expressed in terms of indo-1% saturation or in actual free Ca^{2+} concentration; in vivo values for R_{min} and β were measured using procedures previously described [18]. R_{max} was determined at the end of the experiments after damaging the fibre under study with a thin needle until complete contracture. An estimation of the Ca^{2+} release flux underlying the calculated global $[Ca^{2+}]$ transients was performed as described previously [9, 31]. Details of the procedure used for Ca^{2+} release calculation are given in the Electronic supplementary material.

Fluo-4 changes in fluorescence were expressed as F/F_0, where F_0 is the resting (or baseline) fluorescence level. Changes in [Ca^{2+}] were calculated from the fluo-4 signals using the pseudo-ratio equation [5] assuming a basal [Ca^{2+}] of 100 nM and a K_d of fluo-4 for Ca^{2+} of 1 μM [17]. No correction was made for the fluo-4 binding kinetics.

Measurements of SR Ca^{2+} content in intact fibres

For this, we used a protocol similar to the one we described in a previous study [1]. In brief, the cytosol of *fdb* fibres was dialyzed through the voltage-clamp pipette with the intracellular-like solution also containing 20 mM EGTA, 8 mM Ca, 0.2 mM indo-1 with or without PtdIns(3)*P* (0.1 mM). Following a 30-min period of equilibration, five 200-ms-long pulses from −80 to +10 mV were applied every minute, while the portion of fibre under study was superfused with the standard extracellular solution using a local perfusion system operating by gravity. The portion of fibre was then superfused for 2 min with the extracellular solution also containing 0.1 mM cyclopiazonic acid (CPA) in order to block SR Ca^{2+} uptake. Pulses of 200 ms duration from −80 to + 10 mV were then applied again, at a frequency of 1 Hz in order to rapidly release SR Ca^{2+}. Under these conditions, following the first pulses in the presence of CPA, indo-1 saturation reached an elevated steady level indicating that most of the SR content had been released. We took the difference between this elevated steady level and the initial resting saturation level in each fibre to estimate how much calcium had been released, assuming that saturation of EGTA was the same as saturation of indo-1 and that 20 mM EGTA was present in the cytosol.

Measurements of elementary Ca^{2+} release events (ECREs) in permeabilized muscle fibres

Isolated mouse skeletal muscle fibres from the *fdb* were permeabilized with saponin and loaded with 0.1 mM fluo-3 using previously described experimental solutions and procedures [11]. Briefly, fibres were bathed in a relaxing solution (see Solutions) containing 0.002% saponin for 2–3 min. Permeabilization of the surface membrane was monitored by imaging the fluorescence of fluo-3 present at a concentration of 0.1 mM in the solution. This solution was then replaced by the recording solution (see Solutions). Images were captured with a Zeiss LSM 510 LIVE confocal microscope (Zeiss, Oberkochen, Germany) equipped with a 40× oil immersion objective (NA=1.3). Fluo-3 was excited with the 488-nm line of an argon laser and the emitted fluorescent light was measured at wavelengths >505 nm. Unless otherwise specified, 15 min following application of the recording solution, eight consecutive series of 200 512×512 (x,y) images captured every 67 ms were collected in each tested fibre. Test experiments were carried out in the presence of 0.1 mM of a given PtdIns*P* species (diC8; Echelon Biosciences Inc.) in the recording solution. For each series of test measurements in fibres bathed in the presence of a given PtdIns*P*, a parallel series of control measurements (with no PtdIns*P*) was made using fibres isolated from the same muscles. For analysis, results from a given PtdIns*P* condition were compared to those from the corresponding group of control fibres. Measurements with PtdIns(3,5)P_2, PtdIns(3)*P*) and PtdIns(5)*P* were performed within the same series of experiments whereas measurements with PtdIns were performed 6 months later.

ECRE detection and analysis were performed using modified methods and algorithms described previously by Szabó et al. [36]: details are given in the Electronic supplementary material.

Quantification of PtdIns*P*s in muscle fibres

The concentration level of endogenous PtdIns*P*s in muscle fibres was achieved using the high-performance liquid chromatography–mass spectrometry technique described by Clark et al. [7]. Experiments were conducted at the Lipidomic Core Facility Platform at University of Toulouse. Measurements were carried out on muscle fibres isolated from five *fdb* muscles. Muscles were treated with collagenase as described above. Each *fdb* muscle was then mechanically triturated in a 2-ml volume of Tyrode solution containing 10 mM EGTA. Mechanical trituration of each muscle was achieved so as to release a large number of muscle fibres in the sample; the total number of muscle fibres isolated from each muscle was determined from counting the fibres present in a 50-μl volume of this solution. Each sample was frozen in liquid nitrogen and maintained at −80°C until use. High-performance liquid chromatography was performed on each sample using an Agilent 1290 Infinity, equipped with an autosampler, coupled online to an Agilent 6460 triple quadrupole MS (Agilent Technologies) equipped with electrospray ionization (ESI) source. ESI was performed in positive ion mode. After optimization, the source parameters used were as follows: source temperature was set at 250°C, nebulizer gas (nitrogen) flow rate was 12 l/min, sheath gas temperature was 250°C, sheath gas (nitrogen) flow rate was 12 l/min and the spray voltage was adjusted to 4,000 V. Results expressed in ng of PtdIns*P* PtdInsP_2 and PtdInsP_3 present in each sample were converted into concentration level *per* muscle fibre using the total number of fibres estimated in each sample and assuming a fibre volume of ~2×10^{-7} ml (from an average fibre diameter and length estimated to be 25 and 300 μm, respectively, assuming fibres to be cylindrical).

Solutions

The extracellular solution used for whole-cell voltage-clamp contained (in mM) 140 TEA-methanesulfonate, 2.5 $CaCl_2$, 2 $MgCl_2$, 10 TEA-HEPES and 0.002 tetrodotoxin. In certain

szentesi.peter_292_24

series of measurements, 4-aminopyridine was also present at 1 mM. The intracellular-like solution for whole-cell voltage-clamp contained (in mM) 120 K-glutamate, 5 Na_2 ATP, 5 Na_2 phosphocreatine, 5.5 $MgCl_2$, 5 glucose, 5 HEPES. For indo-1 fluorescence measurements, the dye was present at 1 mM in the injected intracellular-like solution. PtdIns*P*s (diC8; Echelon Biosciences Inc.) were present at 1 mM in the injected solution. LY294002 (Echelon Biosciences Inc.) was prepared in DMSO at a concentration of 10 mM and diluted at 1 mM in the injection solution; DMSO at the same concentration was injected in the control fibres from that series of measurements. For confocal line-scan fluo-4 fluorescence measurements under voltage-clamp conditions, the injected solution contained (in mM) 100 EGTA, 40 $CaCl_2$ and 1 fluo-4. For measurements of ECREs in permeabilized fibres, the relaxing solution contained (in mM) 125 K-glutamate, 10 HEPES, 1 EGTA, 6 $MgCl_2$, 5 Na_2-ATP, 10 Na-phosphocreatine, 10 glucose, 0.13 $CaCl_2$ and the recording solution contained (in mM) 95 K_2SO_4, 10 HEPES, 1 EGTA, 6 $MgCl_2$, 5 Na_2-ATP, 10 Na-phosphocreatine, 10 glucose, 0.13 $CaCl_2$, respectively. All solutions were adjusted to pH 7.20.

Statistics

Least-squares fits were performed using a Marquardt–Levenberg algorithm routine included in Microcal Origin (Originlab, Northampton, MA, USA). Data values are presented as means ± SEM for n fibres. Statistical significance was determined using a Student's t-test: *$p \leq 0.05$, **$p \leq 0.01$, ***$p \leq 0.001$.

Results

PtdIns(3,5)P_2 and PtdIns(3)*P* depress voltage-activated Ca^{2+} release

Since MTM1 deficiency produces a severe impairment of E–C coupling [1], we were specifically interested in the effect of substrates and products of its phosphatase activity. Soluble forms of PtdIns(3,5)P_2, PtdIns(3)*P*, PtdIns(5)*P* or PtdIns were thus micro-injected in separate batches of single isolated muscle fibres and intracellular Ca^{2+} was measured under voltage-clamp conditions. PtdIns*P*s injection was performed so as to reach a final concentration expected to be within the 100 μM range, matching the maximum levels of PtdIns*P*s shown to affect [^{3}H] ryanodine binding to SR as well as single channel activity of RyR1 in bilayer [34]. Mean resting [Ca^{2+}] did not differ between control fibres (0.16±0.02 μM, n=16) and any of the PtdIns*P*s-injected fibre group, but was significantly elevated in fibres injected with either PtdIns(3,5)P_2 (0.21±0.02 μM, n=8) or PtdIns(3)*P* (0.20±0.02 μM, n=8) as compared to fibres injected with PtdIns(5)*P* (0.14±0.01 μM, n=7) or PtdIns (0.12±0.02 μM, n=6).

In order to evaluate the effect of the different PtdIns*P*s on the properties of Ca^{2+} transients and Ca^{2+} release, fibres were stimulated by a voltage-clamp protocol consisting in successive 20-ms-long depolarizing pulses of increasing amplitude from −80 mV. This protocol was repeated five times in each fibre and the traces were averaged. Figure S1 shows an illustrative average indo-1 saturation trace obtained in a control fibre in response to this protocol as well as the corresponding Ca^{2+} release trace calculated as described in Materials and methods and an expanded view of a portion of that same trace centered on the last transient. Figure 1 shows mean indo-1 saturation traces obtained in response to this protocol in the different batches of fibres. The grey shading superimposed to each trace corresponds to the SEM. There was no obvious alteration in the qualitative kinetic properties of the transients in the presence of any of the PtdIns*P*s. However, the peak amplitude was depressed in the presence of PtdIns(3)*P* and, to a lesser extent also in the presence of PtdIns(3,5)P_2. The graphs on the right side in Fig. 1 report the voltage dependence of the mean value for peak Ca^{2+} release in each corresponding condition. The voltage dependence of peak Ca^{2+} release was fitted in each fibre with a Boltzmann function. Corresponding mean values for maximum peak Ca^{2+} release ($d[Ca]_T/dt$ max), voltage of half-activation ($V_{0.5}$) and steepness factor (k) are reported in Fig. 2; as compared to control fibres, maximum Ca^{2+} release was depressed by 50% and 30% in the presence of PtdIns(3)*P* (p<0.001) and PtdIns(3,5)P_2 (p=0.02), respectively, whereas the steepness factor was slightly but significantly enhanced in the presence of PtdIns(3,5)P_2 (p=0.001) and PtdIns(5)*P* (p=0.03). It is worth stressing that indo-1 is a rather high-affinity Ca^{2+} dye with limited kinetic properties precluding fully reliable detection of large fast changes in [Ca^{2+}]. Still, when used in combination with voltage-clamp, the possibility of measuring Ca^{2+} transients in response to small levels of depolarization for which the dye remains far from saturation limits the high-saturation hazardous effects. In other words indo-1 limitations should in no case affect the qualitative effects of PtdIns*P*s observed here but the exact extent of inhibition of Ca^{2+} release by PtdIns(3)*P* and PtdIns(3,5)P_2 may have been somewhat underestimated.

Analysis of the decay phase of the transients (see Fig. S2) indicated that the rate of cytosolic Ca^{2+} removal tended to be significantly slower in fibres injected with PtdIns(3)*P*; since Ca^{2+} release was calculated assuming identical Ca^{2+} removal properties in all fibre groups, this likely indicates that the extent of decrease in peak Ca^{2+} release in PtdIns(3)*P* injected fibres was underestimated.

One important issue was whether the depressed Ca^{2+} release resulted from a depleted SR Ca^{2+} content. In order to address the question a specific series of experiments was

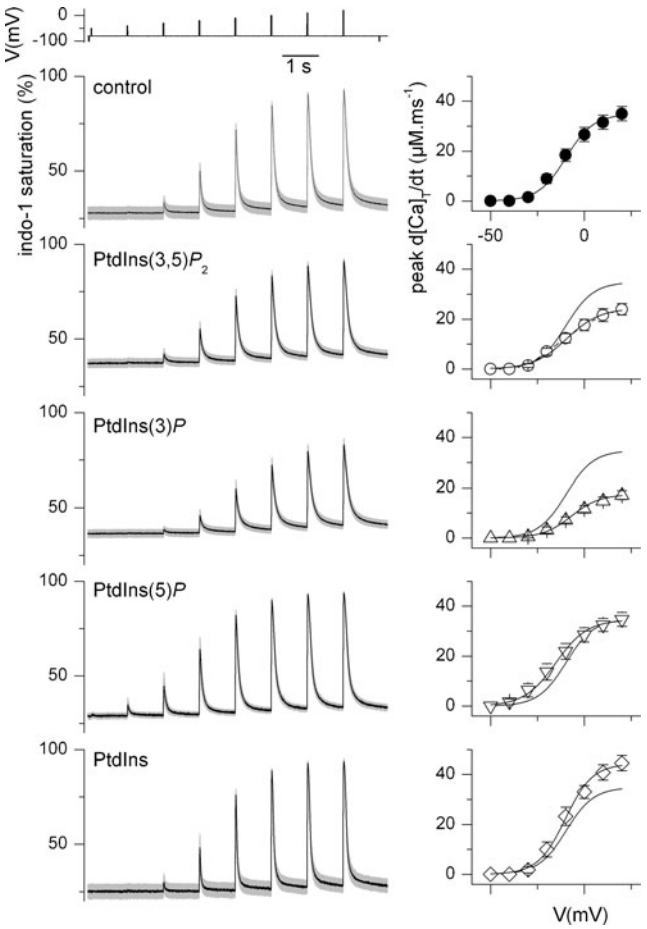


Fig. 1 Voltage-activated Ca^{2+} release in muscle fibres injected with PtdIns*P*s. *Left panel*: mean (±SEM, *grey shading*) indo-1 saturation signal measured in the groups of muscle fibres injected with, from top to bottom, indo-1 with no PtdIns*P* (n=16) and indo-1 with PtdIns(3,5)P_2 (n=8), PtdIns(3)*P* (n=8), PtdIns(5)*P* (n=7), PtdIns (n=6), respectively. The voltage-clamp pulse protocol is shown at the *top*. The voltage-dependence of mean values for peak Ca^{2+} release in each condition is shown on the *right*, next to each corresponding indo-1 trace. The trace superimposed to each set of data points corresponds to a Boltzmann function calculated with the mean parameters obtained from an individual fit of the function to the data points in each fibre

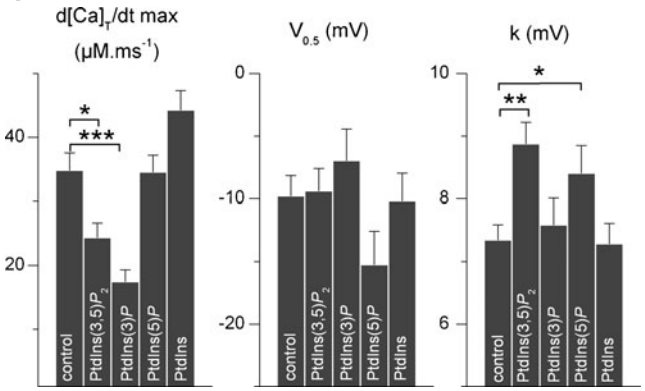


Fig. 2 Mean values for the Boltzmann parameters of the voltage-dependence of Ca^{2+} release in PtdIns*P*s-injected fibres. Mean values for maximal peak rate of Ca^{2+} release, half-activation voltage and steepness were obtained in the different groups of PtdIns*P*s injected fibres from a Boltzmann fit to the peak Ca^{2+} release versus voltage data in each fibre

performed to estimate the SR Ca^{2+} content in control fibres and in fibres containing the PtdIns*P* producing the most effective depression of Ca^{2+} release (PtdIns(3)*P*). For this, we used a protocol consisting in releasing the SR Ca^{2+} content into the cytosol in the presence of a large concentration of EGTA (see Materials and methods). From measurements taken in five control fibres and in six fibres equilibrated with 0.1 mM PtdIns(3)*P* in the intracellular solution, the mean SR Ca^{2+} content was 2.1±0.5 and 2.6±0.4, respectively, which was not statistically different. This thus tends to exclude the possibility that voltage-activated SR Ca^{2+} release was depressed as a consequence of a decreased SR content.

In order to test whether the function of the DHPR was affected and potentially responsible for the above-described effects, we analyzed the membrane current records taken during these experiments. Results from this analysis are presented in Fig. S3 and in the corresponding text section of the Electronic supplementary material. Overall, the results demonstrated that neither the voltage-sensing function of the DHPR nor its Ca^{2+} channel function was substantially affected by PtdIns*P*s.

While testing the effect of PtdIns*P*s on Ca^{2+} transients, we questioned the possibility that voltage-dependent inactivation of Ca^{2+} release would be affected. To test for this, we measured indo-1 transients in response to a pair of 20-ms long pulses to −20 and 0 mV from increasing levels of holding potential. The two pulses were used in order to ensure that heavy saturation of indo-1 for the largest pulse would not hinder detection of a decrease in the Ca^{2+} transient amplitude when changing the holding potential towards more depolarized levels. The pulse protocol and the corresponding mean (±SEM) indo-1 saturation traces obtained in control fibres are shown in Fig. S4a,b. In each fibre, the peak Ca^{2+} transient amplitude calculated from the indo-1 signal was normalized to the initial value measured from the holding potential of −80 mV. We found no indication that any of the four tested PtdIns*P*s affected the inactivation process; this is illustrated in Fig. S4c, where the mean normalized peak amplitude of the Ca^{2+} transient versus the holding potential in the different groups of fibres are shown. Fitting a Boltzmann function to the data in each fibre gave mean values for half-inactivation voltage and steepness factor that did not differ between control fibres and any of the four groups of PtdIns*P*s-injected fibres.

PtdIns(3,5)P_2, PtdIns(3)*P* and PtdIns(5)*P* depress the frequency of ECREs in permeabilized muscle fibres

Measurement of spontaneous ECREs in permeabilized muscle fibres provides a way to study the functional properties of the ryanodine receptor in its native environment, freed from the DHPR control (e.g., [19, 26]). We used this approach to

szentesi.peter_292_24

test whether PtdIns*P*s would directly affect RyR-mediated Ca^{2+} release activity and get insights into the underlying mechanism. Spontaneous ECREs were measured using fast confocal (*x*,*y*) imaging, 15 min following equilibration of fibres with a given PtdIns*P* and properties of the events were compared to those of fibres from the same muscles equilibrated for 15 min with the standard experimental solution. Figure 3a shows an illustrative (*x*,*y*) confocal record of fluo-3 fluorescence from one fibre in each group. Each frame represents the cumulated ECRE activity recorded during a series of 200 consecutive images, covering a period of approximately 13 s. There was a substantial reduction of the number of detected ECREs in the fibres equilibrated with PtdIns(3,5)P_2, PtdIns(3)*P* and PtdIns(5)*P*, the effect being most important with PtdIns(3,5)P_2. Figure 3b shows the mean values for the measured parameters. ECRE frequency was strongly depressed in the presence of each of the three tested phosphorylated forms of PtdIns*P* with the drop amounting to 98% in the presence of PtdIns(3,5)P_2. The mean ECRE amplitude was slightly but significantly increased in the presence of PtdIns(5)*P* whereas the FWHM along both the *x* and *y* directions was depressed by ~10% in the presence of PtdIns(3,5)P_2. Altogether, the tested PtdIns*P*s appeared to modestly, if any, affect the individual ECRE amplitude and spatial properties while severely impairing the occurrence of the events. From that series of measurements we could also check that the observed decrease in ECRE frequency in the presence of PtdIns(3,5)P_2, PtdIns(3)*P* and PtdIns(5)*P* was present right when we started taking measurements: for instance, during the first series of 200 images, the average ECRE frequency was depressed by 92% in fibres equilibrated with PtdIns(3,5)P_2 as compared to the frequency in their control counterparts.

We also performed a specific series of measurements designed to study the time course of ECRE activity earlier in time following application of the PtdIns*P* that was found the most effective on ECRE frequency (PtdIns(3,5)P_2). This was expected to reveal whether or not a putative PtdIns(3,5)P_2-induced early transient increase in spark activity may have occurred during our experiments so as to induce SR Ca^{2+} depletion and thus compromise ECRE occurrence during the measurements that were started 15 min following application of the recording solution. For this, we started taking images 3 min following application of the recording (either control or PtdIns(3,5)P_2-containing) solution and a series of 200 images was then taken every 3 min. ECREs were counted within each series. Results from measurements in five control fibres and three fibres in the presence PtdIns(3,5)P_2 showed that there was no significant change in spark frequency over time in both groups of fibres (not illustrated). In terms of absolute values, the mean frequency in the three PtdIns(3,5)P_2 fibres was depressed by 65–80% as compared to the corresponding values in the control fibres. Although this was somewhat less of an effect than in the set of measurements illustrated in Fig. 3, results clearly demonstrated that there was no sign whatsoever of any stimulating effect of PtdIns(3,5)P_2 on ECRE activity. Finally, in two of the three fibres tested in the presence of PtdIns(3,5)P_2, the experiment was ended by exchanging the test solution with the same solution also containing 0.4 mM 4-chloro-*m*-cresol (CMC) and 4 μM thapsigargin (Tg) to promote global SR Ca^{2+} release and 50 μM *N*-benzyl-*p*-toluenesulfonamide (BTS) to prevent contraction. In both fibres, this produced a strong rise in fluo-3 fluorescence indicating that Ca^{2+} was well available in the SR compartment.

LY2940002 does not affect voltage-activated Ca^{2+} release

As results from Ca^{2+} transients in intact fibres suggested that accumulation of PtdIns(3,5)P_2 and/or PtdIns(3)*P* is capable of reducing voltage-activated Ca^{2+} release, it was of specific interest to explore the effect of manoeuvres intended to reduce the endogenous level of these compounds. For this, we first used LY294002, a classical pharmacological inhibitor of the different classes of PtdIns 3-kinases. Figure 4 compares indo-1 Ca^{2+} transients measured in a batch of control fibres and fibres injected with LY294002 so the final intracellular concentration was expected to be in the 0.1 mM range, well within the range expected to effectively block all classes of PtdIns 3-kinases (e.g., [21]). Fibres were subjected to the same voltage-clamp stimulation protocol as in Fig. 1 (Fig. 4a). Figure 4b shows the mean (±SEM) indo-1 saturation trace from the control (DMSO-injected) and from the LY294002-injected fibres and Fig. 4c shows the corresponding voltage dependence of peak Ca^{2+} release. Presence of the inhibitor clearly had no effect on Ca^{2+} release.

Overexpression of MTM1 does not affect voltage-activated Ca^{2+} release

PtdIns(3,5)P_2 and PtdIns(3)*P* are the main substrates of the PtdIns*P* phosphatase MTM1. An alternative possibility for reducing the level of these two PtdIns*Ps* was thus to overexpress MTM1; this was also of particularly strong interest since loss of activity of this phosphatase is responsible for severe pathological E–C coupling defects [1]. Figure 5 shows the expression pattern of a mCherry-tagged version of MTM1 expressed in a *fdb* muscle fibre, following in vivo transfection (see Material and Methods). Figure 5a–c illustrates the facts that mCherry-MTM1 was distributed throughout the entire volume of the fibres and, interestingly, that the fluorescence yielded a clear transversally striated component forming double rows spaced by ~2 μm, reminiscent of the triadic region. This was confirmed by co-localization of the mCherry fluorescence with that of t-tubule stained with di-8 anepps (Fig. 5d–f). Figure 6 shows the effect of exogenous MTM1

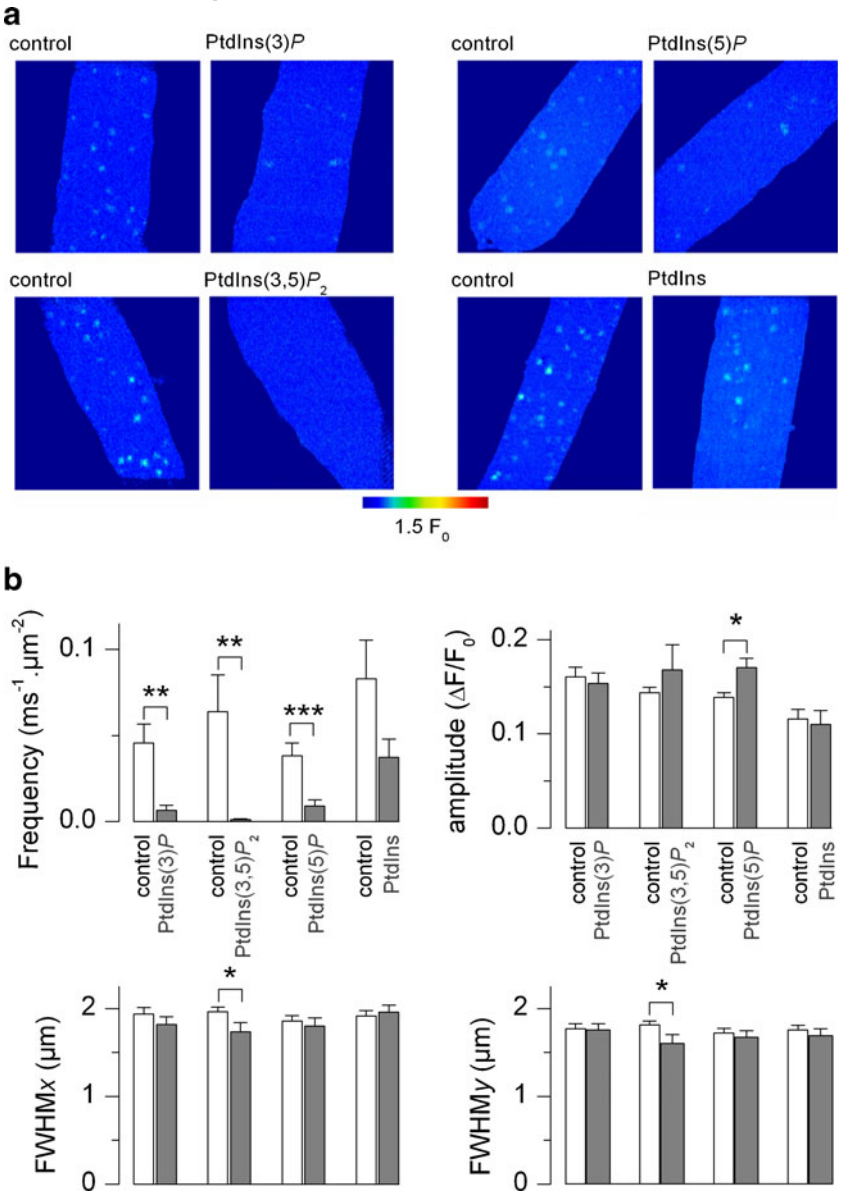


Fig. 3 Effect of PtdIns*P*s on spontaneous elementary Ca^{2+} release events in permeabilised muscle fibres. **a** Cumulated ECRE activity recorded with fluo-3 over a series of 200 consecutive confocal frames in fibres equilibrated with the indicated PtdIns*P* and in control fibres. **b** Mean values for the measured ECRE parameters in the different group of fibres. The number of fibres in the presence of a given PtdIns*P* and in the corresponding control group was 27 and 28 (PtdIns(3,5)P_2), 29 and 28 (PtdIns(3)*P*), 36 and 40 (PtdIns(5)*P*), 12 and 11 (PtdIns), respectively. All images are 84×84 µm

expression on voltage-activated Ca^{2+} release measured with indo-1. Figure 6b shows mean (±SEM) indo-1 saturation traces obtained from 11 control fibres and 11 mCherry-MTM1 expressing fibres in response to the pulse protocol shown in Fig. 6a; the corresponding voltage dependency of peak Ca^{2+} release is shown in Fig. 6c. Although there was a tendency for a slight reduction in peak Ca^{2+} release in the fibres overexpressing MTM1 as compared to control fibres, the difference was not statistically significant. Fitting a Boltzmann function to the data in each fibre gave mean values for maximum peak Ca^{2+} release, voltage of half-activation and steepness factor of 32.5±3 µM ms^{-1}, −7.2±1 mV, 6.8±0.2 mV and 28.2 ±3 µM ms^{-1}, −5.6±1 mV, 6.5±0.4 mV in control and MTM1-overexpressing fibres, respectively.

Indo-1 is a high-affinity dye that gets heavily saturated for large levels of step depolarization, a situation that could be thought to hamper detection of a putative enhancing effect of MTM1 overexpression on Ca^{2+} release; in order to make sure, Ca^{2+} transients from transfected fibres were also measured with fluo-4 in the presence of a high concentration of EGTA (see Materials and methods). In agreement with the indo-1 data, we — also in these conditions — found no indication that overexpression of MTM1 affected voltage-activated Ca^{2+} release: corresponding results are presented in Fig. S5 which shows the mean (±SEM) fluo-4 transients evoked by a 0.5-s-long depolarization from −80 to +30 mV in control fibres (n=5) and in fibres expressing mCherry-MTM1 (n=7), while Fig. S5c shows the corresponding Ca^{2+} release traces.

The possibility that the mCherry tag could somehow affect the activity of MTM1 so as to preclude a functional outcome was tested by measuring Ca^{2+} transients in fibres co-transfected with a plasmid encoding tag-free MTM1 and a plasmid

szentesi.peter_292_24

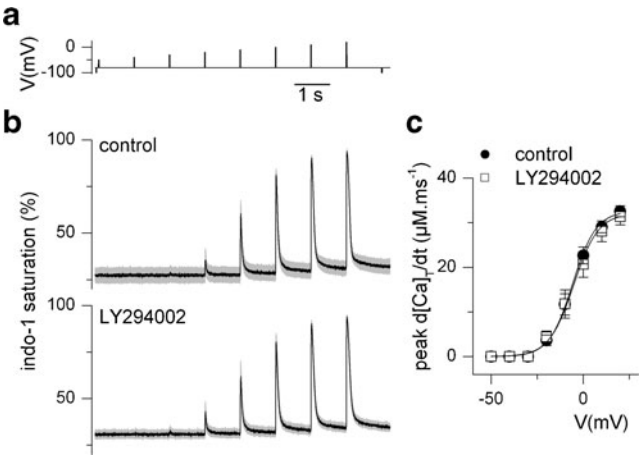


Fig. 4 Voltage-dependent Ca^{2+} release in fibres injected with the PtdIns-3 kinase inhibitor LY294002. **a** Voltage-clamp pulse protocol. **b** Mean (±SEM, *grey shading*) indo-1 saturation signal measured in fibres injected with LY294002 (n=6) and in the corresponding batch of control fibres (n=6). **c** Voltage dependence of mean peak values of Ca^{2+} release in the two groups of fibres. The trace superimposed to each set of data points corresponds to a Boltzmann function calculated with the mean parameters obtained from an individual fit of the function to the data points in each fibre. Mean values for maximum peak Ca^{2+} release, voltage of half-activation and steepness factor were 32.6±1 μM ms^{-1}, −5.8±2 mV, 6.4±0.3 mV and 32.1±2 μM ms^{-1}, −5.3±3 mV, 6.7±0.2 mV in control and LY294002-injected fibres, respectively

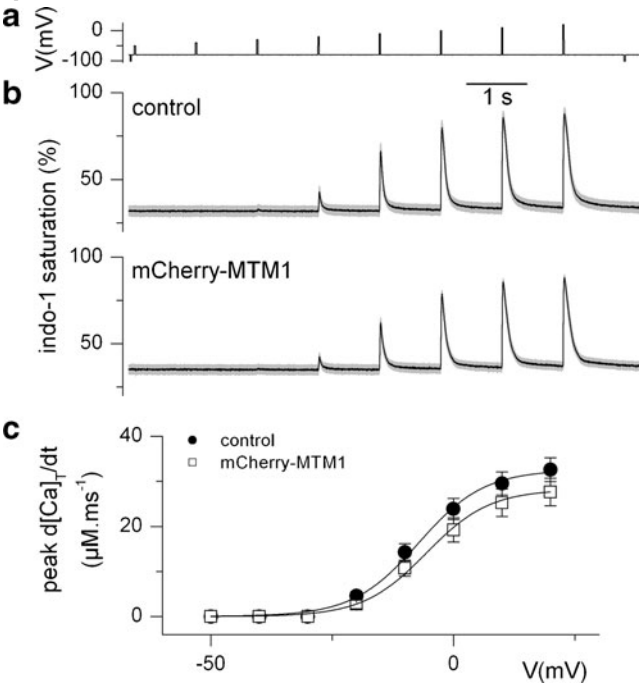


Fig. 6 Voltage-dependent Ca^{2+} release in fibres expressing mCherry-tagged MTM1. **a** Pulse protocol. **b** Mean (±SEM, *grey shading*) indo-1 saturation trace from control fibres (n=11) and from mCherry-MTM1 positive fibres (n=11). **c** Corresponding mean voltage dependence of peak Ca^{2+} release in the two sets of fibres

encoding EGFP. Voltage-activated Ca^{2+} transients in these fibres were compared to those measured in fibres transfected only with the EGFP plasmid. Results from these measurements are detailed in the Electronic supplementary material. They gave no indication that tag-free MTM1 would be more efficient than mCherry MTM1 in altering Ca^{2+} release. Finally, in another series of experiments, we also tested the possibility that the presence of exogenous MTM1 could affect Ca^{2+} release under more stringent conditions of muscle function. For this, Ca^{2+} transients were measured in fibres challenged by repeated trains of membrane depolarization; as described in Fig. S6 and in the corresponding text in the Electronic supplementary material, results also gave no insight into a possible effect of MTM1 overexpression on Ca^{2+} release.

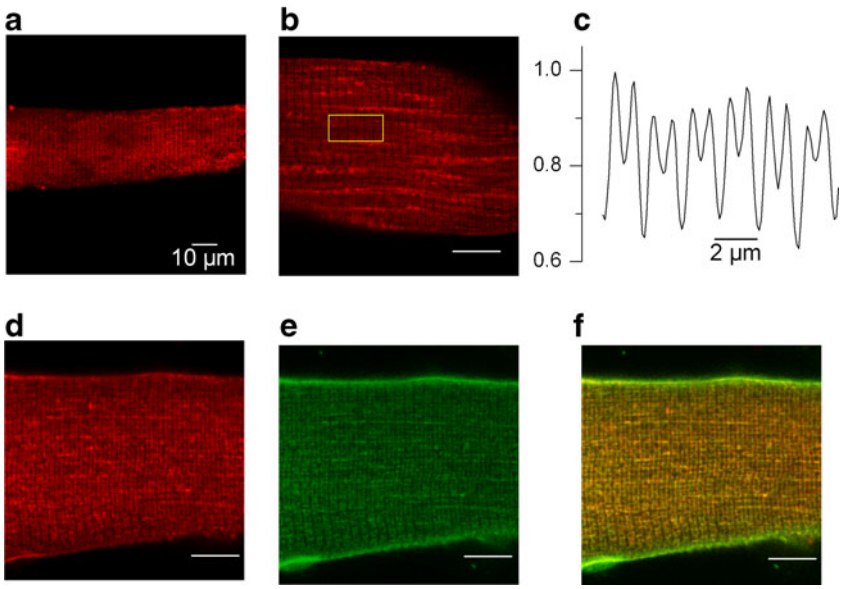


Fig. 5 Expression of the PtdIns*P*s phosphatase MTM1 in mouse muscle fibres. **a**–**b** Representative confocal images of the mCherry fluorescence from fibres expressing mCherry-tagged MTM1. **c** mCherry fluorescence profile along the x axis of the yellow box in **b**. **d**–**f** Co-localization of mCherry and di-8-anneps (*green*) fluorescence. Scale bars in the images all correspond to 10 μm

Concentration levels of PtdIns*P*s in muscle fibres

In order to estimate the physiological concentration levels of PtdIns*P*s in muscle fibres we used a high-performance liquid chromatography–mass spectrometry technique [7]. Although the technique cannot differentiate between the several mono- di- and tri-phosphorylated forms of PtdIns*P*, results were nevertheless anticipated to be informative in regard to the 100 μM concentration level of the several PtdIns*P*s forms we used in our injection experiments. The amount of PtdIns*P*, PtdInsP_2 and PtdInsP_3 present in fibres isolated from five *fdb* muscles is reported in Table 1; the estimated number of fibres in each sample is indicated in the right-end column. From these numbers, the mean concentration level of PtdIns*P* and of PtdInsP_2 was found to be 411±55 and 181±50 μM, respectively (n=5).

Discussion

The present work provides insights into a so-far-unexplored aspect of the E–C coupling function that has direct relevance to a fatal muscle disease. Indeed, the recent discovery that myotubular myopathy is associated with a severe alteration of Ca^{2+} release has highlighted the potentially critical role of PtdIns*P*s metabolism in the maintenance and/or regulation of this process. However, details of how PtdIns*P*s are involved in E–C coupling remain very mysterious.

We show that intracellular application of either PtdIns(3,5)P_2 or PtdIns(3)*P* depresses global voltage-activated Ca^{2+} release in intact muscle fibres. Conversely, we also show that two experimental strategies intended to reduce the level of these two 3-OH phosphorylated PtdIns have no effect on Ca^{2+} release, suggesting that they are maintained at an ineffective low-level in regard to this effect, in normal conditions.

Evidence for a role of PtdIns*P*s in the regulation of muscle Ca^{2+} homeostasis and/or E–C coupling is sparse: mainly, measurements of single RyR channel activity, Ca^{2+} release from SR vesicles and tension from skinned fibres suggested that PtdIns(4,5)P_2 has the potency to activate RyR1 [6, 20, 28] but no clear physiological correlate was ever provided. Our interest here was more specifically focused on the PtdIns*P*s species that are substrates or hydrolyzed products of MTM1. In relation to these, a set of relevant data was collected by Shen et al. [34] indicating that: (a) PtdIns(3,5)P_2 in cultured myotubes resides in the SR; (b) defects in myotubes Ca^{2+} signalling occur upon perfusion with PtdIns(3,5)P_2, PtdIns(3,4)P_2 or PtdIns(3)*P*; (c) all PtdIns*P*s bind to RyR1 with PtdIns(5)*P* yielding the highest binding activity; (d) PtdIns(3,5)P_2, in the 10–100 μM range, directly increases the activity of RyR1 as inferred for instance from the increased number of single RyR1 channel open events in reconstituted lipid bilayers. Although of strong relevance to the present issue, these results provided little insight into whether or not — and if so, how — PtdIns*P*s actually affect RyR1 function and E–C coupling in the native functional environment of an adult muscle fibre.

Our data provide evidence that physiologically triggered RyR1 function is sensitive to certain PtdIns*P*s: indeed data from intact fibres suggest that intracellular levels of PtdIns(3,5)P_2 or PtdIns(3)*P* in the 100 μM range depress voltage-activated Ca^{2+} release. The question of whether this concentration level of soluble di-C8 forms of PtdIns*P*s tested here has physiological relevance may be raised although a completely straightforward answer is harder to come by. From our measurements, we estimated the bulk concentration levels of PtdIns*P* and PtdInsP_2 in muscle fibres to be ~410 and 180 μM, respectively. In mammalian cells, the relative proportion of the three mono-phosphorylated forms of PtdIns*P* is considered to be 0.04 PtdIns(3)*P*, 0.04 PtdIns(5)*P* and 0.93 PtdIns(4)*P* (see [24]) which, according to the above value would correspond to ~16 μM PtdIns(3)*P* and PtdIns(5)*P* and ~380 μM PtdIns(4)*P*. For a muscle fibre assumed to be a cylinder of 25 μm diameter, considering the lipid membrane thickness to be 7 nm, the t-tubule to surface membrane ratio to be 6, the SR volume to represent 5.5% of total fibre volume [15] and the average inner SR radius to be 10 nm, one can calculate that the volume of surface membrane plus t-system membrane represents ~0.3% of the total fibre volume while the SR membrane volume represents ~4% of the total fibre volume. Thus, if distributed uniformly within the surface plus t-system plus SR membrane, the concentration of endogenous PtdIns(3)*P* and PtdIns(5)*P* should amount to 23 times their concentration in the fibre bulk, that is ~370 μM. The 100 μM concentration of PtdIns(3)*P* and PtdIns(5)*P* we used in our injection experiments corresponds to ~6 times the bulk endogenous levels. If the injected PtdIns(3)*P* and PtdIns(5)*P* also partition uniformly within the surface plus t-system plus SR membrane they would also reach a membrane concentration ~6 times larger than the endogenous levels. If they do not partition at all, the added 100 μM bulk level would then increase the concentration by a factor of ~1.3. The actual situation probably lies within these two limits.

Table 1 Quantification of PtdIns*P*s in muscle fibres

Sample	PtdIns*P* (ng)	PtdInsP_2 (ng)	PtdInsP_3 (ng)	Number of fibres
A	123.28	32.94	24.04	1026
B	99.86	32.05	10.94	1767
C	130.26	109.61	9.42	1463
D	96.17	43.88	6.4	1482
E	102.39	33.61	32.77	1273

Amount of mono-, di- and tri-phosphorylated PtdIns*P* measured in samples of muscle fibres isolated from five *fdb* muscles, as described in Materials and methods. The number of fibres estimated in each sample is indicated in the right-end column

szentesi.peter_292_24

Along the same line, the relative proportion of diphosphorylated forms of PtdIns*P* in mammalian cells is considered to be 0.002 PtdIns(3,4)P_2, 0.002 PtdIns(3,5)P_2 and >0.99 PtdIns(4,5)P_2 (see [24]), which according to our estimation of total PtdInsP_2 concentration would give 0.4 μM PtdIns(3,5)P_2. The 100 μM concentration of PtdIns(3.5)P_2 we used in our experiments thus corresponds to ~250 times this bulk level. If endogenous PtdInsP_2 distribute uniformly within the surface plus t-system plus SR membrane, the concentration of PtdIns(3,5)P_2 would amount ~9 μM. If the injected PtdIns(3,5)P_2 also partition entirely in these membranes its membrane concentration will also be 250 times larger than the endogenous level. Conversely, if it does not partition at all, the added 100 μM bulk level will then increase the concentration 11 times. Again, the actual situation has to stand within these two limits.

To summarize, the above estimations suggest that the injected 100 μM concentration of PtdIns*P*s increases the endogenous level of PtdIns(3)*P* and PtdIns(5)*P* by a factor of 1.3–10 and the level of PtdIns(3,5)P_2 by a factor of 11–250.

Increased levels of PtdIns(5)*P* and PtdIns(3,5)P_2 by a factor of 2–30 (which would more or less fit within the above ranges) have been reported in cell systems other than muscle, under various conditions of stress (see [24]). In the A431 epidermoid carcinoma model cell line, siRNA-mediated down-regulation of MTM1 expression resulted in a 1.4–2.5 increase in PtdIns(3)*P* level [4]. Consistently, Mtm1-null skeletal muscle was very recently reported to yield a 2.2-fold increase in PtdIns(3)*P* level as compared to wild-type muscle [2]. Overall, within the limits of the present knowledge, these numbers indicate that the 100 μM concentration of PtdIns*P*s we used may not be so far from the range of levels relevant to physiological or pathological conditions, although it may somewhat exceed such levels in the case of PtdIns(3,5)P_2.

We also examined the effect of PtdIns*P*s on Ca^{2+} release detected under the form of spontaneous elementary events. Normally, ECREs in mammalian muscle do not occur at a frequency that allows appropriate analysis, under physiological conditions. On the other hand, conditions that substantially increase their frequency, such as discussed here after saponin permeabilization, allow a connection between data measured in vitro (whether from vesicles or from artificial bilayers) and global calcium transients measured in intact muscle fibres. In other words, analysis of ECREs offers a way to address discrepancies of RyR1 function between a full in vitro situation and — as full as possible — physiological situation. Also considering that the physiological ECREs that build up the global Ca^{2+} transients in mammalian muscle fibres still remain poorly identified, this approach represents the best one can use to address elementary properties of RyR1-mediated Ca^{2+} release in situ. In qualitative agreement with the reduction of peak voltage-activated Ca^{2+} release by PtdIns(3,5)P_2 and PtdIns(3)*P* that we observed in intact fibres, we also found that the frequency of spontaneous Ca^{2+} release events was reduced by these two PtdIns*P*s in permeabilized fibres, although in contrast with data from intact fibres PtdIns(5)*P* also was effective under these conditions. According to the ECRE parameters, PtdIns*P*s effect on RyR1-mediated Ca^{2+} release is likely to result from a reduced occurrence of RyR1 channel opening than from an alteration of the channel conductance or of the number of coherently operating channels involved in a Ca^{2+} release event.

Our data complement the results of Shen et al. [34] showing that di-C8-PtdIns*P*s, at similar concentrations as used here, enhance the activity of RyR1 in vitro. Although these results may not seem intuitively consistent with the present ones, they may not necessarily be contradictory. Notice along this line that even within our study there was no full consistence between the intact and permeabilized fibre data with respect to PtdIns(5)*P* which had no significant effect on voltage-activated Ca^{2+} release while depressing the ECRE frequency. On the other hand, PtdIns(3,5)P_2 was found to be more effective in altering elementary release events than either PtdIns(3)*P* or PtdIns(5)*P*, in line with the observations made by Shen et al. [34]. Discrepancies may also reflect the different levels of complexity of PtdIns*P*s modulation of the RyR1 channel activity when going from the native intact muscle fibre environment with RyR1 under the control of the DHPR as compared to RyR1 spontaneous activity detected in permeabilized fibres under the form of ECREs and again versus the in vitro situation in vesicles or bilayer. One may for instance picture the possibility that a target other than RyR1 is involved in the effects at the single fibre level. In this respect, our data tend to exclude the DHPR, as evidenced from analysis of the membrane current measurements. Furthermore, the fact that ECRE, presumed to reflect a DHPR-free activity of RyR1 channels, also yield a depressed activity in the presence of PtdIns*P*s does not favour a role for the DHPR as a critical target. The enhanced PtdIns*P*s-induced RyR1 activity observed in vitro [34] could also be speculated to correspond to a specific effect on the resting level of RyR1 activity in the intact fibres; along such line, it is interesting that despite the reduced amplitude of voltage-activated Ca^{2+} release in fibres injected with PtdIns(3,5)P_2 and PtdIns(3)*P*, the resting [Ca^{2+}] level tended to be elevated.

One could have anticipated that under normal conditions, the endogenous level of PtdIns(3,5)P_2 and PtdIns(3)*P* has a chronic effect on Ca^{2+} release that could be overcome by further reducing the level of these molecules. This does not seem to be the case: despite yielding a pattern of expression consistent with the triadic region, overexpression of MTM1 left Ca^{2+} release unchanged. Along the same line, application of a PtdIns 3-kinase inhibitor which would have also been expected to reduce the endogenous level of PtdIns(3,5)P_2 and PtdIns(3)*P* was without effect. Together, these results provide no clue for the existence of a tonic effect of the endogenous

PtdIns*P*s on Ca^{2+} release in normal conditions. Interestingly along this line, recent results showed that ectopic expression in muscle of wild-type MTM1 did not induce any detectable signs of muscle alteration with respect to muscle weight, fibre size and isometric force, in agreement with the present results showing that the steps of E–C coupling remained essentially unaffected [2].

Altogether, although full understanding of the details of how PtdIns*P*s affect Ca^{2+} release in situ will necessitate more efforts, our results represent an important first step towards this goal. Also of importance, data highlight the possibility that accumulation of MTM1 substrates has the potency to depress Ca^{2+} release and to thus contribute to the defective E–C coupling in MTM1-deficient conditions [1]. The mechanism(s) involved and the actual PtdIns*P*s target(s) still remain speculative, and at present we cannot completely rule out that PtdIns*Ps* would act in a cell compartment other than the triadic region. Still, as shown for PtdIns(4,5)P_2 in regard to plasma membrane ion channels, PtdIns(3,5)P_2 and PtdIns(3)*P* may be suggested to exert their effect through a direct interaction with RyR1, and this is supported by the fact that several PtdIns*P*s do bind to RyR1 [34]. Alternatively, they could also be speculated to favor targeting or translocation of another protein in the vicinity of RyR1 or to induce structural changes in the triadic junction by altering membrane curvature [2] that would then be responsible for the observed effects.

Acknowledgements This work was supported by grants from Centre National de la Recherche Scientifique (CNRS), Université Lyon 1, Association Française contre les Myopathies (AFM), Hubert Curien Partnership Balaton (TeT_10-1-2011-0723) and OTKA K107765. E.G.R. was a recipient of a fellowship from the Spanish Ministry of Education and Science (MEC, José Castillejo Program). We thank Bruno Allard for critical comments on the manuscript and helpful discussion.

Ethical standards All experiments comply with the current laws of the two countries (France and Hungary) in which they were performed.

Conflict of interest The authors declare that they have no conflict of interest.

References

1. Al-Qusairi L, Weiss N, Toussaint A, Berbey C, Messaddeq N, Kretz C, Sanoudou D, Beggs AH, Allard B, Mandel JL, Laporte J, Jacquemond V, Buj-Bello A (2009) T-tubule disorganization and defective excitation-contraction coupling in muscle fibres lacking myotubularin lipid phosphatase. Proc Natl Acad Sci U S A 106: 18763–18768
2. Amoasii L, Hnia K, Chicanne G, Brech A, Cowling BS, Müller MM, Schwab Y, Koebel P, Ferry A, Payrastre B, Laporte J (2013) Myotubularin and PtdIns3P remodel the sarcoplasmic reticulum in muscle in vivo. J Cell Sci 126:1806–1819
3. Bolis A, Zordan P, Coviello S, Bolino A (2007) Myotubularin-related (MTMR) phospholipid phosphatase proteins in the peripheral nervous system. Mol Neurobiol 35:308–316
4. Cao C, Backer JM, Laporte J, Bedrick EJ, Wandinger-Ness A (2008) Sequential actions of myotubularin lipid phosphatases regulate endosomal PI(3)P and growth factor receptor trafficking. Mol Biol Cell 19:3334–3346
5. Cheng H, Lederer WJ, Cannell MB (2003) Calcium sparks: elementary events underlying excitation–contraction coupling in heart muscle. Science 262:740–744
6. Chu A, Stefani E (1991) Phosphatidylinositol 4,5-bisphosphate-induced Ca^{2+} release from skeletal muscle sarcoplasmic reticulum terminal cisternal membranes. Ca^{2+} flux and single channel studies. J Biol Chem 266:7699–7705
7. Clark J, Anderson KE, Juvin V, Smith TS, Karpe F, Wakelam MJ, Stephens LR, Hawkins PT (2011) Quantification of PtdInsP3 molecular species in cells and tissues by mass spectrometry. Nat Methods 8:267–272
8. Collet C, Csernoch L, Jacquemond V (2003) Intramembrane charge movement and L-type calcium current in skeletal muscle fibres isolated from control and mdx mice. Biophys J 84:251–265
9. Collet C, Pouvreau S, Csernoch L, Allard B, Jacquemond V (2004) Calcium signaling in isolated skeletal muscle fibres investigated under "Silicone Voltage-Clamp" conditions. Cell Biochem Biophys 40:225–236
10. Csernoch L, Bernengo JC, Szentesi P, Jacquemond V (1998) Measurements of intracellular Mg^{2+} concentration in mouse skeletal muscle fibres with the fluorescent indicator mag-indo-1. Biophys J 75:957–967
11. Csernoch L, Pouvreau S, Ronjat M, Jacquemond V (2008) Voltage-activated elementary calcium release events in isolated mouse skeletal muscle fibres. J Membr Biol 226:43–55
12. Di Paolo G, De Camilli P (2006) Phosphoinositides in cell regulation and membrane dynamics. Nature 443:651–657
13. Dowling JJ, Low SE, Busta AS, Feldman EL (2010) Zebrafish MTMR14 is required for excitation–contraction coupling, developmental motor function and the regulation of autophagy. Hum Mol Genet 19:2668–2681
14. Dowling JJ, Vreede AP, Low SE, Gibbs EM, Kuwada JY, Bonnemann CG, Feldman EL (2009) Loss of myotubularin function results in T-tubule disorganization in zebrafish and human myotubular myopathy. PLoS Genet 5:e1000372. doi:10.1371/journal.pgen.1000372
15. Eisenberg BR (1983) Quantitative ultrastructure of mammalian skeletal muscle. In: Peachey LD, Adrian RH, Geiger SR (eds) Handbook of physiology sect 10: skeletal muscle, 3rd edn. Williams & Wilkins, Baltimore, MD, pp 73–112
16. Hannon JD, Lee NK, Yandong C, Blinks JR (1992) Inositol trisphosphate (InsP3) causes contraction in skeletal muscle only under artificial conditions: evidence that Ca^{2+} release can result from depolarization of T-tubules. J Muscle Res Cell Motil 13:447–456
17. Harkins AB, Kurebayashi N, Baylor SM (1993) Resting myoplasmic free calcium in frog skeletal muscle fibres estimated with fluo-3. Biophys J 65:865–881
18. Jacquemond V (1997) Indo-1 fluorescence signals elicited by membrane depolarization in enzymatically isolated mouse skeletal muscle fibres. Biophys J 73:920–928
19. Kirsch WG, Uttenweiler D, Fink RH (2001) Spark- and ember-like elementary Ca^{2+} release events in skinned fibres of adult mammalian skeletal muscle. J Physiol 537:379–389
20. Kobayashi M, Muroyama A, Ohizumi Y (1989) Phosphatidylinositol 4,5-bisphosphate enhances calcium release from sarcoplasmic reticulum of skeletal muscle. Biochem Biophys Res Commun 163:1487–1491
21. Kong D, Dan S, Yamazaki K, Yamori T (2010) Inhibition profiles of phosphatidylinositol 3-kinase inhibitors against PI3K superfamily and human cancer cell line panel JFCR39. Eur J Cancer 46:1111–1121

szentesi.peter_292_24

22. Lanner JT, Georgiou DK, Joshi AD, Hamilton SL (2010) Ryanodine receptors: structure, expression, molecular details, and function in calcium release. Cold Spring Harb Perspect Biol 2:a003996
23. Laporte J, Hu LJ, Kretz C, Mandel JL, Kioschis P, Coy JF, Klauck SM, Poustka A, Dahl N (1996) A gene mutated in X-linked myotubular myopathy defines a new putative tyrosine phosphatase family conserved in yeast. Nat Genet 13:175–182
24. Lemmon MA (2008) Membrane recognition by phospholipid-binding domains. Nat Rev Mol Cell Bio 9:99–111
25. Logothetis DE, Petrou VI, Adney SK, Mahajan R (2010) Channelopathies linked to plasma membrane phosphoinositides. Pflugers Arch 460:321–341
26. Lukács B, Sztretye M, Almássy J, Sárközi S, Dienes B, Mabrouk K, Simut C, Szabó L, Szentesi P, De Waard M, Ronjat M, Jóna I, Csernoch L (2008) Charged surface area of maurocalcine determines its interaction with the skeletal ryanodine receptor. Biophys J 95: 3497–3509
27. Monnier N, Ferreiro A, Marty I, Labarre-Vila A, Mezin P, Lunardi J (2003) A homozygous splicing mutation causing a depletion of skeletal muscle RYR1 is associated with multi-minicore disease congenital myopathy with ophthalmoplegia. Hum Mol Genet 12:1171–1178
28. Ogawa Y, Harafuji H (1989) Ca-release by phosphoinositides from sarcoplasmic reticulum of frog skeletal muscle. J Biochem 106:864–867
29. Ohizumi Y, Hirata Y, Suzuki A, Kobayashi M (1999) Two novel types of calcium release from skeletal sarcoplasmic reticulum by phosphatidylinositol 4,5-biphosphate. Can J Physiol Pharmacol 77: 276–285
30. Pierson CR, Tomczak K, Agrawal P, Moghadaszadeh B, Beggs AH (2005) X-linked myotubular and centronuclear myopathies. J Neuropathol Exp Neurol 64:555–564
31. Pouvreau S, Csernoch L, Allard B, Sabatier JM, De Waard M, Ronjat M, Jacquemond V (2006) Transient loss of voltage control of Ca^{2+} release in the presence of maurocalcine in skeletal muscle. Biophys J 91:2206–2215
32. Pouvreau S, Jacquemond V (2005) Nitric oxide synthase inhibition affects sarcoplasmic reticulum Ca^{2+} release in skeletal muscle fibres from mouse. J Physiol 567:815–728
33. Romero-Suarez S, Shen J, Brotto L, Hall T, Mo C, Valdivia HH, Andresen J, Wacker M, Nosek TM, Qu CK, Brotto M (2010) Muscle-specific inositide phosphatase (MIP/MTMR14) is reduced with age and its loss accelerates skeletal muscle aging process by altering calcium homeostasis. Aging 2:504–513
34. Shen J, Yu WM, Brotto M, Scherman JA, Guo C, Stoddard C, Nosek TM, Valdivia HH, Qu CK (2009) Deficiency of MIP/MTMR14 phosphatase induces a muscle disorder by disrupting Ca^{2+} homeostasis. Nat Cell Biol 11:769–776
35. Suh BC, Hille B (2008) PIP2 is a necessary cofactor for ion channel function: how and why? Annu Rev Biophys 37:175–195
36. Szabó LZ, Vincze J, Csernoch L, Szentesi P (2010) Improved spark and ember detection using stationary wavelet transforms. J Theor Biol 264:1279–1292
37. Zhou H, Jungbluth H, Sewry CA, Feng L, Bertini E, Bushby K, Straub V, Roper H, Rose MR, Brockington M, Kinali M, Manzur A, Robb S, Appleton R, Messina S, D'Amico A, Quinlivan R, Swash M, Müller CR, Brown S, Treves S, Muntoni F (2007) Molecular mechanisms and phenotypic variation in RYR1-related congenital myopathies. Brain 130:2024–2036
38. Zhou H, Lillis S, Loy RE, Ghassemi F, Rose MR, Norwood F, Mills K, Al-Sarraj S, Lane RJ, Feng L, Matthews E, Sewry CA, Abbs S, Buk S, Hanna M, Treves S, Dirksen RT, Meissner G, Muntoni F, Jungbluth H (2010) Multi-minicore disease and atypical periodic paralysis associated with novel mutations in the skeletal muscle ryanodine receptor (RYR1) gene. Neuromuscul Disord 20:166–173
39. Zhou H, Yamaguchi N, Xu L, Wang Y, Sewry C, Jungbluth H, Zorzato F, Bertini E, Muntoni F, Meissner G, Treves S (2006) Characterization of recessive RYR1 mutations in core myopathies. Hum Mol Genet 15:2791–2803

The Journal of Physiology

Impaired excitation–contraction coupling in muscle fibres from the dynamin2^{R465W} mouse model of centronuclear myopathy

Candice Kutchukian[1], Peter Szentesi[2], Bruno Allard[1], Delphine Trochet[3], Maud Beuvin[3], Christine Berthier[1], Yves Tourneur[4,5], Pascale Guicheney[6], Laszlo Csernoch[2], Marc Bitoun[3] and Vincent Jacquemond[1]

[1] *Univ Lyon, Université Claude Bernard Lyon 1, CNRS UMR-5310, INSERM U-1217, Institut NeuroMyoGène, Villeurbanne, France*
[2] *Department of Physiology, Faculty of Medicine, University of Debrecen, Debrecen, Hungary*
[3] *Research Center for Myology, UPMC Univ Paris 06 and INSERM UMR_S974, Institute of Myology, Paris, France*
[4] *CarMeN, INSERM U1060, Faculté de Médecine Lyon Sud, Oullins, France*
[5] *UFPE Dept Nutrição, Av. Prof. Moraes Rego, Cidade Universitária, Recife, Brazil*
[6] *Sorbonne Universités, UPMC Univ Paris 06, INSERM UMR_S1166, Institute of Cardiometabolism and Nutrition (ICAN), Paris, France*

Edited by: Don Bers & Michael Shattock

Key points

- Dynamin 2 is a ubiquitously expressed protein involved in membrane trafficking processes.
- Mutations in the gene encoding dynamin 2 are responsible for a congenital myopathy associated with centrally located nuclei in the muscle fibres.
- Using muscle fibres from a mouse model of the most common mutation responsible for this disease in humans, we tested whether altered Ca^{2+} signalling and excitation–contraction coupling contribute to muscle weakness.
- The plasma membrane network that carries the electrical excitation is moderately perturbed in the diseased muscle fibres.
- The excitation-activated Ca^{2+} input fluxes across both the plasma membrane and the membrane of the sarcoplasmic reticulum are defective in the diseased fibres, which probably contributes to muscle weakness in patients.

Abstract Mutations in the gene encoding dynamin 2 (DNM2) are responsible for autosomal dominant centronuclear myopathy (AD-CNM). We studied the functional properties of Ca^{2+} signalling and excitation–contraction (EC) coupling in muscle fibres isolated from a knock-in (KI) mouse model of the disease, using confocal imaging and the voltage clamp technique. The transverse-tubule network organization appeared to be unaltered in the diseased fibres, although its density was reduced by ∼10% compared to that in control fibres. The density of Ca^{2+} current through CaV1.1 channels and the rate of voltage-activated sarcoplasmic reticulum Ca^{2+} release were reduced by ∼60% and 30%, respectively, in KI *vs.* control fibres. In addition, Ca^{2+} release in the KI fibres reached its peak value 10–50 ms later than in control ones. Activation of Ca^{2+} transients along the longitudinal axis of the fibres was more heterogeneous in the KI than in the control fibres, with the difference being exacerbated at intermediate membrane voltages. KI fibres exhibited spontaneous Ca^{2+} release events that were almost absent from control fibres. Overall, the results of the present study demonstrate that Ca^{2+} signalling and EC coupling exhibit a number of dysfunctions likely contributing to muscle weakness in *DNM2*-related AD-CNM.

(Resubmitted 24 July 2017; accepted after revision 20 October 2017; first published online 26 October 2017)
Corresponding author V. Jacquemond, Institut NeuroMyoGène, CNRS UMR 5310, INSERM U1217, Université Claude Bernard Lyon 1, Bât. Raphaël Dubois, 43 Boulevard du 11 novembre 1918, F69622 Villeurbanne, France. Email: vincent.jacquemond@univ-lyon1.fr

© 2017 The Authors. The Journal of Physiology © 2017 The Physiological Society DOI: 10.1113/JP274990

Abbreviations AD, autosomal dominant; BIN1, amphiphysin 2; CNM, centronuclear myopathy; DNM2, dynamin 2; EC, excitation–contraction; FDB, flexor digitorum brevis; FWHM, full width at half-maximum; KI, knock-in; MyHC, myosin heavy chain; MTM1, myotubularin; PBS, phosphate-buffered saline; PH, pleckstrin homology; RYR1, type 1 ryanodine receptor; SR, sarcoplasmic reticulum; WT, wild-type.

Introduction

In skeletal muscle, Ca^{2+} released from the sarcoplasmic reticulum (SR) through type 1 ryanodine receptor (RYR1) channels generates the rise in cytosolic Ca^{2+} concentration that triggers contraction. The process is under the control of electrical activity in the transverse invaginations of the plasma membrane (the t-tubules) where it is sensed by the dihydropyridine receptor Ca^{2+} channel CaV1.1, which physically controls RYR1 channel opening (Rios *et al.* 1992; Schneider, 1994; Dulhunty *et al.* 2017). Centronuclear myopathies (CNMs) encompass a group of inherited diseases that yield heterogeneous features in terms of age of onset and muscle weakness severity and progression, with all of them being associated with the presence of nuclei in a central position within the muscle fibres. Most well-known mutations responsible for CNMs affect the genes encoding myotubularin (MTM1; Laporte *et al.* 1996), amphiphysin 2 (BIN1; Nicot *et al.* 2007) and dynamin 2 (DNM2; Bitoun *et al.* 2005). Although great progress has been made in the recent years with respect to the knowledge of the corresponding diseases, the underlying detailed pathophysiological mechanisms still remain unclear (Jungbluth & Gautel, 2014).

DNM2 is an ubiquitously expressed GTPase interacting with actin and microtubules and involved in endocytosis, membrane trafficking and centrosome cohesion (Durieux *et al.* 2010*b*). From the N- to C-terminus, the protein is constituted by a GTPase domain, a 'stalk' region essential for the protein structure, a pleckstrin homology (PH) domain, a GTPase effector domain and a domain enriched in proline and arginine (Cao *et al.* 1998). *DNM2*-related autosomal dominant (AD)-CNM was initially characterized as a slowly-progressing muscle weakness affecting distal muscles with onset in early adulthood, resulting from mutations affecting the stalk domain of the protein (Bitoun *et al.* 2005; Jeub *et al.* 2008). However, mutations affecting the PH domain were subsequently also identified in more severe neonatal sporadic forms of the disease (Bitoun *et al.* 2007). A knock-in (KI) heterozygous mouse model of the most common mutation in the *DNM2* human gene was generated by Durieux *et al.* (2010*a*, KI-*Dnm2*^{R465W}) and found to reproduce the main symptoms of the human disease. In brief, mice develop progressive muscle weakness starting at ∼3 weeks of age, which occurs first with no associated loss in muscle mass or morphological abnormalities. Subsequently, at ∼2 months of age, atrophy develops, together with the appearance of alterations in mitochondria and the reticular membrane network, similar to those reported in biopsies from human patients. Defective membrane trafficking, including altered autophagy, was highlighted as a potentially major mechanism of the disease (Durieux *et al.* 2010*a*, *b*, 2012; Bohm *et al.* 2012). However, a possible contribution of disturbed intracellular Ca^{2+} homeostasis was also highlighted: indeed, the resting Ca^{2+} level and releasable sarcoplasmic reticulum Ca^{2+} content were reported to be elevated in muscle fibres from KI-*Dnm2*^{R465W} mice, in concurrence with impaired contractile properties (Durieux *et al.* 2010*a*; Fraysse *et al.* 2016). Interestingly, defective intracellular Ca^{2+} homeostasis and excitation–contraction (EC) coupling are hallmarks of the centronuclear myopathy resulting from MTM1 deficiency (Al Qusairi *et al.* 2009; Kutchukian *et al.* 2016) and altered Ca^{2+} signals were also reported in muscle fibres down-expressing BIN1 (Tjondrokoesoemo *et al.* 2011). Thus, Ca^{2+} homeostasis and EC coupling may represent commonly affected targets in all CNMs. The present study aimed to contribute to resolving this issue by investigating the detailed properties of voltage clamp-activated sarcoplasmic reticulum Ca^{2+} release in muscle fibres isolated from KI-*Dnm2*^{R465W} mice. Interestingly, the results obtained demonstrate that the pathophysiological consequences of the *Dnm2* mutation on Ca^{2+} signalling and EC coupling share certain specific features with those associated with MTM1 deficiency (Kutchukian *et al.* 2016).

Methods

Ethical approval

All of the experiments and procedures were conducted in accordance with the guidelines of the local animal ethics committee of the University Claude Bernard – Lyon 1, the French Ministry of Agriculture (decree 87/848) and the revised European Directive 2010/63/EU and conform with the principles and regulations as described in Grundy (2015). All experiments were performed at room temperature (20–22°C).

Preparation of the muscle fibres

We used 6-month-old wild-type (WT) and heterozygous KI-*Dnm2*^{R465W} (also referred to as KI) male mice in the C57BL/6 genetic background (Durieux *et al.* 2010*a*). Mice were manipulated and taken care of in accordance with European recommendations on animal experimentation.

© 2017 The Authors. The Journal of Physiology © 2017 The Physiological Society

szentesi_peter_292_24

Single fibres were isolated from the flexor digitorum brevis (FDB) and interosseus muscles in accordance with previously described procedures (Jacquemond, 1997). In brief, mice were anaesthetized with isoflurane and killed by cervical dislocation. Muscles were removed and incubated for 60 min at 37°C in the presence of external Tyrode solution containing 2 mg mL^{-1} collagenase (type 1; Sigma, St Louis, MO, USA). Single fibres were obtained by triturating the collagenase-treated muscles within the experimental chamber. Fibre diameter was estimated from direct microscopic observation of isolated fibres viewed with a 40× objective. Comparisons were always made between groups of fibres issued from the same muscle type (either FDB or interosseous). Experiments were carried out on muscle fibres isolated from the muscles of both hindlimbs from three WT and four KI mice.

Electrophysiology

We used the silicone voltage clamp technique (Jacquemond, 1997; Lefebvre *et al.* 2014). In brief, fibres from the interosseous muscles were partly insulated with silicone grease so that only a short portion (50–100 μm long) of the fibre extremity remained out of the silicone. Fibres were bathed in the standard extracellular solution used for voltage clamp. An RK-400 patch clamp amplifier (Bio-Logic, Claix, France) was used in whole-cell voltage clamp configuration in combination with an analogue–digital converter (Digidata 1440A; Axon Instruments, Foster City, CA, USA) controlled using pClamp 9 software (Axon Instruments). Voltage clamp was performed with a micropipette filled with a solution mimicking the ionic composition of the cytosolic compartment and also containing a high concentration of EGTA and the fluorescent Ca^{2+} -sensitive probe rhod-2. The tip of the micropipette was inserted through the silicone, within the insulated part of the fibre, and it was gently crushed against the bottom of the chamber to ease intracellular equilibration. Analogue compensation was adjusted to further decrease the effective series resistance. Intracellular equilibration of the solution was allowed for a period of 30 min with the holding voltage held at −80 mV before initiating measurements. Membrane depolarizing steps of 0.5 s in duration were applied from a holding command potential of −80 mV. For calcium current analysis, the linear leak component of the membrane current was removed using the appropriately scaled value of the steady change in membrane current elicited by a 20 mV hyperpolarization from the holding potential. The voltage dependence of the peak current was fitted with the equation:

$$I(V) = G_{max}(V - V_{rev})/\{1 + \exp[(V_{0.5} - V)/k]\} \quad (1)$$

where $I(V)$ is the peak current density at the command voltage V, G_{max} is the maximum conductance, V_{rev} is the apparent reversal potential, $V_{0.5}$ is the half-activation potential and k is the steepness factor.

Confocal imaging and analysis

Confocal imaging was conducted with an LSM 5 Exciter microscope (Zeiss, Oberkochen, Germany) equipped with a 63× oil immersion objective (numerical aperture 1.4). For detection of rhod-2 fluorescence, excitation was from the 543 nm line of a HeNe laser and fluorescence was collected above 560 nm. Rhod-2 Ca^{2+} transients were imaged using the line-scan mode (x,t) of the system with the line parallel to the longitudinal axis of the fibres. Images were taken with a scanning frequency of 1.15 ms per line. Rhod-2 fluorescence changes were expressed as F/F_0 where F_0 is the baseline fluorescence. For imaging the t-tubule network, FDB muscle fibres were incubated for 30 min in the presence of 10 μM di-8-anepps in Tyrode solution. For Ca^{2+} sparks measurements, FDB fibres were incubated for 30 min in the presence of Tyrode solution containing 10 μM fluo-4 AM. For both di-8-anepps and fluo-4 imaging, fluorescence was collected above 505 nm with 488 nm excitation. Estimation of the t-tubule density from the di-8-anepps fluorescence was carried out from a largest possible region of interest excluding the plasma membrane, within each fibre. Two images were taken at distinct locations along each fibre. Analysis was carried out with ImageJ (NIH, Bethesda, MD, USA). Automatic thresholding with Otsu's method was used to create a binary image of the surface area occupied by t-tubules. Then, the 'skeletonize' function was used to delineate the t-tubule network. T-tubule density was expressed as the percentage of positive pixels within the region.

Analysis of Ca^{2+} sparks was carried out in accordance with procedures described previously (Csernoch *et al.* 2008; Szabó *et al.* 2010). In brief, the region of the fibre and the background was defined on the first image of each x,y image series. The averaged background fluorescence was subtracted from each pixel of all images in one series. The calcium release events were detected by the stationary wavelet method. The filtering was made by soft thresholding wavelet detection. Finally, the amplitude and full width at half-maximum (FWHM) of the sparks was calculated. Two FWHM values were calculated: perpendicular and parallel with the Z-lines. To detect the Z-lines, the frequency spectrum in each line of all images was calculated using fast Fourier transform. Finally, inverse fast Fourier transform of the frequency components correspond to sarcomeres was used to remove the Z-lines from the images. The analysis of line scan images was performed with automatic event detection software (Szabo *et al.* 2010), which calculated the amplitude (F/F_0), FWHM and the duration of the identified events.

© 2017 The Authors. The Journal of Physiology © 2017 The Physiological Society

szentesi peter_292_24

[Ca^{2+}] and Ca^{2+} release calculation

The Ca^{2+} release flux underlying the rhod-2 Ca^{2+} transients was estimated from the time derivative of the total myoplasmic Ca^{2+} ([Ca_{Tot}]) obtained from the occupancy of intracellular calcium binding sites in accordance with a procedure described previously (Pouvreau *et al.* 2006; Lefebvre *et al.* 2011). For this, changes in [Ca^{2+}] were calculated from the rhod-2 signals using the pseudo-ratio equation (Cheng *et al.* 1993) assuming a basal [Ca^{2+}] of 0.1 μM and a K_d of rhod-2 for Ca^{2+} of 1.2 μM. The model included troponin C (TN) binding sites, parvalbumin binding sites and calcium transport across the SR membrane with the same parameters as those used in Lefebvre *et al.* (2011). Ca^{2+}-binding sites on EGTA provided the major contribution with a total sites concentration of 6 mM, an 'on' rate constant k_{on}, EGTA of 0.056 μM^{-1} ms^{-1} and an 'off' rate constant k_{off}, CaTN of 0.002 ms^{-1}.

Quantification of the spatial heterogeneity of Ca^{2+} release activation was achieved as described previously (Kutchukian *et al.* 2016) by calculating the SD of the time to peak rate of rise in the rhod-2 F/F_0 signal along the scanned line. To reduce noise, analysis was performed on a space- and time-filtered version of the images of rate of change in rhod-2 fluorescence: for this, line-scan images of the rate of change in F/F_0 ($dF/F_0/dt$) were resampled from 512 to 64 pixels (0.1–0.8 μm per pixel) after linear averaging in the space domain, and the time derivative was calculated with a *dt* of 4 pixels (4.6 ms). Furthermore, the value for the time to peak $dF/F_0/dt$ at a given position of the line was discarded if the corresponding absolute $dF/F_0/dt$ value did not exceed five times the SD of the signal amplitude measured at the same line position, after the end of the pulse.

Myosin heavy chain (MyHC) composition

Fibre typing in muscle was determined according to the expression of MyHC isoforms by immunofluorescence analysis. Seven μm thick cryosections of tibialis anterior muscle from 5-month-old mice were made using a CM3050S cryostat (Leica). For immunostaining analysis, tissue sections were blocked for 1 h in 3% bovine serum albumin IgG-free. Monoclonal antibodies against MyHC isoform slow MyHC-1 (BA-D5-s, 1/2) and MyHC-2A (SC-71-s, 1/2) were applied at room temperature for 2 h and then MyHC-2B (BF-F3-s, 1/1) was applied at 4°C overnight. All MyHC antibodies were obtained from DSHB (Iowa City, IA, USA). Sections were respectively revealed by goat anti-mouse IgG2b Cy3-conjugated AffiniPure, goat anti-mouse IgG1 DyLight 488-conjugated AffiniPur and goat anti-mouse IgM AMCA-conjugated AffiniPur (Jackson ImmunoResearch Inc., West Grove, PA, USA) and mounted in Mowiol Medium. Image acquisition was performed using an AZ100 macroscope (Nikon, Tokyo, Japan) and the number of each fibre type was quantified using ImageJ.

Protein extraction and western blotting

Frozen tibialis anterior muscles were homogenized on ice, using a Potter-Elvehjem homogenizer, in lysis buffer containing 50 mM of Tris-HCl pH 7.5, 150 mM NaCl, 1 mM EDTA and NP40 1% supplemented with protease inhibitor cocktail 1% (Sigma-Aldrich, Saint-Quentin-Fallavier, France). After centrifugation (14,000 *g* at 4°C for 15 min), the protein concentration in the supernatant was determined with a BCA Protein Assay Kit (Thermo Scientific Pierce, Villebon sur Yvette, France). Proteins (30 μg) were mixed with loading buffer (50 mM Tris-HCl, SDS 2%, glycerol 10%, β-mercaptoethanol 1% and bromophenol blue). Protein samples were separated on Nupage 4–12% Bis Tris gel (Life Technologies, Saint-Aubin, France) and transferred onto nitrocellulose membranes (0.45 μm pore size; Life Technologies) overnight at 100 mA at 4°C. Membranes were blocked for 1 h at room temperature in phosphate-buffered saline (PBS) containing non-fat dry milk 5% and Tween-20 0.1% and then exposed to mouse monoclonal anti-α1 subunit of DHPR (Merck-Millipore, Saint Quentin en Yvelines, France) or mouse monoclonal anti-α tubulin (Sigma-Aldrich) in PBS-Tween-20 0.1% and milk 1% overnight at 4°C. Membranes were rinsed in PBS-Tween-20 0.1% and incubated for 2 h with HRP-conjugated secondary antibody (anti-mouse from Jackson ImmunoResearch, Newmarket, UK) in PBS-Tween-20 0.1%. Chemiluminescence was detected using an ECL detection Kit (Merck-Millipore) in a G-Box imaging system (Ozyme, Montigny-le-Bretonneux, France) and signal quantification was performed using ImageJ.

Solutions

Tyrode solution contained (in mM): 140 NaCl, 5 KCl, 2.5 $CaCl_2$, 2 $MgCl_2$ and 10 Hepes. The extracellular solution used for voltage clamp contained (in mM) 140 TEA-methanesulphonate, 2.5 $CaCl_2$, 2 $MgCl_2$, 1 4-aminopyridine, 10 Hepes and 0.002 tetrodotoxin. The pipette solution contained (in mM) 120 K-glutamate, 5 Na_2-ATP, 5 Na_2-phosphocreatine, 5.5 $MgCl_2$, 15 EGTA, 6 $CaCl_2$, 0.1 rhod-2, 5 glucose and 5 Hepes. Di-8-anepps and fluo-4 AM were dissolved and stored in dimethyl sulphoxide. All solutions were adjusted to pH 7.20.

Statistical analysis

Statistical analysis was performed using Origin, version 8.0 (OriginLab Corp., Northampton, MA, USA). For all comparisons, only muscle fibres issued from the same type of muscle (either FDB or interosseous) were used.

© 2017 The Authors. The Journal of Physiology © 2017 The Physiological Society

Data values are presented as the mean ± SD for n fibres. Unless otherwise specified, statistical significance was determined using Student's t test ($^{*}P \leq 0.05$, $^{**}P \leq 0.01$, $^{***}P \leq 0.001$). Normality of datasets was checked for each statistical analysis.

Results

Mildly altered t-tubule network in KI-*Dnm2*^{R465W} muscle fibres

An altered t-tubule network is a hallmark of the CNM resulting from MTM1 deficiency and contributes to the associated failing EC coupling (Al Qusairi *et al.* 2009). It was thus of great interest to determine whether a similar process occurs in the KI-*Dnm2*^{R465W} model. Figure 1*A* shows representative confocal frames of di-8-anneps fluorescence from WT and KI-*Dnm2*^{R465W} fibres. The two images, together with corresponding longitudinal profiles of fluorescence intensity (Fig. 1*B*) along the indicated regions of interest, demonstrate that there was no striking difference reproducibly catching the eye between WT and KI fibres. Assuming two t-tubules per sarcomere, sarcomere length was estimated from the number of double-peaks within the profile length. Mean ± SD absolute sarcomere length values were very similar in WT (1.96 ± 0.03, $n = 29$) and KI fibres (1.98 ± 0.04, $n = 37$, $P = 0.04$). To quantify the t-tubule density, the network was outlined as illustrated in Fig. 1*C* (see Methods) and expressed as a percentage of the total surface of the region. Corresponding values for t-tubule density index are shown in Fig. 1*C*.

The mean ± SD density index was reduced by ∼10% in KI (7.97 ± 0.98, $n = 37$) compared to WT fibres (8.67 ± 1.1, $n = 29$, $P = 0.008$). Thus, altogether, the t-tubule network appears far less affected in this model of CNM than in the case of MTM1 deficiency (Al Qusairi *et al.* 2009). However, it should be noted that local defects in the network similar to those reported in MTM1-deficient muscle fibres (Al Qusairi *et al.* 2009; Kutchukian *et al.* 2016) were identified in three out of the 37 imaged KI fibres, with one fibre exhibiting extended alterations giving the lowest value of t-tubule density index (4.8).

Another feature of MTM1-deficiency is muscle atrophy (Buj Bello *et al.* 2002) and this was also a feature associated with impairment of contractile properties of the tibialis anterior of KI-*Dnm2*^{R465W} mice (Durieux *et al.* 2010*a*). We thus checked whether this was also the case for the fibres used in the present study. The mean ± SD diameter was reduced by 8% in the KI group compared to the WT group (42.7 ± 8.5 μm, $n = 81$, *vs.* 39.4 ± 10.7 μm, $n = 95$, respectively, $P = 0.03$).

Depressed CaV1.1 Ca^{2+} current density in KI-*Dnm2*^{R465W} muscle fibres

Membrane currents were measured simultaneously to rhod-2 Ca^{2+} transients in response to voltage clamp depolarizing pulses of 0.5 s duration. The mean ± SD capacitance from WT and KI fibres measured from the change in current elicited by a 20 mV hyperpolarizing pulse from −80 mV was 2.2 ± 0.7 ($n = 22$) and 1.4 ± 0.4 nF ($n = 25$), respectively. The value was thus significantly reduced by 36% ($P < 0.0001$) in the KI fibres. Assuming that, on average, the same fibre length was voltage clamped in the two groups of fibres, this difference is quite substantial. Figure 2*A* shows representative traces of CaV1.1 Ca^{2+} current in response to membrane

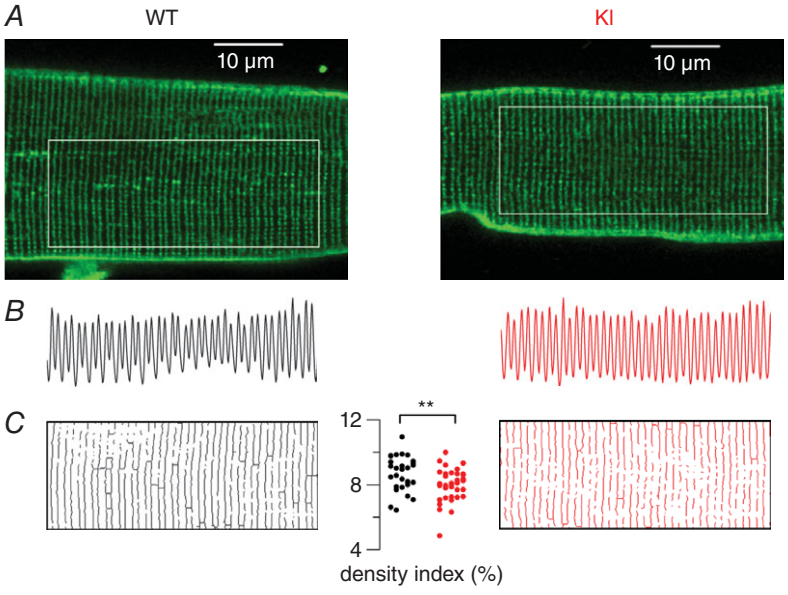


Figure 1. T-tubule network in WT and KI-*Dnm2*^{R465} fibres
A, *x*,*y* fluorescence images of di-8-anepps staining of the t-tubule network in a WT (left) and in a KI (right) muscle fibre. The analysis shown in (*B*) and (*C*) was performed within the region of interest highlighted by a white box in each image. *B*, longitudinal profile of fluorescence along the corresponding region of interest shown in (*A*). *C*, outlined t-tubule network within each region of interest; thresholding was used to create a binary image of the network. The graph in the middle shows values for the t-tubule density index in the two groups of fibres, calculated as the percentage of above-threshold pixels in the regions of interest.

© 2017 The Authors. The Journal of Physiology © 2017 The Physiological Society

depolarizing steps of increasing amplitude in a WT and in a KI muscle fibre. Figure 2*B* shows the mean peak current density *vs.* voltage relationships from 22 WT and 23 KI fibres, whereas the mean parameters obtained from fitting each individual voltage-dependence are shown in Fig. 2*C*. There was a severe decrease in the peak amplitude of the current, which translated into a 70% decrease of the peak conductance associated with an 11 mV negative shift of the half-activation voltage. The apparent reversal voltage also significantly differed between the two groups. However, this difference should be interpreted with caution considering that we did not measure the current at sufficiently large voltages to accurately appreciate this parameter. In any case, the results clearly highlight a severe alteration of CaV1.1-mediated Ca^{2+} entry in the diseased fibres. The time course of inactivation was estimated by fitting a single exponential function to the decaying phase of the current for membrane voltage values between 0 and +40 mV. For voltages between 0 and +30 mV, mean values for the time constant tended

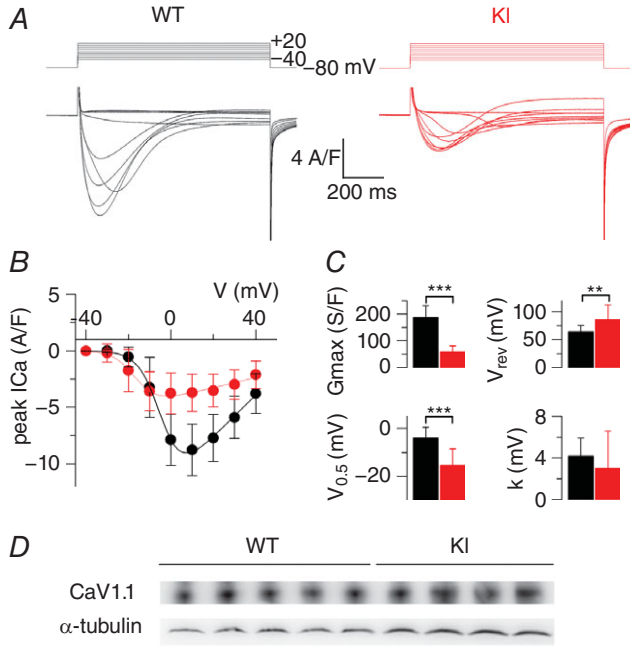


Figure 2. CaV.1.1 Ca^{2+} current in WT and KI-*Dnm2*^{R465} fibres
A, representative Ca^{2+} current traces in a WT and in a KI fibre in response to 0.5 s long depolarizing pulses from −80 mV to the range of indicated values, by 10 mV steps. *B*, mean voltage-dependence of the peak Ca^{2+} current in the two groups of fibres from measurements performed as shown in (*A*). Superimposed continuous lines show the result from fitting the mean WT and KI data points with eqn (1). *C*, mean values for the parameters obtained from fitting each current *vs.* voltage dataset with eqn (1) (see Methods). *D*, expression of CaV1.1 in tibialis anterior muscles: western-blot using an antibody against the α1 subunit of the dihydropyridine receptor was performed on protein extracts from five WT and four KI mice at 5 months of age. An α-tubulin antibody was used as loading control.

to be larger in the KI than in WT fibres (by 10–30%). However differences between the two groups were not significant. For example, at +10 mV, mean ± SD values were 55.5 ± 15.6 ms ($n = 22$) and 73.9 ± 41.7 ms ($n = 25$, $P = 0.056$) in WT and KI fibres, respectively.

To determine whether the depressed Ca^{2+} current density was the result of a reduced amount of CaV1.1 protein, a western blot analysis was performed on protein extracts from tibialis anterior muscles from WT and KI mice, with α-tubulin used as loading control. The results are presented in Fig. 2*D*. On average, the CaV1.1/tubulin ratio was 1.21 ± 0.31 and 0.95 ± 0.06 in extracts from 5 WT and 4 KI muscles, respectively. The difference was statistically not significant ($P = 0.15$; Mann–Whitney *U* test).

Altered SR Ca^{2+} release amplitude and kinetics in KI-*Dnm2*^{R465W} muscle fibres

Figure 3*A* shows rhod-2 Ca^{2+} transients elicited by membrane depolarizing steps of increasing amplitude in a WT and in a KI fibre. As routinely observed under these conditions, transients in WT fibres exhibit a fast rising phase at the onset of the pulse, followed by a slower one at low and intermediate voltages and by a more or less steady or slowly decaying phase for the largest steps. As shown in Fig. 3*A*, KI fibres exhibited an overall similar time-course, although the initial rise of the transients appeared to be less sharp than in the WT fibres, and the maximum level reached during the pulse was somewhat less than in the WT fibres. Figure 3*B* shows corresponding traces for the rate of SR Ca^{2+} release: both WT and KI fibres exhibited an early peak, the amplitude of which increased with the amplitude of the pulse, followed by a spontaneous decay down to a low level. In response to depolarizing steps of same amplitude, the peak Ca^{2+} release was lower in the KI than in the WT fibre. In addition, the time to reach the peak was increased in the KI fibre, as shown in the inset of Fig. 3*B*, which provides an expanded view of peak rates of Ca^{2+} release of similar peak amplitude in the WT (at V = 0 mV) and in the KI fibre (at V = +40 mV).

Mean ± SD values for the amplitude of peak rate of Ca^{2+} release *vs.* voltage are shown in Fig. 3*C* in the two groups of fibres. Fitting the voltage dependence in each fibre with a Boltzmann function gave mean values for maximal rate, mid-voltage and steepness of 83.4 ± 42.5 μM ms^{-1}, −11.3 ± 7.1 mV and 7.4 ± 2.9 mV in WT fibres ($n = 22$) and 59.1 ± 31.2 μM ms^{-1}, −8.1 ± 7.9 mV and 8.2 ± 2.7 mV in KI fibres ($n = 24$), respectively. The mean value for maximal rate was significantly reduced in KI compared to WT fibres by ∼30% (Fig. 3*C*, inset, $P = 0.03$). Figure 3*D* shows corresponding mean values for the total released Ca^{2+} (expressed in terms of myoplasmic volume) calculated from the time integral of the Ca^{2+} release traces. Assuming that some extent of SR Ca^{2+} depletion

© 2017 The Authors. The Journal of Physiology © 2017 The Physiological Society

szentesi_peter_292_24

occurs during the pulses, any severe difference in SR Ca^{2+} content between WT and KI fibres would translate into an alteration of the plateau value of total released Ca^{2+} reached for the large pulses. The results in Fig. 3*D* thus indicate that initial SR Ca^{2+} content was probably similar in the WT and KI fibres. Figure 3*E* shows mean values for time to peak Ca^{2+} release in WT and KI fibres. Mean values were larger in KI fibres by 50 to 10 ms within the −20 to +40 mV range, respectively. To test whether a change in the time course of change in membrane voltage could contribute to the delayed time to peak Ca^{2+} release in KI fibres, an analysis of the time course of the capacitive current was performed. For this, the transient change in membrane current used to calculate the capacitance was fitted by a 2 exponential plus constant function. Mean ± SD values for the fast and slow time constant were 0.62 ± 0.2 ms and 4.8 ± 3.7 ms, respectively, in WT fibres and 0.36 ± 0.08 ms and 4.72 ± 1.16 ms, respectively, in KI fibres, providing no indication that a reduced speed of voltage establishment would contribute to delayed activation of ryanodine receptors in the KI fibres. Thus, altogether, voltage-activated Ca^{2+} release is depressed and slowed in KI fibres, whereas voltage-dependency and SR Ca^{2+} content are unaffected. To determine whether these Ca^{2+} release alterations could be associated with a change in fibre type composition of the muscles, the expression of MyHC isoforms was assessed by immunofluorescence analysis in tibialis anterior muscles. The results are presented in Table 1. They clearly demonstrate that there was no change in fibre type composition in the KI muscles, thus ruling out this possibility.

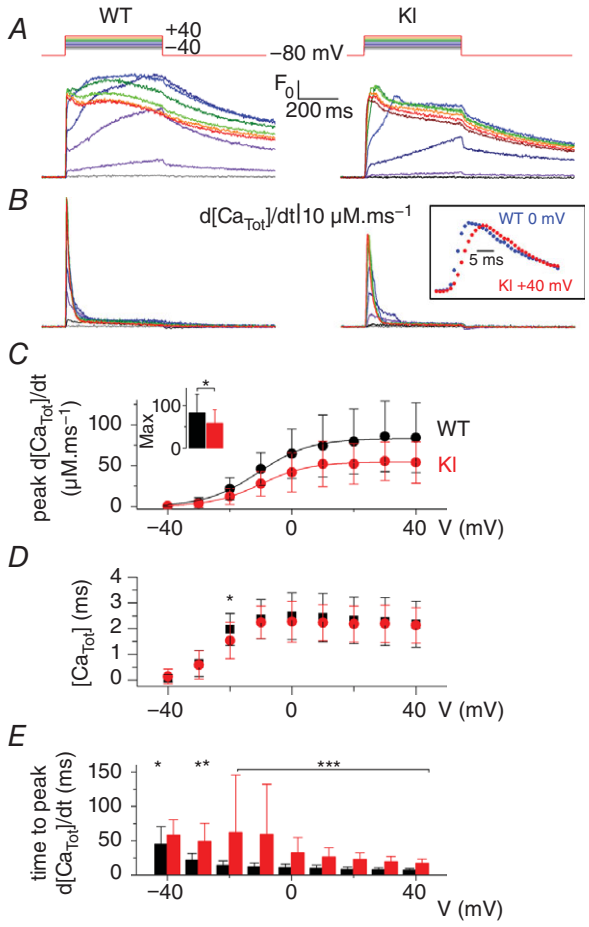


Figure 3. Voltage-activated SR Ca^{2+} release in WT and KI-*Dnm2*^{R465} fibres
A, representative rhod-2 Ca^{2+} transients in a WT and in a KI fibre in response to 0.5 s long depolarizing pulses from −80 mV to the range of indicated values, by 10 mV steps. *B*, corresponding Ca^{2+} release flux ($d[Ca_{Tot}]/dt$) traces calculated as described in the Methods. *C*, mean voltage-dependence of the peak rate of SR Ca^{2+} release in WT and KI fibres. Superimposed continuous lines show the result from fitting the mean WT and KI data points with a Boltzmann equation. The inset shows the mean values for maximal rate of SR Ca^{2+} release in the two groups of fibres, as assessed from Boltzmann fits to data from each fibre. *D*, mean values for the total amount of released Ca^{2+} calculated from the time integral of the Ca^{2+} release traces, in WT and KI fibres. *E*, mean values for the time to peak Ca^{2+} release in WT and KI fibres.

Table 1. Fibre typing in tibialis anterior muscles from 5-month-old WT and KI-*Dnm2*^{R465W} mice

	WT	KI
Type I	0.33 ± 0.09	0.23 ± 0.09
Type IIa	9.42 ± 0.77	7.79 ± 2.63
Type IIb	90.25 ± 0.69	91.98 ± 2.67

Type I, IIa and IIb muscle fibres were counted after co-immunostaining of the three corresponding myosin isoforms on tibialis anterior sections. Values are indicated as the percentage of each fibre type relative to the total number of fibres (mean ± SD from four animals per genotype). Statistical analysis was performed using a Mann–Whitney *U* test (WT *vs.* KI for each fibre type). None of the mean values differed between the two groups ($P > 0.05$).

Spatial variability of Ca^{2+} release in KI-*Dnm2*^{R465W} muscle fibres

Muscle fibres from the *Mtm1*-KO mouse model of CNM were shown to exhibit spatial non uniformity of Ca^{2+} release along their longitudinal axis (Kutchukian *et al.* 2016). It was thus of interest to assess whether similar defects were detectable in the present model of *DNM2*-related CNM. Figure 4*A* shows a line-scan image of rhod-2 fluorescence from a WT (left) and from a KI fibre (right) taken when a pulse from −80 to −10 mV was applied. The traces underneath show the average time course of F/F_0 along the entire line of each corresponding line-scan image. Figure 4*B* shows corresponding images of the time derivative of the fluorescence [$d(F/F_0)/dt$]. The WT fibre exhibited a sharp peak, the time position of which

© 2017 The Authors. The Journal of Physiology © 2017 The Physiological Society

was very well conserved along the line (Fig. 4*C*, left). By contrast, the KI fibre exhibited a delayed peak for which the time position increased from the top to the bottom of the line (Fig. 4*C*, right). Spatial variability of the time to peak Ca^{2+} release could take several forms, as illustrated in Fig. 5, which shows $d(F/F_0)/dt$ images from three KI fibres (Fig. 5*A*–*C*) depolarized at −10 and at +10 mV. Each of these three fibres was from a distinct KI mouse. In all cases, the time to peak Ca^{2+} release tended to vary much more along the line at −10 mV than at +10 mV, irrespective of whether it appeared early or late during the pulse. Figure 5*A* illustrates an example where the time to peak Ca^{2+} release at −10 mV varies along the scanned line but remains close in time to the beginning of the pulse. By contrast, Fig. 5*B* shows an example with time to peak still varying along the line but at very late times during the pulse. Finally, Fig. 5*C* shows an example where two distinct peaks are observed during the pulse.

Figure 4*D* shows mean values for the SD of the time to peak of the derivative in WT and KI fibres at both −10 and +10 mV. The mean value was substantially elevated in the KI fibres at −10 mV and to a lesser extent at +10 mV. Altogether, there was a clear trend for a reduced spatial synchronicity of Ca^{2+} release in KI compared to WT fibres.

Spontaneous Ca^{2+} sparks in KI-*Dnm2*^{R465W} muscle fibres

In differentiated muscle, the tight control of RYR1 channel opening by the t-tubule CaV1.1 voltage-sensors is presumed to repress Ca^{2+}-mediated activation of the channels. Consequently, Ca^{2+} sparks, which are a manifest expression of Ca^{2+}-induced Ca^{2+} release, are very rare in intact mammalian muscle fibres under physiological conditions (Shirokova *et al.* 1998, Zhou *et al.* 2006). We tested whether the present disease situation was associated with a perturbation of this process. Figure 6*A* shows an example of the sum of 10 *x,y* confocal frames of fluo-4 fluorescence taken from a KI fibre. The resulting image was inhomogeneous as a result of transient local increases in fluorescence at various locations throughout the fibre. Figure 6*B* shows the baseline fluorescence-corrected confocal frame exhibiting the brightest event of this series (highlighted in the square box). This event exhibited a peak

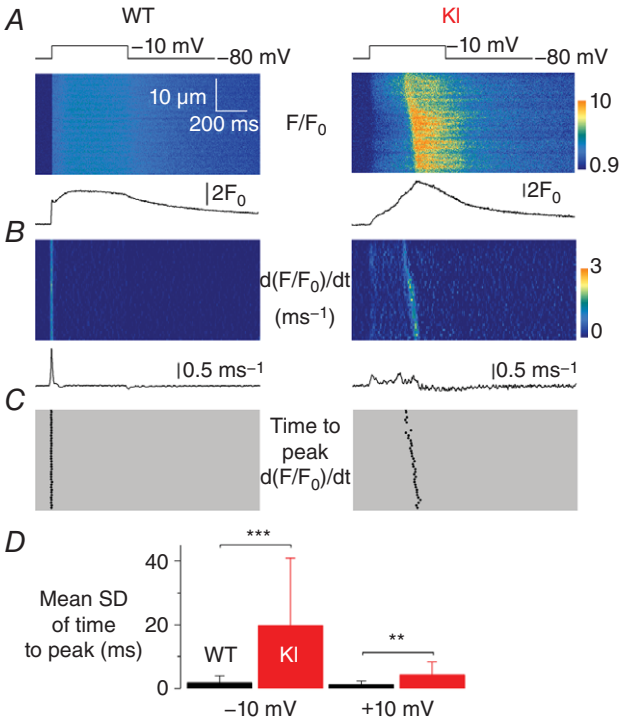


Figure 4. Spatial heterogeneity of time to peak SR Ca^{2+} release in KI-*Dnm2*^{R465} fibres
A, F/F_0 rhod-2 line-scan images taken from a WT and a KI fibre in response to a 0.5 s long depolarizing pulse from −80 to −10 mV. Traces below show the corresponding average F/F_0 signal over the full line. *B*, corresponding images of the rate of change in F/F_0 ($dF/F_0/dt$); these images were resampled from 512 to 64 pixels (0.1–0.8 μm per pixel) after linear averaging in the space domain, and the time derivative was calculated with a dt of 4 pixels (4.6 ms). Traces below show the average rate of change in F/F_0 over the full line. *C*, corresponding distribution of the time to peak rate of change in F/F_0 at each position along the scanned line. *D*, mean ± SD of the time to peak rate of change in rhod-2 F/F_0 in WT ($n = 21$) and KI fibres ($n = 25$), in response to a pulse to −10 mV (left) and to +10 mV (right).

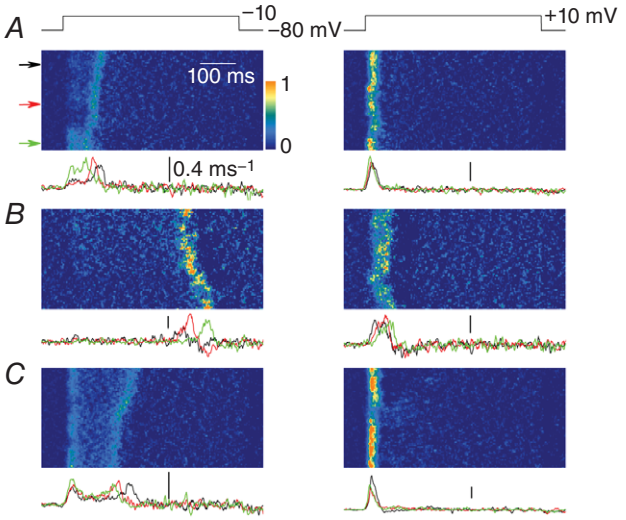


Figure 5. Examples of spatial variability of peak Ca^{2+} release rate in KI-*Dnm2*^{R465W} fibres at −10 and + 10 mV
A–*C*, images of the rate of change in rhod-2 fluorescence ($dF/F_0/dt$) in three distinct KI fibres, respectively, stimulated by a voltage pulse from −80 to −10 mV (left) and by a voltage pulse from −80 to +10 mV (right). Traces underneath each image show the time course of the rate of change in F/F_0 at the three positions indicated by arrows along the line. Scale bars = 0.4 ms^{-1}.

© 2017 The Authors. The Journal of Physiology © 2017 The Physiological Society

szentesi_peter_292_24

amplitude of ~3 F_0 and extended spatially over ~5 μm (Fig. 6*C*). In total, 532 Ca^{2+} sparks were detected in 28 out of 36 KI muscle fibres with a mean ± SD frequency of 153.1 ± 206.2 mm^{-2} s^{-1}. In comparison, only 41 events were detected in 10 out of 30 WT fibres where they appeared with a significantly lower frequency (15.0 ± 33.6 mm^{-2} s^{-1}, $P < 0.001$).

Figure 6*D* and *E* show the distribution of spark amplitude and FWMH in the KI fibres, respectively. The vast majority of events yielded a peak amplitude between 0.5 and 1.5 F_0 (mean of 1.07 ± 0.55) and a FWMH between 1 and 3 μm in both the *x* (mean of 1.94 ± 0.65 μm, black) and *y* (mean of 1.79 ± 0.62 μm, grey) directions. In Fig. 6*D* and *E*, arrows indicate corresponding average values measured in WT fibres, demonstrating not only that the event frequency was enhanced in the KI fibres, but also that the amplitude and spatial spread of the events were significantly larger than those of the rare events detected in WT fibres (mean ± SD amplitude of 0.75 ± 0.36 F_0 and mean ± SD spatial spread of 1.20 ± 0.40 and 1.09 ± 0.44 μm in the *x* and *y* directions, respectively, $P < 0.001$ for all parameters). To characterize their temporal features, events were also detected in line-scan mode in those fibres where the frequency was the largest. Examples are shown in Fig. 7*A*–*C*, indicating the presence of either typical lone sparks (Fig. 7*A*, arrow) or of long-lasting lower amplitude events (Fig. 7*B*, arrow). The amplitude and FWHM distribution of the lone sparks are shown in Fig. 7*D* and *E*. The data originate from 272 events from 16 fibres. Mean ± SD values for event amplitude, FWHM and duration were 1.20 ± 0.74 F_0, 1.33 ± 0.85 μm and 19.7 ± 10.1 ms.

Discussion

The present investigation provides novel insights into the functional features and pathogenic mechanisms involved in *DNM2*-related CNM. The results obtained demonstrate that muscle fibres from the KI-*Dnm2*^{R465W} mouse model of the disease suffer from defective Ca^{2+} homeostasis and EC coupling, which probably contributes to muscle weakness. In addition, the results highlight not only similarities but also discrepancies with other models of CNM.

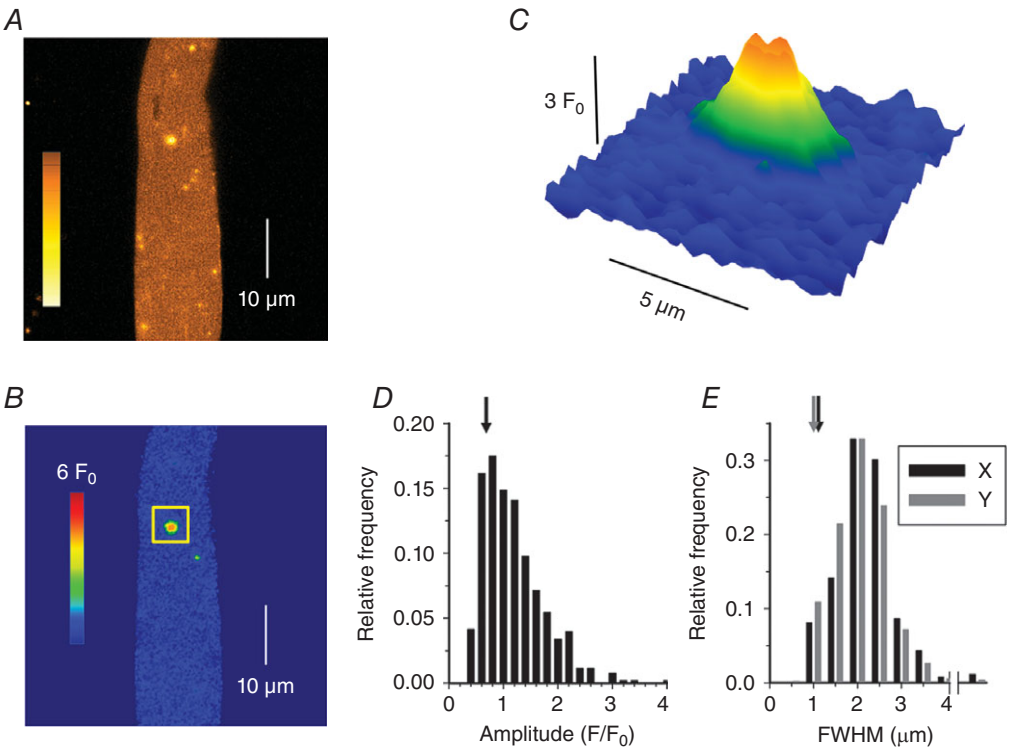


Figure 6. Ca^{2+} sparks in intact KI-*Dnm2*^{R465W} fibres
A, sum of 10 *x,y* confocal images of fluo-4 fluorescence from an isolated KI muscle fibre showing a localized increase in [Ca^{2+}]. Colour bar is in arbitrary units. *B*, first image from the cumulated series shown in (*A*) after correction for baseline fluorescence (F_0) and removal of structure elements (see Methods), expressed as F/F_0. *C*, enlarged view of the individual spark highlighted by the square box in (*B*). Colour bar is the same for (*B*) and (*C*). *D*, Ca^{2+} release events amplitudes. *E*, FWHM of the Ca^{2+} release events, for profiles parallel (X) and perpendicular (Y) to the fibres axis. Arrows in (*D*) and (*E*) indicate the corresponding average values measured for the few events detected in WT fibres.

© 2017 The Authors. The Journal of Physiology © 2017 The Physiological Society

Most well-known CNMs result from mutations in the genes encoding MTM1, DNM2 or BIN1, with all three proteins known to be involved in membrane remodelling and trafficking events. This could provide the basis for a common pathological mechanism (Cowling *et al.* 2012), whereas nuclei mis-localization may represent an offshoot with no or less critical relevance to muscle weakness. Accordingly, it is of particular interest to assess, in all models, the features of processes identified as defective in one of them. Depressed Ca^{2+} release is a hallmark of MTM1 deficiency where it is associated with defective architecture of the t-tubule network (Al Qusairi *et al.* 2009; Kutchukian *et al.* 2016). Defects in t-tubule network linked with alterations in intracellular Ca^{2+} release were also reported following shRNA-mediated knockdown of BIN1in adult muscle fibres (Tjondrokoesoemo *et al.* 2011). By contrast, in the present study, the majority of fibres isolated from 6-month-old KI-*Dnm2*^{R465W} mice did not yield acute destructions of the t-tubule network similar to those reported in the two other models. This is also consistent with previous observations of CaV1.1 immunostaining in muscle fibres from this same mouse model, from which no sign of alteration of the transverse striated expression pattern was detected (Durieux *et al.* 2010*a*). Altogether, this is evidence that critically altered maintenance of the t-tubule network is not a pathogenic hallmark of the present *Dnm2* mutation, whereas it is in the absence of MTM1 or BIN1. Conversely, this also suggests that t-tubule disruption may be critically associated with the degree of severity of a given CNM. Still, the present analysis of the t-tubule density revealed a small but significant reduction in the KI fibres, highlighting a certain extent of reduced t-tubule development. Together with significant atrophy of the muscle fibres, this probably contributed to the observed reduced capacitance of the KI fibres compared to that of WT fibres. However, despite apparently normal integrity, the t-tubule network in KI-*Dnm2* fibres possibly suffered from subtle alterations that remained undetectable from di-8-anepps fluorescence. CNM-related *Dnm2* mutations enhance DNM2 membrane fission activity and thus may be involved in such an effect (Chin *et al.* 2015). Also, reduced t-tubule membrane folding was shown to contribute to reduced capacitance in cardiac cells deleted from BIN1 (Hong *et al.* 2014). Thus, a similar mechanism might occur in the present DNM2 CNM model.

The Ca^{2+} current density through t-tubule CaV1.1 channels was severely reduced in the KI fibres, whereas the protein level was maintained. Because there is evidence in other cell systems that dynamin protein-dependent endocytosis regulates Ca(V) channels density (Yang *et al.* 2010; Di Biase *et al.* 2011), reduced CaV1.1 membrane

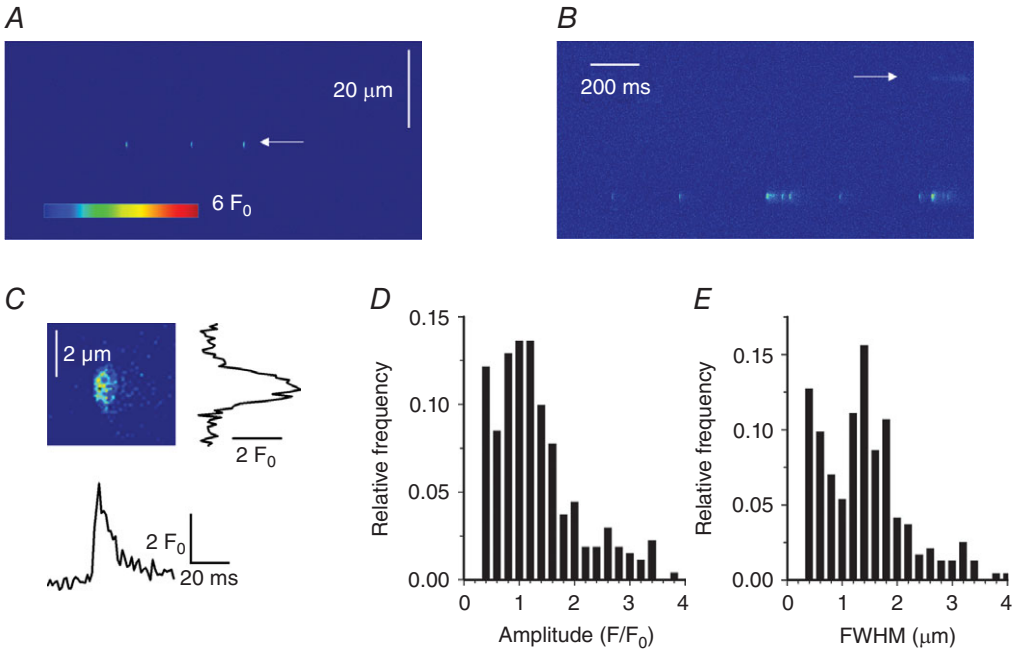


Figure 7. Ca^{2+} sparks in intact KI-*Dnm2*^{R465W} fibres detected in line-scan mode
A and *B*, normalized line-scan images (F/F_0) of fluo-4 fluorescence from two KI fibres showing typical calcium release events corresponding to either lone Ca^{2+} sparks (*A*) or a series of such events (*B*, bottom of the image) or long embers (*B*, marked by arrow). *C*, enlarged portion of the image in (*A*) displaying an individual event at increased temporal and spatial resolution. Traces on the right and underneath show the corresponding spatial distribution and time course of the fluorescence transient, respectively. *D* and *E*, amplitude and FWHM histograms, respectively, of the lone calcium sparks from DNM2 KI fibres.

© 2017 The Authors. The Journal of Physiology © 2017 The Physiological Society

expression could be the underlying mechanism. In MTM1-deficient muscle, CaV1.1 Ca^{2+} current density is also reduced, but this is in association with altered immunostaining and a reduced protein level (Al Qusairi *et al.* 2009). Thus, in the present model, a DNM2-dependent mechanism, possibly related to its trafficking function, is responsible for the loss of Ca^{2+} channel activity in the t-tubule membrane, independent of any reduced protein level.

Voltage-activated SR Ca^{2+} release in the KI-*Dnm2*^{R465W} fibres exhibits a reduced peak amplitude and an increased time-to-peak throughout the voltage range of activation. By contrast, Fraysse *et al.* (2016) reported no difference in peak and time-to-peak Ca^{2+} transients elicited by field stimulation between WT and KI-*Dnm2*^{R465W} fibres. The difference may result from their use of the high-affinity indicator fura-2, which is kinetically limited and easily saturated under non-Ca^{2+}-buffering conditions. Under these conditions, the relatively mild depression of Ca^{2+} release (by 30%) may escape being detected. The Ca^{2+} release alterations observed in the conditions employed in the present study are qualitatively similar to those reported in MTM1-deficient muscle fibres. However, quantitatively, the extent of Ca^{2+} release depression in the present study in muscle fibres from 6-month-old KI-*Dnm2*^{R465W} mice (by ∼30%) was not as dramatic as that observed in muscle fibres from *Mtm1*-KO mice, reaching 60% at 4–5 weeks of age (Kutchukian *et al.* 2016). The much stronger early impairment in *Mtm1*-KO fibres compared to KI-*Dnm2*^{R465W} fibres is probably responsible for the dramatic weakness phenotype in the MTM1 mouse model and in MTM1 patients. Importantly, in the present study, the total amount of released Ca^{2+} for the largest depolarizing pulses did not differ between WT and KI-*Dnm2*^{R465W} fibres, indicating that the SR content was maintained in the diseased fibres and was probably not the reason for the reduced peak rate of Ca^{2+} release. As an underlying mechanism, disturbed DNM2 membrane fission activity, as a consequence of the mutation, may be proposed to alter or destabilize CaV1.1-RYR1 interactions and be responsible for the reduced amplitude of voltage-activated Ca^{2+} release, as well as contribute to the loss of its spatial synchronicity.

The extent of increase in time to peak Ca^{2+} release reported in the present study in KI-*Dnm2*^{R465W} fibres is remarkably similar to that reported in MTM1-deficient muscle fibres. For example, for a pulse to +10 mV, the mean values for time-to-peak Ca^{2+} release in WT and *Mtm1*-KO fibres were 10 and 28 ms, respectively (Kutchukian *et al.* 2016). For the same pulse, the mean values in WT and KI-*Dnm2*^{R465W} fibres are 9 and 26 ms, respectively. Because the disease phenotype is much more severe in the case of MTM1-deficiency, this quantitatively similar alteration probably has no critical role in the loss of muscle force. In *Mtm1*-KO fibres, this effect results, at least in part, from contribution of Ca^{2+}-activated RYR1 channels to voltage-activated Ca^{2+} release because of the presence of CaV1.1-free RYR1 channels (Kutchukian *et al.* 2016) and this process is also considered to contribute to enhanced spatial variability of Ca^{2+} release. The enhanced spatial variability of Ca^{2+} release also observed in the present study in KI-*Dnm2*^{R465W} fibres, together with the propensity for appearance of spontaneous Ca^{2+} sparks, is consistent with enhanced Ca^{2+}-induced Ca^{2+} release activity. This suggests that, despite no apparent acute disruption of the t-tubule network, some RYR1 channels have lost their control by CaV1.1 voltage sensors and can be Ca^{2+}-activated.

The similarity between certain features of altered Ca^{2+} signalling in *Mtm1*-KO fibres and in KI-*Dnm2*^{R465W} fibres prompts the need to highlight the molecular and functional links between MTM1 and DNM2: indeed, both proteins, in association with amphiphysin 2 (BIN1) are considered to be important for membrane tubulation (Royer *et al.* 2013) and a proper balance between the tubulation activity of BIN1 and the fission activity of dynamin 2 has been suggested to be critical for t-tubule maintenance; however, the details of how the three proteins, in association with phosphoinositide metabolism, ensure proper t-tubule homeostasis/maintenance are far from completely understood and the role of MTM1 in the framework is specifically unclear (Hohendahl *et al.* 2016). One other equivocal aspect of this issue is that BIN1 and MTM1 appear to concentrate in the triadic region (Rodriguez *et al.* 2014; Lee *et al.* 2002), which is consistent with a role in t-tubule membrane remodelling, whereas this is not the case for DNM2, which essentially localizes in the vicinity of the Z line (Durieux *et al.* 2010*a*). Thus, either there are different pools of DNM2 of distinct function, localization and concentration, or DNM2 has an indirect distant impact on t-tubule/triad organization, or DNM2 is able to translocate from the Z line region to the triadic area when needed.

By contrast to some of these somewhat uncertain molecular and cellular features, remarkably clear functional links exist between MTM1 and DNM2 at the pathological level: indeed, MTM1-deficiency is associated with overexpression of DNM2 whereas DNM2 down-expression rescues the deleterious consequences of MTM1-deficiency (Cowling *et al.* 2014). In addition, overexpression of DNM2 in normal muscle generates a myopathy phenotype (Cowling *et al.* 2011). Altogether, this is consistent with DNM2 disturbed/enhanced activity playing a role in the MTM1 pathology. Thus, some of the similarities in defective Ca^{2+} signalling between MTM1-deficient fibres and *Dnm2*^{R465W} KI fibres, including the altered time course of Ca^{2+} release, may be a result of enhanced DNM2 expression and enhanced DNM2 activity, respectively. Again, changes in the triadic

© 2017 The Authors. The Journal of Physiology © 2017 The Physiological Society

organization as a result of improperly balanced DNM2 activity may play an important role in these defects.

The Ca^{2+} sparks detected in the present study in the KI fibres occurred, on average, at a frequency one order of magnitude larger than that of the events detected in WT fibres. They also yielded a larger amplitude and spatial spread than in WT fibres. This may indicate that the underlying process does not simply correspond to enhanced activation of the mechanism that generates the erratic events in normal fibres but, instead, that a specific operating mode of the RYR1 channels was promoted in the disease condition. Saponin permeabilization is known to trigger the occurrence of Ca^{2+} sparks in mammalian muscle fibres because of disruption of the normal control of RYR1 by CaV1.1 (Csernoch, 2007). Absolute mean values for peak amplitude and FWHM in the *x* and *y* direction of events measured in the present study in KI fibres were similar to those of events measured with the indicator fluo-3 in saponin-permeabilized muscle fibres from control mice (1.07 *vs.* 1.13 F_0, 1.94 *vs.* 1.92 μm and 1.79 *vs.* 1.76 μm in KI and in permeabilized fibres, respectively, Rodriguez *et al.* 2014). This may be taken as an indication that a similar mechanism was involved, further promoting the possibility that, despite a normal t-tubule network, RYR1 channels in the KI fibres exhibit an enhanced disposition for being activated by Ca^{2+}. The frequency of Ca^{2+} sparks reported in the present study in intact KI fibres was one order of magnitude (~30 times) lower than that reported in permeabilized mouse fibres (Rodriguez *et al.* 2014). Because saponin permeabilization is certainly promoting extensive disruption of RYR1 channel activity control by t-tubule CaV1.1s, the present disease situation appears to be intermediate between the extreme (permeabilized fibres) and the normal (WT) situation. Finally, it is also worth noting that the present model corresponds to the second disease situation promoting spontaneous local Ca^{2+} release events in intact mammalian muscle fibres. Indeed, aberrant expression of the CaV1.1e splice variant, which correlates with muscle weakness in myotonic dystrophy, is also associated with presence of such events (Sultana *et al.* 2016). Accordingly, it is possible that the occurrence of Ca^{2+} sparks in intact mammalian muscle fibres is a feature of other muscle disease conditions and that the spark frequency correlates with the extent of loss of normal control of Ca^{2+} release by t-tubule voltage and thus with the potential severity of altered EC coupling function. In the present disease model, this Ca^{2+} spark activity may have contributed to the increased resting Ca^{2+} level reported by Durieux *et al.* (2010*a*). Conversely, however, there is a low possibility that it affects the SR calcium content. Based on morphological observations and size of sparks, an upper limit of ~4 μm^2 can be assumed for the area that contains one release site in an *x,y* image of a fibre. Because the area of the entire fibre is ~3000–4000 μm^2 in the image, there are close to 1000 release sites per image. If it is assumed that a spark fully depletes its local SR, the total depletion would be the number of sparks per image divided by the number of release sites in the image. Because the average number of sparks per image in DNM2 KI fibres is less than 10, the overall depletion in the SR would be less than 1%.

In conclusion, the results of the present study demonstrate that altered SR Ca^{2+} release probably contributes to the muscle weakness associated with the *Dnm2*^{R465W} CNM mutation. Detailed features of the defects are similar to those observed in MTM1-deficient muscle. However, overall preserved t-tubule architecture and a more limited extent of Ca^{2+} release depression probably make a major contribution to the milder severity of the DNM2 disease compared to MTM1-related CNM. Still, many problems remain unresolved, such as how phosphoinositide 3-kinase inhibition has a beneficial effect in MTM1-deficient muscle (Kutchukian *et al.* 2016) and whether it would also do so in models of DNM2-associated CNM. Overall, a detailed understanding of how DNM2 is involved in the regulation of Ca^{2+} homeostasis and EC coupling will require further studies, which will also probably need to take into account the role of other proteins, including N-WASP (Falcone *et al.* 2014) and SPEG (Agrawal *et al.* 2014).

References

Agrawal PB, Pierson CR, Joshi M, Liu X, Ravenscroft G, Moghadaszadeh B, Talabere T, Viola M, Swanson LC, Haliloğlu G, Talim B, Yau KS, Allcock RJ, Laing NG, Perrella MA & Beggs AH (2014). SPEG interacts with myotubularin, and its deficiency causes centronuclear myopathy with dilated cardiomyopathy. *Am J Hum Genet* **95**, 218–226.

Al-Qusairi L, Weiss N, Toussaint A, Berbey C, Messaddeq N, Kretz C, Sanoudou D, Beggs AH, Allard B, Mandel JL, Laporte J, Jacquemond V & Buj-Bello A (2009). T-tubule disorganization and defective excitation-contraction coupling in muscle fibers lacking myotubularin lipid phosphatase. *Proc Natl Acad Sci USA* **106**, 18763–18768.

Bitoun M, Maugenre S, Jeannet PY, Lacène E, Ferrer X, Laforêt P, Martin JJ, Laporte J, Lochmüller H, Beggs AH, Fardeau M, Eymard B, Romero NB & Guicheney P (2005). Mutations in dynamin 2 cause dominant centronuclear myopathy. *Nat Genet* **37**, 1207–1209.

Bitoun M, Bevilacqua JA, Prudhon B, Maugenre S, Taratuto AL, Monges S, Lubieniecki F, Cances C, Uro-Coste E, Mayer M, Fardeau M, Romero NB & Guicheney P (2007). Dynamin 2 mutations cause sporadic centronuclear myopathy with neonatal onset. *Ann Neurol* **62**, 666–670.

Böhm J, Biancalana V, Dechene ET, Bitoun M, Pierson CR, Schaefer E, Karasoy H, Dempsey MA, Klein F, Dondaine N, Kretz C, Haumesser N, Poirson C, Toussaint A, Greenleaf RS, Barger MA, Mahoney LJ, Kang PB, Zanoteli E, Vissing J, Witting N, Echaniz-Laguna A, Wallgren-Pettersson C, Dowling J, Merlini L, Oldfors A, Bomme Ousager L, Melki J, Krause A, Jern C, Oliveira AS, Petit F, Jacquette A,

© 2017 The Authors. The Journal of Physiology © 2017 The Physiological Society

szentesi_peter_292_24

Chaussenot A, Mowat D, Leheup B, Cristofano M, Poza Aldea JJ, Michel F, Furby A, Llona JE, Van Coster R, Bertini E, Urtizberea JA, Drouin-Garraud V, Béroud C, Prudhon B, Bedford M, Mathews K, Erby LA, Smith SA, Roggenbuck J, Crowe CA, Brennan Spitale A, Johal SC, Amato AA, Demmer LA, Jonas J, Darras BT, Bird TD, Laurino M, Welt SI, Trotter C, Guicheney P, Das S, Mandel JL, Beggs AH & Laporte J (2012). Mutation spectrum in the large GTPase dynamin 2, and genotype-phenotype correlation in autosomal dominant centronuclear myopathy. *Hum Mutat* **33**, 949–959.

Buj-Bello A, Laugel V, Messaddeq N, Zahreddine H, Laporte J, Pellissier JF & Mandel JL (2002). The lipid phosphatase myotubularin is essential for skeletal muscle maintenance but not for myogenesis in mice. *Proc Natl Acad Sci USA* **99**, 15060–15065.

Cao H, Garcia F & McNiven MA (1998). Differential distribution of dynamin isoforms in mammalian cells. *Mol Biol Cell* **9**, 2595–2609.

Chin YH, Lee A, Kan HW, Laiman J, Chuang MC, Hsieh ST & Liu YW (2015). Dynamin-2 mutations associated with centronuclear myopathy are hypermorphic and lead to T-tubule fragmentation. *Hum Mol Genet* **24**, 5542–5554.

Cowling BS, Chevremont T, Prokic I, Kretz C, Ferry A, Coirault C, Koutsopoulos O, Laugel V, Romero NB & Laporte J (2014). Reducing dynamin 2 expression rescues X-linked centronuclear myopathy. *J Clin Invest* **124**, 1350–1363.

Cowling BS, Toussaint A, Amoasii L, Koebel P, Ferry A, Davignon L, Nishino I, Mandel JL & Laporte J (2011). Increased expression of wild-type or a centronuclear myopathy mutant of dynamin 2 in skeletal muscle of adult mice leads to structural defects and muscle weakness. *Am J Pathol* **178**, 2224–2235.

Cowling BS, Toussaint A, Muller J & Laporte J (2012). Defective membrane remodeling in neuromuscular diseases: insights from animal models. *PLoS Genet* **8**, e1002595.

Csernoch L (2007). Sparks and embers of skeletal muscle: the exciting events of contractile activation. *Pflügers Archiv* **454**, 869–878.

Csernoch L, Pouvreau S, Ronjat M & Jacquemond V (2008). Voltage-activated elementary calcium release events in isolated mouse skeletal muscle fibers. *J Membr Biol* **226**, 43–55.

Di Biase V, Tuluc P, Campiglio M, Obermair GJ, Heine M & Flucher BE (2011). Surface traffic of dendritic CaV1.2 calcium channels in hippocampal neurons. *J Neurosci* **31**, 13682–13694.

Dulhunty AF, Wei-LaPierre L, Casarotto MG & Beard NA (2017). Core skeletal muscle ryanodine receptor calcium release complex. *Clin Exp Pharmacol Physiol* **44**, 3–12.

Durieux AC, Prudhon B, Guicheney P & Bitoun M (2010*b*). Dynamin 2 and human diseases. *J Mol Med* **88**, 339–350.

Durieux AC, Vassilopoulos S, Lainé J, Fraysse B, Briñas L, Prudhon B, Castells J, Freyssenet D, Bonne G, Guicheney P & Bitoun M (2012). A centronuclear myopathy–dynamin 2 mutation impairs autophagy in mice. *Traffic* **13**, 869–879.

Durieux AC, Vignaud A, Prudhon B, Viou MT, Beuvin M, Vassilopoulos S, Fraysse B, Ferry A, Lainé J, Romero NB, Guicheney P & Bitoun M (2010*a*). A centronuclear myopathy-dynamin 2 mutation impairs skeletal muscle structure and function in mice. *Hum Mol Genet* **19**, 4820–4836.

Falcone S, Roman W, Hnia K, Gache V, Didier N, Lainé J, Auradé F, Marty I, Nishino I, Charlet-Berguerand N, Romero NB, Marazzi G, Sassoon D, Laporte J & Gomes ER (2014). N-WASP is required for amphiphysin-2/BIN1-dependent nuclear positioning and triad organization in skeletal muscle and is involved in the pathophysiology of centronuclear myopathy. *EMBO Mol Med* **6**, 1455–1475.

Fraysse B, Guicheney P & Bitoun M (2016). Calcium homeostasis alterations in a mouse model of the dynamin 2-related centronuclear myopathy. *Biol Open* **5**, 1691–1696.

Grundy D (2015). Principles and standards for reporting animal experiments in *The Journal of Physiology and Experimental Physiology*. *J Physiol* **593**, 2547–2549.

Hohendahl A, Roux A & Galli V (2016). Structural insights into the centronuclear myopathy-associated functions of BIN1 and dynamin 2. *J Struct Biol* **196**, 37–47.

Hong T, Yang H, Zhang SS, Cho HC, Kalashnikova M, Sun B, Zhang H, Bhargava A, Grabe M, Olgin J, Gorelik J, Marbán E, Jan LY & Shaw RM (2014). Cardiac BIN1 folds T-tubule membrane, controlling ion flux and limiting arrhythmia. *Nat Med* **20**, 624–632.

Jacquemond V (1997). Indo-1 fluorescence signals elicited by membrane depolarization in enzymatically isolated mouse skeletal muscle fibers. *Biophys J* **73**, 920–928.

Jeub M, Bitoun M, Guicheney P, Kappes-Horn K, Strach K, Druschky KF, Weis J & Fischer D (2008). Dynamin 2-related centronuclear myopathy: clinical, histological and genetic aspects of further patients and review of the literature. *Clin Neuropathol* **27**, 430–438.

Jungbluth H & Gautel M (2014). Pathogenic mechanisms in centronuclear myopathies. *Front Aging Neurosci* **6**, 339.

Kutchukian C, Lo Scrudato M, Tourneur Y, Poulard K, Vignaud A, Berthier C, Allard B, Lawlor MW, Buj-Bello A & Jacquemond V (2016). Phosphatidylinositol 3-kinase inhibition restores Ca^{2+} release defects and prolongs survival in myotubularin-deficient mice. *Proc Natl Acad Sci USA* **113**, 14432–14437.

Laporte J, Hu LJ, Kretz C, Mandel JL, Kioschis P, Coy JF, Klauck SM, Poustka A & Dahl N (1996). A gene mutated in X-linked myotubular myopathy defines a new putative tyrosine phosphatase family conserved in yeast. *Nat Genet* **13**, 175–182.

Lee E, Marcucci M, Daniell L, Pypaert M, Weisz OA, Ochoa GC, Farsad K, Wenk MR & De Camilli P (2002). Amphiphysin 2 (Bin1) and T-tubule biogenesis in muscle. *Science* **297**, 1193–1196.

Lefebvre R, Legrand C, González-Rodríguez E, Groom L, Dirksen RT & Jacquemond V (2011). Defects in Ca^{2+} release associated with local expression of pathological ryanodine receptors in mouse muscle fibres. *J Physiol* **589**, 5361–5382.

© 2017 The Authors. The Journal of Physiology © 2017 The Physiological Society

Lefebvre R, Pouvreau S, Collet C, Allard B & Jacquemond V (2014). Whole-cell voltage clamp on skeletal muscle fibers with the silicone-clamp technique. *Methods Mol Biol* **1183**, 159–170.

Nicot AS, Toussaint A, Tosch V, Kretz C, Wallgren-Pettersson C, Iwarsson E, Kingston H, Garnier JM, Biancalana V, Oldfors A, Mandel JL & Laporte J (2007). Mutations in amphiphysin 2 (BIN1) disrupt interaction with dynamin 2 and cause autosomal recessive centronuclear myopathy. *Nat Genet* **39**, 1134–1139.

Pouvreau S, Csernoch L, Allard B, Sabatier JM, De Waard M, Ronjat M & Jacquemond V (2006). Transient loss of voltage control of Ca^{2+} release in the presence of maurocalcine in skeletal muscle. *Biophys J* **91**, 2206–2215.

Ríos E, Pizarro G & Stefani E (1992). Charge movement and the nature of signal transduction in skeletal muscle excitation-contraction coupling. *Annu Rev Physiol* **54**, 109–133.

Rodríguez EG, Lefebvre R, Bodnár D, Legrand C, Szentesi P, Vincze J, Poulard K, Bertrand-Michel J, Csernoch L, Buj-Bello A & Jacquemond V (2014). Phosphoinositide substrates of myotubularin affect voltage-activated Ca^{2+} release in skeletal muscle. *Pflügers Archiv* **466**, 973–985.

Royer B, Hnia K, Gavriilidis C, Tronchère H, Tosch V & Laporte J (2013). The myotubularin-amphiphysin 2 complex in membrane tubulation and centronuclear myopathies. *EMBO Rep* **14**, 907–915.

Shirokova N, García J & Ríos E (1998). Local calcium release in mammalian skeletal muscle. *J Physiol* **512**, 377–384.

Schneider MF (1994). Control of calcium release in functioning skeletal muscle fibers. *Annu Rev Physiol* **56**, 463–484.

Sultana N, Dienes B, Benedetti A, Tuluc P, Szentesi P, Sztretye M, Rainer J, Hess MW, Schwarzer C, Obermair GJ, Csernoch L & Flucher BE (2016). Restricting calcium currents is required for correct fiber type specification in skeletal muscle. *Development* **143**, 1547–1559.

Szabó LZ, Vincze J, Csernoch L & Szentesi P (2010). Improved spark and ember detection using stationary wavelet transforms. *J Theor Biol* **264**, 1279–1292.

Tjondrokoesoemo A, Park KH, Ferrante C, Komazaki S, Lesniak S, Brotto M, Ko JK, Zhou J, Weisleder N & Ma J (2011). Disrupted membrane structure and intracellular Ca^{2+} signaling in adult skeletal muscle with acute knockdown of Bin1. *PLoS ONE* **6**, e25740.

Yang T, Xu X, Kernan T, Wu V & Colecraft HM (2010). Rem, a member of the RGK GTPases, inhibits recombinant CaV1.2 channels using multiple mechanisms that require distinct conformations of the GTPase. *J Physiol* **588**, 1665–1681.

Zhou J, Yi J, Royer L, Launikonis BS, González A, García J & Ríos E (2006). A probable role of dihydropyridine receptors in repression of Ca^{2+} sparks demonstrated in cultured mammalian muscle. *Am J Physiol Cell Physiol* **290**, C539–C553.

Additional information

Competing interests

The authors declare that they have no competing financial interests.

Author contributions

Single muscle fibre experiments were performed at Institut NeuroMyoGène, University Claude Bernard, Lyon 1. Fibre typing and immunoblot measurements were performed at the Research Centre for Myology, UPMC Univ Paris 06. Marc B and PG designed and generated the KI-*Dnm2*^{R465W} mouse model. Marc B and VJ designed the study. CK and VJ performed the electrophysiological and confocal imaging experiments. Marc B, Maud B and DT performed the MyHC and immunoblot experiments and conducted the analysis. CK, PS, BA, DT, Maud B, CB, YT, LC, Marc B and VJ contributed to the analysis and interpretation of data, as well as to the critical revisions of the manuscript. PS and LC specifically performed the calcium spark analysis. All authors approved the final version of the manuscript, agree to be accountable for all aspects of the work in ensuring that questions related to the accuracy or integrity of any part of the work are appropriately investigated and resolved. All persons designated as authors qualify for authorship, and all those who qualify for authorship are listed.

Funding

This work was supported by grants from CNRS, INSERM, the Université Claude Bernard – Lyon 1 and the Association Française contre les Myopathies (AFM-Téléthon: Alliance Myo-NeurALP program) to the Institut NeuroMyoGène, as well as by the Hungarian National Research, Development and Innovation Office (NKFIH NK-115461 to LC) and the Agence Nationale de la Recherche (grant ANR-14-CE12-0009 to MB), and also by a grant from the Société Française de Myologie (SFM) (to CK).

Acknowledgements

We thank the Pitié-Salpêtrière Imaging Platform (PICPS) for providing light microscopy imaging facilities.

© 2017 The Authors. The Journal of Physiology © 2017 The Physiological Society

szentesi.peter_292_24

Cell Calcium 80 (2019) 91–100

Contents lists available at ScienceDirect

Cell Calcium

journal homepage: www.elsevier.com/locate/ceca

Ca^{2+}-induced sarcoplasmic reticulum Ca^{2+} release in myotubularin-deficient muscle fibers

Candice Kutchukian[a], Peter Szentesi[b], Bruno Allard[a], Ana Buj-Bello[c], Laszlo Csernoch[b,**], Vincent Jacquemond[a,*]

[a] Univ Lyon, Université Claude Bernard Lyon 1, CNRS UMR-5310, INSERM U-1217, Institut NeuroMyoGène, 8 avenue Rockefeller, 69373, Lyon, France
[b] Department of Physiology, Faculty of Medicine, University of Debrecen, Debrecen, Hungary
[c] INSERM U951, Evry, University of Evry, UMR_S951, France

ARTICLE INFO

Keywords:
Skeletal muscle
Ryanodine receptor
Sarcoplasmic reticulum Ca^{2+} release
Myotubular myopathy

ABSTRACT

Skeletal muscle deficiency in the 3-phosphoinositide (PtdIns*P*) phosphatase myotubularin (MTM1) causes myotubular myopathy which is associated with severe depression of voltage-activated sarcoplasmic reticulum Ca^{2+} release through ryanodine receptors. In the present study we aimed at further understanding how Ca^{2+} release is altered in MTM1-deficient muscle fibers, at rest and during activation. While in wild-type muscle fibers, SR Ca^{2+} release exhibits fast stereotyped kinetics of activation and decay throughout the voltage range of activation, Ca^{2+} release in MTM1-deficient muscle fibers exhibits slow and unconventional kinetics at intermediate voltages, suggestive of partial loss of the normal control of ryanodine receptor Ca^{2+} channel activity. In addition, the diseased muscle fibers at rest exhibit spontaneous elementary Ca^{2+} release events at a frequency 30 times greater than that of control fibers. Eighty percent of the events have spatiotemporal properties of archetypal Ca^{2+} sparks while the rest take either the form of lower amplitude, longer duration Ca^{2+} release events or of a combination thereof. The events occur at preferred locations in the fibers, indicating spatially uneven distribution of the parameters determining spontaneous ryanodine receptor 1 opening. Spatially large Ca^{2+} release sources were obviously involved in some of these events, suggesting that opening of ryanodine receptors in one cluster can activate opening of ryanodine receptors in a neighboring one. Overall results demonstrate that opening of Ca^{2+}-activated ryanodine receptors is promoted both at rest and during excitation-contraction coupling in MTM1-deficient muscle fibers. Because access to this activation mode is denied to ryanodine receptors in healthy skeletal muscle, this may play an important role in the associated disease situation.

1. Introduction

In differentiated skeletal muscle fibers, contraction is triggered by the increase in cytosolic Ca^{2+} concentration resulting from sarcoplasmic reticulum (SR) Ca^{2+} release. For this, the voltage sensing $Ca_V1.1$ subunit of the dihydropyridine receptor in the transverse (t-) invaginations of the plasma membrane interacts with the type 1 ryanodine receptor (RYR1) Ca^{2+} release channel in the proximate membrane of the junctional SR. This interaction constitutes the switch of excitation-contraction (EC) coupling, allowing turning on and off RYR1 channel activity and consequent SR Ca^{2+} release, in response to t-tubule membrane depolarization and repolarization, respectively [1,2]. RYR channels are also Ca^{2+}-activated channels capable of operating under the Ca^{2+}-induced Ca^{2+} release (CICR) mode, but in healthy differentiated mammalian muscle, the tight control of RYR1 channel activity by $Ca_V1.1$ voltage-sensors is believed to repress Ca^{2+}-mediated activation of the channels [see 3,4].

EC coupling is defective in myotubular myopathy, a disease due to mutations in the gene encoding the PtdIns*P* phosphatase myotubularin (MTM1) [5]. This was established using the MTM1-deficient mouse model which reproduces the main features of human myotubular myopathy [6]: in the absence of MTM1, muscle fibers suffer from

Abbreviations: $Ca_V1.1$, α1 subunit of the dihydropyridine receptor; CNM, centronuclear myopathy; FDB, *flexor digitorum brevis*; EC, excitation-contraction; KO, knock-out; MTM1, myotubularin; RYR1, type 1 ryanodine receptor; SR, sarcoplasmic reticulum; WT, wild-type

* Corresponding author at: Institut NeuroMyoGène, UMR CNRS 5310 - INSERM U1217 - Université Claude Bernard Lyon 1, Faculté de Médecine et de Pharmacie, 8, Avenue Rockefeller, 69373, Lyon, France.
** Corresponding author.
E-mail address: vincent.jacquemond@univ-lyon1.fr (V. Jacquemond).

https://doi.org/10.1016/j.ceca.2019.04.004
Received 15 February 2019; Received in revised form 27 March 2019; Accepted 8 April 2019
Available online 10 April 2019
0143-4160/ © 2019 Elsevier Ltd. All rights reserved.

szentesi.peter_292_24

decreased number of triads (the region where one t-tubule faces two terminal cisternae of junctional SR), disrupted t-tubule network and decreased amounts of $Ca_V1.1$ and RYR1 [7]. At the functional level, voltage-activated SR Ca^{2+} release exhibits reduced peak amplitude, delayed activation kinetics and subcellular non-uniformity [7,8]. Another hallmark of the disease is that loss of MTM1 enzymatic activity is likely playing a critical role in the pathological defects: indeed, MTM1 dephosphorylates PtdIns(3,5)P_2 and PtdIns(3)P at the D3 position of the inositol ring [9,10] and in the disease mouse model both Ca^{2+} release defects in muscle fibers and survival of the animals are improved by PtdIns$P$ 3-kinase inhibition [8,11]. Thus, accumulation of MTM1 substrates may play a key role in the altered SR Ca^{2+} release and associated muscle weakness.

In the present work, we aimed at further characterizing the pathophysiological features of the SR Ca^{2+} release process of MTM1-deficent muscle fibers at rest and during EC coupling. Our results demonstrate that the Ca^{2+}-gated activation mode of RYR channels is promoted under both conditions.

2. Methods

2.1. Preparation of the muscle fibers

All experiments and procedures were in accordance with the guidelines of the local animal ethics committee of the University Claude Bernard - Lyon 1, the French Ministry of Agriculture (decree 87/848) and the revised European Directive 2010/63/EU.

We used 4-5-week old wild type (WT) and *Mtm1*-KO male mice in the 129PAS background [6]. Single fibers were isolated from the *flexor digitorum brevis* (FDB) and interosseus muscles following previously described procedures [12]. In brief, mice were anaesthetized with isoflurane and killed by cervical dislocation. Muscles were removed and incubated for 60 min at 37 °C in the presence of external Tyrode containing 2 $mg.mL^{-1}$ collagenase (Sigma, type 1). Single fibers were obtained by triturating the collagenase-treated muscles within the experimental chamber consisting of a 50-mm-wide culture μ-dish (Ibidi GmbH, Martinsried, Germany). Measurements of Ca^{2+} sparks were carried out on muscle fibers isolated from FDB muscles from 5 WT and 5 *Mtm1*-KO mice. All experiments were performed at room temperature (20–22 °C).

2.2. Electrophysiology

We used the silicone voltage-clamp technique [12,13]. For this, single fibers were partly insulated with silicone grease so that only a short portion (50–100 μm long) of the fiber extremity remained out of the silicone. Voltage-clamp was achieved with a micropipette filled with a solution mimicking the ionic composition of the cytosolic compartment and also containing the fluorescent Ca^{2+}-sensitive dye rhod-2 and a high concentration of EGTA (see Solutions). The tip of the micropipette was inserted through the silicone, within the insulated part of the fiber. The tip was gently crushed against the bottom of the chamber in order to ease intracellular equilibration and decrease series resistance. The chlorided silver wire inside the pipette was connected to an RK-400 patch-clamp amplifier (Bio-Logic, Claix, France) used in whole-cell voltage-clamp configuration, in combination with an analog-digital converter (Digidata 1440 A, Axon Instruments, Foster City, CA) controlled by pClamp 9 software (Axon Instruments). Analog compensation was adjusted to further decrease the effective series resistance. Intracellular equilibration of the solution was allowed for a period of 30 min before initiating measurements. Membrane depolarizing steps of 0.5 s duration were applied from a holding command potential of -80 mV.

2.3. Confocal imaging

Confocal imaging was conducted with a Zeiss LSM 5 Exciter microscope equipped with a 63× oil immersion objective (numerical aperture 1.4). For measurements of voltage-activated Ca^{2+} transients in the presence of high intracellular EGTA we used the dye rhod-2: excitation was from the 543 nm line of a HeNe laser and fluorescence was collected above 560 nm. Rhod-2 Ca^{2+} transients were imaged using the line-scan mode (x,t) of the system with the line parallel to the longitudinal axis of the fibers. Images were taken with a scanning frequency of 1.15 ms per line. Rhod-2 fluorescence changes were expressed as F/F_0 where F_0 is the baseline fluorescence.

For Ca^{2+} sparks measurements, isolated muscle fibers were incubated for 30 min in the presence of Tyrode solution containing 10 μM fluo-4 AM. Fluo-4 fluorescence was detected above 505 nm upon excitation with the 488 nm line of an Argon laser. Fluo-4 fluorescence imaging was performed with either the x,y or the x,t scanning mode of the microscope.

2.4. Ca^{2+} release calculation

The SR Ca^{2+} release flux activated by membrane depolarization was estimated from the time derivative of the total myoplasmic Ca^{2+} ($[Ca_{Tot}]$) calculated from the occupancy of intracellular calcium binding sites according to a previously described procedure [14,15]. For this, changes in $[Ca^{2+}]$ were calculated from the rhod-2 signals assuming a basal $[Ca^{2+}]$ of 0.1 μM and a Kd of rhod-2 for Ca^{2+} of 1.2 μM. The model included troponin C (TN) binding sites, parvalbumin binding sites and calcium transport across the SR membrane with the same parameters as used in [15]. Ca^{2+}-binding sites on EGTA make the major contribution with a total sites concentration of 6 mM, an "on" rate constant $k_{on,\ EGTA}$ of 0.056 $\mu M^{-1}.ms^{-1}$ and an "off" rate constant $k_{off,\ EGTA}$ of 0.002 ms^{-1}.

2.5. Ca^{2+} sparks analysis

Analysis was carried out according to previously described procedures [16,17]. In brief, the region of the fiber and the background was defined on the first image of each x,y image series. The averaged background fluorescence was subtracted from each pixel of all images in one series. The calcium release events were detected by the stationary wavelet method. The filtering was made by soft thresholding wavelet detection. Finally the amplitude and full width at half maximum (FWHM) of the sparks was calculated. Two FWHM values were calculated: perpendicular and parallel with the Z-lines. In order to detect the Z-lines, the frequency spectrum in each line of all images was calculated using fast Fourier transform. Finally inverse FFT of the frequency components corresponding to sarcomeres were used to remove the Z-lines from the images. The analysis of line-scan images was performed with an automatic event detection program [17], which calculated the amplitude (F/F_0), full width at half maximum (FWHM), duration and full time at half maximum (FTHM) of the identified events. Signal mass (SM) was calculated from the amplitudes and FWHM obtained by fitting the spatial profile of the events at every time point [18]. In order to describe the spatial profile of the events, the kurtosis (as defined in statistical mathematics and introduced for calcium sparks by Zhou et al. [19]) was used. Accordingly, a calcium release event was defined as "protoplatykurtic" if it had a flat top right from the first scan detection. The speed of spatial spread of activation was calculated from sequentially activating clusters of RYRs using the angle of the wavefront of propagation of the Ca^{2+} signal, as described earlier [20].

2.6. Solutions

Tyrode solution contained (in mM): 140 NaCl, 5 KCl, 2.5 $CaCl_2$, 2

szentesi.peter_292_24

$MgCl_2$, 10 Hepes. The extracellular solution used for voltage-clamp contained (in mM) 140 TEA-methanesulfonate, 2.5 $CaCl_2$, 2 $MgCl_2$, 1 4-aminopyridine, 10 HEPES and 0.002 tetrodotoxin. The pipette solution contained (in mM) 120 K-glutamate, 5 Na_2-ATP, 5 Na_2-phosphocreatine, 5.5 $MgCl_2$, 12 EGTA, 4.8 $CaCl_2$, 0.1 rhod-2, 5 glucose, 5 HEPES. Fluo-4 AM was dissolved and stored in DMSO. All solutions were adjusted to pH 7.20.

2.7. Statistics

Statistical analysis was performed with Origin 8.0 and GraphPad Prism 6. Unless otherwise specified, data values are presented as means ± S.E.M. for n fibers. For datasets passing the D'Agostino & Pearson omnibus normality test, statistical significance was determined using a Student's *t*-test (*$p \leq 0.05$, **$p \leq 0.01$, ***$p \leq 0.001$). Otherwise Mann Whitney test was applied to assess statistical significance.

3. Results

3.1. Kinetic alterations of voltage-activated SR Ca^{2+} release in MTM1-deficient muscle fibers

Fig. 1 shows a collection of representative line-scan F/F_0 rhod-2 Ca^{2+} transients (top images) and of the corresponding calculated Ca^{2+} release fluxes (bottom images) triggered by voltage-clamp depolarization from -80 mV to -20, -10 and + 10 mV, in 3 WT muscle fibers (A–C) and 3 MTM1-deficient muscle fibers (D–F). Experiments were performed in the presence of 12 mM EGTA to prevent contraction and to simplify Ca^{2+} release calculation. In each fiber, the 3 images were taken at the same Z level with the line positioned parallel at three nearby locations along the transverse axis. For the Ca^{2+} release flux calculation, images were compressed by averaging 10 consecutive rows along the line. The trace below each pair of F/F_0 and corresponding Ca^{2+} release flux images shows the time-course of Ca^{2+} release flux averaged over the entire scanned line.

Ca^{2+} release in WT fibers exhibits stereotyped kinetics, homogeneous along the line, characterized by an early peak, the amplitude of which increases with the pulse, followed by a decay that becomes faster as the peak amplitude gets larger. In MTM1-deficient muscle fibers, we previously reported that voltage-activated Ca^{2+} release exhibits slow onset, reduced peak amplitude and reduced spatial synchrony [8]. Data in Fig. 1 (D–E) illustrates the fact that Ca^{2+} release in the diseased fibers also exhibits specifically marked kinetic alterations at voltage levels near -10 mV. In the example shown in Fig. 1D, Ca^{2+} release triggered by the pulse to -20 mV is heterogeneous along the line, with the top region yielding almost no change at the onset of the pulse as compared to the bottom region of the line. Later during that same pulse, a secondary phase of Ca^{2+} release appears to propagate from the bottom towards the top region of the line, so that within the line region pointed by the red arrow, peak Ca^{2+} release occurs after the end of the pulse (superimposed red Ca^{2+} release trace at the bottom). In the same fiber, upon depolarization to -10 mV (Fig. 1D, middle panel), a delayed release of Ca^{2+} occurs within the same line region, but earlier in time, during the pulse. For the largest pulse, some discrepancy persisted in terms of time to peak Ca^{2+} release between the top and bottom of the line, but to a much more reduced extent.

Severe spatial non-uniformity of Ca^{2+} release as illustrated in Fig. 1D, was not prerequisite to observe the occurrence of a delayed phase of Ca^{2+} release at intermediate activation voltages. This is illustrated in Fig. 1 E–F which shows that, despite reasonable uniformity along the line at the onset of the pulse, Ca^{2+} release was specifically prolonged and tended to exhibit a secondary delayed peak during the pulse to -10 mV. In contrast, during the pulses to -20 and + 10 mV global Ca^{2+} release kinetics, although slower, were qualitatively similar to those in WT fibers.

Fig. 2A shows the mean (± S.D., grey shading) Ca^{2+} release flux in WT and MTM1-deficient muscle fibers triggered by 500-ms long depolarizing pulses from -80 mV to values ranging between -20 and + 20 mV. Mean traces were calculated from line-averaged rhod-2 *x,t* images collected from 20 and 13 fibers, issued from 5 and 5 WT and *Mtm1*-KO mice, respectively. Each of the traces in the two conditions is shown with the *y* scale bar adjusted for best-viewing the time-course of the release flux at each voltage. *y* scale bars of identical length correspond to 3 times lower amplitude in the disease (KO) as compared to the WT condition. The early sharp peak of SR Ca^{2+} release at the onset of the pulse is lost in the MTM1-deficient muscle fibers and the overall time during which Ca^{2+} release remains elevated during the pulses is prolonged. This prolongation was not related to the lower peak amplitude of Ca^{2+} release, as illustrated in Fig. 2B which shows the superimposed mean Ca^{2+} release traces in response to a pulse to -20 mV in WT fibers and in response to a pulse to 0 mV in the MTM1-deficient

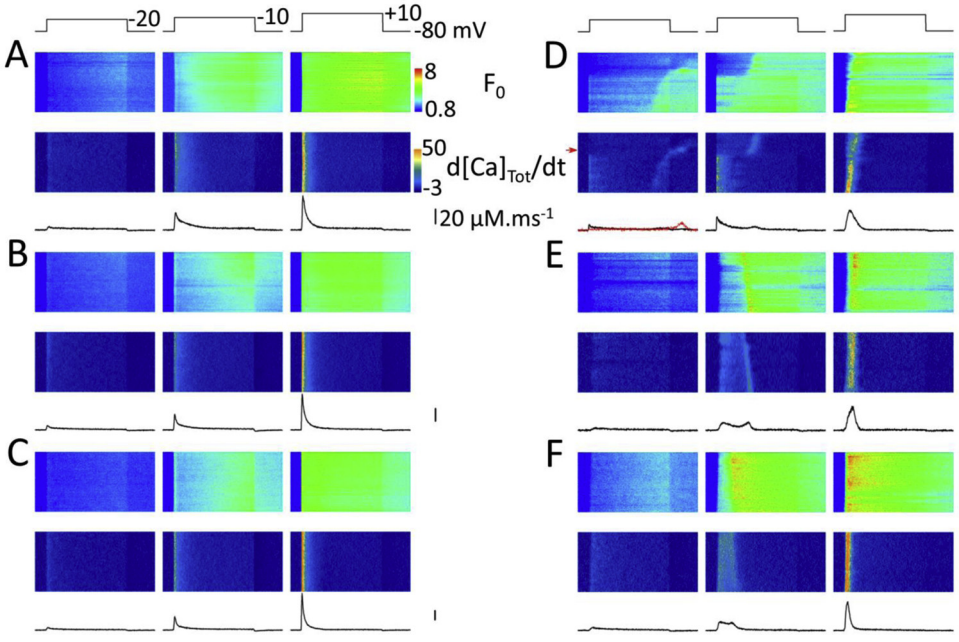


Fig. 1. *x,t* confocal imaging of voltage-activated SR Ca^{2+} release in WT and MTM1-deficient muscle fibers. *A-F*, line-scan image of rhod-2 fluorescence (top image) and of corresponding calculated Ca^{2+} release flux (bottom image) from 3 WT fibers (*A-C*) and 3 MTM1-deficient fibers (*D-F*) stimulated by the voltage clamp pulse shown on top. The trace below each pair of F/F_0 and Ca^{2+} release flux images in a given fiber stimulated by a given pulse corresponds to the average time-course of Ca^{2+} release calculated from the whole image. In *D*, the superimposed red trace shows the time course of Ca^{2+} release at the particular location of the scanned line marked by a red arrow in the corresponding Ca^{2+} release flux image.

szentesi.peter_292_24

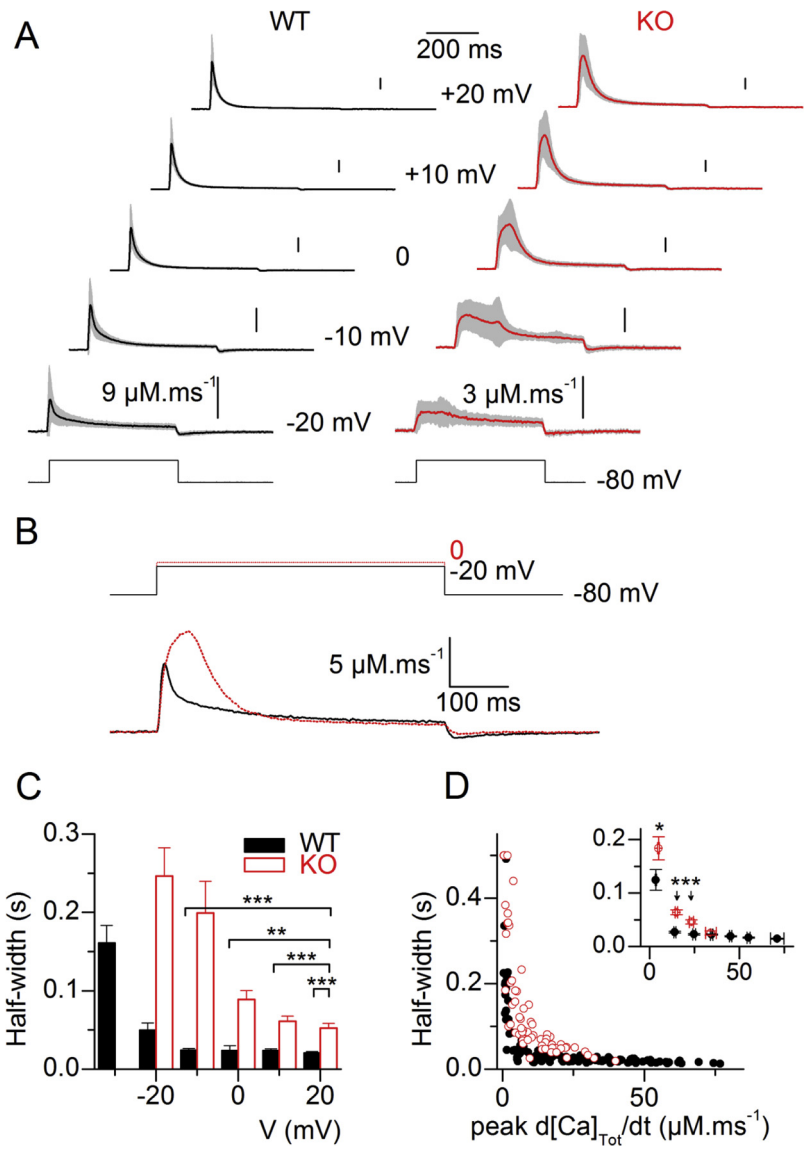


Fig. 2. Altered kinetic features of voltage-activated SR Ca^{2+} release in MTM1-deficient muscle fibers. *A*, mean ± S.D. (grey shading) time course of Ca^{2+} release flux in WT fibers (left, n = 20) and MTM1-deficient fibers (right, n = 13) in response to 500-ms long depolarizing pulses from -80 mV to the indicated values. *y* scale bars all correspond to 9 μM. ms^{-1} and 3 μM. ms^{-1} in the WT and MTM1-deficiency conditions, respectively. *B*, superimposed mean Ca^{2+} release flux evoked by a pulse to -20 mV in WT fibers (continuous trace) and in response to a pulse to 0 mV in MTM1-deficient fibers (dotted trace). *C*, dependence upon voltage of the mean ± S.E.M. half-width of peak Ca^{2+} release in WT fibers (closed bars) and in MTM1-deficient fibers (open bars). *D*, dependence of the half-width of Ca^{2+} release upon its peak amplitude in WT fibers (closed symbols) and MTM1-deficient fibers (open symbols). The inset in Fig. 2D presents mean values for half-width plotted *versus* corresponding mean values for peak amplitude. For this, pairs of peak amplitude/half-width values were sorted according to the peak amplitude. Values for half-width falling within a same range of peak amplitude, following a 10 μM. ms^{-1} increment, were then averaged and plotted versus the corresponding values for mean amplitude.

fibers. Despite a larger peak amplitude in the disease condition, the time-course of Ca^{2+} release was clearly prolonged as compared to that in the WT condition.

The extent of peak Ca^{2+} release duration was estimated by measuring the half-width of the peak in the two groups of fibers. Mean values are reported *versus* membrane voltage in Fig. 2C. The mean value for MTM1-deficient fibers at -30 mV is not presented because Ca^{2+} release was too small and never exhibited an identifiable peak at this voltage so that the half-width would simply correspond to the pulse duration. Nevertheless, values for half-width were significantly larger in MTM1-deficient fibers as compared to WT fibers at all voltages, the difference being the largest at -20 and -10 mV. In fact, the mean half-width in MTM1-deficient fibers in response to a pulse to + 20 mV was significantly larger than that in WT fibers in response to pulses ranging between -10 and + 20 mV. This representation does not take into account the fact that the peak amplitude of Ca^{2+} release is smaller in MTM1-deficient fibers than in WT fibers at all voltages [8]. Fig. 2D presents how the half-width of peak Ca^{2+} release depends on its amplitude for all records. In both groups of fibers the half-width decreases as the peak amplitude of Ca^{2+} release gets larger, with values reaching a minimum level near ~20 ms for the largest values of peak amplitude. However, for peak values between 10 and 30 μM.ms^{-1}, corresponding values for half-width were, on average, close to or more than 2 times larger in MTM1-deficient fibers than in WT ones. This is best viewed in the inset of Fig. 2D where half-width values were binned and averaged according to their corresponding peak Ca^{2+} release amplitude, with an increment of 10 μM. ms^{-1}. For the lowest range of peak amplitudes (0–10 μM. ms^{-1}), half-width values from traces that did not exhibit an identifiable peak were excluded. These results demonstrate that despite slowing the onset and reducing the amplitude of the early peak level of RYR1-mediated Ca^{2+} release, MTM1 deficiency promotes RYR1channels activity over a more prolonged period of time following membrane depolarization at intermediate levels of activation.

3.2. Spontaneous local Ca^{2+} release events at rest in Mtm1-KO muscle fibers

Prolongation of voltage-activated Ca^{2+} release together with recurrent presence of an associated delayed rising phase during the depolarizing pulse (Fig. 1E) and/or of propagating events (Fig. 1D) suggest that RYR1 channels gating in the diseased fibers tends to get deprived from normal control by the t-tubule $Ca_V1.1$ voltage-sensors, a condition under which they may become activated by Ca^{2+} (see [4]). A now classical functional correlate of $Ca_V1.1$-free RYR1 channels in muscle is the presence of spatially localized Ca^{2+} release events taking the form of Ca^{2+} sparks [3,4]. We thus looked for such events in intact

szentesi.peter_292_24

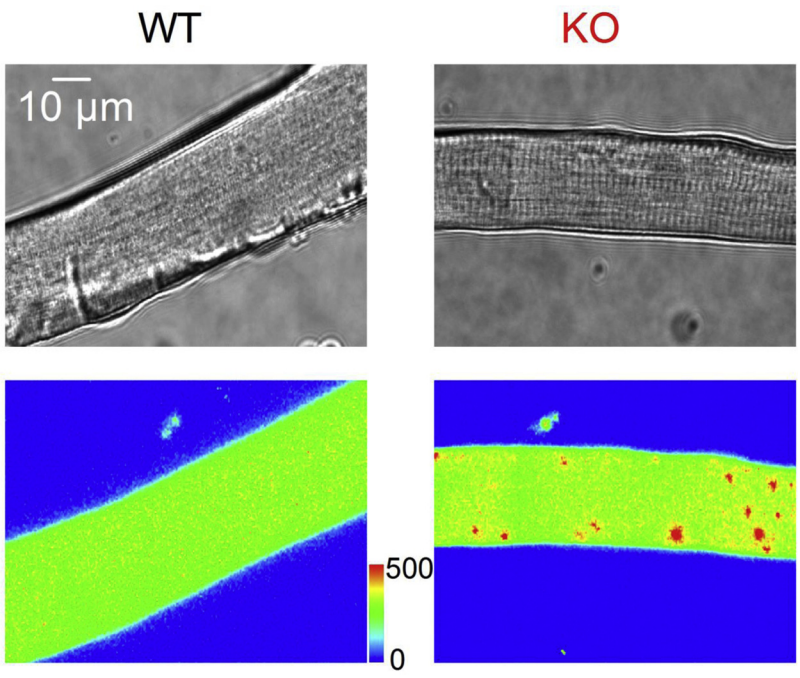


Fig. 3. Ca^{2+} sparks in intact muscle fibers from *Mtm1-KO* mice. *x,y* images of the standard deviation of fluo-4 fluorescence intensity (bottom images) at each pixel position during a sequence of 20 successive frames taken from a WT fiber (left) and from an MTM1-deficient fiber (right). Corresponding transmitted light images of the two fibers are shown above. Note that the original images were resolved on 12 bit (0–4095).

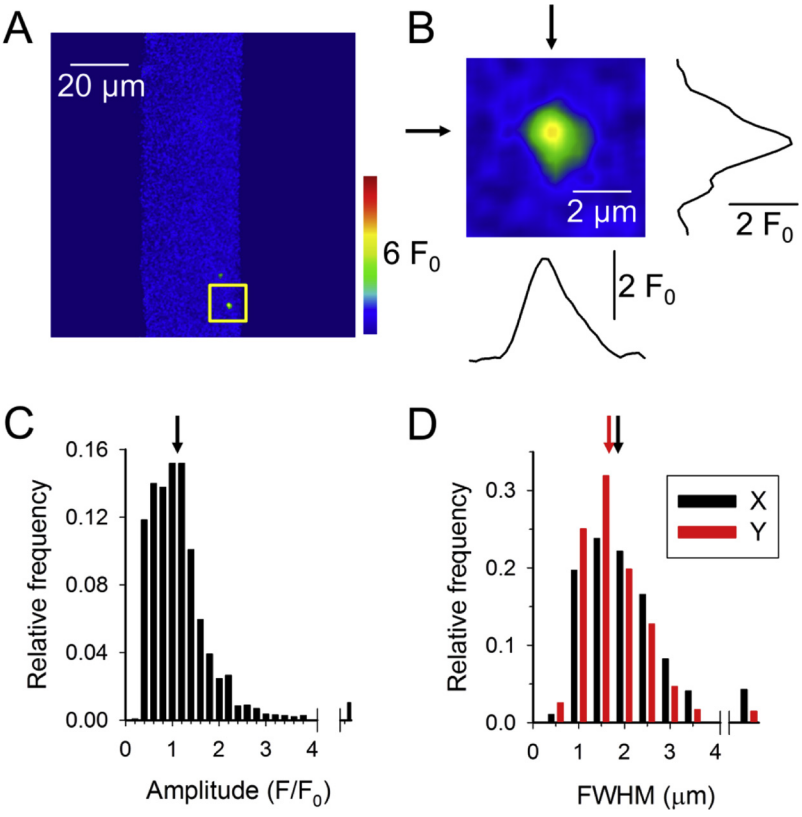


Fig. 4. Spatial features of Ca^{2+} sparks detected with *x,y* confocal imaging in muscle fibers from *Mtm1-KO* mice. *A*, *x,y* image of fluo-4 fluorescence from an intact isolated muscle fiber showing a local increase in Ca^{2+} visualized as the relative increase in fluorescence (F/F_0) after removing the structure elements and correcting for baseline fluorescence (F_0). *B*, enlarged view of the individual spark marked in panel *A*, together with spatial profiles of its amplitude calculated parallel (trace on the right) and perpendicular (trace below) to the main fiber axis at positions indicated by the arrows. Colour bar applies to both *A* and *B*. *C*, histogram of events amplitude. *D*, histograms of FWHM for profiles parallel (X) and perpendicular (Y) to the fiber axis. Arrows in *C* and *D* point to the corresponding mean values from the few events detected in WT fibers.

WT and MTM1-deficient muscle fibers using the dye fluo-4 in the absence of any exogenous Ca^{2+} buffer. The left and right bottom panels in Fig. 3 show the standard deviation of fluo-4 fluorescence intensity over a series of 20 consecutive confocal frames at a given location of a WT and of an MTM1-deficient muscle fiber, respectively. For this, the mean and standard deviation of intensity at each pixel location were calculated. While the WT fiber was basically silent, fluorescence from the MTM1-deficient fiber exhibited local areas of large standard deviation, corresponding to presence of Ca^{2+} release events. Fig. 4 depicts the spatial properties of the events detected in MTM1-deficient fibers using *x,y* confocal laser scanning. Fig. 4A shows one typical Ca^{2+} release event visualized as F/F_0 within an MTM1-deficient fiber, while an enlarged view of this same event is shown in Fig. 4B, together with its spatial profiles at the positions indicated by the arrows. This event exhibited a peak amplitude of ~$3F_0$ and expanded along both the longitudinal and transversal axis of the fiber with a half-width of approximately 2 µm. Fig. 4C shows the frequency histogram of amplitude of the sparks detected in MTM1-deficient fibers while Fig. 4D shows the

szentesi.peter_292_24

Table 1
Mean values for the spark parameters detected in *x,y* images.

	WT (n = 34 events from 43 fibers)	*Mtm1*-KO (n = 1008 events from 51 fibers)
Peak amplitude (F/F_0)	1.01 ± 0.06	1.04 ± 0.02
FWHM-X (μm)	1.71 ± 0.08	2.15 ± 0.02 ***
FWHM-Y (μm)	1.67 ± 0.07	1.78 ± 0.02
Frequency (Hz. mm^{-2})	11.9 ± 5.0	336.7 ± 53.4 ***

histograms of full width at half-maximum (FWHM) for profiles parallel (X) and perpendicular (Y) to the fiber axis. Data are from 2485 events detected from 51 fibers from 5 *Mtm1*-KO mice, respectively. In comparison, 34 events were detected from 45 fibers from 5 WT mice, respectively, the mean amplitude and FWMH of which are indicated with arrows in the histograms of Fig. 4C-D. Table 1 reports mean values for peak amplitude, FWMH and frequency for events detected in WT and MTM1-deficient muscle fibers. For this, only events exhibiting peak amplitude comprised between 0.2 and 10 F/F_0, and FWHM comprised between 0.4 and 10 μm, were selected (34 events from 43 WT fibers and 1008 events from 51 MTM1-deficient fibers). MTM1-deficient fibers yielded events at a frequency more than 20 times that in WT fibers. Mean values for peak amplitude and FWHM along the transverse axis did not differ between the two groups, whereas the FWHM along the longitudinal axis was significantly larger, by ~25%, in the diseased fibers.

The amplitude and spatial features of these Ca^{2+} release events are similar to those of the events that can be detected in saponin-permeabilized muscle fibers, a condition that disrupts the $Ca_V1.1$-RYR1 interaction (e.g. [21]). In contrast to the WT situation, Ca^{2+} release events in intact MTM1-deficient fibers were frequent enough to be easily captured under line-scan imaging configuration. This is illustrated in Fig. 5 which shows typical examples of the spatio-temporal features of the events present in the diseased fibers. They were either lone short events exhibiting features of archetypical Ca^{2+} sparks (Fig. 5A) or series of such Ca^{2+} sparks or long-lasting events of lower amplitude and long duration commonly referred to as Ca^{2+} embers (Fig. 5B, see [3]). Amplitude and FWMH histograms for the lone Ca^{2+} sparks are shown in Fig. 5C and 5D, respectively. Data are from 842 events collected from 38 muscle fibers isolated from 3 mice, respectively. Corresponding mean values for amplitude, rise-time, FWHM, FTHM and duration were 1.18 ± 0.02 F/F_0, 9.4 ± 0.2 ms, 1.71 ± 0.03 μm, 12.7 ± 0.2 ms and 28.6 ± 0.4 ms, respectively.

Fig. 5E shows the distribution of events frequency in individual line-scan images. The superimposed line presents the theoretical Poisson-distribution (λ = 3.99) based on the assumption that the events occur independently of one another, while the inset shows an enlarged part of the graph to emphasize the presence of unexpectedly large number of events on certain images. These results indicate that Ca^{2+} release events did not appear randomly but were more frequent in particular locations of the diseased muscle fibers, suggesting that they did not simply result from uniformly altered RYR1 channel gating.

In Fig.6, we calculated the time-course of calcium release from the SR during lone Ca^{2+} sparks (right panels) and during a repeated series of such events (left panels). The time course of the amount of calcium released was derived as that of the Signal Mass (SM, Fig. 6C and G), calculated from the amplitudes and FWHM obtained by fitting the spatial profile of the events at every time point (for further details see Methods). Fig. 6D and H show the time derivative of SM (d(SM)/dt) representing the time course of SR calcium release flux. Note that in case of the large event presented in Fig. 6A, the hypothetical wrap curve over the individual peaks would follow the same time course as the global release does (see e.g. Fig. 2A), namely, after the rise to an early peak it declines to a maintained steady level. This finding is in line with the expectation that calcium-dependent inactivation of RYR1, if calcium release is maintained, occurs at the local level.

Strikingly, MTM1-deficient fibers were able to generate massive Ca^{2+} release events exhibiting unconventionally large amplitude and spatial width. These represented approximately 5% of the total number of detected events (55 events from 18 fibers from 3 mice, Fig. 5D). One example is shown in Fig. 7A where the event displays peak amplitude larger than 4 F_0 and expands spatially over ~4 μm. Note that the spatial profile of the event is flat just 1.145 ms (i.e. one scanning line) after its onset. The presence of such protoplatycurtic events can only be explained if vast arrays of release channels are activated simultaneously. The distribution of FWHM of such events, selected on the basis of FWHM larger than 3.5 μm is presented in Fig. 7B, showing that approximately 20% of these events yielded a FWHM larger than 5 μm. These included events of giant space-width, as illustrated in Fig. 7C, during which new fiber regions get recruited as time goes. As the spatial profile of the triggered events is also protoplatycurtic (as demonstrated by the F(x) profiles of individual line-scans – 1, 3, …, 11 – into the event) these observations provide further evidence for Ca^{2+} release events triggering the instantaneous activation of large clusters of RYR1 channels. Furthermore they provide the possibility to estimate the speed of spreading of activation presumably via CICR. For the events presented in Fig. 7C this was calculated to be 170 μm/s. In 6 similar events the average speed was found to be 228 ± 47 μm/s. Thus, in this framework, the activation of calcium release channels within junctional clusters would involve intermolecular interactions and therefore appear as instantaneous in our line-scan images, while propagation between neighboring clusters would use CICR.

3.3. *Ca^{2+} sparks do not make a critical contribution to voltage-activated SR Ca^{2+} release in MTM1-deficient muscle fibers*

As compared to the above measurements of resting Ca^{2+} release activity performed with the dye fluo-4 in the absence of exogenous Ca^{2+} buffer, our analysis of voltage-activated SR Ca^{2+} release (Figs. 1 and 2) was conducted with the somewhat lower affinity dye rhod-2 in the presence of a large concentration of intracellular EGTA. As these conditions may either prevent or compromise triggering or detection of Ca^{2+} sparks, we took measurements of voltage-activated fluo-4 transients under non buffering conditions, in order to determine whether Ca^{2+} sparks would be mandatory contributors of voltage-activated SR Ca^{2+} release in the diseased fibers. For this, line-scan images of fluo-4 fluorescence were taken from 3 MTM1-deficient muscle fibers voltage-clamp-depolarized to levels that activated Ca^{2+} release without triggering contraction. As illustrated in Fig. 8, results provided no indication that Ca^{2+} sparks would be systematically associated with voltage-activated Ca^{2+} release in the diseased fibers, as it is the case in frog muscle fibers [22,23].

4. Discussion

The present results show that MTM1-deficient fibers exhibit local spontaneous Ca^{2+} release events at rest and prolonged activity of RYR1 channels during the early phase of voltage-triggered SR Ca^{2+} release. Ca^{2+} release events are very similar to those observed under conditions promoting disruption of $Ca_V1.1$-RYR1 interaction [e.g. 21] and consequent liberty for RYR1s to be gated by Ca^{2+} and to be responsible for Ca^{2+}-induced SR Ca^{2+} release. Accordingly, previous indication that Ca^{2+}-induced Ca^{2+} release also operates during SR Ca^{2+} release activated by t-tubule depolarization [8] is the very likely the reason for the conspicuous alteration of the release flux kinetics.

There is evidence so far that CICR contributes to physiological Ca^{2+} release in muscles containing a substantial fraction of type 3 isoform of ryanodine receptor (RYR3). As compared to RYR1 channels which occupy the junctional SR membrane and directly face $Ca_V1.1$ voltage sensors in the t-tubule membrane, RYR3 channels are believed to reside in a parajunctional position [24], making them unlikely to be activated through a mechanism other than Ca^{2+} gating. The presence of CICR in

szentesi.peter_292_24

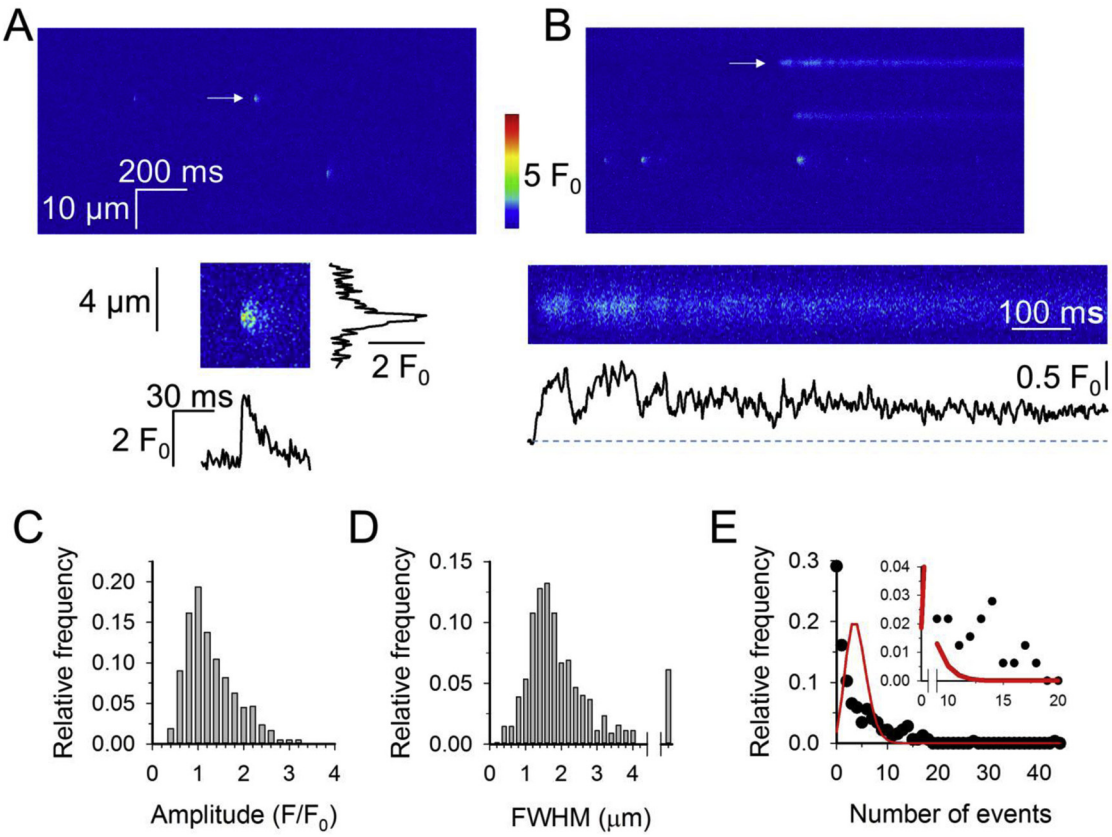


Fig. 5. Spatio-temporal features of Ca^{2+} sparks detected using *x,t* confocal imaging in muscle fibers from *Mtm1-KO* mice. *A-B*, normalized line-scan images (F/F_0) of fluo-4 fluorescence from intact MTM1-deficient fibers showing typical calcium release events that are either lone calcium sparks (*A*) or a series of such events or long embers (*B*). Images shown at the bottom show an enlarged portion of the arrow-pointed regions, displaying the individual events at increased temporal and spatial resolution together with their time course and spatial distribution. *C*, histogram of events amplitude. *D*, histograms of FWHM. *E*, distribution of the event frequencies in individual images. Continuous line presents the theoretical Poisson-distribution ($\lambda = 3.99$) based on the assumption that the events occur independently of one another. Inset shows an enlarged portion of the graph emphasizing the presence of unexpectedly large number of events in certain images.

RYR3-containing muscle was proposed on the basis of specific differences in the kinetic properties of voltage-triggered SR Ca^{2+} release in frog as compared to rat muscle [25], and on kinetic changes observed when frog fibers were challenged by experimental conditions expected to affect CICR, including the presence of various types of Ca^{2+} buffers (see [25–28]). CICR in RYR3-containing muscle was confirmed by the discovery of spontaneous Ca^{2+} sparks at rest [23,29] and by contribution of these events to SR Ca^{2+} release during EC coupling [22,23] (see for review [3,4]).

In contrast, differentiated mammalian muscle contains a negligible proportion of RYR3, and, in coherence, several lines of results tend to exclude contribution of CICR to physiological EC coupling in this tissue

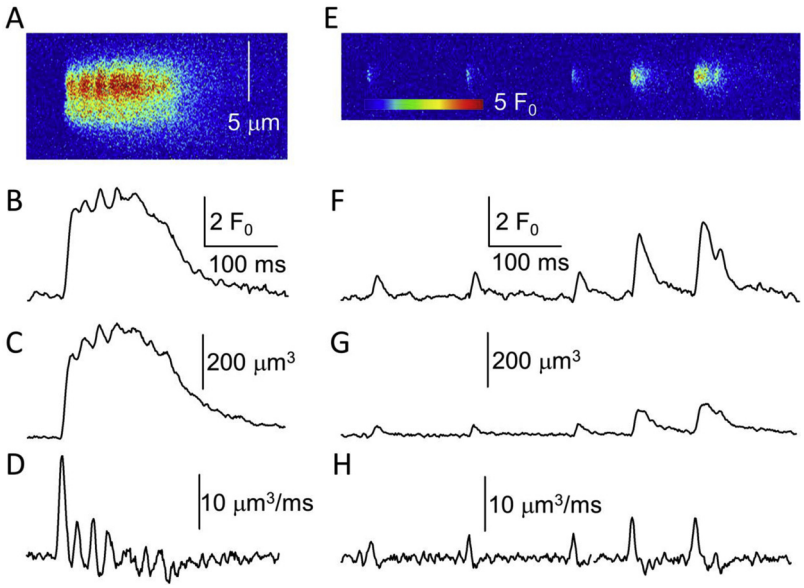


Fig. 6. Rate of SR Ca^{2+} release underlying Ca^{2+} sparks in muscle fibers from *Mtm1-KO* mice. *A*, *E* line-scan images of different types of Ca^{2+} release events corresponding to large (*A*) and small (*E*) repetitive calcium sparks. *B*, *F* corresponding temporal profile of F/F_0. *C, G* corresponding time course of the Signal Mass (SM), calculated from the values for amplitude and FWHM obtained by fitting the spatial profile of the events in *A* and *E* at every time point (for further details see Methods). *D, H* time derivative of SM (d(SM)/dt) representing the time course of calcium release flux from the SR.

szentesi.peter_292_24

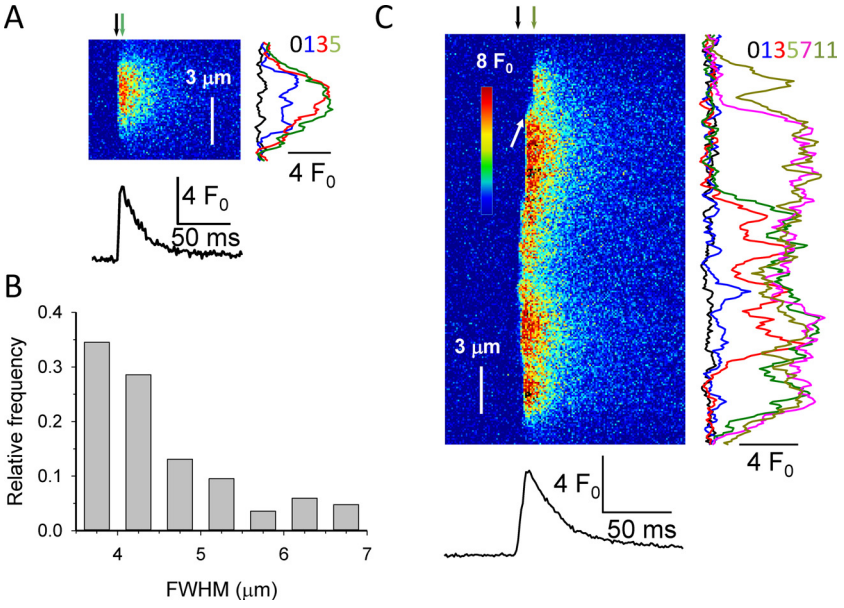


Fig. 7. Vast arrays of RYR1 channels can contribute to spontaneous Ca^{2+} release at rest in MTM1-deficient muscle fibers. *A*, individual protoplatycurtic Ca^{2+} spark with extremely large FWHM. Spatial and temporal profiles are presented next to and below the image, respectively. The several spatial profiles of fluorescence (from left to right) correspond to the one profiles right before the event and then during the 1 st, 3rd, and 5th scan into the event (denoted as 0, 1, 3, and 5, respectively; corresponding to time points 0, 1.15, 3.45, and 5.75 ms, respectively). *B*, distribution of FWHM for Ca^{2+} release events with FWHM greater than 3.5 µm (n = 55). *C*, Ca^{2+} release events trigger additional events in neighboring clusters of ryanodine receptors. The spatial profiles show the fluorescence right before and during the 1 st, 3rd, 5th, 7th, and 11th scan into the event (denoted as 0, 1, 3, 5, 7, and 11, respectively; corresponding to time points 0, 1.15, 3.45, 5.75, 8.05, and 12.65 ms, respectively). Additional positions with an increase in Ca^{2+} appear as time progresses. Arrows in panels A and C above the images show the position of the first (black) and last (grey) scanlines the spatial profiles of which are displayed (in black and grey, respectively) next to the images. White arrow in panel C depicts the position where the speed of spreading of activation was calculated (170 µm/s for the event presented here).

[25,30] including absence of Ca^{2+} sparks at rest and during activation. Still, spontaneous Ca^{2+} sparks are triggered in mammalian muscle under conditions believed to disrupt the $Ca_V1.1$-RYR1 interaction, including osmotic changes and t-tubule membrane permeabilization [31,32]. This indicates that RYR1 channels in differentiated muscle fibers can also be gated open by Ca^{2+} when they are free of the $Ca_V1.1$ control. This could explain the presence of Ca^{2+} sparks at rest in MTM1-deficient muscle fibers. Indeed, in line with our analysis showing that spatial distribution of these events is not random (Fig. 5E) one simple explanation could be that their occurrence spatially correlates with previously described local regions of t-tubule disruption [7,8] and that occasionally observed massive Ca^{2+} release events (Fig. 7) would correspond to RYR1 channels operating within fiber regions yielding extensive loss of t-tubule network. However, there may be as well other parameters either determining or contributing to occurrence of Ca^{2+} sparks in this model. As an example, records in Fig. 8 show that spontaneous Ca^{2+} release can occur at rest within a fiber region where voltage-activated Ca^{2+} release is working and thus where t-tubule structure was preserved. There thus has to be alternative possible explanations for the occurrence of spontaneous Ca^{2+} release events in MTM1-deficient fibers. We previously showed that MTM1 substrates loaded into normal muscle fibers depress voltage-activated Ca^{2+} release and depress the frequency of Ca^{2+} sparks triggered by permeabilization [21]. Along this line, it could be speculated that MTM1 substrates accumulation is spatially heterogeneous in MTM1-deficient fibers so that areas devoid of Ca^{2+} sparks would actually correspond to regions where substrates have accumulated the most and prevent RYR1 channel opening.

In this same context it is also worth emphasizing that muscle fibers from another mouse model of centronuclear myopathy, due to a mutation in the *Dnm2* gene, also exhibit spontaneous Ca^{2+} sparks at rest [33]. However, one major difference between the two models is that *Dnm2* disease fibers exhibit no stringent alterations of the t-tubule network [33] as was observed in MTM1-deficient muscle fibers. Still, considering the close links between MTM1 and DNM2 (see for instance [34]), it is tempting to assume that muscle fibers from the two corresponding disease mouse models share a common mechanism contributing to spontaneous activity of RYR1 channels under the form of Ca^{2+} sparks, independent from t-tubule alterations. In this framework, the fact that sparks frequency in MTM1-deficient fibers is only approximately twice that in *Dnm2* disease fibers further supports the postulate that, despite no apparent disruption of the t-tubule network,

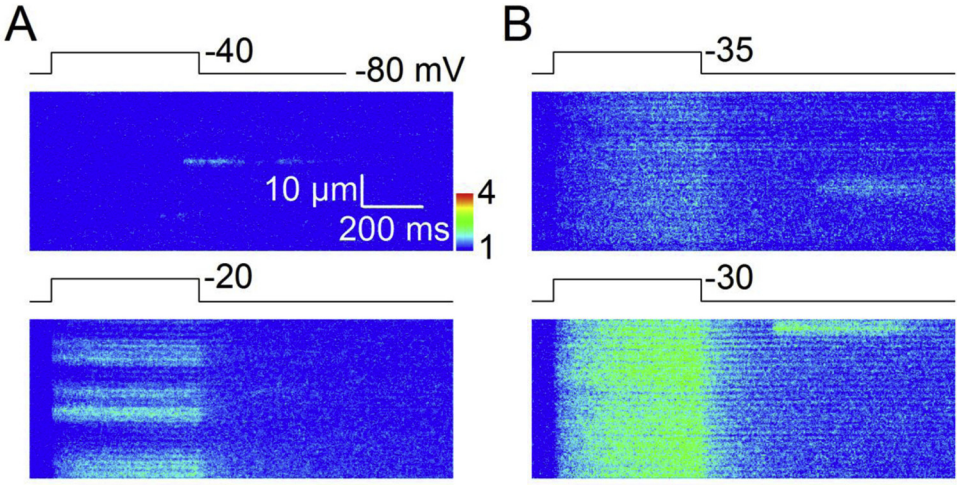


Fig. 8. Ca^{2+} sparks do not underlie voltage-activated SR Ca^{2+} release in MTM1-deficient fibers. Line-scan image of fluo-4 fluorescence from two distinct MTM1-deficient fibers (*A*, *B*) recorded while a voltage-clamp depolarizing pulse from -80 mV to the indicated value was applied.

szentesi.peter_292_24

$Ca_V1.1$ control of RYR1 channels is substantially loosened in that particular disease condition too [33].

At last, it is worth stressing that the situation in MTM1-deficient fibers remains very much distinct from that of RYR3-containing intact muscle fibers. Indeed, although we cannot exclude that extensive series of measurements in MTM1-deficient fibers could have revealed the occasional presence of Ca^{2+} sparks during a depolarizing pulse, these events are not mandatory contributors of voltage-activated SR Ca^{2+} release (Fig. 8) as they are for instance in frog muscle fibers [22,23].

We previously reported that, when measuring Ca^{2+} release under high-EGTA buffering conditions, MTM1-deficient muscle fibers tend to exhibit a delayed phase of Ca^{2+} release onset during depolarizing pulses at intermediate voltages [8], consistent with opening of RYR1 channels triggered when a threshold Ca^{2+} level is reached. Our present analysis now shows that, in these conditions, the early peak phase of SR Ca^{2+} release lasts longer in MTM1-deficient fibers than in WT fibers, at all levels of membrane voltage activation. This occurs even under conditions when Ca^{2+} release is well synchronized all along the scanned line (e.g. Fig. 1F), a situation that excludes severely altered t-tubule network at specific locations of the line. Such difference does not exist between the time-course of voltage-triggered SR Ca^{2+} release in frog and mammals [25], which further supports the dissimilarity between properties of Ca^{2+} release exhibiting CICR contribution in RYR3-containing healthy muscle and Ca^{2+} release alterations in the present disease situation. The increased half-duration of peak Ca^{2+} release in MTM1-deficient fibers reveals that RYR1 channels (or some RYR1 channels) remain open for a prolonged period of time during an activating voltage pulse. An intuitive explanation would be that enhanced propensity for generation of a Ca^{2+}-activated component of Ca^{2+}release at late times during a depolarizing pulse is responsible for this. However, a simple simulation assuming a late component of Ca^{2+} release with properties described previously (peak rate of 3 $\mu M.\ ms^{-1}$, [8]) occurring at random times during a pulse, failed to reproduce the prolonged time-course of Ca^{2+} release observed in MTM1-deficient fibers (not illustrated). One possibility then is that a particular combination of $Ca_V1.1$ controlled RYR1 channels, of $Ca_V1.1$-free RYR1 channels capable of CICR and of non-functional or lost RYR1 channels is necessary to generate the kinetic features of Ca^{2+} release observed here. Future efforts, including mathematical modelling of such combinations may prove able to reproduce the entire kinetic alterations of Ca^{2+} release in MTM1-deficient muscle fibers and to also provide further insights into our understanding of this disease situation with impact for our understanding of normal Ca^{2+} release function.

As for the question of how MTM1 is compulsory for proper function of $Ca_V1.1$-RYR1 coupling, it still remains ambiguous and as discussed earlier, may involve mechanisms implicated both in proper maintenance of t-tubule membrane and triad organization and also directly in RYR1 channel function [8,21,33,34]. In the present context, both may play a role in the promotion of Ca^{2+}-induced Ca^{2+} release because, on the one hand, of loss or loosened control of RYR1 by $Ca_V1.1$ due to triad membrane architecture defects and, on the other hand, of perturbed RYR1 function due to altered availability of MTM1 phosphoinositide substrates and/or products having a regulatory role on the channel activity.

Finally, it is interesting to speculate about the physiological relevance of CICR under MTM1-defciency as well as in analogous disease conditions. Indeed, one may simply picture CICR contribution to Ca^{2+} homeostasis as a collateral consequence of RYR1 channels uncoupling from the t-tubule voltage control, with no specific biological relevance to muscle function. However, one may also consider that the capacity of RYR1 to be gated by Ca^{2+} under conditions when it loses its normal control, grants the muscle fibers with an alternative compensatory mechanism to help sustain EC coupling under such distress situations. Importantly, disruption of the t-tubule network in MTM1-deficient fibers is clearly not accompanied by complete collapse of fiber structure and SR compartment because RYR1 channels are still active in this membrane, capable of generating cytosolic Ca^{2+} changes witnessing a maintained luminal SR content. Nevertheless, this is obviously not sufficient to maintain proper muscle function in myotubular myopathy because the eventual extensive disruption of the t-tubule network precludes any possibility for Ca^{2+} to be raised at sufficient high level to activate contraction throughout the entire cross-section of the fibers. Nevertheless, we propose that Ca^{2+}-gated RYR1 channels contribution to Ca^{2+} release may help sustain muscle function in analogous milder pathological situations. Conversely however, it is undeniable that widespread occurrence of Ca^{2+}-induced Ca^{2+} release will generate uncoordinated Ca^{2+} signals that will be of little help for muscle fiber contractile function. In that case they may instead cause a host of undesired secondary problems adding up to the disease phenotype.

5. Conclusions

Deficient SR Ca^{2+} release is a key determinant of muscle weakness in myotubular myopathy. SR Ca^{2+} release in this disease situation is not only depressed in amplitude but the underlying molecular mechanism substantially differs from the one in healthy muscle as MTM1-deficient fibers exhibit a contribution from Ca^{2+}-gated ryanodine receptors at rest and during EC coupling.

Contributors

All experiments were performed at Institut NeuroMyoGène, University Claude Bernard, Lyon 1. VJ designed the study. AB-B designed and generated the *Mtm1*-KO mouse model. CK and VJ performed the electrophysiological and confocal imaging experiments. PS and LC performed the Ca^{2+} sparks analysis. CK, PS, BA, AB-B, LC and VJ contributed to data interpretation and discussion and to critical revisions of the manuscript.

Declarations of interest

None.

Funding sources

This work was supported by grants from CNRS, INSERM and Université Claude Bernard - Lyon 1 to Institut NeuroMyoGène. This work was also supported by the Association Française contre les Myopathies (AFM-Téléthon: Alliance MyoNeurALP program; project 5.3.4.4 to V. Jacquemond), by grants to L. Csernoch from the Hungarian National Research, Development and Innovation Office (NKFIH K-115461) and from the GINOP-2.3.2-15-2016-00040 project, and by a grant to C. Kutchukian from the Société Française de Myologie (SFM). None of the funding sources had a role in study design, in the collection, analysis and interpretation of data, in the writing of the report. Decision to submit the article for publication was approved by the MyoNeurAlp program.

References

[1] E. Ríos, G. Pizarro, E. Stefani, Charge movement and the nature of signal transduction in skeletal muscle excitation-contraction coupling, Annu. Rev. Physiol. 54 (1992) 109–133.
[2] M.F. Schneider, Control of calcium release in functioning skeletal muscle fibers, Annu. Rev. Physiol. 56 (1994) 463–484.
[3] L. Csernoch, Sparks and embers of skeletal muscle: the exciting events of contractile activation, Pflugers Arch. 454 (2007) 869–878.
[4] E. Ríos, Calcium-induced release of calcium in muscle: 50 years of work and the emerging consensus, J. Gen. Physiol. 150 (2018) 521–537.
[5] J. Laporte, L.J. Hu, C. Kretz, J.L. Mandel, P. Kioschis, J.F. Coy, S.M. Klauck, A. Poustka, N. Dahl, A gene mutated in X-linked myotubular myopathy defines a new putative tyrosine phosphatase family conserved in yeast, Nat. Genet. 13 (1996) 175–182.
[6] A. Buj-Bello, V. Laugel, N. Messaddeq, H. Zahreddine, J. Laporte, J.F. Pellissier, J.L. Mandel, The lipid phosphatase myotubularin is essential for skeletal muscle

maintenance but not for myogenesis in mice, Proc. Natl. Acad. Sci. U. S. A. 99 (2002) 15060–15065.

[7] L. Al-Qusairi, N. Weiss, A. Toussaint, C. Berbey, N. Messaddeq, C. Kretz, D. Sanoudou, A.H. Beggs, B. Allard, J.L. Mandel, J. Laporte, V. Jacquemond, A. Buj-Bello, T-tubule disorganization and defective excitation-contraction coupling in muscle fibers lacking myotubularin lipid phosphatase, Proc. Natl. Acad. Sci. U. S. A. 106 (2009) 18763–18768.

[8] C. Kutchukian, M. Lo Scrudato, Y. Tourneur, K. Poulard, A. Vignaud, C. Berthier, B. Allard, M.W. Lawlor, A. Buj-Bello, V. Jacquemond, Phosphatidylinositol 3-kinase inhibition restores Ca^{2+} release defects and prolongs survival in myotubularin-deficient mice, Proc. Natl. Acad. Sci. U. S. A. 113 (2016) 14432–14437.

[9] G.S. Taylor, T. Maehama, J.E. Dixon, Myotubularin, a protein tyrosine phosphatase mutated in myotubular myopathy, dephosphorylates the lipid second messenger, phosphatidylinositol 3-phosphate, Proc. Natl. Acad. Sci. U. S. A. Proc. Natl. Acad. Sci. U. S. A. 97 (2009) 8910–8915.

[10] H. Tronchère, J. Laporte, C. Pendaries, C. Chaussade, L. Liaubet, L. Pirola, J.L. Mandel, B. Payrastre, Production of phosphatidylinositol 5-phosphate by the phosphoinositide 3-phosphatase myotubularin in mammalian cells, J. Biol. Chem. 279 (2004) 7304–7312.

[11] N. Sabha, J.R. Volpatti, H. Gonorazky, A. Reifler, A.E. Davidson, X. Li, N.M. Eltayeb, C. Dall'Armi, G. Di Paolo, S.V. Brooks, A. Buj-Bello, E.L. Feldman, J.J. Dowling, PIK3C2B inhibition improves function and prolongs survival in myotubular myopathy animal models, J. Clin. Invest. 126 (2016) 3613–3625.

[12] V. Jacquemond, Indo-1 fluorescence signals elicited by membrane depolarization in enzymatically isolated mouse skeletal muscle fibers, Biophys. J. 73 (1997) 920–928.

[13] R. Lefebvre, S. Pouvreau, C. Collet, B. Allard, V. Jacquemond, Whole-cell voltage clamp on skeletal muscle fibers with the silicone-clamp technique, Methods Mol. Biol. 1183 (2014) 159–170.

[14] S. Pouvreau, L. Csernoch, B. Allard, J.M. Sabatier, M. De Waard, M. Ronjat, V. Jacquemond, Transient loss of voltage control of Ca^{2+} release in the presence of maurocalcine in skeletal muscle, Biophys. J. 91 (2006) 2206–2215.

[15] R. Lefebvre, C. Legrand, E. González-Rodríguez, L. Groom, R.T. Dirksen, V. Jacquemond, Defects in Ca^{2+} release associated with local expression of pathological ryanodine receptors in mouse muscle fibres, J. Physiol. 589 (2011) 5361–5382.

[16] L. Csernoch, S. Pouvreau, M. Ronjat, V. Jacquemond, Voltage-activated elementary calcium release events in isolated mouse skeletal muscle fibers, J. Membr. Biol. 226 (2008) 43–55.

[17] L.Z. Szabó, J. Vincze, L. Csernoch, P. Szentesi, Improved spark and ember detection using stationary wavelet transforms, J. Theor. Biol. 264 (2010) 1279–1292.

[18] S. Hollingworth, J. Peet, W.K. Chandler, S.M. Baylor, Calcium sparks in intact skeletal muscle fibers of the frog, J. Gen. Physiol. 118 (2001) 653–678.

[19] J. Zhou, G. Brum, A. González, B.S. Launikonis, M.D. Stern, E. Ríos, Concerted vs. sequential. Two activation patterns of vast arrays of intracellular Ca^{2+} channels in muscle, J. Gen. Physiol. 126 (2005) 301–309.

[20] M. Sztretye, J. Almássy, T. Deli, P. Szentesi, C. Jung, B. Dienes, C.A. Simut, E. Niggli, I. Jona, L. Csernoch, Altered sarcoplasmic reticulum calcium transport in the presence of the heavy metal chelator TPEN, Cell Calcium 46 (2009) 347–355.

[21] E.G. Rodríguez, R. Lefebvre, D. Bodnár, C. Legrand, P. Szentesi, J. Vincze, K. Poulard, J. Bertrand-Michel, L. Csernoch, A. Buj-Bello, V. Jacquemond, Phosphoinositide substrates of myotubularin affect voltage-activated Ca^{2+} release in skeletal muscle, Pflugers Arch. 466 (2014) 973–985.

[22] A. Tsugorka, E. Ríos, L.A. Blatter, Imaging elementary events of calcium release in skeletal muscle cells, Science 269 (1995) 1723–1726.

[23] M.G. Klein, H. Cheng, L.F. Santana, Y.H. Jiang, W.J. Lederer, M.F. Schneider, Two mechanisms of quantized calcium release in skeletal muscle, Nature 379 (1996) 455–458.

[24] E. Felder, C. Franzini-Armstrong, Type 3 ryanodine receptors of skeletal muscle are segregated in a parajunctional position, Proc. Natl. Acad. Sci. U. S. A. 99 (2002) 1695–1700.

[25] N. Shirokova, J. García, G. Pizarro, E. Ríos, Ca^{2+} release from the sarcoplasmic reticulum compared in amphibian and mammalian skeletal muscle, J. Gen. Physiol. 107 (1996) 1–18.

[26] V. Jacquemond, L. Csernoch, M.G. Klein, M.F. Schneider, Voltage-gated and calcium-gated calcium release during depolarization of skeletal muscle fibers, Biophys. J. 60 (1991) 867–873.

[27] L. Csernoch, V. Jacquemond, M.F. Schneider, Microinjection of strong calcium buffers suppresses the peak of calcium release during depolarization in frog skeletal muscle fibers, J. Gen. Physiol. 101 (1993) 297–333.

[28] J.F. Olivera, G. Pizarro, A study of the mechanisms of excitation-contraction coupling in frog skeletal muscle based on measurements of $[Ca^{2+}]$ transients inside the sarcoplasmic reticulum, J. Muscle Res. Cell. Motil. 39 (2018) 41–60.

[29] S. Perni, K.C. Marsden, M. Escobar, S. Hollingworth, S.M. Baylor, C. Franzini-Armstrong, Structural and functional properties of ryanodine receptor type 3 in zebrafish tail muscle, J. Gen. Physiol. 145 (2015) 173–184.

[30] S. Hollingworth, S.M. Baylor, Comparison of myoplasmic calcium movements during excitation-contraction coupling in frog twitch and mouse fast-twitch muscle fibers, J. Gen. Physiol. 141 (2013) 567–583.

[31] W.G. Kirsch, D. Uttenweiler, R.H. Fink, Spark- and ember-like elementary Ca^{2+} release events in skinned fibres of adult mammalian skeletal muscle, J. Physiol. 537 (2001) 379–389.

[32] X. Wang, N. Weisleder, C. Collet, J. Zhou, Y. Chu, Y. Hirata, X. Zhao, Z. Pan, M. Brotto, H. Cheng, J. Ma, Uncontrolled calcium sparks act as a dystrophic signal for mammalian skeletal muscle, Nat. Cell Biol. 7 (2005) 525–530.

[33] C. Kutchukian, P. Szentesi, B. Allard, D. Trochet, M. Beuvin, C. Berthier, Y. Tourneur, P. Guicheney, L. Csernoch, M. Bitoun, V. Jacquemond, Impaired excitation-contraction coupling in muscle fibres from the dynamin2R465W mouse model of centronuclear myopathy, J. Physiol. 595 (2017) 7369–7382.

[34] L. Csernoch, V. Jacquemond, Phosphoinositides in Ca^{2+} signaling and excitation-contraction coupling in skeletal muscle: an old player and newcomers, J. Muscle Res. Cell. Motil. 36 (2015) 491–499.

Charged Surface Area of Maurocalcine Determines Its Interaction with the Skeletal Ryanodine Receptor

Balázs Lukács,* Mónika Sztretye,* János Almássy,* Sándor Sárközi,* Beatrix Dienes,* Kamel Mabrouk,§ Cecilia Simut,* László Szabó,*¶ Péter Szentesi,* Michel De Waard,†‡ Michel Ronjat,†‡ István Jóna,* and László Csernoch*

*Department of Physiology, Research Centre for Molecular Medicine, Medical and Health Science Centre, University of Debrecen, Debrecen, Hungary; †Institut National de la Santé et de la Recherche Médicale, U836, Grenoble, France; ‡Institut des Neurosciences, Université Joseph Fourier, Grenoble, France; §Universités D'Aix-Marseille 1, 2 et 3 Centre National de la Recherche Scientifique-Unite Mixte de Recherche 6517 "Chimie, Biologie et Radicaux Libres," Marseille, France; and ¶Department of Electrical Engineering, Sapientia Hungarian University of Transylvania, Targu Mures, Romania

ABSTRACT The 33 amino acid scorpion toxin maurocalcine (MCa) has been shown to modify the gating of the skeletal-type ryanodine receptor (RyR1). Here we explored the effects of MCa and its mutants ([Ala^{8}]MCa, [Ala^{19}]MCa, [Ala^{20}]MCa, [Ala^{22}]MCa, [Ala^{23}]MCa, and [Ala^{24}]MCa) on RyR1 incorporated into artificial lipid bilayers and on elementary calcium release events (ECRE) in rat and frog skeletal muscle fibers. The peptides induced long-lasting subconductance states (LLSS) on RyR1 that lasted for several seconds. However, their average length and frequency were decreased if the mutation was placed farther away in the 3D structure from the critical ^{24}Arg residue. The effect was strongly dependent on the direction of the current through the channel. If the direction was similar to that followed by calcium during release, the peptides were 8- to 10-fold less effective. In fibers long-lasting calcium release events were observed after the addition of the peptides. The average length of these events correlated well with the duration of LLSS. These data suggest that the effect of the peptide is governed by the large charged surface formed by residues Lys^{20}, Lys^{22}, Arg^{23}, Arg^{24}, and Lys^{8}. Our observations also indicate that the results from bilayer experiments mimic the in situ effects of MCa on RyR1.

INTRODUCTION

Excitation-contraction (EC) coupling in skeletal muscle fibers requires the functional interaction of two calcium channels, the dihydropyridine receptor (DHPR) and the ryanodine receptor (RyR1), residing in the transverse tubular membrane and the membrane of the terminal cisternae of the sarcoplasmic reticulum (SR), respectively. In amphibian skeletal muscle cells, Ca^{2+} release from SR has been proposed to result from the summation of calcium release events, termed sparks, corresponding to the opening of a discrete number of ryanodine receptors (1–3). In contrast, intact adult mammalian skeletal muscle fibers do not give rise to spontaneous Ca^{2+} release events (4). However, as was recently shown, a mild treatment of adult mammalian skeletal fibers with saponin provokes the appearance of Ca^{2+} release events with various morphology (5–7), long events with constant amplitude (called embers) (3), and sparks similar to those observed in frog skeletal muscle cells. It remains to be demonstrated, however, that these events are indeed the elementary building blocks of Ca^{2+} release in mammalian muscle, and that embers represent the opening of a single or a few but coupled (8) RyR1.

Three structurally related scorpion toxins—imperatoxin A (IpTxA), maurocalcine (MCa), and hemicalcin—have been shown to modify RyR1 Ca^{2+} channel properties in vitro (9–11). Two of them have already proved to be useful tools for studying EC coupling and elementary events of Ca^{2+} release. It was also demonstrated that MCa 1), induces Ca^{2+} release from SR vesicles; 2), strongly potentiates [^{3}H]ryanodine binding to SR vesicles; and 3), increases the open probability of the purified RyR1 (12,13). In cultured rat myotubes, MCa induces Ca^{2+} release via the ryanodine receptor but has no effect on the depolarization-evoked Ca^{2+} transient per se. In contrast, MCa does not induce any Ca^{2+} release or Ca^{2+} release events in intact adult mammalian fibers. On the other hand, in saponin-treated adult mammalian cells, MCa had a biphasic effect, inducing first a strong increase in calcium release event frequency and then the appearance of long-lasting embers (14). In addition, under voltage clamp conditions the peptide interfered with the repolarization-induced closure of RyRs, raising the possibility that the binding site of the peptide becomes accessible after the activation by DHPR (15).

Recent results have also drawn attention to the charged amino acid residues around position 24 in MCa as the possible interaction site for the peptide binding to RyR1 (13,14). It is not clear, however, whether alterations in the cluster of positive charges around residue 24 would simply lower the affinity of peptide binding to RyR1 or also have a functional effect on the interaction. It also remains to be experimentally confirmed

Submitted September 7, 2007, and accepted for publication June 3, 2008.

Balázs Lukács and Mónika Sztretye contributed equally to this work.

Address reprint requests to Dr. László Csernoch, Dept. of Physiology, University of Debrecen, PO Box 22, Debrecen, Hungary H-4012. Tel.: 36-52-416-634; Fax: 36-52-432-289; E-mail: csl@phys.dote.hu.

Cecilia Simut's present address is Department of Physics, University of Oradea, Oradea, Romania.

Editor: David S. Weiss.

© 2008 by the Biophysical Society

0006-3495/08/10/3497/13 $2.00

doi: 10.1529/biophysj.107.120840

whether alterations seen on isolated channels incorporated into lipid bilayers will also appear under in situ conditions.

In this study we investigated the effects of different mutations of MCa on the Ca^{2+} release channel of SR and on the spontaneous Ca^{2+} release events in permeabilized adult skeletal muscle fibers from both amphibians and mammals. We show that MCa and its mutants induce, in a concentration-dependent manner, subconductance states in skeletal RyR when applied on the cytosolic side. Analysis of the concentration dependence of different mutants of the peptide suggests that the induction of these long-lasting subconductance states (LLSS) corresponds to a reversible binding and unbinding of MCa at a site that is accessible from the cytosolic side. These results strongly support the hypothesis that the effects of MCa depend on the charged surface region of the peptide.

Part of this work has been presented to the European Muscle Society (16).

MATERIALS AND METHODS

Chemical synthesis and peptide structure

MCa and its analogs were obtained by the solid-phase peptide synthesis (17) using an automated peptide synthesizer (model 433A, Applied Biosystems Inc., Foster City, CA, USA) as described previously (13). Analogues were obtained by point mutation, with Ala replacing one amino acid in the sequence of native-like MCa, and named [Ala^{8}]MCa, [Ala^{19}]MCa, [Ala^{20}]MCa, [Ala^{22}]MCa, [Ala^{23}]MCa, and [Ala^{24}]MCa. Three-dimensional (3D) structures of the peptide and its mutated analogs were calculated using the coordinates obtained from the Swiss Protein Data Bank, based on the NMR measurement in aqueous phase, using Swiss-Pdbviewer 3.7 (SP5) shareware software downloadable from the GalaxoSmithKline server (http://www.expasy.ch).

Preparation of heavy SR vesicles

Heavy SR (HSR) vesicles—containing vesicles formed from membrane fragments of the terminal cisternae of the SR—were isolated from rat skeletal muscle according to Lai and Meissner (18) with slight modifications (19). After a homogenization step in 100 mM NaCl, 20 mM EGTA, 20 mM Na-HEPES, pH = 7.5, first crude microsomes were collected by centrifugation at 40,000 × *g*. After the actomyosin contamination was removed by solubilization in 600 mM KCl, the microsome fraction was collected at 109,000 × *g*. The pellet was resuspended and loaded onto a 20–45% linear sucrose gradient. HSR vesicles were extracted from the 36–38% region of the continuous sucrose gradient, collected by centrifugation, and resuspended in 0.4 M sucrose, 10 mM K-PIPES, pH = 7.0. Protein concentration was measured by the Biuret method.

RyR1 Ca^{2+} channel reconstitution and single-channel recording analysis

Measurements of channel activity were carried out using purified RyR1 incorporated into planar lipid bilayers. RyR1 was purified from rat SR vesicles as previously described (20). The bilayers were formed using phosphatidylethanolamine, phosphatidylserine, and L-phosphatidylcholine in a ratio of 5:4:1 dissolved in *n*-decane up to the final lipid concentration of 20 mg/mL (21). Bilayers were formed across a 200 or 250 μm diameter aperture of a Delrin cap using a symmetrical buffer solution (in mM: 250 KCl, 0.1 EGTA, 0.15 $CaCl_2$, 20 PIPES, pH 7.2). A small aliquot of purified RyR1 was added into the chamber, which was defined as the *cis* (cytoplasmic) side, whereas the other chamber, labeled as the *trans* (luminal) side, was kept on ground potential. To ensure the orientation of the incorporated RyR1, we tested the effect of Ca^{2+} on both sides. After successful incorporation of the RyR1 channel, free calcium concentration in the *cis* chamber was adjusted to 238 nM by the addition of EGTA. Electrical signals were filtered at 1 kHz through an eight-pole low-pass Bessel filter and digitized at 3 kHz using Axopatch 200 and pCLAMP 6.03 (Axon Instruments, Union City, CA, USA). The total recording time in each experiment was 10–20 min for each experimental condition tested. After the conditions were changed, at least 5 min were allowed for equilibration, which appeared to be enough to reach the new equilibrium of the parameters. Single-channel measurements were carried out at 22 ± 1°C. The free Ca^{2+} concentration was calculated using the computer program and affinity constants published by Fabiato (22). Open probabilities were calculated using the common 50% criteria with a medial dead zone of 5%. Current amplitude distribution was analyzed using Origin software (Microcal Software, Northampton, MA, USA). The LLSS ratio was calculated as the fraction of time the channel spent in the LLSS from a given (usually several minutes long) total recording time.

Determination of the ATPase activity

ATPase activity was determined at 37°C by a coupled enzyme assay in a medium containing 100 mM KCl, 20 mM Tris-HCl, 5 mM $MgCl_2$, 5 mM ATP, 0.42 mM phosphoenolpyruvate, 0.001 mM calcimycin (A23187, a Ca^{2+} ionophore), 0.2 mM NADH, 7.5 U/mL pyruvate kinase, and 18 U/mL lactate dehydrogenase (pH 7.5). Total hydrolytic activity was measured as the decrease of optical density at the NADH absorbance wavelength (340 nm) and expressed in micromoles of inorganic phosphate per milligrams of protein per minute (abbreviated as A.U.). The total hydrolytic activity of the HSR vesicles ranged from 6.05 to 6.8 A.U., and Ca^{2+}-dependent ATPase activity was identified as the portion of total hydrolytic activity inhibited by 5 μM thapsigargin (7). The toxin was added to the preparation 5 min before starting measurements of enzyme activity. The assay was performed in the presence of Ca^{2+} and EGTA mixtures, producing the estimated free Ca^{2+} concentration (2 μM) found to induce maximum SERCA activation.

Isolation of single skeletal muscle fibers

Single skeletal muscle fibers were isolated manually from the m. semitendinosus of frogs (*Rana esculenta*) as described previously (23). Briefly, the frogs were killed by rapid decapitation, followed by pithing. The fibers were mechanically separated in Ringer's solution (in mM, 115 NaCl, 2.5 KCI, 1.8 $CaCl_2$, and 5 HEPES) and then transferred to the recording chamber. The fibers were permeabilized by applying the following solution containing 0.004% saponin for 3 min (in mM, 100 K-glutamate, 10 HEPES, 1 EGTA, 5 $MgCl_2$, 5 Na_2-ATP, 10 sodium phosphocreatine, 10 glucose, 0.13 $CaCl_2$ and 8% dextran, 0.05 Fluo-3). After permeabilization the saponin was removed and 100 μM Fluo-4 was applied. The pH of the solutions was set to 7.0.

Single skeletal muscle fibers from the extensor digitorum communis muscles of rats were isolated enzymatically as described previously (23). Briefly, rats of either sex were anesthetized and killed by cervical dislocation. The muscles were removed and treated with collagenase 1.5 mg/mL (Sigma, Type I) for 1–1.5 hr at 37°C. The fibers were allowed to rest for at least 20 min after dissociation. Each selected fiber was transferred to a recording chamber filled with relaxing solution (in mM, 150 K-glutamate, 10 HEPES, 1 EGTA, 2 $MgCl_2$). The surface membrane was permeabilized using a relaxing solution (in mM, 125 potassium glutamate, 10 HEPES, 1 EGTA, 5 $MgCl_2$, 5 Na2-ATP, 10 sodium phosphocreatine, 10 glucose, 0.13 $CaCl_2$ and 8% dextran, 0.05 mM Fluo-3) containing 0.002% saponin. This solution was then changed to a K_2SO_4-based internal solution (in mM, 95 K_2SO_4, 10 Hepes, 1 EGTA, 6 $MgCl_2$, 5 Na_2-ATP, 10 sodium phosphocreatine, 10 glucose, 0.26 $CaCl_2$, 0.1 Fluo-4, and 8% dextran). The pH of the solutions was set to 7.2. The MCa and its mutants were added from 1 mM stock solution. The animals were killed in accordance with the guidelines of the European Community (86/609/EEC) following a protocol approved by the institutional animal care committee.

Measurement of elementary calcium release events

Fibers were imaged with an LSM 510 META laser scanning confocal microscope (Zeiss, Oberkochen, Germany) as reported previously (7). Line-scan images of fluorescence ($F(x,t)$) were taken at 1.54 ms line^{-1} and 512 pixels line^{-1} (pixel size 0.142 μm) parallel to the fiber axis. Fluo-4 was excited at 488 nm and emitted light was collected through a band-pass filter and digitized at 12 bit. Elementary calcium release events (ECRE) were captured using an automatic computer detection method (e.g., Cheng et al. (24)) as described in our previous report (7). The eventless portion of the image was used to calculate baseline fluorescence ($F_0(x)$). The program also determined the amplitude and as $\Delta F/F_0$, the spatial halfwidth measured at the time of the peak (full width at half-maximum (FWHM)) and duration for sparks, and the average amplitude, duration, and FWHM for embers. FWHM was calculated by fitting a Gaussian function to the spatial distribution obtained by averaging three lines at the peak for sparks, or by all lines except the first and last 10 ms of the event for embers.

Chemicals

Protease inhibitors were obtained from Boehringer (Mannheim, Germany), Fluo-3 and Fluo-4 were purchased from Molecular Probes Inc. (Eugene, OR, USA), and all other chemicals, unless otherwise specified, were obtained from Sigma (St. Louis, MO, USA).

RESULTS

Effect of the wild-type MCa on isolated RyR1

The effect of the MCa-RyR interaction on the channel function was tested using RyR1 incorporated into the planar lipid bilayer (Fig. 1). Applying 50 nM MCa on the cytoplasmic (*cis*) side of the channel induced LLSS, which corresponded to ~40% of the full conductance (Fig. 1 *B*). In the case of wild-type MCa, the subconductance state displayed an average LLSS time that was several thousand times longer than that of the mean open time of the unmodified channel (Fig. 1, *A* and *B*). Between LLSS, in the presence of the peptide, the channel showed normal gating with increased activity. This manifested as an ~10-fold increase in the open probability during the inter-LLSS periods in the presence of 50 nM MCa *cis* ($P_{o,control} = 0.02 \pm 0.007$; $P_{o,MCa} = 0.21 \pm 0.016$). The channel retained its ohmic behavior during the inter-LLSS periods, as demonstrated by the linear current-voltage relationship presented in Fig. 1 *C*. This was not the case for the LLSS, as will be addressed below (see Fig. 3 *D*).

It is interesting that the MCa-modified channel retained its ryanodine sensitivity since MCa also induced a subconductance state of the ryanodine-modified RyR1 (Fig. 1 *D*). It should be stressed that in the parallel presence of ryanodine (1 μM) and MCa (200 nM), the effect of ryanodine was the determinant because the channel spent most of its time in the ''half-conductance state'' characteristic for ryanodine, which then alternated with the LLSS induced by the peptide. Note also that the conductance of the MCa-induced LLSS of the ryanodine-modified channel and that of the native channel were not equal. Rather, the wild-type peptide reduced the conductance to ~36% of the full conductance (see also Fig. 3 *C*) and again to ~36% of the already reduced (''half'') conductance, for the native and ryanodine-modified channels, respectively. The duration of the LLSS events was found to be independent of the peptide concentration in the 1–500 nM concentration range; only the time required to get the channel into the LLSS was concentration dependent (data not shown).

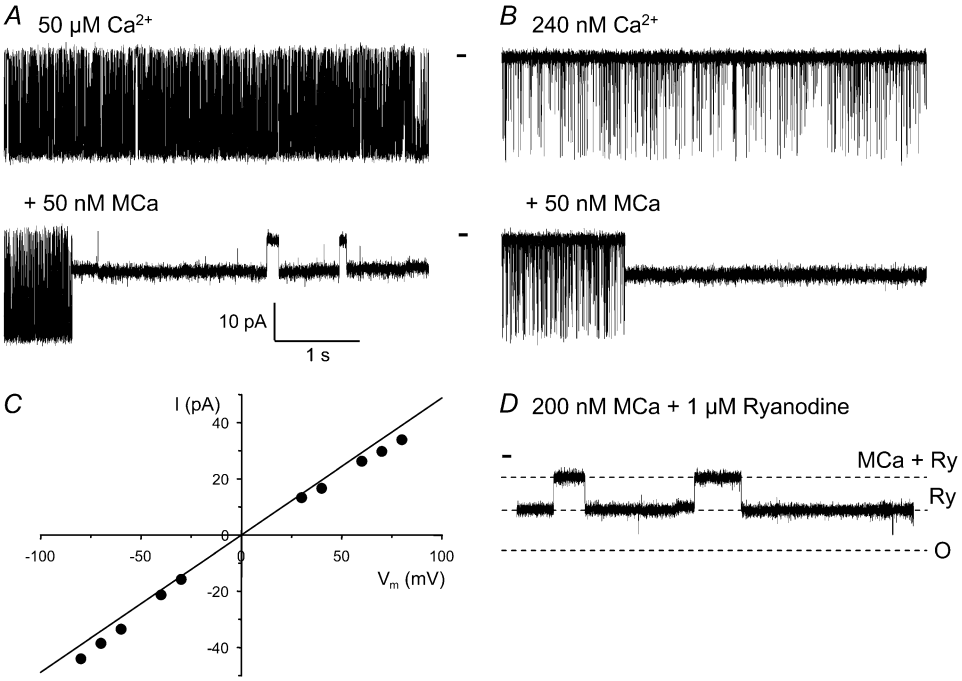


FIGURE 1 Effect of MCa and ryanodine on the calcium channel. The solubilized ryanodine receptor of the rat was incorporated into a lipid bilayer and the channel current was recorded under voltage clamp conditions using +55 mV as the holding potential at two different *cis* [Ca^{2+}] (50 μM, *left*; 240 nM, *right*). The charge carrier was 250 mM KCl; channel openings are represented by downward deflections. The closed state of the channel is marked between the current traces using the symbol —. (*A* and *B*) Single-channel recordings obtained under control conditions and in the presence of 200 nM MCa demonstrating the LLSS, lasting for several seconds, for the latter. (*C*) Current-voltage relationship for the full conductance state calculated from records in the presence of MCa. (*D*) Recording in the presence of 200 nM MCa and 1 μM ryanodine (50 μM [Ca^{2+}] *cis*). The ryanodine-induced specific half conductance state is labeled as Ry, whereas the MCa-induced state in the presence of ryanodine is labeled as MCa + Ry. For reference the full open state is also marked with O.

Effects of mutated analogs of MCa on the isolated RyR1

If, by analogy with other peptide toxin-ion channel associations (25–27), the high-affinity MCa-RyR1 interaction is mediated by electrostatic forces, mutations in the interaction domain of MCa should alter its electrostatic potential and/or the pattern of the subconductance states. Fig. 2 demonstrates that synthetic MCa derivatives activate the isolated RyR and induce subconductance states, in a similar fashion (but to different extents) to the wild-type MCa. Mutations within the cluster of basic amino acids of residues 20–24 elicited dramatic effects. Replacing ^{24}Arg with Ala ([Ala^{24}]MCa mutant) in MCa's sequence essentially abolished the MCa-induced subconductance states (Fig. 2 *G*). Mutants [Ala^{20}]MCa, [Ala^{22}]MCa, and [Ala^{23}]MCa exhibited consequently shorter and shorter transitions to the subconductance state, paralleling the putative 3D distance (28,29) of their mutation with respect to residue 24 (Fig. 2, *D–F*). In contrast, replacing Lys8 or Lys19 with Ala yielded almost the same LLSS as did the wild-type MCa (Fig. 2, *B* and *C*). Not only the temporal characteristics but also the relative amplitude of the subconductance state varied with the mutation, with the wild-type peptide producing the smallest conductance.

Effects of wild-type MCa and its mutated analogs on Ca^{2+}-ATPase activity

We also tested whether the peptides would alter the function of the SR calcium pump. Neither the wild-type toxin nor any of its mutants exhibited any effect on the hydrolytic activity

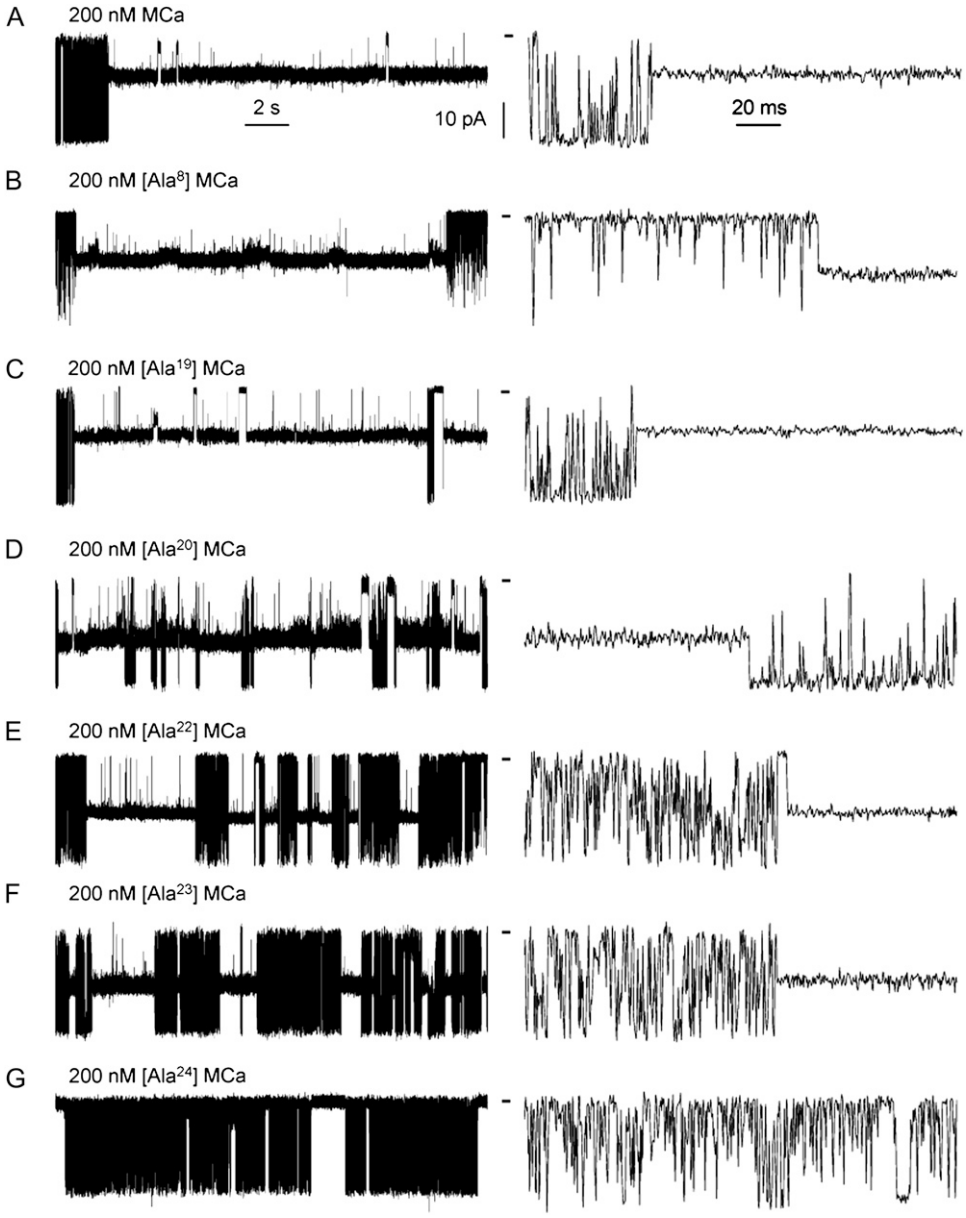


FIGURE 2 Effect of MCa and its mutants on the RyR1 of the rat. (*A–G*) Representative current traces in the presence of MCa (*A*) and its mutants (*B–G*; as marked). Experimental conditions are identical to those for Fig. 1 *A*. The traces in the left and right columns show identical single-channel recordings obtained using different time scales to better visualize the effects of different mutants. Between the two columns the closed state is marked as —. Note that when the place of the mutation is closer to the critical residue ^{24}Arg, the length and the frequency of LLSS decrease while the single-channel conductance corresponding to the full openings of the channel does not change.

of the Ca^{2+}-ATPase (Supplementary Material, Fig. S1 and Fig. S2).

MCa mutants alter the channel gating in two different ways

The effects of the peptide, in the presence of 240 nM ionized calcium, on the LLSS ratio—the relative time the channel spends in LLSS (see Materials and Methods)—and the length of these events are demonstrated in Fig. 3, *A* and *B*. As the site of the mutation became closer and closer to the critical residue 24, the LLSS ratio became smaller and smaller (Fig. 3 *A*). Furthermore, the place of the mutation affected the average LLSS event length more substantially than the LLSS ratio (Fig. 3 *B*). Note also that the LLSS ratio as well as the frequency of the events increased along with the peptide concentration. The average length of the LLSS events, on the other hand, seemed to be independent of the peptide concentration (Fig. 3 *B*).

In addition to affecting the time that channels spend in the LLSS, the mutation altered the relative conductance (the conductance of LLSS as normalized to the full conductance of the channel) as well (Fig. 3 *C*). Although the wild-type peptide reduced the conductance to 35.2% ± 3.7% during the LLSS, other mutants had increasingly smaller effects, again paralleling the spatial distance of their mutation in the putative 3D structure of the peptide.

Polarity dependence of the effects of MCa

The data presented in Fig. 3, *A–C* were obtained with a holding potential of +55 mV. It is important to stress here that the parameters of the LLSS events induced by MCa and its mutants depended on the polarity, and in some cases on the actual value, of the membrane potential, that is, on the direction of the current. When the charge carrier (K^+ or Ca^{2+}) moves from the *trans* to the *cis* side, the current direction is identical to that observed when calcium is released from the SR (''physiological direction''). Using membrane potentials (negative holding potentials) to drive the ions in the physiological direction, the LLSS ratios for each and every mutant were found to be lower as compared to the opposite polarity (''reverse direction''; Table 1). The effect of the peptides, in this respect, appeared to be independent of the actual value of the holding potential in the voltage range of 20–120 mV; only the polarity (current direction) had an appreciable effect. It is also interesting that the effect of MCa on the LLSS ratio was identical at 50 μM and 240 nM free

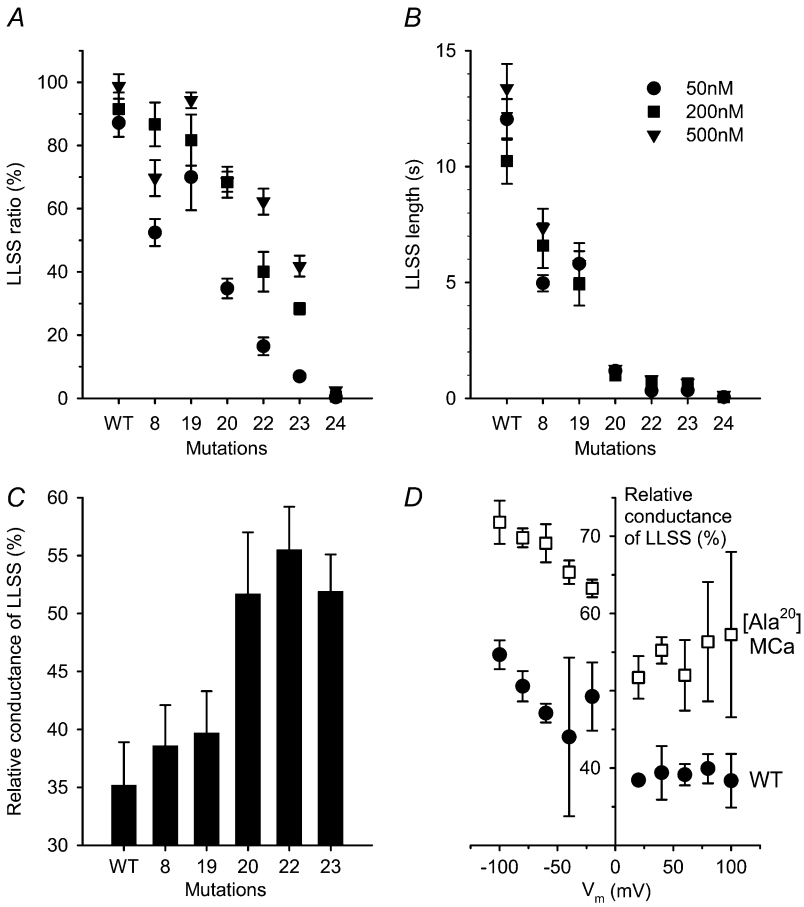


FIGURE 3 Parameters of the LLSS differ for different mutants. (*A* and *B*) Single-channel records were taken at 50 nM (●),200 nM (■), and 500 nM (▼) peptide concentrations, and the LLSS ratio (*A*) and average length of the LLSS events (*B*) were determined. The LLSS ratio was calculated as the ratio of the time spent in the subconductance state over the total time and expressed as percentage. Note that when the site of the mutation is placed more and more distant from the critical residue ^{24}Arg, the channel spends less and less time in the LLSS state. Note also that although the concentration of the peptide did influence the LLSS ratio, it had little effect, if any, on its average length. (*C*) Relative conductance of LLSS for the different mutants was calculated by normalizing the conductance of LLSS to that of the full conductance state. Measurements for panels *A–C* were taken at the holding potential of +55 mV; each symbol represents the mean of at least 20 events taken from at least eight bilayers. (*D*) Voltage dependence of the relative conductance of LLSS for the wild-type MCa (●; 25 nM) and the [Ala^{22}]MCa mutant (□; 250 nM). Values are expressed as a percentage of the full conductance state in panels *C* and *D*.

TABLE 1 Polarity and concentration dependence of LLSS ratio with different MCa mutants

MCa analog	[peptide] (nM)	Reverse direction	Physiological direction*
wild-type	50	88.1 ± 10.5	9.8 ± 1.1
	200	91.5 ± 11.2	43.8 ± 5.2†
[Ala^{8}]MCa	50	52.5 ± 6.1	3.5 ± 0.74
	200	86.7 ± 9.1†	5.4 ± 0.60†
[Ala^{20}]MCa	50	34.8 ± 6.4	3.1 ± 0.72
	200	68.4 ± 8.2†	3.9 ± 0.63
[Ala^{24}]MCa	50	0.34 ± 0.18	not detected
	200	0.62 ± 0.21	not detected

*Physiological direction was defined as the direction in which calcium moves during its release from the SR. The LLSS ratio was determined as described in Materials and Methods and expressed as percentage.
†Indicates that the difference is significant ($p < 0.01$) between the LLSS ratios determined at 50 nM and 200 nM peptide concentration.

calcium concentration in the case of the wild-type MCa (Fig. 1, *A* and *B*) and the [Ala^{8}]MCa mutant, whereas it was slightly lower at low calcium for the other mutants. The length of LLSS was also calcium independent in both current directions (data not shown).

On the other hand, the relative conductance of the MCa-modified channel displayed a clear voltage dependence for the wild-type MCa and all mutated analogs, similar to that presented for MCa and [Ala^{20}]MCa in Fig. 3 *D*. The voltage dependence was present at negative potentials, with a greater conductance at negative holding potentials as compared to the same but positive holding potentials. The relative conductance increased essentially linearly as the holding potential was moved further and further away from 0 mV, indicating again that the effect of the peptides was current-dependent. The wild-type peptide behaved similarly to its mutated analogs at both holding potentials.

To test whether the parameters of the LLSS induced by MCa depend on the presence of an externally applied voltage or on the actual flow of the charge carrier, we tested the effect of the wild-type peptide using a symmetrical (250 mM / 250 mM) charge carrier situation with an externally applied 40 mV membrane potential and an asymmetrical (50 mM / 250 mM) K^+ concentration (corresponding to the same driving force according to the Nernst equation). The former represents the current driven by the electrical field (i.e., potential difference), whereas the latter represents the charge transfer driven by the concentration gradient (measured at zero membrane potential) determined as the short circuit current. These experiments, using the wild-type MCa, revealed that the membrane potential and the concentration gradient—generating the same current—resulted in similar parameters for the LLSS events (data not shown).

These results highlight the existence of a localized binding site of MCa on RyRs and suggest that the MCa-RyR interaction can be modified with the place of the mutation. To further investigate the effect of the different mutations of MCa at the level of EC coupling, ECREs were studied on adult skeletal muscle fibers.

Effects of MCa analogs on event properties of permeabilized mammalian fibers

We have previously shown that MCa can initiate or modify the properties of spontaneous calcium release events in adult mammalian striated muscle fibers (14). We thus tested whether the different mutants of MCa would alter calcium release in a manner similar to their effect on isolated channels. To this end, cells from rat skeletal muscle were permeabilized, placed in a sulfate-based internal solution containing Fluo-4, and imaged with a confocal scanner. Fibers showed spontaneous calcium release events (Fig. 4 *A*) in accordance with previous observations (5,6,14). Shortly after the addition of 50 nM MCa (2–10 min), the frequency at which ECRE occurred increased considerably (Fig. 4 *B*). In addition to sparks, long openings with or without sparks were also observed (Fig. 4 *B*, inset). To test the specificity of the mutants of MCa, we added the [Ala^{8}]MCa analog of MCa, which was found to have similar effects on the occurrence

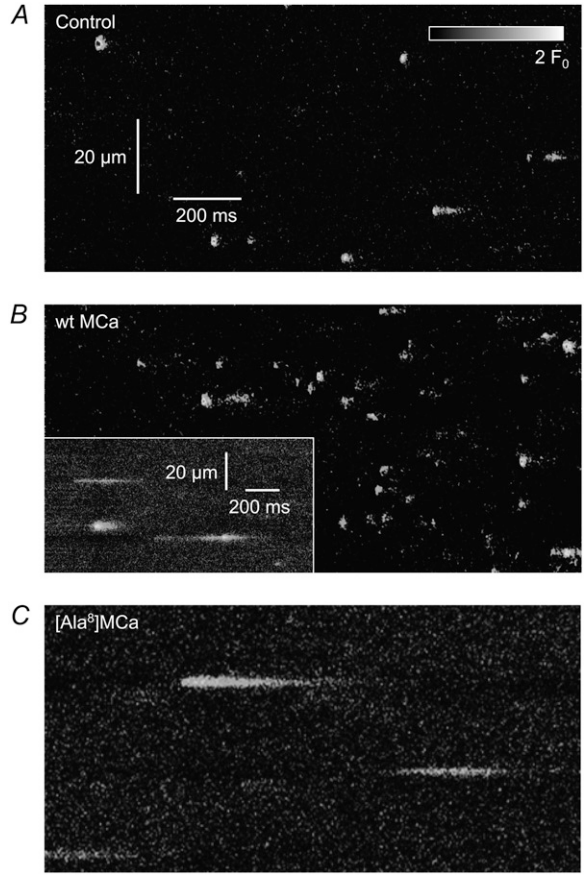


FIGURE 4 Effect of wild-type and mutant MCa on calcium release events in rat skeletal muscle fibers. Line-scan images in control (*A*) and in the presence of wild-type MCa (*B*) and [Ala^{8}]MCa mutant (*C*) in saponin-skinned rat skeletal muscle fibers. Scanning was made parallel with the fiber axis. Images were corrected for background fluorescence (F/F_0) and pseudo-colored. Note the larger number of long-lasting embers as compared to control in the presence of both types of the peptide. The inset shows that wild-type MCa causes similar long events as the [Ala^{8}]MCa mutant.

(Fig. 4 *C*) and duration (187 ± 4 vs. 185 ± 3 ms, $n = 767$ and 1109, for MCa and the mutant, respectively) of embers as the wild-type peptide.

It should be stressed that the above averages are lower estimates of the actual average durations in the presence of the peptides since they inevitably contain durations from events that originate from nonmodified channels. This can be appreciated clearly from the histograms presented in Fig. 5 *A*, where the distribution of event duration is displayed for control fibers and for cells treated with 50 nM MCa. Note that under control conditions the event duration never exceeded 250 ms, whereas in the presence of the peptide events with durations over 250 ms are clearly present. Nevertheless, the majority (95%) of events in the presence of MCa had durations shorter than 250 ms. These latter events most likely originate from nonmodified channels since at this low concentration of the peptide the channel spends less than 10% of its time in the MCa-modified state (see Table 1). To overcome this problem, we also measured the duration of events in the presence of 1 μM MCa, where the majority of events should represent the peptide-modified channels. Fig. 5 *B* demonstrates that the distribution of event duration in the presence of such a high peptide concentration is clearly altered as compared to that in the control. The events with short duration are now suppressed and long events dominate, that is, 15.4% of all events have durations exceeding 1 s (Fig. 5 *B*, *inset*). Although one can still not exclude the possibility that events from MCa-modified channels with durations shorter than 250 ms are still present, their contribution should be greatly reduced. Therefore, to estimate the average duration of these events, we used the above criteria and obtained 1072 ± 49 ms ($n = 459$).

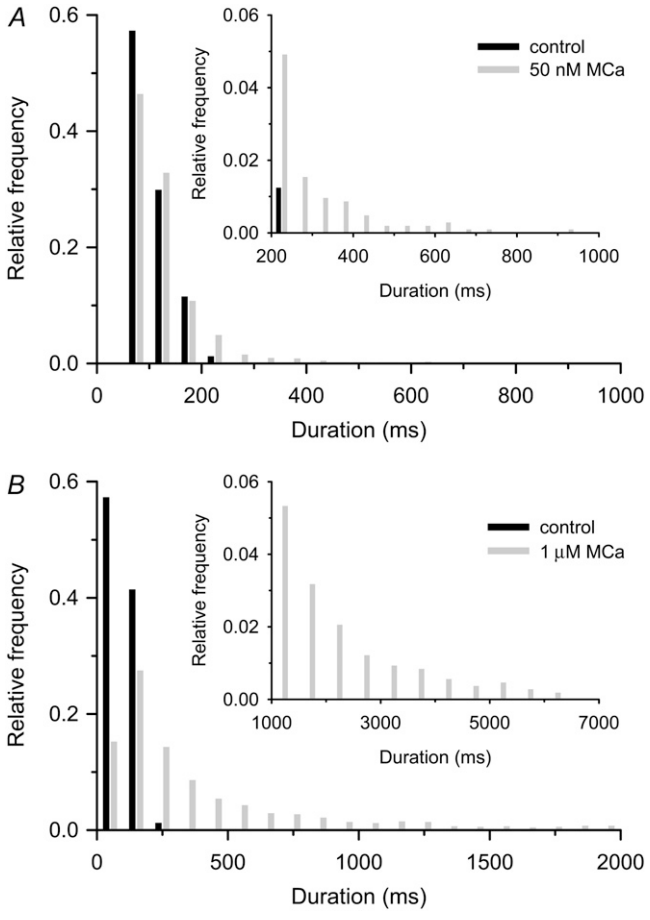


FIGURE 5 Relative distribution of ember durations. (*A*) Event durations were measured under control conditions (*black bars*) and in the presence of 50 nM MCa (*gray bars*). Note the presence of events longer than 250 ms in the presence of the peptide, which were not observed under control conditions. Inset shows the distribution at an expanded *y*-scale for better visualization of the longer events. (*B*) Event durations in the absence and presence of 1 μM of MCa. Note the clear alteration in the shape of the distribution in the presence of the peptide. Inset again shows the distribution at an extended *y*-scale.

To capture events with durations of several seconds in the presence of MCa or the Ala^{19} mutant (see Fig. 6 *A* for an example of the latter), longer imaging times were used. However, to avoid photo-damaging the cells unnecessarily, this was not done routinely. It is also intriguing that, unlike in frogs (see below), where a spark preceded the long ember, the events in rats always started as a sudden step to an increased fluorescence level, which was then maintained during the entire event.

Occasionally (22 events out of 344), however, stepwise changes in fluorescence were detectable, as presented in Fig. 6 *B*. The amplitudes of these steps were slightly greater than the original 158% ± 18% for the second step as normalized to the first, indicating either the opening of an additional but independently gated channel or the transition to the fully conducting state. Although we have no direct evidence to support the latter, it is intriguing to note that the step to the full conductance state from the LLSS in isolated channels was also ~150% of the LLSS state (see, e.g., Fig. 2 or 3 *C*). In addition to simple stepwise changes in fluorescence, events with complex kinetics were also captured (Fig. 6 *B*, *b*). These showed long openings, lasting for several hundreds of milliseconds that alternated with a burst-like pattern clearly resembling that seen for isolated channels (Fig. 2).

Effects of MCa analogs on amphibian fibers

While mammalian fibers readily produce calcium release events of long duration and small amplitude under control conditions, amphibian fibers are normally devoid of such events. To further explore the effects of the mutations of MCa and derive quantitative measures for their duration, we used permeabilized frog skeletal muscle fibers, in which a long event with small amplitude would clearly mark a peptide-modified channel. Fig. 7 thus presents line-scan images recorded under control conditions (Fig. 7 *A*) and in the presence of wild-type MCa, $[Ala^{8}]$MCa, $[Ala^{19}]$MCa, and $[Ala^{22}]$MCa (Fig. 7, *B–E*, respectively). The wild-type peptide and the mutants decreased event frequency but produced long-lasting calcium release events that were

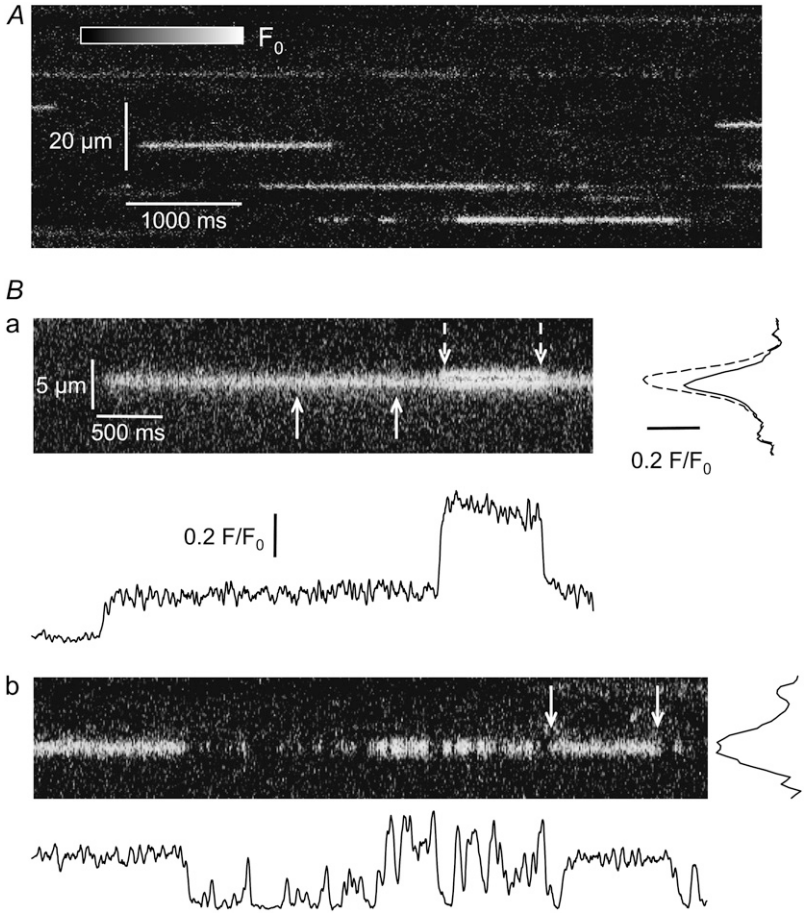


FIGURE 6 Long-lasting calcium events caused by the [Ala^{19}]MCa mutant in rat skeletal muscle fibers. (*A*) Pseudo-colored line-scan image taken in the presence of [Ala^{19}]MCa. The same scanning direction and image correction were applied as in Fig. 4, but the length of acquisition was eight times longer. Note the very long event durations and the presence of endless events on either side of the image. (*B*, *a*) A representative ember with a secondary opening taken from a long scan. (*B*, *b*) A representative event demonstrating the successive reopenings of the channel. The traces below the images show the average of five neighboring lines at the middle of the event, and the traces next to the images represent the spatial spread of the event calculated by averaging the lines between the times marked by white arrows. The solid and dashed traces in panel *B*, *a* correspond to the time windows marked by solid and dashed arrows with calculated FWHMs of 1.54 and 1.44 μm during and before the secondary opening, respectively.

never observed under control conditions in frogs but resembled those reported for IpTxA (30). In line with data from single channels, the [Ala^{22}]MCa mutant caused shorter calcium release events than those produced by the other two mutants (see also Fig. 8 *A*).

Note also that these long events seem to always start with a ''classical'' spark. From the several thousand long events measured in the presence of MCa or its mutants, only a handful (such as the one presented in the inset of Fig. 7 *B* for the wild-type MCa) had no leading spark.

The mutation of MCa alters the morphology of ECRE

We found similar effects of the different mutants of MCa on the length of embers in permeabilized frog skeletal muscle fibers as was shown above on LLSS length. As shown in Fig. 8 *A*, the mutants [Ala^{8}]MCa and [Ala^{19}]MCa were almost as effective as the wild-type MCa at both 50 and 100 nM. In contrast, the [Ala^{22}]MCa mutant induced ~60% and 50% shorter events than did the native peptide at the two concentrations, respectively. We also tested [Ala^{24}]MCa, but in the presence of this analog we did not observe embers as in the peptide-free control solution (data not shown).

As mentioned above, the peptide-modified events, in most cases, displayed a starting spark followed by a prolonged ember. Fig. 8 *B* plots the amplitude and FWHM, as a measure of the spatial spread, of these components for the wild-type peptide. The events that were assumed to be the closest to the confocal plane, as judged by their large amplitude, were selected from those included in panel *A*. As shown in Fig. 8 *B*, the starting sparks had five to six times greater amplitudes and slightly larger FWHMs than the trailing embers.

DISCUSSION

In this work we evaluated how the replacement of different amino acids in the sequence of the wild-type MCa affects its ability to modify the gating of the skeletal-type RyR. We show that mutations of MCa within the cluster of positively charged residues surrounding ^{24}Arg decrease the appearance of LLSS on isolated channels reconstituted into planar lipid bilayers and long-lasting embers in saponin-treated adult striated muscle fibers. The extent of this effect depended on the direction of the current in lipid bilayer experiments, indicating a current- and voltage-dependent interaction of the peptide with the channel.

szentesi.peter_292_24

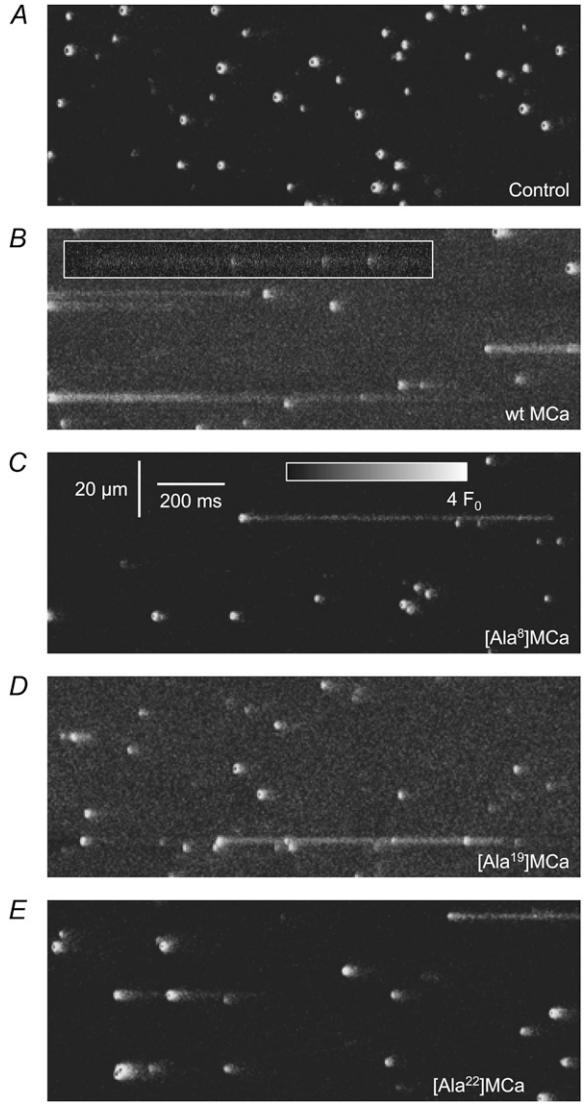


FIGURE 7 Effect of wild-type and mutant MCa on calcium release events in frog skeletal muscle fibers. Pseudo-colored line-scan images under control conditions (*A*) and in the presence of wild-type MCa (*B*) and [Ala^{8}]MCa (*C*), [Ala^{19}]MCa (*D*), and [Ala^{22}]MCa (*E*) mutants in frog skeletal muscle fibers. The same scanning direction and image correction were applied as in Fig. 4. Note the decreased number of long-lasting embers in the presence of [Ala^{22}]MCa as compared to those measured in the presence of wild-type MCa and the other mutants. The inset in panel *B* displays a rare event in which the long opening was not preceded by a spark.

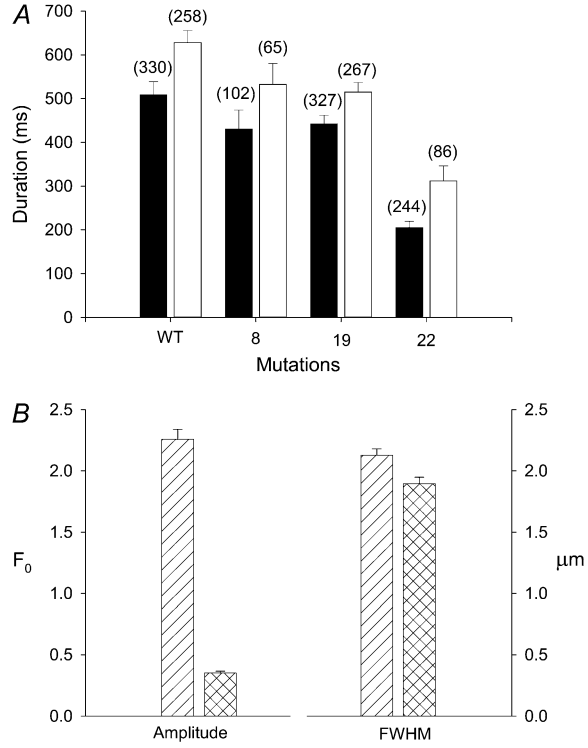


FIGURE 8 Effect of MCa and its mutants on the parameters of calcium release events. (*A*) The average length of the events measured in the presence of wild-type MCa and its different mutants calculated from images similar to those presented in Fig. 7. Empty bars represent averages measured in the presence of 50 nM, and filled bars give values in the presence of 100 nM of the peptides. The numbers above the bars give the number of events included in the average. Only those events whose lengths could reliably be estimated were considered. Note the fewer number of events for the [Ala^{22}]MCa mutant. (*B*) The parameters of the leading spark (*hatched bars*) and the trailing ember (*cross-hatched bars*) for selected large events ($n = 66$) measured in the presence of the wild-type peptide (50 nM). In the case of the trailing ember, the average amplitude is given.

Effect of mutations in MCa on the lengths of LLSS and ECRE

In previous studies we have demonstrated that MCa increases the frequency of ECRE together with a decrease in the amplitude of the individual events in saponin-treated adult mammalian striated muscle fibers (14). In addition, it induces long-lasting embers with durations that usually exceed 200 ms and occasionally last longer than 1.5 s. On purified RyR1 reconstituted into planar lipid bilayers, the peptide induced both an increase in the open probability of the channel and the appearance of long-lasting open events characterized by a reduced conductance (12,13). As a consequence of these effects, MCa caused a dramatic increase in the [^{3}H]ryanodine binding to RyR1, as well as in Ca^{2+} release from SR vesicles. All of these effects were completely abolished by the point mutation of the Arg residue in position 24 of MCa (13,14), supporting the hypothesis that the basic amino acid-rich region is important for the functional effect of MCa on RyR1.

Here we show that the effects of MCa described for LLSS and ECRE depend on the position of mutation of the peptide and correlate with the putative spatial distance of the mutation from the charged surface of MCa as derived from the suggested 3D structure of the peptide (29). Indeed, the effects of [Ala^{8}]MCa and [Ala^{19}]MCa mutants on ECRE were almost identical to those of the wild-type peptide. In the presence of [Ala^{22}]MCa, the length of embers decreased, whereas the [Ala^{24}]MCa analog did not show any effect on ECRE. These results are in direct agreement with the observations originating from lipid bilayer experiments, with these analogs illustrating that the capability for inducing the

LLSS of RyR1 depends on the location of the mutation in the structure.

Changing amino acids at different positions, by substituting a charged amino acid with a neutral one, thus reveals that the dramatic effect of the mutations within the putative 3D cluster of basic amino acids (Fig. 9, *A* and *B*) cannot be solely attributed to the change of the net electrical charge of the peptide since mutations that were distant to the cluster but produced the same change in net electrical charge had relatively minor effects. Since structural changes within MCa due to its triple disulphide bonds are unlikely to accompany the mutations, this cluster is the most likely candidate for the interacting site with the RyR.

The properties of the MCa binding site on RyR

Recent evidence has positioned the MCa binding site to residues 3351–3507 on RyR1 (31). The results presented here suggest that the peptide binding site is distant from the high-affinity calcium binding (regulatory) site because the effects of the peptides were essentially calcium-independent. In addition, it also appears to be distinct from the ryanodine binding site (see below). Finally, it should be noted that the calcium release channel, when gating to the full conductance state, was still ohmic after binding MCa or its mutants, indicating, for this effect, an allosteric modification of the RyR conformation by the peptides.

The fact that the LLSS length was found to be independent of the concentration of MCa, or the concentration of its analogs, suggests that one MCa binds to an RyR channel. On the other hand, the fact that the inter LLSS open probability is higher (by ~10-fold) than under control conditions indicates that an alternative binding site, presumably four on the tetrameric channel, is a precondition for the occupation of the fifth (''in pore'' or central) binding site, for this special type of gating.

Given the above constraints and the reasonable assumption that MCa and its mutants bind to RyR1 via a common structural motif, the corresponding mutations should evoke parallel changes in the affinity if the continuity of the basic surface is essential. Since this was confirmed in all measurements, we can conclude that the orientation of the peptide is likely to be the most important factor in determining its binding to the site that is responsible for the initiation of LLSS, probably because the electric field-induced orientation of the peptide plays an important role in its binding to (or interaction with) the channel. This suggests that this MCa binding site is near the opening of the channel pore, where the electric gradient is extremely large, and thus the electric momentum dominates the orientation of the MCa molecule. In the above framework, due to the necessity of a suitable orientation of the charged surface, the interaction of MCa with the RyR should be influenced by the polarity of the membrane potential. In line with the above reasoning, we

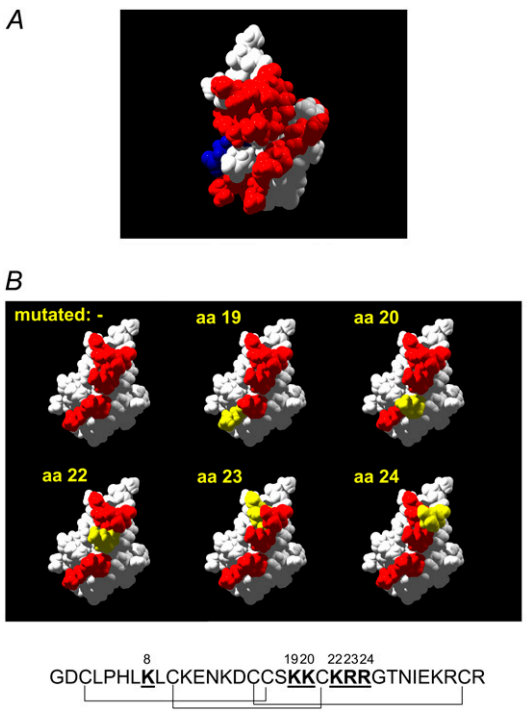


FIGURE 9 3D structure and proposed binding sites of MCa. (*A*) Putative 3D structure of MCa with the basic amino acids (aa) colored red, the acidic aa colored blue, and all others colored white. The presented 3D structure is based on NMR measurements reflecting the structure of the molecule dissolved in an aqueous phase (29). (*B*) Predicted 3D structure of the wild-type and mutated peptides together with the aa sequence. In the first image, the red color shows positively charged aa whose mutations were tested in this study; all other aa are in white. The yellow color in all subsequent images represents the actually mutated aa; these were only recolored without recalculation of the structure. (*C*) Proposed model for the MCa binding sites on the functional channel unit. Each RyR1 monomer has one (identical) binding site (*dotted circles*) and the tetramer has an extra—collective—site (solid circle) positioned in the central part of the channel. Open circles represent unoccupied MCa binding sites, and filled circles represent occupied MCa binding sites. The area of the white central square, the pore, is proportional to the conductance of the channel under the given condition.

found that the dissociation constants of the peptides were polarity-dependent.

We thus propose a model (Fig. 9 *C*) in which four binding sites are located far from the pore on the RyR tetramer (one on each monomer), altering the open probability of the channel in a voltage-independent manner (characterized by normal type of gating). The fifth binding site would, in this framework, be responsible for the potential-dependent (current-direction dependent) LLSS (see Table 1. and Fig. 3.), which is expected to be in the very vicinity of the vestibule of the pore, and must be in direct relation with the other four, as confirmed by the finding that LLSS were always preceded by increased open probability. Once the putative binding site within the pore is occupied, the channel can gate between the LLSS and the closed state, as seen clearly in Fig. 1 *A* for the wild-type MCa and in Fig. 2 *C* for the [Ala^{19}]MCa mutant. Occasionally the channel swaps back to normal gating with higher activity (Fig. 2). This model is also supported by the finding that only the time required to get the channel into the subconductance state varies with the concentration of the peptides. In the case of the wild-type toxin, this was found to be in the 20 min to 20 s range for toxin concentrations in the 1–500 nM range. This type of dose dependence is not unique, being similar to the effect of ryanodine on RyR1 and also to the effect of cyclopiazonic acid on the Ca^{2+} ATPase.

We recently suggested that in intact cells MCa binds preferably to the RyR after its activation via the DHPR (15). It should be noted that this conclusion was derived by comparing the prolonged calcium release after repolarization with that of maximal calcium release during the depolarizing pulse. This prolonged calcium release should correspond to the LLSS seen in lipid bilayer experiments. This suggests that the binding site for the peptide that is responsible for the induction of LLSS is inaccessible or less accessible when the channel is closed. Clearly, a binding site within or in close association to the channel pore would fulfill this criterion. If the binding site is indeed found within the pore, the movement of positively charged ions through the channel (the calcium release process) should hinder the binding of the positively charged peptide. A similar phenomenon is expected to take place in bilayer experiments if the holding potential is set to drive the charge carrying ions in the physiological direction. This is indeed what was observed, strengthening the idea that the binding site is somehow associated with the pore itself.

Combined effect of ryanodine and MCa

Normally, low concentrations of ryanodine induce a characteristic half-conductance state of RyR from which the channel only occasionally closes, and only for a short time (for a few milliseconds), and it never switches back to the full open state unless the ryanodine is removed from the bathing solution (for review see Meissner and el-Hashem (32)). In the case of the simultaneous presence of ryanodine and MCa, the half-conductance state characteristic of the alkaloid dominates channel behavior. Nevertheless, long closing periods due to the presence of MCa become apparent, during which the channel enters a further reduced conductance state, clearly indicating that the binding of the peptide and the alkaloid are independent of one another. The apparently free gating of the channel between these two states ensures that although the binding of MCa or ryanodine might influence the binding of the other, the state into which MCa transforms the channel is independent of that induced by ryanodine.

The binding site for MCa and its effect on ECRE

MCa and its structural analog IpTxA have been shown to induce extremely long calcium release events in amphibian skeletal muscle fibers (14,28,33). These events are most likely a direct consequence of the calcium release channel entering into the LLSS after the binding of the peptide. Several pieces of evidence support this conclusion. First, the length of these long events correlates well with the length of LLSS. We obtained 1.1 s for the average duration of the long embers (Fig. 5 *B*), which should be compared with the average length of LLSS given in Fig. 3 *B* (12 s; wild-type MCa). Note, however, that the values in Fig. 3 were obtained with a positive holding potential (reverse direction of the current; Table 1), whereas in the fiber current flow is in the physiological direction. Second, mutations in MCa caused parallel changes in the ability of the peptide to induce LLSS on isolated channels and to modify the kinetics of ECRE. Third, stepwise changes in event amplitude were observed in peptide-treated cells. Whereas such events were not seen under control conditions, they have been reported for K-201, an immunophylin capable of inducing subconductance states in RyR1 (34). These stepwise changes could be explained by a sudden change in release and/or removal of calcium. Since a very rapid change is unlikely occur in the calcium binding sites (in their concentration or affinity for calcium) within the myoplasm, a possible candidate could be an MCa-induced alteration in the properties of the calcium pump—a reduction in the amount of calcium transported into the SR. However, neither MCa nor its mutated analogs seem to exert any effect on the ATP-ase activity of the calcium pump (Fig. S1 and Fig. S2). This leaves us with the possibility that calcium release is altered suddenly, due either to the opening of an additional channel (or channels) or an increase in the conductance of an already open channel. Whereas we cannot exclude the possibility that the opening of neighboring channel(s) caused the sudden increase, the correlation between the magnitude of the change and the relative conductance of the LLSS as well as the minimal change in FWHM argue in favor of the latter possibility. Finally, neither the wild-type MCa nor its mutated analogs had any effects on the SR calcium pump (data not shown). This, on the one hand, clearly confirms that these long events are a result of the calcium released through a single peptide-modified channel

whereas calcium sparks are generated by the opening of a group of calcium release channels. On the other hand, it gives further insight into the interaction of MCa and the calcium release channel. As discussed above, the peptide seems to prefer the open conformation when it interacts with RyR. If MCa binds only to the open channel, the prediction would be that long events should tail calcium sparks. This is clearly the case for amphibians, in which long events are generally made up of a leading spark and a trailing ember. It should be noted, however, that a few events (2% of those in which long embers were observed) are devoid of the leading ember. This indicates that there is a possibility, albeit a much lower one, for the peptide to bind to the closed channel. We, of course, cannot exclude the possibility that the binding actually occurred right after the opening of the channel and this event then prevented neighboring channels from opening and the spark from being formed. Whereas this scenario is an acceptable, although unlikely, possibility in amphibians, it clearly cannot account for the observation that in mammals all long events are without leading sparks. Taken together, our data are in line with the hypothesis that MCa and its mutants bind preferably but not solely to the open channel.

SUPPLEMENTARY MATERIAL

To view all of the supplemental files associated with this article, visit www.biophysj.org.

The authors are grateful for the technical assistance of Ms R. Őri and Ms É. Sági.

The work was supported by grants from the Hungarian Scientific Research Fund OTKA (T049151, NK61412, K61442).

REFERENCES

1. Tsugorka, A., E. Rios, and L. A. Blatter. 1995. Imaging elementary events of calcium release in skeletal muscle cells. *Science*. 269:1723–1726.
2. Klein, M. G., H. Cheng, L. F. Santana, Y. H. Jang, W. J. Lederer, and M. F. Schneider. 1996. Two mechanisms of quantized calcium release in skeletal muscle. *Nature*. 379:455–458.
3. Gonzalez, A., W. G. Kirsch, N. Shirokova, G. Pizarro, M. D. Stern, and E. Rios. 2000. The park and its ember: separately gated local components of Ca^{2+} release in skeletal muscle. *J. Gen. Physiol.* 115:139–157.
4. Shirokova, N., J. Garcia, and E. Rios. 1998. Local calcium release in mammalian skeletal muscle. *J. Physiol.* 512:377–384.
5. Kirsch, W. G., D. Uttenweiler, and R. H. A. Fink. 2001. Spark- and ember-like elementary Ca^{2+} release events in skinned fibers of adult mammalian skeletal muscle. *J. Physiol.* 537:379–389.
6. Zhou, J., G. Brum, A. Gonzalez, B. S. Launikonis, M. D. Stern, and E. Rios. 2003. Ca^{2+} sparks and embers of mammalian muscles. Properties of the sources. *J. Gen. Physiol.* 122:95–114.
7. Szentesi, P., H. Szappanos, C. Szegedi, M. Gönczi, I. Jona, J. Cseri, L. Kovacs, and L. Csernoch. 2004. Altered elementary calcium release events and enhanced calcium release by thymol in rat skeletal muscle. *Biophys. J.* 86:1436–1453.
8. Marx, S. O., K. Ondrias, and A. R. Marks. 1998. Coupled gating between individual muscle Ca^{2+} release channels (ryanodine receptors). *Science*. 281:818–821.
9. El-Hayek, R., A. J. Lokuta, C. Arevalo, and H. H. Valdivia. 1995. Peptide probe of ryanodine receptor function. Imperatoxin A, a peptide from the venom of the scorpion *Pandinus imperator*, selectively activates skeletal-type ryanodine receptor isoforms. *J. Biol. Chem.* 270: 28696–28704.
10. Fajloun, Z., R. Kharrat, L. Chen, C. Lecomte, E. Di Luccio, D. Bichet, M. El Ayeb, H. Rochat, P. D. Allen, I. N. Pessah, M. DeWaard, and J. M. Sabatier. 2000. Chemical synthesis and characterization of maurocalcine, a scorpion toxin that activates Ca^{2+} release channel/ryanodine receptors. *FEBS Lett.* 469:179–185.
11. Shahbazzadeh, D., N. Srairi-Abid, W. Feng, N. Ram, L. Borchani, M. Ronjat, A. Akbari, I. N. Pessah, M. De Waard, and M. El Ayeb. 2007. Hemicalcin, a new toxin from the Iranian scorpion *Hemiscorpius lepturus* which is active on ryanodine-sensitive Ca^{2+} channels. *Biochem. J.* 404:89–96.
12. Chen, L., E. Estève, J. M. Sabatier, M. Ronjat, M. DeWaard, P. D. Allen, and I. N. Pessah. 2003. Maurocalcine and peptide A stabilize distinct subconductance states of ryanodine receptor type 1, revealing a proportional gating mechanism. *J. Biol. Chem.* 278:16095–16106.
13. Estève, E., S. Smida-Rezgui, S. Sarkozi, C. Szegedi, I. Regaya, L. Chen, X. Altafaj, H. Rochat, P. D. Allen, I. N. Pessah, I. Marty, J. M. Sabatier, I. Jona, M. DeWaard, and M. Ronjat. 2003. Critical amino acid residues determine the binding affinity and the Ca^{2+} release efficacy of maurocalcine in skeletal muscle cells. *J. Biol. Chem.* 278:37823–37831.
14. Szappanos, H., S. Smida-Rezgui, J. Cseri, C. Simut, J. M. Sabatier, M. De Waard, L. Kovacs, L. Csernoch, and M. Ronjat. 2005. Differential effects of maurocalcine on Ca^{2+} release events and depolarization-induced Ca^{2+} release in rat skeletal muscle. *J. Physiol.* 565:843–853.
15. Pouvreau, S., L. Csernoch, B. Allard, J. M. Sabatier, M. De Waard, M. Ronjat, and V. Jacquemond. 2006. Transient loss of voltage control of Ca^{2+} release in the presence of maurocalcine in skeletal muscle. *Biophys. J.* 91:2206–2215.
16. Szentesi, P., J. Almássy, M. Fehér, B. Dienes, C. A. Simut, I. Jona, M. Ronjat, and L. Csernoch. 2006. Mutation in the scorpiotoxin maurocalcine alter its ability to modify the calcium release events in frog skeletal muscle. *J. Muscle Res. Cell Motil.* 27:516–517.
17. Merrifield, B. 1986. Solid phase synthesis. *Science*. 232:341–347.
18. Lai, F. A., and G. Meissner. 1990. Structure of the calcium release channel of skeletal muscle sarcoplasmic reticulum and its regulation by calcium. *Adv. Exp. Med. Biol.* 269:73–77.
19. Sarkozi, S., C. Szegedi, B. Lukacs, M. Ronjat, and I. Jona. 2005. Effect of gadolinium on the ryanodine receptor/sarcoplasmic reticulum calcium release channel of skeletal muscle. *FEBS J.* 272:464–471.
20. Lai, F. A., H. P. Erickson, E. Rousseau, Q. Y. Liu, and G. Meissner. 1988. Purification and reconstitution of the calcium release channel from skeletal muscle. *Nature*. 331:315–319.
21. Herrmann-Frank, A., M. Richter, S. Sarkozi, U. Mohr, and F. Lehmann-Horn. 1996. 4-Chloro-m-cresol, a potent and specific activator of the skeletal muscle ryanodine receptor. *Biochim. Biophys. Acta*. 1289:31–40.
22. Fabiato, A. 1988. Computer programs for calculating total from specified free or free from specified total ionic concentrations in aqueous solutions containing multiple metals and ligands. *Methods Enzymol.* 157:378–417.
23. Szentesi, P., V. Jacquemond, L. Kovacs, and L. Csernoch. 1997. Intramembrane charge movement and sarcoplasmic calcium release in enzymatically isolated mammalian skeletal muscle fibers. *J. Physiol.* 505:371–384.
24. Cheng, H., L. S. Song, N. Shirokova, A. Gonzalez, E. G. Lakatta, E. Rios, and M. D. Stern. 1999. Amplitude distribution of calcium sparks in confocal images: theory and studies with an automatic detection method. *Biophys. J.* 76:606–617.
25. Hidalgo, P., and R. MacKinnon. 1995. Revealing the architecture of a K^+ channel pore through mutant cycles with a peptide inhibitor. *Science*. 268:307–310.
26. Dudley, S. C., H. Todt, G. Lipkind, and H. A. Fozzard. 1995. A muconotoxin-insensitive Na^+ channel mutant: possible localization of a binding site at the outer vestibule. *Biophys. J.* 69:1657–1665.

27. Gurrola, G. B., C. Arevalo, R. Sreekumar, A. J. Lokuta, J. W. Walker, and H. H. Valdivia. 1999. Activation of ryanodine receptors by imperatoxin A and a peptide segment of the II–III loop of the dihydropyridine receptor. *J. Biol. Chem.* 274:7879–7886.

28. Mosbah, A., R. Kharrat, Z. Fajloun, J. G. Renisio, E. Blanc, J. M. Sabatier, M. El Ayeb, and H. Darbon. 2000. A new fold in the scorpion toxin family, associated with an activity on a ryanodine-sensitive calcium channel. *Proteins.* 40:436–442.

29. Lee, C. W., E. H. Lee, K. Takeuchi, H. Takahashi, I. Shimada, K. Sato, S. Y. Shin, D. H. Kim, and J. I. Kim. 2004. Molecular basis of the high-affinity activation of type 1 ryanodine receptors by imperatoxin A. *Biochem. J.* 377:385–394.

30. Shtifman, A., C. W. Ward, J. Wang, H. H. Valdivia, and M. F. Schneider. 2000. Effect of imperatoxin A on local sarcoplasmic reticulum Ca^{2+} release in frog skeletal muscle. *Biophys. J.* 79:814–827.

31. Altafaj, X., W. Cheng, E. Estève, J. Urbani, D. Grunwald, J. M. Sabatier, R. Coronado, M. DeWaard, and M. Ronjat. 2005. Maurocalcine and domain A of the II–III loop of the dihydropyridine receptor Cav 1.1 subunit share common binding sites on the skeletal ryanodine receptor. *J. Biol. Chem.* 280:4013–4016.

32. Meissner, G., and A. el-Hashem. 1992. Ryanodine as a functional probe of the skeletal muscle sarcoplasmic reticulum Ca^{2+} release channel. *Mol. Cell. Biochem.* 114:119–123.

33. Gonzalez, A., W. G. Kirsch, N. Shirokova, G. Pizarro, G. Brum, I. N. Pessah, M. D. Stern, H. Cheng, and E. Rios. 2000. Involvement of multiple intracellular release channels in calcium sparks of skeletal muscle. *Proc. Natl. Acad. Sci. USA.* 97:4380–4385.

34. Almassy, J., M. Sztretye, B. Lukacs, B. Dienes, L. Szabo, P. Szentesi, G. Vassort, L. Csernoch, and I. Jona. 2008. Effects of K-201 on the calcium pump and calcium release channel of rat skeletal muscle. *Pflugers Arch.* 10.1007/s00424–008–0504–7.

szentesi.peter_292_24

International Journal of
Molecular Sciences

MDPI

Article

Calcium Homeostasis Is Modified in Skeletal Muscle Fibers of Small Ankyrin1 Knockout Mice

Enrico Pierantozzi [1,†], Péter Szentesi [2,†], Dána Al-Gaadi [2,3], Tamás Oláh [2], Beatrix Dienes [2], Mónika Sztretye [2], Daniela Rossi [1], Vincenzo Sorrentino [1] and László Csernoch [2,*]

1 Department of Molecular and Developmental Medicine, Molecular Medicine Section, University of Siena, 53100 Siena, Italy
2 Department of Physiology, Medical Faculty, University of Debrecen, H-4002 Debrecen, Hungary
3 Doctoral School of Molecular Medicine, University of Debrecen, H-4002 Debrecen, Hungary
* Correspondence: csl@edu.unideb.hu
† These authors contribute equally to this work.

Received: 8 May 2019; Accepted: 4 July 2019; Published: 9 July 2019



Abstract: Small Ankyrins (sAnk1) are muscle-specific isoforms generated by the *Ank1* gene that participate in the organization of the sarcoplasmic reticulum (SR) of striated muscles. Accordingly, the volume of SR tubules localized around the myofibrils is strongly reduced in skeletal muscle fibers of 4- and 10-month-old sAnk1 knockout (KO) mice, while additional structural alterations only develop with aging. To verify whether the lack of sAnk1 also alters intracellular Ca^{2+} handling, cytosolic Ca^{2+} levels were analyzed in stimulated skeletal muscle fibers from 4- and 10-month-old sAnk1 KO mice. The SR Ca^{2+} content was reduced in sAnk1 KO mice regardless of age. The amplitude of the Ca^{2+} transients induced by depolarizing pulses was decreased in myofibers of sAnk1 KO with respect to wild type (WT) fibers, while their voltage dependence was not affected. Furthermore, analysis of spontaneous Ca^{2+} release events (sparks) on saponin-permeabilized muscle fibers indicated that the frequency of sparks was significantly lower in fibers from 4-month-old KO mice compared to WT. Furthermore, both the amplitude and spatial spread of sparks were significantly smaller in muscle fibers from both 4- and 10-month-old KO mice compared to WT. These data suggest that the absence of sAnk1 results in an impairment of SR Ca^{2+} release, likely as a consequence of a decreased Ca^{2+} store due to the reduction of the SR volume in sAnk1 KO muscle fibers.

Keywords: sarcoplasmic reticulum; sAnk1; calcium release; spark

1. Introduction

The sarcoplasmic reticulum (SR) of skeletal muscle fibers is a convoluted organelle consisting of a network of membrane-limited tubules where Ca^{2+} is stored. Two distinct SR regions can be described: the longitudinal SR (l-SR) and the junctional SR (j-SR). The l-SR surrounds each myofibril throughout its entire length and represents the major site for Ca^{2+} uptake from the cytosol due to the presence of the sarco/endoplasmic reticulum Ca^{2+}-ATPase (SERCA) pumps. The j-SR is formed by the so-called terminal cisternae that are connected to the l-SR tubules. In skeletal muscle, two terminal cisternae are positioned on opposite sides of a transverse (T)-tubule, an in-folding of the sarcolemma, to form the triad. The membrane of the terminal cisternae facing the T-tubule accommodates the ryanodine receptor (RyR1) Ca^{2+} release channels, and additional SR proteins, including triadin, junctin, and calsequestrin, which, together with RyR1 channels, participate in the mechanisms of excitation–contraction (e–c) coupling. This mechanism transduces depolarization-induced activation of the dihydropyridine receptor (DHPR), the voltage sensor on T-tubules, into a release of Ca^{2+} from the SR to allow muscle contraction [1]. Alterations of this mechanism are associated with different skeletal muscle diseases

szentesi.peter_292_24

in humans [2–5], including Central and Multi Mini Core Disease, and centronuclear myopathies associated with mutations in RyR and myotubularin, respectively [6–8].

The correct positioning of the SR around myofibrils and the connection with T-tubules are essential for the efficient regulation of muscle contraction [9]. Ankyrins are a family of protein adaptors involved in the organization of specialized membrane domains. All three ankyrin genes (*Ank1*, *Ank2* and *Ank3*) encode, through multiple splicing events, a large number of ankyrin isoforms that share a common general structure [10]. Interestingly, in striated muscles, all three ankyrin genes code for muscle-specific isoforms [11–14]. In particular, in addition to the high molecular weight (220–130 kDa) that ankyrin isoforms present in most tissues, an internal promoter in the *Ank1* gene drives the expression of small muscle-specific isoforms of 20–25 kDa, collectively known as sAnk1 isoforms (sAnk1.5, sAnk1.6, sAnk1.7 and sAnk1.9). These sAnk1 isoforms lack most of the canonical ankyrin domains and contain a unique hydrophobic domain at their NH_2-terminal, which localizes them in the SR [15–18]. Among these short muscle isoforms, sAnk1.5 is the most abundantly expressed, while the other isoforms are expressed at lower levels [19]. sAnk1.5 contains, within its cytoplasmic tail, a specific sequence that allows direct binding to obscurin [20,21], a sarcomeric protein required for the maintenance of M-band stability in skeletal muscle [22–25]. The interaction between sAnk1.5 and obscurin is crucial to maintain the SR in close proximity to the myofibrils [26]. Knockdown of sAnk1 isoforms in primary cultures of rat *flexor digitorum brevis* (FDB) resulted in a loss of anastomosis within tubules of the l-SR, while the organization of the j-SR was only barely affected [27]. In agreement with this observation, the more recent characterization of the sAnk1 knockout (KO) mouse, an animal model where sAnk1 expression is completely abolished, showed that the lack of sAnk1 results in a significant reduction of the SR volume, although RyRs and SERCA protein levels and localization did not differ in fibers from both fast and slow muscles of sAnk1 KO and WT mice [28]. Notably, almost identical alterations in SR morphology were also observed in skeletal muscle fibers from obscurin KO mice, confirming the relevance of the interaction between sAnk1 and obscurin in preserving SR architecture [29]. Further analysis revealed that, with age, fibers from sAnk1 KO mice developed structural damage of contractile elements, large areas of contracture and tubular aggregates containing SR proteins such as calsequestrin, SERCA1 and triadin, all involved in Ca^{2+} handling. These structural alterations were accompanied by an impairment of electrophysiological properties and force generation in sAnk1 KO muscles [28]. This evidence is consistent with a previous work reporting that cultured fibers where sAnk1 had been knocked down displayed a reduced Ca^{2+} release from the SR [27], indicating that structural alterations generated by the absence or reduced expression of sAnk1 may result in impaired Ca^{2+} handling. However, whether the deletion of sAnk1 also affects Ca^{2+} homeostasis in skeletal muscle fibers with respect to the phenotypes observed in young and old KO mice is far less known. Here, we report results from the analysis of Ca^{2+} fluxes in FDB fibers of sAnk1 KO mice, showing that fibers from KO mice have altered Ca^{2+} transients, and less frequent and smaller spontaneous Ca^{2+} release events compared to WT mice.

2. Results

2.1. Decreased SR Ca^{2+} Content in Skeletal Muscle Fibers from sAnk1 KO Mice

The effects of the deletion of sAnk1 on Ca^{2+} homeostasis were examined in single FDB fibers isolated from 4- and 10-month-old mice. At first, we measured the resting $[Ca^{2+}]_i$ in unstimulated Fura-2 loaded FDB fibers from sAnk1 KO and WT mice. These measurements indicated that the resting Ca^{2+} levels were not significantly different in both 4- and 10-month-old FDB fibers from sAnk1 KO mice compared to WT mice (Figure 1C). In Figure 1A, representative Ca^{2+} transients following treatment with a releasing cocktail in a calcium-free extracellular solution are reported. The removal of Ca^{2+} from the extracellular solution occasionally depolarized the fibers, resulting in a slight increase in $[Ca^{2+}]_i$. The application of the releasing cocktail to muscle fibers from WT mice resulted in a large Ca^{2+} transient that decreased even in the continued presence of the cocktail, as a consequence of store emptying

szentesi.peter_292_24

(Figure 1A). On the contrary, the average change in the amplitude of Ca^{2+} transients ($\Delta[Ca^{2+}]_i$) was significantly smaller in fibers from 4- and 10-month-old KO mice with respect to age-matched control mice (Figure 1A,B), suggesting that the total SR Ca^{2+} content in sAnk1 KO mice is lower than that in WT mice.

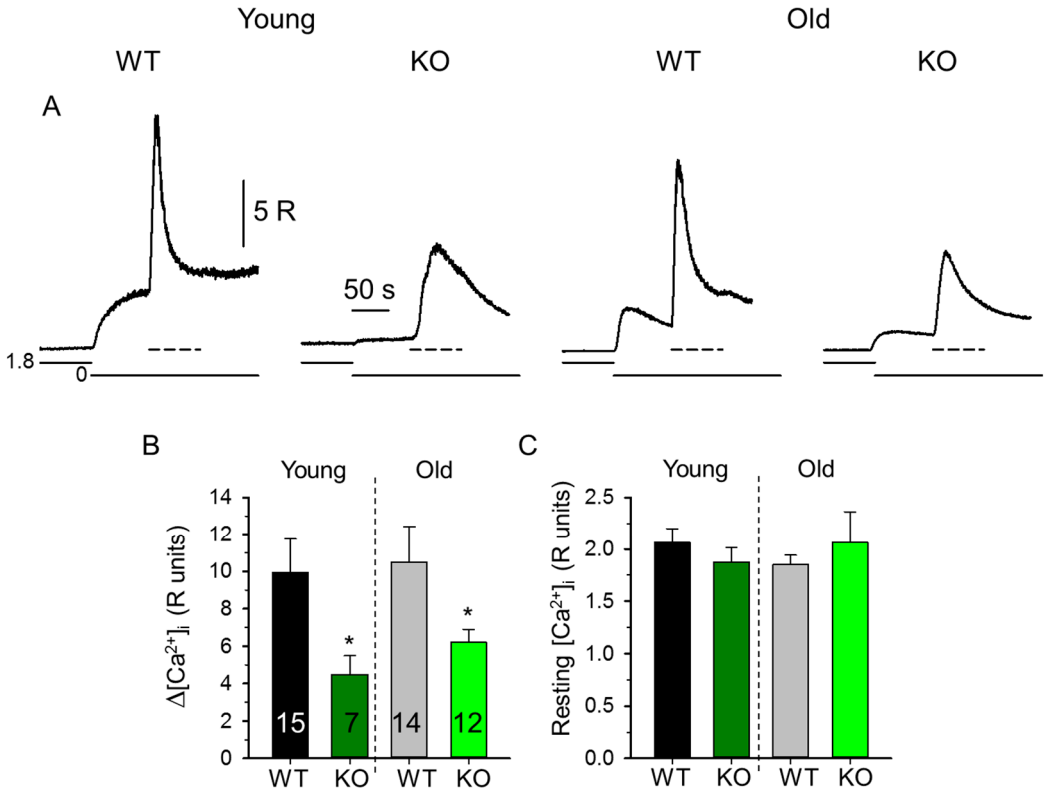


Figure 1. Decreased Ca^{2+} transients in *flexor digitorum brevis* (FDB) fibers from small ankyrin1 (sAnk1) knockout (KO) mice. (**A**) Representative depletion cocktail evoked Ca^{2+} transients measured on fibers isolated from the FDB muscles of 4- and 10-month-old wild type (WT) and sAnk1 KO mice. Pooled data for resting $[Ca^{2+}]_i$ (**C**), and maximal increase in $[Ca^{2+}]_i$ (**B**). The protocol of the solution exchange in panel A was: 0–70 s normal Tyrode's solution (1.8, solid line), 70–300 s Ca^{2+}-free Tyrode's with 5 mM EGTA (0, solid line), 150–220 s releasing cocktail (200 μM 4-chloro-M-cresol and 10 μM cyclopiazonic acid) in Ca^{2+}-free Tyrode's (dashed line). Numbers in columns show the number of fibers averaged. The number of animals in groups varied between 3 and 4. * denotes significant difference from WT at $p < 0.05$.

We next induced changes in $[Ca^{2+}]_i$ under whole-cell voltage-clamp by progressively increasing membrane depolarization between −60 mV and +30 mV (Figures 2 and 3). As shown in Figure 2A,B,D, the average change in the amplitude of Ca^{2+} transients in 4-month-old mice was significantly smaller in fibers from sAnk1 KO mice than from WT mice. When similar experiments were performed with 10-month-old mice (Figure 3A), a small difference between fibers from sAnk1 KO mice and WT was still observed, but it did not reach statistical significance (Figure 3B,D). Similarly, when the total amount of Ca^{2+} released during the depolarizing pulse at +30 mV was calculated, a significant difference between sANK1 KO mice and WT mice was observed in 4-month-old mice, but not in 10-month-old mice (Figures 2E and 3E).

szentesi.peter_292_24

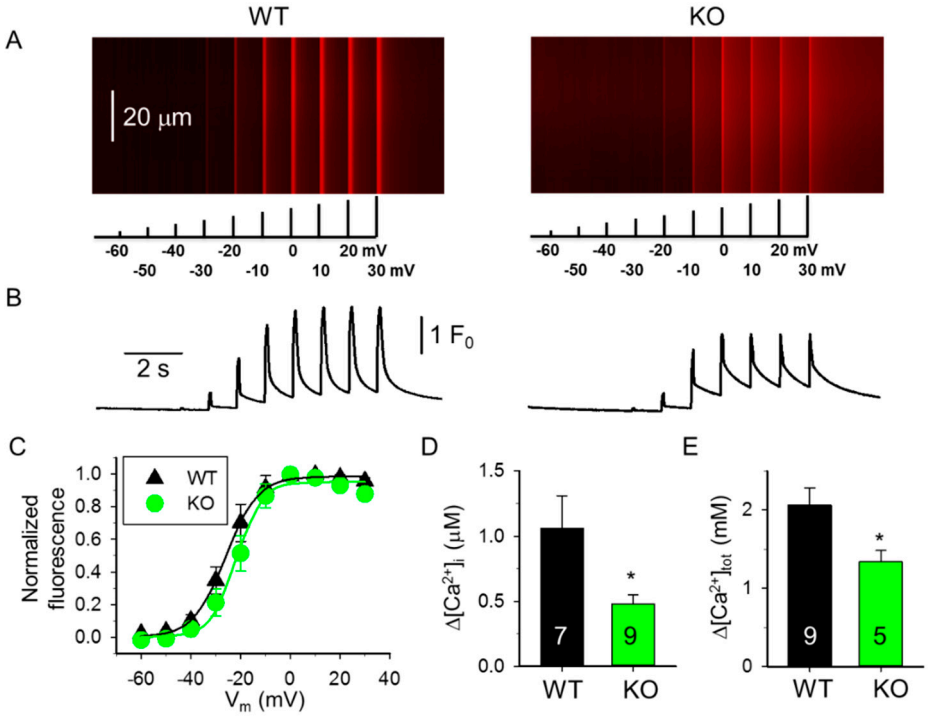


Figure 2. Membrane potential dependence of changes in $[Ca^{2+}]_i$ in fibers from 4-month-old WT and sAnk1 KO mice. (**A**) Line-scan images of changes in $[Ca^{2+}]_i$ elicited under whole-cell voltage-clamp by 100 ms long progressively increasing membrane depolarizations ranging between −60 mV and +30 mV, with 10 mV increments every 500 ms in WT and KO fibers. Each cell was held at −80 mV and perfused with 10 mM EGTA. The scale bar in the left panel corresponds to both line-scans. (**B**) Temporal profile of the changes in $[Ca^{2+}]_i$ calculated from the corresponding images in panel A by averaging 50 lines in the spatial domain normalized to average resting $F_0(x)$. (**C**) Voltage dependence of the changes in $[Ca^{2+}]_i$. Values obtained for individual fibers were first fitted by a Boltzmann function (Equation (1)) and then normalized to the obtained maximum for a given fiber, and finally averaged over the fibers. Continuous lines represent the best fit of the Boltzmann function to the average values with parameters of k = 8.95 and 6.17 mV, and V_{50} = −21.60 and −20.91 mV, for WT (n = 10) and KO (n = 9), respectively. (**D**,**E**) Pooled data for $\Delta[Ca^{2+}]_i$ (**D**) and the total amount of Ca^{2+} released (**E**) at +30 mV depolarization from four WT and five KO mice. To assess the peak change in $[Ca^{2+}]_i$ (**D**) and the amount of Ca^{2+} released (**E**), 100 ms and 1 s long single pulses were used, respectively. Numbers in columns show the number of fibers averaged. * denotes significant difference from WT at $p < 0.05$.

The voltage dependence of the transients was only slightly affected by sAnk1 deletion in both 4-month-old mice (Figure 2C) and 10-month-old mice (Figure 3C), although it was less steep in the older mice. Interestingly, the midpoint voltage of the Boltzmann curves was shifted by almost 20 mV to the right, i.e., to more positive voltages, in both 10-month-old mice groups (Table 1).

Table 1. Parameters describing the voltage dependence of the depolarizing pulse-evoked Ca^{2+} transients in WT and sAnk1 KO fibers.

Boltzmann Parameters †	WT 4-Month-Old (4 Mice) (9 Fibers)	KO 4-Month-Old (5 Mice) (9 Fibers)	WT 10-Month-Old (4 Mice) (9 Fibers)	KO 10-Month-Old (4 Mice) (9 Fibers)
max	1.91 ± 0.27	1.11 ± 0.19 *	1.61 ± 0.34	1.39 ± 0.32
k (mV)	7.25 ± 1.09	5.57 ± 0.85	5.88 ± 0.92	8.67 ± 1.16 #
V_{50} (mV)	−21.84 ± 4.96	−20.68 ± 2.97	−4.76 ± 4.44 #	−3.62 ± 6.17 #

† Parameters were obtained by fitting the voltage dependence of the individual fibers using Equation (1). * indicates significant difference from WT at $p < 0.05$. # indicates significant difference from young mice from the same genetic background at $p < 0.05$.

szentesi.peter_292_24

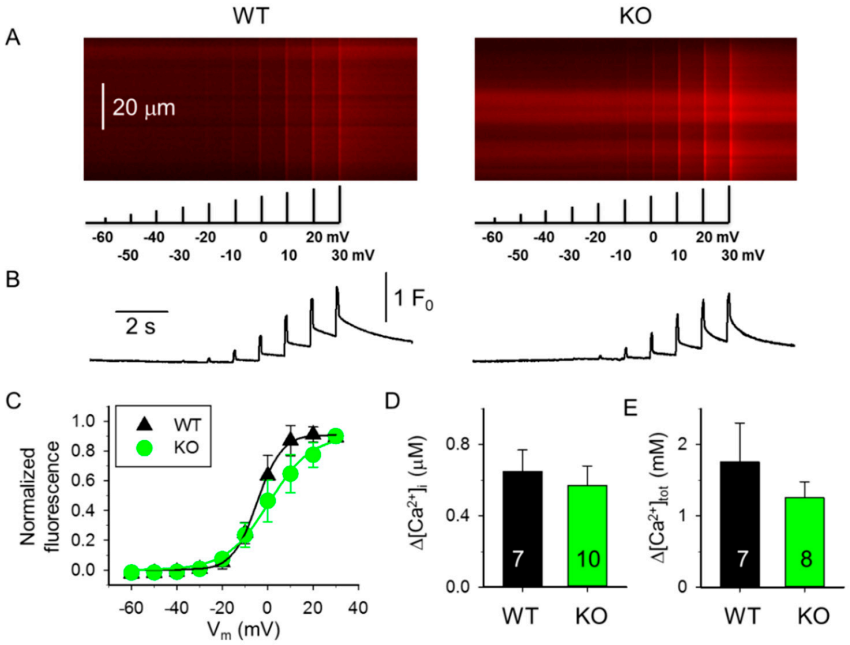


Figure 3. Membrane potential dependence of changes in $[Ca^{2+}]_i$ in 10-month-old WT and sAnk1 KO mice. (**A**) Line-scan images of changes in $[Ca^{2+}]_i$ elicited by the same depolarization protocol as in Figure 2. The scale bar in the left panel corresponds to both line-scans. (**B**) Temporal profile of the changes in $[Ca^{2+}]_i$ calculated from the corresponding images in panel A. (**C**) Voltage dependence of the changes in $[Ca^{2+}]_i$. Values were obtained as described for Figure 2C. Continuous lines represent the best fit of the Boltzmann function to the average values with parameters of k = 8.09 and 14.67 mV, and V_{50} = −5.94 and −7.86 mV, for WT (n = 9) and KO (n = 9), respectively. (**D**,**E**) Pooled data for $\Delta[Ca^{2+}]_i$ (**D**) and amount of Ca^{2+} released (**E**) at +30 mV depolarization for three WT and five KO mice. To assess the peak change in $[Ca^{2+}]_i$ (**D**) and the amount of Ca^{2+} released (**E**), 100 ms and 1 s long single pulses were used, respectively. Numbers in columns show the number of fibers averaged.

To evaluate whether the reduced Ca^{2+} transients observed following treatment with the releasing cocktail or induced by membrane depolarization may have resulted from a decreased Ca^{2+} transport by SERCA pumps, the maximal transport rate (V_{max}) was calculated in fibers from WT and sAnk1 KO mice. This analysis revealed that the V_{max} progressively reduced in old mice compared to young animals, in both WT and sAnk1 KO mice (p = 0.0057 and $p < 0.0001$, respectively). In addition, in old sAnk1 KO mice the V_{max} was significantly lower compared to WT (1.68 ± 0.31 and 3.13 ± 0.49 mM s^{-1}, n = 9 and 8, respectively; p = 0.028). This suggests that the remarkable but not statistically significant reduction in Ca^{2+} transients observed with age may be partially explained by a lower SERCA pump activity. However, the difference in Ca^{2+} transients observed between WT and sAnk1 KO muscle fibers at 4 months of age cannot be ascribed to SERCA pumps, since no difference could be observed between the two genotypes at this age (4.72 ± 0.08 and 4.79 ± 0.07 mM s^{-1}, respectively; p = 0.54, n = 9 in both groups).

2.2. Spontaneous Ca^{2+} Release Events (CREs) Are Reduced in sAnk1 KO Mice

The measurement of spontaneous Ca^{2+} release events in saponin-permeabilized muscle fibers offers the possibility to study the functional properties of RyR1 in its native environment, independently from the control of the DHPR [30,31]. We used this method to test whether the lack of sAnk1 would affect the spontaneous Ca^{2+} release activity from the SR. Spontaneous CREs were measured using confocal XY imaging in fluo-3 loaded fibers isolated from 4- and 10-month-old KO and WT mice. Events shown in Figure 4 represent the cumulated CRE activity recorded during a series of 120 consecutive images, covering a period of approximately 20 s.

szentesi.peter_292_24

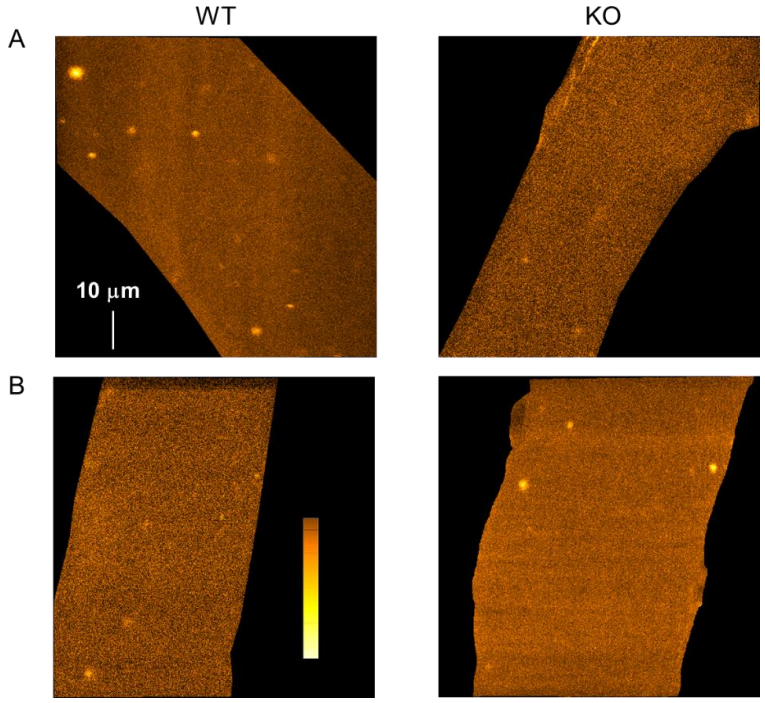


Figure 4. Spontaneous Ca^{2+} release events in saponin-permeabilized FDB fibers. Representative composite XY images from 4-month-old (**A**) and 10-month-old (**B**) WT (left panels) and sAnk1 KO (right panels) mice. Changes in $[Ca^{2+}]_i$ were visualized by loading the fibers with fluo-3. Each image is the composite of 120 images recorded with a frequency of 16 Hz. The scale bar in the top left image corresponds to all images. The color bar in the bottom left image corresponds to all images. Lighter colors represent a higher change in $[Ca^{2+}]_i$.

Single XY images and CREs from 4- and 10-month-old mice are shown on an enlarged scale in Figures 5A and 6A, respectively. A significant reduction in the frequency of CREs was detected in fibers from 4-month-old sAnk1 KO mice as compared to age-matched WT mice (Figure 5B, Table 2). The frequency of CREs declines in fibers from 10-month-old WT mice, and no further difference was observed between KO and WT mice (Figure 6B, Table 2).

Table 2. Parameters of CREs in WT and sAnk1 KO fibers.

	WT 4-Month-Old (3 Mice) (43 Fibers)	**KO 4-Month-Old (9 Mice) (87 Fibers)**	**WT 10-Month-Old (3 Mice) (76 Fibers)**	**KO 10-Month-Old (4 Mice) (105 Fibers)**
Number of sparks	1084	1231	1063	1646
Amplitude (F/F_0)	0.216 ± 0.005	0.158 ± 0.003 ***	0.205 ± 0.006	0.171 ± 0.003 ***,##
FWHM-x (μm)	2.239 ± 0.023	2.048 ± 0.020 ***	2.312 ± 0.025 #	1.972 ± 0.020 ***,##
FWHM-y (μm)	1.968 ± 0.020	1.784 ± 0.017 ***	1.991 ± 0.022	1.761 ± 0.017 ***
Signal mass (SM) (μm^3)	3.195 ± 0.130	1.852 ± 0.090 ***	2.909 ± 0.124	1.996 ± 0.088 ***
Frequency ($mm^{-2}\ s^{-1}$)	65.8 ± 13.8	28.8 ± 8.6 *	35.0 ± 5.7 #	39.1 ± 6.9

* and *** indicate significant difference from WT at $p < 0.05$ and $p < 0.001$, respectively. # and ## indicate significant difference from young mice from the same genetic background at $p < 0.05$ and $p < 0.01$, respectively.

szentesi.peter_292_24

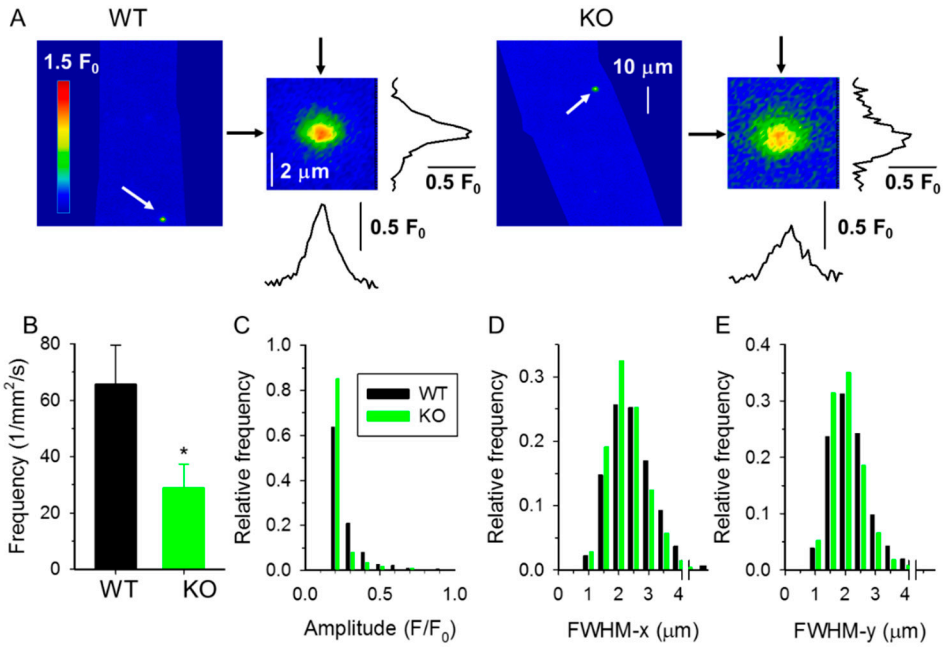


Figure 5. Parameters of Ca^{2+} release events in 4-month-old WT and sAnk1 KO mice. (**A**) A single XY image of normalized fluorescence (F/F_0). The images were obtained by selecting one image from a series (as presented in Figure 4) and normalizing to baseline fluorescence (F_0) after removing the background (determined outside of the fiber). Enlarged portions (black arrows) present the Ca^{2+} release events (CREs) marked in the original image together with their spatial profiles parallel (x) or perpendicular (y) to the longitudinal axis of the fiber. (**B**–**E**) Pooled data for CRE frequency (**B**), amplitude (**C**), and full width at half maximum (FWHM) in x (**D**) and in y (**E**) directions for WT (number of events, n = 1084) and KO (n = 1231) fibers.

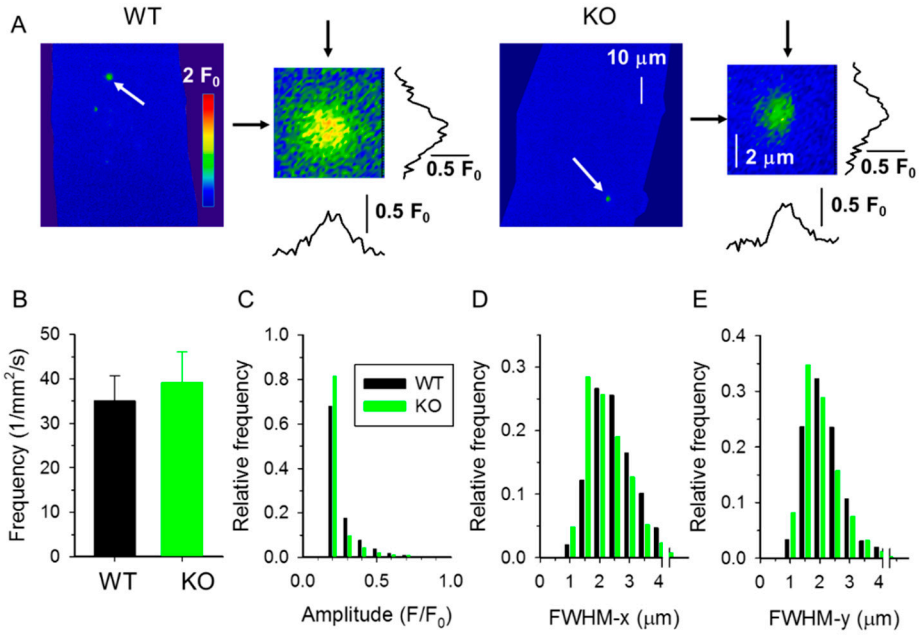


Figure 6. Parameters of Ca^{2+} release events in 10-month-old WT and sAnk1 KO mice. (**A**) A single XY image of normalized fluorescence (F/F_0). The images were obtained as described for Figure 5A. (**B**–**E**) Pooled data for CREs frequency (**B**), amplitude (**C**), and FWHM in x (**D**) and in y (**E**) directions for WT (number of events, n = 1063) and KO (n = 1646) fibers.

We next analyzed the mean CRE amplitude (F/F_0) and observed a significant decrease in 4- and 10-month-old KO mice compared to their age-matched WT counterparts (Table 2). The analysis of the distribution of the amplitude of CREs revealed a higher frequency of CREs with a small amplitude in KO fibers compared to age-matched WT fibers (Figures 5C and 6C). When the spatial widths of CREs, namely full widths at half maximum (FWHMs) perpendicular to, and parallel to, the Z-lines (i.e., FWHM-x and FWHM-y) were analyzed, a significant reduction of these parameters was observed in fibers from both 4- and 10-month-old KO mice (Table 2), with an increased number of small CREs in fibers from KO mice (Figure 5D,E, and Figure 6D,E). These alterations were clearly reflected in the calculated amount of Ca^{2+} released, estimated as the Signal Mass (SM) during the CREs. As reported in Table 2, the absence of sAnk1 was accompanied by a marked reduction in SM, independently of the age of the mice. These data indicate that there is either a reduction in the Ca^{2+} available for immediate release in the SR or an impaired opening of the Ca^{2+} release channels, or both.

3. Discussion

In skeletal muscle fibers, the SR has acquired specific morphological adaptations to efficiently sustain Ca^{2+} release for muscle contraction [1,32,33]. In particular, sAnk1, localized on the SR membrane, binds to the sarcomeric giant protein obscurin. This protein–protein interaction is necessary for the accurate positioning of the SR tubules, where Ca^{2+} is stored, around the myofibrils, in order to regulate muscle contraction. We previously showed that a lack of sAnk1 results in SR volume reduction in 4-month-old mice, with the appearance of contractures, tubular aggregates and myofibrillar disarray in aging sAnk1 KO mice. All these events are compatible with imbalanced intracellular Ca^{2+} levels [25], which, with age, may lead to the muscle damage observed in old animals.

In this study, we investigated the effect of deletion of sAnk1 on Ca^{2+} homeostasis in skeletal muscle fibers from 4- and 10-month-old sAnk1 KO mice. Our results indicate that total SR Ca^{2+} content was reduced in 4- and 10-month-old sAnk1 KO mice compared to age-matched WT mice, as revealed by the use of a releasing cocktail. Ca^{2+} transients induced in voltage-clamped fibers were reduced also in muscle from 4- but not from 10-month-old sAnk1 KO mice, compared to those from age-matched WT mice. Indeed, the amplitude of Ca^{2+} transients in 10-month-old WT mice was reduced compared to that observed in 4-month-old WT mice. This is in agreement with previously reported data indicating that aging leads to a physiological decline of Ca^{2+} release from the SR [34]. On the contrary, voltage-induced Ca^{2+} transients in fibers from 4-month-old sAnk1 KO mice were similar to those obtained from fibers isolated from 10-month-old sAnk1 KO mice. This is not surprising since the amplitude of Ca^{2+} transients in 4-month-old sAnk1 KO mice was reduced compared to that of age-matched WT mice. The voltage-induced Ca^{2+} transients measured in 10-month-old sAnk1 mice were comparable to those observed in 10-month-old WT mice. These results are consistent with the finding that sAnk1 KO mice show a reduction in the SR volume already in young animals, which may explain the decrease in the amplitude of Ca^{2+} transients. Interestingly, the voltage dependence of SR Ca^{2+} release was not affected in sAnk1 KO fibers, suggesting that the altered Ca^{2+} release observed in sAnk1 KO fibers might reflect a reduction of the Ca^{2+} store, likely due to the decrease in l-SR volume observed in sAnk1 KO mice [28], rather than to a defect in the DHPR-induced RYR1 activation.

An additional piece of evidence suggesting a reduction of the Ca^{2+} store in skeletal muscle fibers from sAnk1 KO mice was obtained by measuring CRE parameters. CREs represent elementary events of Ca^{2+} release through RyR1 channels, activated by cytosolic and/or luminal Ca^{2+} [35]. Results obtained with saponin-permeabilized fibers, which represent an experimental model where luminal Ca^{2+} content is the most relevant driving force for sparks to occur, clearly showed that the amplitude, spatial spread and frequency of CREs were all reduced in muscle fibers from KO mice compared to WT. In addition, signal mass values calculated from spark parameters, which in turn represent an indirect assessment of the Ca^{2+} released [36], were significantly lower in sAnk1 KO fibers, further supporting a decreased Ca^{2+} content in the SR of fibers lacking sAnk1. Given that RyRs have a calcium sensor

szentesi.peter_292_24

on their luminal side which, if occupied, stimulates the opening of the channel [37], it is possible to envisage that the reduced SR content might be responsible for the reduced spark frequency.

Furthermore, the indirect measurement of SERCA pump activity in WT and sAnk1 KO mice did not reveal a significant difference between the two genotypes in young animals. Only in 10-month-old sAnk1 KO mice, the V_{max} of SERCA pump resulted to be significantly decreased. Considering that the reduction in SR volume is comparable between young and old sAnk1 KO mice, the marked decrease in SERCA pump activity observed in 10-month-old sAnk1 KO mice may not be caused by the SR morphology nor by a loss of interaction between sAnk1.5 and SERCA and/or sarcolipin [38,39], but it may rather result from the structural alterations observed in skeletal muscles of old sAnk1 KO mice [28], although yet unidentified additional cues cannot actually be ruled out. Alternatively, compensatory events that may be active in young sAnk1 KO mice may no longer suffice in 10-month-old sAnk1 KO mice.

In conclusion, our results show that the deletion of sAnk1.5 results in an impairment of Ca^{2+} homeostasis in skeletal muscle fibers of young sAnk1 KO mice, compared to age-matched controls. The observed difference in Ca^{2+} homeostasis becomes less evident when, with age, Ca^{2+} release efficiency also decreases in the skeletal muscle of old WT mice [34]. This suggests that in young sAnk1 KO mice Ca^{2+} handling is already compromised at levels comparable to those observed in old WT mice. On the other hand, with age, KO mice develop structural alterations, like tubular aggregates and contractures that are not present in WT mice. Future work is required to better address the mechanisms affected by the deletion of sAnK1, impaired Ca^{2+} homeostasis and the development of structural alterations.

4. Materials and Methods

4.1. Animal Care

The generation of sAnk1 KO mice has been described in Giacomello et al. [28]. The mouse colony was maintained by intercrossing heterozygous mice, and the genotype of the progeny was determined by polymerase chain reaction as previously described [28]. The experiments were carried out on sAnk1 KO and littermate wild type mice weighing 20–30 g. The animals were kept under standard laboratory conditions (12 h light/dark cycle, room temperature 22–25 °C) with free access to tap water and pelleted mouse chow in their plastic cages, which have mesh covers. Animal experiments followed the guidelines of the European Community (86/609/EEC) and the experimental protocol (31/2012/DE MAB) was approved by the institutional Animal Care Committee of the University of Debrecen.

Animals were anaesthetized and sacrificed following a protocol (22/2011/DE MÁB, 2012) approved by the Animal Care Committee of the University of Debrecen. After pentobarbital anesthesia (27 mg/kg) and cervical dislocation, the *m. flexor digitorum brevis* from the hind limbs were dissected.

4.2. Isolation of Single Skeletal Muscle Fibers

All Ca^{2+} concentration measurements were carried out on skeletal muscle fibers from the FDB muscles of control (WT) and sAnk1 deficient (KO) male mice of both 4 and 10 months of age. Ca^{2+} free Tyrode's solution (in mM: 137 NaCl, 5.4 KCl, 0.5 $MgCl_2$, 1.8 $CaCl_2$, 11.8 Hepes-NaOH, 1 g/L glucose, pH 7.4) was used during the dissection of the muscle. Single muscle fibers from FDB were enzymatically dissociated in a minimal essential medium containing 0.2% Type I collagenase (Sigma, St Louis, MO, USA) at 37 °C for 35 min [37]. To obtain single intact fibers, FDB muscles were triturated gently in normal Tyrode's solution (1.8 mM $CaCl_2$). Fibers were then placed in culture dishes and stored at 4 °C in refrigerator until use.

4.3. Whole Cell Intracellular Ca^{2+} Concentration Measurements

Changes in intracellular Ca^{2+} concentration ($[Ca^{2+}]_i$) in different extracellular solutions were measured using a Fura-2 fluorescent calcium indicator as described previously [40]. Briefly, enzymatically

szentesi.peter_292_24

isolated single FDB fibers were mounted on a laminin-coated glass cover slip and loaded with 5 μM Fura-2 acetoxymethyl ester (AM) for 1 h. Fibers were then kept in normal Tyrode's solution for half an hour at room temperature. Measurements were carried out on an inverted fluorescence microscope (Nikon Diapoth, Nikon, Tokyo, Japan). A microcomputer-controlled dual-wavelength monochromator alternated the excitation wavelength with 50 Hz between 340 and 380 nm (Deltascan, Photon Technology International, New Brunswick, NJ, USA), whereas a photomultiplier measured the emission signal at 510 nm with a 10 Hz acquisition rate at room temperature. To measure SR Ca^{2+} content, isolated FDB fibers were permanently washed with Tyrode's solution using a background perfusion system, then a calcium-free Tyrode's solution with 5 mM EGTA was applied through a local perfusion system, which was positioned in close proximity to the selected fiber. Intracellular Ca^{2+} stores were emptied using a depleting cocktail (200 μM 4-chloro-M-cresol and 10 μM cyclopiazonic acid) in calcium-free Tyrode's resulting in a massive Ca^{2+}-release from the SR via RyRs. All solutions contained 50 μM BTS to minimize fiber movement artefacts during calcium release. $[Ca^{2+}]_i$ was assessed as the ratio of measured fluorescence intensities (F_{340}/F_{380}). Resting $[Ca^{2+}]_i$ was calculated from averaging the ratio in normal Tyrode's. The SR Ca^{2+} content was calculated as the difference between resting $[Ca^{2+}]_i$ and the maximum of the ratio measured during the application of the releasing cocktail.

4.4. Measurement of Ca^{2+} Release Events (CREs) in Permeabilized Muscle Fibers

Isolated FDB muscle fibers were permeabilized with saponin and loaded with 0.1 mM fluo-3 using experimental solutions and procedures previously described [41]. In brief, fibers were bathed in a relaxing solution (in mM: 6 $MgCl_2$, 5 Na_2-ATP, 125 K-glutamate, 10 HEPES, 1 EGTA, 0.13 $CaCl_2$, 10 glucose, 10 Na-phosphocreatine, pH 7.2) containing 0.002% saponin for 2–3 min. Permeabilization of the surface membrane by the detergent was monitored by imaging how the fluorescence of fluo-3 increases in the muscle fiber. This solution was then replaced by a recording solution (in mM: 6 $MgCl_2$, 5 Na_2-ATP, 95 K_2SO_4, 10 HEPES, 1 EGTA, 0.13 $CaCl_2$, 10 glucose, 10 Na-phosphocreatine, pH 7.2). Images were recorded with a 40× oil immersion objective (NA = 1.3) on a Zeiss LSM 5 LIVE laser scanning confocal microscope (Zeiss, Oberkochen, Germany). The 488 nm line of an argon laser excited fluo-3 in the fibers, and the emitted fluorescent light was collected above 505 nm wavelength. Fifteen minutes following the application of the recording solution, eight consecutive series of hundred and twenty 512 × 512 (x, y) images captured every 67 ms were collected in each tested fiber. CRE detection and analysis were performed using modified methods and algorithms previously described in [42]. In brief, the region of the background and the contour of the fiber were defined on the first image of each series. Then, the averaged background fluorescence calculated from the selected area was subtracted from each pixel of all images in one series. To detect the Z-lines in the fiber, the frequency spectrum in each line of all images was calculated using fast Fourier transform (FFT). Then, inverse FFT of the frequency components corresponding to sarcomeres was used to remove the Z-lines from the images. The stationary wavelet method with soft threshold filtering was used to detect Ca^{2+} release events on the fibers. Finally, the following spark parameters were calculated: the amplitude and two full widths at half maximum (FWHMs), perpendicular to (FWHM-x) and parallel with (FWHM-y) the Z-lines.

To assess the amount of Ca^{2+} released during a CRE, the Signal Mass (SM) was calculated as described in [43]. To estimate FWHM in the z direction (i.e., the optical axis), the average of the two FWHMs in the focal plane (x and y directions) was used.

4.5. Voltage Clamp and Ca^{2+} Transient Analysis

The experimental design was similar to the one described in [44]. Briefly, isolated fibers were voltage-clamped (Axoclamp 2B, Axon Instruments, Foster City, CA, USA) and imaged using a confocal microscope (Zeiss LSM 5 Live) in external solution (in mM: 140 TEA-CH_3SO_3, 1 $CaCl_2$, 3.5 $MgCl_2$, 10 Hepes, 1 4-Aminopyridine, 0.5 $CdCl_2$, 0.3 $LaCl_3$, 0.001 TTX, and 0.05 BTS, pH 7.2, osmolality 320 mOsm). Fibers were dialyzed with rhod-2 containing internal solution (in mM: 110

szentesi.peter_292_24

N-methylglucamine, 110 L-glutamic acid, 10 EGTA, 10 Tris, 10 glucose, 5 Na ATP, 5 phosphocreatine Tris, 0.1 rhod-2, 3.56 $CaCl_2$, and 7.4 mM $MgCl_2$, pH 7.2, osmolality 320 mOsm). All experiments were conducted at 20–22 °C and the resting holding potential was kept at −80 mV. The pipette resistance varied in the range of 1–2 MΩ. Analog compensation was used to correct the linear capacitive currents.

Ca^{2+} transients were analyzed by fitting a removal model that calculates release flux. This takes into account the evolution of $[Ca^{2+}]_i(t)$ in a single compartment including quantitatively specified processes of removal, such as the maximal rate of the SERCA pump (V_{max}) [45]. The experiments were performed in the presence of calcium buffer (10 mM EGTA), thus the endogenous buffers were considered almost negligible in the removal process. The Boltzmann function was used to describe the voltage dependence of the activation of Ca^{2+} release:

$$\Delta[Ca^{2+}]_{i,max}/(1 + \exp(-(V_m - V_{50})/k) \quad (1)$$

where V_{50} is the midpoint voltage and the reciprocal of k is the limiting logarithmic of the slope. Line-scan images were analyzed by a custom-made program using the following parameters: $K_{d\ rhod\text{-}2}$ = 18 μM and k_{ON} = 0.7 10^8 $M^{-1}s^{-1}$. From the release flux (the flux exiting through the release channels), the net flux leaving the SR can be derived by subtraction of the pump removal flux. The integral of the net flux provides the SR content releasable by depolarization or otherwise termed the amount of Ca^{2+} released ($\Delta[Ca^{2+}]_{tot}$).

4.6. Chemicals and Statistical Analysis

Chemicals, unless otherwise stated, were purchased from Sigma (St. Louis, MO, USA) and were of analytical grade.

Pooled data were expressed as mean ± standard error of the mean (SEM). The differences between control and sAnk1 KO mice with different ages were assessed using two-way analysis of variance (ANOVA) and all pairwise multiple comparison procedures (Student-Newman-Keuls Method) with Prism (GraphPad Software, San Diego, CA, USA). An f-test was used to test the significance and a *p* value of less than 0.05 was considered statistically significant.

Author Contributions: L.C. and V.S. designed the experiments; E.P. L.C. P.S. D.R. and V.S. wrote the manuscript, contributed to discussion and reviewed/edited the manuscript; E.P. and P.S. participated in CRE experiments; T.O. and D.A.-G. participated in whole cell Ca^{2+} experiments; B.D. and M.S. performed the patch clamp experiments; D.A-G.. and P.S. did the data and statistical analysis. All authors contributed to discussion, laboratory support, and reviewed/edited the manuscript.

Funding: This work was supported by grants from the Hungarian National Research, Development and Innovation Office (NKFIH K-115461), by the GINOP-2.3.2-15-2016-00040 project, and EFOP-3.6.2-16-2017-00006 to L. Csernoch, by the Italian Ministry of Health (grant RF-2013-02356787), and the Italian Ministry of Research (MIUR PRIN 2015 grant 2015ZZR4W3) to V. Sorrentino. Bolyai Janos Fellowship and ÚNKP-18-4-DE-157 to M. Sztretye.

Acknowledgments: The authors thank R. Ori for her excellent technical assistance. We thank Luanne L. Peters and the late Connie Birkenmeier, Jackson Laboratory, Bar Harbor, Maine for providing the original sAnk1 KO mice.

Conflicts of Interest: There is no conflict of interest between the authors and the results presented in this study.

References

1. Franzini-Armstrong, C. The relationship between form and function throughout the history of excitation–contraction coupling. *J. Gen. Physiol.* **2018**, *150*, 189–210. [CrossRef] [PubMed]
2. Dowling, J.J.; Lawlor, M.W.; Dirksen, R.T. Triadopathies: An emerging class of skeletal muscle diseases. *Neurotherapeutics.* **2014**, *11*, 773–785. [CrossRef] [PubMed]
3. Ríos, E.; Figueroa, L.; Manno, C.; Kraeva, N.; Riazi, S. The couplonopathies: A comparative approach to a class of diseases of skeletal and cardiac muscle. *J. Gen. Physiol.* **2015**, *145*, 459–474. [CrossRef] [PubMed]
4. Rossi, D.; Vezzani, B.; Galli, L.; Paolini, C.; Toniolo, L.; Pierantozzi, E.; Spinozzi, S.; Barone, V.; Pegoraro, E.; Bello, L.; et al. A Mutation in the CASQ1 Gene Causes a Vacuolar Myopathy with Accumulation of Sarcoplasmic Reticulum Protein Aggregates. *Hum Mutat.* **2014**, *35*, 1163–1170. [CrossRef] [PubMed]

szentesi.peter_292_24

5. Barone, V.; Del Re, V.; Gamberucci, A.; Polverino, V.; Galli, L.; Rossi, D.; Costanzi, E.; Toniolo, L.; Berti, G.; Malandrini, A.; et al. Identification and characterization of three novel mutations in the CASQ1 gene in four patients with tubular aggregate myopathy. *Hum Mutat.* **2017**, *38*, 1761–1773. [CrossRef] [PubMed]
6. Jungbluth, H.; Treves, S.; Zorzato, F.; Sarkozy, A.; Ochala, J.; Sewry, C.; Phadke, R.; Gautel, M.; Muntoni, F. Congenital myopathies: Disorders of excitation-contraction coupling and muscle contraction. *Nat Rev Neurol.* **2018**, *14*, 151–167. [CrossRef] [PubMed]
7. Smolenicka, Z.; Guerini, D.; Carafoli, E.; Kress, W.; Liechti-Gallati, S. Detection of a new polymorphism in the plasma-membrane Ca2+ ATPase isoform-3 gene and its exclusion as a candidate for X-linked myotubular myopathy (MTM1). *Hum. Genet.* **1996**, *98*, 681–684. [CrossRef]
8. Kutchukian, C.; Szentesi, P.; Allard, B.; Trochet, D.; Beuvin, M.; Berthier, C.; Tourneur, Y.; Guicheney, P.; Csernoch, L.; Bitoun, M.; et al. Impaired excitation-contraction coupling in muscle fibres from the dynamin2R465W mouse model of centronuclear myopathy. *J Physiol.* **2017**, *595*, 7369–7382. [CrossRef]
9. Sorrentino, V. Sarcoplasmic reticulum: Structural determinants and protein dynamics. *Int. J. Biochem. Cell Biol.* **2011**, *43*, 1075–1078. [CrossRef]
10. Bennett, V.; Chen, L. Ankyrins and cellular targeting of diverse membrane proteins to physiological sites. *Curr. Opin. Cell Biol.* **2001**, *13*, 61–67. [CrossRef]
11. Bennett, V.; Healy, J. Membrane Domains Based on Ankyrin and Spectrin Associated with Cell–Cell Interaction. *Cold Spring Harb. Perspect. Biol.* **2009**, *1*, a003012. [CrossRef] [PubMed]
12. Tee, J.M.; Peppelenbosch, M.P. Anchoring skeletal muscle development and disease: The role of ankyrin repeat domain containing proteins in muscle physiology. *Crit. Rev. Biochem. Mol. Biol.* **2010**, *45*, 318–330. [CrossRef] [PubMed]
13. Cunha, S.R.; Mohler, P.J. Ankyrin-based cellular pathways for cardiac ion channel and transporter targeting and regulation. *Semin. Cell Dev. Biol.* **2011**, *22*, 166–170. [CrossRef] [PubMed]
14. Randazzo, D.; Giacomello, E.; Lorenzini, S.; Rossi, D.; Pierantozzi, E.; Blaauw, B.; Reggiani, C.; Lange, S.; Peter, A.K.; Chen, J.; et al. Obscurin is required for ankyrinB-dependent dystrophin localization and sarcolemma integrity. *J Cell Biol.* **2013**, *200*, 523–536. [CrossRef] [PubMed]
15. Zhou, D.; Birkenmeier, C.S.; Williams, M.W.; Sharp, J.J.; Barker, J.E.; Bloch, R.J. Small, membrane-bound, alternatively spliced forms of ankyrin 1 associated with the sarcoplasmic reticulum of mammalian skeletal muscle. *J. Cell Biol.* **1997**, *136*, 621–631. [CrossRef] [PubMed]
16. Gallagher, P.G.; Forget, B.G. An alternate promoter directs expression of a truncated, muscle-specific isoform of the human ankyrin 1 gene. *J. Biol. Chem.* **1998**, *273*, 1339–1348. [CrossRef]
17. Kordeli, E.; Ludosky, M.A.; Deprette, C.; Frappier, T.; Cartaud, J. AnkyrinG is associated with the postsynaptic membrane and the sarcoplasmic reticulum in the skeletal muscle fiber. *J. Cell Sci.* **1998**, *1*, 2197–2207.
18. Tuvia, S.; Buhusi, M.L.; Davis, M.; Reedy, V. Bennett, Ankyrin-B Is Required for Intracellular Sorting of Structurally Diverse Ca^{2+} Homeostasis Proteins. *J. Cell Biol.* **1999**, *147*, 995–1008.
19. Armani, A.; Galli, S.; Giacomello, E.; Bagnato, P.; Barone, V.; Rossi, D.; Sorrentino, V. Molecular interactions with obscurin are involved in the localization of muscle-specific small ankyrin1 isoforms to subcompartments of the sarcoplasmic reticulum. *Exp. Cell Res.* **2006**, *312*, 3546–3558. [CrossRef]
20. Bagnato, P.; Barone, V.; Giacomello, E.; Rossi, D.; Sorrentino, V. Binding of an ankyrin-1 isoform to obscurin suggests a molecular link between the sarcoplasmic reticulum and myofibrils in striated muscles. *J. Cell Biol.* **2003**, *160*, 245–253. [CrossRef]
21. Kontrogianni-Konstantopoulos, A.; Jones, E.M.; Van Rossum, D.B.; Bloch, R.J. Obscurin is a ligand for small ankyrin 1 in skeletal muscle. *Mol. Biol. Cell* **2003**, *14*, 1138–1148. [CrossRef] [PubMed]
22. Kontrogianni-Konstantopoulos, A.; Catino, D.H.; Strong, J.C.; Sutter, S.; Borisov, A.B.; Pumplin, D.W.; Russell, M.W.; Bloch, R.J. Obscurin modulates the assembly and organization of sarcomeres and the sarcoplasmic reticulum. *FASEB J.* **2006**, *20*, 2102–2121. [CrossRef] [PubMed]
23. Randazzo, D.; Blaauw, B.; Paolini, C.; Pierantozzi, E.; Spinozzi, S.; Lange, S.; Chen, J.; Protasi, F.; Reggiani, C.; Sorrentino, V. Exercise-induced alterations and loss of sarcomeric M-line organization in the diaphragm muscle of obscurin knockout mice. *Am. J. Physiol.-Cell Physiol.* **2017**, *312*, C16–C28. [CrossRef] [PubMed]
24. Randazzo, D.; Pierantozzi, E.; Rossi, D.; Sorrentino, V. The potential of obscurin as a therapeutic target in muscle disorders. *Expert Opin. Ther. Targets.* **2017**, *21*, 897–910. [CrossRef] [PubMed]

szentesi.peter_292_24

25. Rossi, D.; Palmio, J.; Evilä, A.; Galli, L.; Barone, V.; Caldwell, T.A.; Policke, R.A.; Aldkheil, E.; Berndsen, C.E.; Wright, N.T.; et al. A novel FLNC frameshift and an OBSCN variant in a family with distal muscular dystrophy. *PLoS ONE* **2017**, *12*, e0186642. [CrossRef] [PubMed]
26. Barone, V.; Randazzo, D.; Del Re, V.; Sorrentino, V.D. Rossi, Organization of junctional sarcoplasmic reticulum proteins in skeletal muscle fibers. *J. Muscle Res. Cell Motil.* **2015**, *36*, 501–515. [CrossRef] [PubMed]
27. Ackermann, M.A.; Ziman, A.P.; Strong, J.; Zhang, Y.; Hartford, A.K.; Ward, C.W.; Randall, W.R.; Kontrogianni-Konstantopoulos, A.; Bloch, R.J. Integrity of the network sarcoplasmic reticulum in skeletal muscle requires small ankyrin 1. *J. Cell Sci.* **2011**, *124*, 3619–3630. [CrossRef] [PubMed]
28. Giacomello, E.; Quarta, M.; Paolini, C.; Squecco, R.; Fusco, P.; Toniolo, L.; Blaauw, B.; Formoso, L.; Rossi, D.; Birkenmeier, C.; et al. Deletion of small ankyrin 1 (sAnk1) isoforms results in structural and functional alterations in aging skeletal muscle fibers. *Am. J. Physiol.-Cell Physiol.* **2015**, *308*, C123–C138. [CrossRef] [PubMed]
29. Lange, S.; Ouyang, K.; Meyer, G.; Cui, L.; Cheng, H.; Lieber, R.L.; Chen, J. Obscurin determines the architecture of the longitudinal sarcoplasmic reticulum. *J. Cell Sci.* **2009**, *122*, 2640–2650. [CrossRef]
30. Kirsch, W.G.; Uttenweiler, D.; Fink, R.H. Spark- and ember-like elementary Ca^{2+} release events in skinned fibres of adult mammalian skeletal muscle. *J. Physiol.* **2001**, *537*, 379–389. [CrossRef] [PubMed]
31. Lukács, B.; Sztretye, M.; Almássy, J.; Sárközi, S.; Dienes, B.; Mabrouk, K.; Simut, C.; Szabó, L.; Szentesi, P.; De Waard, M.; et al. Charged surface area of maurocalcine determines its interaction with the skeletal ryanodine receptor. *Biophys. J.* **2008**, *95*, 3497–3509. [CrossRef]
32. Reggiani, C. Calcium handling in muscle fibers of mice and men: Evolutionary adaptation in different species to optimize performance and save energy. *J. Physiol.* **2014**, *592*, 1173–1174. [CrossRef]
33. Rossi, A.E.; Dirksen, R.T. Sarcoplasmic reticulum: The dynamic calcium governor of muscle. *Muscle Nerve* **2006**, *33*, 715–731. [CrossRef]
34. Jiménez-Moreno, R.; Wang, Z.M.; Gerring, R.C.; Delbono, O. Sarcoplasmic Reticulum Ca^{2+} Release Declines in Muscle Fibers from Aging Mice. *Biophys. J.* **2008**, *94*, 3178–3188. [CrossRef]
35. Cheng, H.; Lederer, W.J. Calcium Sparks. *Physiol. Rev.* **2008**, *88*, 1491–1545. [CrossRef]
36. Ríos, E.; Stern, M.D.; González, A.; Pizarro, G.; Shirokova, N. Calcium Release Flux Underlying Ca^{2+} Sparks of Frog Skeletal Muscle. *J. Gen. Physiol.* **1999**, *114*, 31–48. [CrossRef]
37. Burdakov, D.; Petersen, O.H.; Verkhratsky, A. Intraluminal calcium as a primary regulatorof endoplasmic reticulum function. *Cell Calcium* **2005**, *38*, 303–310. [CrossRef]
38. Desmond, P.F.; Muriel, J.; Markwardt, M.L.; Rizzo, M.A.; Bloch, R.J. Identification of Small Ankyrin 1 as a Novel Sarco(endo)plasmic Reticulum Ca^{2+}-ATPase 1 (SERCA1) Regulatory Protein in Skeletal Muscle. *J. Biol. Chem.* **2015**, *290*, 27854–27867. [CrossRef]
39. Desmond, P.F.; Labuza, A.; Muriel, J. Interactions between small ankyrin 1 and sarcolipin coordinately regulate activity of the sarco(endo)plasmic reticulum Ca^{2+}-ATPase (SERCA1). *J. Biol. Chem.* **2017**, *292*, 10961–10972. [CrossRef]
40. Fodor, J.; Gönczi, M.; Sztretye, M.; Dienes, B.; Oláh, T.; Szabó, L.; Csoma, E.; Szentesi, P.; Szigeti, G.P.; Marty, I.; et al. Altered expression of triadin 95 causes parallel changes in localized Ca^{2+} release events and global Ca^{2+} signals in skeletal muscle cells in culture. *J. Physiol.* **2008**, *586*, 5803–5818. [CrossRef]
41. Csernoch, L.; Pouvreau, S.; Ronjat, M.; Jacquemond, V. Voltage-activated elementary calcium release events in isolated mouse skeletal muscle fibers. *J. Membr. Biol.* **2008**, *226*, 43–55. [CrossRef]
42. Szabó, L.Z.; Vincze, J.; Csernoch, L.; Szentesi, P. Improved spark and ember detection using stationary wavelet transforms. *J. Theor. Biol.* **2010**, *264*, 1279–1292. [CrossRef]
43. Hollingworth, S.; Peet, J.; Chandler, W.K.; Baylor, S.M. Calcium sparks in intact skeletal muscle fibers of the frog. *J. Gen. Physiol.* **2001**, *118*, 653–678. [CrossRef]
44. Royer, L.; Pouvreau, S.; Ríos, E. Evolution and modulation of intracellular calcium release during long-lasting, depleting depolarization in mouse muscle. *J. Physiol.* **2008**, *586*, 4609–4629. [CrossRef]
45. Melzer, W.; Rios, E.; Schneider, M.F. Time course of calcium release and removal in skeletal muscle fibers. *Biophys. J.* **1984**, *45*, 637–641. [CrossRef]



© 2019 by the authors. Licensee MDPI, Basel, Switzerland. This article is an open access article distributed under the terms and conditions of the Creative Commons Attribution (CC BY) license (http://creativecommons.org/licenses/by/4.0/).

© 2016. Published by The Company of Biologists Ltd | Development (2016) 143, 1547-1559 doi:10.1242/dev.129676
szentesi.peter_292_24

RESEARCH ARTICLE

Restricting calcium currents is required for correct fiber type specification in skeletal muscle

Nasreen Sultana[1], Beatrix Dienes[2], Ariane Benedetti[1], Petronel Tuluc[3], Peter Szentesi[2], Monika Sztretye[2], Johannes Rainer[4], Michael W. Hess[5], Christoph Schwarzer[6], Gerald J. Obermair[1], Laszlo Csernoch[2] and Bernhard E. Flucher[1,*]

ABSTRACT

Skeletal muscle excitation-contraction (EC) coupling is independent of calcium influx. In fact, alternative splicing of the voltage-gated calcium channel $Ca_V1.1$ actively suppresses calcium currents in mature muscle. Whether this is necessary for normal development and function of muscle is not known. However, splicing defects that cause aberrant expression of the calcium-conducting developmental $Ca_V1.1e$ splice variant correlate with muscle weakness in myotonic dystrophy. Here, we deleted *$Ca_V1.1$* (*Cacna1s*) exon 29 in mice. These mice displayed normal overall motor performance, although grip force and voluntary running were reduced. Continued expression of the developmental $Ca_V1.1e$ splice variant in adult mice caused increased calcium influx during EC coupling, altered calcium homeostasis, and spontaneous calcium sparklets in isolated muscle fibers. Contractile force was reduced and endurance enhanced. Key regulators of fiber type specification were dysregulated and the fiber type composition was shifted toward slower fibers. However, oxidative enzyme activity and mitochondrial content declined. These findings indicate that limiting calcium influx during skeletal muscle EC coupling is important for the secondary function of the calcium signal in the activity-dependent regulation of fiber type composition and to prevent muscle disease.

KEY WORDS: Voltage-gated calcium channel, Skeletal muscle excitation-contraction coupling, Muscle fiber type specification, Mouse

INTRODUCTION

Calcium is the principal second messenger regulating skeletal muscle contraction, growth and differentiation. In excitation-contraction (EC) coupling, cytoplasmic calcium levels are rapidly increased in response to action potentials and the magnitude of these calcium signals regulates the force of contraction. In skeletal muscle, voltage-gated calcium channels ($Ca_V1.1$) and calcium release channels (type 1 ryanodine receptors, RyR1) are physically coupled to one another so that voltage-dependent activation of $Ca_V1.1$ can directly activate opening of the RyR1. In mature muscles, calcium is released from the sarcoplasmic reticulum (SR) calcium stores, whereas calcium influx is dispensable for skeletal muscle EC coupling (Melzer et al., 1995). Actually, calcium currents through the major $Ca_V1.1a$ splice variant are small and activate slowly, only at strong membrane depolarizations.

Interestingly, during maturation of mammalian skeletal muscles activity-dependent calcium influx is actively suppressed by alternative splicing of $Ca_V1.1$. In fetal muscles, exclusion of exon 29 produces a $Ca_V1.1e$ channel variant that conducts sizable L-type calcium currents and activates in parallel to SR calcium release at physiological voltages (Tuluc et al., 2009). However, after birth, the developmental $Ca_V1.1e$ splice variant is almost completely replaced by the adult, poorly conducting $Ca_V1.1a$ splice variant that includes exon 29 (Flucher and Tuluc, 2011; Tang et al., 2012). Why calcium influx is present in developing muscle but is then curtailed in mature skeletal muscles is not known. Conversely, it remains to be determined whether continued expression of the calcium-conducting $Ca_V1.1e$ splice variant alters contractile properties of mature skeletal muscles.

In addition to their primary role in EC coupling, activity-induced calcium signals in skeletal muscle are important for maintaining calcium homeostasis and for the regulation of muscle growth and differentiation. For example, calcium signals regulate the transcription of genes involved in the adaptive response to exercise (Bassel-Duby and Olson, 2006). Therefore, the tight control of calcium influx by alternative splicing of the $Ca_V1.1$ channel is probably important for tuning muscle function to varying activity levels. Conversely, calcium influx through $Ca_V1.1e$ channels in mature muscles might be harmful. Abnormal expression of the embryonic, calcium-conducting $Ca_V1.1e$ splice variant in myotonic dystrophy type 1 (DM1) patients correlates with their degree of muscle weakness (Tang et al., 2012). Moreover, aberrant splicing of calcium channels and transporters in cultured myotubes from DM1 patients leads to altered intracellular calcium signaling (Santoro et al., 2014), and experimentally induced skipping of exon 29 aggravated the disease phenotype in muscles of a myotonia mouse model (Tang et al., 2012).

To identify the physiological importance of curtailing calcium influx through $Ca_V1.1$ channels in adult skeletal muscle and to reveal a possible involvement of aberrant calcium signaling in DM1, we generated a genetic mouse model in which exon 29 has been permanently deleted. As expected, skeletal muscles of $Ca_V1.1^{\Delta E29/\Delta E29}$ knockout mice experienced increased calcium influx during EC coupling and at rest. In addition, their contractile properties were altered, calcium-activated downstream regulators were upregulated, and the fiber type composition was shifted towards slower fiber types. However, mitochondrial content and oxidative enzyme activity were reduced. Together, these findings

[1]Department of Physiology and Medical Physics, Medical University Innsbruck, Innsbruck 6020, Austria. [2]Department of Physiology, Faculty of Medicine, University of Debrecen, Debrecen 4032, Hungary. [3]Department of Pharmacology, University of Innsbruck, Innsbruck 6020, Austria. [4]Division of Molecular Pathophysiology, Biocenter, Medical University Innsbruck, Innsbruck 6020, Austria. [5]Division of Histology and Embryology, Medical University Innsbruck, Innsbruck 6020, Austria. [6]Department of Pharmacology, Medical University Innsbruck, Innsbruck 6020, Austria.

*Author for correspondence (Bernhard.E.Flucher@i-med.ac.at)

This is an Open Access article distributed under the terms of the Creative Commons Attribution License (http://creativecommons.org/licenses/by/3.0), which permits unrestricted use, distribution and reproduction in any medium provided that the original work is properly attributed.

Received 11 August 2015; Accepted 29 February 2016

Development (2016) 143, 1547-1559 doi:10.1242/dev.129676

szentesi.peter_292_24

indicate that chronically increased calcium influx through the developmental $Ca_V1.1e$ isoform has little effect on EC coupling, but disturbs the normal regulation of muscle fiber type composition. Furthermore, the increased calcium influx causes mitochondrial damage and may thus contribute to muscle wasting in DM1. Conversely, these results suggest that, during normal development, limiting L-type calcium currents is important to enable the proper specification of fiber type composition and to protect the muscles from calcium-induced damage.

RESULTS

Selective deletion of *$Ca_V1.1$* exon 29 prevents the developmental switch from the $Ca_V1.1e$ to the $Ca_V1.1a$ isoform

In order to study the importance of the isoform switch from the calcium-conducting developmental $Ca_V1.1e$ splice variant to the poorly conducting adult $Ca_V1.1a$ splice variant we generated a mouse model with a constitutive knockout of exon 29 of the *$Ca_V1.1$* (*Cacna1s*) gene (Fig. 1A). We reasoned that because the short transcript *$Ca_V1.1e$* is predominant during fetal development, *$Ca_V1.1^{\Delta E29}$* mice would develop normally up to birth, but that the aberrant continuing expression of the high-conductance developmental calcium channel splice variant throughout postnatal development and adult life would reveal any influence of the extra calcium influx on EC coupling and/or other calcium-mediated signaling processes regulating muscle growth and differentiation. Furthermore, the *$Ca_V1.1^{\Delta E29}$* mouse will expose whether aberrant splicing of $Ca_V1.1$ is itself sufficient to cause a disease phenotype reminiscent of DM1.

Heterozygous *$Ca_V1.1^{+/\Delta E29}$* and homozygous *$Ca_V1.1^{\Delta E29/\Delta E29}$* mice were viable, they developed normally, and home cage activity of *$Ca_V1.1^{\Delta E29}$* mice was not significantly different from that of wild-type siblings (Fig. 1B, Fig. S1A). Expression of the two *$Ca_V1.1$* transcripts at different developmental stages was analyzed in the predominantly slow/oxidative soleus muscle, the predominantly fast/glycolytic extensor digitorum longus (EDL) muscle, and the mixed diaphragm muscle. Quantitative RT-PCR demonstrated that wild-type fetal muscles express moderate levels of both splice variants, with a higher proportion of the splice variant lacking exon 29 ($Ca_V1.1e$) (Fig. 1C). After birth, wild-type muscles experienced a strong upregulation of the *$Ca_V1.1a$* transcript, whereas expression of the *$Ca_V1.1e$* transcript declined to less than 3% in 16-week-old mice. In muscles of ageing mice (15-18 months), total *$Ca_V1.1$* transcript levels declined but the overall predominance of the $Ca_V1.1a$ variant was maintained. As expected, in homozygous *$Ca_V1.1^{\Delta E29/\Delta E29}$* mice the *$Ca_V1.1e$* transcript was found exclusively. At all developmental stages its expression levels resembled those of total *$Ca_V1.1$* transcripts in wild-type mice. Western blot analysis confirmed normal expression levels of total $Ca_V1.1$ protein in soleus (Fig. 1D). However, in EDL muscle total $Ca_V1.1$ protein was reduced. This might, at least in part, reflect a reduced content of triad junctions due to the fiber type shift observed in *$Ca_V1.1^{\Delta E29}$* muscles (see below).

Aberrant expression of the developmental $Ca_V1.1e$ isoform in mature muscles is not sufficient to cause severe myotonic dystrophy symptoms in mice

Because aberrant expression of $Ca_V1.1e$ in adults has been linked to the DM1 phenotype in mouse and human (Santoro et al., 2014; Tang et al., 2012), we subjected *$Ca_V1.1^{\Delta E29}$* mice at 2 and 8 months of age to a range of behavioral tests to examine different aspects of muscle performance (Fig. 2). A wire hang test was used to assess muscle strength. Endurance was tested by making the mice run on a treadmill at accelerating speed until exhaustion. Overall motor performance was examined with the Rotarod test. In none of these tests was a significant difference in the performance of wild-type, heterozygous *$Ca_V1.1^{+/\Delta E29}$* and homozygous *$Ca_V1.1^{\Delta E29/\Delta E29}$* mice observed. However, directly measuring grip strength revealed that the grip force of the front paws was significantly reduced in homozygous *$Ca_V1.1^{\Delta E29/\Delta E29}$* mice (Fig. 2D). Finally, voluntary running of the mice in a running wheel was recorded over the period of 7 days. Both the distance run and the duration the mice spent running per day were significantly reduced in homozygous *$Ca_V1.1^{\Delta E29/\Delta E29}$* mice compared with wild-type controls (Fig. 2E). These behavioral and functional analyses indicate that aberrant expression of $Ca_V1.1e$ alters muscle performance without causing severe motor deficits as assessed in tests that revealed the disease phenotype in other DM mouse models (Gomes-Pereira et al., 2011). Also, histological staining of muscle sections did not reveal an increase in centrally located nuclei in *$Ca_V1.1^{\Delta E29/\Delta E29}$* muscles (Fig. S1B).

Aberrant expression of the developmental $Ca_V1.1e$ isoform in mature muscles alters the contractile properties of isolated slow and fast muscles

Because the reduced grip force and voluntary running indicated altered muscle performance, we next determined the contractile properties directly in isolated mouse muscles. The contractile force of soleus and EDL muscles was recorded in response to a single electrical stimulus (twitch) and in response to high-frequency trains of stimuli (tetanus) (Fig. 3A). Both were significantly reduced in both muscles types of *$Ca_V1.1^{\Delta E29/\Delta E29}$* mice (Fig. 3B, Table 1). The relative decline of muscle force during a continuous series of repetitive tetanic stimulations is a measure of the fatigability of the muscle (Fig. 3C). Slow soleus muscles are more fatigue resistant than fast EDL muscles. In *$Ca_V1.1^{\Delta E29/\Delta E29}$* mice, both muscle types display significantly reduced fatigue compared with wild-type controls (Fig. 3D, Table 1). Finally the tetanic fusion frequency was assessed by recording tetanic force during a series of stimulus trains of increasing frequency (Fig. 3E). *$Ca_V1.1^{\Delta E29/\Delta E29}$* muscles reached the half-maximal value and the plateau of contractile force at lower frequencies than control muscles. This is reflected by a left shift of the force frequency curve (Fig. 3F) and a reduction of the frequency of the half-maximal tetanic force (Fig. 3G) in both soleus and EDL muscles. Together, these tests on isolated muscles demonstrate that expression of $Ca_V1.1e$ in adult *$Ca_V1.1^{\Delta E29/\Delta E29}$* mice significantly reduces the contractile force, increases the fatigue resistance, and lowers the tetanic fusion frequency of slow and fast muscles.

Aberrant expression of the developmental $Ca_V1.1e$ isoform in mature muscles alters calcium signals during EC coupling and in resting muscle fibers

To clarify the cellular mechanisms underlying the altered muscle properties of *$Ca_V1.1^{\Delta E29/\Delta E29}$* mice we analyzed calcium currents and cytoplasmic calcium signals directly in isolated flexor digitorum brevis (FDB) muscle fibers using several experimental paradigms. First, combined patch-clamp and cytoplasmic calcium recording was performed in FDB fibers loaded with the fluorescent calcium indicator Rhod-2. In line with the current properties of the $Ca_V1.1e$ splice variant previously determined in reconstituted dysgenic myotubes (Tuluc et al., 2009), *$Ca_V1.1^{\Delta E29/\Delta E29}$* FDB fibers displayed sizable calcium currents starting at test potentials of −30 mV (Fig. 4A). Under the same conditions (1.8 mM extracellular calcium, 100 ms test pulses), control FDB fibers did

Development (2016) 143, 1547-1559 doi:10.1242/dev.129676

szentesi.peter_292_24

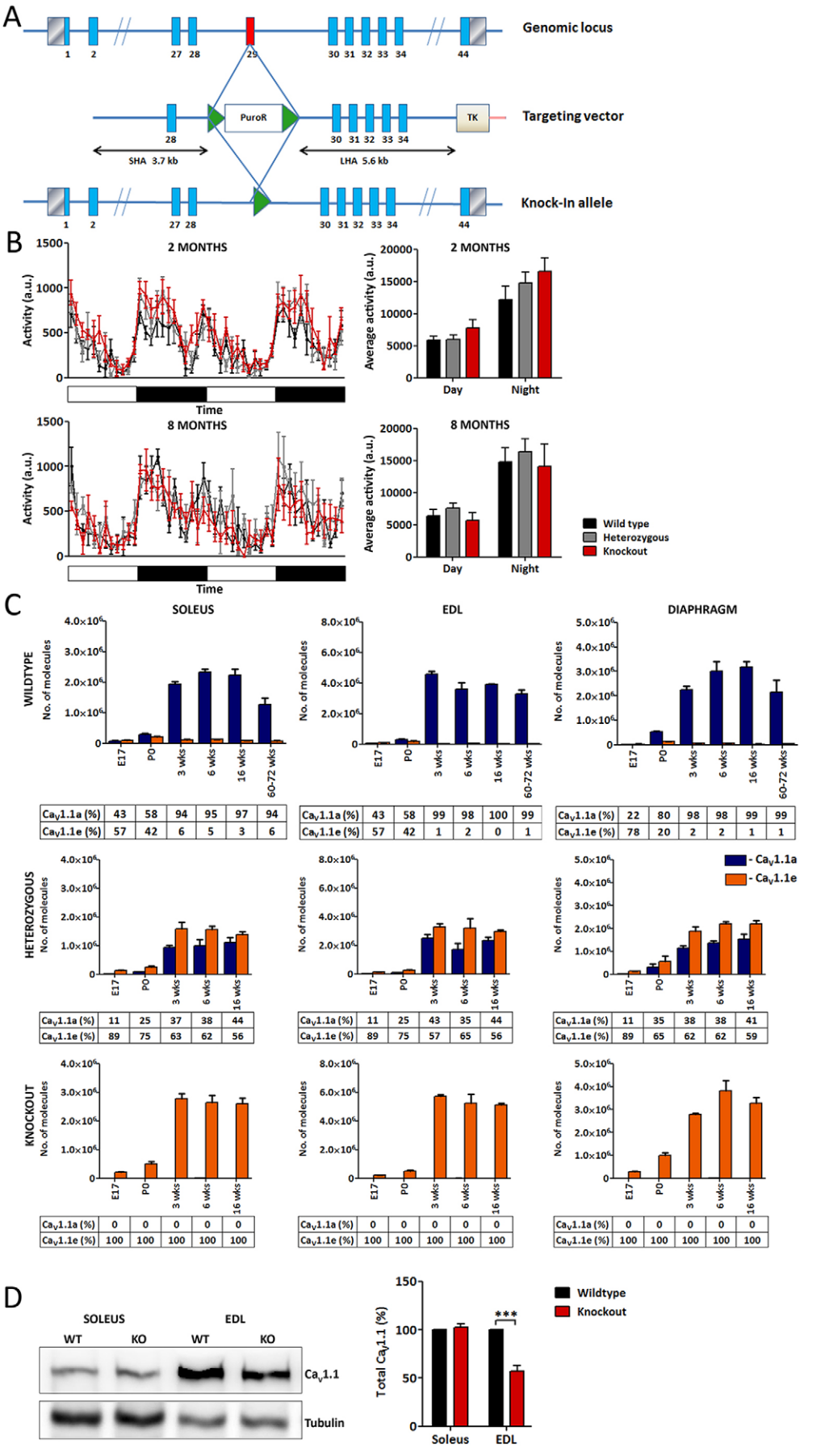


Fig. 1. Characterization of the $Ca_V1.1^{\Delta E29}$ mouse. (A) Targeting strategy for generating the $Ca_V1.1$ exon 29 knockout allele. (B) Voluntary home cage activity at 2 and 8 months of age is similar in $Ca_V1.1^{\Delta E29/\Delta E29}$ mice compared with wild-type and $Ca_V1.1^{+/\Delta E29}$ siblings (*N*=5). (C) Expression levels of $Ca_V1.1a$ and $Ca_V1.1e$ mRNAs in wild-type, $Ca_V1.1^{+/\Delta E29}$ and $Ca_V1.1^{\Delta E29/\Delta E29}$ mice were measured by quantitative RT-PCR (TaqMan) in soleus, EDL and diaphragm muscle at different developmental stages (*N*=3). Numbers beneath show the fractional content of the two $Ca_V1.1$ transcripts. (D) Western blot analysis of total $Ca_V1.1$ protein (both splice variants) in soleus and EDL muscle of wild-type and $Ca_V1.1^{\Delta E29}$ mice (*N*=3; ***P<0.001). Mean±s.e.m. See also Fig. S1.

Development (2016) 143, 1547-1559 doi:10.1242/dev.129676

szentesi.peter_292_24

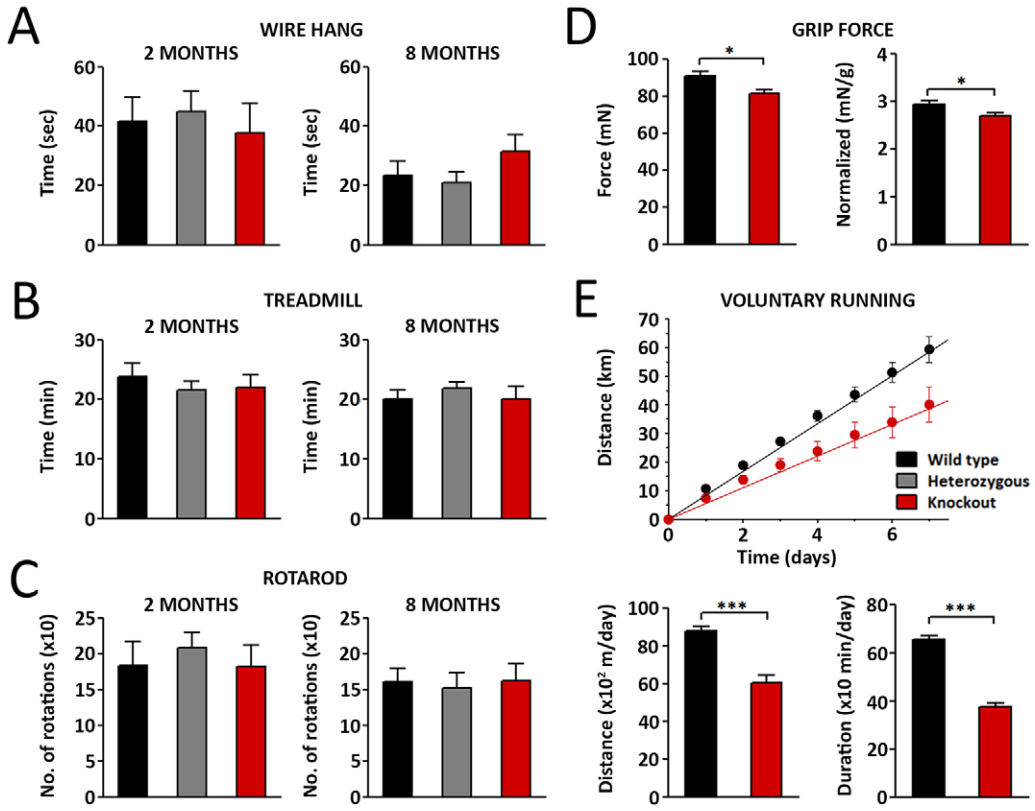


Fig. 2. $Ca_V1.1^{\Delta E29}$ mice show normal motor performance but reduced muscle strength. (A-C) Strength, endurance and motor skills were examined in wild-type, $Ca_V1.1^{+/\Delta E29}$ and $Ca_V1.1^{\Delta E29/\Delta E29}$ mice using the wire hang test (A), treadmill running to exhaustion (B) and the Rotarod test (C). At 2 and 8 months of age, the performance of $Ca_V1.1^{\Delta E29}$ mice did not differ from that of the other genotypes (N=5-8; P>0.05). (D) Direct measurement of front paw strength revealed reduced grip force (both in absolute value and force normalized to body weight) in 6-month-old $Ca_V1.1^{\Delta E29/\Delta E29}$ mice compared with wild-type siblings (N=5-8; *P<0.05). (E) Analysis of voluntary wheel running over a period of 7 days showed that the running distance and duration per day were decreased in $Ca_V1.1^{\Delta E29/\Delta E29}$ mice compared with the wild type (N=8; ***P<0.001). Mean±s.e.m.

not display measurable currents at any test potential. In order to compare voltage sensitivity between the two genotypes, recordings in control fibers were repeated using 5 mM extracellular calcium and 500 ms test pulses. The current-voltage and current-conductance curves indicate that in $Ca_V1.1^{\Delta E29/\Delta E29}$ fibers half-maximal current activation is shifted by 38.5±3.1 mV in the hyperpolarizing direction (Fig. 4B). Accordingly, the simultaneously recorded calcium transients in $Ca_V1.1^{\Delta E29/\Delta E29}$ fibers showed a pronounced voltage-dependent component that peaked at −20 mV and declined in parallel with the current density at positive potentials (Fig. 4C).

From the calcium transients the total calcium flux (influx and SR release) during the depolarizing pulses was calculated (Fig. 4A lower trace, Fig. S2). These calcium flux traces characteristically showed an early peak followed by a steady-state plateau phase (Szentesi et al., 1997). In control muscle, the voltage dependence of both the peak and plateau calcium fluxes displayed a monotonic increase, which could be fitted with a two-state Boltzmann function. This is consistent with a model of skeletal muscle EC coupling in which both parameters of the calcium flux (peak and plateau) represent a single process, i.e. calcium release from the SR. In $Ca_V1.1^{\Delta E29/\Delta E29}$ muscle fibers, the peak calcium flux behaved like that in controls, whereas the voltage dependence of the plateau flux was non-monotonous. At intermediate voltages the plateau flux was significantly larger than that of controls. Thus, the additional component in $Ca_V1.1^{\Delta E29/\Delta E29}$ muscles compared with controls corresponds to voltage-dependent calcium influx, which peaks at −20 mV where most $Ca_V1.1e$ channels are activated and then decreases in parallel with the declining driving force at positive membrane potentials. Together, these analyses clearly demonstrate that, during EC coupling, muscle fibers of $Ca_V1.1^{\Delta E29/\Delta E29}$ mice experience increased calcium signals due to a substantial component of calcium influx that is not observed in muscle fibers of wild-type mice.

In addition to its immediate role in EC coupling, this extra calcium influx in $Ca_V1.1^{\Delta E29/\Delta E29}$ mice might alter the calcium homeostasis in muscle cells. Analysis of cytoplasmic calcium concentrations in Fura-2-loaded isolated FDB fibers revealed no difference in resting calcium levels of $Ca_V1.1^{\Delta E29/\Delta E29}$ mice compared with wild-type controls (45.77±0.96 nM and 46.14±1.14 nM, respectively; P>0.5). Next, we examined a possible contribution of L-type calcium currents to refilling of SR calcium stores. Both SR depletion and refilling resulted in a robust cytoplasmic calcium transient (Fig. 4D), the relative magnitude of which was expressed as the external to SR calcium transient ratio. In wild-type muscle fibers this ratio was not affected by the application of the L-type calcium channel blocker nisoldipine. However, in $Ca_V1.1^{\Delta E29/\Delta E29}$ muscle fibers 5 µM nisoldipine dramatically reduced the ratio, indicating that in $Ca_V1.1e$-expressing muscle SR refilling is predominantly carried out by calcium influx through L-type channels (i.e. $Ca_V1.1e$).

Finally, the spontaneous occurrence of focal calcium transients – so called calcium sparklets – in resting muscle fibers was investigated. Because similar local calcium release events are exclusive to muscle cells expressing calcium-conducting Ca_V

Development (2016) 143, 1547-1559 doi:10.1242/dev.129676

szentesi.peter_292_24

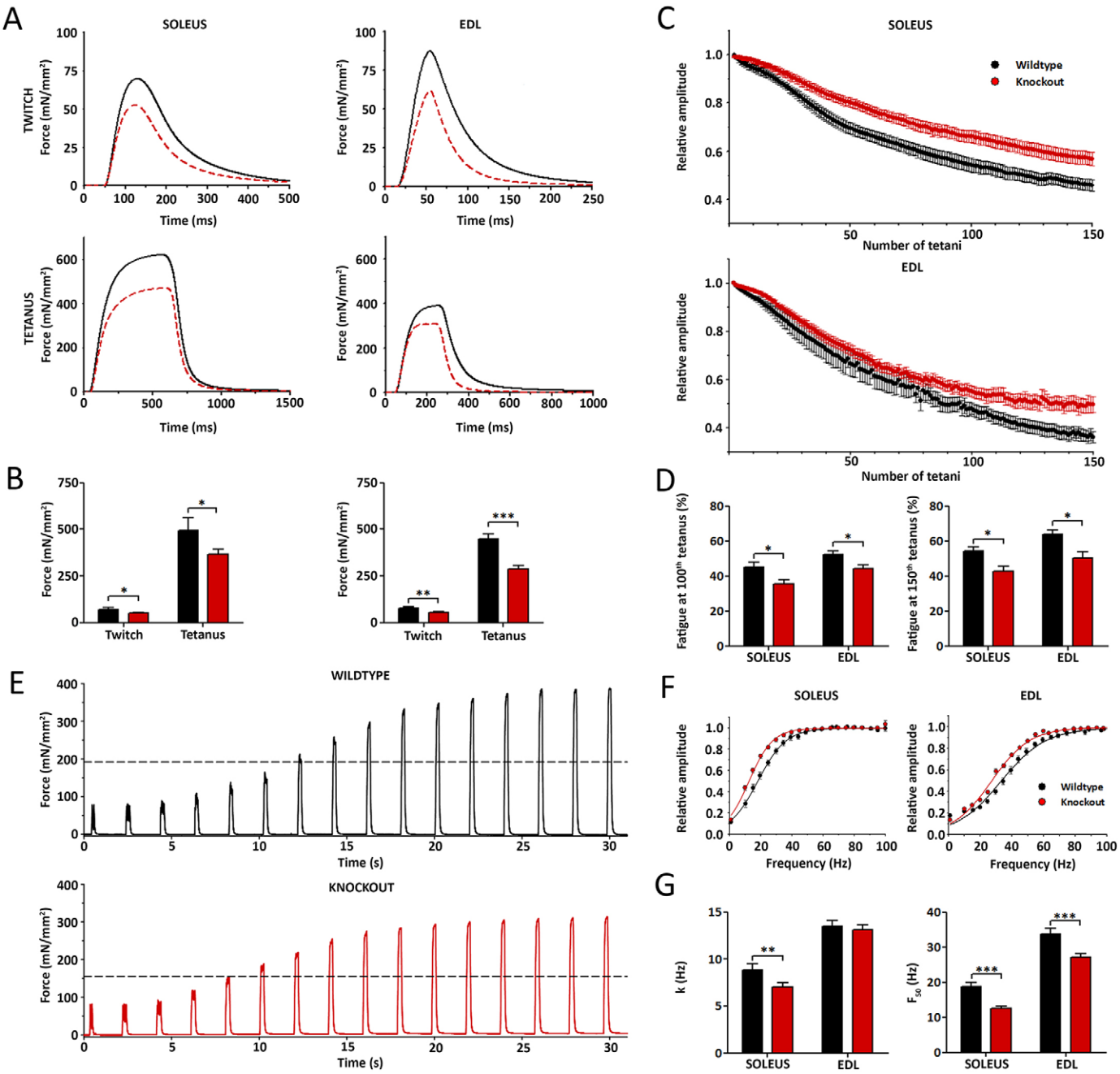


Fig. 3. Contractile properties of isolated slow and fast skeletal muscles are altered in $Ca_V1.1^{\Delta E29/\Delta E29}$ mice. (A) Representative recordings of twitch and tetanic contractions in isolated soleus and EDL muscles of 3- to 6-month-old wild-type (black; *N*=5) and $Ca_V1.1^{\Delta E29/\Delta E29}$ (red; *N*=15) mice. Muscle twitches were elicited by a single 2 ms supramaximal electrical pulse (top), tetani by stimulation trains at 100 Hz for 500 ms in soleus (lower left) or at 200 Hz for 200 ms in EDL (lower right). (B) Maximal twitch and tetanic forces are significantly reduced in $Ca_V1.1^{\Delta E29/\Delta E29}$ compared with control muscles (control *N*=5, $Ca_V1.1^{\Delta E29/\Delta E29}$ *N*=15). (C) Decline of maximal force during 150 repetitive tetani in soleus (upper) and EDL (lower) muscles of wild-type (black) and $Ca_V1.1^{\Delta E29/\Delta E29}$ (red) mice (stimulation as in A, repeated at 0.5 Hz; normalized to the first tetanus; control *N*=5, $Ca_V1.1^{\Delta E29/\Delta E29}$ *N*=15). (D) Relative reduction of force at the 100th and 150th tetanus was significantly lower in $Ca_V1.1^{\Delta E29/\Delta E29}$ than in wild-type muscles. (E) Representative force transients of isolated EDL muscle stimulated with increasing frequencies (10 to 85 Hz, with 0.5 Hz increment) from wild-type (black) and $Ca_V1.1^{\Delta E29/\Delta E29}$ (red) mice. Note that 50% of maximal force (dashed line) is reached at 40 Hz (seventh transient) in wild-type and at 30 Hz (fifth transient) in $Ca_V1.1^{\Delta E29/\Delta E29}$ muscles. (F) Relative force-frequency curves are left shifted in soleus (left) and EDL (right) muscles of $Ca_V1.1^{\Delta E29/\Delta E29}$ (red) compared with wild-type (black) mice. (G) The frequency required for producing half-maximal force was significantly lower in soleus and EDL muscles of $Ca_V1.1^{\Delta E29/\Delta E29}$ compared with wild type (control *N*=7, $Ca_V1.1^{\Delta E29/\Delta E29}$ *N*=12). **P*<0.05, ***P*<0.01, ****P*<0.001. Mean±s.e.m.

channels (e.g. $Ca_V1.2$ in cardiac myocytes), we hypothesized that aberrant expression of $Ca_V1.1e$ might also bring about calcium sparklets in mature muscle fibers of $Ca_V1.1^{\Delta E29/\Delta E29}$ mice. Indeed, isolated FDB fibers from $Ca_V1.1^{\Delta E29/\Delta E29}$ mice loaded with Fluo-8 AM displayed spontaneous calcium sparklet-like behavior (Fig. 4E). The average amplitude of these calcium sparklets was 0.140±0.001 [ΔF/F]. The average amplitude, full width and half maxima of these calcium sparklets resembled those described by Rodríguez et al. (2014). In 5 mM extracellular calcium, these calcium sparklets occurred at a frequency of 0.724 ±0.211 10^{-3} s^{-1} mm^{-1}. When the extracellular calcium concentration was reduced to 1.8 mM, or when L-type calcium

Development (2016) 143, 1547-1559 doi:10.1242/dev.129676

szentesi.peter_292_24

Table 1. Contractile properties of soleus and EDL muscles of $Ca_V1.1^{\Delta E29/\Delta E29}$ and wild-type mice

	Soleus			EDL		
Property	Wild type (*N*=5)	Knockout (*N*=15)		Wild type (*N*=5)	Knockout (*N*=15)	
Twitch force (mN/mm^2)	70.3±10.0	50.2±4.8	*P*<0.05	78.0±7.3	54.2±4.1	*P*<0.01
Tetanic force (mN/mm^2)	492.4±67.4	368.1±22.8	*P*<0.05	447.6±27.3	289.1±19.3	*P*<0.001
Fatigue (100th tetanus) %	45.2±2.8	35.3±2.7	*P*<0.05	52.1±2.3	44.9±2.2	*P*<0.05
Fatigue (150th tetanus) %	54.2±2.4	42.8±2.8	*P*<0.05	64.0±2.3	50.4±3.3	*P*<0.05
Force-frequency (slope, k)	9.20±0.67	6.90±0.45	*P*<0.01	13.74±0.67	12.90±0.54	*P*>0.05
Force-frequency (F_{50}, Hz)*	19.74±0.85	11.97±0.44	*P*<0.001	34.75±1.61	27.09±1.02	*P*>0.001

Values represent mean±s.e.m.
*Frequency of half-maximal force.

channels were blocked with 10 µM nisoldipine, the calcium sparklets were completely abolished, indicating their dependence on calcium influx through $Ca_V1.1e$. In wild-type control muscle fibers no such calcium release events were observed in normal or high extracellular calcium concentrations. Together, these findings demonstrate that calcium influx through the $Ca_V1.1e$ splice variant not only alters calcium handling during EC coupling and during refilling of SR calcium stores, but also causes spontaneous calcium signals in resting intact muscle fibers.

Muscles of $Ca_V1.1e$-expressing mice display an altered fiber type composition and oxidative metabolism

In skeletal muscle, calcium signals also regulate activity-dependent control of muscle growth and fiber type specification. Moreover, the observed changes in contractile properties – decreased force, increased fatigue resistance and lower tetanic fusion frequency – are all reminiscent of the differences between fast and slow muscle types. Therefore, we hypothesized that the altered calcium signaling in $Ca_V1.1^{\Delta E29/\Delta E29}$ mice might affect contractile properties indirectly by a dysregulation of fiber type specification.

To analyze the fiber type composition of slow and fast muscles in wild-type and $Ca_V1.1^{\Delta E29/\Delta E29}$ mice, we immunostained sections of soleus and EDL muscle with antibodies against specific myosin heavy chain isoforms. The representative images in Fig. 5A,D demonstrate a substantial shift towards slower fiber types in both soleus and EDL muscles of $Ca_V1.1^{\Delta E29/\Delta E29}$ mice. Soleus muscles of $Ca_V1.1^{\Delta E29/\Delta E29}$ mice experienced a 48% increase in the fraction of type I fibers, mainly at the cost of type IIA and mixed fibers (Fig. 5A-C). In EDL muscle of $Ca_V1.1^{\Delta E29/\Delta E29}$ mice the fraction of type IIB fibers was reduced by 26%, whereas the fractions of IIA, IIX and mixed fibers increased 2- to 3-fold (Fig. 5D-F). Type I fibers were not detected in $Ca_V1.1^{\Delta E29/\Delta E29}$ EDL muscles. These findings indicate that expression of the calcium-conducting $Ca_V1.1e$ splice variant in skeletal muscles of adult $Ca_V1.1^{\Delta E29/\Delta E29}$ mice causes a substantial shift in fiber type composition towards slower fiber types.

Aberrant expression of $Ca_V1.1e$ in mature skeletal muscle causes mitochondrial damage

A slower fiber type composition is expected to be accompanied by an increase in oxidative metabolism. Indeed, staining of succinate dehydrogenase (SDH) in soleus and EDL muscles of 7-week-old $Ca_V1.1^{\Delta E29/\Delta E29}$ mice revealed a marked increase in SDH activity compared with wild-type controls (Fig. 6A). In soleus, a loss of fibers with lower SDH activity was evident, probably reflecting the increase in type I fibers relative to type IIA fibers. In EDL, an increase in high SDH activity fibers occurred, consistent with the increased fraction of oxidative IIA fibers relative to glycolytic fiber types (see Fig. 5). Unexpectedly, in 6- and 12-month-old $Ca_V1.1^{\Delta E29/\Delta E29}$ mice the SDH activity was significantly reduced compared with the wild type (Fig. 6B, Fig. S3A). The left shift of the intensity distribution diagrams was more pronounced in soleus, but it was still significant in EDL. It equally affected fibers with low and high SDH activity. Together, these results show that the initial increase of oxidative metabolism in young $Ca_V1.1^{\Delta E29/\Delta E29}$ mice is lost and even reversed at 6 months and older.

Because decreased SDH activity could arise from either a reduction in mitochondrial activity or content, we analyzed mitochondria in electron microscopy preparations. Consistent with the overall healthy state and normal motor performance of the $Ca_V1.1^{\Delta E29/\Delta E29}$ mice, electron microscopy did not reveal any defects in the myofibrils and EC coupling membranes (Fig. 6C). However, the mitochondria were distorted in $Ca_V1.1^{\Delta E29/\Delta E29}$ muscles. Morphometric analysis revealed that the mitochondrial content was significantly reduced in $Ca_V1.1^{\Delta E29/\Delta E29}$ mice to approximately half that in wild-type controls (Fig. 6D, Fig. S3B). This loss of intact mitochondria was paralleled by an increase in the fraction of damaged mitochondria up to 4.5-fold compared with wild-type controls, as well as a decrease in the average size of the healthy mitochondria. These findings explain the significantly reduced SDH activity observed in $Ca_V1.1^{\Delta E29/\Delta E29}$ compared with wild-type muscles of the same age.

Aberrant expression of $Ca_V1.1e$ changes key activity- and calcium-dependent regulators of fiber type specification and mitochondrial biogenesis

If the altered calcium signals in $Ca_V1.1e$-expressing muscles impact the regulation of fiber type specification this might be reflected in the activity and/or expression levels of major calcium- and activity-regulated signaling proteins. In skeletal muscle, the calcium-dependent protein phosphatase calcineurin (protein phosphatase 2B) and the calmodulin-dependent protein kinase II (CaMKII) decode fiber type-specific activation patterns and function as master regulators of fast to slow fiber type changes (Chin et al., 1998; Wu et al., 2001; Chin, 2005). Using a colorimetric phosphatase assay we show that steady-state calcineurin activity is significantly increased in $Ca_V1.1^{\Delta E29/\Delta E29}$ soleus and EDL muscles (Fig. 7A). Western blot analysis using a phospho-specific antibody demonstrated that the activated forms of all three CaMKII isoforms were significantly increased in cytoplasmic fractions of soleus muscle (Fig. 7B), whereas in EDL muscles no changes in CaMKII activation were observed. A differential activation of CaMKII in slow versus fast muscles is consistent with its suggested role in differentially decoding slow and fast muscle calcium signals (Tavi and Westerblad, 2011).

Interestingly, expression of their respective downstream transcriptional regulators, NFATC1 and HDAC4, in the cytoplasm and nuclei of $Ca_V1.1^{\Delta E29/\Delta E29}$ muscles was not altered (Fig. 7C,D, Fig. S4A,B). However, expression of peroxisome

Development (2016) 143, 1547-1559 doi:10.1242/dev.129676

szentesi.peter_292_24

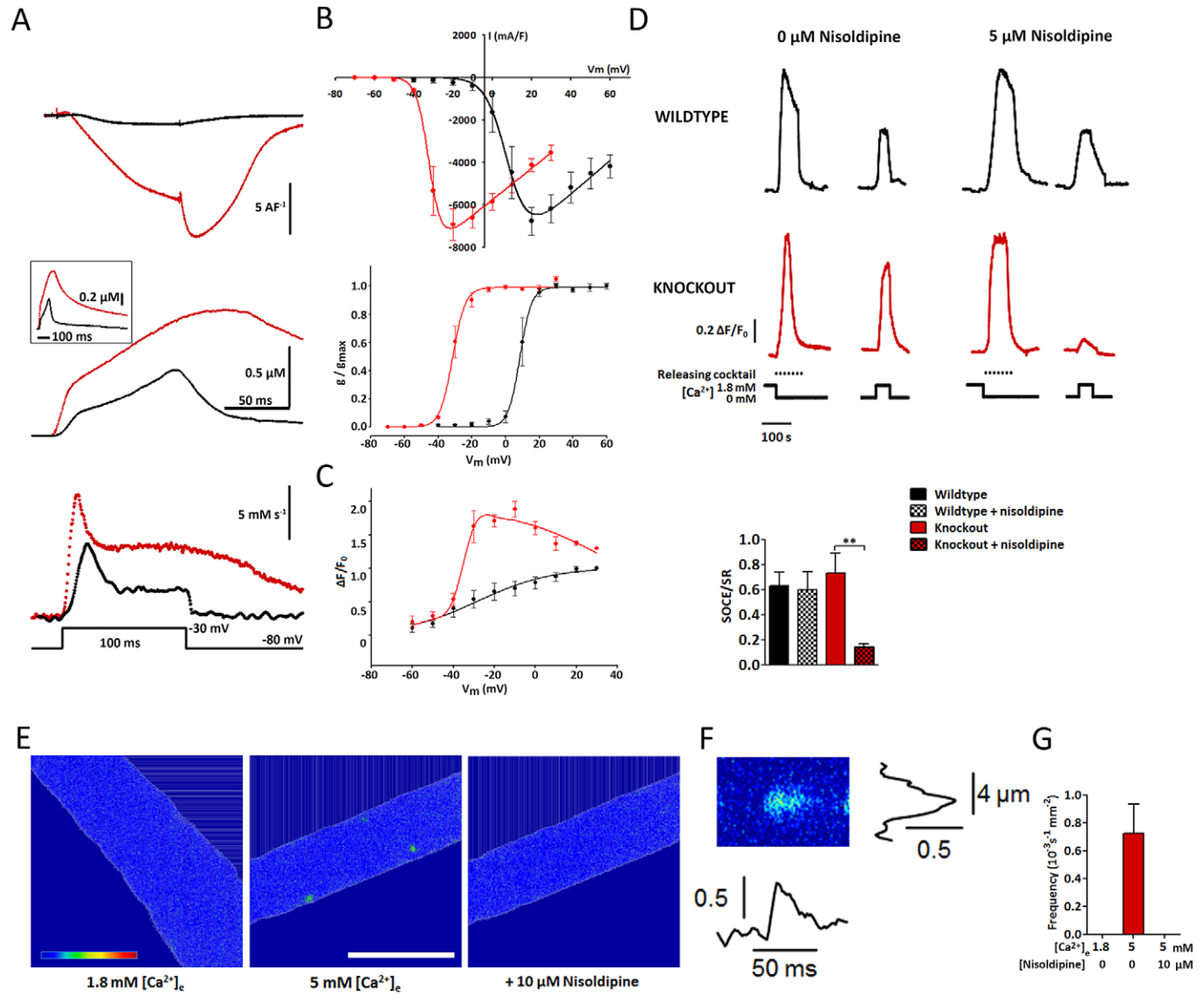


Fig. 4. Altered calcium signaling in isolated muscle fibers of $Ca_V1.1^{\Delta E29/\Delta E29}$ mice. Enzymatically isolated FDB fibers from 3- to 4-month-old $Ca_V1.1^{\Delta E29/\Delta E29}$ (red) and wild-type (black) mice were loaded with Rhod-2 (A-C) or Fluo-8 AM (D-G). (A) Representative voltage-clamp recording of calcium currents and parallel recording of cytoplasmic free calcium during a 100 ms depolarization to −30 mV. Bottom trace is the calculated total calcium flux. (B) Voltage dependence of peak current densities and conductance display the 38.5±3.1 mV shift of channel activation in $Ca_V1.1^{\Delta E29/\Delta E29}$ fibers. Note that $Ca_V1.1^{\Delta E29/\Delta E29}$ fibers were recorded in 1.8 mM extracellular calcium during 100 ms test pulses and control fibers in 5 mM calcium during 500 ms test pulses to experimentally normalize current densities. (C) Calcium transient amplitudes display a striking increase in $Ca_V1.1^{\Delta E29/\Delta E29}$ muscle fibers at intermediate voltages, indicative of the calcium influx through $Ca_V1.1e$. (D) Representative calcium recordings of wild-type and $Ca_V1.1^{\Delta E29/\Delta E29}$ fibers during an SR calcium release and reloading protocol. Note that the relative magnitude of the release and reloading transients is significantly decreased upon nisoldipine block of Ca_V1 channels in $Ca_V1.1^{\Delta E29/\Delta E29}$ but not in wild-type muscle (**P<0.01). (E) Representative confocal images of a resting $Ca_V1.1^{\Delta E29/\Delta E29}$ FDB fiber in 1.8 mM and 5 mM calcium. Spontaneous calcium release events occur only in 5 mM calcium and are blocked by addition of 10 µM nisoldipine. (F) Spatiotemporal properties in line-scan images identify the localized calcium signals as calcium sparklets. (G) The sparklets are sensitive to the extracellular calcium concentration and L-type channel block. n=32 images/N=4 animals (1.8 mM), n=183/N=7 (5 mM) and n=24/N=3 (5 mM+nisoldipine). Mean±s.e.m. See also Fig. S2.

proliferator-activated receptor γ co-activator 1α (*PGC1α*; *Ppargc1a*), a key downstream regulator of mitochondrial biogenesis and of oxidative metabolism in muscle (Handschin et al., 2007; Lin et al., 2002), was significantly increased in soleus muscle of $Ca_V1.1^{\Delta E29/\Delta E29}$ mice compared with wild-type controls (Fig. 7E). In EDL muscle, *PGC1α* expression was not significantly altered. Expression of *Six1*, a key regulator of the fast fiber program (Grifone et al., 2004; Wu et al., 2013), was not affected.

To further examine potential effects on the expression patterns of the slow and fast program and on mitochondrial biogenesis, Affymetrix expression profiling was performed on mRNA preparations from soleus and EDL muscles of wild-type and $Ca_V1.1^{\Delta E29/\Delta E29}$ mice. Although the analysis showed differential gene expression in soleus versus EDL muscles of both genotypes, comparison of wild-type versus $Ca_V1.1^{\Delta E29/\Delta E29}$ soleus and EDL muscles did not reveal any significant differences (Fig. S4C). Also, the specific analysis of genes involved in mitochondrial fusion and fission revealed only small differences between slow and fast muscles but not between wild-type and $Ca_V1.1^{\Delta E29/\Delta E29}$ mice. Thus, the increased calcium influx through $Ca_V1.1e$ chronically hyperactivates calcineurin, CaMKII and PGC1α signaling and, over time, produces the observed changes in fiber type composition

Development (2016) 143, 1547-1559 doi:10.1242/dev.129676

szentesi.peter_292_24

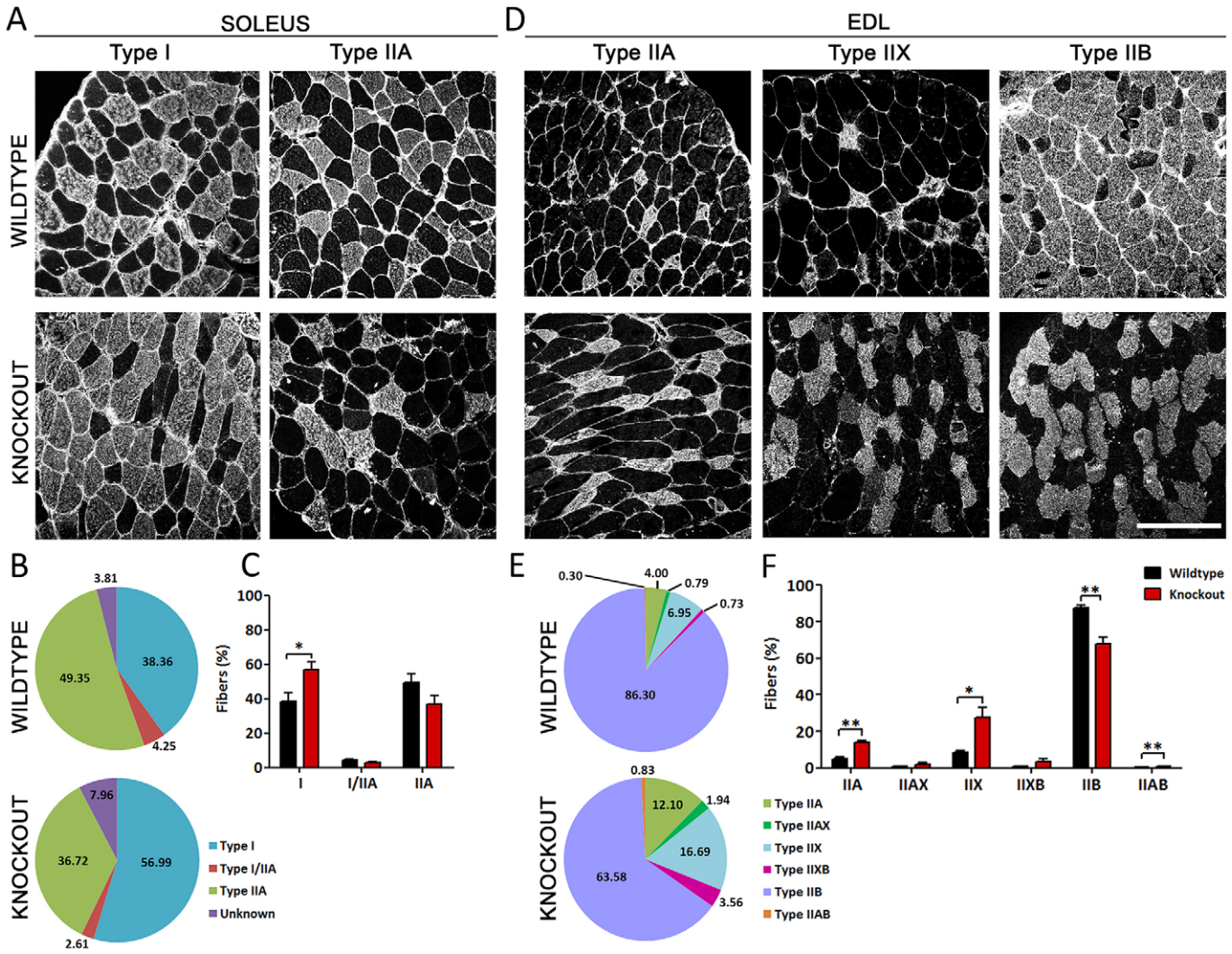


Fig. 5. Changes in fiber type composition and metabolic properties of soleus and EDL muscles in $Ca_V1.1^{\Delta E29/\Delta E29}$ mice. (A,D) Representative transverse sections of soleus and EDL muscles from 5- to 6-month-old wild-type and $Ca_V1.1^{\Delta E29/\Delta E29}$ mice immunostained with fiber type-specific myosin heavy chain antibodies. Scale bar: 100 µm. Note the increase of type I fibers and decrease of type IIA fibers in $Ca_V1.1^{\Delta E29/\Delta E29}$ soleus (A), and the increase of IIA and IIX fibers in parallel with the decrease of IIB fibers in $Ca_V1.1^{\Delta E29/\Delta E29}$ EDL (D). (B,E) The fractional redistribution of fiber types in $Ca_V1.1^{\Delta E29/\Delta E29}$ soleus and EDL muscles. (C,F) The relative magnitude and statistical significance of the changes in individual fiber types. N=3; *P<0.05, **P<0.01. Mean±s.e.m.

without, however, a major induction of the slow muscle gene program at basal activity levels in adult mice.

DISCUSSION

The developmental switch of $Ca_V1.1$ splice variants is important for the correct specification of skeletal muscle fiber types

Several lines of evidence at the molecular, functional and behavioral level demonstrate that the continued expression of the developmental $Ca_V1.1e$ splice variant in mature muscles of $Ca_V1.1^{\Delta E29/\Delta E29}$ mice alters the fiber type composition in the slow direction: (1) in soleus muscle the fraction of type I fibers increases at the expense of type IIA fibers, and in EDL muscles type IIA, IIX and mixed fibers increase at the expense of type IIB fibers; (2) in isolated soleus and EDL muscles maximal twitch and tetanic forces are reduced, fatigue resistance is increased, and tetanic fusion of contractions occurs at lower frequencies; (3) grip force and the duration of voluntary wheel running are reduced; (4) calcineurin and CaMKII activity and expression of PGC1α are upregulated. However, in mature mice the increased slow fiber content and the increased expression of PGC1α were no longer accompanied by the expected increase in oxidative enzyme activity, most likely because the increased calcium influx in $Ca_V1.1^{\Delta E29/\Delta E29}$ muscles also caused a severe loss of mitochondria.

The fiber type composition of skeletal muscles is primarily a genetically determined adaptation of muscle properties to their specific physiological functions. Furthermore, it is subject to continuous dynamic adaptation to altered demand. The changes in fiber type composition and contractile properties observed in the $Ca_V1.1^{\Delta E29/\Delta E29}$ mice are reminiscent of adaptations occurring in response to endurance training. The magnitude of the observed shift in fiber type composition is within the range observed in mice subjected to stringent endurance training protocols (Allen et al., 2001; Krüger et al., 2013). However, neither monitoring home cage activity nor the behavioral tests revealed increased spontaneous activity. If anything, $Ca_V1.1^{\Delta E29/\Delta E29}$ mice spent less time voluntarily running than wild-type controls. Therefore, the observed changes in fiber type composition cannot be explained

Development (2016) 143, 1547-1559 doi:10.1242/dev.129676

szentesi.peter_292_24

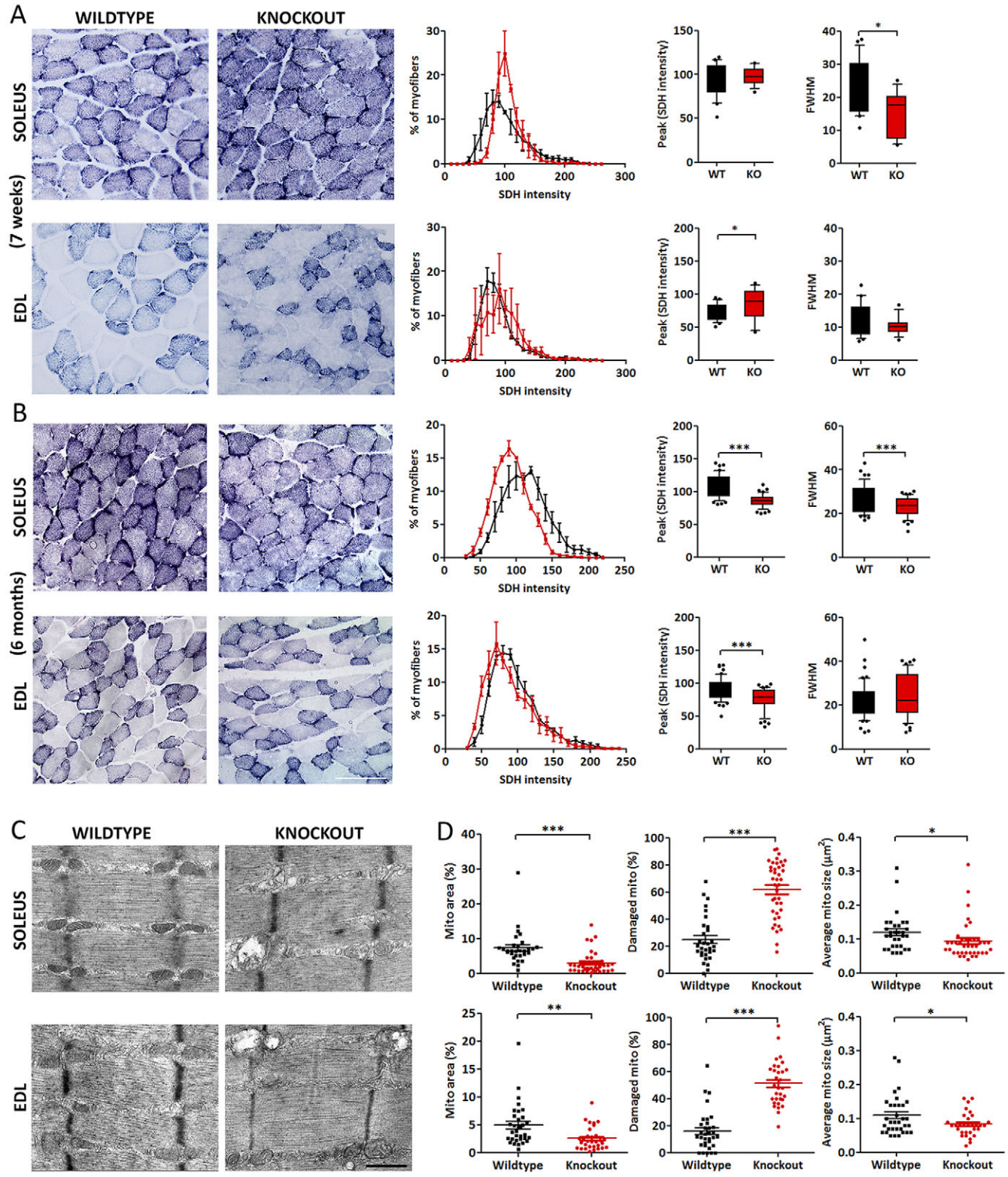


Fig. 6. Mitochondrial content and enzyme activity are reduced in $Ca_V1.1^{\Delta E29/\Delta E29}$ muscles. (A,B) SDH activity was analyzed in sections of wild-type (black) and $Ca_V1.1^{\Delta E29/\Delta E29}$ (red) mice. Staining intensity was measured in each fiber profile and plotted in intensity distribution diagrams. (A) In 7-week-old mice, SDH activity is markedly increased in $Ca_V1.1^{\Delta E29/\Delta E29}$ soleus and EDL muscles, as seen by the right-shifted intensity distribution histogram. (B) In 6-month-old mice, SDH activity is significantly reduced in $Ca_V1.1^{\Delta E29/\Delta E29}$ soleus muscle and in EDL muscles. In EDL also the full width at half maximum (FWHM) was reduced. *N*=3. (C) Electron micrographs of 4- and 5-month-old wild-type and $Ca_V1.1^{\Delta E29/\Delta E29}$ soleus and EDL muscles. Whereas myofibrils and EC coupling membranes appear normal, dilated and lysed mitochondria are found in $Ca_V1.1^{\Delta E29/\Delta E29}$ muscles. (D) Morphometric analysis demonstrates significantly decreased fractional content (percentage area occupied by intact mitochondria) in both $Ca_V1.1^{\Delta E29/\Delta E29}$ muscle types. Mitochondrial size is decreased in $Ca_V1.1^{\Delta E29/\Delta E29}$ muscles and the fraction of damaged mitochondria increased in $Ca_V1.1^{\Delta E29/\Delta E29}$ soleus muscles. *N*=30-40 images of two biological replicates per condition. **P*<0.05, ***P*<0.01, ****P*<0.001. Mean±s.e.m. See also Fig. S3. Scale bars: 100 µm in A,B; 0.5 µm in C.

Development (2016) 143, 1547-1559 doi:10.1242/dev.129676

szentesi.peter_292_24

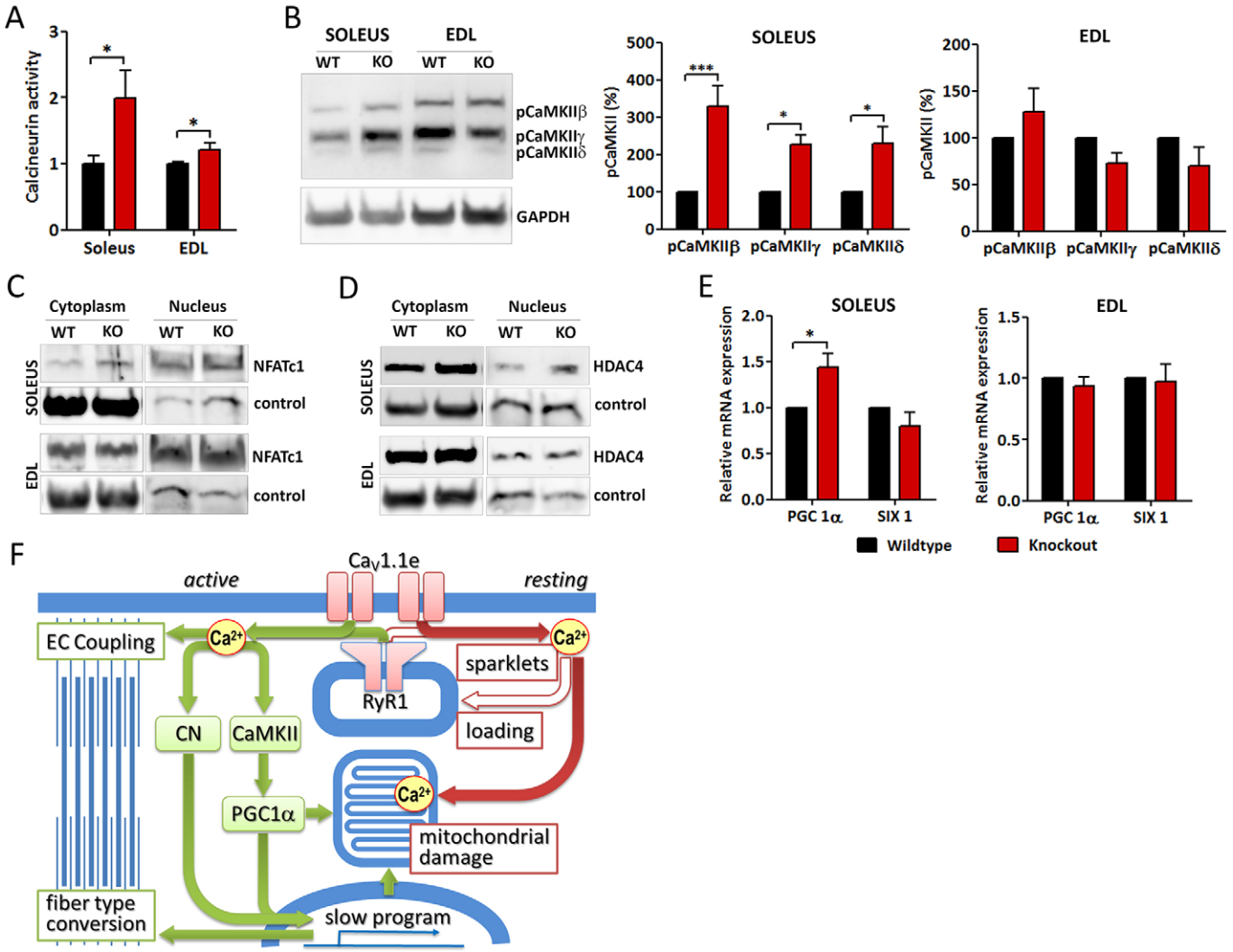


Fig. 7. Altered expression of regulators of fiber type specification and mitochondrial biogenesis in slow and fast muscles of $Ca_V1.1^{\Delta E29/\Delta E29}$ mice. (A) Basal enzymatic activity of calcineurin is significantly increased in $Ca_V1.1^{\Delta E29/\Delta E29}$ soleus and EDL muscles (red) compared with wild type (black). (B) Western blot analysis shows a significant increase of activated CaMKII β, γ and δ isoforms (phosphorylated at Thr286) in soleus but not EDL muscle of $Ca_V1.1^{\Delta E29/\Delta E29}$. (C,D) Cytoplasmic and nuclear localization of NFATC1 and HDAC4 does not differ between the genotypes (age of mice 6-8 months). Controls for the cytoplasm and nuclear fraction are GAPDH and histone H3, respectively. *N*=3. (E) Quantitative RT-PCR analysis demonstrates that expression of *PGC1α* (*Ppargc1a*) mRNA is significantly increased in $Ca_V1.1^{\Delta E29/\Delta E29}$ soleus muscles, whereas the decline of *PGC1α* in EDL and of *Six1* expression in both muscles is not significant. *N*=3. **P*<0.05, ****P*<0.001. Mean±s.e.m. (F) Model of signaling pathways causing fiber type shift and mitochondrial damage in $Ca_V1.1^{\Delta E29/\Delta E29}$ muscles. During EC coupling, increased calcium influx through Ca$_V$1.1e activates calcineurin (CN), CaMKII and PGC1α, the primary regulators of fiber type specification and mitochondrial biogenesis. The shift in fiber type composition in the slow direction offsets the direct effects of increased calcium signals on EC coupling. Parallel upregulation of oxidative metabolism by PGC1α is counteracted by mitochondrial damage caused by calcium overload due to increased activity-dependent and spontaneous calcium influx and altered calcium homeostasis. See also Fig. S4.

as a normal adaptive response to altered activity, but represent a dysregulation of fiber type composition owing to the absence of postnatal inclusion of *Ca$_V$1.1* exon 29 in $Ca_V1.1^{\Delta E29/\Delta E29}$ mice. Since Ca$_V$1.1 is almost exclusively expressed in skeletal muscle and the functional effects (e.g. reduced force, increased fatigue resistance) were observed in isolated muscles, muscle-intrinsic mechanisms are likely to be responsible for the altered muscle fiber type composition in $Ca_V1.1^{\Delta E29/\Delta E29}$ mice.

Expression of Ca$_V$1.1e alters skeletal muscle calcium signaling and activates the pathways for the slow twitch fiber program

Calcium is the principal second messenger regulating adaptive changes of muscle properties in response to training or experimentally altered innervation patterns (Bassel-Duby and Olson, 2006; Chin et al., 1998; Liu et al., 2005). As the primary defects in the $Ca_V1.1^{\Delta E29/\Delta E29}$ mice are altered gating and conduction properties of the skeletal muscle L-type calcium channel expressed in adult mice, a role of increased calcium influx in determining the fiber type composition is very likely. In cultured dysgenic myotubes reconstituted with either of two Ca$_V$1.1 splice variants, we previously reported that exclusion of exon 29 caused a 30 mV left-shifted voltage dependence of current activation and an 8-fold increase in current density (Tuluc et al., 2009). Here, we demonstrate that also in isolated muscle fibers of $Ca_V1.1^{\Delta E29/\Delta E29}$ mice, sole expression of the Ca$_V$1.1e splice variant causes an equally large left shift of voltage sensitivity and a substantially increased calcium influx during EC coupling. Interestingly, the calcium influx on top of the calcium released from the SR was not reflected in a parallel increase in contractile

Development (2016) 143, 1547-1559 doi:10.1242/dev.129676

szentesi.peter_292_24

strength. This indicates that, with respect to muscle contraction, the effects of increased calcium influx are counteracted by other consequences of the altered calcium signaling in $Ca_V1.1^{\Delta E29/\Delta E29}$ mice. In fact, the observed fiber type shift to slower, and thus weaker, fiber types could be part of a compensatory response of the muscle cell to an increased calcium load during EC coupling. The effects of continued expression of the calcium-conducting $Ca_V1.1e$ splice variant on fatigability and fiber type composition are consistent with recently published results obtained in a *$Ca_V1.1$* mutant (Lee et al., 2015). A knock-in mouse with a mutation in the $Ca_V1.1$ pore that abolished calcium binding and conduction showed increased fatigability and type IIB fiber content. Together, the two studies demonstrate that fiber type specification in skeletal muscle is highly sensitive to the magnitude of L-type calcium currents. The loss of calcium influx through $Ca_V1.1$ shifts the muscles towards a faster phenotype, whereas an increase of calcium currents causes a shift towards a slower phenotype.

In addition to altered calcium transients during EC coupling, a nisoldipine-sensitive component of calcium influx was observed in a store-refilling protocol, indicating that the extra calcium influx through the developmental $Ca_V1.1e$ splice variant also contributes to mechanisms of calcium homeostasis. Functionally, increased store filling probably contributes to the increased fatigue resistance observed in muscles of $Ca_V1.1^{\Delta E29/\Delta E29}$mice. Consistent with this notion, the opposite effects – decreased store filling and decreased fatigue resistance – were observed in the calcium permeation mutant mouse (Lee et al., 2015).

Furthermore, at rest muscle fibers of $Ca_V1.1^{\Delta E29/\Delta E29}$ mice generated focal calcium transients – so called calcium sparklets. Although calcium sparks are common in cardiac muscle cells, in developing skeletal muscle fibers and in cultured myotubes, they have never before been observed in mature muscle fibers of healthy mice (Cheng and Lederer, 2008; Weisleder and Ma, 2006). The calcium sparklets observed in $Ca_V1.1^{\Delta E29/\Delta E29}$ mice were dependent on the extracellular calcium concentration and were sensitive to the L-type channel blocker nisoldipine. Thus, there can be little doubt that calcium influx through $Ca_V1.1e$ channels contributed directly or indirectly to this phenomenon. As calcium sparks in cardiac myocytes can be activated by the opening of even a single $Ca_V1.2$ channel (Lopez-Lopez et al., 1995), it is conceivable that in skeletal muscles spontaneous openings of $Ca_V1.1e$ channels trigger the opening of RyR1 and thus activate calcium sparklets by calcium-induced calcium release. In wild-type mice this is limited to developing myotubes, which naturally express the $Ca_V1.1e$ splice variant. In $Ca_V1.1^{\Delta E29/\Delta E29}$ mice these spontaneous calcium signals occur also in differentiated muscles, where they might affect signaling pathways regulating fiber type composition and cause mitochondrial damage.

Downstream of calcium, it is calcineurin and CaMKII that are the key regulators of fast to slow twitch fiber type changes (Chin et al., 1998). Calcineurin regulates transcription of muscle genes via the classical NFAT pathway, CaMKII via HDAC4. Both converge on MEF2, but have also been reported to activate PGC1α (Tavi and Westerblad, 2011). A key feature of these parallel signaling pathways is their ability to distinguish between calcium signals in response to chronic, repetitive (slow fiber type) activation patterns and those in response to phasic (fast fiber type) activation patterns (Liu et al., 2005; Tavi and Westerblad, 2011). Apparently, expression of a calcium-conducting $Ca_V1.1e$ splice variant in adult muscles tips the balance of this delicate calcium sensing mechanism and leads to constitutive activation of the signaling pathway for the slow muscle program (Fig. 7F). Consistent with this notion, we observed that calcineurin and CaMKII activity, as well as expression of PGC1α, were constitutively upregulated in skeletal muscles of $Ca_V1.1^{\Delta E29/\Delta E29}$ mice, and that activation of CaMKII and PGC1α was specific to slow muscles. In accordance with this, altered CaMKII signaling was also observed in the calcium permeation *$Ca_V1.1$* mutant (Lee et al., 2015).

Thus, in $Ca_V1.1^{\Delta E29/\Delta E29}$ mice the continuous expression of $Ca_V1.1e$ causes increased calcium influx during EC coupling, in homeostatic calcium regulation, and at rest. Which of these calcium influx events contribute to the activation of the slow muscle pathway remains to be determined. Because calcineurin and CaMKII signaling is highly sensitive to the calcium signaling patterns in response to slow fiber type-specific activity, we favor a role of altered calcium signal during EC coupling. In any case, if aberrant activation of these signaling pathways causes an increase in slow fibers in $Ca_V1.1^{\Delta E29/\Delta E29}$ mice, during normal development the alternative splicing event causing the shift from a calcium-conducting to a non-conducting $Ca_V1.1$ variant might be an important prerequisite for the proper regulation of fiber type composition at basal activity levels as well as in response to exercise.

The contribution of aberrant $Ca_V1.1$ splicing to myotonic dystrophy

Splicing defects of important muscle proteins, including the CLCN1 chloride channel, insulin receptor, SERCA1 (ATP2A1) and $Ca_V1.1$, lead to DM1 (Thornton, 2014). The myotonia is likely to be caused by a hyperexcitability of muscles due to the loss of CLCN1 function (Lueck et al., 2007). Because aberrant expression of the $Ca_V1.1e$ splice variant correlates with the degree of muscle weakness in DM1 patients, and forced missplicing of *$Ca_V1.1$* exon 29 caused centrally localized nuclei in a myotonia mouse model, it has been suggested that increased calcium influx through the developmental $Ca_V1.1e$ splice variant may contribute to the myopathy (Santoro et al., 2014; Tang et al., 2012). This hypothesis is in line with the known role of increased calcium influx via various entry pathways in muscular dystrophy (Allen et al., 2010; Whitehead et al., 2006). Here, we examined whether aberrant missplicing of *$Ca_V1.1$* exon 29 by itself is sufficient to cause DM-like symptoms. At the organismal level this was not the case. Homozygous $Ca_V1.1^{\Delta E29/\Delta E29}$ mice, which exclusively express the developmental $Ca_V1.1e$ splice variant, did not show severe muscle weakness, and their muscle sections did not reveal centrally located nuclei, which is a histopathological hallmark of dystrophic muscle. Although the contractile force of isolated muscles was reduced, this was accompanied by increased fatigue resistance and might therefore be the consequence of the fiber type shift rather than a symptom of DM1.

We observed decreased SDH activity and severe mitochondrial damage in muscles of mature and aged $Ca_V1.1^{\Delta E29/\Delta E29}$ mice. Similar mitochondrial damage has been described in other mouse muscle disease models with aberrant calcium signaling (Irwin et al., 2003). Calcium overload leads to mitochondrial damage and ultimately produces the symptomatic central cores in the diseased muscles (Boncompagni et al., 2009; Brookes et al., 2004). Similarly, the $Ca_V1.1e$-mediated spontaneous calcium sparklets, or the increased calcium influx after store depletion, might overburden the mitochondrial calcium handling capacity and cause their loss in $Ca_V1.1^{\Delta E29/\Delta E29}$ muscles. In fact, both calcium sparks and store-operated calcium currents have previously been implicated in the pathophysiology of muscular dystrophy (Goonasekera et al., 2014; Weisleder and Ma, 2006). Thus, the mitochondrial damage observed in $Ca_V1.1^{\Delta E29/\Delta E29}$ mice might precede the appearance of histopathological and clinical features of DM1.

Development (2016) 143, 1547-1559 doi:10.1242/dev.129676

szentesi.peter_292_24

We conclude that, by itself, missplicing of exon 29 in $Ca_V1.1$ is not sufficient to reproduce the full spectrum of DM1 symptoms in mice. As the disease phenotype in dystrophy and myotonia mouse models is often less severe than in human disease, this does not preclude the possibility that missplicing of $Ca_V1.1$ makes a notable contribution to the disease in DM1 patients. Furthermore, it is likely that in combination with the splicing defects in other muscle genes involved in calcium handling (*Serca1*) and excitability (*Clcn1*), the mitochondrial damage observed in the $Ca_V1.1^{\Delta E29/\Delta E29}$ mice might be aggravated, and thus contribute to the myopathy (Tang et al., 2012). If so, the use of clinically approved L-type calcium channel blockers to target $Ca_V1.1e$ currents might be a viable strategy to alleviate the symptoms of DM1 (Benedetti et al., 2015).

In conclusion, the effects of $Ca_V1.1$ missplicing in the $Ca_V1.1^{\Delta E29/\Delta E29}$ mice revealed a novel role of increased L-type calcium currents in the dysregulation of muscle fiber type composition. With regard to normal muscle physiology these findings suggest that, during development, skeletal muscles actively suppress L-type calcium currents by alternative splicing of $Ca_V1.1$, so as to prevent unrestrained calcium influx during EC coupling from interfering with the second calcium signaling function in regulating muscle fiber type composition. Furthermore, aberrant expression of the developmental $Ca_V1.1e$ splice variant in mature muscles causes mitochondrial damage, which might contribute to the pathology of DM1.

MATERIALS AND METHODS

Mice and animal care

$Ca_V1.1^{\Delta E29}$ mice were generated in a C57BL/6N background at Taconic Artemis (Cologne, Germany). All experimental protocols conformed to guidelines of the European Community (86/609/EEC) and were approved by the Austrian Ministry of Science (BMWF-66.011/0069-II/10b/2010) and by the Institutional Animal Care Committee of the University of Debrecen (22/2011/DE MAB). Genotyping is described in the supplementary Materials and Methods.

Quantitative RT-PCR

RNA was isolated from muscles of wild-type and $Ca_V1.1^{\Delta E29}$ mice using the RNeasy Fibrous Tissue Mini Kit (Qiagen). After reverse transcription (SuperScript II reverse transcriptase, Invitrogen) the absolute number of transcripts was assessed by quantitative TaqMan PCR (50 cycles). For primer sequences and experimental details, see the supplementary Materials and Methods and Table S1.

Microarray

Affymetrix GeneChip analysis of mRNA expression in soleus and EDL muscles of wild-type and $Ca_V1.1^{\Delta E29/\Delta E29}$ mice was performed as detailed in the supplementary Materials and Methods.

Behavioral experiments

The following tests were performed on 2- and 8-month-old wild-type, heterozygous $Ca_V1.1^{+/\Delta E29}$ and homozygous $Ca_V1.1^{\Delta E29/\Delta E29}$ mice: home cage activity, voluntary running, Rotarod test, wire hang test, grip force measurements. For details, see the supplementary Materials and Methods.

Force measurements

Contractile force of isolated EDL and soleus muscles of 3- to 6-month-old mice in response to twitch and tetanic stimulations were recorded with a capacitative mechanoelectric force transducer as described in the supplementary Materials and Methods.

Single fiber measurements

Single fibers were isolated from FDB muscles and used for voltage-clamp recordings of calcium currents with an Axoclamp 2B amplifier (Axon Instruments), and cytoplasmic calcium signals were recorded using fluorescent calcium indicators and imaging with a Zeiss 5 Live confocal microscope (20× objective). Further experimental details and data analysis are described in the supplementary Materials and Methods.

Immunohistochemistry and SDH activity assay

Cryosections of EDL and soleus muscles from 6-month-old wild-type and $Ca_V1.1^{\Delta E29/\Delta E29}$ mice were immunostained with antibodies against specific myosin heavy chain isoforms (Developmental Studies Hybridoma Bank, University of Iowa, Iowa, USA). Histochemical staining of SDH activity was performed with succinic acid and nitroblue tetrazolium for 1 h. For information on the antibodies used and further details of experimental and quantification procedures, see the supplementary Materials and Methods and Table S2.

Western blot and calcineurin assay

Cytoplasmic and nuclear protein fractions were prepared from 6-month-old wild-type and $Ca_V1.1^{\Delta E29/\Delta E29}$ mice and separated on 6-10% bis-Tris gels for western blotting. Calcineurin activity was determined using a Calcineurin Phosphatase Activity Colorimetric Assay (Abcam) according to the manufacturer's instructions. For antibodies and experimental details, see the supplementary Materials and Methods.

Electron microscopy

Tissue processing for transmission electron microscopy of EDL and soleus muscles, and the analysis of mitochondria, were performed as detailed in the supplementary Materials and Methods.

Statistical analysis

A two-way ANOVA with Bonferroni post-hoc test was used for home cage activity and fiber type analysis. One-way ANOVA was used for the other behavioral tests. Student's *t*-test and Mann–Whitney U-test were used to calculate the statistical significance for fiber type and contractile properties analysis. *N* represents the number of animals. Data are presented as mean± s.e.m. The statistical analysis was performed with GraphPad Prism. For further details see the supplementary Materials and Methods.

Acknowledgements

We thank Dr C. Humpel for providing muscle samples of aged mice; Dr S. Schiaffino for helpful advice on fiber type analysis; Dr B. Lontay for assistance with calcineurin activity measurements; and R. Őri, K. Gutleben and B. Witting for excellent technical assistance.

Competing interests

The authors declare no competing or financial interests.

Author contributions

B.E.F., N.S. and L.C. designed research and wrote the manuscript. N.S., B.D., A.B., P.T., P.S., M.S., J.R., M.W.H., C.S. and G.J.O. performed experiments and/or analyzed data.

Funding

This work was supported by grants from the Austrian Science Fund (FWF) [P23479 and W1101] to B.E.F.; from the Hungarian Scientific Research Fund (OTKA) [NN-107765]; from the European Union and the State of Hungary, co-financed by the European Social Fund in the framework of TÁMOP-4.1.2.E-13/1/KONV-2013-0010 and TÁMOP-4.2.4.A/2-11/1-2012-0001 'National Excellence Program' to B.D. Deposited in PMC for immediate release.

Data availability

The raw and preprocessed microarray data are available at Gene Expression Omnibus under accession number GSE67803.

Supplementary information

Supplementary information available online at
http://dev.biologists.org/lookup/suppl/doi:10.1242/dev.129676/-/DC1

References

Allen, D. L., Harrison, B. C., Maass, A., Bell, M. L., Byrnes, W. C. and Leinwand, L. A. (2001). Cardiac and skeletal muscle adaptations to voluntary wheel running in the mouse. *J. Appl. Physiol.* **90**, 1900-1908.

Allen, D. G., Gervasio, O. L., Yeung, E. W. and Whitehead, N. P. (2010). Calcium and the damage pathways in muscular dystrophy. *Can. J. Physiol. Pharmacol.* **88**, 83-91.

Development (2016) 143, 1547-1559 doi:10.1242/dev.129676

szentesi.peter_292_24

Bassel-Duby, R. and Olson, E. N. (2006). Signaling pathways in skeletal muscle remodeling. *Annu. Rev. Biochem.* **75**, 19-37.

Benedetti, B., Tuluc, P., Mastrolia, V., Dlaska, C. and Flucher, B. E. (2015). Physiological and pharmacological modulation of the embryonic skeletal muscle calcium channel splice variant CaV1.1e. *Biophys. J.* **108**, 1072-1080.

Boncompagni, S., Rossi, A. E., Micaroni, M., Hamilton, S. L., Dirksen, R. T., Franzini-Armstrong, C. and Protasi, F. (2009). Characterization and temporal development of cores in a mouse model of malignant hyperthermia. *Proc. Natl. Acad. Sci. USA* **106**, 21996-22001.

Brookes, P. S., Yoon, Y., Robotham, J. L., Anders, M. W. and Sheu, S.-S. (2004). Calcium, ATP, and ROS: a mitochondrial love-hate triangle. *Am. J. Physiol. Cell Physiol.* **287**, C817-C833.

Cheng, H. and Lederer, W. J. (2008). Calcium sparks. *Physiol. Rev.* **88**, 1491-1545.

Chin, E. R. (2005). Role of Ca2+/calmodulin-dependent kinases in skeletal muscle plasticity. *J. Appl. Physiol.* **99**, 414-423.

Chin, E. R., Olson, E. N., Richardson, J. A., Yang, Q., Humphries, C., Shelton, J. M., Wu, H., Zhu, W., Bassel-Duby, R. and Williams, R. S. (1998). A calcineurin-dependent transcriptional pathway controls skeletal muscle fiber type. *Genes Dev.* **12**, 2499-2509.

Flucher, B. E. and Tuluc, P. (2011). A new L-type calcium channel isoform required for normal patterning of the developing neuromuscular junction. *Channels* **5**, 518-524.

Gomes-Pereira, M., Cooper, T. A. and Gourdon, G. (2011). Myotonic dystrophy mouse models: towards rational therapy development. *Trends Mol. Med.* **17**, 506-517.

Goonasekera, S. A., Davis, J., Kwong, J. Q., Accornero, F., Wei-LaPierre, L., Sargent, M. A., Dirksen, R. T. and Molkentin, J. D. (2014). Enhanced Ca(2)(+) influx from STIM1-Orai1 induces muscle pathology in mouse models of muscular dystrophy. *Hum. Mol. Genet.* **23**, 3706-3715.

Grifone, R., Laclef, C., Spitz, F., Lopez, S., Demignon, J., Guidotti, J.-E., Kawakami, K., Xu, P.-X., Kelly, R., Petrof, B. J. et al. (2004). Six1 and Eya1 expression can reprogram adult muscle from the slow-twitch phenotype into the fast-twitch phenotype. *Mol. Cell. Biol.* **24**, 6253-6267.

Handschin, C., Chin, S., Li, P., Liu, F., Maratos-Flier, E., LeBrasseur, N. K., Yan, Z. and Spiegelman, B. M. (2007). Skeletal muscle fiber-type switching, exercise intolerance, and myopathy in PGC-1alpha muscle-specific knock-out animals. *J. Biol. Chem.* **282**, 30014-30021.

Irwin, W. A., Bergamin, N., Sabatelli, P., Reggiani, C., Megighian, A., Merlini, L., Braghetta, P., Columbaro, M., Volpin, D., Bressan, G. M. et al. (2003). Mitochondrial dysfunction and apoptosis in myopathic mice with collagen VI deficiency. *Nat. Genet.* **35**, 367-371.

Krüger, K., Gessner, D. K., Seimetz, M., Banisch, J., Ringseis, R., Eder, K., Weissmann, N. and Mooren, F. C. (2013). Functional and muscular adaptations in an experimental model for isometric strength training in mice. *PLoS ONE* **8**, e79069.

Lee, C. S., Dagnino-Acosta, A., Yarotskyy, V., Hanna, A., Lyfenko, A., Knoblauch, M., Georgiou, D. K., Poché, R. A., Swank, M. W., Long, C. et al. (2015). Ca(2+) permeation and/or binding to CaV1.1 fine-tunes skeletal muscle Ca(2+) signaling to sustain muscle function. *Skeletal Muscle* **5**, 4.

Lin, J., Wu, H., Tarr, P. T., Zhang, C.-Y., Wu, Z., Boss, O., Michael, L. F., Puigserver, P., Isotani, E., Olson, E. N. et al. (2002). Transcriptional co-activator PGC-1 alpha drives the formation of slow-twitch muscle fibres. *Nature* **418**, 797-801.

Liu, Y., Randall, W. R. and Schneider, M. F. (2005). Activity-dependent and -independent nuclear fluxes of HDAC4 mediated by different kinases in adult skeletal muscle. *J. Cell Biol.* **168**, 887-897.

Lopez-Lopez, J. R., Shacklock, P. S., Balke, C. W. and Wier, W. G. (1995). Local calcium transients triggered by single L-type calcium channel currents in cardiac cells. *Science* **268**, 1042-1045.

Lueck, J. D., Mankodi, A., Swanson, M. S., Thornton, C. A. and Dirksen, R. T. (2007). Muscle chloride channel dysfunction in two mouse models of myotonic dystrophy. *J. Gen. Physiol.* **129**, 79-94.

Melzer, W., Herrmann-Frank, A. and Lüttgau, H. C. (1995). The role of Ca2+ ions in excitation-contraction coupling of skeletal muscle fibres. *Biochim. Biophys. Acta* **1241**, 59-116.

Rodríguez, E. G., Lefebvre, R., Bodnár, D., Legrand, C., Szentesi, P., Vincze, J., Poulard, K., Bertrand-Michel, J., Csernoch, L., Buj-Bello, A. et al. (2014). Phosphoinositide substrates of myotubularin affect voltage-activated Ca(2)(+) release in skeletal muscle. *Pflugers Arch.* **466**, 973-985.

Santoro, M., Piacentini, R., Masciullo, M., Bianchi, M. L. E., Modoni, A., Podda, M. V., Ricci, E., Silvestri, G. and Grassi, C. (2014). Alternative splicing alterations of Ca2+ handling genes are associated with Ca2+ signal dysregulation in myotonic dystrophy type 1 (DM1) and type 2 (DM2) myotubes. *Neuropathol. Appl. Neurobiol.* **40**, 464-476.

Szentesi, P., Jacquemond, V., Kovács, L. and Csernoch, L. (1997). Intramembrane charge movement and sarcoplasmic calcium release in enzymatically isolated mammalian skeletal muscle fibres. *J. Physiol.* **505**, 371-384.

Tang, Z. Z., Yarotskyy, V., Wei, L., Sobczak, K., Nakamori, M., Eichinger, K., Moxley, R. T., Dirksen, R. T. and Thornton, C. A. (2012). Muscle weakness in myotonic dystrophy associated with misregulated splicing and altered gating of Ca (V)1.1 calcium channel. *Hum. Mol. Genet.* **21**, 1312-1324.

Tavi, P. and Westerblad, H. (2011). The role of in vivo Ca(2)(+) signals acting on Ca (2)(+)-calmodulin-dependent proteins for skeletal muscle plasticity. *J. Physiol.* **589**, 5021-5031.

Thornton, C. A. (2014). Myotonic dystrophy. *Neurol. Clin.* **32**, 705-719, viii.

Tuluc, P., Molenda, N., Schlick, B., Obermair, G. J., Flucher, B. E. and Jurkat-Rott, K. (2009). A CaV1.1 Ca2+ channel splice variant with high conductance and voltage-sensitivity alters EC coupling in developing skeletal muscle. *Biophys. J.* **96**, 35-44.

Weisleder, N. and Ma, J.-j. (2006). Ca2+ sparks as a plastic signal for skeletal muscle health, aging, and dystrophy. *Acta Pharmacol. Sin.* **27**, 791-798.

Whitehead, N. P., Yeung, E. W. and Allen, D. G. (2006). Muscle damage in mdx (dystrophic) mice: role of calcium and reactive oxygen species. *Clin. Exp. Pharmacol. Physiol.* **33**, 657-662.

Wu, H., Rothermel, B., Kanatous, S., Rosenberg, P., Naya, F. J., Shelton, J. M., Hutcheson, K. A., DiMaio, J. M., Olson, E. N., Bassel-Duby, R. et al. (2001). Activation of MEF2 by muscle activity is mediated through a calcineurin-dependent pathway. *EMBO J.* **20**, 6414-6423.

Wu, W., Ren, Z., Zhang, L., Liu, Y., Li, H. and Xiong, Y. (2013). Overexpression of Six1 gene suppresses proliferation and enhances expression of fast-type muscle genes in C2C12 myoblasts. *Mol. Cell. Biochem.* **380**, 23-32.

Author's personal copy

szentesi.peter_292_24

Journal of Theoretical Biology 264 (2010) 1279–1292

Contents lists available at ScienceDirect

Journal of Theoretical Biology

journal homepage: www.elsevier.com/locate/yjtbi

Improved spark and ember detection using stationary wavelet transforms

László Zsolt Szabó [a,b], János Vincze [a], László Csernoch [a], Péter Szentesi [a,*]

[a] Department of Physiology, Medical and Health Science Centre, University of Debrecen, Debrecen, Hungary
[b] Department of Electrical Engineering, Sapientia Hungarian University of Transylvania, Târgu Mureș, Romania

ARTICLE INFO

Article history:
Received 9 February 2010
Received in revised form
31 March 2010
Accepted 6 April 2010
Available online 9 April 2010

Keywords:
Calcium spark
Ember
Automatic detection
Wavelet analysis

ABSTRACT

Calcium sparks and embers are localized intracellular events of calcium release in muscle cells studied frequently by confocal microscopy using line-scan imaging. The large quantity of images and large number of events require automatic detection procedures based on signal processing methods. In the past decades these methods were based on thresholding procedures. Although, recently, wavelet transforms were also introduced, they have not become widespread. We have implemented a set of algorithms based on one- and two-dimensional versions of the à trous wavelet transform. The algorithms were used to perform spike filtering, denoising and detection procedures. Due to the dependence of the algorithms on user adjustable parameters, their effect on the efficiency of the algorithm was studied in detail. We give methods to avoid false positive detections which are the consequence of the background noise in confocal images. In order to establish the efficiency and reliability of the algorithms, various tests were performed on artificial and experimental images. Spark parameters (amplitude, full width-at-half maximum) calculated using the traditional and the wavelet methods were compared. We found that the latter method is capable of identifying more events with better accuracy on experimental images. Furthermore, we extended the wavelet-based transform from calcium sparks to long-lasting small-amplitude events as calcium embers. The method not only solved their automatic detection but enabled the identification of events with small amplitude that otherwise escaped the eye, rendering the determination of their characteristic parameters more accurate.

© 2010 Elsevier Ltd. All rights reserved.

1. Introduction

The key step in excitation–contraction coupling of muscle cells is the increase in intracellular calcium concentration. In skeletal muscle calcium ions are released from their internal stores, the sarcoplasmic reticulum through calcium release channels (ryanodine receptors; RyR). The opening of one or a few RyR gives rise to localized calcium release events (LCRE; Cheng et al., 1993; Schneider and Klein, 1996) which are assumed to be the building blocks of the global calcium signal. To study these events confocal microscopy and calcium sensitive fluorescent dyes are used (e.g. Klein and Schneider, 2006; Csernoch, 2007; Cheng and Lederer, 2008).

Due to the spatial and temporal characteristics of the events seen in line-scan (x-t) images they have been termed calcium sparks (high-amplitude and short-duration events; Cheng et al., 1993; Schneider and Klein, 1996) or embers (small-amplitude and long-lasting events; González et al., 2000) (for recent reviews see Csernoch, 2007; Cheng and Lederer, 2008). In these studies large quantities of images are produced, hundreds or thousands of events are analyzed, and statistical methods are used because of the bias introduced in imaging and calculation processes.

Therefore, to detect calcium release events on confocal images, automatic detection methods have been developed. The goal of these algorithms is to detect and then isolate the area of each event from the noisy background, and, finally, to extract the characteristic parameters of the events. Most of these methods are based on a double threshold algorithm (this will be referred to as the *conventional method*) proposed by Cheng et al. (1999). Modified versions of the algorithm were used in several studies (Ríos et al., 2001; Zhou et al., 2003; Sebille et al., 2005; Picht et al., 2007). However, due to the unreliable detection caused by the large variety of event morphology—especially those of embers in images from mammalian muscles—and the presence of various noise patterns, emphasis has also been placed on interactive procedures (manual selection of regions of interest and removing false positive detections).

To overcome these difficulties, methods based on wavelet transforms were also introduced in recent years for image enhancement and detection (Wegner et al., 2006, 2007). Wavelet transforms are time–frequency signal decomposition methods, their theory has been developed starting from the mid 1980s. In biomedical image processing wavelets are used for image

* Corresponding author. Tel.: +36 52 255 575; fax: +36 52 255 116.
E-mail address: szp@phys.dote.hu (P. Szentesi).
URL: http://phys.dote.hu/ (P. Szentesi).

0022-5193/$ - see front matter © 2010 Elsevier Ltd. All rights reserved.
doi:10.1016/j.jtbi.2010.04.005

Author's personal copy

szentesi.peter_292_24

enhancement, noise reduction and object detection (Unser and Aldroubi, 1996). Although the à trous wavelet transform has excellent image enhancing and object detection characteristics on noisy images, to achieve fully automatic detection for events with variable size, parameters of the algorithm have to be properly adjusted. For images burdened with photon or shot-noise tuning of the algorithm to achieve reliable detection brings up further difficulties.

Nevertheless, a fully automatic detection remains the main goal of these procedures. In case of sparks, current methods are able to detect events reliably enough to analyze data without manual intervention. However, in case of embers, previously described algorithms did not provide satisfactory results unless manual detection was also included.

We have developed a program in MATLAB (The MathWorks Inc., Natick, USA) to have a Graphical User Interface to carry out calcium event detection. The program uses wavelet-based analysis, utilizing the à trous transform with cubic B-spline as scaling function. This transform has been proposed by Starck (1993) and his coworker, Murtagh (1994) in astronomical image analysis and was first introduced by Wegner and coworkers (2006) for confocal images in calcium spark analysis. While using the conventional method manual user intervention was necessary to modify automatically selected events, with the wavelet-based analysis developed here a fully automatic analysis has been achieved for sparks and an essentially automatic analysis has been achieved for embers.

We designed procedures to test the algorithm and compared the results with previous works and the conventional method. Since experimental images may contain various noise patterns, derived mostly from shot noise produced by the detector, we give a method to use the algorithm on noisy experimental images. Moreover, we test the algorithm for simultaneous detection of high- and low-amplitude events, and thus propose procedures to detect embers, when both sparks and embers are present on the same experimental image.

2. Methods

The algorithm was tested on both experimental and simulated images. The latter, with noisy backgrounds generated by the computer, were used to establish the basic values for the parameters of the algorithm. Modified experimental images were then used to study the effects of real noise patterns especially that of shot noise, on the detection process. Finally, a set of experimental images were used to evaluate the detection methods for embers.

2.1. Implementation of the traditional method

The implementation of the traditional method is a modified version of the algorithm given in a previous work (Cheng et al., 1999). In brief, the original $F(x,t)$ image is filtered with a 3×3 median filter. Pixels above $mean+CRI\cdot\sigma$ are excluded from the image. CRI is an adjustable parameter between 1.6 and 2.0; the mean and standard deviation (σ) is calculated for each spatial position (pixels at a given location at different points in time). A binary mask is formed from the excluded pixels, and continuous regions are searched for to give a binary mask of potential events. Then the image is normalized to the mean of the baseline fluorescence for each spatial position. Values $mean_2$ and σ_2 are calculated for the normalized image (excluding regions of potential LCRE). A region is accepted as an LCRE, if pixel values above $mean_2+CRI_2\cdot\sigma_2$ exist in the region. The criterion CRI_2 is a number above 3, for best detection CRI_2 between 3.4 and 3.7 is used. The test for pixels above CRI_2 is a simple test for existence of pixels or might be a strict test for continuous regions also.

2.2. Implementation of the à trous wavelet transform for spark detection

The algorithm used here is an implementation of the à trous wavelet transform (Holschneider et al., 1989; Mallat, 1999; Shensa, 1992). We followed the implementation that Starck (1993) and Starck and Murtagh (1994) used for denoising and object detection in astronomical images. As a scaling function the transform uses the B-spline of degree 3 (Starck, 1993) utilizing its multi-resolution properties (Unser, 1997). The details of the transform are presented in Appendix 1. To handle the boundaries when performing the convolution one can use either symmetric or circular continuity, it has little influence on the wavelet coefficients (not shown). In our implementation the circular convolution was used. We demonstrate the results of the application of the two-dimensional wavelet transform on a synthetic image containing sparks of various sizes in Fig. 1.

2.2.1. Image denoising

For denoising the multi-resolution support (Starck and Murtagh, 1998) based on the à trous transform was used. Applying the transform for L successive levels and then rebuilding the signal with the inverse transform from levels limited by a proper threshold, gives the denoised signal. Threshold selection is thus a vital step in this method. The selection of threshold values is derived from the standard deviation of the noise in the signal (Starck and Murtagh, 1998; Starck et al., 1998). The algorithm in detail is presented in Appendix 2, and contains a user adjustable parameter δ, to control the threshold level.

2.2.2. Detection algorithm for sparks

The same wavelet transform was used for the detection procedure, but now starting with the denoised image. A thresholding value T_S is applied for each wavelet plane,

$$T_{Sj}=\sigma_j\cdot\tau, \tag{1}$$

where σ_j is the standard deviation of noise for level j (for details see Appendix 2), and τ is a user adjustable parameter. This results in the construction of binary masks for each plane. Small sized (in terms of signal processing high frequency) events as sparks appear on planes 2 and 3, while larger sized (lower frequencies) events as embers, on higher level planes (see section Automatic ember detection in Results). In case of sparks, from the binary masks of levels 2 and 3 (through a logical or operation) the connecting areas are formed, limiting the high-frequency transition borders of sparks. For experimental images with less noise wavelet level 4 might also be used (Fig. 1).

Besides the areas containing LCRE, small areas may also be detected as events, due to specific noise patterns. These should, therefore, be discarded. When used for object detection, the à trous wavelet method is not robust enough in relation to false positive detections. High-amplitude, stand-alone pixels together with noise patterns (2–3 neighboring pixels of higher value than background mean) can disturb the detection process (Starck and Murtagh, 2002). These appear frequently on fluorescence images with higher levels of shot noise.

As a measure of the detected area the number of pixels forming the connected area is thus introduced, and is termed *event size*. When performing the detection, events with sizes below a user adjustable β are discarded; hence, β is the third parameter of the algorithm.

Author's personal copy

szentesi.peter_292_24

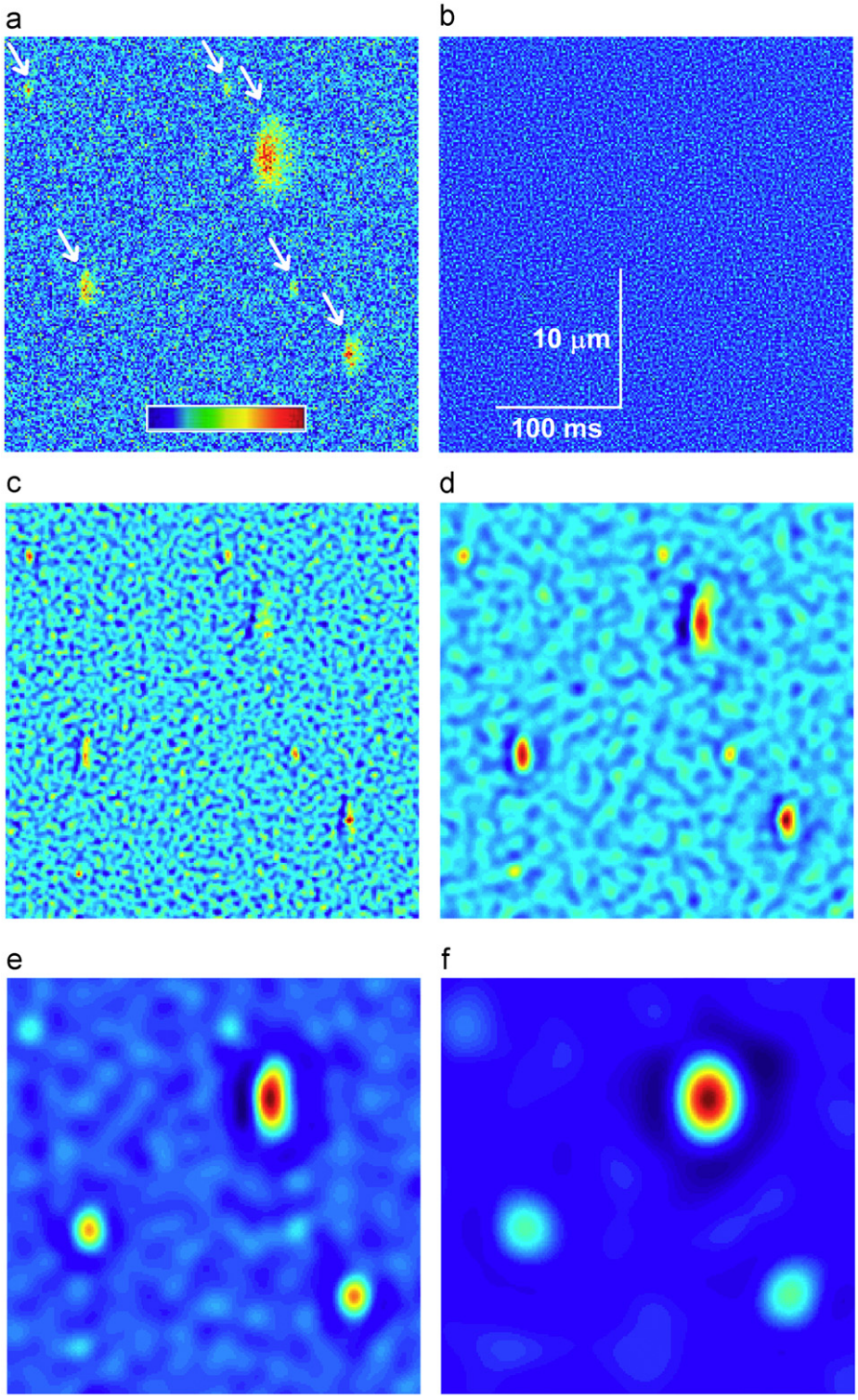


Fig. 1. A simulated image and its wavelet decomposition. (a) Simulated image with Gaussian noise pattern containing 6 sparks (arrows; with relative amplitudes of 0.33, 0.45, 0.57, 0.93, 1.0 and 1.2 F_0) and one single pixel set to shot-noise level. (b–f) Wavelet decomposition levels 1 through 5 of the simulated image. On all panels, warmer colors indicate higher values. Scale bars on panel b apply for all images.

2.3. *Event parameter calculation*

2.3.1. *Sparks*

For sparks, event parameters were calculated according to the usual procedure (Hollingworth et al., 2001). In case of the conventional method, the calculations were done on data extracted for sparks from the normalized image. In case of the wavelet method the normalized and denoised images were used for the calculations. In order to compare values obtained from the denoised data with values obtained from the normalized image in some tests the calculations were carried out for both. Event parameters, full width at half maximum (FWHM), full time at half maximum (FTHM) and amplitude, were calculated by averaging three neighboring lines in space and time, respectively,

Author's personal copy

szentesi.peter_292_24

passing through the pixel within the spark mask having the highest value on the denoised image.

2.3.2. Embers

Before the analysis of the parameters of embers, background fluorescence estimates were updated for each spatial position from the mean fluorescence level of pixels not within a spark or ember mask. The raw image was then renormalized with the updated background level. This normalized image (F_{ne}), now correctly representing embers, was used to calculate the parameters as well as to recalculate the parameters of sparks.

Within the ember mask, the beginning and the end of the plateau phase were marked by the positions where the pixel values reach 80% of the maximal amplitude. We consider the duration of the ember to be the temporal distance between these two marks. All pixel values of F_{ne} between the two marks and not within a spark area were averaged in the spatial domain, showing the spatial distribution of fluorescence during the plateau phase of the ember. A Gaussian fit was applied to these mean values, from which the FWHM and amplitude parameters were derived (Lukacs et al., 2008).

2.4. Images used for the evaluation of the algorithms

2.4.1. Experimental procedures for obtaining images containing sparks

Skeletal muscle fibers isolated from frogs or rats were loaded with 0.1 mM Fluo-3 to record LCRE. Images were captured using an LSM 510 META laser scanning confocal microscope (Zeiss, Oberkochen, Germany) as described earlier (Lukacs et al., 2008). In brief, line-scan images were taken at 1.54 ms/line and 512 pixels/line (pixel size 0.142 μm) with a 63x water immersion objective (1.2 n.a., Zeiss). Fluo-3 was excited with an Argon ion laser (at 488 nm), emitted light was collected through a band-pass filter and digitized at 12 bit.

The noise level of the image—expressed as the ratio of mean (m) and standard deviation (σ) of the background of the image—is an important parameter of algorithm testing. We will refer to it as signal-to-noise ratio of the background $BSNR=m/\sigma$. For experimental images, this was calculated by excluding pixels containing the events. In our experiments (including 700 randomly selected images into the analysis) BSNR varied between 3.2 and 5.4. Consequently, we will consider in our tests BSNR of 2.5 as the worst case, 3.5 as intermediate and 4.5 as good experimental conditions.

2.4.2. Artificial images

We used two methods to construct the background for our simulated images. First, the background was approximated by a generated noise with Gaussian distribution (Cheng et al., 1999; Wegner et al., 2006). This is a good approximation for images with low levels of shot noise. Second, we used experimental images to reconstruct the heavy shot-noise patterns. Images used to generate such a background were first tested for having no positive detection of LCRE. Moreover, the scan lines were shuffled randomly to eliminate the possibility of undetected sparks in the image.

In order to test the accuracy of detecting sparks, synthetic model sparks were embedded in the background. The model spark (see Fig. 6 insets) was obtained by averaging the image of 10 experimental sparks (similar size in x and t directions) and smoothing the obtained image, and had a FWHM of ~1.7 μm, FTHM of ~9 ms and a duration of ~14 ms, values which correspond to sparks detected in our experimental images. It was then scaled to have various amplitudes. The sparks, six for each image, were distributed randomly in the image; no overlapping regions between sparks were permitted (Fig. 1a).

2.4.3. Images containing embers

Since embers are more diverse in their morphology than sparks, we decided not to generate simulated images containing embers, but to evaluate the effectiveness of the detection method on a set of images from experiments containing embers. We have previously shown that the scorpion toxin maurocalcine causes frequent long-lasting calcium release events (embers) on skeletal muscle fibers (Lukacs et al., 2008). A set of 74 images from these experiments were used to evaluate the detection algorithm. Images contain both sparks and embers (sometimes as combined events) with relatively high frequency and varying duration for embers made them ideal for the evaluation of the detection algorithm. Positions of the embers were manually determined by a person experienced in confocal image analysis. The result of the detection algorithm was compared to this manual selection on all images, minor differences in position were not considered as false detections since they do not affect the parameters of the ember.

2.5. Methods used to test the algorithm

To test the algorithm, 240 images with randomly embedded events (see above) were analyzed for a given set of parameters. During the repeated execution, parameters of the sparks were calculated and collected. In addition, true positive (TP; event found at the location where it was originally placed), false positive (FP; an event found at a location where originally no event was placed) and false negative (FN; an originally positioned event that was not found) detection counts were retained. To evaluate the performance and reliability of the algorithm the sensitivity (S; defined as $TP/(TP+FN)$) and the positive predictive value (PPV, as defined in signal detection theory $TP/(TP+FN)$) were calculated. To characterize the functions, the values S_{50} and PPV_{50}, defined as the relative event amplitude where S and PPV reach 50% detection probability, were used (Wegner et al., 2006). Statistical analysis was made using the SigmaStat (Aspire Software International, Ashburn, USA) program. Mann–Whitney Rank Sum test was used to compare median values and Brown–Forsythe test was used to compare standard deviations. In both cases P-value 0.001 was defined as significant.

3. Results

3.1. Artificial images

First the performance of the traditional and the wavelet-based detection methods were compared on artificial images (Fig. 3) where the background was generated from experimental images (panels a and b; see Methods, Artificial images) or using Gaussian noise (panels c and d). In case of the former the traditional method can be set to give satisfactory sensitivity in the 0.2–0.5 amplitude region (Fig. 3a), which is the region where sparks are most abundant in mammalian muscle. However, in the same amplitude region, using the same parameters ($\tau=3$, $\delta=4$) the positive predictive value of the detection was extremely low (less than 0.2, Fig. 3b), indicating that the traditional method requires an extensive manual post-processing. In contrast, if used on simulated images with Gaussian noise, the traditional method gives high positive predictive values (Fig. 3d) even for low-amplitude events emphasizing the importance of the noise pattern used.

Author's personal copy

szentesi.peter_292_24

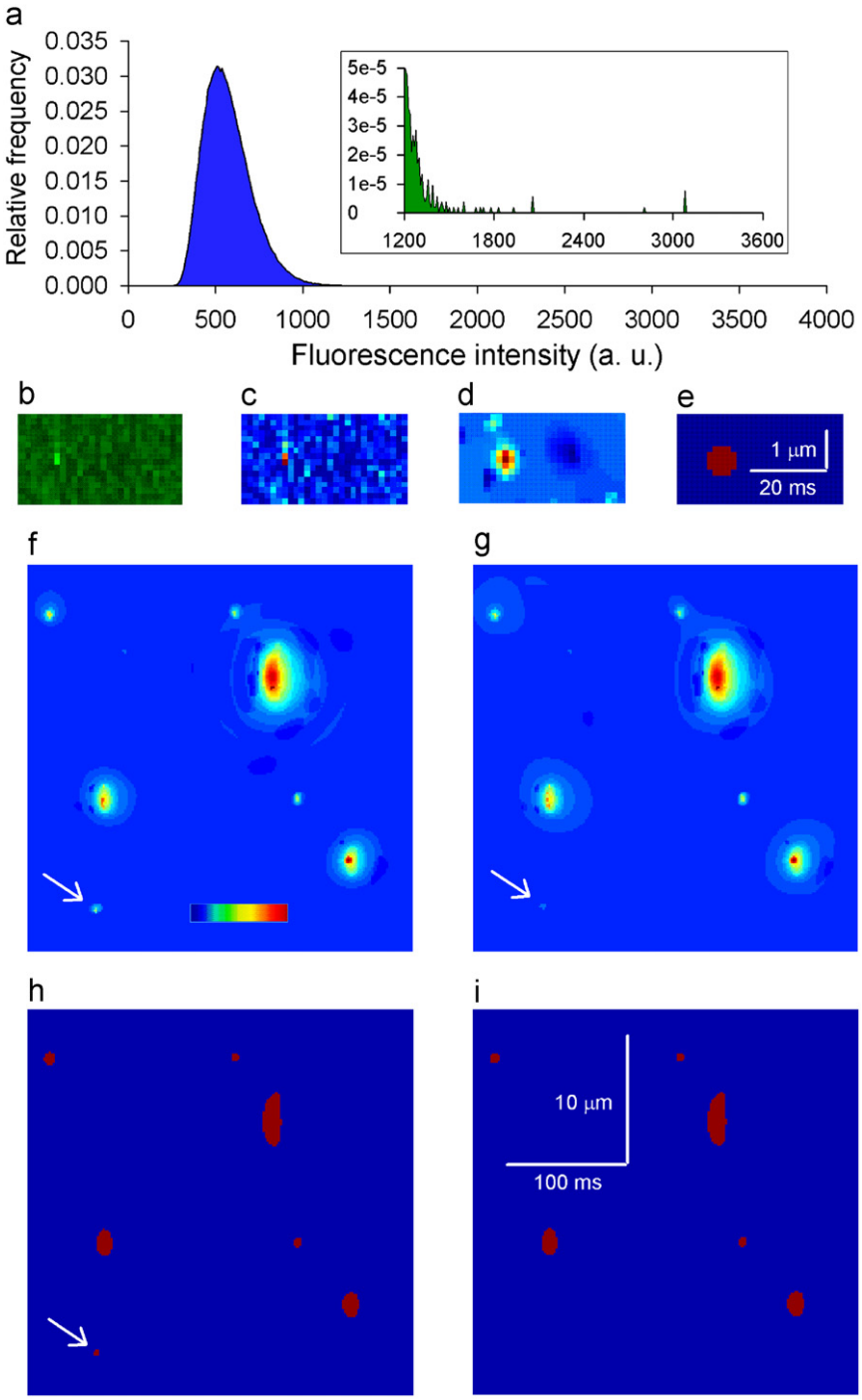


Fig. 2. Spikes and the background noise distribution of a confocal line-scan image. (a) Histogram of a shot noise affected experimental image that does not contain sparks. Inset shows the histogram on an expanded *y*-scale to demonstrate the presence of pixels with high fluorescence. (b–e) Appearance of spikes following wavelet decomposition. (b) Shot-noise pattern (a few neighboring pixels with high fluorescence intensity) from an experimental image. Brighter green indicates higher fluorescence intensity. (c) The shot-noise pattern on the normalized image. (d) The shot-noise pattern on the wavelet-denoised image. (e) Detection mask of the shot-noise pattern obtained with the wavelet method. Scale bars in panel e apply for all images in b–e. (f) Denoised image of the simulated image of Fig. 1d without the spike filter. (g) Denoised image of the simulated image of Fig. 1d with the spike filter. (h and i) Detection masks obtained without and with spike filter for images in f and g, respectively. Arrow points to the spike caused by the shot noise. Note the lack of spike on panel i. Scale bars in panel i apply for all images in f–i. Color scale in panel f applies for panel c, d, f and g.

While the sensitivity of the wavelet-based detection method was essentially the same as that of the traditional method for both backgrounds (Fig. 3a and c), it performed substantially better in the detection of similar amplitudes on images with experimental noise. The PPV_{50} value was, in this case, lower by more than 0.3 (0.287 vs. 0.592) relative fluorescence units as compared to the traditional method (Fig. 3b). The PPV curve was, however, less steep than in the case of the traditional method and it also did not match the steepness previously described in case of a similar algorithm (Wegner et al., 2006). After a close examination, it was found that most of this difference could be attributed to false positive events—termed "spikes" from hereon—which are not present on simulated images with Gaussian-distributed background noise. The background noise profile of experimental

Author's personal copy

szentesi.peter_292_24

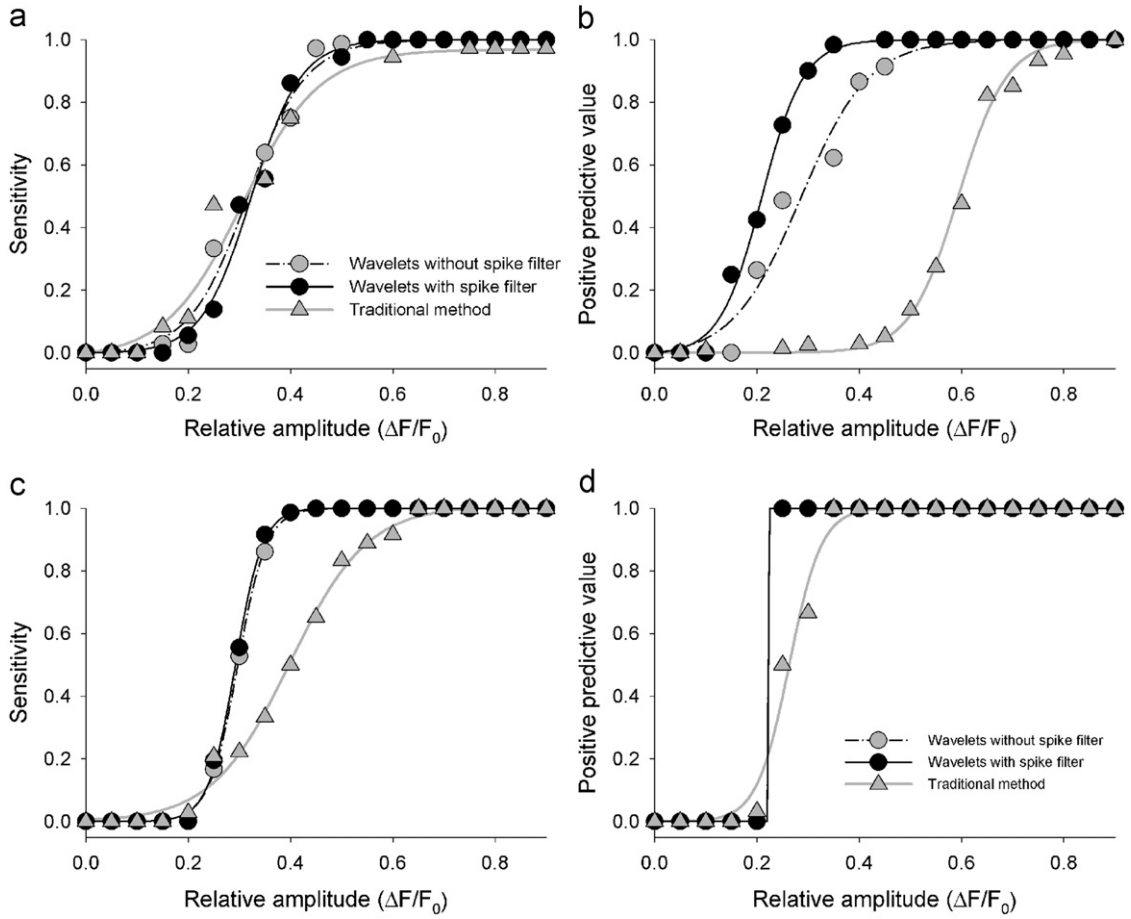


Fig. 3. Sensitivity (a and c) and positive predictive values (b and d) as a function of event amplitude for different detection algorithms. Simulated images with synthetic model sparks on backgrounds generated from experimental images (a and b) and with Gaussian noise (c and d) were used to test the accuracy of the algorithms. Three different algorithms were tested, the traditional method (with $CRI_2=3.6$), the wavelet-based method without and with spike filter (with $H=4.5$, $\tau=3$, $\delta=4$, wavelet levels 2 and 3). Curves for each data set were drawn by eye with S_{50} and PPV_{50} values of 0.315, 0.315, 0.325 on panel a, 0.285, 0.21, 0.595 on panel b, 0.3, 0.3, 0.41 on panel c and 0.23, 0.23, 0.26 on panel d for the wavelet without and with spike filter and for the traditional methods, respectively.

images is not perfectly Gaussian- or even Poisson-like since high-amplitude pixels are more abundant than predicted by those distributions (Fig. 2a). Spikes are created by the wavelet-based denoising procedure when 2 or 3 pixels with high amplitude are next to each other (Fig. 2d and f). These areas are then detected as false positive events (Fig. 2e and h). We compared the detection statistics of the algorithm on images with different distributions of the background noise using the same parameters (Table 1). A difference of about 0.3 units in PPV_{50} was found between images with typical experimental backgrounds (BSNR 3.24) and with Gaussian backgrounds with similar BSNR. In case of extremely noisy experimental backgrounds ($BSNR < 2.5$) the difference was even more pronounced (not shown).

Table 1
Effect of background noise on detection[a] statistics.

Background noise distribution	BSNR	S_{50}	PPV_{50}
Gaussian	2.0	0.37	0.28
Experimental	2.38	0.47	0.90
Gaussian	2.5	0.37	0.28
Experimental	3.24	0.35	0.58
Gaussian	3.5	0.30	0.23

[a] Parameters used in the wavelet-based detection were $\delta=3.5$; $\tau=3.5$.

3.1.1. The threshold operator

The selection of the threshold operator also has an influence on the detection of false positive events in noisy images. Of the three operators described in Appendix 2, soft thresholding produces the smoothest denoised images, but it modifies all coefficients, therefore substantially influences the calculated event parameters. The affine threshold operator produces a smoother denoised image than hard thresholding, but as an effect of inclusion of small wavelet coefficients, it is vulnerable to spikes (data not shown). Consequently, the hard threshold operator was used during the tests for image denoising.

3.1.2. Event size

Since spikes are generated by the denoising algorithm from a small number of neighboring pixels, they are generally smaller in time and space than detectable true events. Therefore, at first, it seemed feasible to eliminate spikes by setting a threshold—parameter β—for the size of the events during detection (Fig. 2h and i).

We evaluated different settings of β between 2 and 40 (in Fig. 4 data for $\beta=2$, 10 and 40 shown). We did not try β values lower than 2, as that would mean the inclusion of "events" containing

Author's personal copy

szentesi.peter_292_24

only 1 pixel. Even if these hits were true positives, they would be indistinguishable from the background. With $\beta=40$ we could already reach 100% PPV at all amplitudes where we could detect events, so any further increase in β would only shift PPV_{50} to the right, but not improve sensitivity.

From the detailed evaluation of different β parameters, we concluded that size-based event selection is not an efficient method of eliminating false positive hits caused by spikes. Its moderate increase only slightly improves one part of the PPV curve (Fig. 4b, compare curves for $\beta=2$ and $\beta=10$) while a β set high enough to improve PPV substantially worsens sensitivity (Fig. 4a).

3.1.3. Spike filter

As selecting higher β values did not prove useful for the exclusion of spike-induced false positive events, we applied a filter, also based on the à trous wavelet transform to find and remove the high-amplitude pixels forming spikes. This "spike filter" was applied to the normalized image, which was obtained by the same procedure as described for the traditional method, except for the introductory median filtering and smoothing. Before denoising, the high-frequency components of the image were selected (Koshino et al., 2002). The à trous transform was calculated for wavelet levels 1 and 2. For the $F_n(t,x)$ image:

$$F_n(t,x) = c_2(t,x) + \sum_{i=1}^{2} w_i(t,x). \tag{2}$$

The backward transform was performed including only the wavelet coefficients (and excluding the background obtained for level 2):

$$\mathrm{hf}(t,x) = \sum_{i=1}^{2} w_i(t,x). \tag{3}$$

Mean and standard deviation (m,σ) of $\mathrm{hf}(t,x)$ were calculated. A threshold was applied:

$$|hf(t,x) - m| > H \cdot \sigma \tag{4}$$

resulting in a binary image $B(x,y)$, revealing the high-frequency pixels (edges, spikes). H is the parameter of tuning the threshold level; in case of our line-scan images the best results were obtained using values between 3.5 and 4.5.

Connected regions of 2 or more pixels were discarded. This can be achieved by convolving the binary image B with the

$$\begin{matrix} \frac{1}{9} & \frac{1}{9} & \frac{1}{9} \\ \frac{1}{9} & \frac{1}{9} & \frac{1}{9} \\ \frac{1}{9} & \frac{1}{9} & \frac{1}{9} \end{matrix} \tag{5}$$

kernel and discarding more than 2 connected pixels. This step prevented us from smoothing regions of pixels with high-fluorescence values that appear in areas of sparks. Solitaire high-amplitude pixels were replaced by the mean of their eight neighbors. The difference between results of the denoising procedure with and without spike filtering is shown in Fig. 2f–i.

Spike filters are generally not perfect, i.e. they may attenuate real sparks with small areas that have similar morphology to spikes, therefore, the application of the spike filter will at least slightly influence the detection of small-sized events. According to our results a minor decrease in sensitivity is indeed present, but definitely not as serious as when using high β values. We obtained the best PPV for $H=3.5$, and even at this setting the decrease in sensitivity was moderate (data not shown).

These results could be further improved by applying the spike filter locally. As spike-induced false positives are limited in event area, we can use the spike filter as an exclusion technique on events with small areas. In practice, the wavelet-based detection procedure is run without spike filtering, and after the detection phase one tests the small sized events for spikes (in practice we limit the test to events with areas below 50 pixel). The method is the same as described above, but the application area is limited to pixels within the detection mask of the event from the normalized image. After the test, small-sized events identified as spikes are excluded, since the presence of pixels having high values in a small spark is improbable. This local test does not affect sparks with higher event size and amplitude.

With this improved method we could reach good spike filtering with practically no loss in sensitivity (Fig. 3a). In conclusion, we found that on our system the optimal parameter set for mammalian spark detection is $\delta=4.0$, $\tau=3$, $\beta=2$, and the spike filter should be applied with $H=4.5$, since it produces marked gain in PPV with no visible loss in sensitivity.

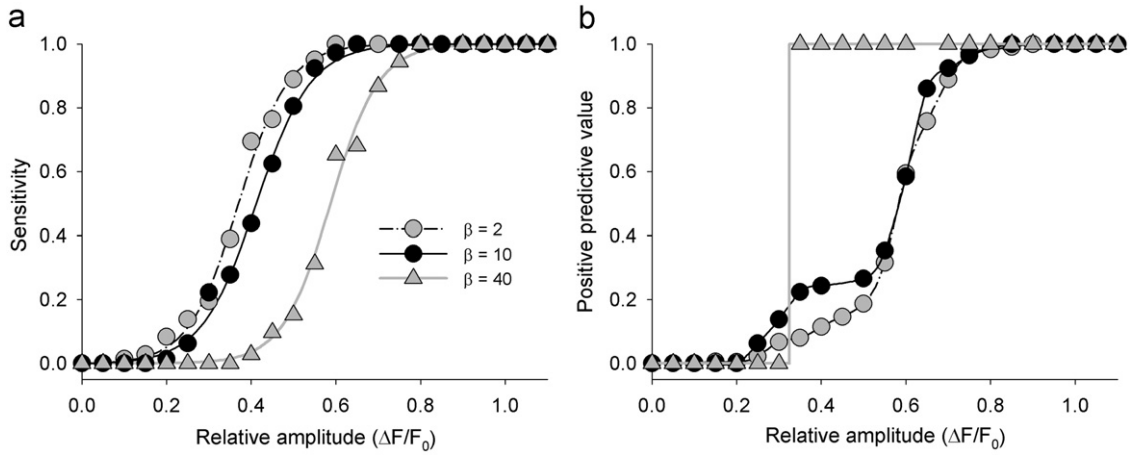


Fig. 4. Sensitivity (a) and positive predictive values (b) as a function of event amplitude if the events below a predefined area (event size, parameter β) are excluded. The wavelet method without the spike filter was used for event detection. Images were generated as described for Fig. 3. Results are shown for three (2, 10 and 40) different β values. Curves for each data set were drawn by eye with S_{50} and PPV_{50} values of 0.37, 0.41, 0.585 and 0.583, 0.576, 0.325 for $\beta=2$, 10 and 40, respectively. (For further details, see text.)

Author's personal copy

szentesi.peter_292_24

3.1.4. Parameters of the detected events

To test the accuracy of the calculation of event parameters, we compared the calculated parameters of differently scaled events embedded in synthetic images (Fig. 6). We used three scaled versions of the model spark: the one used in all other tests (hereafter referred to as normal sized; FWHM = 1.78 μm and FTHM = 18.4 ms) together with its half- and double-sized versions. Scaling was performed in both spatial and temporal dimensions. For each scaled version we generated images containing sparks between amplitudes 0.2 and 0.9 $\Delta F/F_0$.

We found that the calculated amplitude is a linear function of the generated amplitude at all FWHM values if the generated amplitude is at or above 0.4. Note that sparks with amplitudes higher than 0.4, could be detected with practically 100% sensitivity. The non-linearity in amplitude values below 0.4 is caused by the fact that in the case of smaller amplitudes, a spark has greater chance to be detected if positive noise is added on it. Therefore, for sparks with small amplitudes the calculated event amplitude is a biased estimate of the original event amplitude. Another interesting fact about the relationship between the generated and the calculated event amplitude is that the slope of the linear part of the function is itself a monotonically increasing function of FWHM (i.e., it was the smallest for the half sized and the largest for the double-sized events). In case of the normal-sized model spark, the slope was around unity (Fig. 6b).

We also compared the calculated FWHM values to those of the different scaled model sparks. As a general finding, the calculated FWHM at most equals that of the model spark, usually the calculation underestimates the FWHM. In case of the half-sized model spark, the calculated FWHM was smaller than the original FWHM at all tested amplitudes and was independent of event amplitude (Fig. 6a). In other cases the detected FWHM definitely increased as the relative amplitude of events increased, and reached 90% of the generated value at amplitude levels 0.64 and 0.4 in the case of normal (Fig. 6b) and double-sized (Fig. 6c) model sparks, respectively.

3.1.5. Experimental images

To compare data obtained by the new wavelet-based method to data obtained by the previously used traditional method, we evaluated the results of both methods on a set of experimental images. First, the wavelet-based detection identifies a number of events that are not found by the traditional method. In addition, both in case of the detected amplitude and in the case of the detected FWHM, the mean from the wavelet-based method (0.490 ± 0.005 $\Delta F/F_0$ and 1.90 ± 0.01 μm) was significantly ($p < 0.001$) lower than those of the traditional method (0.523 ± 0.006 $\Delta F/F_0$ and 2.33 ± 0.03 μm) (Fig. 5). In case of FWHM it is also apparent that the standard deviation is smaller (0.706 vs. 1.787 in the wavelet-based and in the traditional method, respectively), i.e. there are fewer events with FWHM much different from mean FWHM. This difference is also significant ($p < 0.001$).

We attribute these differences mainly to two factors. First, the wavelet-based method has better sensitivity and PPV at smaller amplitudes, therefore small sparks had higher probability to be detected by the wavelet transformation. Second, the denoising produces based on the wavelet transforms generate much cleaner images than the median filter used in the traditional method, therefore curve fittings are more accurate. We visually compared several sparks where the result of fitting was different for the two algorithms and verified that the fitting on the wavelet–denoised image was better.

Izu et al. (1998) pointed out that if simple assumptions for the RyR hold true—the duration of all release channel openings are equal—the reciprocal of the relative number of events should be a linear function of event amplitude. As presented in Fig. 5a inset the relationship is a convex rather than a linear function, suggesting that the sparks were generated by channels whose open times were exponentially distributed as discussed by Izu et al. (1998).

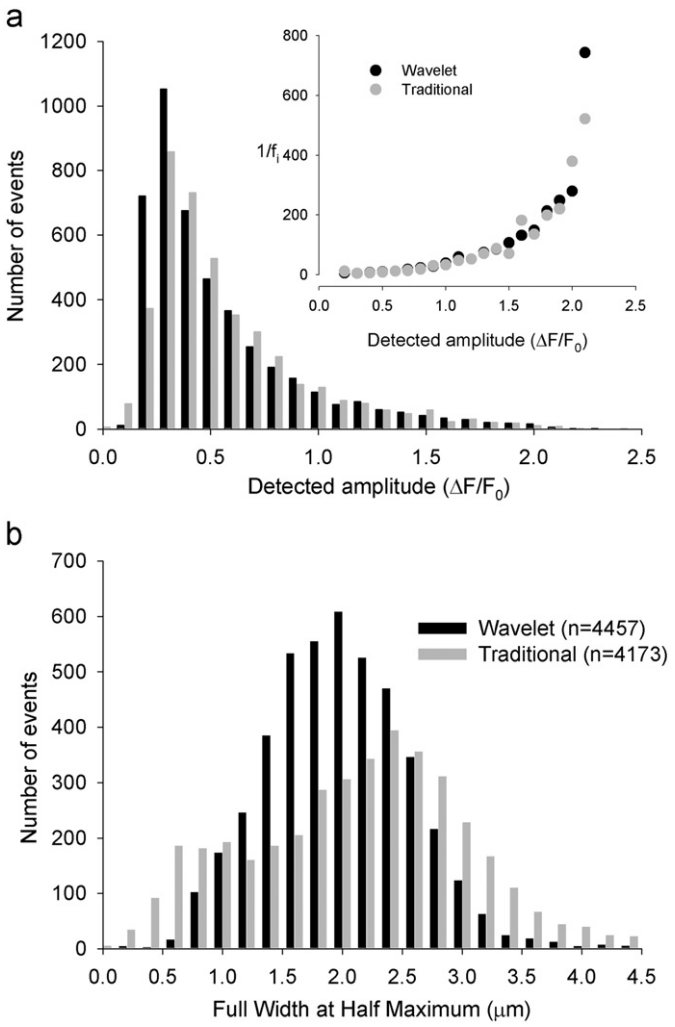


Fig. 5. Distribution of spark parameters, amplitude (a) and FWHM (b). Events were identified with the traditional (gray) and the wavelet-based (black) methods using the spike filter for the latter. 300 images were included into the analysis. Event parameters were calculated as described in Methods. All identified events, regardless of their parameters were included into the histograms. Inset in panel a shows the reciprocal of the relative number of events as a function of event amplitude for data in this panel.

3.2. Automatic ember detection

3.2.1. Image preprocessing for ember detection

Our ember detection method uses the raw fluorescence image as its input (Fig. 7a), but sparks are excised from it. This excision is achieved by the multiplication of the original image with the inverse of the spark mask generated in the final step of spark detection, containing 0 if a pixel is within a spark rectangle and 1 otherwise (Fig. 7a, rectangles). In order not to generate sharp amplitude steps causing undesired signals on lower frequency (i.e., higher) wavelet levels, pixels with zero values are filled with the values of a randomly positioned set of pixels from the same

Author's personal copy

szentesi.peter_292_24

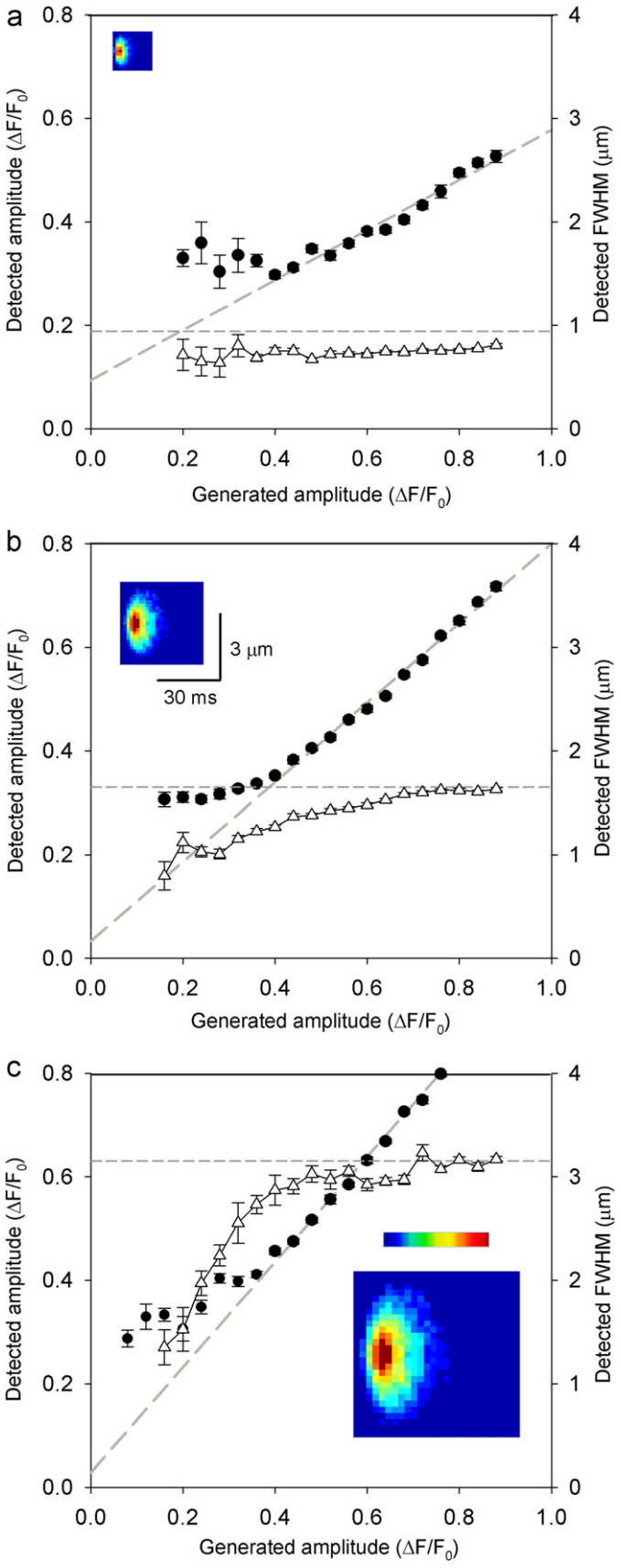


Fig. 6. Evaluation of how the detected event parameters—amplitude (●) and FWHM (Δ)—depend on the original event parameters. Generated model sparks, shown in the insets, were scaled to have different amplitudes and then embedded in images with backgrounds generated from experimental images. Horizontal short dashed lines in a–c give the FWHM of the original sparks. Long dashed lines are linear fits to data points obtained for sparks with amplitudes 0.4 and above with slopes of 0.48, 0.76 and 1.02, respectively. Scale bars on panel b and the grey scale in panel c apply for all images.

time line not within any spark rectangle. Let the image generated this way be denoted as F_e (Fig. 7c). Note that the described filling method also ensures that even if consecutive sparks are present in a column, they are filled with different background pixels. Without random sampling from the column, unwanted low-frequency patterns may arise, significantly lowering the positive predictive value of the algorithm. This image is further enhanced by spike filtering (see section Spike filter), eliminating shot-noise patterns that can cause a significant signal even on high wavelet levels. In conclusion, F_e is suitable for use in all further steps of ember detection.

3.2.2. Wavelet transform and ember detection

We propose two slightly different methods for ember detection, both based on the á trous wavelet transform. Both algorithms have clear advantages over the other, so we provide a detailed analysis and comparison of the two.

3.3. Method a—two-dimensional wavelet transform

Due to the characteristics of the wavelet transformation, lower frequency signal components, like those representing embers, are found on higher wavelet levels. We found in our preliminary studies that embers of typical duration (90 ms to 1300 ms, i.e. 60–850 pixels under the condition used here) appear mostly on the fifth wavelet level (w_5; Fig. 7d) if the above-described two-dimensional wavelet transform is performed. To localize embers on this wavelet plane a double thresholding is applied:

$$M_A(x,y) = \begin{cases} 0, \text{ if } w_5(x,y) < \mu \cdot \varepsilon, \\ 1, \text{ if } \mu \cdot \varepsilon \le w_5(x,y) < \mu \cdot \zeta \\ 2, \text{ if } \mu \cdot \zeta \le w_5(x,y). \end{cases} \quad (6)$$

where μ is the image mean, ε is the lower criterion and ζ is the higher criterion. Connected areas of $M_A \ge 1$ containing at least 10 pixels with $M_A=2$ are considered to be embers (Fig. 7e). For further analysis, their bounding rectangle is determined by adding 30 pixels in each temporal direction and 10 pixels in each spatial direction to the minimum bounding rectangle of the area (Fig. 7i; rectangles with short dashed lines).

3.4. Method b—one-dimensional wavelet transform

In contrast to the two-dimensional wavelet transform used for spark detection and in *Methods A* and *B* we apply a one-dimensional wavelet transform in the time dimension on each image line separately. This choice was made to account for the spatiotemporal characteristics of embers (i.e., their width in the space domain is in the order of 25 pixels while their length in the time domain can be more than ten times larger) and for the lack of uniform background level in the absence of normalization.

Apart from the difference in the number of dimensions, we use the same wavelet transform and base function as described in section Implementation of the à trous wavelet transform for spark detection. Let the wavelet levels of the so decomposed signal be denoted as w_k, where k is the number of the level. As shown on Fig. 7f and g, embers of typical duration yield the most distinctive signal on levels 8 and 9. In case of longer embers, the signal on level 8 is more pronounced around the beginning and the end of the event and the signal on level 9 is more pronounced in the middle. We, therefore, perform double thresholding on the combined image generated by the following function from

Author's personal copy

szentesi.peter_292_24

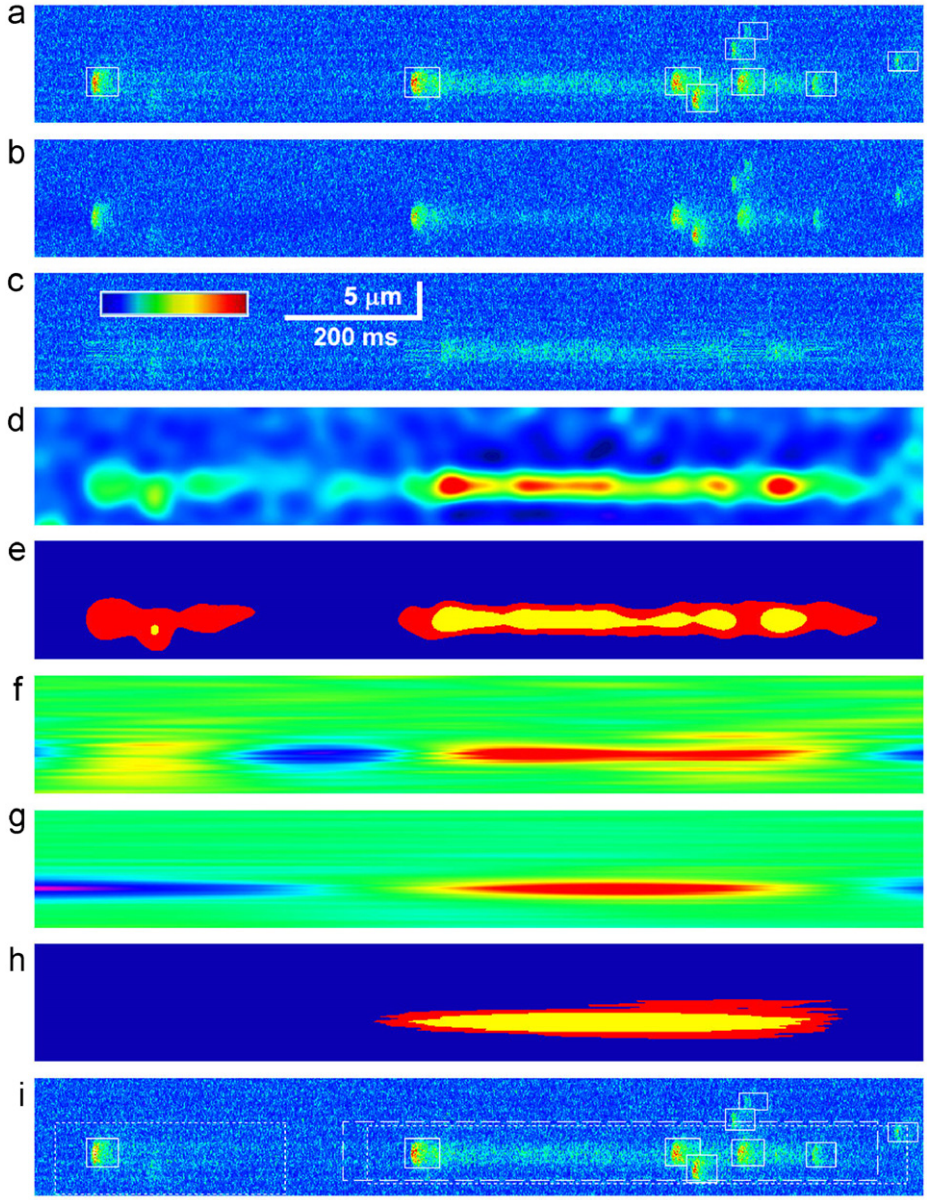


Fig. 7. Detection of embers using the wavelet method. (a) Sparks and embers on an experimental image. As a first step sparks are identified (rectangles). (b) Normalized image, note the problem of normalization at the spatial position of the ember. (c) Image with excised sparks. (d) Wavelet transform—level 5—of the image in panel c. (e) Mask obtained from the image in panel d with the double threshold method. (f and g) Wavelet transform levels 8 and 9 of the image in panel c. (h) Mask obtained with a simple threshold method from the images in panels f and g. (i) Identified sparks and embers, the latter are marked by dashed rectangles. For further details, see text. Scale bars on panel c apply for all panels. The color scale on panel c apply for all panels except e and h. On panels e and h blue means mask value 0, red mask value 1 and yellow mask value 2.

wavelet levels 8 and 9:

$$w'_{8+9} = \max(w'_8, w'_9) \tag{7}$$

The resulting mask of double thresholding (M_B) is generated using the image mean (μ), lower (ε) and higher (γ) criteria:

$$M_B(x,y) = \begin{cases} 0, \text{ if } w'_{8+9}(x,y) < \mu \cdot \varepsilon, \\ 1, \text{ if } \mu \cdot \varepsilon \le w'_{8+9}(x,y) < \mu \cdot \gamma \\ 2, \text{ if } \mu \cdot \gamma \le w'_{8+9}(x,y). \end{cases} \tag{8}$$

Again, connected areas of $M_B \ge 1$ containing at least 10 pixels with $M_B = 2$ are considered to be embers (Fig. 7h). For further analysis, their bounding rectangle is determined by adding 30 pixels in each temporal direction and 10 pixels in each spatial direction to the minimum bounding rectangle of the area (Fig. 7i; rectangles with long dashed lines).

3.4.1. Ember detection statistics

Detailed analysis of the events detected as embers by our algorithms shows that both algorithms are generally capable for automatic ember detection. When tested on all 74 images method B based on the one-dimensional wavelet transform always had higher positive predictive value for a given sensitivity than method A (Fig. 8). However, method A has characteristics that can yield better detection parameters in certain applications. First, it is able to find relatively shorter, but wider events (Fig. 7i). Second, it is capable of detecting events that span the entire image. In conclusion, we found that images similar to those analyzed here can be most effectively processed with method B, using parameters $\varepsilon = 0.015$ and $\gamma = 0.035$ (resulting in a PPV of 0.84 at 0.71 sensitivity). Under the same conditions method A reached 0.64 PPV at 0.73 sensitivity ($\varepsilon = 0.015$, $\zeta = 0.055$).

Author's personal copy

szentesi.peter_292_24

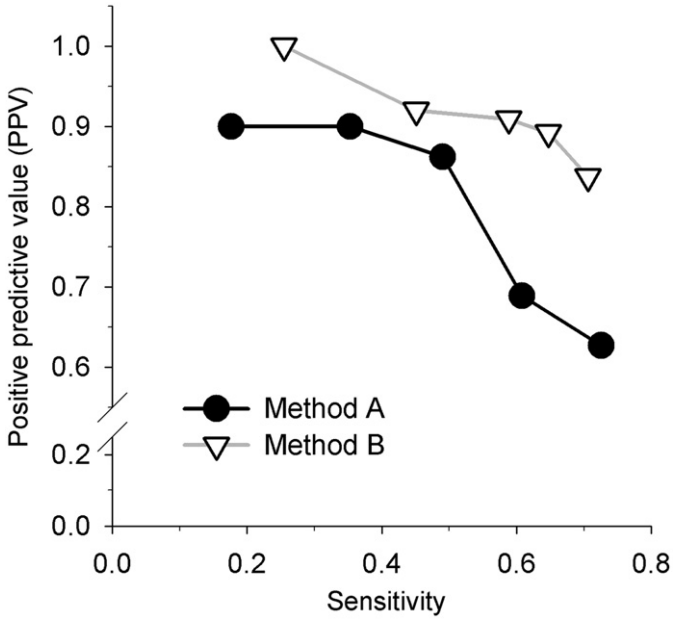


Fig. 8. Accuracy of ember detection using one- and two-dimensional wavelet transforms. For testing 74 experimental images were used. Note that the one-dimensional wavelet transform (method B) always had a higher positive predictive value for a given sensitivity than did the two-dimensional based transform (method A). For details on methods A and B, see text.

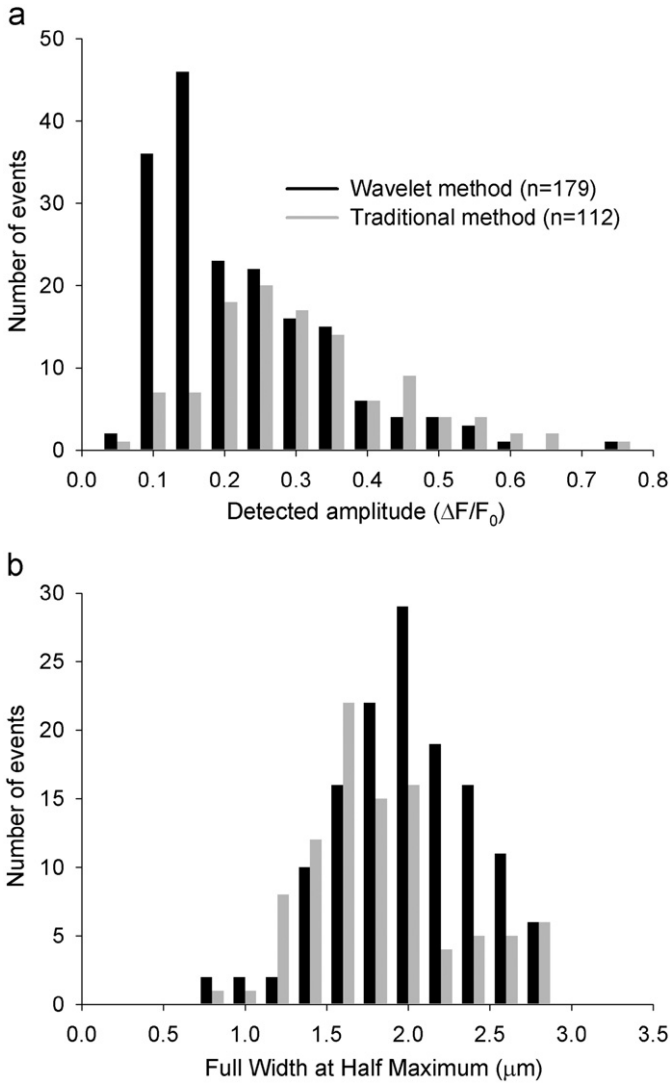


Fig. 9. Distribution of ember parameters, amplitude (a) and FWHM (b). Events were identified with the traditional and the wavelet-based methods using the spike filter for the latter. 140 images were included into the analysis. Event parameters were calculated as described in Methods. All identified events, regardless of their parameters were included into the histograms.

We next compared the parameters of long-lasting events identified by the wavelet transform to those identified by eye. First, it is important to stress that the wavelet-based method recognized more events (179 vs. 112 in the 140 images tested). It is clear from the distributions of event amplitudes presented in Fig. 9a that these extra events had smaller amplitudes. Noteworthy is the fact that the amplitude distribution, which had a shallow rising phase for the events identified by eye, became more exponential, as expected theoretically. This resulted in a clear change in the average amplitude to smaller values, from 0.231 ± 0.013 to 0.197 ± 0.009, for events identified by eye and by the wavelet method, respectively.

On the other hand, the distributions of FWHM for the two methods (Fig. 9b) were not as different as for the amplitudes, indicating that the extra events found by the wavelet method indeed belong to the same group as the others. This observation was confirmed by the fact that only a small, albeit significant difference was detected in the average values of FWHM, 1.93 ± 0.05 vs. $2.09 \pm 0.04\,\mu m$.

Taken together, these observations not only confirm that the wavelet-based method is capable of identifying long-lasting events as embers, but prove that it gives a more accurate detection than a simple identification by eye does.

4. Discussion

In this work the à trous wavelet transform was implemented to detect localized calcium release events in fluorescence images from skeletal muscle fibers. We used the transform to develop algorithms for denoising, event detection and spike filtering. The method proved to be a valuable tool in analyzing these two-dimensional fluorescence signals (x-t images) embedded in a noisy background. Besides the use of the transform to detect calcium sparks—events with large amplitude and relatively short duration—we established a procedure to isolate long-lasting, low-amplitude events, as embers. The results presented here imply that these multi-resolution methods are, on the one hand, adequate for analyzing confocal images and, on the other hand, indicate that they are a better choice than the traditionally applied thresholding algorithms.

Wavelet-based methods in biological data/image processing have been used extensively. Nevertheless, these algorithms in calcium imaging have not gained ground, and only a few reports are available for comparison (Wegner et al., 2006, 2007). The important difference between the tests presented in those reports and the tests presented here is that we used backgrounds generated from experimental images rather than backgrounds generated using mathematical distributions. This difference becomes significant if positive predictive values and sensitivities are compared since experimental images are burdened with shot noise. Clearly, the values of PPV_{50} and S_{50} reported by Wegner et al. (2006) are smaller than the values obtained here with the simple (without spike filter) wavelet method. We believe that this difference is due to the presence of pixels with high fluorescence intensity in experimental images.

Author's personal copy

szentesi.peter_292_24

Importantly, therefore, if one uses the transform on experimental images from mammalian muscle images that are usually affected by high levels of shot noise, one must face the high sensitivity of the detection procedure, resulting in a large number of false positive detections (Figs. 1–3). This renders the simple wavelet method inconvenient for event detection since an extensive manual post-processing (removing of false positive events by an experienced person) would be required. This could explain why wavelet-based detection has not become widespread. As a result, we present here a procedure—the spike filter; also based on the wavelet method—to avoid false positive detections. If the traditional technique for spark detection and the method based on the wavelet transform (including the spike filter) are compared, a higher sensitivity and better positive predictive values can be achieved by the latter (Fig. 3).

We thus used data from the denoised images for calculating the parameters of calcium sparks. This permitted better curve fitting and more accurate determination of the parameters. It should be emphasized here that the amplitude was only slightly affected by the denoising, while the signal-to-noise ratios in the analyzed images had been improved. Comparing the event parameters obtained with the wavelet method to data derived with the traditional method revealed significant differences. Most importantly, a number of events that were not recognized by the traditional method—mostly events with small amplitudes (Fig. 5a)—were clearly identified by the wavelet-based algorithms. In addition, the distribution of event parameters was more consistent for the latter, showing that the identified events are indeed derived from a single population. It is important to stress here that the distribution of FWHM obtained with the traditional method shows a slight increase at small FHWM values. This is clearly due to the fact that no manual selection of the events was permitted resulting in a number of false positive detections using the traditional method. In conclusion, the wavelet-based method provides better parameter estimation in the case of experimental images than the traditional method, because the cleaner denoised images result in better curve fitting. However, there is a significant difference in the distributions of event parameters; therefore images processed using the traditional method should be reprocessed before comparing their results to new data obtained with the wavelet-based detection algorithm.

Previously published LCRE detection methods for *x-t* images rely on column-by-column normalization of the raw image in order to eliminate the variation of background fluorescence and produce relative fluorescence signal. This normalization technique is suitable when the combined event duration is only a fraction of the total scan time. It will, however, not produce the desired result if this condition is not fulfilled, e.g. on images containing long embers. Embers are effectively smoothed into the background and, more importantly, darker areas may appear before and after the event, rendering them undetectable by the normalization (Fig. 7b). Therefore, using previously published methods for spark detection, embers usually have to be manually selected on raw images. Manual selection is not only impractical on large amount of data, but may also lead to bias in ember parameters, similarly to the bias in case of spark amplitudes as described in previous studies (Song et al., 1997).

The two, wavelet-based ember detection algorithms described here proved to be effective aids in analyzing images containing embers. Although their detection efficiency (sensitivity and positive predictive value) may not be as good as those of the spark detection algorithm (compare Figs. 3 and 7), it is evident that they can greatly reduce the human workload. Under favorable circumstances, they may even be capable of reliable and fully automatic ember detection. In addition, it is clear that the parameters derived from the events identified by the wavelet method represent a more accurate estimation of the actual values than those obtained with the traditional methods.

If detection accuracy is analyzed in detail two problems with the wavelet-based detection can be identified. It is clear from the distributions presented in Fig. 9 that there are events which were identified by eye and not by the wavelet method. Individually looking at these undetected events revealed that they either represent short embers trailing a spark or were events very closely following one another. In case of the former the ember was included into the spark by the automatic detection, while in case of the latter they were taken as a single event. The number of these events was, however, small, less than 10%, rendering the detection accuracy still quite acceptable.

Despite these slight problems the methods presented here are an important step forward in automatic ember detection. Furthermore, these algorithms, especially the one-dimensional wavelet transform based variant, can also be used as a basis for algorithms of spark detection on recently introduced high-speed line-scan images, since on those images the morphology of a spark is very similar to that of an ember if measured with a normal-speed confocal scanner.

Acknowledgment

The authors are grateful to Dr. Beatrix Dienes. The work was supported by grants from the Hungarian Scientific Research Fund OTKA (K75604, NK78398) and ETT (186-09).

Appendix 1

The à trous transform is an undecimated discrete wavelet transform, consequently permits the exact temporal and spatial localization of various frequencies and signal intensities found in the analyzed data. Detailed mathematical description is given by Mallat (1999), Shensa (1992) and Bijaoui et al. (1994). We used both of the one- and two-dimensional à trous transform.

According to Starck and Murtagh (1994), for the one-dimensional transform, the wavelet function $\psi(x)$ is defined as:

$$\frac{1}{2}\psi\left(\frac{x}{2}\right)=\phi(x)-\frac{1}{2}\phi\left(\frac{x}{2}\right). \tag{A.1}$$

where $\phi(x)$ is the scaling function, satisfying the dilation equation:

$$\frac{1}{2}\phi\left(\frac{x}{2}\right)=\sum_l h(l)\phi(x-l). \tag{A.2}$$

with h as a discrete low pass filter associated with the scaling function.

For the one-dimensional case, the sampled data $\{c_0(k)\}$,$k=1\ldots N$, is considered as the scalar product at pixels k of the function $f(x)$ with the scaling function $\phi(x)$, used as a low pass filter:

$$c_0(k)=\langle f(x),\phi(x\text{-}k)\rangle. \tag{A.3}$$

The low pass filtered data at a resolution level i and position k is obtained by

$$c_i(k)=\frac{1}{2^i}\langle f(x),\phi\left(\frac{x-k}{2^i}\right)\rangle. \tag{A.4}$$

Computationally this is obtained by the convolution:

$$c_i(k)=\sum_l h(l)c_{i-1}(k+2^{i-1}l). \tag{A.5}$$

Author's personal copy

szentesi.peter_292_24

The wavelet coefficients are resulting from the signal difference between two successive convolution steps:

$$w_i(k) = c_{i-1}(k) - c_i(k), \text{ or} \tag{A.6}$$

$$w_i(k) = \frac{1}{2^i} \langle f(x), \psi\left(\frac{x-k}{2^i}\right) \rangle. \tag{A.7}$$

The wavelet function is defined by (A1). The calculations are reduced to the following algorithm (Starck and Murtagh, 1994):

1. i is set to 0, and the algorithm starts with the original data set $\{c_i(k)\}$;
2. $i=i+1$, and a discrete convolution is carried out using the filter h;
3. the discrete wavelet transform is obtained after the convolution step from the difference: $w_i(k)=c_{i-1}(k)-c_i(k)$;
4. if i < L, L being the level of resolution to compute, go to step 2;
5. the set $w_1, w_2, \ldots, w_L, c_L$ is the wavelet transform of the data. c_L is the low-frequency background of the data. The algorithm is extensible to two dimensions.

As convolution masks we used the values derived from cubic B-spline: $(1/16)\times[1,4,6,4,1]$ for the one dimensional, and

$$\frac{1}{256} \times \begin{bmatrix} 1 & 4 & 6 & 4 & 1 \\ 4 & 16 & 24 & 16 & 4 \\ 6 & 24 & 36 & 24 & 6 \\ 4 & 16 & 24 & 16 & 4 \\ 1 & 4 & 6 & 4 & 1 \end{bmatrix} \tag{A.8}$$

for the two-dimensional case.

The inverse à trous transform is defined by

$$c_0(k) = c_L(k) + \sum_{i=1}^{L} w_i(k). \tag{A.9}$$

The set defined by $w_i(k)$ is called wavelet plane i. A wavelet plane contains the same number of pixels as the original data set.

Appendix 2

In the first phase of the denoising procedure we approximate the general noise level of the image (Starck and Murtagh, 1998). This approximation is performed iteratively in the following steps:

1. Estimate the standard deviation of the noise in the original image: eliminate pixels above image $mean+3\cdot\sigma$ and calculate the standard deviation of the remaining pixels; we have σ_{I0}.
2. Compute the wavelet transform of the image for L levels and obtain

$$f(x,y) = c_L(x,y) + \sum_{i=1}^{L} w_i(x,y). \tag{A.10}$$

   The noise in the low-frequency background c_L is negligible.
3. Set n to 0.
4. Compute multi-resolution support $M(j,x,t)$, $j=1, L$ resulted from wavelet coefficients and σ_{In}. Wavelet coefficients $>3\cdot\sigma_j$ are considered significant, σ_j is calculated according to (A.11).
5. A binary mask is formed. Pixels are set to 1 where $M(j,x,t)$ is below threshold in each wavelet plane (insignificant wavelet coefficients that are considered belonging to noise). From pixels selected by this mask the background $c_L(x,y)$ is subtracted (the background is not included in the noise estimation).
6. $n=n+1$, compute σ_{In} from the selected pixels.
7. If $|\sigma_{I_n}-\sigma_{I_{n-1}}|/\sigma_{I_n} > \varepsilon$, go to step 4.

The method converges in a few steps, resulting in σ_I of the noise in the image.

After that the standard deviation of the noise σ_j for level j is determined from the standard deviation of the noise in the original image:

$$\sigma_j = \sigma_I \cdot \sigma_{j0}, \tag{A.11}$$

where σ_{j0}, $j=1, L$, is the standard deviation of wavelet transform level j of a Gaussian noise with standard deviation 1, and σ_I is the estimate of the standard deviation of the noise in the original image. From this a threshold level for each wavelet level is determined:

$$T_{Dj} = \delta \cdot \sigma_j, \tag{A.12}$$

where δ is one of the user adjustable parameters of the algorithm. The last step of the denoising algorithm is to perform thresholding on each wavelet level using one of the following functions (Jin et al., 2005).

Hard threshold:

$$g_{hT}(x) = \begin{cases} x, \text{if } |x| > T_{Dj} \\ 0, \text{if } |x| \le T_{Dj} \end{cases} \tag{A.13}$$

Soft threshold:

$$g_{sT}(x) = \begin{cases} x - T_{Dj}, \text{ if } x \ge T_{Dj} \\ x + T_{Dj}, \text{ if } x \le -T_{Dj} \\ 0 \text{ if } |x| < T_{Dj} \end{cases}. \tag{A.14}$$

Affine (firm) threshold:

$$g_{aT}(x) = \begin{cases} x, \text{ if } |x| \ge T_{Dj} \\ 2\cdot x + T_{Dj}, \text{ if } -T_{Dj} \le x \le -\frac{T_{Dj}}{2} \\ 2\cdot x - T_{Dj}, \text{ if } \frac{T_{Dj}}{2} \le x \le T_{Dj} \\ 0 \text{ if } |x| < \frac{T_{Dj}}{2} \end{cases} \tag{A.15}$$

References

Bijaoui, A., Starck, J.L., Murtagh, F., 1994. Restauration des images multi-échelles par l'algorithme à trous. Traitement du Signal 11, 229–243.

Cheng, H., Lederer, W.J., Cannell, M.B., 1993. Calcium sparks: elementary events underlying excitation–contraction coupling in heart muscle. Science 262, 740–744.

Cheng, H., Song, L.S., Shirokova, N., Gonzalez, A., Lakatta, E.G., Rios, E., Stern, M.D., 1999. Amplitude distribution of calcium sparks in confocal images: theory and studies with an automatic detection method. Biophys. J. 76, 606–617.

Cheng, H., Lederer, W.J., 2008. Calcium sparks. Physiol. Rev. 88, 1491–1545.

Csernoch, L., 2007. Sparks and embers of skeletal muscle: the exciting events of contractile activation. Pflügers Archiv.: Eur. J. Physiol. 454, 869–878.

González, A., Kirsch W, G., Shirokova, N., Pizarro, G., Stern M, D., Ríos, E., 2000. The spark and its ember. J. Gen. Physiol. 115, 139–157.

Hollingworth, S., Peet, J., Chandler, W.K., Baylor, S.M., 2001. Calcium sparks in intact skeletal muscle fibers of the frog. J. Gen. Physiol. 118, 653–678.

Holschneider, M., Morlet, M., Kronland-Martinet, R., Tchamitchian, P., 1989. Wavelets Time Frequency Methods and Phase Space. Springer Verlag, Berlin, pp. 289–297.

Izu, L.T., Wier, W.G., Balke, C.W., 1998. Theoretical analysis of the Ca^{2+} spark amplitude distribution. Biophy. J. 75, 1144–1162.

Jin, Y., Angelini, E., Laine, A., 2005. Wavelets in medical image processing: denoising, segmentation, and registration. In: Handbook of Biomedical Image Analysis. Springer, Berlin, pp. 319–324.

Klein, M.G., Schneider, M.F., 2006. Ca^{2+} sparks in skeletal muscle (review). Progress Biophys. Mol. Biol. 92, 308–332.

Koshino, K., Saito, N., Suzuki, S., Tamaki, J., 2002. Spike noise removal in the scanning laser microscopic image of diamond abrasive grain using a wavelet transform. Opt. Commun. 211, 73–83.

Lukacs, B., Sztretye, M., Almassy, J., Sarkozi, S., Dienes, B., Mabrouk, K., Simut, C., Szabo, L., Szentesi, P., De Waard, M., Ronjat, M., Jona, I., Csernoch, L., 2008. Charged surface area of maurocalcine determines its interaction with the skeletal ryanodine receptor. Biophy. J. 95, 3497–3509.

Mallat, S.G., 1999. A Wavelet Tour of Signal Processing, second ed. Academic Press, London.

Author's personal copy

szentesi.peter_292_24

Picht, E., Zima, A., Blatter, L.A., Bers, D.M., 2007. SparkMaster-automated calcium spark analysis with ImageJ. Am. J. Physiol. Cell Physiol. 293, C1073–C1081.

Ríos, E., Shirokova, N., Kirsch, G., Pizarro, G., Stern, M.D., Cheng, H., González, A., 2001. A preferred amplitude of calcium sparks in skeletal muscle. Biophys. J. 80, 169–183.

Schneider, M.F., Klein, M.G., 1996. Sarcomeric calcium sparks activated by fiber depolarization and by cytosolic Ca^{2+} in skeletal muscle. Cell Calcium 20, 123–128.

Sebille, S., Cantereau, A., Vandebrouck, C., Balghi, H., Constantin, B., 2005. Calcium sparks in muscle cells: interactive procedures for automatic detection and measurements on line-scan confocal images series. Comput. Methods Programs Biomed. 77, 57–70.

Shensa, M.J., 1992. The discrete wavelet transform: wedding the À Trous and Mallat algorithms. IEEE T Signal P 40 (10), 2464–2482.

Song, L.S., Stern, M.D., Lakatta, E.G., Cheng, H., 1997. Partial depletion of sarcoplasmic reticulum calcium does not prevent calcium sparks in rat ventricular myocytes. J. Physiol. 505, 665–675.

Starck, J.L., 1993. The à trous algorithm. In: ESO-MIDAS User's Guide, Volume B. ESO European Organization for Astronomical Research in the Southern Hemisphere. 〈http://www.eso.org/sci/data-processing/software/esomidas〉. Accessed 26 May 2009.

Starck, J.L., Murtagh, F., 1994. Image restoration with noise suppression using the wavelet transform. Astron. Astrophys. 288, 342–348.

Starck, J.L., Murtagh, F., 1998. Automatic noise estimation from the multiresolution support. Publ. Astron. Soc. Pac. 110, 193–199.

Starck, J.L., Murtagh, F., Bijaoui, A., 1998. Image Processing and Data Analysis: The Multiscale Approach. Cambridge University Press, London.

Starck, J.L., Murtagh, F., 2002. Astronomical Image and Data Analysis. Springer, Berlin.

Unser, M., Aldroubi, A., 1996. A review of wavelets in biomedical applications. P IEEE 84 (4), 626–638.

Unser, M., 1997. Ten Good Reasons for Using Spline. Proc. SPIE Vol. 3169, Wavelets Applications in Signal and Image Processing V:422–431.

Wegner, F.V., Both, M., Fink, R.H.A., 2006. Automated detection of elementary calcium release events using the À Trous wavelet transform. Biophys. J. 90, 2151–2163.

Wegner, F.V., Both, M., Fink, R.H.A., Friedrich, O., 2007. Fast XYT imaging of elementary calcium release events in muscle with multifocal multiphoton microscopy and wavelet denoising and detection. IEEE Transact. Med. Im. 26 (7), 925–934.

Zhou, J., Brum, G., González, A., Launikonis, B.S., Stern, M.D., Ríos, E., 2003. Sparks and embers of mammalian muscle. Prop. Sources J. Gen. Physiol. 122, 95–114.

szentesi.peter_292_24

Journal of Physiology (1997), **505.2**, *pp.*371–384

Intramembrane charge movement and sarcoplasmic calcium release in enzymatically isolated mammalian skeletal muscle fibres

Péter Szentesi, Vincent Jacquemond *, László Kovács and László Csernoch †

*Department of Physiology, University Medical School of Debrecen, H-4012, Hungary and *Laboratoire de Physiologie des Eléments Excitables, CNRS UMR 5578, Université Lyon I, Villeurbanne, France*

1. Single muscle fibres were dissociated enzymatically from the extensor digitorum longus and communis muscles of rats and guinea-pigs. The fibres were mounted into a double Vaseline gap experimental chamber and the events in excitation–contraction coupling were studied under voltage clamp conditions.

2. The voltage dependence of intramembrane charge movement followed a two-state Boltzmann distribution with maximal available charge of 26·1 ± 1·5 and 26·1 ± 1·3 nC μF^{-1}, mid-point voltage of −35·1 ± 5·0 and −42·2 ± 1·2 mV and steepness of 16·7 ± 2·2 and 17·0 ± 1·9 mV (means ± S.E.M., $n = 7$ and 4) in rats and guinea-pigs, respectively.

3. Intracellular calcium concentration ($[Ca^{2+}]_i$) was monitored using the calcium-sensitive dyes antipyrylazo III, fura-2 and mag-fura-5. Resting $[Ca^{2+}]_i$ was similar in rats and guinea-pigs with 125 ± 18 and 115 ± 8 nM ($n = 10$ and 9), respectively, while the maximal increase for a 100 ms depolarization to 0 mV was larger in rats (6·3 ± 1·0 μM; $n = 7$), than in guinea-pigs (2·8 ± 0·3; $n = 4$).

4. The rate of calcium release (R_{rel}) from the sarcoplasmic reticulum (SR) displayed an early peak followed by a fast and a slow decline to a quasi maintained steady level. After normalizing R_{rel} to the estimated SR calcium content (1·2 ± 0·1 and 0·9 ± 0·1 mM in rats and guinea-pigs, respectively) and correcting for depletion of calcium in the SR the peak and steady levels at 0 mV, respectively, were found to be 2·50 ± 0·08 and 0·81 ± 0·06 % ms^{-1} in rats and 2·43 ± 0·25 and 0·88 ± 0·01 % ms^{-1} in guinea-pigs. The voltage dependence was essentially the same in both species, but different from that in amphibians.

5. These experiments show that enzymatic isolation yields functionally intact mammalian skeletal muscle fibres for Vaseline gap experiments. The data also suggest a close connection in the regulation of the different kinetic components of SR calcium release in mammalian skeletal muscle.

In the past decade considerable knowledge has been accumulated concerning the molecular events of excitation–contraction (E–C) coupling in skeletal muscle. It is now widely accepted that it involves the direct interaction of two proteins, namely the dihydropyrydine (DHP) receptor, located in the membranes of the transverse (T)- tubules, and the ryanodine receptor (RyR) found in the sarcoplasmic reticulum (SR). While the former acts as a voltage sensor (Tanabe, Beam, Powell & Numa, 1988; Ríos & Pizarro, 1991) the latter is a calcium release channel (Smith, Imagawa, Ma, Fill, Campbell & Coronado, 1988; Meissner, 1994) through which calcium enters the myoplasmic space from its internal store, the SR.

Most of our knowledge regarding the actual time course of calcium release from the SR in conditions similar to those *in vivo* was obtained from measurements on frog skeletal muscle fibres (Baylor, Chandler & Marshall, 1983; Melzer, Ríos & Schneider, 1984). In amphibians calcium release evoked by a long depolarizing pulse displays an early inactivating peak and a maintained steady level (Melzer *et al.* 1984; Schneider & Simon, 1988).

The regulation of the SR calcium release channel, on the other hand, was studied using isolated RyR from mammalian skeletal muscle that expresses only a single RyR isoform (Marks *et al.* 1989; Takeshima *et al.* 1989).

† To whom correspondence should be addressed.

Downloaded from jp.physoc.org at Medical University, Central Library, H-4012 DEBRECEN, Hungary on March 9, 2006

szentesi.peter_292_24

Hence there is deep interest in comparing the regulation of calcium release in amphibian and mammalian skeletal muscle. However, only a few groups have published calcium transients from the latter muscle type. The lack of data is mainly due to problems in obtaining single fibres from this tissue. Furthermore, the published values for intracellular calcium concentration ($[Ca^{2+}]_i$) changes and calcium release waveforms differ for every laboratory.

To overcome the problems of obtaining single fibres from mammalian skeletal muscle we developed a novel method of enzymatically dissociating these fibres and mounting them into a double Vaseline gap chamber. Using this method we successfully measured intramembrane charge movement and sarcoplasmic calcium release in fibres from rats and guinea-pigs. The calculated rate of release displayed an early peak and then declined to a maintained steady level. The peak and steady levels followed the same voltage dependence, that is the peak to steady level ratio remained constant over the examined voltage range.

METHODS

Enzymatic dissociation and solutions

A novel method was developed to isolate enzymatically single skeletal muscle fibres from the rat and the guinea-pig and to mount them into a double Vaseline gap chamber. The 3- to 5-month-old Wistar rats or guinea-pigs of either sex were anaesthetized with ether and killed by cervical dislocation. The extensor digitorum longus (EDL) and extensor digitorum communis (EDC) muscles were removed and placed into modified Krebs solution (the composition of all solutions is given in Table 1).

The muscles were dissected into three or four smaller pieces and placed into Dulbecco's Modified Eagle's Medium (Sigma) supplemented with 1·25 mg l^{-1} Amphotericin B, 50 000 units l^{-1} penicillin, 50 mg l^{-1} streptomycin and 4 % fetal calf serum (FCS). The muscle pieces were placed into an incubator (IG 150; Jouan, Saint Herblain, France) at 37 °C and treated with collagenase (Sigma, Type I, 1 mg ml^{-1}) for 1½ h. After the dissociation the muscles were washed with modified Krebs solution with no Ca^{2+} added (0 Ca^{2+} Krebs solution) and stored at 4 °C until further use.

To obtain single fibres the muscles were triturated in 0 Ca^{2+} Krebs solution supplemented with 10 % FCS. Fibres were allowed to rest for 10 min in the modified Krebs solution and only those that showed no signs of membrane damage were used. For checking fibre integrity a CK2 inverted microscope (Olympus, Tokyo, Japan) at ×100 magnification was used. The selected fibre was gently sucked into a glass capillary (inner diameter, 0·85 mm) then transferred to the recording chamber (Kovács, Ríos & Schneider, 1983). The chamber was prepared and filled with relaxing solution in advance to expose the Vaseline to bovine serum albumin (BSA) and FCS.

Vaseline was placed upon the fibre to isolate the three compartments in the recording chamber. It should be noted that the Vaseline isolation required the presence of BSA and FCS in the relaxing solution to prevent the development of a contracture under the seals. To permeabilize the fibre segment the relaxing solution in the open-end pools was exchanged for 30 s to a relaxing solution containing 0·01 % saponin. The solution in the open-end pools was then changed to internal solution. The internal solution contained 1 mM antipyrylazo III (APIII) and 100 μM fura-2 or 200 μM mag-fura-5 for the detection of intracellular calcium concentration. The solution in the middle pool was first exchanged for a 0 Ca^{2+} external solution supplemented with 10 % FCS which was then changed to regular external solution.

Fibres obtained from rats were thicker than those from guinea-pigs. The mean ± S.E.M. diameters of the fibres used for calculating the voltage dependence of intramembrane charge and SR calcium release were 57 ± 2 and 37 ± 2 μm for rats and guinea-pigs ($n = 10$ and 9), respectively.

The length of the fibre segment in the middle pool was set to 500 μm. The sarcomere length (SL) was either set to 2·4–2·7 μm (slack fibre) or the fibre was stretched beyond filament overlap (SL ⩾ 3·6 μm). It should be noted that stretching more often caused membrane damage in these enzymatically treated mammalian fibres than it did in mechanically dissociated frog fibres.

Mag-fura-5 and fura-2 were purchased from Molecular Probes, APIII from ICN Biomedicals (Aurora, OH, USA) and all other chemicals were of analytical grade (Sigma). All measurements were carried out at 17–20 °C.

Experimental set-up and data acquisition

The experimental set-up and data acqusition have been described in detail in our earlier reports (e.g. Sárközi, Szentesi, Jona & Csernoch, 1996). In brief, the fibre was transilluminated using a tungsten–halogen light source ($\lambda > 600$ nm) and was also epi-illuminated at 380 nm or at the isosbestic wavelength of fura-2 or mag-fura-5 using a 75 W xenon arch lamp (Oriel 60 000; Stratford, CT, USA). The actual arrangement of interference filters and dichroic mirrors (Klein, Simon, Szücs & Schneider, 1988) enabled the simultaneous recording of light intensities at 510, 720 and 850 nm for the detection of APIII absorbance and fura-2 or mag-fura-5 fluorescence. Fibres were voltage clamped, and the holding potential (V_h) was set to −90 or −100 mV.

Calculation of non-linear capacitative currents and $[Ca^{2+}]_i$

Non-linear capacitive currents (I_Q) representing intramembrane charge movement were calculated as described earlier (Sárközi *et al.* 1996). In brief, hyperpolarizing pulses of −20 mV and 100 ms were applied and the accompanying currents (negative controls) were scaled and subtracted from the current records measured with depolarizing pulses. The membrane potential (V_m) dependence of charge transferred ($Q(V_m)$) was fitted with the two-state Boltzmann function:

$$Q(V_m) = Q_{max}/(1 + \exp\{-(V_m - V')/k\}), \quad (1)$$

where Q_{max} is the maximal available charge, V' is the mid-point voltage and k is the slope factor. The rate of charge transition (α) was assessed by fitting single exponentials to the charge movement currents starting 2 ms after the peak. Its membrane potential dependence was fitted with the linear Eyring rate model:

$$\alpha(V_m) = \alpha_{min}\,(V_m - V')\coth\{(V_m - V')/2k\}/2k, \quad (2)$$

where α_{min} is the rate constant when $V_m = V'$, coth is the cotangent hyperbolic function and all other parameters have their usual meaning.

Changes in the myoplasmic free calcium concentration were calculated from APIII absorbance (APIII calcium transient) as described by Kovács *et al.* (1983) using the correction for intrinsic fibre absorbance at 850 nm following the procedure in Melzer, Ríos & Schneider (1986). Changes in fura-2 fluorescence were used to calculate the resting $[Ca^{2+}]$. To calculate the $[Ca^{2+}]$ from the fura-2 signals the procedure described by Klein *et al.* (1988) was used.

Downloaded from jp.physoc.org at Medical University, Central Library, H-4012 DEBRECEN, Hungary on March 9, 2006

szentesi.peter_292_24

Table 1. Composition of solutions used (mM)

Solution	$[Na^+]$	$[K^+]$	$[Cs^+]$	$[Ca^{2+}]$	$[Mg^{2+}]$	$[TEA^+]$	$[Cl^-]$	$[SO_4^{2-}]$	$[CH_3SO_3^-]$	[Glutamate]	[Hepes]	[Glucose]
Modified Krebs*	145	5	—	2·5	1	—	155	1	—	—	10	10
Relaxing†	—	150	—	—	2	—	4	—	—	150	10	—
Internal‡	20	—	130	0·0082	5·5	—	11	—	—	130	5	5
External	—	—	—	2	2	150	8	—	150	—	5	—

* Supplemented with 10% FCS. † Supplemented with 2% BSA and 10% FCS. ‡ Also contained 5 mM ATP, 5 mM creatine phosphate and the calcium-sensitive dyes (estimated free $[Ca^{2+}]$, 0·1 μM; $[Mg^{2+}]$, 1 mM). The external solution contained 10^{-7} g ml^{-1} tetrodotoxin. All solutions were adjusted to pH 7·2 and 300 mosmol l^{-1}.

Using mag-fura-5 as calcium indicator

Changes in mag-fura-5 fluorescence were used as an alternative method to detect changes in $[Ca^{2+}]_i$. The dye was excited either at 380 nm or at the isosbestic wavelength. The latter was obtained by tilting an interference filter until no change was seen in fluorescence when APIII signals were still present upon fibre depolarization. $[Ca^{2+}]_i$ was calculated from the ratio (R) of fluorescence intensities with 380 nm (F_{380}) or the isosbestic wavelength (F_{iso}) being the incident light ($R = F_{380}/F_{iso}$) as described for fura-2 (Klein *et al.* 1988). First the saturation of the dye (S_m) was calculated:

$$S_m = (R - R_{min}) / (R_{max} - R_{min}), \quad (3)$$

where R_{max} is the ratio at saturating and R_{min} is the ratio at 0 $[Ca^{2+}]$. It should be noted that the R_{min} used in this study does not represent the ratio in metal-free conditions due to the presence of Mg^{2+}. This renders the determination of resting $[Ca^{2+}]_i$ inadequate under these conditions.

Figure 1*A* and *B* demonstrate how R_{min} and R_{max} were determined. The internal solution was supplemented with 2 mM EGTA, no added Ca^{2+}, and the myoplasmic space was allowed to equilibrate with the solutions in the open-end pools. The diffusion of mag-fura-5 was complete after 2 h (Fig. 1*C*). This corresponded to a diffusion coefficient (obtained by fitting the diffusion as described by Kovács *et al.* 1983) of $6{\cdot}12 \times 10^{-3}$ mm^2 min^{-1}, a value four times greater than that found for APIII in this fibre. The quasi steady value of R during equilibration (horizontal line at 1·96; Fig. 1*B*) was used as R_{min}. To obtain R_{max} the calcium ionophore 4-bromo-A23187 was added into the external solution (indicated by arrows in Fig. 1). This resulted in a rapid decline in F_{380} and,

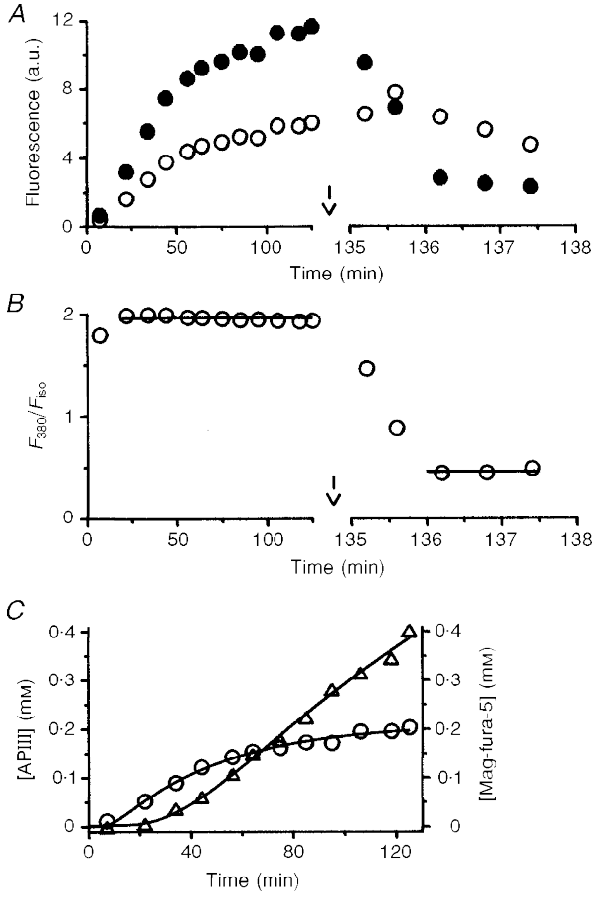


Figure 1. Calibration of mag-fura-5 fluorescence

A, fluorescence intensities (a.u., arbitrary units) with excitation at 380 nm (F_{380}, ●) and the isosbestic wavelength (F_{iso}, ○). The internal solution, supplemented with 2 mM EGTA, no added Ca^{2+}, was applied at time 0. After F_{iso} reached a steady value the calcium ionophore 4-bromo-A23187 (final concentration, 10 μM) was added (arrow indicates time of addition) into the external solution. *B*, calculated ratio ($R = F_{380}/F_{iso}$) of fluorescence intensities from *A*. Horizontal lines at 1·96 and 0·46 indicate estimated R_{min} and R_{max}, respectively. Note that the time scales in *A* and *B* change after the addition of the ionophore. *C*, changes in dye concentration with time. Curves represent the least-squares fit of the equation describing the diffusion (see text) with diffusion coefficients of 1·50 and $6{\cdot}12 \times 10^{-3}$ mm^2 min^{-1} and final concentrations of 991 and 211 μM for APIII (△) and mag-fura-5 (○), respectively. Fibre 354; EDC; path length (PL), 50 μm.

Downloaded from jp.physoc.org at Medical University, Central Library, H-4012 DEBRECEN, Hungary on March 9, 2006

szentesi.peter_292_24

consequently, in R. Again, the steady value of R (horizontal line at 0·46; Fig. 1*B*) was taken as R_{max}.

Using the calculated saturation $[Ca^{2+}]_i$ was determined assuming instantaneous equilibrium:

$$[Ca^{2+}]_i = K_{d,m} S_m/(1 - S_m), \quad (4)$$

where $K_{d,m}$ is the dissociation constant of calcium from mag-fura-5. The value of $K_{d,m}$ was taken as 28 μM (Haugland, 1996).

It should be noted that using the ratio for determining $[Ca^{2+}]_i$ enabled us to use slack fibres that contracted upon stimulation (Fig. 5). Although large contractions did increase the overall fluorescence (by 50% in F_{iso}) this 'movement artifact' was not present in the ratio.

Calculation of R_{rel}

The rate of calcium release from the SR (R_{rel}) was calculated from the calcium transient using the procedure described in Sárközi *et al.* (1996). Originally three parameters of the removal model were fitted simultaneously, $k_{off,M\text{-}P}$ (Mg^{2+} off rate from parvalbumin), PV_{max} (maximal transport rate of SR calcium pump) and [parv] (concentration of parvalbumin). This yielded values above 2 mM for the concentration of the Ca^{2+}–Mg^{2+} binding sites on parvalbumin. Since mammalian muscle was shown to contain lesser amount of this calcium binding protein (Heizmann, Berchtold & Rowlerson, 1982) a fixed value of 690 μM, as calculated by García & Schneider (1993), was used throughout the calculations. To estimate the time course and number of open release channels in the SR membrane the calculated R_{rel} records were corrected for the depletion of calcium in the SR and expressed as percentage of SR content (Csernoch, Jacquemond & Schneider, 1993).

The voltage dependence of either component of calcium release ($R_i(V_m)$, where i = peak or steady level) was assessed by fitting the two-state Boltzmann function:

$$R_i(V_m) = R_{i,max}/(1 + \exp\{-(V_m - V')/k\}), \quad (5)$$

where $R_{i,max}$ is the maximal release and V' and k have the same meaning as above, to the calculated data.

In statistical analyses all values were expressed as means ± S.E.M.; statistical significance was calculated using Student's t test assuming significance for $P \leqslant 0{\cdot}05$.

RESULTS

Since all of the previous reports used rat fibres we first demonstrate our findings in this species. The data from guinea-pigs, although referred to in connection to results from rats, are presented at the end of this section. During the course of the experiments we found no difference between fibres from EDL and EDC. Mean values, therefore, include fibres from both muscles.

Intramembranous charge movement

To ensure that the fibres obtained by the enzymatic dissociation were functionally intact first their electrical

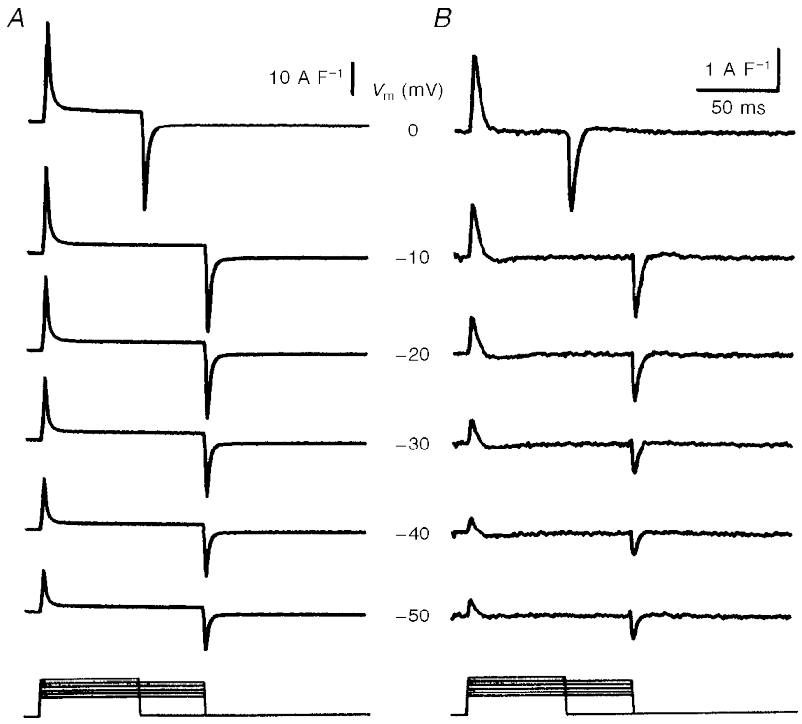


Figure 2. Intramembrane charge movement in rat fibres

A, total membrane currents obtained in response to depolarizations to the indicated test potentials to demonstrate the absence of ionic currents. No leak or capacitive subtraction was carried out, however, the transients were normalized to fibre capacitance. *B*, non-linear capacitive currents that remain after subtracting a 'negative control', representing intramembranous charge displacement. Voltage excursion is given below the current records. EDL; PL, 48 μm; holding potential (V_h), −100 mV; linear capacitance (LC), 8·9 nF.

Downloaded from jp.physoc.org at Medical University, Central Library, H-4012 DEBRECEN, Hungary on March 9, 2006

szentesi.peter_292_24

properties were carefully examined. The linear capacitance of the fibres (8·2 ± 1·9 and 6·8 ± 1·0 nF, $n = 7$ and 4, for rats and guinea-pigs, respectively) fell within the same range as reported in earlier studies (Shirokova, García, Pizarro & Ríos, 1996). No significant difference ($P > 0·7$) was found between the linear capacitance of rat and guinea-pig fibres if the measured values were normalized to surface area (assuming similar T-tubular networks). Fibres were electrically stable for 30–60 min (in a few cases for even longer periods) after setting the holding potential to −100 mV allowing the determination of the voltage dependence of intramembrane charge movement and/or SR calcium release.

As demonstrated in Fig. 2*A*, under our conditions – the given external and internal solutions – 60–100 ms depolarizing pulses did not elicit significant ionic currents. It should be noted that longer pulses usually induced the activation of an inward current with a threshold for activation of −20 mV and a time to peak of about 200 ms at 0 mV (data not shown). Although these properties suggest that the current was carried by Ca^{2+} through L-type channels the characterization of this current is not included in this study.

Using negative controls the intramembrane charge displacement currents were calculated from the total membrane currents (Fig. 2*B*). These showed all the characteristics presented previously on intact mammalian fibres. No secondary slow components at and around the threshold of SR calcium release were observed; however, specific pulse protocols to enhance such delayed currents were not applied. To obtain the amount of charge transferred at every given membrane potential the currents were integrated. The calculated charge was then normalized to the measured linear capacitance and its voltage dependence was assessed by fitting eqn (1) to the data. For the fibre presented in Fig. 2 the fit yielded Q_{max} of 22·0 nC μF^{-1}, V' of −28·9 mV and k of 14·2 mV.

To compare the voltage dependence of intramembranous charge movement in different fibres Q_{max} was determined separately in each individual fibre resulting in an average Q_{max} of 26·1 ± 1·5 nC μF^{-1}, V' of −35·1 ± 5·0 mV and k of 16·7 ± 2·2 mV ($n = 7$). The amount of charge moved at a given membrane potential was then normalized to Q_{max} in that fibre and the mean for seven fibres was plotted as a function of membrane voltage (Fig. 3*A*). Including all normalized data into the fit an overall V' of −30·8 mV and k of 20·8 mV was obtained. These results, together with those from guinea-pigs (Fig. 8*D*), indicate a somewhat lower voltage sensor density in mammals compared with frogs. Although the membrane potential dependence of intramembrane charge movement was shifted to lower membrane potentials in mammals its steepness was rather similar to that in amphibians (Huang, 1989).

The decay phase of the charge movement currents were well fitted by a single exponential. The rates of decay for the fibres used in Fig. 3*A* were averaged and displayed as a function of the membrane potential (Fig. 3*B*). The data point corresponding to −100 mV represents the value obtained by fitting the 'off" part of the currents, whereas all other values were calculated from the 'on' transients. As

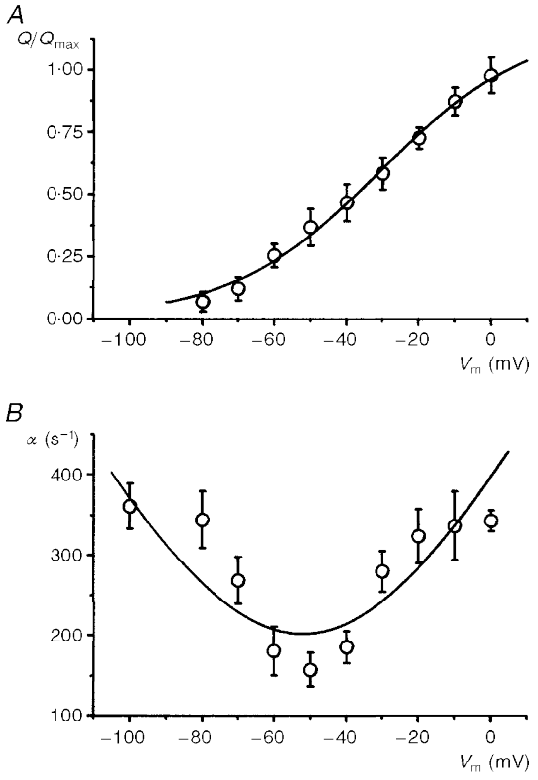


Figure 3. Voltage-dependent properties of intramembrane charge movement

A, voltage dependence of charge transferred from 7 fibres (means ± S.E.M.). Each data point was first normalized to the maximal charge in that particular fibre and then averaged. The continuous line represents the least-squares fit of eqn (1) to all data points with $V' = -30·8$ mV and $k = 20·8$ mV. *B*, charge movement currents were fitted with a single exponential and the obtained rate constants averaged (± S.E.M., same 7 fibres as in *A*) for every membrane potential. The data, including all individual data points, were fitted with eqn (2); the continuous line represents the calculated voltage dependence with $\alpha_{min} = 202$ s^{-1}, $V' = -52·1$ mV and $k = 13·9$ mV.

Downloaded from jp.physoc.org at Medical University, Central Library, H-4012 DEBRECEN, Hungary on March 9, 2006

szentesi.peter_292_24

shown in the figure the rate constant was the lowest at intermediate voltages and increased with increasing or decreasing the membrane potential. The data were fitted assuming a one-barrier linear Eyring model (eqn (2)), including all individual observations. The obtained parameters were $\alpha_{min} = 202\ s^{-1}$, $V' = -52{\cdot}1$ mV and $k = 13{\cdot}9$ mV; the continuous line in Fig. 3*B* represents the voltage dependence calculated with these values. In the framework of the model the mid-point voltage and the slope factor should be the same as those determined by fitting the Boltzmann function to the charge *vs.* membrane potential data. The difference might represent the presence of a slow component on the current records that activated around −60 mV. Again, the corresponding values for guinea-pigs were essentially the same (see below) strengthening the similarity between the two species.

Calcium transients evoked by membrane depolarization

Depolarizing pulses, if they exceeded the threshold, were accompanied by changes in $[Ca^{2+}]_i$. The threshold, determined from the smallest depolarization necessary to evoke a transient rise in fura-2 saturation, was similar in rats and guinea-pigs averaging -59 ± 2 and -55 ± 3 mV ($n = 10$ and 9), respectively. The resting $[Ca^{2+}]_i$ values were also similar, 125 ± 18 and 115 ± 8 nM (same fibres as above), respectively.

As shown in Fig. 4*A* increasing depolarizations brought about increasingly larger changes in $[Ca^{2+}]_i$ if measured with APIII. The calcium transients displayed a characteristic change in the slope of the rising phase; an early fast elevation was followed by a gradual increase that

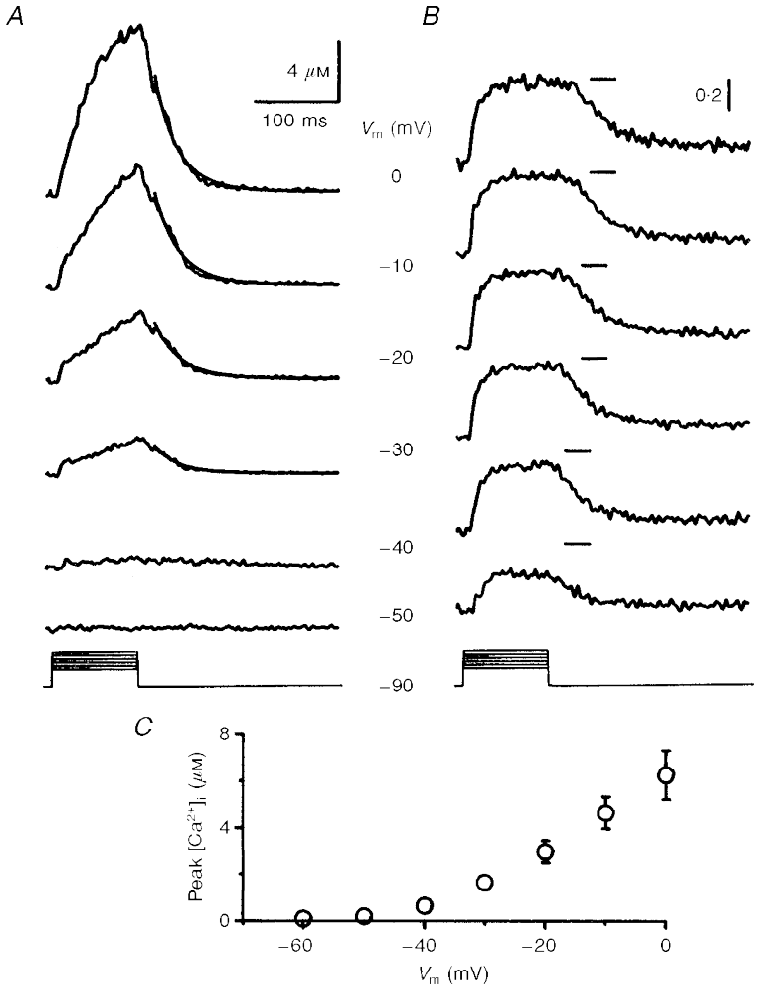


Figure 4. Voltage dependence of $[Ca^{2+}]_i$ in rat fibres

A, calcium transients calculated from APIII absorbance changes elicited by 100 ms depolarizing pulses. The voltage excursion is given below the traces, and the membrane potential during the test is shown in each row. Note that the transients display two distinct rising phases. *B*, changes in fura-2 saturation calculated from the simultaneously measured fluorescence intensities. Horizontal bars next to each record mark complete saturation ($S_f = 1$) of the dye with Ca^{2+}. EDC; PL, 43 μm; SL, 3·9 μm; [APIII], 320–339 μM; [fura-2], 49·6–56·0 μM; V_h, −90 mV. *C*, voltage dependence of the maximal $[Ca^{2+}]_i$ during a 100 ms pulse. Values represent means ± S.E.M. from 8 fibres.

Downloaded from jp.physoc.org at Medical University, Central Library, H-4012 DEBRECEN, Hungary on March 9, 2006

szentesi.peter_292_24

lasted until the end of the depolarizing pulse. After repolarization $[Ca^{2+}]_i$ declined, following a single exponential, to its prestimulation level. The time constant of the decrease in $[Ca^{2+}]_i$ was $39{\cdot}2 \pm 7{\cdot}9$ ms for depolarizations to 0 mV ($n = 7$).

The actual values and the voltage dependence of the maximal increase in $[Ca^{2+}]_i$ (Fig. 4*C*) resembled those measured in amphibians. The mean increase at 0 mV was $6{\cdot}3 \pm 1{\cdot}0$ μM ($n = 7$) and the first detectable signal appeared around −50 mV. The time course of the calcium transients qualitatively resembled those reported by García & Schneider (1993), who used APIII and fura-2 as calcium indicators. However, the increase in $[Ca^{2+}]_i$ in our measurements were larger by a factor of 3–5 than reported by the above authors. Due to this large elevation in myoplasmic $[Ca^{2+}]$ fura-2 became fully saturated early into and remained saturated during most of the depolarizing pulse at and beyond −30 mV (Fig. 4*B*). Nevertheless its resting saturation prior to each depolarizing pulse has been used to estimate the resting $[Ca^{2+}]_i$.

Our calcium transients were similar in size to, but had different time courses compared with, those reported by Delbono & Stefani (1993) who used mag-fura-2 or mag-fura-5 as the calcium indicator. It was thus of interest to determine whether the observed difference was due to the different method of obtaining the fibres (mechanical dissection *versus* enzymatic dissociation) or the two dyes giving different values for $[Ca^{2+}]_i$. Furthermore, since the fibres obtained by enzymatic dissociation were sensitive to stretch we tested whether mag-fura-5 could be used as a calcium indicator on moving 'slack' fibres.

Figure 5 demonstrates a calcium transient on a moving fibre evoked by a 100 ms depolarization to 0 mV. F_{iso} displayed a slow increase (by 48%, reached 220 ms after the onset of the depolarizing pulse) due to the contraction (Fig. 5*A*). In stretched fibres F_{iso} remained constant during the pulse. Using 380 nm as the excitation wavelength the fluorescence light intensity first decreased then increased almost in parallel with F_{iso}. The calculated change in the saturation of mag-fura-5 (Fig. 5*B*) displayed no delayed slow components only a transient rise that started to decline as the membrane potential was returned to −100 mV. It should be noted that F_{iso} was heavily smoothed (smoothed record is shown superimposed on the original trace in Fig. 5*A*) prior to

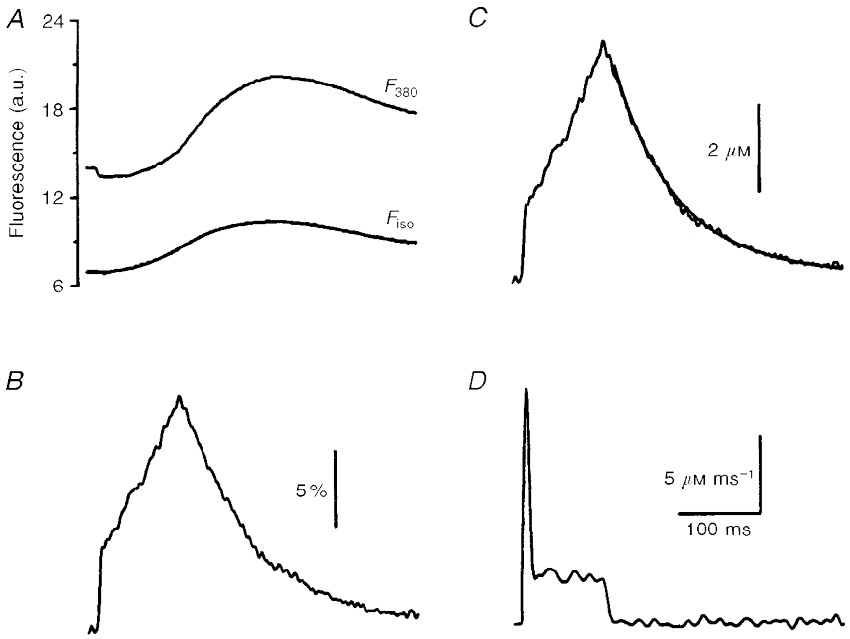


Figure 5. Calcium release in a slack fibre measured with mag-fura-5

A, mag-fura-5 fluorescence, detected at 510 nm with 380 nm (F_{380}) or the isosbestic (F_{iso}) as the excitation wavelength, in response to a 100 ms depolarization to 0 mV. While F_{380} displayed two components, a calcium-dependent downward deflection and a related movement, the former was missing from F_{iso}. To decrease the noise in the ratio, F_{iso} was heavily smoothed (smoothed record is shown superimposed on the raw signal). *B*, the ratio of the two signals in *A* was used to calculate the change in mag-fura-5 saturation (S_m) according to eqn (3). *C*, the intracellular calcium transient corresponding to S_m in *B* calculated using eqn (4). Note the two distinct rising phases during the test pulse. Superimposed after repolarization is the predicted decay after fitting a removal model to the calcium transient as described in Methods. *D*, the rate of calcium release (R_{rel}) from the SR calculated with the parameters obtained by fitting the removal model. Note that R_{rel} displayed an early peak followed by a fast and a slow declining phase during the test pulse. EDL; PL, 51 μm; SL, 2·5 μm; V_h, −100 mV; [APIII], 601 μM; [mag-fura-5], 239 μM. In the removal model PV_{max} was 3·86 mM s^{-1}; $k_{off,M\text{-}P}$ was 6·8 s^{-1} and resting $[Ca^{2+}]_i$ was assumed to be 0·15 μM.

Downloaded from jp.physoc.org at Medical University, Central Library, H-4012 DEBRECEN, Hungary on March 9, 2006

szentesi.peter_292_24

calculating S_m. This smoothing reduced the noise considerably without affecting the actual time course of the calculated transients.

Using eqn (4) the change in $[Ca^{2+}]_i$ was calculated from the saturation of mag-fura-5 (Fig. 5*C*). The calcium transient closely resembled those measured with APIII. During the depolarizing pulse an early fast rise was followed by a less steep increase in $[Ca^{2+}]_i$. As the membrane potential was returned to −100 mV $[Ca^{2+}]_i$ declined to its resting value. It should be noted that the maximal increase in $[Ca^{2+}]_i$, 5·5 μM for the fibre in Fig. 4, was comparable in fibres containing APIII or mag-fura-5.

The declining phase of the calcium transient was fitted with a removal model as described in Methods. The model successfully described the change in $[Ca^{2+}]_i$, in most cases until its return to the resting value, as shown by the superimposed theoretical decline in Fig. 5*C*. The obtained values ($n = 12$, fibres with APIII and mag-fura-5) for maximal SR pump rate, $3{\cdot}9 \pm 0{\cdot}3$ mM s^{-1}, and the dissociation rate of Mg^{2+} from parvalbumin, $11{\cdot}0 \pm 1{\cdot}1$ s^{-1}, were in the range published earlier (García & Schneider, 1993) for similar conditions.

These observations clearly demonstrate that enzymatically dissociated rat fibres display normal calcium transients with magnitudes and time courses resembling those seen in amphibians. They also show that mag-fura-5 can reliably detect changes in $[Ca^{2+}]_i$ on slack fibres.

Calcium release from the SR

Using the parameters obtained by fitting the removal model to the decline of the calcium transients after repolarization the rate of calcium release from the SR can be calculated. Figure 5*D* displays the result of such a calculation. It should be noted that mag-fura-5 is not capable of detecting the resting $[Ca^{2+}]_i$ due to uncertainties in free $[Mg^{2+}]_i$. Therefore a value of 150 nM was assumed in the calculations. The obtained waveform of R_{rel} was strikingly similar to that seen in amphibians: an early peak followed by a rapid and a slow decline to a quasi maintained steady level. The magnitude of the early peak, 15·1 μM ms^{-1} for the fibre in Fig. 5, was slightly smaller than those published for frog from our laboratory. After repolarization SR calcium release rapidly (in 12 ms) ceased.

To compare our data with earlier reports SR calcium release was calculated in fibres containing APIII and fura-2. Figure 6 shows R_{rel} in a wide voltage range calculated from the changes in APIII absorbance. The resting $[Ca^{2+}]_i$ was estimated from the fluorescence of fura-2 prior to each depolarization. At every examined membrane potential

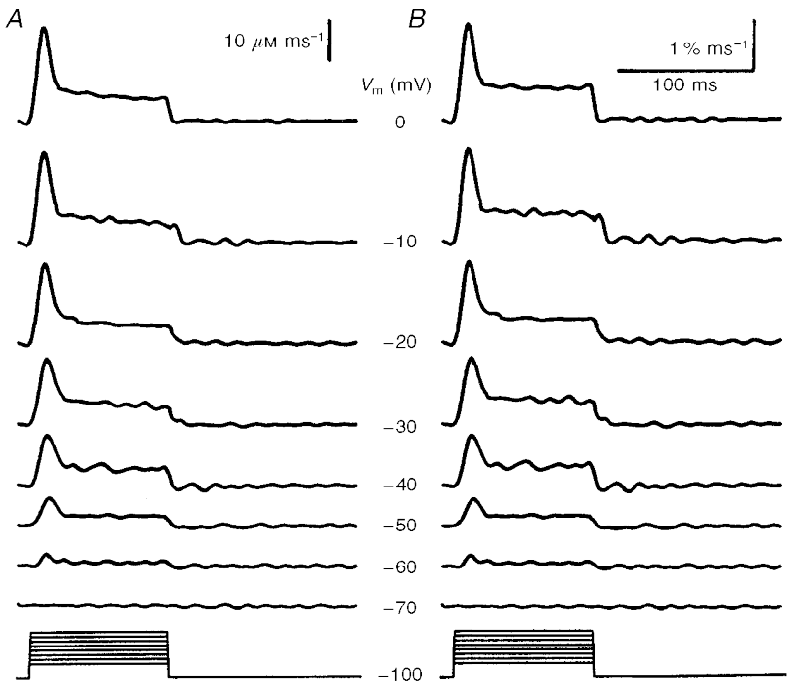


Figure 6. SR calcium release rate in a wide voltage range

A, R_{rel} calculated from APIII calcium transients and fura-2 saturation. The membrane potential was changed to the indicated values for 100 ms (pulse protocol shown at the bottom). Note that both the waveform and the magnitude of SR calcium release derived from APIII signals resembled that using mag-fura-5 (Fig. 5). *B*, to demonstrate the change in SR permeability (R_{rel}*/C_0) during the depolarizing steps the records in *A* were corrected for depletion of Ca^{2+} in the SR and expressed as percentage of SR content prior to the pulse (C_0, 1·3 mM). EDL; PL, 43 μm; SL, 3·6 μm; V_h, −100 mV; [APIII], 976–1004 μM; [fura-2], 99·1–119·4 μM; PV_{max}, 4·78 mM s^{-1}; $k_{off,M\text{-}P}$, 13·2 s^{-1}.

Downloaded from jp.physoc.org at Medical University, Central Library, H-4012 DEBRECEN, Hungary on March 9, 2006

szentesi.peter_292_24

the time course of the calculated R_{rel} resembled that measured in amphibians. It reached an early peak that was followed by a rapid and a slow decline. As discussed by others (e.g. Delbono, 1995) the former, most probably, represents the inactivation of the calcium release channels mediated by calcium, while the latter is due to the depletion of calcium in the SR. It should be noted that R_{rel} presented in Fig. 6*A* (top trace) and Fig. 5*D* were very similar, both in magnitude and in kinetics, showing that both dyes were capable of accurately detecting the release of calcium from the SR.

As shown in Fig. 6*A* R_{rel} was measurable for depolarizations exceeding −60 mV and increased with increasing test pulse amplitude. For the depolarization to 0 mV (top trace) R_{rel} reached its peak 10 ms after the onset of the depolarization and was 23·3 μM ms^{-1}. On average the peak of R_{rel} at 0 mV was found to be 30·0 ± 3·7 μM ms^{-1} ($n = 7$) resembling that, or somewhat smaller than, in amphibians (e.g. Baylor *et al.* 1983; Melzer *et al.* 1984). To determine the permeability of the SR membrane the calculated R_{rel} was corrected for the depletion of calcium in the SR and expressed as normalized to the estimated SR content (Fig. 6*B*). The obtained SR calcium content was 1·3 mM for the fibre in Fig. 5 and 1·2 ± 0·1 mM on average. Thus the calculated SR permeability for the largest depolarization in Fig. 6*B* was 1·86 and 0·68 % ms^{-1} for the early peak and the maintained component, respectively.

Although both the amplitude and the threshold of appearance of SR calcium release in rats resembled those in amphibians, there were distinct differences. We did not observe the damped oscillation described in amphibians that accompanies the negative phase in intramembrane charge movement in that preparation (Shirokova, Pizarro & Ríos, 1994). Furthermore, the ratio of peak to steady level seemed smaller in rats than in frogs. To quantify this observation the voltage dependence of the peak and of the steady level of $R_{rel}*/C_0$ was plotted together with their ratio in Fig. 7.

Figure 7*A* presents the average of the calculated peak (open symbols) and steady level (filled symbols) of the SR permeability ($R_{rel}*/C_0$) *versus* the membrane potential during the test pulse from seven fibres. To assess the voltage dependence of the two components eqn (5) was fitted to the data; the theoretical distributions are shown in Fig. 7*A* as continuous lines. The two membrane potential dependencies were strikingly similar with mid-point voltages of −29·5 and −28·0 mV and steepness factors of 9·4 and 9·8 mV. As demonstrated in connection with Fig. 8 similar voltage dependencies were observed in guinea-pigs. Although these membrane potential dependencies were centred at the same voltage as the distribution of intramembrane charge displacement the steepness of the latter was significantly lower. Furthermore, a considerable amount of charge was already transferred to its new position below the threshold of the appearance of SR calcium release.

The similar voltage dependence of the peak and steady level suggested that, unlike in amphibians (e.g. Shirokova *et al.* 1996), the peak to steady level should be independent of the membrane potential. To demonstrate this prediction quantitatively the peak of each $R_{rel}*/C_0$ transient was normalized to its steady level and averaged from the seven fibres used in Fig. 7*A*. As shown in Fig. 7*B* the average ratio was between 3·0 and 3·6, the lowest value obtained at

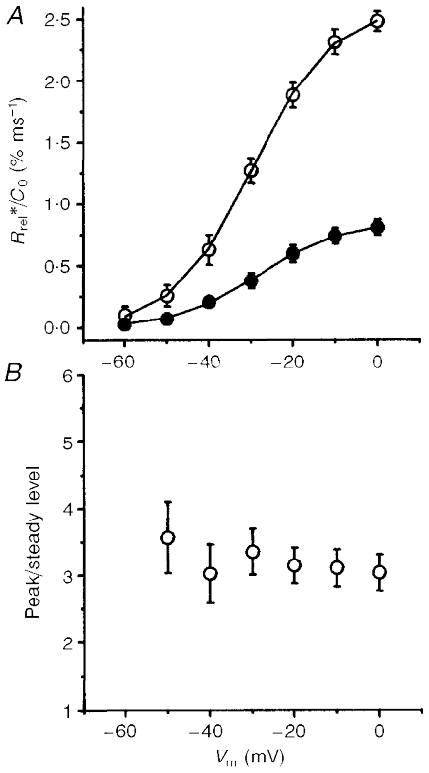


Figure 7. Membrane potential dependence of the components of $R_{rel}*/C_0$

A, the changes in SR permeability, induced by 100 ms depolarizing pulses, were calculated in 7 fibres from APIII and fura-2 signals in a wide voltage range. Open symbols represent the membrane potential dependence of the early peak while the filled symbols show that of the steady component (means ± S.E.M.). The continuous lines were generated according to eqn (5), with the least-squares fit parameters of $R_{max} = 2{\cdot}59$ and 0·86 % ms^{-1}, $V' = -29{\cdot}5$ and −28·0 mV, $k = 9{\cdot}4$ and 9·8 mV for the peak and the steady level, respectively. *B*, the peak to steady level ratio was calculated for every trace and then averaged over the 7 fibres. Symbols present the ratio as means ± S.E.M.; none of the differences between the values at different membrane potentials was found to be significant ($P > 0{\cdot}1$). Note that the value at −60 mV was omitted, since the low value of the steady level introduced a large scatter into the calculated ratio.

Downloaded from jp.physoc.org at Medical University, Central Library, H-4012 DEBRECEN, Hungary on March 9, 2006

szentesi.peter_292_24

−40 mV. Note that the value at −60 mV is not shown due to the large scatter introduced by the very low values of the steady level (the denominator) at this membrane potential. Although there seemed to be a small decrease in peak to steady level ratio with increasing depolarization this change was not statistically significant for any membrane potential pair.

The data presented in Figs 5–7 demonstrate that SR calcium release can be readily measured in enzymatically dissociated mammalian skeletal muscle fibres. The magnitude and overall time course of R_{rel} resembled those in amphibians; however, the peak to steady level ratio was smaller and did not depend on the amplitude of the depolarization.

Voltage dependence of E–C coupling events in guinea-pigs

It was of interest to see whether our method that was successful in obtaining rat fibres could be adopted for other species as well, and to see whether the properties of intramembrane charge movement and SR calcium release would be similar in different mammals. Figure 8 demonstrates that fibres from guinea-pigs were successfully isolated enabling the study of the events in E–C coupling.

Intramembrane charge movement currents were similar both in size and in time course to those from rats. The current evoked by a 120 ms depolarization to 0 mV (Fig. 8*A*) was comparable to that shown in Fig. 2*B*. The voltage dependence of the charge transferred followed a two-state Boltzmann distribution. The membrane potential dependence was assessed as described in connection with Fig. 3*A*. First the Q_{max} of each individual fibre was determined then the normalized charge was averaged for every depolarization and plotted *vs.* the membrane voltage in Fig. 8*D*. The maximal charge was found to be 26·1 ± 1·3 nC μF^{-1} ($n = 4$). Fitting eqn (1) to all normalized data yielded a mid-point voltage of −41·0 mV and a steepness factor of 17·0 mV so generating the theoretical distribution (continuous line) in Fig. 8*D*. Averaging the parameters of fits to individual fibres gave V' of −42·2 ± 1·2 mV and k of 17·0 ± 1·9 mV. These values were not significantly different ($P > 0{\cdot}15$) from those obtained for rat fibres showing that different mammals probably have similar intramembrane charge movements. This similarity was also present in the rate of charge transfer. Fitting single exponentials to the individual charge movement current records and carrying out the analysis detailed in connection with Fig. 3*B* yielded α_{min} of 221 s^{-1}, V' of −61·4 mV and k of 16·6 mV. Note, that the difference

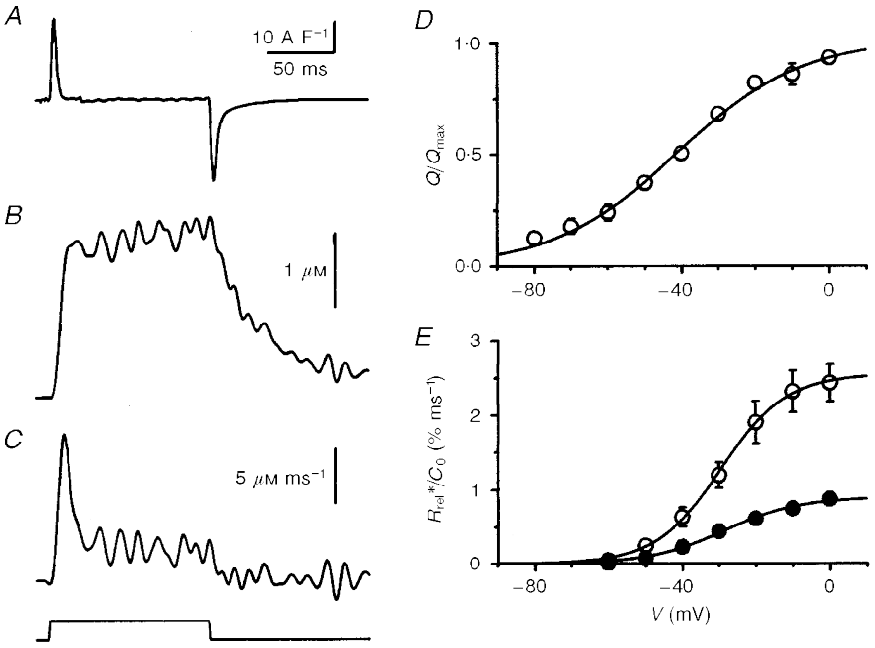


Figure 8. Intramembrane charge movement and SR calcium release in guinea-pigs

A, intramembrane charge movement current in response to a 120 ms depolarization to 0 mV. *B*, the accompanying increase in $[Ca^{2+}]_i$ measured with APIII and fura-2. Note that part of the noise is due to the small diameter of the fibre. *C*, the calculated SR calcium release rate using the calcium transient in *B*. EDL; V_h, −100 mV; LC, 7·7 nF; PL, 34 μm; SL, 3·6 μm; [APIII], 609 μM; [fura-2], 34 μM; $k_{off,M\text{-}P}$, 4·4 s^{-1}; PV_{max}, 4·0 ms^{-1}. *D*, voltage dependence of intramembrane charge movement averaged from 4 fibres. Before averaging data were normalized to the maximal available charge in the given fibre. Continuous line represents the least-squares fit of eqn (1) with V' of −41·0 mV and k of 17·0 mV. *E*, membrane potential dependence of the peak (○) and of the steady level (●) of SR permeability ($R_{rel}*/C_0$) in the same fibres. Fitting eqn (5) yielded V' of −29·4 and −28·5 mV and k of 9·0 and 10·2 mV for the peak and the steady level, respectively. Continuous lines represent the theoretical curves generated with the above parameters.

Downloaded from jp.physoc.org at Medical University, Central Library, H-4012 DEBRECEN, Hungary on March 9, 2006

szentesi.peter_292_24

between the two species was, again, a negative shift in the voltage dependence of the guinea-pig compared with the rat.

One consequence of the guinea-pig fibres having a smaller diameter was an increase in the relative noise in the optical records. As shown in Fig. 8*B* the calcium transient accompanying the depolarizing pulse displayed more noise than those obtained from rats. Furthermore, the magnitude of the maximal increase in $[Ca^{2+}]_i$ was smaller than in rats, 2·4 μM for the fibre in Fig. 8 for a depolarization to 0 mV. Not only this fibre but most guinea-pig fibres displayed smaller calcium transients than those observed with rats. The mean value obtained from four fibres, $2{\cdot}8 \pm 0{\cdot}3$ μM, proved significantly ($P < 0{\cdot}05$) smaller than that in rats. Furthermore, the secondary rising phase of calcium transients, although present, was much less marked in guinea-pigs.

The calcium release calculated using the calcium transient in Fig. 8*B* had a time course resembling that measured in rats (Fig. 6). During the test pulse an early peak, reached 12 ms after the onset of the depolarization, was followed by a fast and a slow decline. After repolarization calcium release rapidly ceased. Measured at other membrane potentials the kinetics of SR calcium release were similar to that presented in Fig. 8*C* (data not shown). The smaller calcium transient already suggested that the SR calcium release was smaller in guinea-pigs than in rats. The magnitude of the peak of the calculated R_{rel} in Fig. 8*C* was 13·4 μM ms^{-1}. On average, a depolarization to 0 mV brought about an SR calcium release with a peak of $19{\cdot}3 \pm 3{\cdot}5$ μM ms^{-1} ($n = 4$). Although the difference is not statistically significant ($P > 0{\cdot}1$), this value is about two-thirds of that measured in rats. The possible explanations for this difference would be either a decreased SR permeability or a decreased driving force for calcium, or both.

To compare the voltage dependence of SR permeability in guinea-pigs with that in rats R_{rel} was corrected for the depletion of calcium in the SR and normalized to the estimated SR contents. Figure 8*E* presents the voltage dependence of the peak (open symbols) and the steady level (filled symbols) of $R_{rel}{}^*/C_0$ from four fibres. The estimated SR contents, $0{\cdot}9 \pm 0{\cdot}1$ mM, were smaller than the values obtained in rats. Although this difference was not significantly different ($P > 0{\cdot}15$), it nevertheless accounted for most, if not all (see below), the lower R_{rel} seen in guinea-pigs compared with rats.

The calculated SR permeability, due to the lower SR content, was strikingly similar in guinea-pig and rat fibres averaging, in the former, $2{\cdot}43 \pm 0{\cdot}25$ % ms^{-1} for the peak and $0{\cdot}88 \pm 0{\cdot}1$ % ms^{-1} for the steady level. Not only was the magnitude of $R_{rel}{}^*/C_0$ similar in the two species but its voltage dependence was, essentially, identical, too. As shown by the continuous lines in Fig. 8*E* the two-state Boltzmann distribution correctly described the voltage dependence of the peak and the steady level. The parameters obtained by fitting eqn (5) to the data from all fibres gave −29·4 and −28·5 mV for the mid-point voltage and 9·0 and 10·2 mV for the steepness factor in case of the peak and the steady level, respectively. These values were almost the same as those obtained in rats and, furthermore, as in rats, the voltage dependences of the two components of $R_{rel}{}^*/C_0$ were also very similar. This resulted in a voltage independent peak to steady level ratio (data not shown) in the range 3–4.

These data clearly demonstrate that, apart from a somewhat smaller SR content in guinea-pigs, all the other key parameters of E–C coupling were identical in the two species.

DISCUSSION

In this study we have demonstrated that enzymatic dissociation of mammalian skeletal muscle fibres can be used to obtain single cells suitable for Vaseline gap voltage clamp measurements. This novel technique should prove fruitful in studying excitation–contraction coupling events in mammalian striated muscle especially in the investigation of genetic disorders.

Using these enzymatically isolated fibres we successfully measured intramembranous charge movement and intracellular calcium transients, the two key events in E–C coupling. The magnitude of the latter was found to be similar to, or somewhat lower than, that previously seen in amphibians. Although the calculated SR calcium release also displayed an early peak followed by a rapid and a slower decline to a maintained steady level, the peak to steady level ratio was independent of membrane voltage suggesting a different control of R_{rel} in mammals than in frogs.

Enzymatic dissociation for obtaining single fibres

Dissociation of skeletal muscle using collagenase and trituration to obtain single isolated fibres has been a widely applied technique and has been used for studying, amongst other things, intracellular calcium homeostasis (e.g. Williams, Head, Bakker & Stephenson, 1990; Carroll, Klein & Schneider, 1995; Allard, Bernengo, Rougier & Jacquemond, 1996). The isolated fibres were, however, usually stimulated externally and responded with a single, or a train of, action potentials. The kinetics of calcium release from the SR and intramembrane charge movement, on the other hand, are better studied in Vaseline gap voltage clamp conditions. Since, to our knowledge, no previous work has been conducted on enzymatically isolated fibres undergoing double Vaseline gap voltage clamp, the first problem was to determine suitable conditions and the muscle to be studied.

Previous studies (e.g. Bekoff & Betz, 1977; Carroll *et al.* 1995), including our own (Allard *et al.* 1996), used flexor digitorum brevis (FDB) which yields relatively short (~1 mm) fibres. When trying to adopt this existing method these cells were found to be too short to enable successful mounting which requires a fibre of 3·5–4·5 mm before stretching. On the other hand, we observed that the longer

Downloaded from jp.physoc.org at Medical University, Central Library, H-4012 DEBRECEN, Hungary on March 9, 2006

szentesi.peter_292_24

the fibres in a given muscle the lower the number of fibres that survive the trituration. Taken together with the fact that data on SR calcium release was obtained mostly from EDL (e.g. García & Schneider, 1993; Delbono & Stefani, 1993), we decided to use this and the analogous muscle (EDC) from the front leg.

Although transferring the fibres into the recording chamber could be done without any damage to the cell membrane, covering them with Vaseline resulted in the development of a contracture. In our experience there was no other way to prevent this except to add BSA and FCS to the solution in which mounting was performed. Furthermore, the longer (up to 15–20 min) the Vaseline had contact with the BSA- and FCS-containing solution before mounting the better was the survival of the fibres. In this study we have demonstrated that using this method of dissociation the fibres kept their electrical integrity and the capability of releasing calcium from the SR, rendering the enzymatic dissociation a convenient tool for obtaining fibres for Vaseline gap measurements.

Properties of intramembrane charge movement

Intramembrane charge movement has been extensively studied not only in amphibian but also in mammalian skeletal muscle fibres. Although several different mammalian species and muscle types, including rat EDL (e.g. Hollingworth & Marshall, 1981; Dulhunty & Gage, 1983), rat omohyoid (Simon & Beam, 1985), rabbit sternomastoid (Lamb, 1986) and human quadriceps (Delbono, Rourke & Ettinger, 1995), have previously been examined the amount and voltage dependence of intramembrane charge is still not clear. For rat EDL and Q_{max} there is a factor of four difference between the lowest (12·1 nC μF^{-1}; García, Gambia-Aldeco & Stefani, 1990) and highest (48·9 nC μF^{-1}; Hollingworth & Marshall, 1981) values reported so far. Values from other reports (Dulhunty & Gage, 1983; Lamb, 1986) and the value obtained in these experiments, 26·1 nC μF^{-1}, are, on the other hand, very similar and lie midway between these two extremes. Although different muscles might have different available charge (Lamb, 1986) the similarity between the value reported here for the rat and the guinea-pig suggests that the same muscle has the same voltage sensor density regardless of species.

The reports are more consistent on the voltage dependence of intramembrane charge movement in rat EDL fibres. From the parameters, obtained by fitting a two-state Boltzmann distribution (eqn (1)), the steepness was essentially the same as in earlier studies. The mid-point voltage was similar to that reported by García *et al.* (1990) who used double Vaseline gap voltage clamp but was more negative than the value from microelectrode voltage clamp studies (Hollingworth & Marshall, 1981; Dulhunty & Gage, 1983). There is no clear reason why using the Vaseline gap should result in a more negative voltage dependence.

The kinetics of intramembrane charge movement are much less well documented for rat muscle fibres than its voltage dependence. Although only microelectrode studies are available for comparison (EDL: Hollingworth & Marshall, 1981; omohyoid: Simon & Beam, 1985) the obtained α_{min}, 202 s^{-1}, was remarkably similar to that reported earlier. It should be noted that the mid-point voltage was, as for the charge distribution, more negative than in those studies. Slow components of intramembrane charge (for review see Huang, 1989) might have, to some extent, distorted the values obtained in this study.

Calcium release in mammalian skeletal muscle

Enzymatically isolated intact mammalian skeletal muscle fibres respond with transient elevation in $[Ca^{2+}]_i$ to electrical stimulation. The peak $[Ca^{2+}]_i$ evoked by an action potential was reported to be around 0·6 μM (most available data from FDB; Turner, Westwood, Regen & Steinhardt, 1988; Carroll *et al.* 1995). This value is considerably smaller than that found in this study (6·3 and 2·8 μM for rats and guinea-pigs, respectively). A possible explanation for the difference could be the duration of the depolarization. However, Carroll *et al.* (1995) found that a train of action potentials did not elevate $[Ca^{2+}]_i$ significantly more than did a single action potential. On the other hand, these authors described that a small elevation in resting $[Ca^{2+}]_i$ considerably increased the peak of the calcium transient. Comparing the resting $[Ca^{2+}]_i$ found in intact fibres (40 nM; Turner *et al.* 1988; Carroll *et al.* 1995) with that reported here (120 nM) suggests that part of the larger maximal elevation in $[Ca^{2+}]_i$ could have been due to the higher resting calcium levels. It should be noted that Williams *et al.* (1990) found the resting $[Ca^{2+}]_i$ to be 90 nM in enzymatically dissociated EDL fibres.

The change in calcium concentration induced by a depolarizing pulse in our study is, nevertheless, comparable with data from EDL including both intact fibres (Hollingworth, Zhao & Baylor, 1996) and mechanically dissected cut fibres mounted into a Vaseline gap. Although data on the actual maximum of $[Ca^{2+}]_i$ increase for the latter are diverse in the literature, reported values ranging from 1 μM (García & Schneider, 1993) to 10 μM (Delbono & Stefani, 1993), the values found in this study fall within the above range. It should be noted that although the magnitude of the calcium concentration change was closer to that reported by Delbono & Stefani (1993) the time course of our transients resembled those of García & Schneider (1993). As shown in Fig. 5, this was true even when the same dye, mag-fura-5, was used as in the study of Delbono & Stefani (1993).

The calculated SR release flux, as expected from the similar calcium transients, resembled those of García & Schneider (1993). Furthermore, the estimated properties of the intracellular calcium buffers and the SR calcium pump were essentially the same, too. On the other hand, the SR release flux was different from that reported by Delbono & Stefani (1993) or Delbono (1995) even using the same calcium-sensitive dye; no secondary peaks were detected. The absence of the secondary peak clearly originates from the

Downloaded from jp.physoc.org at Medical University, Central Library, H-4012 DEBRECEN, Hungary on March 9, 2006

szentesi.peter_292_24

fact that our calcium transients differ from those of Delbono & Stefani (1993). At the moment there is no explanation for this observation, and therefore further experiments are needed to clarify the difference. We also found, in agreement with Shirokova *et al.* (1996), that the peak to steady ratio of SR calcium release flux, unlike that in amphibians, was voltage independent in mammals. These similarities are strong proof that enzymatic dissociation can replace the mechanical dissection for obtaining single mammalian fibres.

Allard, B., Bernengo, J. C., Rougier, O. & Jacquemond, V. (1996). Intracellular Ca^{2+} changes and Ca^{2+}-activated K^+ channel activation induced by acetylcholine at the endplate of mouse skeletal muscle fibres. *Journal of Physiology* **494**, 337–349.

Baylor, S. M., Chandler, W. K. & Marshall, M. W. (1983). Sarcoplasmic reticulum calcium release in frog skeletal muscle fibres estimated from Arsenazo III calcium transients. *Journal of Physiology* **344**, 625–666.

Bekoff, A. & Betz, W. J. (1977). Physiological properties of dissociated muscle fibres obtained from innervated and denervated adult rat muscle. *Journal of Physiology* **271**, 25–40.

Carroll, S. L., Klein, M. G. & Schneider, M. F. (1995). Calcium transients in intact rat skeketal muscle fibers in agarose gel. *American Journal of Physiology* **269**, C28–34.

Csernoch, L., Jacquemond, V. & Schneider, M. F. (1993). Microinjection of strong calcium buffers suppresses the peak of calcium release in frog skeletal muscle fibres. *Journal of General Physiology* **101**, 297–333.

Delbono, O. (1995). Ca^{2+} modulation of sarcoplasmic reticulum Ca^{2+} release in rat skeletal muscle fibres. *Journal of Membrane Biology* **146**, 91–99.

Delbono, O., Rourke, K. S. & Ettinger, W. H. (1995). Excitation-calcium release uncoupling in aged single human skeletal muscle fibers. *Journal of Membrane Biology* **148**, 211–222.

Delbono, O. & Stefani, E. (1993). Calcium transients in single mammalian skeletal muscle fibres. *Journal of Physiology* **463**, 689–707.

Dulhunty, A. F. & Gage, P. W. (1983). Asymetrical charge movement in slow- and fast-twitch mammalian muscle fibres in normal and paraplegic rats. *Journal of Physiology* **341**, 213–231.

Garcia, J., Gamboa-Aldeco, R. & Stefani, E. (1990). Charge movement and calcium currents in skeletal muscle fibers are enhanced by GTPγS. *Pflügers Archiv* **417**, 114–116.

García, J. & Schneider, M. F. (1993). Calcium transients and calcium release in rat fast-twitch skeletal muscle fibres. *Journal of Physiology* **463**, 709–728.

Haugland, R. P. (1996). *Handbook of Fluorescent Probes and Research Chemicals*. Molecular Probes, Inc., Eugene, OR, USA.

Heizmann, C. W., Berchtold, M. W. & Rowlerson, A. M. (1982). Correlation of parvalbumin concentration with relaxation speed in mammalian muscles. *Proceedings of the National Academy of Sciences of the USA* **79**, 7243–7247.

Hollingworth, S. & Marshall, M. W. (1981). A comparative study of charge movement in rat and frog skeletal muscle fibres. *Journal of Physiology* **321**, 583–602.

Hollingworth, S., Zhao, M. & Baylor, S. M. (1996). The amplitude and time course of the myoplasmic free $[Ca^{2+}]$ transient in fast-twitch fibres of mouse muscle. *Journal of General Physiology* **108**, 455–469.

Huang, C. L.-H. (1989). Intramembrane charge movements in skeletal muscle. *Physiological Reviews* **68**, 1197–1247.

Klein, M. G., Simon, B. J., Szücs, G. & Schneider, M. F. (1988). Simultaneous recording of calcium transients in skeletal muscle using high and low affinity calcium indicators. *Biophysical Journal* **55**, 971–988.

Kovács, L., Ríos, E. & Schneider, M. F. (1983). Measurement and modification of free calcium transients in frog skeletal muscle fibres by a metallochromic indicator dye. *Journal of Physiology* **343**, 161–196.

Lamb, G. D. (1986). Assymetric charge movement in contracting muscle fibres in the rabbit. *Journal of Physiology* **376**, 63–83.

Lamb, G. D. & Walsh, T. (1987). Calcium currents, charge movementand dihydropyridine binding in fast- and slow-twitch muscles of rat and rabbit. *Journal of Physiology* **393**, 595–617.

Marks, A. R., Tempst, P., Hwang, K. S., Taubman, M. B., Inui, M., Chadwick, C., Fleischer, S. & Nadal-Ginard, B. (1989). Molecular cloning and characterization of the ryanodine receptor/junctional channel complex cDNA from skeletal sarcoplasmic reticulum. *Proceedings of the National Academy of Sciences of the USA* **86**, 8683–8687.

Meissner, G. (1994). Ryanodine receptor/Ca^{2+} release channels and their regulation by endogenous effectors. *Annual Review of Physiology* **56**, 485–508.

Melzer, W., Ríos, E. & Schneider, M. F. (1984). Time course of calcium release and removal in skeletal muscle fibres. *Biophysical Journal* **45**, 637–641.

Melzer, W., Ríos, E. & Schneider, M. F. (1986). The removal of myoplasmic free calcium following calcium release in frog skeletal muscle. *Journal of Physiology* **372**, 261–292.

Ríos, E. & Pizarro, G. (1991). Voltage sensor of excitation–contraction coupling in skeletal muscle. *Physiological Reviews* **71**, 849–908.

Sárközi, S., Szentesi, P., Jona, I. & Csernoch, L. (1996). Effects of cardiac glycosides on excitation–contraction coupling in frog skeletal muscle fibres. *Journal of Physiology* **495**, 611–626.

Schneider, M. F. & Simon, B. J. (1988). Inactivation of calcium release from the sarcoplasmic reticulum in frog skeletal muscle. *Journal of Physiology* **405**, 727–745.

Shirokova, N., García, J., Pizarro, G. & Ríos, E. (1996). Ca^{2+} release from the sarcoplasmic reticulum compared in amphibian and mammalian skeletal muscle. *Journal of General Physiology* **107**, 1–18.

Shirokova, N., Pizarro, G. & Ríos, E. (1994). A damped oscillation in the intramembranous charge movement and calcium release flux of frog skeletal muscle. *Journal of General Physiology* **104**, 449–477.

Simon, B. J. & Beam, K. G. (1985). Slow charge movement in mammalian skeletal muscle. *Journal of General Physiology* **85**, 1–19.

Smith, J. S., Imagawa, T., Ma, J., Fill, M., Campbell, K. P. & Coronado, R. (1988). Purified ryanodine receptor from rabbit skeletal muscle is the calcium-release channel of sarcoplasmic reticulum. *Journal of General Physiology* **92**, 1–26.

Takeshima, H., Nishimura, S., Matsumoto, T., Ishida, H., Ueda, M., Hanaoka, M., Hirose, T. & Numa, S. (1989). Primary structure and expression from complementary DNA of skeletal muscle ryanodine receptor. *Nature* **339**, 439–445.

Downloaded from jp.physoc.org at Medical University, Central Library, H-4012 DEBRECEN, Hungary on March 9, 2006

szentesi.peter_292_24

Tanabe, T., Beam, K. G., Powell, J. A. & Numa, S. (1988). Restoration of excitation–contraction coupling and slow calcium current in dysgenic muscle by dihydropyridine receptor complementary DNA. *Nature* **336**, 134–139.

Turner, P. R., Westwood, T., Regen, C. M. & Steinhardt, R. A. (1988). Increased protein degradation results from elevated free calcium levels found in muscle from mdx mice. *Nature* **335**, 735–738.

Williams, D. A., Head, S. I., Bakker, A. J. & Stephenson, G. (1990). Resting calcium concentrations in isolated skeletal muscle fibres of dystrophic mice. *Journal of Physiology* **428**, 243–256.

Acknowledgements

The authors wish to thank Ms R. Öri for skillful technical assistance. This work was supported by Hungarian research grants (OTKA T016957, ETT095/1996, FKFP1289/1997). The visit of Dr Jacquemond to Debrecen was financed by a French–Hungarian intergovernmental program (Balaton 95012).

Received 28 April 1997; *accepted 11 August 1997.*

Downloaded from jp.physoc.org at Medical University, Central Library, H-4012 DEBRECEN, Hungary on March 9, 2006

szentesi.peter_292_24
Biophysical Journal Volume 86 March 2004 1436–1453

Altered Elementary Calcium Release Events and Enhanced Calcium Release by Thymol in Rat Skeletal Muscle

Péter Szentesi,* Henrietta Szappanos,* Csaba Szegedi,* Monika Gönczi,† István Jona,* Julianna Cseri,* László Kovács,*† and László Csernoch*†

*Department of Physiology and †Cell Physiology Research Group of the Hungarian Academy of Sciences, Research Center for Molecular Medicine, Medical and Health Science Center, University of Debrecen, Debrecen, Hungary

ABSTRACT The effects of thymol on steps of excitation-contraction coupling were studied on fast-twitch muscles of rodents. Thymol was found to increase the depolarization-induced release of calcium from the sarcoplasmic reticulum, which could not be attributed to a decreased calcium-dependent inactivation of calcium release channels/ryanodine receptors or altered intramembrane charge movement, but rather to a more efficient coupling of depolarization to channel opening. Thymol increased ryanodine binding to heavy sarcoplasmic reticulum vesicles, with a half-activating concentration of 144 μM and a Hill coefficient of 1.89, and the open probability of the isolated and reconstituted ryanodine receptors, from 0.09 $\pm$ 0.03 to 0.22 $\pm$ 0.04 at 30 μM. At higher concentrations the drug induced long-lasting open events on a full conducting state. Elementary calcium release events imaged using laser scanning confocal microscopy in the line-scan mode were reduced in size, 0.92 $\pm$ 0.01 vs. 0.70 $\pm$ 0.01, but increased in duration, 56 $\pm$ 1 vs. 79 $\pm$ 1 ms, by 30 μM thymol, with an increase in the relative proportion of lone embers. Higher concentrations favored long events, resembling embers in control, with duration often exceeding 500 ms. These findings provide direct experimental evidence that the opening of a single release channel will generate an ember, rather than a spark, in mammalian skeletal muscle.

INTRODUCTION

Excitation-contraction coupling (E-C coupling) in skeletal muscle critically depends on the concerted action of two proteins, the dihydropyridine receptors (DHPRs) and ryanodine receptors (RyRs). The former, residing in the transverse-tubular (T-tubular) membrane, serves as the voltage sensor and can also carry the L-type calcium current (Ríos and Pizarro, 1991). The latter is the calcium release channel of the sarcoplasmic reticulum (SR) through which calcium ions enter the myoplasmic space upon stimulation (e.g., Meissner, 1994).

Spontaneous openings of RyRs in situ appear as elementary calcium release events in confocal images (Cheng et al., 1993). In mammalian muscle they can be subdivided into sparks and embers (Kirsch et al., 2001), the former resembling the *sparks* first described in heart (Cheng et al., 1993) and then in amphibian skeletal muscle (Tsugorka et al., 1995; Klein et al., 1996). *Embers*, a term introduced by González and co-workers (2000b) to denote events having long duration with constant fluorescence seem, on the other hand, to be more frequent in mammalian striated muscle as compared to sparks (Kirsch et al., 2001). Not only do mammalian calcium release events differ from those of frogs in their appearance, they seem to be affected less by classic drugs, e.g., caffeine, that influence E-C coupling and calcium sparks in amphibians (González et al., 2000a). Understanding this morphological variability and resistance to external influences should lead to a better understanding of how calcium release channels are regulated in mammalian striated muscle.

A wide range of phenol derivatives, including 4-chloro-meta-cresol (4CmC; Herrmann-Frank et al., 1996) and methyl *p*-hydroxybenzoate (Cavagna et al., 2000), were shown to alter RyR function. In a concentration of 0.2 mM and up, these substances increase the open probability of isolated RyRs and augment calcium release from intracellular calcium stores. It is interesting to note that a well known and widely used member of this group, thymol, has also been shown to alter calcium handling in a variety of cells, including skeletal muscle (Koshita and Oba, 1989; Kostyuk et al., 1991). In rabbit skeletal muscle, thymol first reduced the Ca^{2+}-ATPase activity, then increased the calcium permeability of the SR membrane. On neurons or on smooth muscle preparations, calcium transients could occur spontaneously in the presence of thymol, and the drug was found to increase the intracellular calcium concentration (Kostyuk et al., 1991; Hisayama and Takayanagi, 1986). Thymol is of special interest not only because it is widely used as a food preservative, but also because it is the stabilizer of liquid halothane, and its concentration might build up in the vaporizer during anesthesia. Despite its general use and definite actions on calcium homeostasis, no detailed analysis has so far been carried out to investigate the effects of thymol on E-C coupling in depth. Furthermore, no attempts were made to correlate the drug-induced alterations of SR calcium release and RyR function with the parameters of elementary calcium release events.

Here we show that thymol, at a concentration as low as 30 μM, enhances SR calcium release without major effects on the voltage sensor. Thymol is also shown to increase both

Submitted August 13, 2003, and accepted for publication October 21, 2003.

Address reprint requests to Dr. László Csernoch, Dept. of Physiology, University of Debrecen, PO Box 22, Debrecen H-4012, Hungary. Tel.: 36-52-416-634; Fax: 36-52-432-289; E-mail: csl@phys.dote.hu.

© 2004 by the Biophysical Society

0006-3495/04/03/1436/18 $2.00

[^{3}H]ryanodine binding to heavy SR vesicles and the open probability (P_o) of the isolated and reconstituted RyRs through inducing long-lasting open events with full conductance at concentrations above 100 μM. These findings establish thymol as an ideal tool to study elementary calcium release events in mammalian muscle. Indeed, the drug altered the morphology of these events by increasing both their duration and the relative proportion of embers as compared to sparks. Higher concentrations of the drug induced extremely long embers that, in all likelihood, originate from a drug-modified channel, providing direct experimental evidence that embers, rather than sparks, represent the opening of a single RyR in mammalian skeletal muscle. Some of these results were presented to the Biophysical Society (Csernoch et al., 2002).

MATERIALS AND METHODS

Enzymatic isolation and voltage-clamping of single fibers

Single skeletal muscle fibers, isolated enzymatically from the *extensor digitorum communis* muscles of rats, were mounted into a double Vaseline-gap chamber as described earlier (Szentesi et al., 1997). In brief, rats of either sex were anesthetized and killed by cervical dislocation in accordance with the guidelines of the European Community (86/609/EEC) following a protocol approved by the institutional Animal Care Committee. The muscles were removed and were treated with collagenase (Type I, Sigma, St. Louis, MO) for 1–1.5 h at 37°C. After the dissociation, fibers were allowed to rest for at least 20 min.

The selected fiber was transferred into the recording chamber filled with relaxing solution (150 mM K-glutamate, 2 mM $MgCl_2$, 10 mM HEPES, and 1 mM EGTA). The fiber segments in the open-end pools were permeabilized using 0.01% saponin. Solutions were then exchanged to internal solution in the open-end pools (120 mM Cs-glutamate, 5.5 mM $MgCl_2$, 5 mM Na_2-ATP, 10 mM Na-phosphocreatine, 10 mM glucose, 5 mM HEPES, and 5 mM EGTA) and to external solution in the middle pool (140 mM tetraethylammonium-CH_3SO_3, 2 mM $CaCl_2$, 2 mM $MgCl_2$, 5 mM HEPES, 0.0003 mM tetrodotoxin, and 1 mM 3,4diamino-pyridine). All solutions were adjusted to pH 7.2 and 300 mosmol/l. The internal solution also contained 1 mM Antipyrylazo III (APIII) and 100 μM Fura-2 for the detection of $[Ca^{2+}]_i$. The length of the fiber segment in the middle pool was set to 500 μm.

The experimental setup and the data acquisition have been described in detail in our earlier reports (e.g., Csernoch et al., 1999b). The fiber was transilluminated using a tungsten halogen light source ($\lambda > 600$ nm) and was epiilluminated at 380 nm or at the isosbestic wavelength of Fura-2 using a 75-W Xenon arc lamp (Oriel 60000, Oriel Instruments, Stratford, CT). Light intensities were simultaneously recorded at 510, 720, and 850 nm for the detection of APIII absorbance and Fura-2 fluorescence. Fibers were voltage-clamped and the holding potential was set to −100 mV. All experiments were performed at 16–18°C.

Preparation of SR vesicles and RyRs

Heavy SR (HSR) vesicles were isolated from either rabbit or rat skeletal muscle as described earlier (Szegedi et al., 1999, and Csernoch et al., 1999b, respectively). Rabbit HSR vesicles were used for ryanodine binding experiments, whereas the ryanodine receptor calcium release channel was isolated from rat HSR vesicles. In brief, skeletal muscles were removed from the *longissimus dorsii* (rabbit) or from the front and hind legs of those rats that were used in the Vaseline-gap experiments. The muscles were cut into small pieces, quickly frozen using liquid nitrogen, and stored at −70°C until further use. Vesicles were obtained by first homogenizing the tissue then removing the unsolubilized particles in a clinical centrifuge. Crude membrane fraction was collected from the supernatant by centrifugation at 40,000 × g (30 min). The actomyosin content of the pellet was then dissolved in 600 mM KCl and the crude microsome fraction was collected by centrifugation at 109,000 × g (30 min). The microsome was loaded onto a 20–45% linear sucrose gradient and spun for 16 h at 90,000 × g (4°C) in a swingout (SW-27) Beckman rotor (Beckman-Coulter, Fullerton, CA). The protein-ring corresponding to the HSR fraction was extracted from the 36–38% region. Vesicles were collected at 124,000 × g for 60 min then resuspended in 92.5 mM KCl and 18.5 mM K-MOPS at pH = 7.0 for vesicular measurements or in 0.4 M sucrose and 10 mM K-PIPES at pH = 7.2 for RyR preparation. Samples were stored at −70°C until further use.

For preparation of RyR, the rat HSR vesicles (3 mg/ml) were solubilized for 2 h at 4°C with 1% CHAPS (3[(3-chloramidopropyl)dimethyl-amino]-1-propanesulfonate) in a solution containing 1 M NaCl, 100 μM EGTA, 150 μM $CaCl_2$, 5 mM AMP, 0.45% phosphatidylcholine, 20 mM Na-PIPES at pH = 7.2, and protease inhibitors (Csernoch et al., 1999b). Unsolubilized proteins were removed by centrifugation at 59,000 × g, and subsequently the supernatant was layered on top of a 10–28% sucrose gradient also containing 1% CHAPS, 0.7 M NaCl, 10 mM AMP, 0.5% phosphatidylcholine, 70 μM EGTA, 100 μM $CaCl_2$, 1 mM DTT (dithiothreitol), and 13 mM Na-PIPES at pH = 7.2. Solubilized SR membranes were centrifuged through the sucrose gradient for 16 h at 90,000 × g (4°C) in a swingout (SW-27) Beckman rotor. Fractions containing RyRs were collected in small aliquots. They were then rapidly frozen in liquid nitrogen and stored at −70°C.

Calculation of $[Ca^{2+}]_i$ and R_{rel}

In Vaseline-gap experiments the changes in myoplasmic free calcium concentration ($[Ca^{2+}]_i$) were calculated from APIII absorbance with the correction for intrinsic fiber absorbance at 850 nm and from Fura-2 fluorescence using the kinetic correction. Resting, as well as small changes in $[Ca^{2+}]_i$ were determined from changes in Fura-2 saturation, whereas large increases in $[Ca^{2+}]_i$ were determined from changes in APIII absorbance.

The rate of calcium release from the SR (R_{rel}) was calculated from the calcium transients using the procedure described in Szentesi et al. (1997). In brief, four parameters of the removal model were fitted simultaneously, $k_{off,M-P}$ (Mg^{2+} off rate from parvalbumin), PV_{max} (maximal transport rate of SR calcium pump), and $k_{off,Ca-E}$ and $k_{on,Ca-E}$ (the rate constants of calcium binding to EGTA). The calculated R_{rel} records were corrected for the depletion of calcium in the SR and expressed as a percentage of SR content. The voltage dependence (V_m) of either component of calcium release, $R_{rel,i}(V_m)$, where i = peak or steady level, was assessed by fitting the two-state Boltzmann function

$$R_{rel,i}(V_m) = R_{rel,i}[max]/(1 + \exp\{-(V_m - V_{50})/k\}), \quad (1)$$

where $R_{rel,i}[max]$ is the maximal release rate, V_{50} is the voltage at half-maximal release rate, and k is the slope factor, to the calculated data.

Intramembrane charge movement

Intramembrane charge transfer was calculated by measuring membrane currents in response to depolarizing and hyperpolarizing pulses as described in detail previously (Szentesi et al., 1997). Briefly, the linear capacitive current was determined from hyperpolarizing pulses of −20 mV in amplitude. This current was then scaled and subtracted from those measured during depolarizing steps. The nonlinear capacitive current, representing intramembranous charge transfer, was integrated to give the amount of charge moved during the pulse (Q). To assess the membrane potential dependence of charge transfer, $Q(V_m)$, the measured charge was fitted with the Boltzmann function

$$Q(V_m) = Q_{max}/(1 + \exp\{-(V_m - V_{50})/k\}), \quad (2)$$

where Q_{max} is the maximal available charge, and V_{50} and k have their usual meaning.

Ryanodine binding

Ryanodine binding assay was carried out using [^{3}H]ryanodine in an incubation medium of 1 M NaCl, 25 mM Na-PIPES at pH 7.1, 1 mM Pefabloc, (Fluka, Buchs, Switzerland), 300 μM $CaCl_2$, and 205 μM EGTA. 50 μl aliquots, containing 25 μg protein were incubated at 37°C for 2 h, with the various concentrations of the radioligand and of thymol (Herrmann-Frank et al., 1996). The reaction was terminated by immediately filtering the samples on a Bio-Dot 96 well filter apparatus (Bio-RAD Lab., Hercules, CA) using Millipore-50 filter paper (Millipore, Billerica, MA). The dots were than rinsed with equal aliquots of washing medium without ryanodine (hot and cold), that were otherwise identical to the incubation medium. Filter papers were cut into appropriate pieces and their radioactivity was determined using a liquid scintillation counter. Nonspecific binding was determined in the presence of 50–100 μM ryanodine, added to the incubation mixture before the radioligand. Thymol was found not to affect the nonspecific binding. Binding data, as well as the concentration-dependent effects of thymol on binding, were fitted using the Hill equation

$$B/B_{max} = [X]^n/([EC_{50}]^n + [X]^n), \quad (3)$$

where B is the concentration of the bound form, B_{max} is the theoretical maximum of B, X is the ligand in question (ryanodine or thymol), and n is the Hill coefficient. Experiments were carried out in quadruplets and the averaged data were used in the calculations.

Planar lipid bilayer measurements

CHAPS-solubilized ryanodine receptors (Tripathy and Meissner, 1996) were incorporated into planar lipid bilayers formed across a 200-μm aperture of a nolrene cup using a lipid mixture composed of phosphatidylethanolamine, phosphatidylserine, and phosphatidylcholine in the weight ratio of 5:4:1. Lipids were dissolved in *n*-decane up to a final concentration of 20 mg/ml as described in our previous reports (e.g., Csernoch et al., 1999b). Reconstitution was initiated in symmetric buffer solution (250 mM KCl, 100 μM EGTA, 150 μM $CaCl_2$, and 20 mM PIPES, at pH 7.2), by adding a small aliquot of the solubilized receptor to the *cis* (cytoplasmic) side. The current signal was filtered at 1 kHz through an eight-pole low-pass Bessel filter and digitized at 6 kHz using an Axopatch 200 amplifier and pClamp software (Axon Instruments, Foster City, CA). Channels with conductance >400 pS were accepted as RyRs. Open probability values were calculated from 1-min-long segments of the current traces. Measurements were carried out at 22–25°C, and thymol was applied in the *cis* chamber.

Measurement of calcium sparks

Single fibers, isolated as detailed above, were mounted into a chamber with glass bottom. Cells were treated with a modified relaxing solution (125 mM K-glutamate, 10 mM HEPES, 1 mM EGTA, 6 mM $MgCl_2$, 5 mM Na_2-ATP, 10 mM Na-phosphocreatine, 10 mM glucose, 0.13 mM $CaCl_2$, and 8% dextran) containing 0.002% saponin for 2–3 min. Permeabilization of the surface membrane was monitored by the addition of 50 μM fluo-3 into the solution and imaging of the fiber. This solution was then exchanged to a K_2SO_4-based internal solution (95 mM K_2SO_4, 10 mM HEPES, 1 mM EGTA, 6 mM $MgCl_2$, 5 mM Na_2-ATP, 10 mM Na-phosphocreatine, 10 mM glucose, 0.13 mM $CaCl_2$, 0.1 mM fluo-3, and 8% dextran) since the presence of sulfate was shown to increase the spark frequency without affecting the spark morphology in mammalian preparations (Csernoch et al., 2003; Zhou et al., 2003).

Fibers were imaged using an LSM 510 laser scanning confocal microscope (Zeiss, Oberkochen, Germany). Line-scan images ([x,t]) were taken at 1.54 ms/line and 512 pixels/line (pixel size 0.142 μm) with a 40× water immersion objective (1.2 NA; Zeiss) parallel to the fiber axis. Fluo-3 was excited with an argon ion laser (at 488 nm; 5% laser intensity), and emitted light was collected through a bandpath filter and digitized at 12 bits. Any bleaching of the dye was corrected for. To avoid photodamage, the same position was not imaged twice. The bleaching-corrected images (F[x,t]) were then normalized to baseline fluorescence (F_0[x]).

Elementary calcium release events were captured using an automatic computer detection method based on those described earlier (e.g., Cheng et al., 1999). In brief, the program identified elementary events as regions with fluorescence above a relative threshold, calculated from the noise in the images, and having amplitudes >0.3 $\Delta F/F_0$ units. The eventless portion of the image was used to calculate bleaching (averaged over the x axis and smoothed) and F_0[x] (averaged, but not smoothed over the t axis). The program also determined the parameters of the identified events: amplitude (as $\Delta F/F_0$); spatial half-width measured at the time of the peak (full width at half-maximum, FWHM); duration; and rise time for sparks and sparks with embers. For the lone embers, the average amplitude, duration, and FWHM parameters were determined. FWHM was obtained from fitting a Gaussian function to the spatial distribution obtained by averaging three lines at the peak for sparks or by all lines except the first and last 10 ms of the event for lone embers.

Chemicals and statistics

Fura-2 and Fluo-3 were purchased from Molecular Probes (Eugene, OR), whereas APIII was purchased from ICN Biomedicals (Aurora, OH). Protease inhibitors were from Boehringer (Mannheim, Germany), from Merck (Darmstadt, Germany), and from Sigma (St. Louis, MO). Lipids were obtained from Avanti Polar Lipids (Alabaster, AL), [^{3}H]ryanodine was from Dupont (Boston, MA), and all other chemicals were from Sigma. Thymol was prepared as a stock of 300 mM in DMSO.

In statistical analyses all values were expressed as mean ± SE. Statistical significance was calculated with Student's t-test assuming significance for $p < 0.05$.

RESULTS

Thymol has modest effects on intramembrane charge movement

Recent reports demonstrated the suppression of L-type calcium currents by thymol on cardiac (Magyar et al., 2002) as well as skeletal (Szentandrássy et al., 2003) muscle cells with half-inhibitory concentration above 100 μM. To understand the effects of the drug on E-C coupling we first tested the involvement of the voltage sensor as a putative binding site of thymol. Intramembrane charge movements were thus measured on rat skeletal muscle fibers mounted into the double Vaseline-gap chamber.

Fig. 1 *A* presents nonlinear capacitive currents in the absence and presence of the drug. The transients were recorded in response to 100-ms-long depolarizing pulses exploring the −80–0 mV voltage range. The actual intramembrane charge movement currents were normalized to fiber capacitance to take into account the differences in fiber size or any possible change in passive electrical properties during the experiments. It should be noted, however, that the linear capacitance, on average, did not change significantly

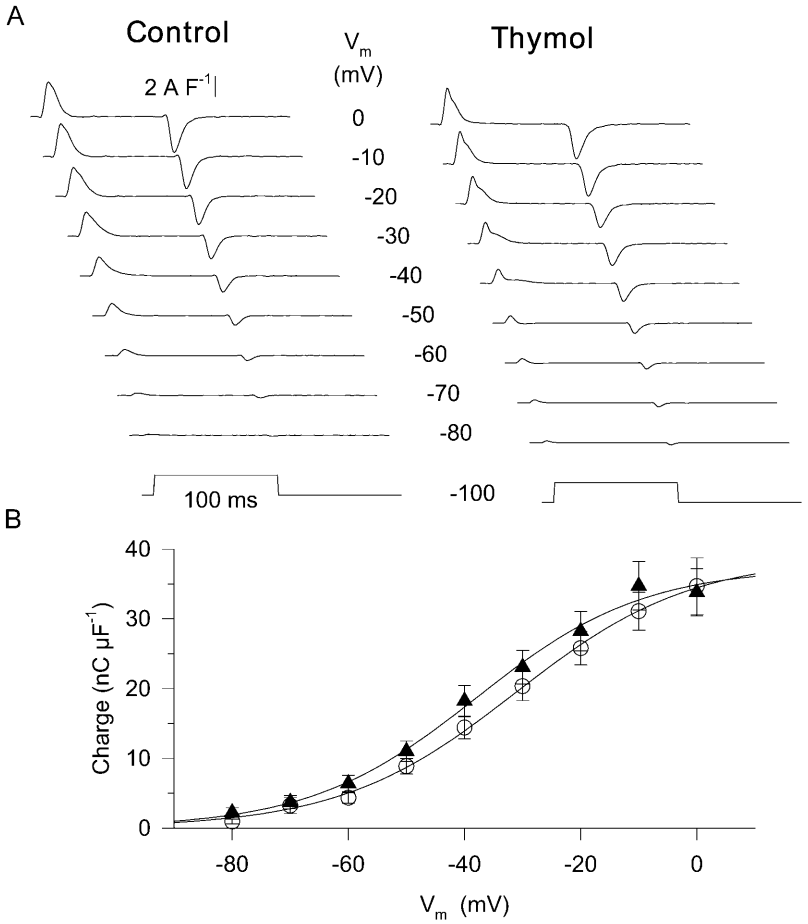


FIGURE 1 The effect of thymol on intramembrane charge movement. (*A*) Nonlinear capacitive currents in the absence and presence of 300 μM thymol. The holding potential was set to −100 mV and the currents representing the intramembrane charge displacement were recorded in response to 100-ms-long depolarizing pulses. The membrane potentials during the pulses are given in each row. The current traces were normalized to the linear capacitance (10.5 nC) of the fiber. (*B*) The Boltzmann distribution of intramembrane charge. The current records presented in *A* and six other fibers were integrated and the calculated charges at corresponding voltages were averaged. Eq. 1 was fitted to the data points to assess the voltage dependence of charge displacement. Superimposed curves were generated using the parameters obtained from the fits (Q_{max} = 38.8 and 37.4 nC μF^{-1}; V_{50} = −31.2 and −38.0 mV; k = 15.1; and 14.4 mV in control (○) and in thymol (▲), respectively).

during the course of these experiments since it was found to be 11.3 ± 1.1 nF (n = 7) under control conditions and 9.4 ± 1.7 nF on the same cells after the addition of 300 μM thymol.

To assess the voltage dependence of charge transfer, the currents were integrated and Eq. 2 was fitted to the charge versus voltage data both before and after the addition of thymol. Average values of the parameters from these fits are presented in Table 1. To visualize the effects of thymol on the voltage dependence of charge transfer, Fig. 1 *B* plots the charge as a function of membrane potential during the test pulse. Thymol, at the concentration tested, shifted the voltage dependence to the left along the voltage axis, by 10 mV, together with a slight decrease in Q_{max} (the maximally available charge). Whereas the changes in V_{50} were statistically significant, the changes in Q_{max} and in the steepness remained, on average, within the limits of statistical variation. As it will be detailed below, thymol already had significant effects on SR calcium release at a concentration of 30 μM. Table 1, therefore, presents average values for the voltage dependence of charge movement at this concentration.

These data, on the one hand, establish that the suppression of L-type calcium currents seen in earlier studies with phenol analogs (Fusi et al., 2001) or with thymol itself cannot be accounted for by an effect on the voltage sensor. Furthermore, the slight shift in the voltage dependence of intramembrane charge movement could also not explain its effects on previously reported effects on calcium handling.

Thymol increases the calcium transients

Fig. 2 illustrates the effect of extracellular application of 30 μM thymol on the calcium transients elicited by 60–100-ms-long depolarizing pulses under voltage-clamp conditions. Fig. 2 *A* shows a series of calcium transients, measured with APIII, elicited by depolarizing pulses of various lengths from −40 to 0 mV. Measurements in thymol were taken 5−10 min after the solution exchange. This was believed to be long enough for the drug to reach its binding site and exert its full effect. Application of thymol produced an ~50% increase in the maximal amplitude of the calcium transient from 1.5 ± 0.3 to 2.2 ± 0.4 μM (n = 9). The transients showed a continuous increase in control and after the addition of 30 μM thymol. The increase was present both in the rate of rise and in the amplitude of the calcium signals. Fig. 2 *B* shows the voltage dependence of the mean (n = 9) maximum change in $[Ca^{2+}]_i$ reached in control conditions (*open symbols*), and upon thymol application (*solid symbols*). In

TABLE 1 Effect of thymol on intramembrane charge movement

	Q_{max} (nC μF^{-1})	V_{50} (mV)	k (mV)
Control ($n = 7$)	35.2 ± 3.1	−25.9 ± 2.6	12.0 ± 1.5
30 μM thymol	34.0 ± 4.4	−34.8 ± 2.7*	11.6 ± 0.9
Control ($n = 8$)	35.4 ± 2.7	−27.8 ± 2.4	11.4 ± 1.2
300 μM thymol	35.8 ± 3.8	−39.8 ± 2.9*	13.7 ± 0.6

Parameter values obtained by fitting Eq. 2 to the voltage dependence of intramembrane charge movement.
*Significant difference from control.

average, the drug produced a 58% elevation of the peak calcium transient. This effect of thymol was associated with a slight, but not significant, change in resting $[Ca^{2+}]_i$, which, within this series of measurements, exhibited a mean value of 51 ± 6 and 72 ± 9 nM before and after addition of the drug.

SR permeability is augmented by thymol

Fig. 3 presents the rate of calcium release from the SR (R_{rel}; see Methods) calculated from calcium transients shown in Fig. 2. The figure demonstrates that the above-mentioned effects of thymol on $[Ca^{2+}]_i$ were present on R_{rel} at every membrane potential tested. Thymol increased both the early peak and the sustained steady level of the calcium release. On average the maximal increase in the peak in 30 μM thymol was found to be 28.4 ± 4.0 μM ms^{-1} ($n = 10$) for a 100-ms-long depolarization to 0 mV as compared to 17.8 ± 2.2 μM ms^{-1} measured on the same fibers under control conditions. Whereas the maximal increase in the steady level was found to be 10.6 ± 2.0 μM ms^{-1} ($n = 10$) in the presence of the drug and 7.3 ± 1.0 μM ms^{-1} was measured on the same fibers under control conditions, the effect of thymol was reversible. After washout, the peak returned to

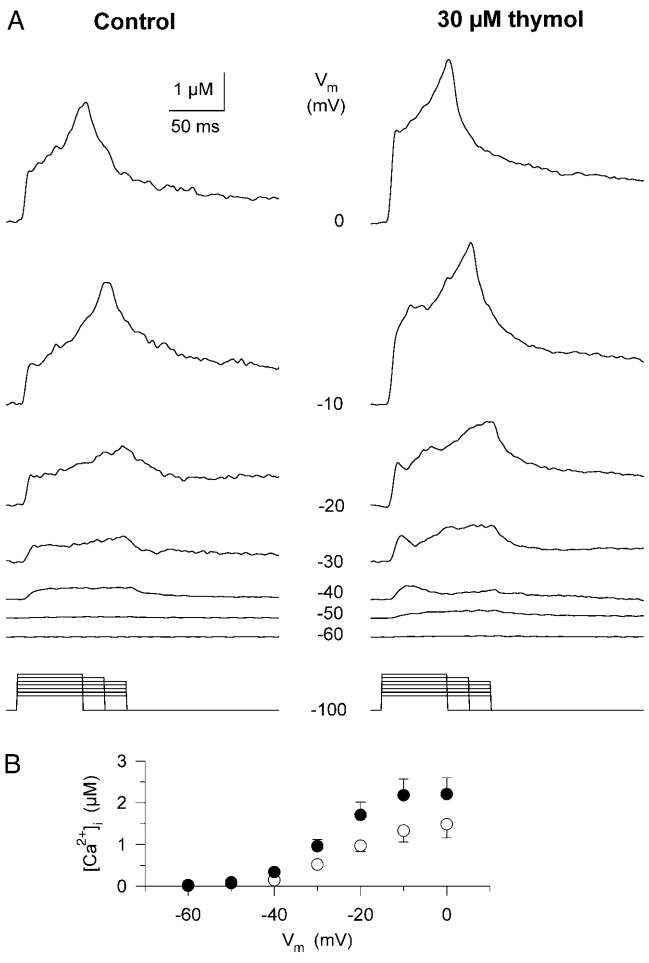


FIGURE 2 Effect of 30 μM thymol on the calcium transients. (*A*) Changes in $[Ca^{2+}]_i$ measured with APIII before and after the addition of the drug. The holding potential was set to −100 mV and the fiber was then depolarized to the indicated voltages for 60–100 ms. [APIII] = 680–1380 μM. (*B*) The maximal increase in $[Ca^{2+}]_i$ during the calcium transients was averaged from 10 fibers and plotted as a function of the membrane potential during the depolarizing pulses.

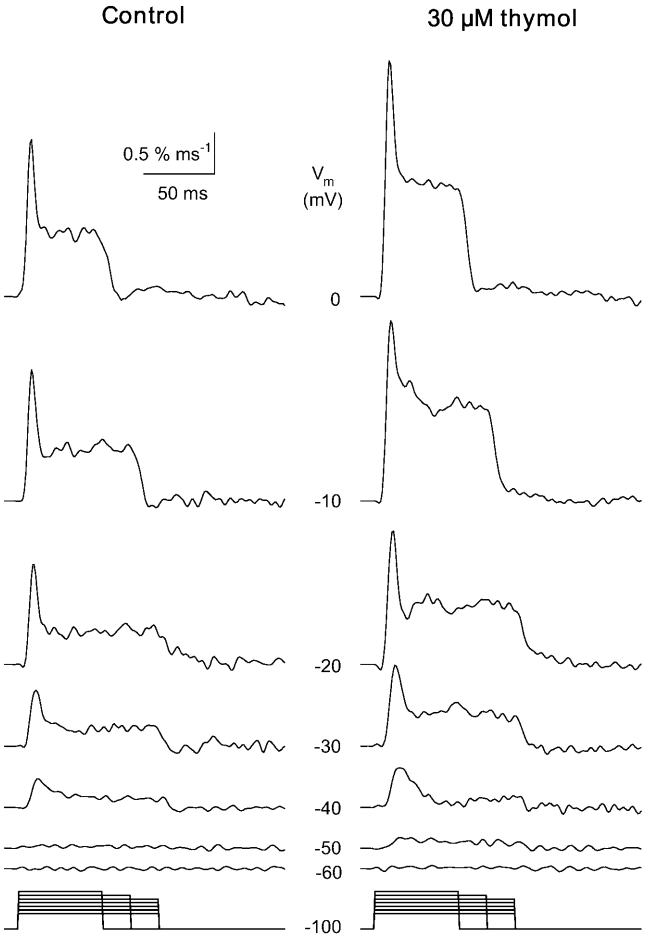


FIGURE 3 Effect of 30 μM thymol on SR permeability. Calcium release from the SR was calculated from the transients presented in Fig. 2 and then corrected for the depletion of calcium in the SR. The parameters of the removal model used in the calculation of SR calcium release were $k_{off,Mg-P} = 9.4$ s^{-1}, $PV_{max} = 2.4$ mM s^{-1}, $k_{on,Ca-E} = 0.76$ μM^{-1} s^{-1}, and $k_{off,Ca-E} = 6.3$ s^{-1}. SR calcium content, 2.0 mM, was determined from the transient obtained in response to the depolarization to 0 mV in control, and used throughout.

szentesi.peter_292_24

82 ± 9% whereas the steady level returned to 82 ± 6% of the control level.

To describe the effect of thymol on the calcium release process the rate of calcium release was corrected for depletion of calcium in the SR and the obtained transients were normalized to SR contents. This content was found to be fairly stable over the fibers included into the present study (1.7 ± 0.2 mM; $n = 10$) and to be unaltered by the treatment with 30 μM thymol. All calculation used, therefore, the same SR content in a given fiber in the absence and presence of the drug. Similarly, thymol left the parameters of the removal model essentially unaltered. The corresponding values of the parameters, if fitted independently in control and in the presence of the drug, were $k_{off,M-P} = 7.4 \pm 1.3$ and $4.5 \pm 0.7\ s^{-1}$; $PV_{max} = 2.5 \pm 0.6$ and $2.2 \pm 0.4\ mM\ s^{-1}$; $k_{off,C-E} = 7.2 \pm 1.4$ and $6.0 \pm 0.8\ s^{-1}$; and $k_{on,C-E} = 1.4 \pm 0.3$ and $2.2 \pm 0.9\ \mu M\ s^{-1}$.

The effect of thymol on calcium release is presented in Fig. 4, where pooled data of the two kinetic components of SR permeability are shown as a function of membrane potential in control, in the presence of the drug and after wash. The individual data points were normalized before averaging. To this end Eq. 1 was fitted to the data—peak or steady level versus voltage—in control for each and every fiber and the obtained maximum ($R_{rel,i}[max]$ in Eq. 1) was used for normalization. Fig. 4 reveals an elevation of both the early peak and the steady component of SR permeability reaching >50% in 30 μM thymol. It also shows that significant recovery was achieved after the removal of the drug.

To quantify the increase caused by the drug, Eq. 1 was fitted to the data—peak or steady level versus voltage—in the presence and absence of thymol and after wash in every fiber. The obtained parameters, P_{max} or Sl_{max} ($R_{rel,i}[max]$ in Eq. 1 with i = peak or steady level, respectively), the midpoint voltage, and the slope factor, are presented in Table 2, after averaging. The data reveal that 30 μM thymol significantly ($p < 0.05$) elevated the early peak and the steady level, although the effect on the steady level was somewhat smaller than on the peak (51 ± 17 vs. 62 ± 17%).

Comparing the voltage dependence of the different components as well as the effect of thymol on the voltage dependence did not reveal any systematic difference or trend. The fact that thymol had very little effect on the voltage dependence of either component suggested a voltage-independent activation of SR permeability by the drug.

These data establish that thymol elevates SR permeability in a voltage-independent manner. The extent of elevation is equal for the two kinetic components, peak and steady level, of SR permeability.

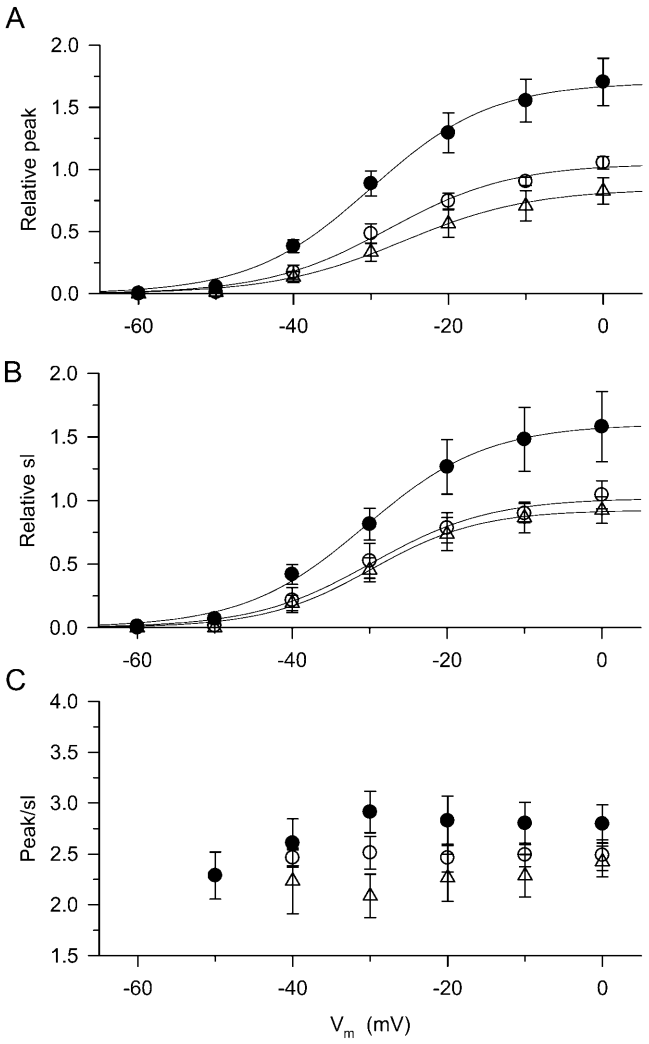


FIGURE 4 Effects of thymol on the kinetic components of SR permeability. (*A*) Voltage dependence of the peak component of SR permeability. The voltage dependence of the peak of SR permeability was first fitted with Eq. 1 in control. The obtained maximum was used to normalize all values in the given fiber both before (○) and after the addition (●), and after the removal of the drug (△). The normalized values from 10 fibers were averaged before plotting them. Superimposed curves present the least-squares fit of Eq. 1 with $Max = 1.05 \pm 0.04$, 1.70 ± 0.04, and 0.84 ± 0.03; $V_{50} = -27.7 \pm 1.2$, -29.9 ± 0.8, and -25.9 ± 1.0 mV; and $k = 7.9 \pm 0.9$, 7.8 ± 0.6, and 8.4 ± 0.7 mV in control, in the presence of thymol, and after wash. (*B*) Voltage dependence of the steady component of SR permeability. The steady level for a given transient was calculated as the average of the last 20 points during the depolarizing pulse. The values were then normalized and averaged as described in *A*. Superimposed curves again represent the fit of Eq. 1 with $Max = 1.02 \pm 0.04$, 1.70 ± 0.03, and 0.93 ± 0.02; $V_{50} = -29.7 \pm 1.2$, -30.5 ± 0.7, and -29.7 ± 0.7 mV; and $k = 7.6 \pm 0.9$, 7.9 ± 0.5, and 6.9 ± 0.6 mV in control, in the presence of thymol, and after wash. (*C*) Voltage dependence of the peak/steady ratio. At voltages <-40 mV, with the exception of data in thymol at -50 mV, the values were too small to allow a reliable determination of the ratio.

Inactivation of R_{rel} is unaffected by thymol

Previous sections have demonstrated that thymol enhances the permeability of the SR membrane when stimulated through the voltage sensors. This augmentation could, in general, occur through increased activation, decreased inactivation, or both. In the following we tested whether

TABLE 2 Voltage dependence of SR calcium permeability

	Peak			Steady level		
	Max* (μM ms^{-1})	V_{50} (mV)	k (mV)	Max* (μM ms^{-1})	V_{50} (mV)	k (mV)
Control ($n = 10$)	16.9 ± 1.9	−28.5 ± 2.3	6.5 ± 0.5	6.2 ± 0.8	−28.7 ± 2.6	6.4 ± 0.7
30 μM thymol	25.6 ± 3.1†	−31.0 ± 1.2	7.0 ± 0.5	8.6 ± 0.9†	−31.5 ± 1.0	7.6 ± 0.5
Wash	13.3 ± 1.6	−22.8 ± 3.5	8.6 ± 0.9†	5.2 ± 0.5	−26.7 ± 2.3	7.4 ± 0.5

Parameter values obtained by fitting Eq. 1 to the voltage dependence of SR permeability. Values represent mean ± SE.
*Denoted as $R_{rel,i}[max]$ with i = peak or steady level in Eq. 1.
†Significant difference from control.

the drug alters the inactivation of the calcium release channels.

To study the calcium-dependent inactivation of calcium release, double pulses, separated by 10-ms-long repolarization to −120 mV to facilitate the return of intramembranous charge to its resting state, were applied with varying the amplitude of the first (pre-) pulse and keeping the second (test) constant. The increase in $[Ca^{2+}]_i$ during the prepulse caused a marked suppression of the peak during the test pulse (Simon et al., 1991; Szentesi et al., 2000) which corresponded to the inactivation of the channels. Fig. 5 presents SR permeability elicited by double pulses in the absence (*left panel*) and in the presence of 30 μM thymol (*right panel*). The steady-state inactivation was assessed as the relative suppression of the inactivating component (peak minus steady level = P–Sl) during the test pulse (Szentesi et al., 2000), which was the largest when no prepulse was applied (P_0–Sl_0). The effect of a prepulse, if it elicited measurable calcium release, was to suppress the inactivating component of the subsequent test pulse (P_1–Sl_1) without affecting the steady level. The figure shows that 30 μM thymol did not cause any visible change in how the channels inactivate, although it enhanced calcium release both during the prepulse and the test pulse.

Previous studies revealed that the relative suppression—the inactivating component of a conditioned test pulse that is normalized to the inactivating component of a non-conditioned test pulse, (P_1–Sl_1)/(P_0–Sl_0)—is a good measure of channel inactivation (Pizarro et al., 1997). Fig. 6 *A* thus presents the relative suppression as a function of the maximal SR calcium release during the prepulse in control and in the presence of 30 μM thymol. In control the relationship is linear as shown previously (Pizarro et al., 1997; Szentesi et al., 2000). It describes a direct link between the calcium concentration reached in the triad and the number of channels that were inactivated during the test pulse. In the presence of thymol the linear relationship was maintained although, due to the larger release in the presence of the drug, it was shifted to the right. Furthermore, if the data were normalized to the maximum release on the given fiber in control and in thymol, respectively, the linear functions were identical in the absence and the presence of the drug (Fig. 6 *B*).

By plotting the absolute suppression, $\Delta(P\text{–}Sl) = (P_0\text{–}Sl_0) - (P_1\text{–}Sl_1)$, as a function of the inactivating component of the prepulse from different fibers (Fig. 6, *open symbols* in control, *solid symbols* in thymol), the relationship became independent of V_{test}, resembling a straight line (Fig. 6 *C*). Fitting straight lines to the data, independently to the values in control and in the presence of the drug, gave regression coefficients close to unity suggesting that exactly those channels were lost from the test pulse that were inactivated

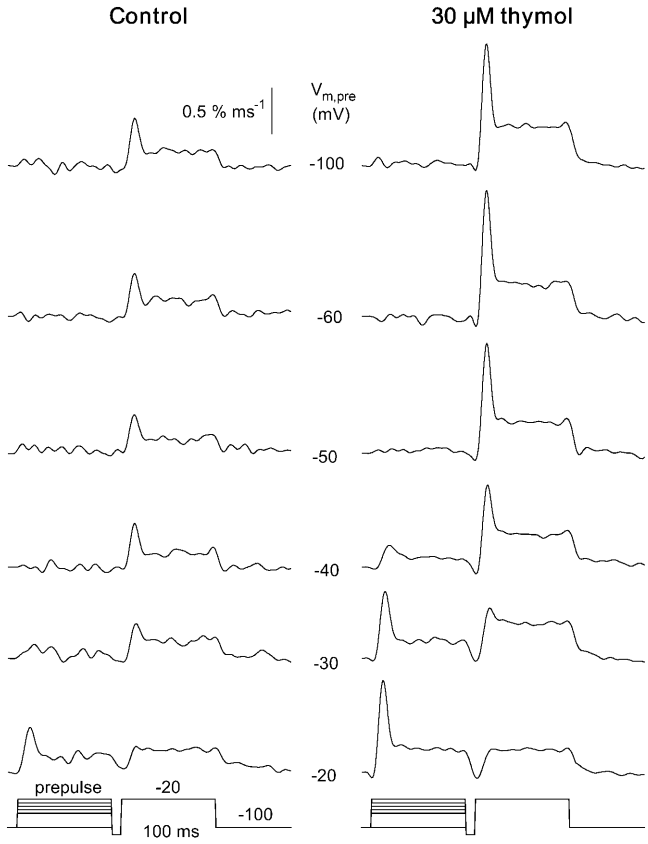


FIGURE 5 Inactivation of SR calcium release in the presence of thymol. SR permeability was measured with double pulses. The test pulse was always a depolarization to −20 mV, whereas the membrane potential during the prepulse was varied between −100 mV, the holding potential, and −20 mV (values indicated between the traces). The depletion factor, 2.0 mM, was determined in control and used throughout the experiment. The parameters of the removal model were $k_{off,Mg\text{–}P} = 16.0\ s^{-1}$, $PV_{max} = 1.6\ mM\ s^{-1}$, $k_{on,Ca\text{–}E} = 0.51\ \mu M^{-1}\ s^{-1}$, and $k_{off,Ca\text{–}E} = 3.0\ s^{-1}$.

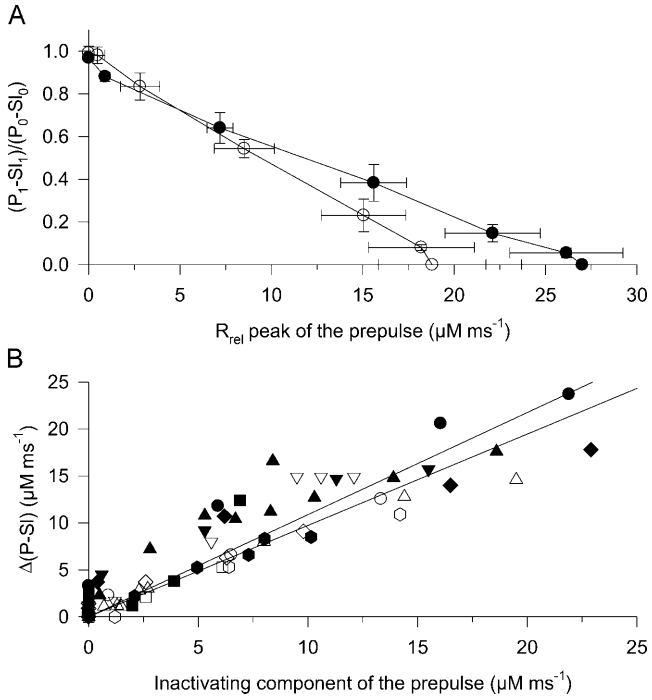


FIGURE 6 Suppression of the inactivating component of SR permeability. The inactivating component was calculated as the difference between the peak (P) and the steady level (Sl). Open symbols represent measurements in the absence, whereas solid symbols represent data obtained in the presence (30 μM) of the drug. (A) The normalized inactivating component as a function of SR calcium release during the prepulse. Values obtained with a given membrane potential during the prepulse were averaged from eight fibers. For normalization the inactivating component of the nonconditioned (prepulse voltage = −100 mV) transient (P_0–Sl_0) was used. (B) Same data as in A, but calcium release during the prepulse was normalized to the maximal release in the given fiber as described in Fig. 5. (C) The suppression of the inactivating component, $\Delta(P–Sl) = (P_0–Sl_0) - (P–Sl)$, as a function of the inactivating component of the prepulse. Different symbols represent different fibers. Solid lines represent the least-squares fit of a linear function, constrained to go through the origin, to the data point with a slope of 0.973 and 1.088 in the presence and absence of thymol.

during the prepulse (Pizarro et al., 1997; Szentesi et al., 2000), in both cases.

These results clearly establish that the calcium-dependent inactivation of the calcium release channels is not suppressed in the presence of thymol. They, furthermore, argue in favor of the hypothesis that the drug does not influence the inactivation process of the channels at all, other than altering the $[Ca^{2+}]_i$ in the triadic junction.

Thymol induces a change in the transfer function

The data presented in the previous sections clearly demonstrate that thymol alters the way in which T-tubular depolarization affects the consequent increase in SR permeability. This alteration cannot be explained by the changes in the properties of intramembrane charge movement (see Fig. 1). To characterize the transmission of information from the T-tubular to the SR membrane, the transfer function of the triadic events, that is, SR permeability as a function of the amount of charge transferred, was calculated (Csernoch et al., 1999a).

Fig. 7 shows the change in transfer function induced by the application of 30 μM thymol. To obtain the data points, the mean normalized steady level of SR permeability was plotted as a function of the mean normalized charge. The presence of the drug clearly changed the coupling between charge movement and the SR permeability increase. As demonstrated in Fig. 1, the charge movement was practically unaffected by the thymol (slightly suppressed and shifted to the left), whereas the steady level of SR permeability was increased. This is evident from the transfer functions, which demonstrate that the same amount of charge moved brought about a larger calcium release in the presence of the drug. To describe the transfer function and the change induced by the thymol in detail, a straight line was fitted to the data points above the threshold for the appearance of detectable calcium release. The transfer function is then characterized by the slope (m) and the x-axis intercept ($Q_{th,r}$) of the straight line. The slope indicates the efficiency of the coupling whereas the intercept is the relative amount of charge moved before any measurable calcium release occurs. As the superimposed traces in Fig. 7 demonstrate, thymol increased the slope of the transfer function significantly, from 1.26 ± 0.09 to 2.37 ± 0.12, indicating a more efficient coupling between the voltage sensors and the calcium release channels. On the other hand, the drug did not alter $Q_{th,r}$ significantly (from 0.08 ± 0.06 to 0.16 ± 0.08).

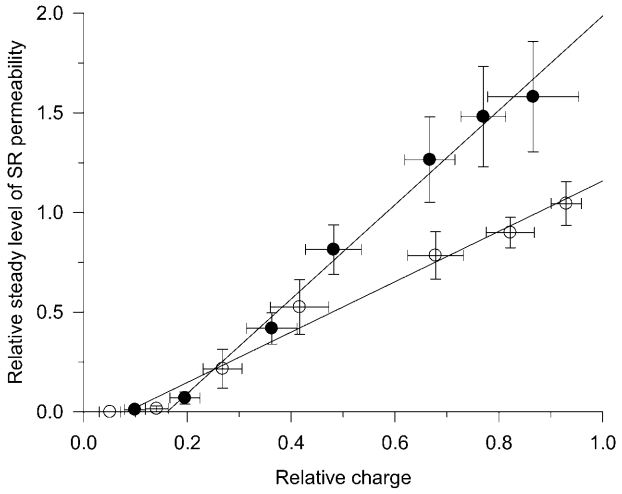


FIGURE 7 The change in transfer function induced by the application of 30 μM thymol. The mean steady level of SR permeability was plotted as a function of the mean normalized charge. The transfer function was characterized by the slope (m) and the x axis intercept ($Q_{th,r}$) of the straight line fitted to the data points. Thymol increased m (from 1.26 to 2.37), but did not significantly alter $Q_{th,r}$ (from 0.08 to 0.16) of the transfer function.

Thymol increases ryanodine binding to heavy SR vesicles

We have, so far, demonstrated that 30 μM thymol increases SR permeability by ~50% without altering the voltage-sensing function of the DHPRs. The results do not, however, exclude the presence of a putative binding site that might influence the interaction of DHPRs and RyRs. To exclude this possibility HSR vesicles were prepared and the effect of thymol was tested on ryanodine binding.

Ryanodine binding under control conditions was characterized by a single binding site (Fig. 8). The fit of Eq. 1 to data points in Fig. 8 *A* revealed a dissociation constant of 25.3 ± 1.4 nM and a B_{max} of 8.7 ± 0.3 pmol/mg protein. The presence of a single binding site per RyR was confirmed in the Scatchard plot (Fig. 8 *B*), where the straight line was constructed using the same parameters as above. The addition of 300 μM thymol caused a massive increase in ryanodine binding to HSR vesicles as demonstrated in Fig. 8, *A* and *B*. The drug increased both the affinity of the binding site (dissociation constant decreased to 15.5 ± 1.0 nM) and the amount bound (B_{max} increased to 14.7 ± 0.5 pmol/mg protein).

To describe the concentration dependence of thymol action, the amount of [^{3}H]ryanodine bound, at a concentration of 6 nM, was determined at different concentrations of thymol (Fig. 8 *C*). The data were then fitted with the Hill equation. This revealed a half-activating concentration of 144 ± 11 μM and a Hill coefficient of 1.89 ± 0.27.

Thymol was thus found to enhance ryanodine binding to HSR vesicles close to threefold. This observation, together with the results on SR permeability, points to a direct, stimulating action of thymol on the calcium release channel.

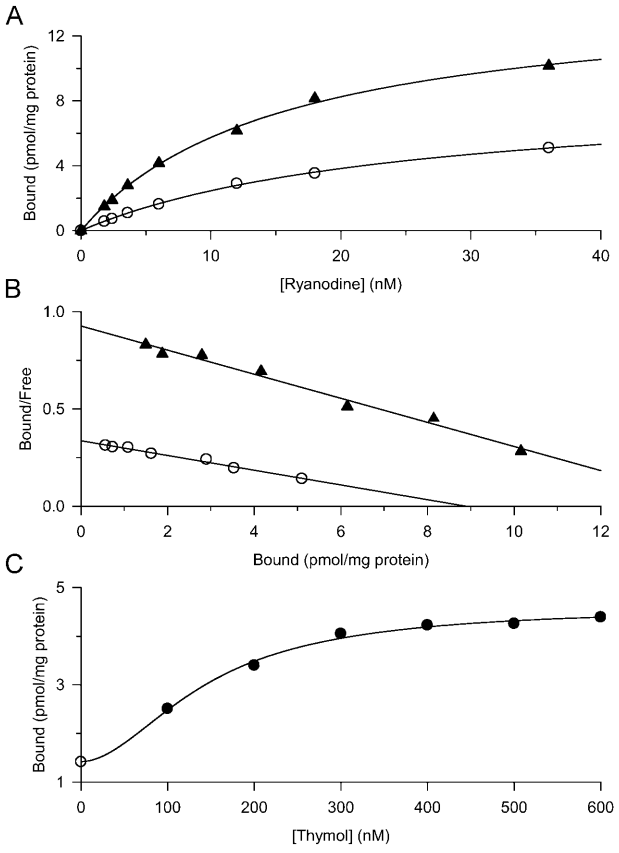


FIGURE 8 Effects of thymol on ryanodine binding to heavy SR vesicles. (*A*) Ryanodine binding determined in the absence (○) and presence (▲) of 300 μM thymol at different [^{3}H]ryanodine concentrations. Assuming a single binding site the Hill fit resulted in k_{50} = 25.3 ± 1.4 nM and B_{max} = 8.67 ± 0.26 pmol/mg protein in control, whereas k_{50} = 15.5 ± 1.0 nM and B_{max} = 14.65 ± 0.45 pmol/mg protein in the presence of the drug. (*B*) The data presented in *A* were used for constructing the Scatchard plot. Straight lines were drawn using the parameters given above. (*C*) Concentration-dependent effect of thymol on ryanodine binding. Ryanodine binding was determined in the absence and presence of various concentrations of thymol at 6 nM [^{3}H]ryanodine concentrations. Fitting the Hill equation resulted in a half-activating concentration of 144 ± 11 μM, a Hill coefficient of 1.89 ± 0.27, and approximately three times higher ryanodine binding at saturating thymol concentration than in control.

Thymol stimulates the isolated RyRs

To test the direct effect of thymol on the calcium release channel, isolated RyRs were incorporated into planar lipid bilayers and the properties of channel gating were determined. Under our experimental conditions the channels displayed a low open probability (P_o = 0.063 in Fig. 9 *A*). After the addition of 30 μM thymol the P_o increased (to 0.105 in Fig. 9 *B*), demonstrating a direct activating effect of the drug on the calcium release channel. This effect was present for all channels tested; the P_o increased from 0.089 ± 0.034 to 0.221 ± 0.044. Fig. 9 also demonstrates that thymol did not interfere with the ability of ryanodine to lock the calcium release channel in the characteristic, half-conducting state.

Examining the current records in Fig. 9, *A* and *B*, reveals that the size of the current, when the channel was open, was the same before and after the addition of the drug. This observation suggests that thymol does not influence the conductance of RyRs. This hypothesis was tested in the experiment presented in Fig. 9 *C*, where the current amplitude is plotted as a function of the holding potential both before (*open symbols*) and after (*solid symbols*) the addition of the drug. Fitting straight lines, constrained to go through the origin, to the data points, revealed a slope of 545 pS in control and 543 pS in the presence of the drug.

To further explore the action of thymol on channel gating the drug was applied in concentrations of 150 (Fig. 10 *B*) and 300 μM (Fig. 10 *C*). Together with the increased open probability long-lasting open events were observed. These events had, on average, the same lengths ($p > 0.4$) in the presence of 150 μM thymol (287 ± 21 s; 235 events) and in the presence of 300 μM thymol (317 ± 41 s; 159 events).

The experiments with isolated and reconstituted RyRs demonstrated that thymol is a potent activator of the calcium

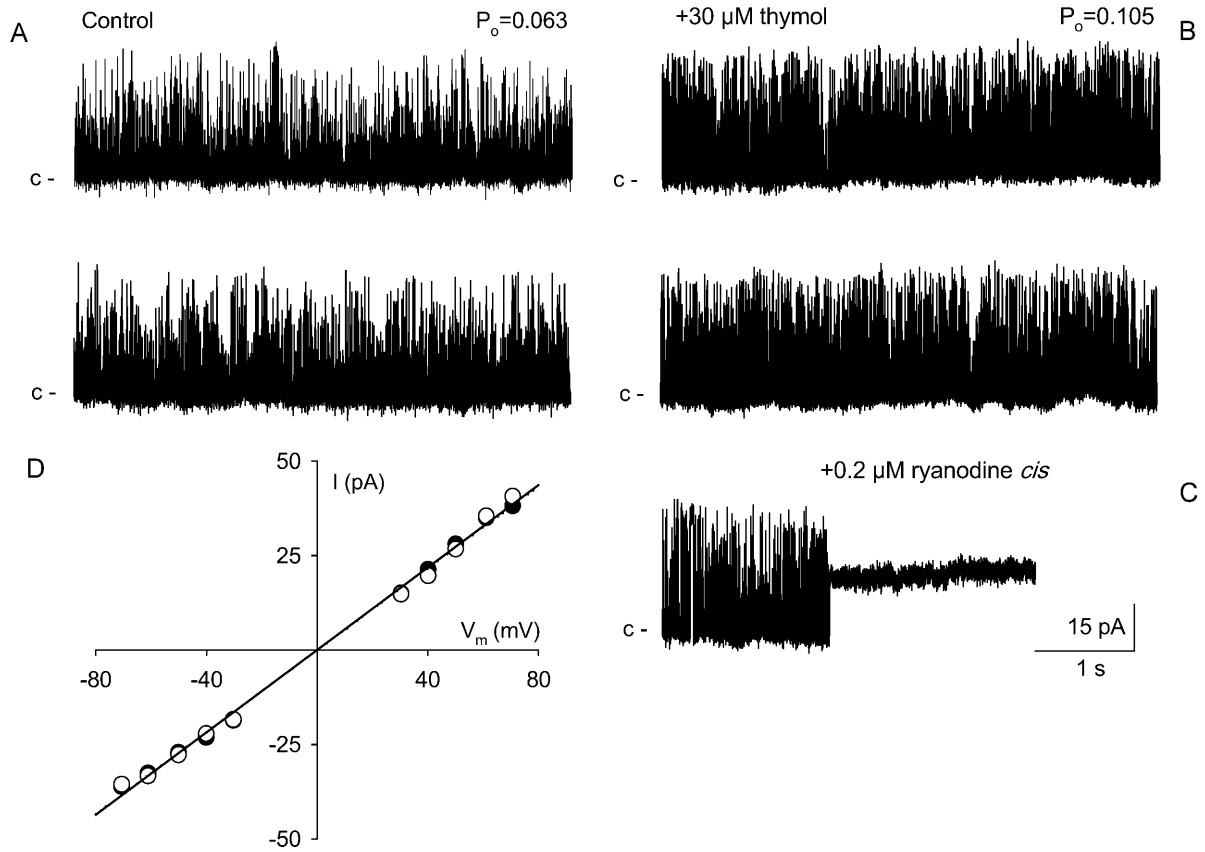


FIGURE 9 Effect of 30 μM thymol on the isolated RyRs. Incorporation was initiated in symmetric 250 mM KCl, holding potential was 61 mV; channel openings are upward deflections. Horizontal lines before each current record mark the closed state. (*A*) Single channel recordings in control conditions. (*B*) Representative segments of single channel behavior taken 5 min after the additions of thymol. (*C*) Single channel currents measured after the successive addition of 0.2 μM ryanodine into the *cis* chamber. (*D*) Single channel currents plotted as a function of the holding potential. Open symbols represent measurements under control conditions, whereas solid symbols represent those in the presence of thymol. Straight lines correspond to a single channel conductance of 545 and 543 pS in control and in the presence of the drug, respectively. All recordings are from a single experiment.

release channel—one which increases the open probability of the channel without significantly modifying the single channel conductance.

Elementary calcium release events are altered by thymol

Elementary calcium release events in mammalian muscle fibers exhibit a wide morphological variety. Calcium sparks, resembling those in frog fibers, can be preceded and/or followed by embers, or embers can occur on their own (Kirsch et al., 2001; Zhou et al., 2003). Since thymol was found to activate RyRs it was of interest to see if it modified the properties or appearance of the calcium release events. Calcium sparks and embers were thus measured on permeabilized fibers and their relative numbers and morphological properties compared in the absence and presence of the drug.

Under control conditions, calcium release events occurred with an appreciable frequency (0.0587 $\pm$ 0.0020 s^{-1} sarcomere^{-1}; Fig. 11 *A*) and displayed all the morphological characteristics described earlier (e.g., Kirsch et al., 2001). Most abundant were lone sparks (63%; Fig. 11 *Ba*), but lone embers (22%; Fig. 11 *Bb*) or sparks with trailing embers (Fig. 11 *Bc*) were also readily observable. Sparks with leading embers (Fig. 11 *Bd*) were rare (1.1% of all events). In the presence of thymol, the frequency increased to 0.0654 $\pm$ 0.0016 s^{-1} sarcomere^{-1} (Fig. 11 *C*; $p < 0.01$). More noticeable was the change in overall event characteristics, inasmuch as longer and more complex events dominated the images, with lone sparks (Fig. 11 *Da*) decreasing in relative proportion (41%). Lone embers (35%, Fig. 11 *Db*) and sparks with trailing embers (Fig. 11 *Dc*) were still readily distinguishable, with sparks with leading embers (Fig. 11 *Dd*) increasing in proportion to >4% of all events.

A total of 2030 vs. 2478 events from 20 vs. 9 fibers were analyzed under control conditions and in the presence of 30 μM thymol, respectively, and their characteristic parameters are presented in Table 3. The drug decreased the amplitude or average amplitude of both sparks and embers by 20–24% leaving the rise time and FWHM essentially constant. The decrease in spark amplitude was attributable to a decrease in

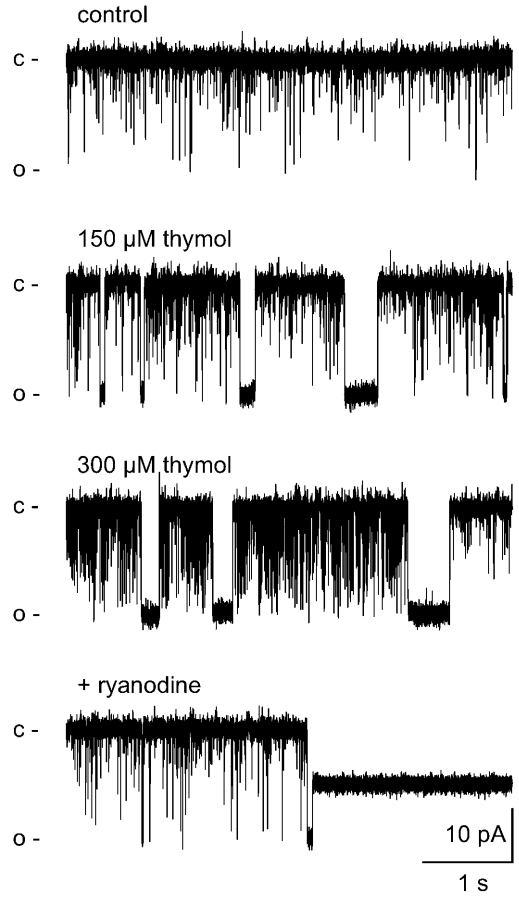


FIGURE 10 Effect of higher thymol concentrations on calcium release channel activity. Measurements were carried out under the same conditions as in Fig. 9 with the holding potential being −61 mV, and thus channel openings are downward deflections. Horizontal lines mark the closed state. The fast gating of the channel seen in control (*top*) is interrupted by long open events in the presence of both 150 (*second from top*) and 300 μM (*second from bottom*) thymol. Note that the channel opens to a full conducting state during the long open events. (*Bottom*) Ryanodine was capable of interfering with the thymol-induced alteration in channel gating. Note that the transition to the half-conducting state, characteristic to the ryanodine-modified channel, occurred during a long open event.

the number of large sparks as depicted in Fig. 11 *E*. In parallel, the duration of the calcium release events increased considerably. As evidenced from Fig. 12 and its inset, the drug, although reducing the relative proportion of shorter events, induced events that had durations of several hundred milliseconds.

Higher concentrations of thymol were found to induce long open events on isolated RyRs (Fig. 10). The application of 150 and especially 300 μM thymol to permeabilized fibers, to investigate their effects on elementary calcium release events, was in many cases disastrous. A massive release of calcium followed the addition of the drug, as evidenced from the sudden increase in fluorescence and contraction of the fiber (not shown). In only a few occasions were we successful in recording calcium release events in the presence of such high concentrations of the drug. Although this prevented a detailed statistical analysis, the events could still be characterized.

As shown in Fig. 12, sparks were hardly ever observed in the presence of 150 μM thymol. Rather, long events resembling lone embers were detected. Their duration, however, often exceeded 500 ms, sometimes lasting >1.5 s, the duration of the image. These events had characteristic amplitudes and full widths similar to the embers measured in the presence of low thymol concentrations. The fact that the amplitude of the fluorescence was steady over the entire event (Fig. 12) suggests that the channel(s) involved were continuously open.

These data clearly indicate that the long calcium release events correspond to the long-lasting open events seen for the thymol-modified isolated RyRs. Since the long calcium release events were neither preceded nor followed by a spark, they should be considered as the opening of a single release channel or the concerted opening of a small group of channels. It should be stressed, however, that were the latter the actual arrangement, the channels opening synchronously must always open together—which would constitute the elementary release unit. These findings thus strongly argue in favor of the lone ember being the elementary building block of calcium release in mammalian skeletal muscle.

DISCUSSION

These experiments give, for the first time, a complete account of the effects of thymol on steps of excitation-contraction coupling, from intramembrane charge movement to elementary calcium release events, in mammalian skeletal muscle fibers. Thymol was found to only slightly interfere with the voltage-sensing event but to augment SR calcium permeability by 50% already at 30 μM. The drug enhanced ryanodine binding to HSR vesicles by increasing both the affinity and the amount bound. The isolated and reconstituted calcium release channel displayed an increased open probability in the presence of thymol with the appearance of long-lasting open events at concentration above 100 μM. Elementary calcium release events were also modified in their characteristics with embers becoming more frequent and of longer duration. At high concentrations of thymol lone embers with extremely long duration dominated the images. These experiments argue that in mammalian skeletal muscle, embers arise from the opening of a single release channel, or a release unit, and thus represent the elementary event of calcium release.

Calcium release from the SR in the presence of thymol

Thymol has been known to affect calcium handling in a variety of cell types (Hisayama and Takayanagi, 1986; Kostyuk et al., 1991). In particular, Palade (1987) used it to

szentesi.peter_292_24

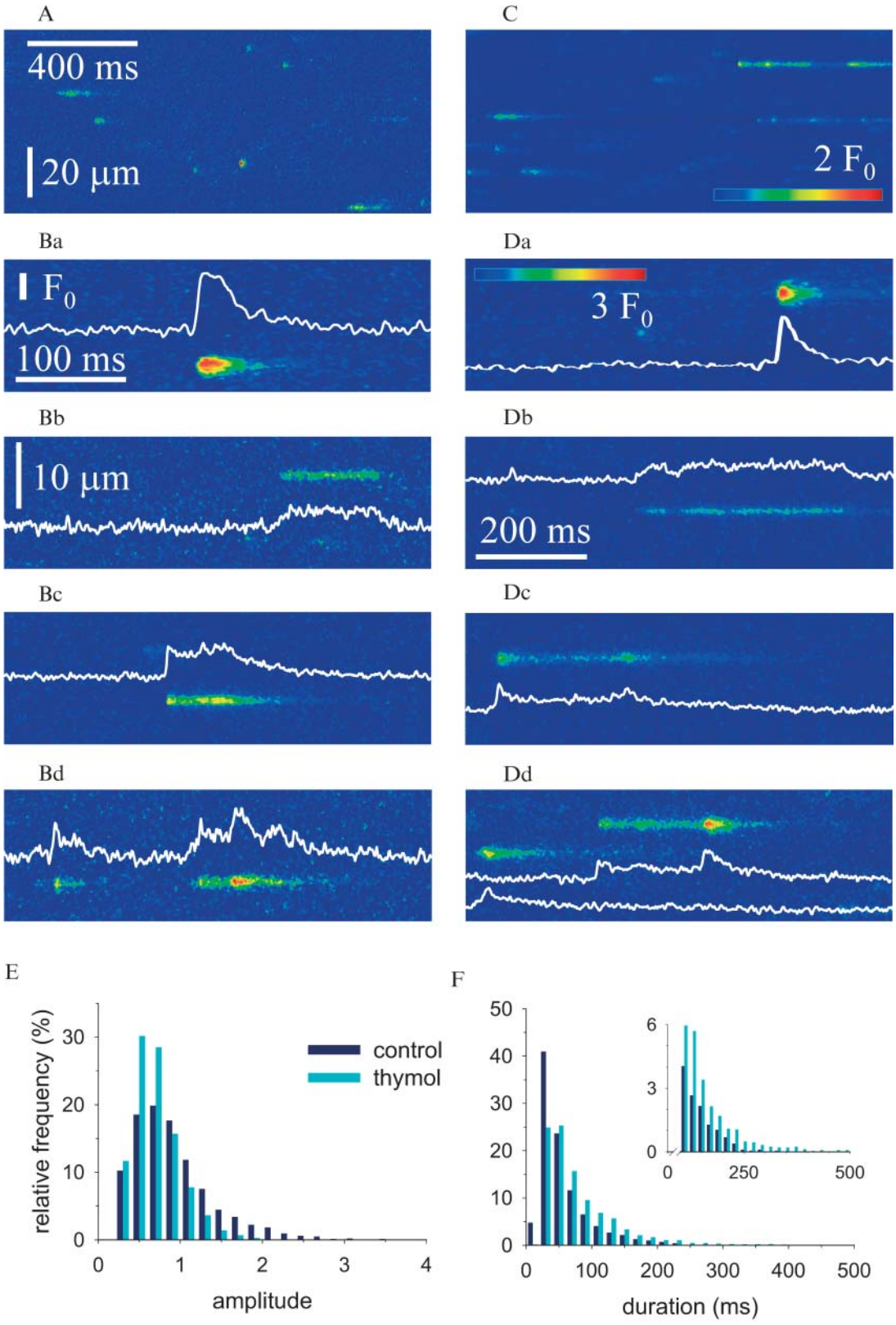


FIGURE 11 Modified elementary calcium release events in the presence of 30 μM thymol. (*A* and *B*) Calcium release events under control conditions. The large image (*A*) illustrates the frequency whereas the smaller images (*Ba–Bd*) demonstrate the wide variety in morphology of the events, namely, a lone spark (*Ba*), a lone ember (*Bb*), a spark with trailing (*Bc*), and a leading ember (*Bd*). (*C* and *D*) Calcium release events in the presence of thymol. The organization of the images is the same as in *A* and *B*, respectively. Note, however, the longer events in *Db–Dd*, characteristic to the thymol-treated cells. Traces in all images

TABLE 3 Thymol-induced changes in the morphological characteristics of elementary calcium release events

	Control		30 μM thymol	
	Spark (n = 1576)	Ember (n = 454)	Spark (n = 1605)	Ember (n = 873)
Amplitude	0.92 ± 0.01	0.210 ± 0.004	0.70 ± 0.01*	0.168 ± 0.002*
FWHM (μM)	1.81 ± 0.03	1.76 ± 0.03	1.74 ± 0.01*	1.77 ± 0.02
Rise time (ms)	9.4 ± 0.1	–	9.6 ± 0.1	–
Duration (ms)	56 ± 1	87 ± 2	79 ± 1*	102 ± 2*

Values represent mean ± SE. All events with sparks were grouped under Spark, whereas the parameters of lone embers are given under Ember. In the case of embers, the average amplitude is given.
*Significant differences between data in control and in the presence of thymol.

initiate calcium release from HSR vesicles isolated from rabbit skeletal muscle. Furthermore, thymol is used to stabilize liquid halothane, in which the added thymol can be as high as 0.1–0.7% (Thompson and Carlson, 1989). Taking the usual concentration of halothane in the in vitro contracture tests (1–2 mM), the thymol present can easily reach the concentration (30 μM) used in this study. Nevertheless, no account on the effects of the drug on SR calcium release has been published so far. Not only is this true for mammalian skeletal muscle, but to our knowledge, it is also true for striated muscle cells from other classes of vertebrates or invertebrates.

It is thus important to note that thymol, on its own, will facilitate calcium release from the SR, averaging an ~50% increase at 30 μM (see Table 2). In this respect its action is similar to that of caffeine (Klein et al., 1990; Csernoch et al., 1999a) or 4CmC (Struk and Melzer, 1999), although it seems to be more potent than either one. Its action further resembles that of caffeine inasmuch as 1), only slight differences between the effects of thymol on the two kinetic components, peak and steady level, of SR permeability (e.g., Table 2) were found and 2), the transfer function was altered in a way that suggests a more efficient coupling between the voltage sensors and the RyRs. These findings further strengthen the close and tight coupling between the two kinetic components of SR calcium release and favor the hypothesis that they both originate from the skeletal isoform of RyRs. Nevertheless, the mode of action of thymol is clearly distinct from that of caffeine or 4CmC, as evidenced from its effects on RyRs.

Effects of thymol on RyRs

Thymol is known to induce calcium release from heavy SR vesicles and was thus used in previous experiments to assess the action of other drugs on RyR function (Palade, 1987; Szentesi et al., 2001). Those experiments used concentrations of 300 μM. Data from [^{3}H]ryanodine binding experiments presented in this study (Fig. 8) demonstrate that thymol in that concentration would cause an approximately threefold increase in ryanodine binding, which is close to its maximal effect.

The half-activating concentration of thymol in the [^{3}H]ryanodine binding experiments was found to be 144 μM. This is approximately fivefold higher than the concentration in which the drug was capable of augmenting the calcium transients (Fig. 2) or SR calcium release (Fig. 3). On the other hand, it is consistent with the observation that the resting $[Ca^{2+}]_i$ was only slightly (20 nM) elevated by the drug in this low concentration. One would predict, based on these data, that higher concentrations of thymol, especially at several hundred μM, will initiate large efflux of calcium from the SR even under resting conditions and would, therefore, hinder the comparison of SR calcium release in control conditions and in the presence of the drug. Due to this foreseen difficulty such experiments were not included in the present study.

The [^{3}H]ryanodine binding data, however, call attention to an additional point. The Hill coefficient of thymol action was found to be 1.89—that is, close to 2 (see Fig. 8). This indicates that two thymol molecules, acting cooperatively, are needed to induce the observed stimulating effect.

Analyzing the action of 30 μM thymol on the isolated and reconstituted RyRs revealed an ~60% increase in open probability (Fig. 9) with no change in single channel conductance. In this respect the effect of the drug is similar to that of caffeine (Rousseau et al., 1988) or 4CmC (Herrmann-Frank et al., 1996). Unlike 4CmC or caffeine, however, thymol was found to induce long-lasting open events, which raises the need for finding an alternative explanation for its mode of action. Such alternative explanation could be based on the antioxidant effect of the drug since the calcium release channel is regulated by its redox state (e.g., Feng et al., 2000; Sun et al., 2001). Although possible redox regulation of SR calcium release will be discussed later it should be mentioned here that sulfhydryl

(A–D) represent the timecourse of F/F_0 measured at the position of the peak (events with spark) or in the middle of the event (lone ember) by averaging three neighboring pixels in the x direction. (E) Relative distribution of the amplitudes of events with sparks. (F) Relative distribution of the duration of all events. Inset shows the lower portion of the graph to demonstrate the presence of events with long duration in the presence of the drug.

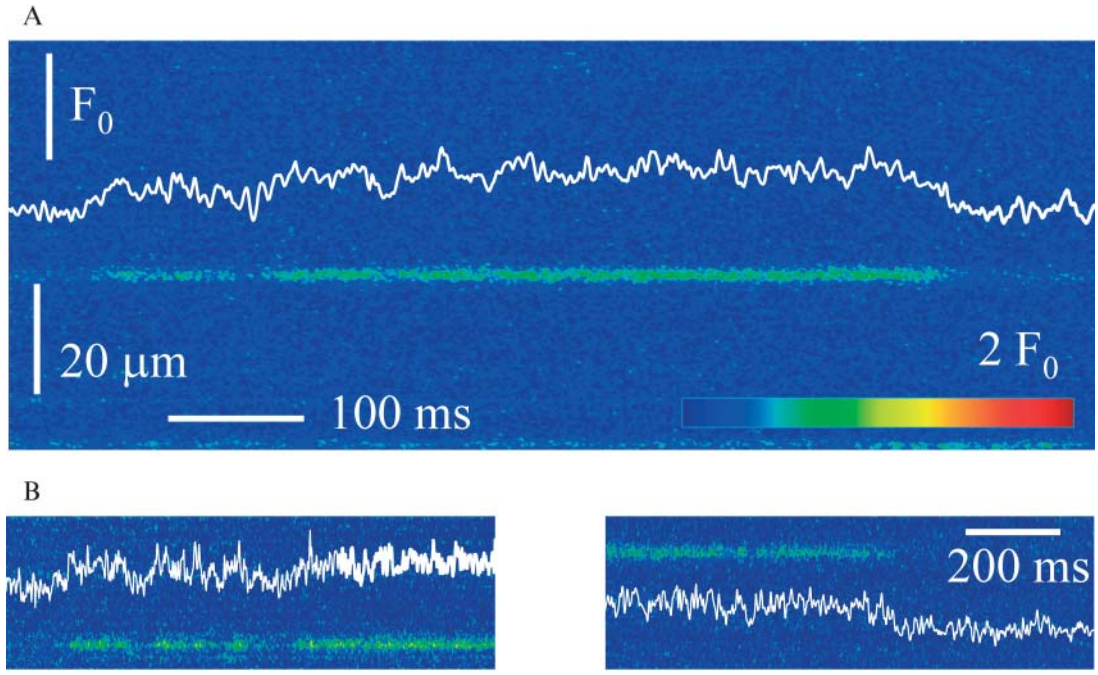


FIGURE 12 Calcium release events in the presence of 150 μM thymol. Representative images showing events with extremely long duration, otherwise resembling embers measured under control conditions. Note that the fluorescence (F/F_0) and the spatial width of these long events stay essentially constant over hundreds of milliseconds (*A*). Note also that the release unit can reopen (*B*) and give rise to an event with the same spatial and temporal characteristics. Traces in the images were calculated as described in Fig. 11 for lone embers.

oxidation, rather than reduction, was found to increase the P_o of the reconstituted channel (e.g., Suko et al., 2000).

On the other hand, the long-lasting open events with full conductance observed in the presence of thymol resemble those measured with bastadin 10 (Chen et al., 1999). The effects of bastadin 10 were interpreted as a shift in the free energy of the open state of the drug-modified RyRs. Furthermore, the removal of FKBP12 from the RyRs interfered with the action of bastadin 10 (Chen et al., 1999). Although the present experiments did not test the FKBP12 sensitivity of effect of thymol, it is, nevertheless, likely that the two drugs share the capability of lowering the free energy of the open state of RyRs.

As mentioned above, the value of close to 2 for the Hill coefficient indicates that two thymol-binding sites are present for each calcium release channel. Noteworthy is the observation that channel activity in between long-lasting open events, in the presence of higher thymol concentrations, was found to have higher open probability than in control conditions. This raises the possibility that the binding of the first thymol molecule would already activate the channel and thus increase its P_o. The binding of the second molecule could then shift the channel to the long-lasting open state.

Effects of thymol on DHPR function

To our knowledge no previous work has examined the effects of thymol on the voltage sensor of E-C coupling. Recent experiments have, on the other hand, demonstrated that the L-type calcium currents from cardiac (Magyar et al., 2002) as well as skeletal (Szentandrássy et al., 2003) muscle are suppressed by the drug. Thymol neither altered the voltage dependence of current activation nor the reversal potential for calcium, but attenuated the conductance of the channels. In cardiac preparations the voltage dependence of steady-state inactivation was shifted to more negative membrane potentials (Magyar et al., 2002). In the above changes thymol had a half-effective concentration ~200 μM. In the experiments presented here thymol failed to induce marked alterations in intramembrane charge movement even at 300 μM (Fig. 1 and Table 1). Since Q_{max} did not change significantly it cannot account for the >50% reduction in conductance seen in the previous reports. This observation suggests that either the alteration described for the calcium current represents specific effects of thymol on ion permeation of the L-type calcium channels or, alternatively, that intramembrane charge movement and L-type calcium current originate from distinct subpopulations of DHPRs.

To interpret the slight change in the voltage dependence of intramembrane charge movement (see Fig. 1 *B* and Table 1) one should consider the large amount of evidence supporting the idea that altered SR calcium release influences intramembrane charge movement (Pizarro et al., 1991; Pape et al., 1996; Shirokova and Ríos, 1996). Results obtained here, such as little effect on Q_{max} and a

leftward shift in V_{50}, closely resemble those published earlier for compounds such as caffeine or perchlorate that enhance SR calcium release (e.g., González and Ríos, 1993; Csernoch et al., 1999a). Noteworthy here is the observation that intramembrane charge movement displayed clear delayed components in the presence of thymol (see Fig. 1). This again is consistent with previous data suggesting that calcium released from the SR influences charge movement (e.g., Pizarro et al., 1991). It should be stressed, however, that mammalian fibers under control conditions hardly ever show such slow components on their charge movement currents (e.g., Szentesi et al., 1997). The observation that thymol can alter charge movement in such a way that this component becomes visible suggests that it is present in mammalian muscle, albeit masked under control conditions.

Redox regulation of the calcium release channel

Thymol, under most conditions, is used as an antioxidant. A number of studies have called the attention to the redox sensor function of RyRs (e.g., Abramson and Salama, 1988; Marengo et al., 1998). The calcium release channel is known to contain a large number of reactive cysteines, a number of which can undergo oxidation or reduction under appropriate conditions (Moore et al., 1999; Sun et al., 2001). RyRs were, recently, shown to respond to changes in the redox state of the intracellular environment and thus serve as a redox sensor (Feng et al., 2000; Xia et al., 2000). Changes in the redox potential established across the SR membrane by the reduced and oxidized forms of glutathione, as well as the oxidation or reduction of reactive cysteines on the RyRs, have also been shown to alter the open probability of the calcium release channel (Feng et al., 2000; Sun et al., 2001). The fact that most studies on SR calcium release in intact or cut fiber preparations were conducted under ambient oxygen levels, whereas in situ functioning muscle is an environment with much lower oxygen content and antioxidants such as methyl *p*-hydroxybenzoate (Cavagna et al., 2000) and thymol (this study) alter RyR function and SR calcium release, makes the question of redox regulation even more intriguing.

On the other hand, the treatment of mechanically skinned mammalian fibers working at ambient oxygen levels with the strong oxidant H_2O_2 increased, rather than reduced, SR calcium release (Posterino et al., 2003). Furthermore, reducing reagents (as dithiothreitol or reduced glutathione) affected the calcium sensitivity of the contractile apparatus and not the calcium release process (Posterino et al., 2003). Finally, the massive release of calcium from the SR in the presence of larger thymol concentrations cannot be explained in a framework where the drug would solely relieve a block caused by massive oxidation. Taken the above, alternative explanations must be considered to understand the effects of thymol.

Due to its lipid solubility thymol is expected to enter all membranes and possibly influence their fluidity and thus the interaction between the membrane and its integral proteins, channels, and pumps. Work on aging rats has indeed revealed that the administration of thyme oil (or thymol itself) can have beneficial effect on the polyunsaturated fatty acid composition of certain membranes (Youdim and Deans, 1999). This raises the possibility that the actions of thymol seen at larger ($>100\ \mu$M) concentrations are influenced by thymol's effect on the lipids or on the lipid-protein interaction resulting, as discussed above, in the reduction of the free energy associated with the open state of the channel.

Calcium release events in permeabilized fibers

Elementary calcium release events in mammalian skeletal muscle preparations have recently been reported from a number of laboratories (Conklin et al., 2000; Kirsch et al., 2001; Zhou et al., 2003). These events differ from those measured in amphibians (Tsugorka et al., 1995, Klein et al, 1996) mainly in their morphological variability, namely, that sparks and embers coexist, and in their relative frequency, events are more numerous in frogs. In line with previous studies (e.g., Shirokova et al., 1998) we were also unable to detect calcium sparks in intact (Fluo-3 AM loaded) or notched fibers (data not shown) and, therefore, followed the idea of Kirsch et al. (2001) to chemically skin the fibers. The removal of the surface membrane with saponin proved to be successful, and elementary calcium release events were recorded routinely on these fibers. However, their frequency was still far too low to enable decent statistical comparison between control and drug-modified states. To increase the number of events the measurements were carried out with sulfate as the major anion in the bathing solution. This indeed resulted in an appreciable frequency (Fig. 11) without any marked alterations in the characteristics of the events as described earlier (Csernoch et al., 2003).

Under these conditions the proportion of events with embers (lone embers and sparks with embers) was found to be 37% (22% for lone embers) in good agreement with the report by Zhou and collaborators (2003), but slightly lower than that reported by Kirsch et al. (2001; 33% for lone embers). It should be noted, however, that the composition of the solutions used here more closely resembled that applied in the former study and, furthermore, a similar automatic computerized detection method was used.

The calcium sparks and embers detected in this study were morphologically similar to those reported earlier. They had a smaller average amplitude than those reported by Kirsch et al. (2001), as expected from the use of sulfate and the consequent lowering of the SR calcium content due to the precipitation of $CaSO_4$ inside the SR (Csernoch et al., 2003). The measured FWHM and rise time were essentially identical with previous values, although the FWHM more

closely resembled the value reported by Kirsch et al. (2001; 1.85 μm) than that reported by Csernoch et al. (2003; 2.04 μm). Noteworthy is the difference that Kirsch et al. (2001) found it sufficient to draw an *FDHM* (full duration at half-maximum) $>$ 50 ms selection criteria for distinguishing embers from sparks, whereas here, lone embers shorter than 50 ms were, occasionally, also observed. Taken together, the methods used here were clearly capable of detecting elementary calcium release events with the spatial and temporal characteristics observed on previous occasions. This enabled us to compare the events before and after the addition of thymol and to analyze the action of the drug.

Calcium release events in the presence of thymol

Thymol, in a concentration of 30 μM, has slightly increased the frequency of the elementary calcium release events, from 0.0587 to 0.0654 s^{-1} sarcomere^{-1}, which is in agreement with its effects on the calcium release measured on cut fibers and on the open probability of isolated RyRs. The increase in event frequency was, however, not as marked as the increase in global calcium release. Nevertheless, the relative proportion of embers, which, as it will be discussed later, are more likely to be the elementary events in mammals, were increased more than the actual frequency.

In higher concentrations the drug resulted, in most cases, in a massive release of calcium, rendering the detection of individual events impossible. (This global release could be interpreted as a drastic increase in event frequency, in line with the effects described above.) In the few cases where the fiber survived the addition of 150 μM thymol, the frequency of the events was reduced and the relative proportion of embers was further increased.

Comparing the average amplitudes of sparks or embers before (0.93 and 0.21) and after (0.70 and 0.17) the addition of thymol (Table 3) reveals a 20–24% decrease in both cases. This suppression of event amplitude can only be explained as a drop in SR content due to an increased leak of calcium from the SR. Together with the decrease in amplitude, the rise time and the duration of events were increased from 9.4 to 9.6, and from 56 to 79 ms, respectively. The increase in rise time and duration is, on the one hand, likely to be due to the effect of thymol on the open time of the release channel. On the other hand, the decrease in the amplitude of sparks reflects a lower concentration of calcium at the release site and, therefore, a possibly less prominent negative feedback of the released calcium.

The number of channels involved in the generation of a spark in mammalian muscle

One of the most intriguing findings of this study is the appearance of long events observed in the presence of thymol, especially with the higher, 150 μM, concentration of the drug. These calcium release events resemble those measured in frog skeletal muscle treated with imperatoxin A (González et al., 2000a; Shtifman et al., 2000) or bastadin 10 (González et al., 2000a). They are most likely due to the drug-induced alteration in channel gating, namely, the long-lasting open events seen in lipid bilayer experiments. The fact that the calcium release events displayed steady fluorescence and essentially equal spatial width during their entire timecourse implies that the released calcium reached a steady state with the diffusion and binding of calcium.

Unlike imperatoxin, which locks the channel in a subconductance state (Tripathy et al., 1998), but similarly to bastadin 10 (Chen et al., 1999), thymol did not affect the conductance of the channel. The change in fluorescence during the long events should, therefore, provide an upper limit to the ΔF, if a single channel, or the elementary release unit if it is more than a single channel, opens to a full conductance state. Since the embers measured in the absence of the drug had an average amplitude comparable to that of the long events—the slight difference, as discussed above, is most likely due to the difference in SR contents—they must represent the opening of an elementary release unit under control conditions. This unit must either 1), consist of a single channel, inasmuch as no stepwise increase (only occasional closings as in Fig. 12 *B*) in fluorescence was observed during the long events that could have indicated the opening or closing of a channel or 2), the channels involved gate synchronously (Marx et al., 1998; Zhou et al., 2003).

To estimate the number of channels involved in generating a spark, note that the largest sparks had an average amplitude of 2.96 and a FWHM of 2.09 μm (15 largest events). Similar parameters for large embers were 0.43 and 1.72 μm, respectively. As discussed earlier (e.g., Ríos et al., 1999; Jiang et al., 1999) large events represent scans close to the source and, therefore, give the best possible resolution. Signal mass (*SM*; introduced by Sun et al., 1998) was shown to be proportional to the amplitude and FWHM^3 (Chandler et al., 2003), whereas its first derivative is at the onset of the event to release current (ZhuGe et al., 2000). It follows, therefore, that the ratio of release currents, and thus of the number of channels (N) involved, is

$$N_s/N_e = \{d(A_s \times FWHM_s^3)/dt\}/\{d(A_e \times FWHM_e^3)/dt\}, \quad (4)$$

where the subscripts s and e denote spark and ember, respectively, and A and *FWHM* should be calculated for every time point.

There are two possible routes to evaluate Eq. 4. In the direct approach, A and *FWHM* are determined by fitting Gaussian functions to each line, $F[x,t = constant]$, in the line-scan image. SM is then plotted as a function of time and its derivative is calculated. For the above-mentioned sparks and embers, the rate of change in SM was found to be on average 8.4 $\pm$ 1.0 and 0.29 $\pm$ 0.7 pl s^{-1}, respectively. This

yields 29 for the relative number of channels involved in generating a spark. Note, however, that the scatter for $d(SM)/dt$ for embers is large. This is due to the poor estimation of the parameters of the Gaussian function since, for these small events, the signal/noise ratio is high.

The indirect approach utilizes the observation that SM increases linearly in time until the channel is open, inasmuch as channel conductance remains the same and no appreciable depletion occurs at early times. Therefore SM measured at the time of the peak and divided by the rise time is a good estimate of $d(SM)/dt$. Note also that the time to reach steady width for the large embers (10 ms) was comparable with the rise time of the large sparks (9 ms). Since the spatial spread of embers reaches a maximum and then stays constant thereafter, FWHM, calculated as described in Methods, represents the upper limit of FWHM during the evolution of the ember. Thus the indirect approach gives a simple way to get a lower limit for N_s over N_e. With the data given above for A and $FWHM$, N_s over N_e calculates to be 11 in agreement with the value obtained with the direct method.

In other words, ~20–30 times more channels open during a spark than during an ember. If embers represent single channel events, sparks are generated when some 20–30 channels open. On the other hand, if embers are generated by a number of synchronously opening channels, the number of channels opened during a spark could easily reach 100—that is, the entire couplon (Stern et al., 1997).

On the other hand, following the line of reasoning given by ZhuGe et al. (2000), one can estimate $d(SM)/dt$ for a single channel. Using 0.5 pA for single channel current, 150 nM free $[Ca^{2+}]_i$ and 100 μM for the concentration of the dye $d(SM)/dt$ calculates to be 0.18 pl s^{-1}. This value suggests that 1–2 channels are involved in generating an ember and some 50 channels in generating a spark.

These experiments have demonstrated that thymol enhances SR calcium release by acting directly on the RyR calcium release channels. On purified channels reconstituted into lipid bilayers it increases the open probability and induces long-lasting open events. In parallel, elementary calcium release events with long duration, resembling embers, are observed in line-scan images. These data constitute the first full description, from the voltage-sensing event to calcium release, of drug-modified E-C coupling in mammalian skeletal muscle and give an experimental estimation of the relative number of release channels involved in generating a mammalian spark. They also argue in favor of the ember representing the opening of the elementary calcium release unit, either as a single channel or a group of channels always opening together, in mammalian skeletal muscle.

The authors thank Ms. R. Őri and É. Sági for skillful technical assistance.

This work was supported by research grants from the Hungarian government (OTKA T034894, T037727, and TS040773; FKFP 0193/2001; and ETT 250/2003).

REFERENCES

Abramson, J. J., and G. Salama. 1988. Sulfhydryl oxidation and Ca^{2+} release from sarcoplasmic reticulum. *Mol. Cell Biochem.* 82:81–84.

Cavagna, D., F. Zorzato, E. Babini, G. Prestipino, and S. Treves. 2000. Methyl *p*-hydroxybenzoate (E-218) a preservative for drugs and food is an activator of the ryanodine receptor Ca^{2+} release channel. *Br. J. Pharmacol.* 131:335–341.

Chandler, W. K., S. Hollingworth, and S. M. Baylor. 2003. Simulation of calcium sparks in cut skeletal muscle fibers of the frog. *J. Gen. Physiol.* 121:311–324.

Chen, L., T. F. Molinski, and I. N. Pessah. 1999. Bastadin 10 stabilizes the open conformation of the ryanodine-sensitive Ca^{2+} channel in an FKBP12-dependent manner. *J. Biol. Chem.* 274:32603–32612.

Cheng, H., W. J. Lederer, and M. B. Cannel. 1993. Calcium sparks: elementary events underlying excitation-contraction coupling in heart muscle. *Science.* 262:740–744.

Cheng, H., L. S. Song, N. Shirokova, A. González, E. G. Lakatta, E. Ríos, and M. D. Stern. 1999. Amplitude distribution of calcium sparks in confocal images. Theory and studies with an automatic detection method. *Biophys. J.* 76:606–617.

Conklin, M. W., C. A. Ahern, P. Vallejo, V. Sorrentino, H. Takeshima, and R. Coronado. 2000. Comparison of Ca^{2+} sparks produced independently by two ryanodine receptor isoforms (type 1 or type 3). *Biophys. J.* 78:1777–1785.

Csernoch, L., P. Szentesi, and L. Kovács. 1999a. Differential effects of caffeine and perchlorate on excitation-contraction coupling in mammalian skeletal muscle. *J. Physiol.* 520:217–230.

Csernoch, L., P. Szentesi, S. Sárközi, C. Szegedi, and I. Jona. 1999b. Effects of tetracaine on sarcoplasmic calcium release in mammalian skeletal muscle fibers. *J. Physiol.* 515:843–857.

Csernoch, L., P. Szentesi, and L. Kovács. 2002. Increased calcium release from the sarcoplasmic reticulum (SR) in the presence of thymol in mammalian skeletal muscle fibers. *Biophys. J.* 21:641a.

Csernoch, L., J. Zhou, B. Launikonis, A. González, M. D. Stern, G. Brum, and E. Ríos. 2003. The effects of SO_4^{2-}, a Ca^{2+}-precipitating buffer, on Ca^{2+} sparks of mammalian and batrachian twitch muscle. *Biophys. J.* 84:386a.

Feng, W., G. Liu, P. D. Allen, and I. N. Pessah. 2000. Transmembrane redox sensor of ryanodine receptor complex. *J. Biol. Chem.* 275:35902–35907.

Fusi, F., S. Saponara, H. Gagov, and G. Sgaragli. 2001. Effects of some sterically hindered phenols on whole-cell Ca^{2+} current of guinea-pig gastric fundus smooth muscle cells. *Br. J. Pharmacol.* 132:1326–1332.

González, A., W. G. Kirsch, N. Shirokova, G. Pizarro, G. Brum, I. N. Pessah, M. D. Stern, H. Cheng, and E. Ríos. 2000a. Involvement of multiple intracellular release channels in calcium sparks of skeletal muscle. *Proc. Natl. Acad. Sci. USA.* 97:4380–4385.

González, A., W. G. Kirsch, N. Shirokova, G. Pizarro, M. D. Stern, and E. Ríos. 2000b. The spark and its ember: separately gated local components of Ca^{2+} release in skeletal muscle. *J. Gen. Physiol.* 115:139–158.

González, A., and E. Ríos. 1993. Perchlorate enhances transmission in skeletal muscle excitation-contraction coupling. *J. Gen. Physiol.* 102: 373–421.

Herrmann-Frank, A., M. Richter, S. Sárközi, U. Mohr, and F. Lehmann-Horn. 1996. 4-Chloro-*m*-cresol, a potent and specific activator of the skeletal muscle ryanodine receptor. *Biochim. Biophys. Acta.* 1289:31–40.

Hisayama, T., and I. Takayanagi. 1986. Some properties and mechanisms of thymol-induced release of calcium from the calcium-store in guinea-pig taenia caecum. *Jpn. J. Pharmacol.* 40:69–82.

Jiang, Y.-H., M. G. Klein, and M. F. Schneider. 1999. Numerical simulation of Ca^{2+} ''sparks'' in skeletal muscle. *Biophys. J.* 77:2333–2357.

Kirsch, W. G., D. Uttenweiler, and R. H. A. Fink. 2001. Spark- and ember-like elementary Ca^{2+} release events in skinned fibres of adult mammalian skeletal muscle. *J. Physiol.* 537:379–389.

Klein, M. G., H. Cheng, L. F. Santana, Y.-H. Jiang, W. J. Lederer, and M. F. Schneider. 1996. Two mechanisms of quantized calcium release in skeletal muscle. *Nature*. 379:455–458.

Klein, M. G., B. J. Simon, and M. F. Schneider. 1990. Effects of caffeine on calcium release from the sarcoplasmic reticulum in frog skeletal muscle fibers. *J. Physiol.* 425:599–626.

Koshita, M., and T. Oba. 1989. Caffeine treatment inhibits drug-induced calcium release from sarcoplasmic reticulum and caffeine contracture but not tetanus in frog skeletal muscle. *Can. J. Physiol. Pharmacol.* 67:890–895.

Kostyuk, P. G., P. V. Belan, and A. V. Tepikin. 1991. Free calcium transients and oscillations in nerve cells. *Exp. Brain Res.* 83:459–464.

Magyar, J., N. Szentandrássy, T. Bányász, L. Fülöp, A. Varró, and P. P. Nánási. 2002. Effects of thymol on calcium and potassium currents in canine and human ventricular cardiomyocytes. *Br. J. Pharmacol.* 136:330–338.

Marengo, J. J., C. Hidalgo, and R. Bull. 1998. Sulfhydryl oxidation modifies the calcium dependence of ryanodine-sensitive calcium channels of excitable cells. *Biophys. J.* 74:1263–1277.

Marx, S. O., K. Ondrias, and A. R. Marks. 1998. Coupled gating between individual skeletal muscle Ca^{2+} release channels (ryanodine receptors). *Science*. 281:818–821.

Meissner, G. 1994. Ryanodine receptor/Ca^{2+} release channels and their regulation by endogenous effectors. *Annu. Rev. Physiol.* 56:485–508.

Moore, C. P., J.-Z. Zhang, and S. L. Hamilton. 1999. A role for cysteine 3635 of RYR1 in redox modulation and calmodulin binding. *J. Biol. Chem.* 274:36831–36834.

Palade, P. 1987. Drug-induced Ca^{2+} release from isolated sarcoplasmic reticulum. II. Releases involving a Ca^{2+} induced Ca^{2+} release channel. *J. Biol. Chem.* 262:6142–6148.

Pape, P. C., D. S. Jong, and W. K. Chandler. 1996. A slow component of intramembranous charge movement during sarcoplasmic reticulum calcium release in frog cut muscle fibers. *J. Gen. Physiol.* 107:79–101.

Pizarro, G., L. Csernoch, I. Uribe, M. Rodriguez, and E. Ríos. 1991. The relationship between Q_γ and Ca release from the sarcoplasmic reticulum in skeletal muscle. *J. Gen. Physiol.* 97:913–947.

Pizarro, G., N. Shirokova, A. Tsugorka, and E. Ríos. 1997. ''Quantal'' calcium release operated by membrane voltage in frog skeletal muscle. *J. Physiol.* 501:289–303.

Posterino, G. S., M. A. Cellini, and G. D. Lamb. 2003. Effects of oxidation and cytosolic redox conditions on excitation-contraction coupling in rat skeletal muscle. *J. Physiol.* 547:807–823.

Ríos, E., and G. Pizarro. 1991. Voltage sensor of excitation-contraction coupling in skeletal muscle. *Physiol. Rev.* 71:849–908.

Ríos, E., M. D. Stern, A. Gonzáles, G. Pizarro, and N. Shirokova. 1999. Calcium release flux underlying Ca^{2+} sparks of frog skeletal muscle. *J. Gen. Physiol.* 114:31–48.

Rousseau, E., J. LaDine, Q. Y. Liu, and G. Meissner. 1988. Activation of the Ca^{2+} release channel of skeletal muscle sarcoplasmic reticulum by caffeine and related compounds. *Arch. Biochem. Biophys.* 267:75–86.

Shirokova, N., J. García, and E. Ríos. 1998. Local calcium release in mammalian skeletal muscle. *J. Physiol.* 512:377–384.

Shirokova, N., and E. Ríos. 1996. Caffeine enhances intramembranous charge movement in frog skeletal muscle by increasing cytoplasmic Ca^{2+} concentration. *J. Physiol.* 493:341–356.

Shtifman, A., C. W. Ward, J. Wang, H. H. Valdivia, and M. F. Schneider. 2000. Effects of imperatoxin A on local sarcoplasmic reticulum Ca^{2+} release in frog skeletal muscle. *Biophys. J.* 79:814–827.

Simon, B. J., M. G. Klein, and M. F. Schneider. 1991. Calcium dependence of inactivation of calcium release from the sarcoplasmic reticulum in skeletal muscle fibers. *J. Gen. Physiol.* 97:437–471.

Stern, M. D., G. Pizarro, and E. Ríos. 1997. Local control model of excitation-contraction coupling in skeletal muscle. *J. Gen. Physiol.* 110: 415–440.

Struk, A., and W. Melzer. 1999. Modification of excitation-contraction coupling by 4-chloro-*m*-cresol in voltage-clamped cut muscle fibers of the frog (*R. pipiens*). *J. Physiol.* 515:221–231.

Suko, J., G. Hellmann, and H. Drobny. 2000. Modulation of the calmodulin-induced inhibition of sarcoplasmic reticulum calcium release channel (ryanodine receptor) by sulfhydryl oxidation in single channel current recordings and [^{3}H]ryanodine binding. *J. Membr. Biol.* 174:105–120.

Sun, J., L. Xu, J. P. Eu, J. S. Stamler, and G. Meissner. 2001. Classes of thiols that influence the activity of the skeletal muscle calcium release channel. *J. Biol. Chem.* 276:15625–15630.

Szegedi, C., S. Sárközi, A. Herzog, I. Jona, and M. Varsanyi. 1999. Calsequestrin: more than ''only'' a luminal Ca^{2+} buffer inside the sarcoplasmic reticulum. *Biochem. J.* 337:19–22.

Szentandrássy, N., P. Szentesi, J. Magyar, P. P. Nanasi, and L. Csernoch. 2003. Effect of thymol on kinetic properties of Ca and K currents in rat skeletal muscle. *BMC Pharmacology*. 3:9.

Szentesi, P., C. Collet, S. Sárközi, C. Szegedi, I. Jona, V. Jacquemond, L Kovács, and L. Csernoch. 2001. Effects of dantrolene on steps of excitation-contraction coupling in mammalian skeletal muscle fibers. *J. Gen. Physiol.* 118:355–375.

Szentesi, P., V. Jacquemond, L. Kovács, and L. Csernoch. 1997. Intramembrane charge movement and sarcoplasmic calcium release in enzymatically isolated mammalian skeletal muscle fibers. *J. Physiol.* 505:371–384.

Szentesi, P., L. Kovács, and L. Csernoch. 2000. Deterministic inactivation of calcium release in mammalian skeletal muscle. *J. Physiol.* 528:447–456.

Sun, X.-P., N. Callamaras, J. S. Marchant, and I. Parker. 1998. A continuum of $InsP_3$-mediated elementary Ca^{2+} signalling events in *Xenopus* oocytes. *J. Physiol.* 509:67–80.

Thompson, R. D., and M. Carlson. 1989. Determination of thymol in halothane anaesthetic preparations by high-performance liquid chromatography. *J. Pharm. Biomed. Anal.* 7:1199–1206.

Tripathy, A., and G. Meissner. 1996. Sarcoplasmic reticulum luminal Ca^{2+} has access to cytosolic activation and inactivation sites of skeletal muscle Ca^{2+} release channel. *Biophys. J.* 70:2600–2615.

Tripathy, A., W. Resch, L. Xu, H. H. Valdivia, and G. Meissner. 1998. Imperatoxin A induces subconductance states in Ca^{2+} release channels (ryanodine receptors) of cardiac and skeletal muscle. *J. Gen. Physiol.* 111:679–690.

Tsugorka, A., E. Ríos, and L. A. Blatter. 1995. Imaging elementary of calcium release in skeletal muscle cells. *Science*. 269:1723–1726.

Xia, R., T. Stangler, and J. J. Abramson. 2000. Skeletal muscle ryanodine receptor is a redox sensor with a well defined redox potential that is sensitive to channel modulators. *J. Biol. Chem.* 275:36556–36561.

Youdim, K. A., and S. G. Deans. 1999. Beneficial effects of thyme oil on age-related changes in the phospholipid C20 and C22 polyunsaturated fatty acid composition of various rat tissues. *Biochim. Biophys. Acta*. 1438:140–146.

Zhou, J., G. Brum, A. González, B. Launikonis, M. D. Stern, and E. Ríos. 2003. Ca^{2+} sparks and embers of mammalian muscle. Properties of the sources. *J. Gen. Physiol.* 122:95–114.

ZhuGe, R., K. E. Fogarty, R. A. Tuft, L. M. Lifshitz, K. Sayar, and J. V. Walsh, Jr. 2000. Dynamics of signaling between Ca^{2+} sparks and Ca^{2+}-activated K^+ channels studied with a novel image-based method for direct intracellular measurement of ryanodine receptor Ca^{2+} current. *J. Gen. Physiol.* 116:845–864.

Pflugers Arch - Eur J Physiol (2007) 455:541–553
DOI 10.1007/s00424-007-0298-z
szentesi.peter_292_24

SKELETAL MUSCLE

Alterations in the calcium homeostasis of skeletal muscle from postmyocardial infarcted rats

Gyula Péter Szigeti · János Almássy · Mónika Sztretye · Beatrix Dienes · László Szabó · Péter Szentesi · Guy Vassort · Sándor Sárközi · László Csernoch · István Jóna

Received: 13 February 2007 / Revised: 25 April 2007 / Accepted: 21 May 2007 / Published online: 9 June 2007
© Springer-Verlag 2007

Abstract In chronic heart failure, skeletal muscles develop a weakness that is not associated to an impaired circulatory function but rather to alterations in the skeletal muscle fibers themselves. To understand these changes, the steps in excitation–contraction coupling of rats that underwent a left anterior coronary artery occlusion were studied. About 24 weeks after the myocardial infarction, neither the total amount nor the voltage dependence of intramembrane charge were altered. In contrast, calcium release from the sarcoplasmic reticulum was considerably suppressed, and its voltage dependence shifted toward more positive voltages. Elementary calcium-release events showed altered morphology as the relative proportion of embers increased. Calcium sparks were smaller in amplitude and had larger time-to-peak values. Isolated ryanodine receptors (RyR) displayed an unusual rectification with increased single-channel conductance at positive (*cis* vs *trans*) voltages. In addition, the bell-shaped calcium dependence of channel activity was broader, with a slight shift of activation to lower and a larger shift in inactivation to higher calcium concentrations. These data indicate that the number of channels that open during a calcium-release event is decreased and that RyR function is altered; thus, calcium-release is suppressed after a myocardial infarction. These observations give an explanation for the impaired skeletal muscle function in these animals.

Keywords Charge movement · Calcium transients · Calcium sparks · Ryanodine receptor · Single channel · Myocardial infarction

G. P. Szigeti · J. Almássy · M. Sztretye · B. Dienes · L. Szabó · P. Szentesi · S. Sárközi · L. Csernoch · I. Jóna (✉)
Department of Physiology, Medical and Health Science Center, University of Debrecen,
P.O. Box 22, Debrecen, Hungary 4012
e-mail: csl@phys.dote.hu

L. Szabó
Department of Electrical Engineering,
Sapientia Hungarian University of Transilvania,
Targu Mures, Romania

G. Vassort
INSERM U-637, Physiopathologie Cardiovasculaire,
Université Montpellier1,
Montpellier, France

Introduction

Chronic heart failure (CHF) is characterized by an energetic failure of both cardiac and skeletal muscles. The failing heart wastes energy because of anatomical changes, while skeletal muscle undergoes atrophy. The alterations in the energetic level, the gene expression, and the cell contractility are rather well understood in cardiac cells in CHF; however, the underlying reasons of these modifications in skeletal muscle are still less clear [27].

Exercise intolerance is one of the major hallmarks of CHF. Numerous studies have explained different aspects of skeletal muscle dysfunction in clinical and experimental heart failure. The low cardiac output and reduced muscle blood flow for a given work rate, a decreased skeletal muscle mass, and disorders at the cellular and subcellular level have been identified as contributing causes to altered muscle aerobic metabolism during exercise. However, insufficient cardiac output and/or muscle blood flow are unlikely to cause the abnormal skeletal muscle metabolism that occurs during exercise in CHF [4, 30].

Some authors speculate that CHF causes a specific decrease in skeletal muscle oxidative capacity, possibly because of impaired mitochondria causing diminished

szentesi.peter_292_24

exercise capacity, slower oxygen kinetics, and an early increase in blood lactate [3, 5, 12, 21, 26, 35, 43]. The altered O_2 transport and substrate supply or defective energy and metabolic signal transfers within the cell result that mitochondrial oxidative capacity is intrinsically altered [24, 36]. This means that in CHF patients during exercise, skeletal muscles produce high-energy phosphates at a slower rate than in healthy subjects. It has also been suggested that the CHF causes a decreased proportion of type I (fatigue-resistant, oxidative) and an increased proportion of type II (fatigable, glycolytic) fibers in animal models [9, 32]. On the other hand, the few studies that directly assessed intrinsic skeletal muscle oxidative capacity in CHF reported that it was decreased in both oxidative and glycolytic muscles in a rat model [9].

Together with the changes in oxidative capacity, functional alterations were also observed in skeletal muscle of animals of postmyocardial infarction (PMI) [9]. Reduced twitch tension and suppressed sarcoplasmic reticulum (SR) function both accompany CHF [18–20, 28, 29, 34, 42]. Although this modification could partially be due to the altered energetic, recent reports suggest that modified calcium handling, both release from and reuptake into the SR, are also responsible for these functional changes [31, 41].

Excitation–contraction (EC) coupling involves membrane depolarization that activates the dihydropyridine receptors (DHPRs), which in turn activate the ryanodine receptors (RyRs), leading to SR Ca^{2+} release and muscle contraction. The global increase in myoplasmic Ca^{2+} during muscle fiber depolarization consists of the summation of large numbers of local, elementary Ca^{2+} release events (Ca^{2+} sparks and embers). Reduced SR calcium release could thus result from the suppression of DHPR function, RyR channel behavior, or SR calcium load [14].

The aim of this study was to show how the calcium homeostasis is changed in skeletal muscle in CHF using PMI rats as an animal model of the disease. In this investigation, we evaluated the alterations in intramembrane charge movement and of the ryanodine-sensitive Ca^{2+}-release channels by analyzing global and local Ca^{2+} signaling and its single channel properties.

Materials and methods

Experimental model

Male Wistar rats were subjected to coronary artery ligation to produce PMI, and sham-operated animals served as controls [41]. In brief, rats (180–220 g) were anesthetized (pentobarbital, 60 mg/kg) and ventilated. After left-median thoracotomy, the left anterior coronary artery was occluded with a 7–0 silk suture at the most proximal position. Sham-operated animals were subjected to the same surgical operation without any ligation of the coronary artery. PMI rats were used ~24 weeks after surgery and were arbitrarily selected according to the visible level of remodeling estimated by the size (at least 50%) of the fibrotic area on the left ventricle.

All experiments were performed in accordance with Hungarian and French national guidelines and were in compliance with the National Institutes of Health guidelines for the care and use of laboratory animals.

Enzymatic dissociation and solutions

Single skeletal muscle fibers from the fast extensor digitorum communis muscles of coronary operated Wistar rats and sham-operated controls were isolated enzymatically as described previously [37]. Briefly, rats of either sex were anesthetized and killed by cervical dislocation in accordance with the guidelines of the European Community (86/609/EEC) following a protocol approved by the Institutional Animal Care Committee. After removal, the muscles were treated with collagenase (Type I, Sigma Chemicals, St Louis, MO) for 1–1.5 h at 37°C. Fibers were allowed to rest for at least 20 min after dissociation.

The selected fiber was transferred into the recording chamber filled with relaxing solution (in mM, 150 K-glutamate, 2 $MgCl_2$, 10 4-(2-hydroxyethyl)-1-piperazineethanesulfonic acid [HEPES], 1 ethylene glycol tetraacetic acid [EGTA]). The fiber segments in the open-end pools were permeabilized using 0.01% saponin. Solutions in the open-end pools were then exchanged to the internal solution (in mM, 120 Cs-glutamate, 5.5 $MgCl_2$, 5 Na_2-ATP, 10 Na-phosphocreatine, 10 glucose, 5 HEPES, 10 EGTA) and to the external solution in the middle pool (in mM, 140 tetraethylammonium–CH_3SO_3, 2 $CaCl_2$, 2 $MgCl_2$, 5 HEPES, 0.0003 tetrodotoxin, 1 3,4-diaminopyridine). All solutions were adjusted to pH 7.2 and 300 mosmol/l. The internal solution also contained 1 mM Antipyrylazo III (APIII) and 100 μM Fura-2 for the detection of $[Ca^{2+}]_i$. The length of the fiber segment in the middle pool was set to 500 μm.

Experimental setup and data acquisition for cut-fiber experiments

The experimental setup and data acquisition have been described in detail in our earlier reports [38]. In brief, the fiber was *trans*-illuminated using a tungsten–halogen light source (λ>600 nm) and was also epi-illuminated at 380 nm or at the isosbestic wavelength of Fura-2 using a 75-W xenon arch lamp (Oriel 60 000; Stratford, CT). The actual arrangement of interference filters and dichroic mirrors [15] enabled the simultaneous recording of light intensities at

szentesi.peter_292_24

510, 720, and 850 nm for the detection of APIII absorbance and Fura-2 fluorescence. Fibers were voltage clamped, and the holding potential (V_h) was set to −90 or −100 mV. All measurements were carried out at 15–17°C.

Calculation of nonlinear capacitative currents and $[Ca^{2+}]_i$

Nonlinear capacitive currents (IQ) representing intramembrane charge movement were calculated as described earlier [37]. In brief, hyperpolarizing pulses of −20 mV and 100 ms were applied, and the accompanying currents (negative controls) were scaled and subtracted from the current records measured with depolarizing pulses. The membrane potential (V_m) dependence of charge transferred ($Q(V_m)$) was fitted with the two-state Boltzmann function:

$$Q(V_m) = Q_{max}/(1 + \exp\{-(V_m - V')/k\}), \quad (1)$$

where Q_{max} is the maximal available charge, V' is the midpoint voltage, and k is the slope factor.

Changes in the myoplasmic free calcium concentration were calculated from APIII absorbance as described by Kovács et al. [15] using the correction for intrinsic fiber absorbance at 850 nm [25] and dye kinetics [6]. For large depolarizations, the APIII signal was used for small depolarizations, and for the estimation of the resting $[Ca^{2+}]_i$, the Fura-2 signal was used [33]. Because the internal solution contained 10 mM EGTA, the time course of the calcium transient was used to estimate that of SR calcium release. To determine its voltage dependence, Eq. 1 was used with $[Ca^{2+}]_{i,max}$—maximal intracellular calcium concentration—instead of Q_{max} as one of the fitted parameters.

Measurement of elementary calcium-release events

After dissociation, the selected fiber was transferred to the recording chamber with a glass bottom filled with relaxing solution (in mM: 100 K-glutamate, 10 HEPES, 1 EGTA, 5.5 $MgCl_2$, 5 Na_2-ATP, 10 Na-phosphocreatine, 10 glucose, 0.13 $CaCl_2$, and 8% dextran, pH 7.0). The surface membrane was permeabilized using a relaxing solution containing 0.002% saponin for 2–3 min, 50 μM Fluo-3, and 4% dextran. This solution was then changed to a K_2SO_4-based internal solution (in mM: 95 K_2SO_4, 10 HEPES, 1 EGTA, 6 $MgCl_2$, 5 Na_2-ATP, 10 Na-phosphocreatine, 10 glucose, 0.26 $CaCl_2$, 0.1 Fluo-3, and 8% dextran) to record the calcium-release events. The free calcium concentration in the cytosol was calculated to be pCa=7.4 with the computer program of Fabiato [10].

Fibers were imaged using an LSM 510 META laser scanning confocal microscope (Zeiss, Oberkochen, Germany) as described earlier [38]. Line-scan images ([x,t]) were taken at 1.54 ms/line and 512 pixels/line (pixel size 0.142 μm) with a 63× water immersion objective (numerical aperture=1.2; Zeiss). Fluo-3 was excited with an Argon ion laser at 488 nm; the emitted light was collected through a band-pass filter (505–570 nm) and digitized at 12 bit. To avoid photodamage, the same position was not imaged twice. All measurements were carried out at room temperature (22°C).

Elementary Ca^{2+}-release events were captured using an automatic computer detection routine based on those described earlier (e.g., [2, 38]). In brief, the program identified elementary events as regions with fluorescence above a relative threshold, calculated from the noise in the images. If the event was longer than 40 pixels in time and had a clear plateau, it was identified as an ember; otherwise, it was taken to be a spark. Events longer than 40 pixels that had a definite peak were treated as "spark + ember" and were not included in this analysis. The program also determined the parameters of the identified events, namely amplitude (as $\Delta F/F_0$), spatial half-width measured at the time of the peak (full width at half maximum, FWHM), duration, and rise time. FWHM was obtained from fitting a Gaussian function to the spatial distribution obtained by averaging three lines at the peak. In case of embers, the average amplitude was calculated instead of the peak amplitude. Namely, after determination of the mask of an ember (rectangular), all lines excluding the first and last ten at every time point were averaged, and the amplitude of the temporal average was calculated. Sparks with amplitudes smaller than 0.2 $\Delta F/F_0$ units and embers with average amplitudes smaller than 0.05 $\Delta F/F_0$ units were excluded from the analysis.

The signal mass (SM) of the events was calculated as a function of time using the equation

$$SM(t) = 1.206 \times A(t) \times FWHM(t)^3, \quad (2)$$

where $A(t)$ and FWHM(t) are the amplitude and FWHM, respectively, of the Gaussian function fitted to the spatial profile of the spark at time t [11]. Rate of SM production was calculated by fitting a linear function to the rising phase of SM(t).

Preparation of the solubilized RyR1

Heavy SR (HSR) vesicles—containing vesicles formed from membrane fragments of the terminal cisternae of the SR—were isolated from rat skeletal muscle according to Lai and Meissner [16] with slight modifications. After a homogenization in 100 mM NaCl, 20 mM EGTA, and 20 mM Na-HEPES, pH 7.5, first crude microsomes were collected by centrifugation at 40,000×g. After removing the actomyosin contamination, by solubilization in 600 mM KCl, the microsome fraction was collected at 109,000×g. The pellet was resuspended and loaded onto a 20–45% linear sucrose gradient in a SW-27 rotor and centrifuged for 16 h at 21,000 rpm (90,000×g at the bottom). HSR vesicles were extracted from the 36–38% region of the continuous

szentesi.peter_292_24

sucrose gradient, collected by centrifugation and resuspended in 0.4 M sucrose, 10 mM K-PIPES, pH 7.0. Resuspended vesicles were solubilized in 3-[(3-cholamido-propyl)dimethylammonio]-1-propane-sulfonate (CHAPS)-containing medium and were layered on the top of a 10–28% sucrose gradient, centrifuged for 16 h at 90,000×*g* using a Beckman SW-27 rotor. Fractions—containing the solubilized receptor complex—were collected, rapidly frozen in liquid N_2, and stored at −70°C. Several protease inhibitors were included in the solutions to prevent proteolysis during the isolation [38]. Protein concentrations were determined according to Lowry, using bovine serum albumin standard.

Single-channel measurements

The CHAPS-solubilized RyR1 was incorporated into a Müller–Rudin-type planar lipid bilayer [39]. Bilayers were formed across a 250-μm aperture on the delrin cup (Warner Instruments, Campden, NJ) using a mixture of phosphatidylethanolamine, phosphatidylserine, and phosphatidylcholine at a weight ratio of 5:4:1 dissolved in *n*-decane up to a final concentration of 20 mg/ml. Incorporation of the RyR1 into the bilayer was initiated in symmetric buffer solution (250 mM KCl, 100 μM EGTA, 150 μM $CaCl_2$, 20 mM PIPES, pH 7.2) containing 50 μM ionized (free) calcium. Small aliquots of the solubilized receptor were added to one side of the bilayer chamber defined as the *cis* (cytoplasmic) side, as in 90% of the cases, this orientation was verified by the pharmacology of the channel. Successful incorporation was detected as a step-like increase of membrane current. Electric potential is given as potential of the (assumed) *cis* chamber relative to the potential of the *trans* chamber, which was kept at ground potential. Orientation of the incorporated receptor was verified at the last step of each single experiment using ryanodine or ruthenium red additions. Records that failed the verification (opposite incorporation) were discarded. Current signals were filtered at 1 kHz using an eight-pole low-pass Bessel filter, and the filtered signal was digitized at 3.3 kHz at a 12-bit resolution using an Axopatch 200 amplifier with Digidata 1200 interface (Axon Instruments, Union City, CA). Pilot experiments were carried out in which the calculated channel parameters (as mean open time, P_o, and maximum current) were determined using 3-kHz filter and 10-kHz sampling frequency vs 1- and 3.3-kHz sampling frequency for collecting the data of the same channel. These experiments revealed that these (data collection) settings do not influence the calculated channel parameters. After changing the conditions in the chamber, at least 5 min were allowed to reach the new equilibrium, and total recording time was more than 5 min for each experimental condition. Open probability (P_o) values were calculated from representative data segments of 50–100 s in duration using the pClamp 6.02 software package of Axon Instruments, with the common 50% criteria with a 2.5% dead zone. Maximal current was determined for each record, and levels were set accordingly. Channel conductance was determined for each channel, and voltage–current relationship was tested occasionally before the verification of the channel orientation. To determine the conductance of the channel, the frequency–conductance histogram was fitted with one or two Gaussian peaks using Origin 7.0 software (OriginLab, Northampton, MA). For statistical comparison of the open probabilities, Student's *t* test and *F* test were used with a significance limit of 0.05 or 0.01. Free [Ca^{2+}] was calculated according to Fabiato [10]. The concentration-dependent effects of Ca^{2+} on the P_o were fitted using the Hill equations:

$$P_o \Big/ P_{o,\max} = \left[Ca^{2+}\right]^{nA} \Big/ \left([EC_{50}]^{nA} + \left[Ca^{2+}\right]^{nA} \right) \times \left(1 - \left[Ca^{2+}\right]^{nI} \Big/ \left([IC_{50}]^{nI} + \left[Ca^{2+}\right]^{nI} \right), \quad (3)$$

where P_o is the open probability, $P_{o,\max}$ is the theoretical maximum of P_o, [EC_{50}] and [IC_{50}] are the half effective concentrations, while n_A and n_I are the Hill coefficients during activation and inhibition, respectively. Experiments were carried out in quadruplets, and the averaged data were used in the calculations.

Chemicals

Fura-2 and Fluo-3 were purchased from Molecular Probes (Eugene, OR), APIII from ICN Biomedicals (Aurora, OH), and all other chemicals were of analytical grade (Sigma).

Statistics

All values were expressed as mean ± SE of mean of *n* data. For testing significant differences between control and PMI data, the Microsoft Office Excels' built-in *t* test for two samples assuming equal variance statistical test was used at 0.05 confidence level. To find the coefficients (parameters) of the independent variable(s) that give the "best fit" between the equation and the data, built-in functions and methods of SigmaPlot (SPSS, Chicago, IL) were used that apply the Marquardt–Levenberg algorithm. The results of the fits are present as the parameters ± error of the fit.

Results

Intramembrane charge movement

To ensure that the fibers obtained by the enzymatic dissociation were functionally intact, their electrical properties were first carefully examined. The linear capacitance

szentesi.peter_292_24

of the fibers (9.3±1.6 and 11.1±1.9 nF, n=5 and 4, for control and PMI rats, respectively) fell within the same range as reported in earlier studies [37]. No significant difference (p>0.2) was found between the linear capacitance of the two groups if the measured values were normalized to surface area (assuming similar T-tubular networks). Fibers were electrically stable for 30–60 min (in a few cases for even longer periods) after setting the holding potential to −100 mV allowing the determination of the voltage dependence of intramembrane charge movement and/or SR calcium release.

Under our conditions—the given external and internal solutions—60- to 100-ms depolarizing pulses did not elicit significant ionic currents. It should be noted that longer pulses usually induced the activation of an inward current with a threshold for activation of −20 mV and a time to peak of about 200 ms at 0 mV (data not shown). Although these properties suggest that the current was carried by Ca^{2+} through L-type channels, the characterization of this current is not included in this study.

Using negative controls, the intramembrane charge displacement currents (Fig. 1a) were calculated from the total membrane currents measured on PMI rats. These showed all the characteristics presented previously on control mammalian fibers. No secondary slow components at and around the threshold of SR calcium release were observed; however, specific pulse protocols to enhance such delayed currents were not applied. To obtain the amount of charge transferred at every given membrane potential, the currents were integrated. The calculated charge was then normalized to the measured linear capacitance, and its voltage dependence was assessed by fitting a Boltzmann equation (Eq. 1) to the data. For the fiber presented in Fig. 1a, the fit yielded Q_{max} of 22.0 nC/μF, V' of −28.9 mV, and k of 14.2 mV. Carrying out similar fits in every fiber resulted in an average Q_{max} of 32.2±3.4 nC/μF, V' of −28.3±2.7 mV, and k of 12.1±2.0 mV (n=5) under the control condition, while Q_{max} of 33.4±4.3 nC/μF, V' of −28.0±4.3 mV, and k of 14.9±2.0 mV (n=4) in PMI rats. There was no significant difference (p>0.1) between the parameters obtained under control conditions and in PMI rats.

To compare the voltage dependence of intramembrane charge movement in different fibers, the amount of charge moved at a given membrane potential was normalized to Q_{max} determined in that fiber and pooled data from all fibers was plotted as a function of the membrane potential (Fig. 1b). There was no significant difference (p>0.05) between the mean charge moved at different membrane potentials except for those at −60 and −50 mV. Including all normalized data into the fit, an overall V' of −27.6±0.6 mV and k of 11.5±0.5 mV was obtained under control conditions, while a V' of −27.7±2.2 mV and k of 17.2±1.5 mV in fibers from PMI rats.

Calcium transients evoked by membrane depolarization

Depolarizing pulses, if they exceeded the threshold, were accompanied by changes in $[Ca^{2+}]_i$. As shown in Fig. 2a and b, increasing depolarizations brought about increasingly larger changes in $[Ca^{2+}]_i$ if measured with APIII. The calcium transients displayed the characteristic peaky time course resembling that of SR calcium release because of the presence of high concentrations of the intracellular calcium buffer. After repolarization, the decline of $[Ca^{2+}]_i$ to its

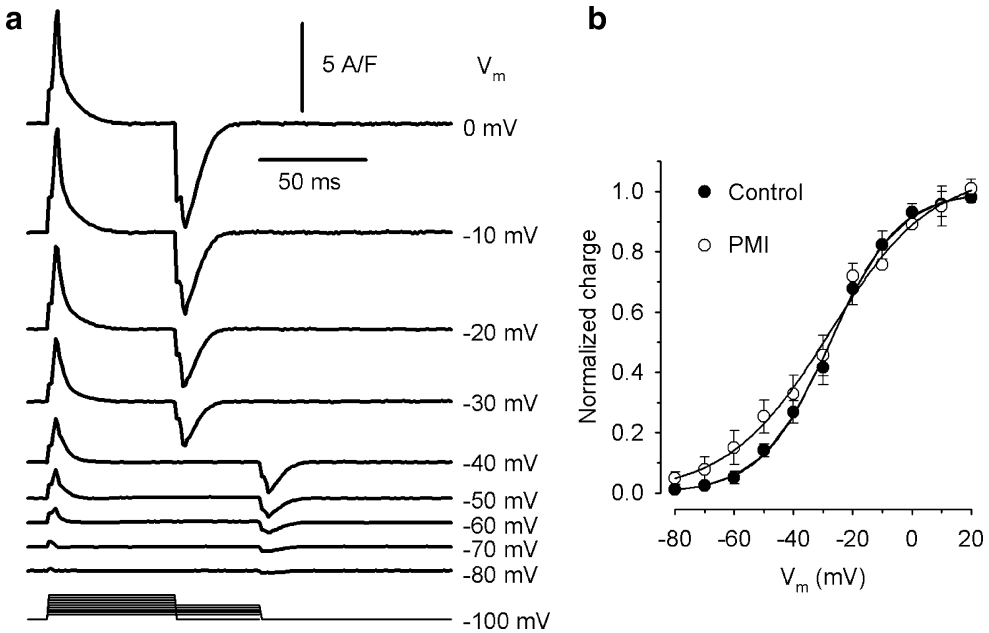


Fig. 1 Voltage dependence of intramembrane charge movement in control and PMI rat fibers. **a** Nonlinear capacitive currents that remain after subtracting a "negative control," representing intramembrane charge displacement in fibers from a PMI rat. Voltage excursion is given below the current records. Holding potential (V_h), −100 mV; linear capacitance, 13.3 nF. **b** Voltage dependence of charge transferred from five and four fibers (means ± SEM) in sham-operated and PMI rats, respectively. Each data point was first normalized to the maximal charge in that particular fiber and then averaged. The *continuous line* represents the least-squares fit of the Boltzmann equation (Eq. 1) to all data points

szentesi.peter_292_24

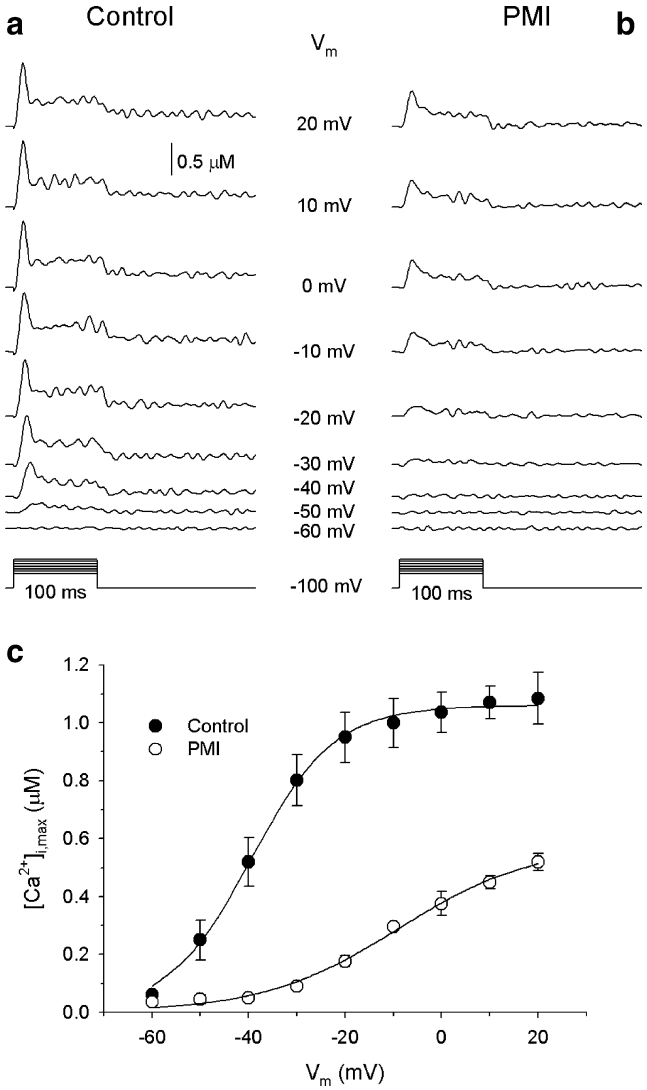


Fig. 2 Voltage dependence of $[Ca^{2+}]_i$ in control and PMI rat fibers. **a** Calcium transients calculated from APIII absorbance changes elicited by 100-ms depolarizing pulses in control rats (path length, 70 μm; [APIII], 290–440 μM; V_h, −100 mV). The voltage excursion is given *below the traces*, and the membrane potential during the test is shown in each *row*. Note that the transients display a peaky time course because of the presence of high [EGTA]. **b** Calcium transients in PMI rats (path length, 43 μm; [APIII], 550–1,380 μM; V_h, −100 mV). **c** Voltage dependence of the maximal $[Ca^{2+}]_i$ during a 100-ms pulse. Values represent means ± SEM from five and three fibers in control and PMI rats, respectively. The *continuous lines* represent the least-squares fit of Eq. 1 to the two sets of mean values

prestimulation level was slowed again as expected from the presence of the buffer.

The voltage dependence of change in $[Ca^{2+}]_i$ was assessed by fitting Eq. 1 to the data points yielding $[Ca^{2+}]_{i,max}$ of 0.96±0.02 and 0.51±0.04 μM, V' of −39.8±1.1 and −14.6±2.9 mV, and k of 7.2±1.0 and 12.7±1.9 mV for the control conditions (Fig. 2a) and for the PMI rat (Fig. 2b), respectively. Repeating the fit for each individual fiber resulted in an average $[Ca^{2+}]_{i,max}$ of 1.00±0.10 μM, an average V' of −40.0±1.9 mV, and an average k of 7.2±1.1 mV (n=5) under control conditions, while $[Ca^{2+}]_{i,max}$ of 0.55±0.03 μM, V' of −11.7±1.6 mV, and k of 14.9±2.0 mV (n=4) in PMI rats. All these parameters were significantly different ($p<0.01$) between control and PMI rats.

Values from individual experiments were pooled and plotted in Fig. 2c. The voltage dependence of the maximal increase in $[Ca^{2+}]_i$ under control conditions resembled those measured earlier. The first detectable signal appeared around −50 mV. To compare the voltage dependence of calcium transients, the mean values were fitted with the Boltzmann function. The fit to the pooled data featured similar changes in the parameters as the averaged data from the individual fits. $[Ca^{2+}]_{i,max}$ was reduced (from 1.06±0.01 to 0.58±0.03 μM), the midpoint voltage was shifted to more positive voltages (from −39.5±0.5 to −8.8±2.3 mV), while the slope factor was increased (from 8.6±0.5 to 14.1±1.3 mV) in PMI as compared to sham-operated rats.

To explore the changes in the kinetics of the calcium transients, the peak-to-steady level ratio (P/Sl) and the time-to-peak (TTP) were calculated from the calcium transients measured at 0 mV. There was no significant difference ($p>0.1$) in P/Sl between the control (2.34±0.07) and PMI (2.14±0.18) rats. On the other hand, the TTP at 0 mV was increased significantly ($p<0.05$) from 15.4±1.2 ms in the control to 21.3±2.9 ms in PMI rats.

Elementary calcium-release events

Elementary calcium-release events in mammalian muscle fibers exhibit a wide morphological variety: short rise in $[Ca^{2+}]_i$ (calcium sparks) and long elevation of cytosolic calcium (embers) [13, 44]. Because whole-cell calcium handling is modified in PMI rats, it was of interest to see whether the properties and appearance of the calcium-release events are altered in these rats. Calcium sparks and embers were thus measured on permeabilized fibers, and their relative numbers and morphological properties were compared in the two populations of rats.

Under control conditions (Fig. 3a), calcium-release events occurred with an appreciable frequency (0.038±0.001 s^{-1} sarcomere^{-1}, 733 images from ten fibers) and displayed all the morphological characteristics described earlier (e.g., [38]). In PMI rats (Fig. 3b), the frequency increased slightly but not significantly to 0.041±0.001 s^{-1} sarcomere^{-1} (522 images from eight fibers, $p>0.8$). On the other hand, the ratio of embers to sparks found in all experiments was altered. While in control animals, 63.2% of all events were sparks, 22.4% were embers, and the rest (14.4%) were found to be "spark + ember," this was modified to 40.1, 32.7, and 27.2%, respectively, in PMI rats. Averaging the ember-to-spark ratio of individual fibers

szentesi.peter_292_24

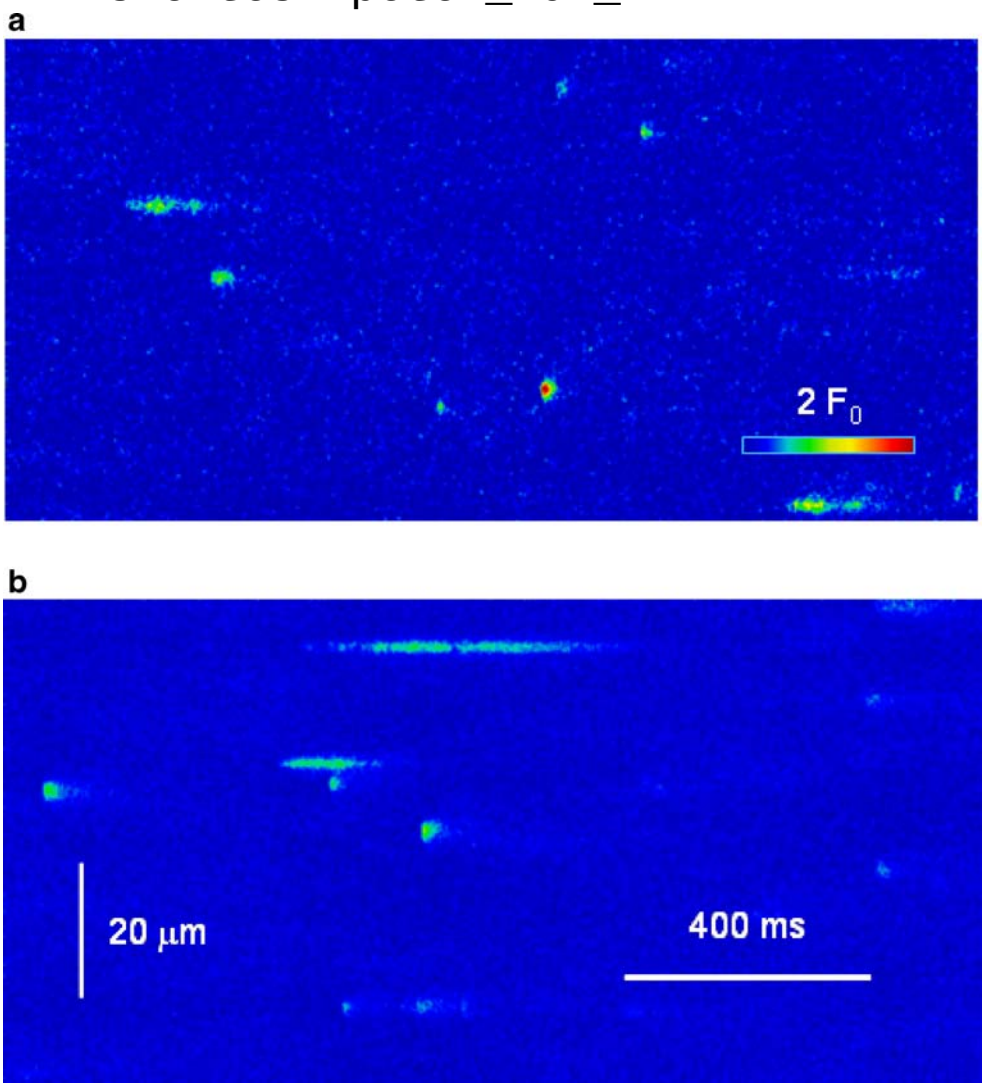


Fig. 3 Calcium release events in control animals and PMI rats. Line-scan images of two fibers from a sham-operated (**a**) and from a PMI (**b**) rat. Scanning was made parallel with the fiber axis. Images were corrected for background fluorescence (F/F_0) and pseudo-colored. Note the smaller amplitude of events and the relatively larger number of embers as compared to sparks in the PMI rat

revealed a significant ($p<0.05$) increase from 0.39±0.17 in the control to 1.48±0.61 in PMI animals.

A total of 1,284 vs 937 sparks and 454 vs 765 embers from ten vs eight fibers (six vs four animals) were analyzed under control conditions and in PMI rats, respectively, and their characteristic parameters are presented in Table 1. In PMI rats, the average amplitude of sparks decreased by 40% leaving FWHM essentially constant (Fig. 4c). The decrease in spark amplitude was attributable to a decrease in the number of large sparks as depicted in Fig. 4a. Together with the decrease in amplitude, the rise time of the sparks increased significantly ($p<0.001$; Table 1). The average amplitude of embers was also decreased in PMI rats by 20% (Fig. 4b), and there was a small increase of

Table 1 Characteristic parameters of the calcium-release events from control and PMI rats

	Spark		Ember[a]	
	Control, $n=1,284$	PMI, $n=937$	Control, $n=454$	PMI, $n=765$
Amplitude[b]	0.81±0.01	0.48±0.01[c]	0.21±0.004	0.17±0.003[c]
Rise time (ms)	12.4±0.2	14.6±0.3[c]	–	–
FWHM (μm)	1.72±0.02	1.66±0.02[c]	1.78±0.02	1.81±0.02
Duration (ms)	34.6±0.4	35.6±0.6	87.9±0.4	88.6±2.1

[a] Embers containing sparks were not included into the calculations.
[b] In case of embers, the average amplitude was calculated instead of amplitude.
[c] Indicates significant difference between the control and PMI

szentesi.peter_292_24

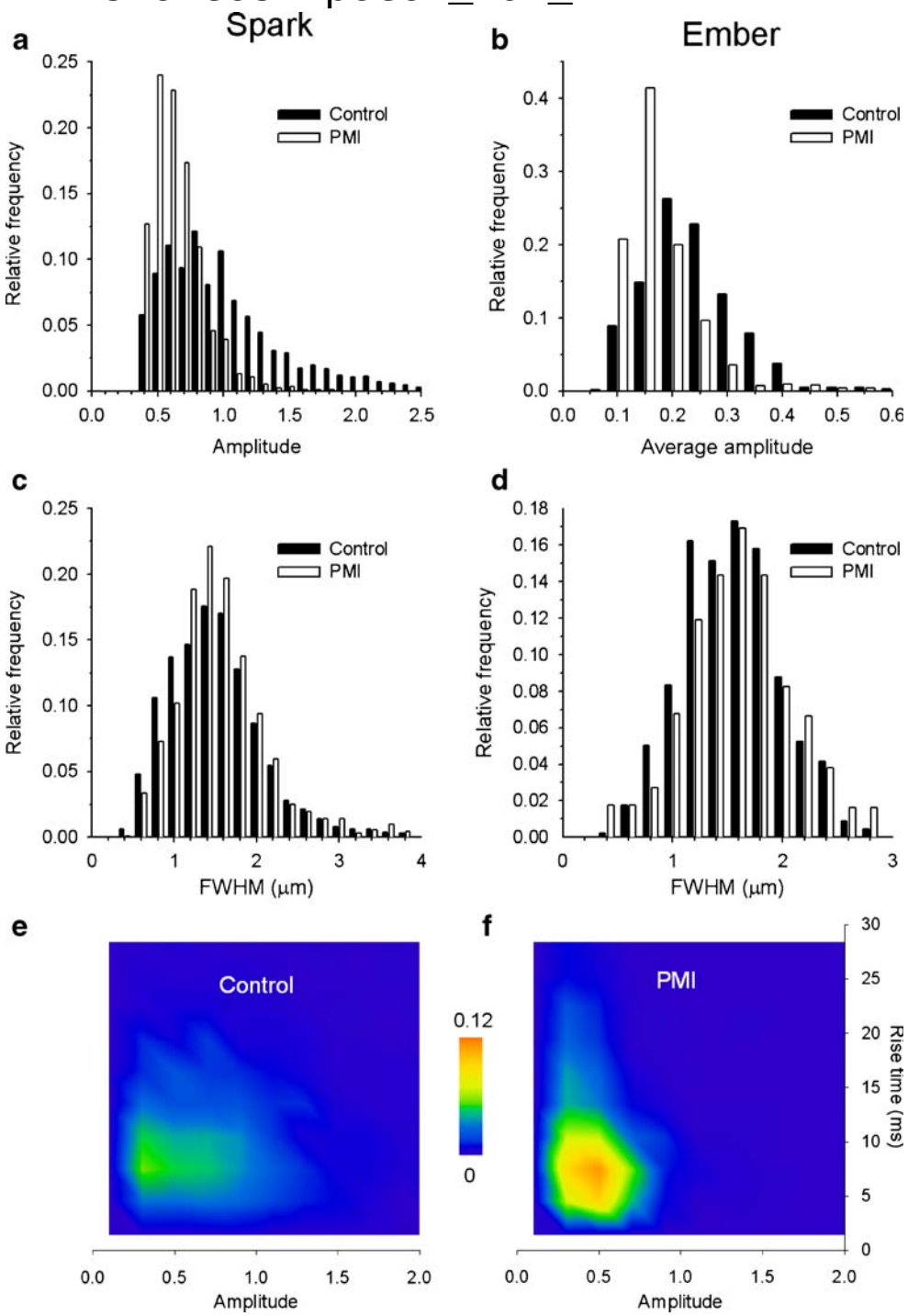


Fig. 4 Distribution of the characteristic parameters of sparks and embers. The amplitude (**a**), average amplitude (**b**), and full width at half maximum (**c** and **d**) of sparks (*left*) and of embers (*right*) in skeletal muscle fibers of sham-operated (*control*) and PMI rats. Note the shift to smaller values in the amplitude, with no appreciable change in the FWHM histograms. Distribution of the amplitudes and rise times of the calcium sparks in control (**e**) and in PMI animals (**f**). Amplitude and rise time values were binned and the relative frequencies plotted as a pseudo-colored two-dimensional surface. The mean values of the parameters presented here are given in Table 1

FWHM comparing the values obtained from sham-operated rats (Fig. 4d).

To visualize the alteration in the morphology of the calcium sparks, the two dimensional distribution of the amplitudes and rise times are presented in Fig. 4e and f for the control and for the PMI events, respectively. To this end, amplitudes and rise times were binned, and the relative frequency of the events that fell into a given bin for both the amplitude and the rise time were plotted as a surface. The distributions clearly reveal a shift to smaller amplitudes and larger rise times in PMI rats.

To estimate the calcium flux during the events, the rate of production of SM(t) was determined. Figure 5 presents two typical sparks of large amplitude measured in a control and in a PMI rat fiber (Fig. 5a) together with their time courses (Fig. 5b). Gaussian functions were fitted to the spatial profiles of the sparks at each point in time, and SM (t) was calculated using Eq. 2 in both cases (Fig. 5c). Signal

szentesi.peter_292_24

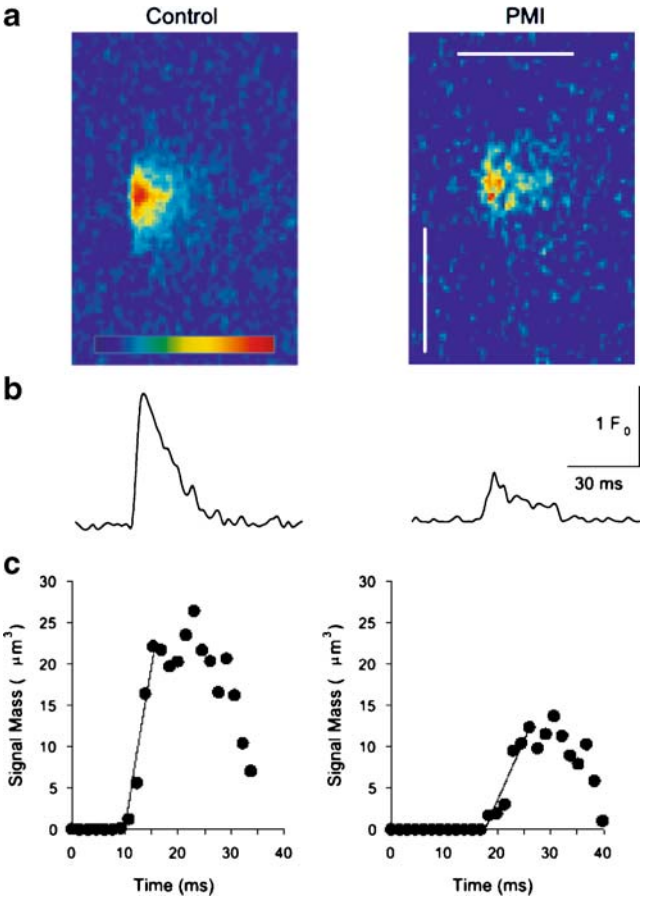


Fig. 5 Signal mass of sparks. **a** Two typical sparks of large amplitude from a control animal and from a PMI rat. **b** Time course of the sparks presented in **a**. The amplitudes were 1.79 and 0.70 in control and in the PMI rat, respectively. **c** Signal mass estimated using Eq. 2 after fitting Gaussian functions to the spatial spread of the events at each and every point in time. *Straight lines* represent a linear fit to the rising phase of SM(t) functions with slopes of 3.80 and 1.44 $\mu m^3\ ms^{-1}$ for the control and the PMI rat, respectively

mass production was estimated as the slope of the straight line fitted to the rising phase of SM(*t*) (Fig. 5c). It was roughly constant during the rise time of the spark and was found to be 3.80 and 1.79 μm^3/ms for the control spark and for the spark measured on the fiber from the PMI rat, respectively. Selecting the ten largest sparks, assumed to represent events closest to the confocal plane, the average rate of SM production calculated from control sparks was significantly greater than that of PMI rats (2.59± 0.24 and 1.42±0.25 μm^3/ms, respectively; $p<0.01$). This observation clearly indicates that the calcium flux associated with the calcium-release events were depressed in animals with CHF.

Conductance of the rat SR calcium-release channel

Channels were incorporated at 50 μM free Ca^{2+} *cis* and *trans*, to get open probabilities high enough to detect the incorporation immediately. The charge carrier was 250 mM potassium, and the channel current was recorded as described in "Materials and methods," using positive (Fig. 6a left) and negative (Fig. 6a right) holding potentials. In some experiments, stepwise changes in holding potential were applied to construct the *I–V* characteristics (Fig. 6b) of the channel. This revealed an ohmic behavior with an average conductance of 544.3±0.2 pS under the control condition and 546.9±0.5 pS at negative while 796.6±

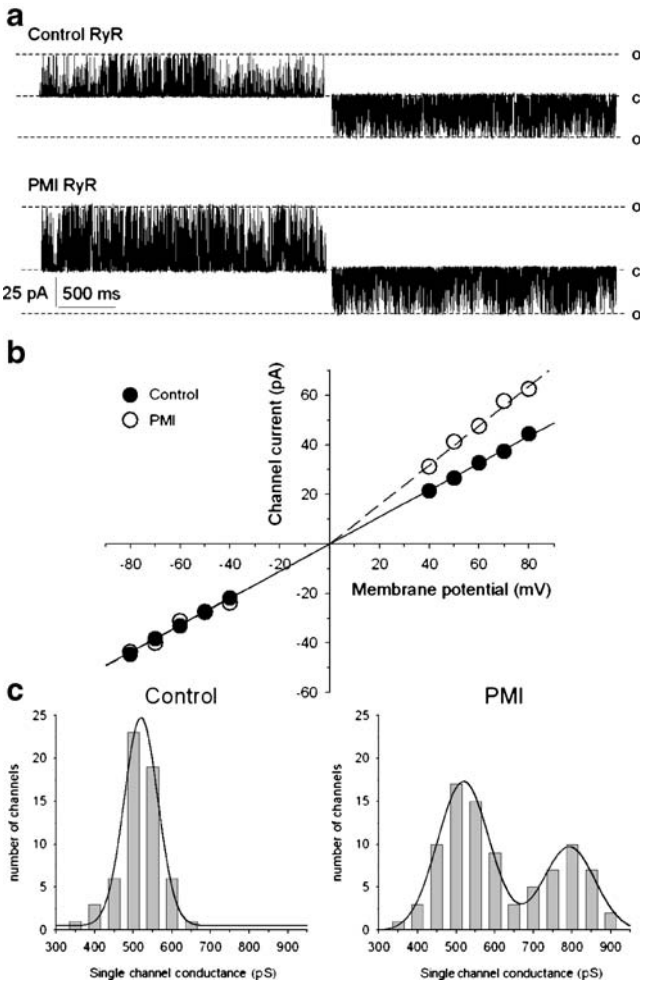


Fig. 6 Current voltage characteristics of the channel. **a** Single-channel currents obtained at symmetrical 50 μM free calcium concentration using 250 mM KCl as charge carrier. Holding potential was set to 70 (*left*) or to −70 mV (*right*) for the records. The open and the closed state of the channel are labeled as *O* and *C*. **b** Representative channel currents were measured at various voltages as described in "Materials and methods." A *continuous line* was fitted to the *filled circles* representing data from control rats, while *dashed lines* were fitted, independently to the data for negative and positive holding potential, to the *open circles* representing data from PMI rats. **c** Single-channel conductance histograms were constructed using 50-pS binning including all channels studied. Conductance of the individual channels was determined at positive holding potentials for the control animals (*left*) and for the PMI rats (*right*). Histograms were fitted with one or two Gaussian functions giving 520.3±2.1 pS for the control and 519.5± 3.2 and 793.1±5.7 pS for the PMI channels

szentesi.peter_292_24

0.7 pS at positive potentials in PMI for the channels presented in Fig. 6a. The average conductance of the control channels (n=57) was 535±32 pS. However, in PMI rats, at negative potentials, the average conductance of RyR was not significantly different from the control (575± 31 pS, p>0.2), while reaching a significant increase (785± 28 pS, p<0.001) at positive potentials (n=89).

It should be stressed that only a group of channels isolated from PMI animals displayed this increased conductance at positive potentials. To present this dual behavior frequency, histograms were constructed including all channels (Fig. 6c), and the conductance for each condition was also determined by fitting a single (control, R^2=0.98) or a double Gaussian peak (PMI, R^2=0.98) to the distributions. At positive holding potentials, the estimated conductance—represented by the center of the distribution—was 520.3± 2.1 pS for the control while 519.5±3.2 and 793.1±5.7 pS for the PMI channels (Fig. 6c). At negative holding potentials, the Gaussian fits gave for channels conductance 529.2± 3.8 pS under control conditions and 573±4.3 pS for the PMI rats (histograms not shown).

Regulation of rat RyR activity by *cis* Ca^{2+}

Ca^{2+} concentration (in the pCa=3–8 range) was adjusted on the *cis* side of the bilayer by the addition of the required amounts of EGTA or $CaCl_2$ stocks (Fig. 7). The open probability was calculated from single-channel records at different Ca^{2+} concentrations after reaching equilibrium. The solubilized and incorporated RyR was most active in the 50–100 μM *cis* Ca^{2+} range in both animal groups (Fig. 7). Average mean open time at 50 μM Ca^{2+} *cis* was 0.436±0.057 (control) and 0.473±0.041 ms (PMI), while at 472 nM Ca^{2+} *cis*, it was 0.417±0.054 (control) and 0.431± 0.041 ms (PMI). These differences are not significant (p> 0.8). Raising the *cis* calcium concentration from 50 to 500 μM Ca^{2+} *cis*, the mean open time significantly (p< 0.02) decreased to 0.247±0.032 (control) and to 0.221± 0.027 ms (PMI). Decreasing the calcium concentration from 50 μM Ca^{2+} *cis* into the submicromolar range drastically reduced P_o (Fig. 7a and b), mainly because of the lesser number of open events and not to the decrease in the mean open time. Similarly, if Ca^{2+} *cis* was increased above 100 μM, the open probability decreased (Fig. 7a and b). This was, on the other hand, not only the result of the decreased number of open events but also of the decrease in the mean open time. Fitting the open probabilities using the Hill equation (Eq. 3) revealed Hill coefficients close to unity for the ascending (0.84±0.07 in sham-operated and 0.92±0.12 in PMI rats) and for the descending (1.19±0.1 in sham-operated and 1.03±0.27 in PMI rats) limbs (Fig. 7c) in agreement with the presence of one activatory and one inhibitory calcium binding site. There was only a slight

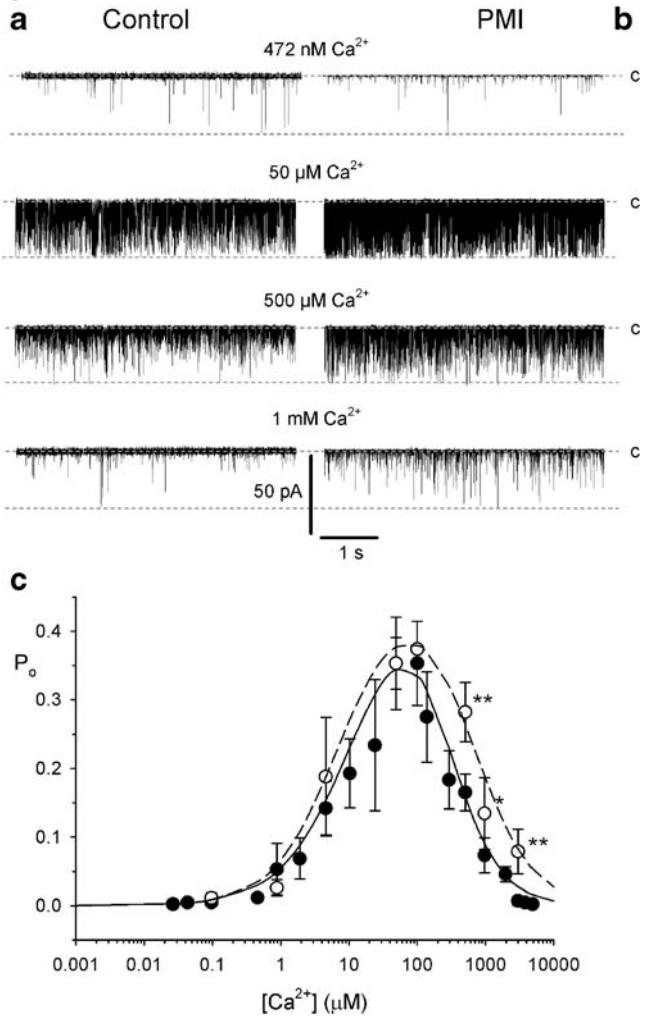


Fig. 7 Calcium dependence of open probability. **a**, **b** Representative single channel currents recorded using −70 mV holding potential in the presence of various free *cis*-calcium concentrations using 250 mM K^+ as charge carrier. Channel openings are indicated by downward deflections. **c** Open probabilities plotted as a function of free *cis*-calcium concentration expressed as pCa. *Filled symbols* represent values obtained using RyR1 from the control animals while *open circles* represent data obtained using RyR1 prepared from PMI rats. Data from control (*continuous line*) and PMI animals (*dashed line*) were fitted with the Hill equation (Eq. 3) to obtain the apparent dissociation constants and Hill coefficients for the activatory and inhibitory calcium binding sites. Significantly different open probabilities were indicated by *asterisks* (p<0.05) or *double asterisks* (p<0.01)

difference between the two animal groups in the half activatory concentrations (12.3±1.3 and 7.1±1.3 μM, in sham-operated and PMI rats, respectively). However, the half inactivatory concentration was moved to considerably higher values in PMI rats (274.8±23.4 vs 675.8±15.9 μM, in sham-operated and PMI rats, respectively) showing that the calcium sensitivity of inactivation is particularly reduced in PMI rats.

szentesi.peter_292_24

Discussion

In this investigation, the steps in EC coupling of the skeletal muscle of sham-operated and PMI rats were evaluated. Intramembrane charge movement and the depolarization-activated Ca^{2+} transients were studied with a double-Vaseline gap voltage clamp. While the overall voltage dependence of charge movements, associated with the conformational changes in the voltage sensor DHPRs, was not significantly altered in PMI rats, the calcium release from the SR was considerably depressed, and its voltage dependence shifted toward more positive voltages. To understand the reasons for this reduction, elementary Ca^{2+}-release events were measured using laser scanning confocal imaging in individual saponin-permeabilized and Fluo-3-loaded fibers of the extensor digitorum communis muscle. Both types of the events, sparks (short release with high amplitude) and embers (longer response with low amplitude), were detected after myocardial infarction; however, the relative proportion of the latter was considerably increased. In addition, the amplitude of the events was reduced in PMI rats, and moreover, the Ca^{2+} fluxes during the events were also depressed. Consistent with the increased time to peak of the global calcium transients in PMI rats, the rise time of the calcium sparks was also significantly lengthened in these animals. These observations are consistent with a reduced Ca^{2+} content of the SR or with alterations in RyR function. To evaluate whether intrinsic changes of RyR accompany CHF, the single-channel properties of the calcium-release channel were studied under voltage-clamp conditions. The conductance of RyR1 was unaltered at negative but increased at positive potentials, and the bell-shaped curve that describes its Ca^{2+} sensitivity was slightly broader in PMI rats. These results are consistent with the idea that either the averaged number of RyR channels that open during a calcium-release event or the driving force for Ca^{2+} to leave the SR is (or both are) reduced in CHF.

Alterations of global Ca^{2+} signaling in fast-twitch muscle

The extensor digitorum longus (EDL) muscle fibers from PMI rats exhibit alterations in both Ca^{2+} release and uptake properties of the SR. Perreault et al. [28] first reported a reduction in the magnitude and a slowing of SR Ca^{2+} uptake in association with reductions in force in the rat EDL muscle during CHF. Recent reports by Lunde et al. [18], in contrast with those of Ward et al. [41] and Perreault et al. [28], showed no differences in the twitch or tetanic forces in the fast flexor digitorum brevis muscle with no changes in the force–Ca^{2+} relationship. However, they reported alterations in the contractile properties of the slow-twitch soleus muscle during fatigue, which they suggested to be consistent with reduced SR Ca^{2+} release and uptake.

Ward et al. [41] published the first report of single-fiber Ca^{2+} transients elicited by action potential stimulation in intact PMI rat skeletal muscle. Using multiphoton imaging, they found that EDL fibers from PMI rats exhibited weaker and slower Ca^{2+} dynamics, with a 40% reduction in amplitude and a 43% reduction in the initial rate of rise of the transients. In addition, the decay in fluorescence was significantly slower, and consequently, the TTP of transients was slightly increased. Thus, EDL muscle fibers from PMI rats exhibit alterations in both Ca^{2+}-release and Ca^{2+}-uptake properties of the SR.

In our investigation, the intramembrane charge movement and the calcium transients were measured using the double-Vaseline gap voltage clamp technique. There were no differences in the voltage dependence of the intramembrane charge movement between the sham-operated and PMI rats suggesting that the function and voltage dependence of the skeletal muscle-type DHPR are not altered after myocardial infarction. However, the global Ca^{2+} transients evoked by membrane depolarization displayed a characteristic reduction in the average amplitude and a lengthening of the rising phase, apparent as an increase in the TTP values, in PMI rats. There are at least three reasons that could underline this alteration: (1) the coupling between the DHPR and the RyR is modified, (2) the function, conductivity, and/or Ca^{2+} sensitivity of the RyR is altered, or (3) the calcium content of the SR is reduced under the diseased condition. To answer these questions, the elementary Ca^{2+}-release events and the function of the RyR were studied using confocal microscopy and lipid bilayer technique.

Alterations in local Ca^{2+} signaling and in RyR function

Ward et al. [41] showed alterations in the spatiotemporal properties of spontaneous Ca^{2+} sparks in EDL muscle from PMI rats. Populations of sparks from EDL fibers were significantly lower in amplitude and had slower temporal kinetics in CHF muscle, without evidence of alteration in SR Ca^{2+} load. Although mitochondria have been recently shown to contribute to the spatiotemporal time course of Ca^{2+} sparks, their lack of contribution in the global Ca^{2+} transient and the high buffering capacity in the myoplasm make it unlikely that mitochondria significantly affected Ca^{2+} sparks in our experiments.

Ward et al. [41] also demonstrated that RyR1 in PMI muscle is protein kinase A (PKA)-hyperphosphorylated and depleted of FKBP12. They suggested that the altered global and local Ca^{2+} signaling seen in the PMI model results from a PKA-dependent mechanism inducing a disruption of the FKBP12 interaction with the RyR1 and RyR1–DHPR. Our

szentesi.peter_292_24

data on the single channel characteristics showed that the voltage dependence of the RyRs is altered in PMI rats in positive potentials. However, there is no difference in the voltage dependence between the two groups in the physiological (more negative) voltages. In addition, we did not observe any clear subconductance states in RyR gating questioning any significant depletion of FKBP12 of RyR1. One could, however, speculate that while the depletion of FKBP12 seen by Ward et al. [41] was not enough to disrupt intersubunit interactions, it was sufficient to alter the coupling between neighboring channel complexes [23]. This would explain the reduced number of channels seen in the elementary events of calcium release (see above). Another difference in the biophysical properties of the RyR is the Ca^{2+} dependence of the channel activation and inactivation. The Ca^{2+} dependence of the activation of RyRs isolated from PMI rats is slightly shifted to the left; the Ca^{2+} dependence of the channel inactivation is shifted to higher cytoplasmic Ca^{2+} concentrations meaning that the Ca^{2+} sensitivity of the channel is reduced in PMI rats. These data suggest that the function, conductivity, and Ca^{2+} sensitivity of the RyR are altered in PMI rats.

Our data indicate that the single channel conductance of the control rats is around 520 pS in agreement with previous reports from our [7, 38] as well as from other laboratories [8, 17]. On the other hand, higher conductance—around 800 pS—has also been reported in a partially similar ionic environment [16, 40]. One explanation might be that in those measurements, liposome incorporated RyR1s were fused with the bilayer, while we and others [8] use CHAPS-solubilized RyR1. In addition, the different redox state of the preparations may also contribute to the observed differences.

Altered open probability and gating behavior of RyR1 of PMI rats were reported earlier and attributed to the different levels in their phosphorylation [31] or that of calstabin [22] without significant changes in the calcium current through RyR1 driven by the calcium gradient. In addition, PKA phosphorylation was reported to markedly increase the P_o and significantly elevate the specific conductance of RyR2 with an increase of about 39% in the single channel conductance [1]. However, no rectifying effect of PKA phosphorylation was observed. Our data shows an increase of about 46% in the single channel conductance in a rectifying fashion; that is, increased conductivity is present only at positive voltages, when cations move from the cytoplasmic toward the luminal side of the channel.

Taken together, our data are not inconsistent with the following framework of events. Because RyR conductance at negative voltages was found to be unaltered and SR calcium load was previously reported unchanged, the reduced amplitude and SM of calcium sparks together with an increased proportion of embers clearly indicates that in CHF, the number of calcium-release channels that open during a spontaneous calcium-release event is considerably reduced. Although the increased rise time of the calcium sparks may intrinsically originate from their smaller amplitude, the altered Ca^{2+} concentration dependence of RyR inactivation observed in these experiments could also contribute. All in all, the reduction in functioning calcium-release channels, their altered kinetics, and modified recruitment readily explain the suppression and the prolonged TTP of the global calcium transient in this animal model. These specific alterations in EC coupling could thus play a significant role in the skeletal muscle-specific force decrements and reduced exercise tolerance seen in humans and in experimental models of myocardial overload. Moreover, because cellular Ca^{2+} homeostasis has been shown to play a crucial role in the determination of muscle fiber type, these alterations in RyR1-dependent Ca^{2+} release may play a determinant role in the remodeling of the skeletal muscle that occurs secondary to chronic myocardial overload and CHF. These alterations in the Ca^{2+} handling of the skeletal muscle may answer the reduced contractility of skeletal muscle in patients with CHF.

Acknowledgments The authors are indebted for the excellent technical assistance from R. Öri. G.P. Szigeti holds a Bolyai Fellowship from the Hungarian Academy of Sciences. This work was supported by OTKA T049151, T61442 and NK61412. Guy Vassort held an INSERM position. He would like to thank A. Lacampagne for a very stimulating discussion.

References

1. Carter S, Colyer J, Sitsapesan R (2006) Maximum phosphorylation of the cardiac ryanodine receptor at serine-2809 by protein kinase a produces unique modifications to channel gating and conductance not observed at lower levels of phosphorylation. Circ Res 98:1506–1513
2. Cheng H, Song LS, Shirokova N, Gonzalez A, Lakatta EG, Rios E, Stern MD (1999) Amplitude distribution of calcium sparks in confocal images: theory and studies with an automatic detection method. Biophys J 76:606–617
3. Clark AL, Poole-Wilson PA, Coats A (1996) Exercise limitation in chronic heart failure: central role of the periphery. J Am Coll Cardiol 28:1092–1102
4. Coats AJ (1996) The "muscle hypothesis" of chronic heart failure. J Mol Cell Cardiol 28:2255–2262
5. Cohn JN, Johnson GR, Shabetai R, Loeb H, Tristani F, Rector T, Smith R, Fletcher R (1993) Ejection fraction, peak exercise oxygen consumption, cardiothoracic ratio, ventricular arrhythmias, and plasma norepinephrine as determinants of prognosis in heart failure. The V-HeFT VA Cooperative Studies Group. Circulation 87:VI5–V16
6. Csernoch L, Pizarro G, Uribe I, Rodriguez M, Rios E (1991) Interfering with calcium release suppresses I gamma, the "hump" component of intramembranous charge movement in skeletal muscle. J Gen Physiol 97:845–884

7. Csernoch L, Szentesi P, Sarkozi S, Szegedi Cs, Jona I, Kovacs L (1999) Effects of tetracaine on sarcoplasmic calcium release in mammalian skeletal muscle fibres. J Physiol 515:843–857
8. Delbono O, Chu A (1995) Ca^{2+} release channels in rat denervated skeletal muscle. Exp Physiol 80:561–574
9. De Sousa E, Veksler V, Bigard X, Mateo P, Ventura-Clapier R (2000) Heart failure affects mitochondrial but not myofibrillar intrinsic properties of skeletal muscle. Circulation 102:1847–1853
10. Fabiato A (1988) Computer programs for calculating total from specified free or free from specified total ionic concentrations in aqueous solutions containing multiple metals and ligands. Methods Enzymol 157:378–417
11. Hollingworth S, Peet J, Chandler WK, Baylor SM (2001) Calcium sparks in intact skeletal muscle fibers of the frog. J Gen Physiol 118:653–678
12. Jondeau G, Katz SD, Zohman L, Goldberger M, McCarthy M, Bourdarias J-P, LeJemtel TH (1992) Active skeletal muscle mass and cardiopulmonary reserve. Failure to attain peak aerobic capacity during maximal bicycle exercise in patients with severe congestive heart failure. Circulation 86:1351–1356
13. Kirsch WG, Uttenweiler D, Fink RHA (2001) Spark- and ember-like elementary Ca^{2+} release events in skinned fibers of adult mammalian skeletal muscle. J Physiol 537:379–389
14. Klein MG, Lacampagne A, Schneider MF (1997) Voltage dependence of the pattern and frequency of discrete Ca^{2+} release events after brief repriming in frog skeletal muscle. Proc Natl Acad Sci USA 94:11061–11066
15. Kovács L, Rios E, Schneider MF (1983) Measurement and modification of free calcium transients in frog skeletal muscle fibres by a metallochromic indicator dye. J Physiol 343:161–196
16. Lai FA, Meissner G (1990) Structure of the calcium release channel of skeletal muscle sarcoplasmic reticulum and its regulation by calcium. Adv Exp Med Biol 269:73–77
17. Laver DR, Eager KR, Taoube L, Lamb GD (2000) Effects of cytoplasmic and luminal pH on Ca^{2+} release channels from rabbit skeletal muscle. Biophys J 78:1835–1851
18. Lunde PK, Sejersted OM, Thorud HM, Tonnessen T, Henriksen UL, Christensen G, Westerblad H, Bruton J (2006) Effects of congestive heart failure on Ca^{2+} handling in skeletal muscle during fatigue. Circ Res 98:1514–1519
19. Lunde PK, Dahlstedt AJ, Bruton JD, Lannergren J, Thoren P, Sejersted OM, Westerblad H (2001) Contraction and intracellular Ca^{2+} handling in isolated skeletal muscle of rats with congestive heart failure. Circ Res 88:1299–1305
20. Lunde PK, Verburg E, Eriksen M, Sejersted OM (2002) Contractile properties of in situ perfused skeletal muscles from rats with congestive heart failure. J Physiol 540:571–580
21. Mancini D, LeJemtel T, Aaronson K (2000) Peak VO(2): a simple yet enduring standard. Circulation 101:1080–1082
22. Marks AR (2002) Ryanodine receptors, FKBP12, and heart failure. Front Biosci 7:d970–d977
23. Marx SO, Ondrias K, Marks AR (1998) Coupled gating between individual muscle Ca^{2+} release channels (ryanodine receptors). Science 281:818–821
24. Massie BM, Conway M, Rajagopalan B, Yonge R, Frostick S, Ledingham J, Sleight P, Radda G (1988) Skeletal muscle metabolism during exercise under ischemic conditions in congestive heart failure. Evidence for abnormalities unrelated to blood flow. Circulation 78:320–326
25. Melzer W, Rios E, Schneider MF (1986) The removal of myoplasmic free calcium following calcium release in frog skeletal muscle. J Physiol 372:261–292
26. Mettauer B, Lampert E, Petitjean P, Bogui P, Epailly E, Schnedecker B, Geny BEB, Haberey P, Lonsdorfer J (1996) Persistent exercise intolerance following cardiac transplantation despite normal oxygen transport. Int J Sports Med 17:277–286
27. Mettauer B, Zoll J, Garnier A, Ventura-Clapier R (2006) Heart failure: a model of cardiac and skeletal muscle energetic failure. Pflugers Arch 452:653–666
28. Perreault CL, Gonzalez-Serratos H, Litwin SE, Sun X, Franzini-Armstrong C, Morgan JP (1993) Alterations in contractility and intracellular Ca^{2+} transients in isolated bundles of skeletal muscle fibers from rats with chronic heart failure. Circ Res 73:405–412
29. Peters DG, Mitchell HL, McCune SA, Park S, Williams JH, Kandarian SC (1997) Skeletal muscle sarcoplasmic reticulum Ca^{2+}-ATPase gene expression in congestive heart failure. Circ Res 81:703–710
30. Poole-Wilson PA, Ferrari R (1996) Role of skeletal muscle in the syndrome of chronic heart failure. J Mol Cell Cardiol 28:2275–2285
31. Reiken S, Lacampagne A, Zhou H, Kherani A, Lehnart SE, Ward C, Huang F, Gaburjakova M, Gaburjakova J, Rosemblit N, Warren MS, He KL, Yi GH, Wang J, Burkhoff D, Vassort G, Marks AR (2003) PKA phosphorylation activates the calcium release channel (ryanodine receptor) in skeletal muscle: defective regulation in heart failure. J Cell Biol 160:919–928
32. Sabbah HN, Hansen-Smith F, Sharov VG, Kono T, Lesch M, Gengo PJ, Steffen RP, Levine TB, Goldstein S (1993) Decreased proportion of type I myofibers in skeletal muscle of dogs with chronic heart failure. Circulation 87:1729–1737
33. Sarkozi S, Szentesi P, Jona I, Csernoch L (1996) Effects of cardiac glycosides on excitation–contraction coupling in frog skeletal muscle fibres. J Physiol 495:611–626
34. Simonini A, Chang K, Yue P, Long CS, Massie BM (1999) Expression of skeletal muscle sarcoplasmic reticulum calcium-ATPase is reduced in rats with postinfarction heart failure. Heart 81:303–307
35. Stratton JR, Kemp GJ, Daly RC, Yacoub M, Rajagopalan B (1994) Effects of cardiac transplantation on bioenergetic abnormalities of skeletal muscle in congestive heart failure. Circulation 89:1624–1631
36. Sullivan MJ, Knight JD, Higginbotham MB, Cobb FR (1989) Relation between central and peripheral hemodynamics during exercise in patients with chronic heart failure. Muscle blood flow is reduced with maintenance of arterial perfusion pressure. Circulation 80:769–781
37. Szentesi P, Jacquemond V, Kovacs L, Csernoch L (1997) Intramembrane charge movement and sarcoplasmic calcium release in enzymatically isolated mammalian skeletal muscle fibres. J Physiol 505:371–384
38. Szentesi P, Szappanos H, Szegedi C, Gonczi M, Jona I, Cseri J, Kovacs L, Csernoch L (2004) Altered elementary calcium release events and enhanced calcium release by thymol in rat skeletal muscle. Biophys J 86:1436–1453
39. Tripathy A, Meissner G (1996) Sarcoplasmic reticulum lumenal Ca^{2+} has access to cytosolic activation and inactivation sites of skeletal muscle Ca^{2+} release channel. Biophys J 70:2600–2615
40. Wang Y, Xu L, Pasek DA, Gillespie D, Meissner G (2005) Probing the role of negatively charged amino acid residues in ion permeation of skeletal muscle ryanodine receptor. Biophys J 89:256–265
41. Ward CW, Reiken S, Marks AR, Marty I, Vassort G, Lacampagne A (2003) Defects in ryanodine receptor calcium release in skeletal muscle from post-myocardial infarct rats. FASEB J 17:1517–1519
42. Williams JH, Ward CW (1998) Changes in skeletal muscle sarcoplasmic reticulum function and force production following myocardial infarction in rats. Exp Physiol 83:85–94
43. Wilson JR, Groves J, Rayos G (1996) Circulatory status and response to cardiac rehabilitation in patients with heart failure. Circulation 94:1567–1572
44. Zhou J, Brum G, Gonzalez A, Launikonis BS, Stern MD, Rios E (2003) Ca^{2+} sparks and embers of mammalian muscles. Properties of the sources. J Gen Physiol 122:95–114

Author's personal copy

szentesi.peter_292_24

Cell Calcium 46 (2009) 347–355

Contents lists available at ScienceDirect

Cell Calcium

journal homepage: www.elsevier.com/locate/ceca

Altered sarcoplasmic reticulum calcium transport in the presence of the heavy metal chelator TPEN

Mónika Sztretye[a,1], János Almássy[a], Tamás Deli[a], Péter Szentesi[a], Carole Jung[b,2], Beatrix Dienes[a], Cecilia A. Simut[a], Ernst Niggli[b], István Jona[a], László Csernoch[a,*]

[a] Department of Physiology, Medical and Health Science Center, University of Debrecen, Nagyerdei krt. 98, H-4012 Debrecen, Hungary
[b] Department of Physiology, University of Bern, Buehlplatz 5, 3012 Bern, Switzerland

ARTICLE INFO

Article history:
Received 13 January 2009
Received in revised form 1 October 2009
Accepted 5 October 2009
Available online 8 November 2009

Keywords:
TPEN
Ryanodine receptor
Sarcoplasmic reticulum
Ca^{2+} spark
Ca^{2+} pump
Lipid bilayer
Confocal microscopy
Ca^{2+} homeostasis

ABSTRACT

TPEN (N,N,N′,N′-tetrakis(2-pyridylmethyl)-ethylenediamine) is a membrane-permeable heavy-metal ion chelator with a dissociation constant for Ca^{2+} comparable to the Ca^{2+} concentration ($[Ca^{2+}]$) within the intracellular Ca^{2+} stores. It has been used as modulator of intracellular heavy metals and of free intraluminal $[Ca^{2+}]$, without influencing the cytosolic $[Ca^{2+}]$ that falls in the nanomolar range. In our previous studies, we gave evidence that TPEN modifies the Ca^{2+} homeostasis of striated muscle independent of this buffering ability. Here we describe the direct interaction of TPEN with the ryanodine receptor (RyR) Ca^{2+} release channel and the sarcoplasmic reticulum (SR) Ca^{2+} pump (SERCA). In lipid bilayers, at negative potentials and low $[Ca^{2+}]$, TPEN increased the open probability of RyR, while at positive potentials it inhibited channel activity. On permeabilized skeletal muscle fibers of the frog, but not of the rat, 50 μM TPEN increased the number of spontaneous Ca^{2+} sparks and induced propagating events with a velocity of 273 ± 7 μm/s. Determining the hydrolytic activity of the SR revealed that TPEN inhibits the SERCA pump, with an $IC_{50} = 692 \pm 62$ μM and a Hill coefficient of 0.88 ± 0.10. These findings provide experimental evidence that TPEN directly modifies both the release of Ca^{2+} from and its reuptake into the SR.

© 2009 Elsevier Ltd. All rights reserved.

1. Introduction

Excitation–contraction (E–C) coupling in skeletal muscle critically depends on the concerted action of two proteins, dihydropyridine receptors (DHPR) and ryanodine receptors (RyR). DHPR serves as the voltage sensor while RyR is the Ca^{2+} release channel of the sarcoplasmic reticulum (SR) susceptible to activation and inhibition by Ca^{2+} [1,2]. The arrival of the action potential at the transverse (T)-tubule initiates the release of Ca^{2+} through RyR; while the released calcium was suggested to trigger the activation of neighboring RyRs [3] via the Ca^{2+}-induced Ca^{2+} release mechanism (CICR).

While CICR has been shown to have a limited role in intact mammalian skeletal muscle [4,48], it plays a fundamental role in cardiac cells [5–7]. CICR is also important in amphibian skeletal muscle [3,8,9]. Different molecular makeup and supramolecular assembly of their E–C coupling devices may explain the differences observed between the species [4,10–12]. Furthermore, CICR becomes active after fiber permeabilization [13] and after mechanical stress [14] in mammalian skeletal muscle.

Global changes in intracellular Ca^{2+} concentration ($[Ca^{2+}]_i$) and the underlying SR Ca^{2+} release is made up of elementary calcium release events (ECRE) reflecting the opening of a single or a small cluster of RyR. ECRE termed Ca^{2+} sparks were first observed and described in cardiac myocytes [15,16] followed by their characterization in frog skeletal muscle [9,17]. RyR and thus Ca^{2+} sparks are modulated by a variety of intracellular second messengers and ions, including Ca^{2+} and Mg^{2+} [1]. The latter was shown to inhibit CICR [18–20] resulting in a strong negative correlation between spark frequency and intracellular Mg^{2+} concentration ($[Mg^{2+}]_I$) [21]. Not only the intracellular environment but also the SR Ca^{2+} content seems to play an important role in the regulation of ECRE [22,23].

Heavy metal ions have also been reported to influence $[Ca^{2+}]_i$ of cells in numerous ways. Zn^{2+} alters Ca^{2+} currents of L-type Ca^{2+} channels in cardiomyocytes [51], while Hg^{2+} induces sustained increases in $[Ca^{2+}]_i$ and triggers Ca^{2+} waves in RTH-149 hepatoma cells [24]. Salama et al. [25] showed that Hg^{2+}, Cu^{2+}, Cd^{2+}, Ag^{+} and Ni^{2+} elicit contractions of rabbit skeletal muscle fibers by oxidizing

* Corresponding author at: Department of Physiology, University of Debrecen, P.O. Box 22, H-4012 Debrecen, Hungary. Tel.: +36 52 255 575; fax: +36 52 255 116.
E-mail address: csl@phys.dote.hu (L. Csernoch).
[1] Present address: Department of Molecular Biophysics and Physiology, Rush University Medical Center, 1750 W. Harrison Street, Chicago, IL 60612, USA.
[2] Present address: Laboratory of Molecular Physiology and Channelopathies, Dept. Ciències Experimentals i de la Salut, Universitat Pompeu Fabra, C\ Dr. Aiguader 80, Barcelona 08003, Spain.

0143-4160/$ – see front matter © 2009 Elsevier Ltd. All rights reserved.
doi:10.1016/j.ceca.2009.10.002

Author's personal copy

szentesi.peter_292_24

reactive sulfhydryl sites on an SR protein to open SR Ca^{2+} release channels.

These observations suggest that a heavy metal chelator and membrane permeable Ca^{2+} buffer that is able to modulate SR calcium content should strongly influence Ca^{2+} homeostasis and E–C coupling. Indeed, a number of studies have utilized TPEN (N,N,N′,N′-tetrakis-(2-pyridylmethyl)-ethylenediamine) to modify the intracellular ionic composition of cells (e.g. [26]). In recent studies, the hypothesis that TPEN is capable of modulating EC coupling was tested on striated muscle in detail [27,50]. Quite unexpectedly, we found that low concentrations (20–50 μM) of the buffer initiated Ca^{2+} waves in cardiac myocytes and triggered SR Ca^{2+} release in cultured C2C12 cells. At higher concentrations (above 100 μM) of the buffer suppressed caffeine-induced Ca^{2+} transients and slowed the removal of Ca^{2+} from the myoplasm.

Although a few studies have focused on the possible effects of TPEN on Ca^{2+} homeostasis in muscle cells, little is known regarding its interaction with the two most important proteins participating in Ca^{2+} homeostasis, the skeletal muscle Ca^{2+} release channel and the SR Ca^{2+} ATPase (SERCA). Here we demonstrate that low concentrations (~50 μM) of the drug increase the open probability of RyRs incorporated into planar lipid bilayers at membrane potentials below −20 mV. We also found that the same concentration of TPEN increases the frequency of spontaneous Ca^{2+} sparks and gives rise to propagating events on permeabilized muscle fibers of frogs but not of rats. In addition, increasing $[Mg^{2+}]_i$ interfered with the ability of TPEN to augment Ca^{2+} sparks. On the other hand, concentrations that are an order of magnitude greater (~500 μM) suppressed the open probability of RyR and decreased the hydrolytic activity of SERCA. These results clearly establish that TPEN directly interferes with the function of both key players of E–C coupling, the SR Ca^{2+} release channel and the SR Ca^{2+} pump.

2. Materials and methods

2.1. Isolation of single fibers and preparation of HSR vesicles

For measuring Ca^{2+} sparks single fibers were either isolated enzymatically from the *m. extensor digitorum communis* of the rat or dissected manually from the *m. semitendinosus* of the frog (*Rana esculenta*) as described earlier [28]. Both muscles contain more than 95% fast twitch fibre [29,30].

For planar lipid bilayer experiments and measurement of the SR Ca^{2+} pump activity, heavy SR (HSR) vesicles were isolated from rabbit skeletal muscles (*m. longissimus dorsi*) according to the method described by Lai and Meissner [31] with slight modifications [32]. Bands corresponding to the HSR fractions were collected from the 36–38% region of continuous sucrose gradient, pelleted at 124,000 × *g* for 60 min, resuspended in 0.4 mM sucrose, 10 mM K^+ PIPES, pH 7.0. HSR vesicles were then either snap frozen in liquid nitrogen and stored at −70° C for ATPase activity measurements or were instantly used for ryanodine receptor purification as described earlier [33]. Protein concentration was determined by the Lowry method [34].

All animals included in this study were sacrificed in accordance with the guidelines of the European Community (86/609/EEC) following a protocol approved by the institutional Animal Care Committee of the University of Debrecen.

2.2. Measurement of Ca^{2+} sparks

Isolated skeletal muscle fibers were mounted into a chamber with glass bottom and treated with a modified relaxing solution (in mM: 100 K-glutamate for rats or 140 K-glutamate for frogs, 10 HEPES, 1 EGTA, 5.5 $MgCl_2$, 5 Na_2-ATP, 10 Na-phosphocreatine, 10 glucose, 0.13 $CaCl_2$ and 8% dextran, pH 7.2 for rats and pH 7.0 for frogs) containing 0.002% and 0.004% saponin, respectively, for 2–3 min as described in Szentesi et al. [35]. Permeabilization of the surface membrane was monitored by the addition of 50 μM fluo-3 into the solution while imaging of the fiber. This solution was then exchanged to an internal solution (K-glutamate in case of frogs or K_2SO_4-based relaxing solution in case of rats) supplemented with 0.1 mM fluo-3. Unless otherwise stated the internal solution contained 5.5 or 6 mM total $MgCl_2$, in case of frogs and rats, respectively. The solution containing lowered Mg^{2+} concentration for frogs had 5 mM total $MgCl_2$.

The chamber was mounted on the stage of an inverted microscope (Axiovert 200, Zeiss, Oberkochen, Germany) equipped for confocal scanning of laser-excited fluorescence (LSM 510 META, Zeiss,) as described earlier [35]. Line scan images ($[x,t]$) were taken at 1.53 ms/line and 512 pixels/line (pixel size 0.142 μm) with a 63× water immersion objective (numerical aperture = 1.2; Zeiss). Fluo-3 was excited with an Argon ion laser (at 488 nm), emitted light was collected through a band-pass filter (505–570 nm) and digitized at 12 bit. The images ($F[x,t]$) were normalized to baseline fluorescence ($F_0[x]$). All measurements were carried out at room temperature (22–23 °C).

Elementary Ca^{2+} release events were captured using an automatic computer detection routine (e.g. [36]) as described in our earlier reports [35,37]. Sparks with amplitudes smaller than 0.2 $\Delta F/F_0$ units and embers with average amplitudes smaller than 0.05 $\Delta F/F_0$ units were excluded from the analysis. If the event was longer than 40 pixels in time and had a clear plateau, it was identified as an ember; otherwise, it was taken to be a spark.

2.3. Planar lipid bilayer measurements

CHAPS solubilized ryanodine receptors [38] were incorporated into planar lipid bilayers formed across a 250 μm aperture of a nolrene cup using a lipid mixture composed of phosphatidyl-ethanolamine, phosphatidyl-serine and phosphatidyl-choline in the weight ratio of 5:4:1. Lipids were obtained from Avanti Polar Lipids (Alabaster, AL, USA) and dissolved in *n*-decane up to a final concentration of 20 mg/ml as described in our previous reports [32]. Reconstitution was initiated in symmetric buffer solution (250 mM KCl, 100 μM EGTA, 150 μM $CaCl_2$, 20 mM PIPES, pH 7.4), by adding a small aliquot of the solubilized receptor to the *cis* (cytoplasmic) side. The current signal was filtered at 1 kHz through an 8-pole low-pass Bessel filter and digitized at 5 kHz using an Axopatch 200 amplifier and pClamp software (Axon Instruments, Foster City, CA, USA). Channels with conductance higher than 400 pS were accepted as RyR. Open probability values were calculated from 1- to 2-min-long segments of the current traces. Measurements were carried out at 22–25 °C, TPEN was applied in the *cis* chamber. After the addition of TPEN 5 min were allowed to reach the new equilibrium.

2.4. Measurement of the SERCA activity

ATPase activity was determined at 37 °C by a coupled enzyme assay in a medium containing 100 mM KCl, 20 mM Tris–HCl, 5 mM $MgCl_2$, 5 mM ATP, 0.42 mM phospho(ε) pyruvate, 0.001 mM A23187 (calcium ionophore), 0.2 mM NADH, 7.5 U/ml pyruvate-kinase, 18 U/ml lactate-dehydrogenase (pH 7.4). Total hydrolytic activity was measured as the decrease of optical density at the NADH absorbance wavelength (342 nm), and is expressed in μmol Pi/mg protein/min, abbreviated as I.U. throughout the text and figures. Total hydrolytic activity ranged from 6.83 to 7.56 I.U. SERCA-dependent ATPase activity was identified as the portion of total hydrolytic activity inhibited by thapsigargin (5 μM). TPEN was added to the vesicles 5 min before starting measurements of

Author's personal copy

szentesi.peter_292_24

enzyme activity. The assay was performed in the presence of Ca^{2+} and EGTA mixture producing estimated free Ca^{2+} concentration of 2.9 μM [47] which was found to induce maximum SERCA activation.

The concentration dependent effects of TPEN on the ATPase activity were fitted with the Hill equation:

$$\frac{\text{ATPase activity}}{\text{ATPase activity max}} = 1 - \frac{[Ca^{2+}]^n}{[IC_{50}]^n + [Ca^{2+}]^n} \quad (1)$$

where ATPase activity is the activity of SERCA, ATPase activity_{max} is the theoretical maximum of the activity, $[IC_{50}]$ is the half effective inhibitory concentrations while n_l is the Hill coefficient.

2.5. Chemicals

Fluo-3 was purchased from Molecular Probes (Eugene, OR, USA) while all other chemicals were of analytical grade (Sigma).

2.6. Statistics

Data are presented as the mean ± standard error (SE) of the mean. The statistical significance between experimental groups was assessed using Student's *t*-test assuming significant difference for $p < 0.05$.

3. Results

3.1. TPEN inhibits ECRE on isolated rat muscle fibers

Our former experiments on isolated cardiac [27] as well as on cultured skeletal muscle cells [50] suggested an activation of RyRs by low TPEN concentrations (20–50 μM). To better understand the effects of this buffer on Ca^{2+} release and to study the TPEN–RyR interaction *in situ*, elementary calcium release events were measured in isolated adult mammalian muscle fibers of the rat.

As expected (see e.g. [13,34]), both Ca^{2+} sparks and embers were readily observed under control conditions after permeabilization (Fig. 1A). Surprisingly, compared to what was described on cardiac muscle [27] the addition of 50 μM TPEN resulted in suppression rather than augmentation of spontaneous spark activity. A total of 574, 159 and 197 sparks were detected and analyzed under control conditions, in the presence of 50 and 500 μM TPEN, respectively. The number of embers decreased (from the control value of 154) to the extent 6 in the presence of 50 μM TPEN that prevented reliable analysis and comparison. The following experiments thus focus on Ca^{2+} sparks.

The characteristic parameters of Ca^{2+} sparks are presented in Table 1. Under control conditions, sparks occurred with an appreciable frequency ($0.032 \pm 0.005\ s^{-1}$ sarcomere^{-1}) and displayed all the characteristic parameters described earlier (e.g. [13,34]). Although the frequency of Ca^{2+} sparks did not change significantly in the presence of 50 μM TPEN ($0.031 \pm 0.014\ s^{-1}$ sarcomere^{-1}, $p > 0.9$; Fig. 1B), increasing the concentration of the buffer to 500 μM significantly reduced the frequency ($0.021 \pm 0.026\ s^{-1}$ sarcomere^{-1}, $p < 0.05$; Fig. 1C). Together with the decrease in the number of events their morphology was also altered by TPEN with a significant reduction in event amplitude, duration and FWHM for the latter concentration (see Table 1). These alterations in amplitude and FWHM are clearly visible from the histograms presented in Fig. 1D. Note especially the shift to smaller values with increasing TPEN concentrations resulting in a steeper decline of the amplitude histograms. A similar shift to the left is present in the histogram of FWHM for 500 μM TPEN.

3.2. TPEN alters the frequency and morphology of Ca^{2+} sparks in isolated frog muscle fibers

The notable difference in the process of SR Ca^{2+} release between adult mammalian skeletal muscle fibers *versus* cardiac and cultured skeletal muscle cells are attributed to a lack of CICR in the former. Since it is now generally accepted for amphibian skeletal muscle fibers that CICR plays an important role in recruiting neighboring Ca^{2+} release channels during a Ca^{2+} spark, we explored how TPEN modifies spontaneously occurring Ca^{2+} release events using single skeletal muscle fibers from adult frogs. To facilitate CICR a slightly reduced $[Mg^{2+}]_i$ (see Section 2) was used.

A total of 4365, 9885 and 286 sparks were detected and analyzed under control conditions and in the presence of 50 and 200 μM TPEN, respectively, and their characteristic parameters are presented in Table 2. Low concentrations of the buffer (50 μM) clearly enhanced (Fig. 2A), while higher concentrations (200 μM) inhibited (Fig. 2B) the spontaneous spark activity of the fibers as indicated by changes in most of the parameters of Ca^{2+} sparks from which the most striking was the change in event frequency. While under control conditions the frequency was $0.23 \pm 0.05\ s^{-1}$ sarcomere^{-1}, in the presence of 50 μM TPEN it increased to 143% of control. 200 μM of the drug, on the other hand, decreased it to 39% of control.

Not only did the application of 50 μM TPEN modify the frequency, it also clearly altered the morphology of Ca^{2+} sparks as can be assessed by comparing the *x–y* (Fig. 2A) and line scan images of permeabilized fibers (Fig. 2B) and of individual events (Fig. 2C). Most strikingly, the presence of 50 μM of the drug gave rise to propagating Ca^{2+} sparks. Three typical examples of such propagating events are presented in Fig. 2D on an extended scale: a spark propagating in one (left panel), or propagating in two directions (middle panel) from a single source and two sparks converging from two sources (right panel). In the latter case, the two sources were close enough and the propagation directions were opposite, thus colliding sparks annihilated each other. All these features, together with the straight wave front are all characteristics of CICR-based propagation [35]. The velocity of propagation of Ca^{2+} release could be calculated from the cotangent of the angle of the spark's wave front as depicted in Fig. 2D. Its average was found to be $273 \pm 7\ \mu m\ s^{-1}$ ($n = 62$), in good agreement with previous results [39].

The buffer altered not only the global appearance but also the characteristic parameters of Ca^{2+} sparks. Control values for the duration (41.3 ± 0.2 ms), FWHM (2.12 ± 0.01 μm) and amplitude (0.92 ± 0.005) were modified to 102.3%, 113.6% and 84.7% of the control by 50 μM, and to 73.4%, 82% and 70.6% of the control by 200 μM TPEN, respectively (see Table 2). The increase in FWHM in 50 μM TPEN presumably reflects an increased number of neighboring release channels that were opened by the released Ca^{2+}, that is, a more effective CICR during the event.

Noteworthy is the observation that 200 μM TPEN had in some cases, as for the frequency and FWHM, opposite effects as 50 μM did. In addition, propagating events were never observed in the presence of 200 μM TPEN. These observations clearly indicate the presence of at least two separate mechanisms that are differently affected by low and high concentrations of TPEN, respectively.

To further test the concept that the presence of CICR is important in the effect of 50 μM TPEN, measurements were carried out after slightly elevating $[Mg^{2+}]_i$ in the internal solution to obtain a condition which is known to suppress CICR. As shown in Table 2 50 μM TPEN had essentially the opposite effects to those measured at lower $[Mg^{2+}]_i$. The buffer suppressed rather than increased both the frequency and the FWHM of Ca^{2+} sparks. In addition, a slight increase in event amplitude was also observed.

To visualize the alteration in the morphology of Ca^{2+} sparks, the two-dimensional distribution of the amplitudes and FWHM are presented in Fig. 3 for control conditions (Fig. 3A and C) and

Author's personal copy

szentesi.peter_292_24

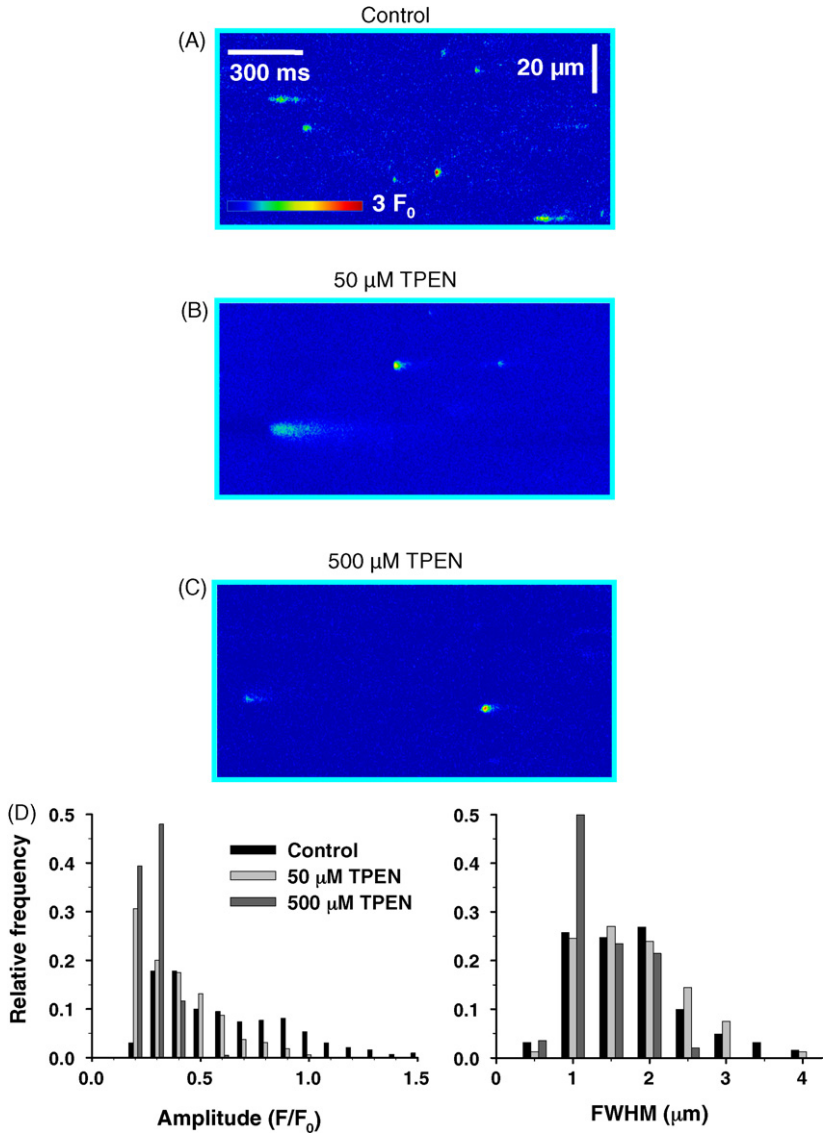


Fig. 1. Calcium release events in control and in the presence of TPEN in rat skeletal muscle fibers. Line-scan images of a fiber in control (A), in 50 μM (B) and 500 μM TPEN (C). Scanning was made parallel with the fiber axis. Images were corrected for background fluorescence (F/F_0) and pseudo-colored. Note the small number of events in 500 μM TPEN. (D) Histograms for the amplitude and FWHM of Ca^{2+} sparks measured under control conditions and in the presence of 50 and 500 μM TPEN. The mean values of the parameters of Ca^{2+} sparks are given in Table 1.

Table 1
Characteristic parameters of Ca^{2+} sparks from rats.

	n	Amplitude ($\Delta F/F_0$)	FWHM (μm)	Duration (ms)	Frequency (s^{-1} sarcomere^{-1})
Control	574	0.80 ± 0.01	1.52 ± 0.03	41.84 ± 0.63	0.032 ± 0.005
50 μM TPEN	159	0.43 ± 0.01*	1.54 ± 0.05	34.81 ± 1.06*	0.031 ± 0.014
500 μM TPEN	197	0.32 ± 0.01*	1.09 ± 0.03*	36.68 ± 0.98*	0.021 ± 0.026

* Significant difference ($p < 0.001$) between the control and TPEN.

Table 2
Characteristic parameters of Ca^{2+} sparks from frogs.

	Total $[Mg^{2+}]_i$ (mM)	n	Amplitude ($\Delta F/F_0$)	FWHM (μm)	Duration (ms)	Frequency (s^{-1} sarcomere^{-1})
Control	5.5	1561	0.84 ± 0.01	2.16 ± 0.02	34.8 ± 0.3	0.19 ± 0.02
50 μM TPEN	5.5	2101	0.95 ± 0.01*	1.95 ± 0.02*	29.1 ± 0.1*	0.10 ± 0.01**
Control	5	4365	0.92 ± 0.005	2.12 ± 0.01	41.3 ± 0.2	0.23 ± 0.05
50 μM TPEN	5	9885	0.78 ± 0.003*	2.41 ± 0.01*	42.3 ± 0.2*	0.33 ± 0.02**
200 μM TPEN	5	286	0.65 ± 0.03*	1.74 ± 0.04*	30.3 ± 0.8*	0.09 ± 0.02**

* Significant difference ($p < 0.001$) between the control and TPEN.
** Significant difference ($p < 0.05$) between the control and TPEN.

Author's personal copy

szentesi.peter_292_24

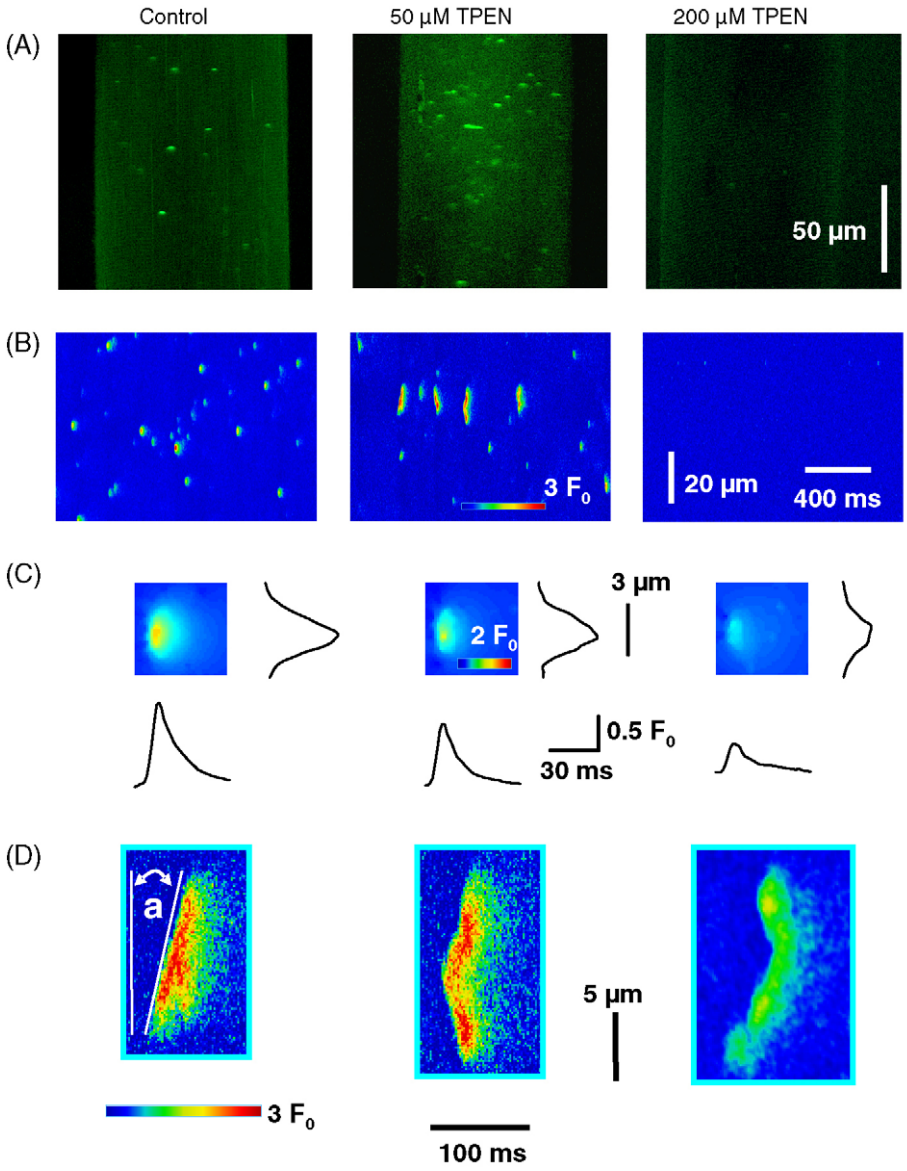


Fig. 2. Alteration of elementary calcium release events in the presence of TPEN. (A) *x*–*y* images of saponin permeabilized frog fibers immersed into a low-magnesium internal solution. Note the presence of large sparks in 50 µM and the absence of sparks in 200 µM TPEN. (B) Line-scan images of fibers presented in (A). Scanning was made perpendicular to the fiber axis. Note the traveling sparks in the presence of 50 µM of the calcium buffer. (C) Typical examples of Ca^{2+} sparks measured in the absence and presence of TPEN. The time course and spatial spread of each spark, displayed below and next to the images, respectively, were calculated by averaging three neighboring lines. (D) Three typical examples of the propagating Ca^{2+} sparks seen in 50 µM TPEN. The angle of the wave front (α in the leftmost image) was used to estimate the speed of propagation (proportional to ctg(α)) and was found to be 299 µm s^{-1} for this particular event.

in the presence 50 µM TPEN (Fig. 3B and D) at both $[Mg^{2+}]_i$ used. To this end, amplitudes and FWHM were binned and the relative frequency of the events that fell into a given bin for both the amplitude and FWHM were plotted as a surface. The distributions clearly demonstrate that the effects of 50 µM TPEN on event amplitude and FWHM depended on the $[Mg^{2+}]_i$ used. Note especially the shift to higher FWHM values for 50 µM TPEN in the presence of lowered $[Mg^{2+}]_i$.

3.3. *TPEN affects the open probability of isolated RyRs in a concentration and voltage dependent manner*

Data in the previous sections suggested that TPEN might directly influence the activity of the Ca^{2+} release channel itself. To test this hypothesis isolated Ca^{2+} release channels (RyR1 tetramers) were incorporated into planar lipid bilayers and the properties of channel gating were determined.

At 470 nM (ionized) Ca^{2+} concentration the channels displayed low open probability ($P_o = 0.0076 \pm 0.0018$, Fig. 4A and B). Following the addition of 50, 100, and 200 µM TPEN the open probability increased, demonstrating a direct activation of the Ca^{2+} release channel by the drug at negative membrane potentials. This activation by TPEN at negative potentials was also present at 50 µM free Ca^{2+} concentration, with slightly different parameters (Fig. 4). At positive (+85 mV) potentials, the effect of TPEN was quite the opposite. The addition of 50 µM of the drug resulted in a substantial decrease in open probability (Fig. 5) from $P_{o,contr} = 0.208 \pm 0.024$ to $P_{o,TPEN} = 0.0014 \pm 0.002$ (Fig. 5A, traces a and b), while at −85 mV the activation was still present (Fig. 5A, traces d and e). Fig. 5A also demonstrates that TPEN did not interfere with the ability of ryanodine to lock the Ca^{2+} release channel in the characteristic, half-conducting state (traces c and f).

The voltage dependence of how TPEN alters RyR function was also tested by determining the relative open probability, comparing

Author's personal copy

szentesi.peter_292_24

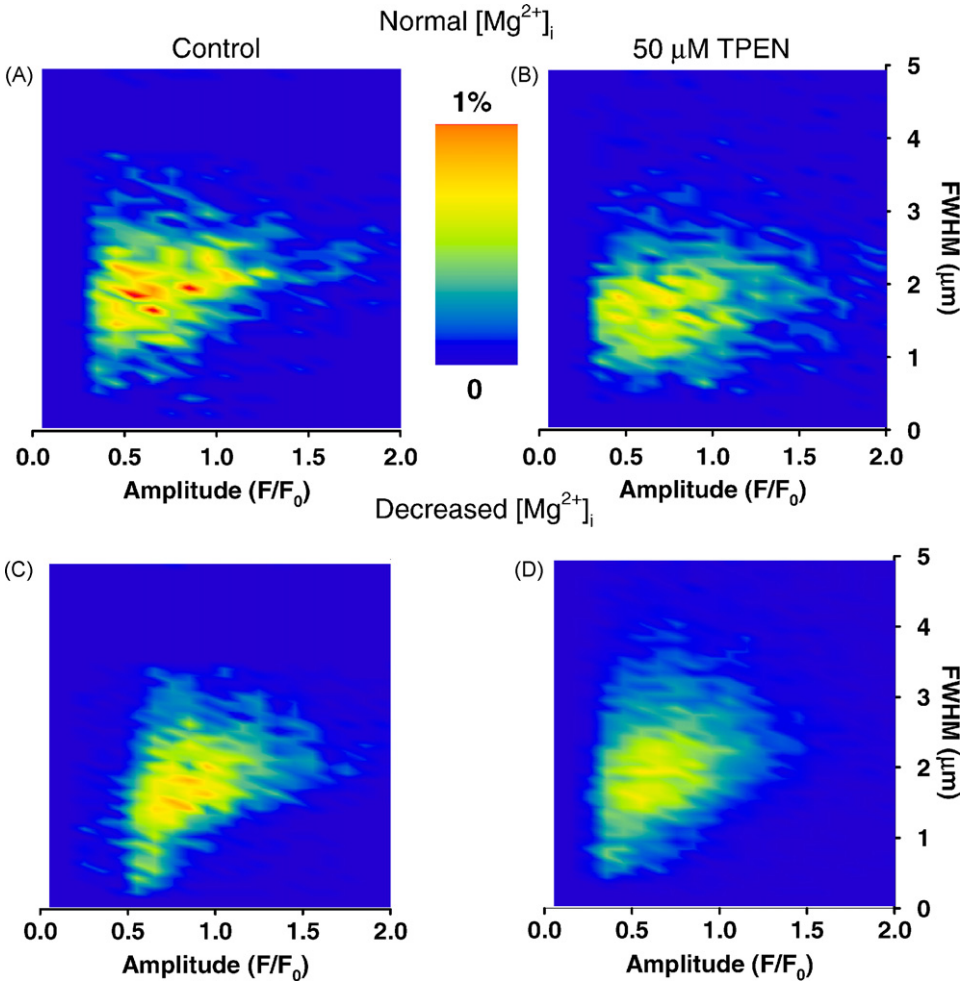


Fig. 3. Distribution of the amplitudes and FWHM of the Ca^{2+} sparks. Amplitude and FWHM values of Ca^{2+} sparks measured under control conditions (left) and in the presence of TPEN (right) in normal (top) and in decreased $[Mg^{2+}]_i$ (bottom) were binned and the relative frequencies plotted as a pseudo-colored two-dimensional surface. Note the differences in the distributions between normal and decreased $[Mg^{2+}]_i$.

the P_o values in the absence and in the presence of TPEN (50, 100 and 200 μM) at different voltages (Fig. 5B). The figure demonstrates clear voltage dependence, with profound inhibition at positive but slight and concentration dependent activation at negative voltages.

Examining the current records in Fig. 6A also reveals that the magnitude of the single channel current was the same before and after the addition of the drug. This observation suggests that TPEN does not influence the conductance of RyR.

3.4. TPEN inhibits the activity of the SR Ca^{2+} pump

In our previous report [50] we have indicated that TPEN might interfere with the reuptake of Ca^{2+} into the SR since it slowed the decay of the Ca^{2+} transients following a KCl-induced depolarization on C2C12 cells. To confirm that this was indeed due to a direct interaction of TPEN with the Ca^{2+} pump, the activity of the SERCA pump was examined in isolated SR vesicle preparations.

To estimate the magnitude of the effect, the hydrolytic activity of HSR vesicles was determined at different TPEN concentrations. Fig. 6 shows pooled data from five independent experiments indicating that TPEN inhibits the ATPase activity of the Ca^{2+} pump. Data were then fitted with the Hill-equation (Eq. (1)) to obtain an IC_{50} of 692 ± 62 μM and a Hill coefficient of 0.88 ± 0.10 for the inhibition.

4. Discussion

In the present study we demonstrate that TPEN modifies the calcium homeostasis of skeletal muscle cells via altering the activity of two of the most important SR membrane proteins, the RyR and the SERCA pump. Examination of Ca^{2+} sparks in amphibian single skeletal muscle fibers indicates that low concentrations of the drug (50 μM) increase the frequency of these elementary calcium release events and promote CICR. The lipid bilayer studies clearly identified the corresponding target to be the Ca^{2+} release channel of the SR (RyR). On the other hand, high concentrations (200 or 500 μM) of TPEN seem to hinder the movement of Ca^{2+} through the SR membrane in either direction. Proper consideration of these findings seems an important prerequisite for the correct interpretation of any experimental data regarding the interaction of TPEN and cellular Ca^{2+} homeostasis.

Ever since TPEN was first used as a heavy metal ion chelator in biological systems [40] several, often contradictory observations have been linked to its ability of binding different heavy metal ions, especially Zn^{2+} [41,42]. It is important to stress that the effects seen in this study are unlikely to be due to the chelation of heavy metals since the affinity of the buffer for these ions is so high (dissociation constants are smaller than 10^{-10} M [40]) that 50 μM TPEN should already have bound all heavy metal ions in the solution. This renders the concentration dependence, and, therefore, the effects of TPEN presented in this study independent of heavy metal chelation.

Author's personal copy

szentesi.peter_292_24

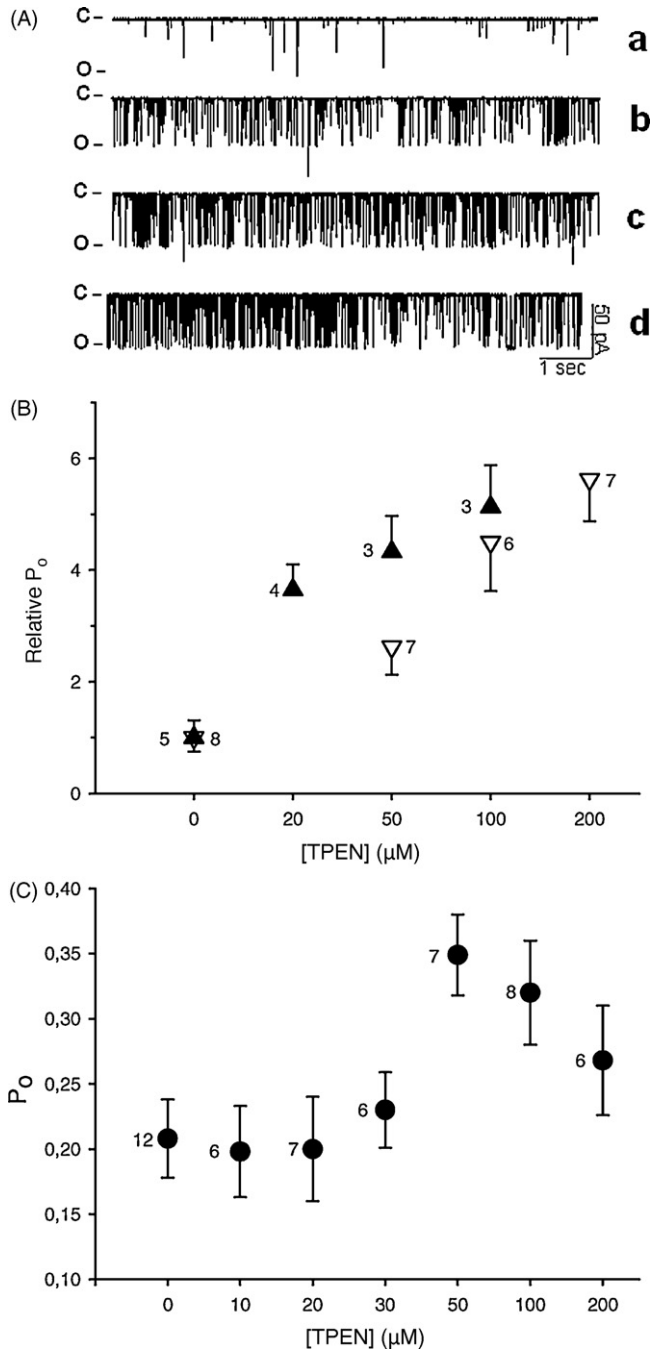


Fig. 4. Activation of the Ca^{2+} release channel RyR by TPEN at negative potentials. (A) Representative current records obtained at various TPEN concentrations. RyRs were incorporated into the bilayer in symmetrical 50 μM *cis* and *trans* Ca^{2+}, followed by the decrease of *cis* Ca^{2+} to 470 nM. Channel openings are represented by downward deflections. Current traces were recorded under control conditions (a) and after increasing *cis* [TPEN] to 50 (b), 100 (c) and 200 μM (d). (B and C) Concentration dependence of channel activation by *cis* TPEN at low (B) and high [Ca^{2+}] (C). The open probabilities of the channel were determined from 60 to 120 s long current records and plotted as a function of *cis* [TPEN]. Free [Ca^{2+}] was adjusted to 50 μM *trans* and either 470 nM (B) or 50 μM (C) *cis*. The symbols represent pooled data of open probabilities from several bilayers. Numbers next to the symbols represent the number of data averaged. In all experiments the holding potential was set to −85 mV and the charge carrier was 250 mM K^+.

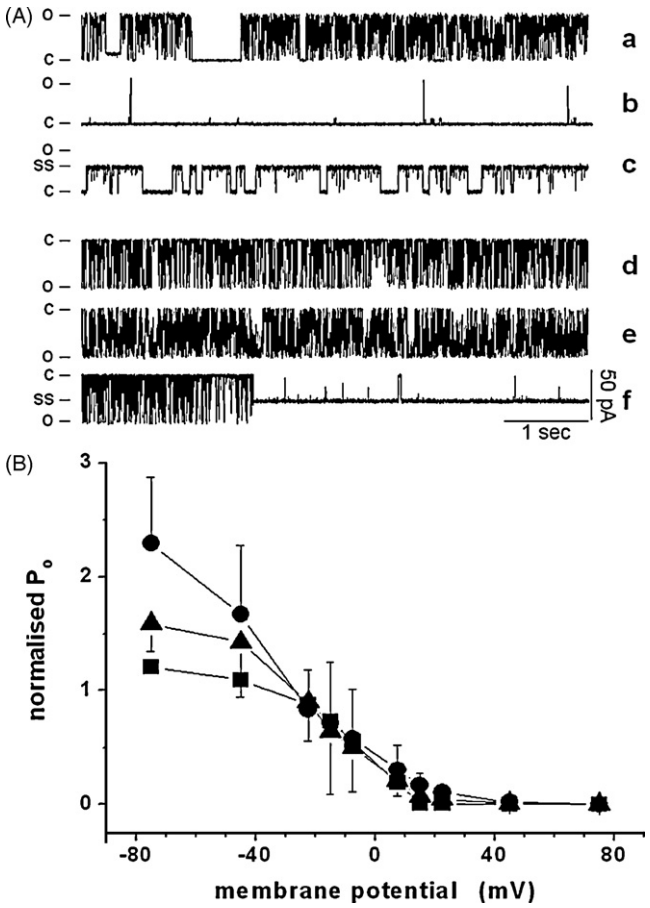


Fig. 5. Voltage dependent interaction of TPEN with RyR. RyRs were incorporated into the bilayer in symmetrical 50 μM *cis* and *trans* Ca^{2+}, with 250 mM K^+ as charge carrier. (A) Representative current records obtained at +85 mV (traces a, b and c) and at −85 mV (traces d, e and f) membrane potentials. The open and the closed states of the channel are represented by o and c respectively, while ss stands for the ryanodine induced characteristic subconductance state. Current traces show control conditions (a and d), records obtained after the addition of 50 μM TPEN *cis* (b and e) and then adding 2 μM Ryanodine to the TPEN modified channel (c and f). (B) Relative open probabilities shown in the presence of 50 (circles), 100 (triangles) and 200 μM TPEN (squares). The open probabilities of the channel were determined from 120 s long current records at various voltages, normalized to control values measured at the given voltage and plotted as function of the membrane potential. The *symbols* represent the average; error bars not shown for the data at 200 μM TPEN for clarity.

Our experiments on skeletal muscle fibers indicated that 50 μM TPEN is able to promote spontaneous Ca^{2+} release events. The buffer not only increased the frequency of Ca^{2+} sparks but it also induced propagating events on frog skeletal muscle fibers (Fig. 2). Importantly, these effects were neither seen on mammalian skeletal muscle (Fig. 1 and Table 1) nor did they appear on frog fibers when $[Mg^{2+}]_i$ was elevated (Table 2). In addition, our earlier experiments also demonstrated that TPEN at this concentration was able to induce propagating Ca^{2+} waves on cardiac myocytes [27]. These observations clearly indicate that TPEN promoted CICR, that is, the further activation of RyR by calcium. In line with this observation the buffer at 50 μM had a more pronounced effect on the isolated channel incorporated into planar lipid bilayers when the *cis* [Ca^{2+}] was 50 μM as compared to that when it was 470 nM.

Further increasing the concentration of TPEN, in contrast, inhibited Ca^{2+} release events in frog skeletal muscle even at the lower $[Mg^{2+}]_i$ tested. This manifested in a decrease in event frequency as well as in the suppression of the amplitude and FWHM of Ca^{2+} sparks. At least three independent mechanisms could be responsible for this observation. If the increased TPEN concentration would further stimulate the opening of RyR this could result in the deple-

Author's personal copy

szentesi.peter_292_24

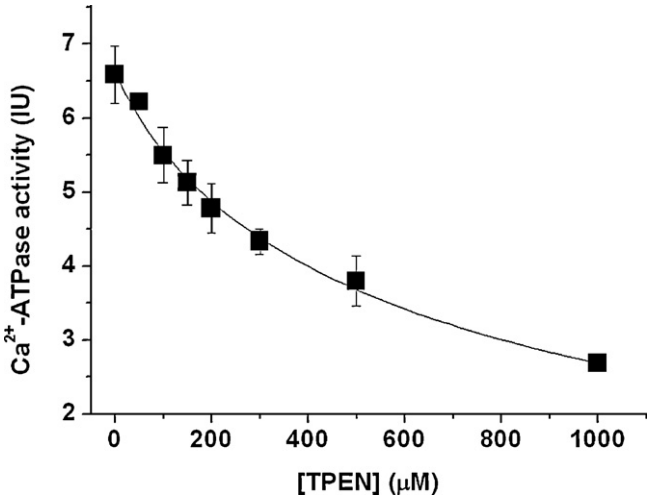


Fig. 6. Inhibition of the hydrolytic activity of the SR Ca^{2+} pump by TPEN. ATPase activity was determined using the coupled enzyme assay as described in Section 2. The *symbols* represent the average of five independent measurements. Data were fitted with the Hill-equation. The curve superimposed on the data was generated with the best fit parameters for IC_{50}, 692 μM, and the Hill coefficient, 0.88.

tion of Ca^{2+} in the SR. TPEN could inhibit the reuptake of Ca^{2+} into the SR via the SR Ca^{2+} pump, again resulting in a depletion of the internal stores. Finally, the buffer could inhibit RyR at higher concentrations. Measurements conducted on isolated systems gave indication for all above possibilities.

Examination of isolated RyR in lipid bilayers revealed that at negative membrane potentials increasing the concentration of TPEN on the *cis* side results in greater open probability of the RyR (Fig. 4) when *cis* $[Ca^{2+}]$ was low. Under these conditions TPEN concentrations above 50 μM further increased the P_o of the channel. However, were this the case an increase in $[Ca^{2+}]_i$ due to the leakage from the SR should have been detected. As a rise in $[Ca^{2+}]_i$ was never observed upon the addition of 500 μM TPEN alone in cellular systems [50], it is unlikely that the drug exerts its inhibition only through activating the Ca^{2+} release channels and depleting the releasable calcium in the SR.

Our data clearly establish that TPEN inhibits the hydrolytic activity of the SR Ca^{2+} pump. This inhibition, however, occurs at relatively high (EC_{50} is greater than 600 μM) concentrations of the buffer. Assuming, nevertheless, that the 45% inhibition of SERCA by 500 μM TPEN would have been sufficient to prevent SR refilling would also imply an increase in $[Ca^{2+}]_i$, similarly to what is seen upon the administration of other blockers of SERCA (as thapsigargin, see e.g. [43]) or to the situation of an increased leak, unless accompanied by blockage of the RyR. Since this was not observed, as explained above, this leaves the third possibility, that is, a direct inhibition of RyR itself, as the most likely candidate to explain the observed suppression of SR calcium release.

Indeed, in high *cis* $[Ca^{2+}]$ the activation of the Ca^{2+} release channel was maximal at 50 μM and less pronounced at higher concentrations. In addition, at positive membrane potentials, a clear inhibition is observed for higher TPEN concentrations.

Although our findings with lipid bilayers clearly show that the activation of the RyR by TPEN depends on the *cis* Ca^{2+} concentration, they do not allow us to tell exactly how. We can, however, exclude the possibility that it is simply due to the chelation of Ca^{2+} by the buffer since in the lipid bilayer experiments special care was taken to keep the free $[Ca^{2+}]$ constant at every TPEN concentration tested.

Taken together, the experiments on Ca^{2+} release events and on lipid bilayers suggest a possible mode of action for the buffer. Assuming that TPEN sensitizes RyR towards both the activating and inactivating Ca^{2+}, increasing TPEN concentrations would generate an increasing leftward shift of the bell-shaped Ca^{2+}-activation and -activation curve described in numerous reports (e.g. [43]). At low $[Ca^{2+}]$, one, therefore, obtains an increasing activation with increasing buffer concentration describing only the rising phase of the bell-shaped curve. At higher $[Ca^{2+}]$ the declining phase of the Ca^{2+}-activation and -inhibition curve of the RyR is also reached, that is, an inhibition at higher TPEN concentrations is observed.

It should be emphasized, however, that TPEN has been suggested to be efficient in inhibiting malignant cell proliferation [44] and promoting apoptosis by activating the p53 pathway (e.g. [45]). Although these actions of TPEN have been associated with the chelation of Zn^{2+}, calcium binding proteins can also modulate the p53 apoptosis pathway (e.g. [46]). In this study we provide evidence from experiments on living systems as well as on isolated RyRs, that low concentrations of TPEN (~50 μM) can activate the RyR. We also demonstrate that high concentrations of the buffer (~500 μM) clearly inhibit the SERCA pump and also the RyR. The range of putative effects as well as the effective concentrations of TPEN is, therefore, wide and their understanding is essential in elucidating certain aspects of cellular Ca^{2+} homeostasis and programmed cell death.

Conflicts of interest

There are no conflicts of interest.

Acknowledgements

The authors are grateful for the technical assistance of Ms. R. Öri and Ms. É. Sági. The work was supported by grants from the Hungarian Scientific Research Fund OTKA (T049151, K61442, K75604 and NK61412), from the Swiss National Science Foundation (109693.05 to E.N.), from the Swiss Cardiovascular Research and Training Network (SCRTN) and the State Secretariat for Education and Research (SER).

References

[1] C. Franzini-Armstrong, F. Protasi, Ryanodine receptors of striated muscles: a complex channel capable of multiple interactions, Physiol. Rev. 77 (1997) 699–729.
[2] P. Leong, D.H. MacLennan, Complex interactions between skeletal muscle ryanodine receptor and dihydropyridine receptor proteins, Biochem. Cell Biol. 76 (1998) 681–694.
[3] E. Rios, G. Pizarro, Voltage sensors and calcium channels of excitation–contraction coupling, News Physiol. Sci. 3 (1988) 223–227.
[4] J. Zhou, B.S. Launikonis, E. Rios, G. Brum, Regulation of Ca^{2+} sparks by Ca^{2+} and Mg^{2+} in mammalian and amphibian muscle. An RyR isoform-specific role in excitation–contraction coupling? J. Gen. Physiol. 124 (2004) 409–428.
[5] M. Endo, M. Tanaka, Y. Ogawa, Calcium induced release of calcium from the sarcoplasmic reticulum of skinned skeletal muscle fibres, Nature 228 (1970) 34–36.
[6] L.E. Ford, R.J. Podolsky, Regenerative calcium release within muscle cells, Science 167 (1970) 58–59.
[7] A. Fabiato, Calcium-induced release of calcium from the cardiac sarcoplasmic reticulum, Am. J. Physiol. 245 (1985) C1–C14.
[8] D. McKemy, A. Ivanenko, J.L. Kenyon, A. Airey, J.L. Sutko, The c~RyR influences the type of E–C coupling used in embryonic chicken skeletal muscle, Biophys. J. 68 (1995) A50 (Abstract).
[9] M.G. Klein, H. Cheng, L.F. Santana, Y.-H. Jiang, W.J. Lederer, M.F. Schneider, Two mechanisms of quantized calcium release in skeletal muscle, Nature (London) 379 (1996) 455–458.
[10] Y. Ogawa, N. Kurebayashi, T. Murayama, Ryanodine receptor isoforms in excitation–contraction coupling, Adv. Biophys. 36 (1999) 27–64.
[11] S. Pouvreau, L. Royer, J. Yi, G. Brum, G. Meissner, E. Ríos, J. Zhou, Ca(2+) sparks operated by membrane depolarization require isoform 3 ryanodine receptor channels in skeletal muscle, Proc. Natl. Acad. Sci. U.S.A. 104 (2007) 5235–5240.
[12] C. Legrand, E. Giacomello, C. Berthier, B. Allard, V. Sorrentino, V. Jacquemond, Spontaneous and voltage-activated Ca^{2+} release in adult mouse skeletal muscle fibres expressing the type 3 ryanodine receptor, J. Physiol. 586 (2008) 441–457.
[13] W.G. Kirsch, D. Uttenweiler, R.H. Fink, Spark- and ember-like elementary Ca^{2+} release events in skinned fibres of adult mammalian skeletal muscle, J. Physiol. 537 (2001) 379–389.

Author's personal copy

szentesi.peter_292_24

[14] A.S. Martins, V.M. Shkryl, M.C. Nowycky, N. Shirokova, Reactive oxygen species contribute to Ca^{2+} signals produced by osmotic stress in mouse skeletal muscle fibres, J. Physiol. 586 (2008) 197–210.

[15] H. Cheng, W.J. Lederer, M.B. Cannell, Calcium sparks: elementary events underlying excitation–contraction coupling in heart muscle, Science 262 (5134) (1993) 740–744.

[16] P. Lipp, E. Niggli, Modulation of Ca^{2+} release in cultured neonatal rat cardiac myocytes. Insight from subcellular release patterns revealed by confocal microscopy, Circ. Res. 74 (5) (1994) 979–990.

[17] A. Tsugorka, E. Ríos, L.A. Blatter, Imaging elementary events of calcium release in skeletal muscle cells, Science 269 (5231) (1995) 1723–1726.

[18] G. Meissner, E. Darling, J. Eveleth, Kinetics of rapid Ca^{2+} release by sarcoplasmic reticulum. Effects of Ca^{2+}, Mg^{2+}, and adenine nucleotides, Biochemistry 25 (1986) 236–244.

[19] V. Shoshan-Barmatz, R.H. Ashley, The structure, function, and cellular regulation of ryanodine-sensitive Ca^{2+} release channels, Int. Rev. Cytol. 183 (1998) 185–270.

[20] D.R. Laver, E.R. O'Neill, G.D. Lamb, Luminal Ca^{2+}-regulated Mg^{2+} inhibition of skeletal RyRs reconstituted as isolated channels or coupled clusters, J. Gen. Physiol. 124 (2004) 741–758.

[21] A. Lacampagne, M.G. Klein, M.F. Schneider, Modulation of the frequency of spontaneous sarcoplasmic reticulum Ca^{2+} release events (Ca^{2+} sparks) by myoplasmic $[Mg^{2+}]$ in frog skeletal muscle, J. Gen. Physiol. 111 (1998) 207–224.

[22] S. Györke, I. Györke, V. Lukyanenko, D. Terentyev, S. Viatchenko-Karpinski, T.F. Wiesner, Regulation of sarcoplasmic reticulum calcium release by luminal calcium in cardiac muscle, Front. Biosci. 7 (2002) d1454–d1463.

[23] E. Rios, B.S. Launikosnis, L. Royer, G. Brum, J. Zhou, The elusive role of store depletion in the control of intracellular calcium release, J. Muscle Res. Cell Motil. 27 (2006) 337–350.

[24] B. Burlando, M. Bonomo, E. Fabbri, F. Dondero, A. Viarengo, Hg^{2+} signaling in trout hepatoma (RTH-149) cells: involvement of Ca^{2+}-induced Ca^{2+} release, Cell Calcium 34 (2003) 285–293.

[25] G. Salama, J.J. Abramson, G.K. Pike, Sulphydryl reagents trigger Ca^{2+} release from the sarcoplasmic reticulum of skinned rabbit psoas fibres, J. Physiol. 454 (1992) 389–420.

[26] X. Liu, I.S. Ambudkar, Characteristics of a store-operated calcium-permeable channel: sarcoendoplasmic reticulum calcium pump function controls channel gating, J. Biol. Chem. 276 (2001) 29891–29898.

[27] C. Jung, A.V. Zima, P. Szentesi, I. Jona, L.A. Blatter, E. Niggli, Ca^{2+} release from the sarcoplasmic reticulum activated by the low affinity Ca^{2+} chelator TPEN in ventricular myocytes, Cell Calcium 41 (2007) 187–194.

[28] P. Szentesi, V. Jacquemond, L. Kovacs, L. Csernoch, Intramembrane charge movement and sarcoplasmic calcium release in enzymatically isolated mammalian skeletal muscle fibers, J. Physiol. 505 (1997) 371–384.

[29] S. Ausoni, L. Gorza, S. Schiaffino, K. Gundersen, T. Lømo, Expression of myosin heavy chain isoforms in stimulated fast and slow rat muscles, J. Neurosci. 10 (1990) 153–160.

[30] J.G. Lutz, S. Bremner, N. Lajevardi, R.L. Lieber, L.C. Rome, Quantitative analysis of muscle fibre type and myosin heavy chain distribution in the frog hindlimb: implications for locomotory design, J. Muscle Res. Cell Motil. 19 (1998) 717–731.

[31] F.A. Lai, G. Meissner, Structure of the calcium release channel of skeletal muscle sarcoplasmic reticulum and its regulation by calcium, Adv. Exp. Med. Biol. 269 (1990) 73–77.

[32] S. Sárközi, C. Szegedi, B. Lukács, M. Ronjat, I. Jóna, Effect of gadolinium on the ryanodine receptor/sarcoplasmic reticulum calcium release channel of skeletal muscle, FEBS J. 272 (2005) 464–471.

[33] F.A. Lai, H.P. Eriksson, E. Rousseau, Q.Y. Lio, G. Meissner, Purification and reconstitution of the calcium release channel from skeletal muscle, Nature 331 (1988) 315–319.

[34] O.H. Lowry, N.J. Rosenbrough, A.L. Farr, R.J. Randall, Protein measurement with the Folin phenol reagent, J. Biol. Chem. 193 (1951) 265–275.

[35] P. Szentesi, H. Szappanos, Cs. Szegedi, M. Gönczi, I. Jóna, J. Cseri, L. Kovács, L. Csernoch, Altered elementary calcium release events and enhanced calcium release by thymol in rat skeletal muscle, Biophys. J. 86 (2004) 1436–1453.

[36] H. Cheng, M.R. Lederer, W.J. Lederer, M.B. Cannell, Calcium sparks and $[Ca^{2+}]_i$ waves in cardiac myocytes, Am. J. Physiol. 270 (1996) 148–159.

[37] Gy.P. Szigeti, J. Almássy, M. Sztretye, B. Dienes, L. Szabó, P. Szentesi, G. Vassort, S. Sárközi, L. Csernoch, I. Jóna, Alterations in the calcium homeostasis of skeletal muscle from postmyocardial infarcted rats, Pflugers Arch. 455 (2007) 541–553.

[38] A. Tripathy, G. Meissner, Sarcoplasmic reticulum luminal Ca^{2+} has access to cytosolic activation and inactivation sites of skeletal muscle Ca^{2+} release channel, Biophys. J. 70 (1996) 2600–2615.

[39] J. Zhou, G. Brum, A. Gonzalez, B.S. Launikonis, M.D. Stern, E. Rios, Concerted vs. sequential. Two activation patterns of vast arrays of intracellular Ca^{2+} channels in muscle, J. Gen. Physiol. 126 (2005) 301–309.

[40] P. Arslan, F. Di Virgilio, M. Beltrame, R.Y. Tsien, T. Pozzan, Cytosolic Ca^{2+} homeostasis in Ehrlich and Yoshida carcinomas. A new, membrane-permeant chelator of heavy metals reveals that these ascites tumor cell lines have normal cytosolic free Ca^{2+}, J. Biol. Chem. 260 (1985) 2719–2727.

[41] D.K. Shumaker, L.R. Vann, M.W. Goldberg, T.D. Allen, K.L. Wilson, TPEN, a Zn^{2+}/Fe^{2+} chelator with low affinity for Ca^{2+}, inhibits lamin assembly, destabilizes nuclear architecture and may independently protect nuclei from apoptosis in vitro, Cell Calcium 23 (1998) 151–164.

[42] F. Chimienti, M. Seve, S. Richard, J. Mathieu, A. Favier, Role of cellular zinc in programmed cell death: temporal relationship between zinc depletion, activation of caspases, and cleavage of Sp family transcription factors, Biochem. Pharmacol. 62 (2001) 51–62.

[43] S. Sárközi, Cs. Szegedi, P. Szentesi, L. Csernoch, L. Kovács, I. Jóna, Regulation of the rat sarcoplasmic reticulum calcium release channel by calcium, J. Muscle Res. Cell Motil. 21 (2000) 131–138.

[44] M. Donadelli, E. Dalla Pozza, C. Costanzo, M.T. Scupoli, A. Scarpa, M. Palmieri, Zinc depletion efficiently inhibits pancreatic cancer cell growth by increasing the ratio of antiproliferative/proliferative genes, J. Cell Biochem. 104 (2008) 202–212.

[45] H. Ra, H.L. Kim, H.W. Lee, Y.H. Kim, Essential role of p53 in TPEN-induced neuronal apoptosis, FEBS Lett. 583 (2009) 1516–1520.

[46] C. Li, H. Chen, F. Ding, Y. Zhang, A. Luo, M. Wang, Z. Liu, A novel p53 target gene, S100A9, induces p53-dependent cellular apoptosis and mediates the p53 apoptosis pathway, Biochem. J. 422 (2009) 363–372.

[47] A. Fabiato, Computer programs for calculating total from specified free or free from specified total ionic concentrations in aqueous solutions containing multiple metals and ligands, Methods Enzymol. 157 (1988) 371–384.

[48] N. Shirokova, E. Rios, Activation of Ca^{2+} release by caffeine and voltage in frog skeletal muscle, J. Physiol. 493 (1996) 317–339.

[50] M. Sztretye, T. Deli, P. Szentesi, Gy.P. Szigeti, L. Csernoch, Effect of TPEN on the calcium release of cultured C2C12 mouse myotubes, J. Muscle Res. Cell Motil. 28 (2007) 421–428.

[51] B. Turan, Zinc-induced changes in ionic currents of cardiomyocytes, Biol. Trace Elem. Res. 94 (2003) 49–60.

J Muscle Res Cell Motil (2015) 36:263–274
DOI 10.1007/s10974-015-9413-5

szentesi.peter_292_24

CrossMark

ORIGINAL PAPER

Effects of fluvastatin and coenzyme Q_{10} on skeletal muscle in normo- and hypercholesterolaemic rats

J. Vincze[1] · Á. Jenes[1] · M. Füzi[1] · J. Almássy[1] · R. Németh[1] · G. Szigeti[1] · B. Dienes[1] · Z. Gaál[1] · P. Szentesi[1] · I. Jóna[1] · P. Kertai[2] · G. Paragh[3] · L. Csernoch[1]

Received: 13 January 2015 / Accepted: 21 April 2015 / Published online: 29 April 2015
© Springer International Publishing Switzerland 2015

Abstract Myalgia and muscle weakness may appreciably contribute to the poor adherence to statin therapy. Although the pathomechanism of statin-induced myopathy is not completely understood, changes in calcium homeostasis and reduced coenzyme Q_{10} levels are hypothesized to play important roles. In our experiments, fluvastatin and/or coenzyme Q_{10} was administered chronically to normocholesterolaemic or hypercholaestherolaemic rats, and the modifications of the calcium homeostasis and the strength of their muscles were investigated. While hypercholesterolaemia did not change the frequency of sparks, fluvastatin increased it on muscles both from normocholesterolaemic and from hypercholesterolaemic rats. This effect, however, was not mediated by a chronic modification of the ryanodine receptor as shown by the unchanged ryanodine binding in the latter group. While coenzyme Q_{10} supplementation significantly reduced the frequency of the spontaneous calcium release events, it did not affect their amplitude and spatial spread in muscles from fluvastatin-treated rats. This indicates that coenzyme Q_{10} supplementation prevented the spark frequency increasing effect of fluvastatin without having a major effect on the amount of calcium released during individual sparks. In conclusion, we have found that fluvastatin, independently of the cholesterol level in the blood, consistently and specifically increased the frequency of calcium sparks in skeletal muscle cells, an effect which could be prevented by the addition of coenzyme Q_{10} to the diet. These results support theories favouring the role of calcium handling in the pathophysiology of statin-induced myopathy and provide a possible pathway for the protective effect of coenzyme Q_{10} in statin treated patients symptomatic of this condition.

Keywords Skeletal muscle · Calcium homeostase · Force · Spark · Statin · Q_{10} · Myopathy

Introduction

Statins are the most frequently prescribed drugs for lowering the high blood cholesterol level worldwide. Statins competitively inhibit 3-hydroxy-3-methylglutaryl coenzyme A (HMG-CoA) reductase, the enzyme catalysing the rate-limiting step of cholesterol biosynthesis. The major indications for the prescription of statins are high blood cholesterol level and primary or secondary prevention of cardiovascular events. Clinical trials have demonstrated that statins are beneficial for the prophylaxis of cardiovascular morbidity and mortality in at-risk patients, even if patients have normal levels of cholesterol, consequently, a large population of patients are on these drugs (Mihaylova et al. 2012; Taylor et al. 2013). Statins take their effect not only by lowering blood cholesterol level, but also by decreasing inflammation and oxidative stress, by stabilising the atherosclerotic plaques, and by inhibiting the thrombogenic response of blood vessels (Gerber et al. 2013; Guarini and Marzilli 2013).

J. Vincze and Á. Jenes have contributed equally to this work.

✉ L. Csernoch
csl@edu.unideb.hu

[1] Department of Physiology, Faculty of Medicine, University of Debrecen, Nagyerdei krt. 98, P.O. Box 22, Debrecen 4012, Hungary

[2] Department of Preventive Medicine, Faculty of Public Health, University of Debrecen, Debrecen, Hungary

[3] Clinical Center, Institute of Medicine, University of Debrecen, Debrecen, Hungary

szentesi.peter_292_24

The main adverse effect of statins is myopathy (Bruckert et al. 2005). Skeletal muscle related side effects are associated with all commonly used statins and are dose dependent (Tomlinson and Mangione 2005). Since no validated survey or standardized diagnostic criteria have yet been established to assess muscle pain or muscle weakness in statin trials, the incidence of myalgia is problematic to determine. The reports of muscle complaints vary between 0.3 and 33 % (Daugird et al. 2003). Generally, myalgia and myopathy seem to be underreported, the incidence of statin-induced muscle toxicity in randomized controlled trials is probably lower than noticed in routine clinical practice. Half of the patients discontinue statin therapy within a year (Jackevicius et al. 2002; Evans et al. 2009; Fernandez et al. 2011). The side effects, especially myalgia and muscle weakness, may appreciably contribute to the poor adherence to statin medications.

The pathomechanism of statin-induced myopathy is highly studied yet not completely understood. Many theories have been offered as to the mechanism by which statins may cause muscle-related adverse effects, and the majority of these theories are related to the Ca^{2+} homeostasis of the skeletal muscle and to deficiencies of synthetic products of the HMG-CoA reductase pathway. The most common explanations invoke the deficiency of one of three main end-products: cholesterol, coenzyme Q_{10} or prenylated proteins (Antons et al. 2006). Cholesterol deficiency impairs membrane integrity, potentially leading to secondary abnormal membrane behaviour (Waclawik et al. 1993; Nakahara et al. 1998). Coenzyme Q_{10} deficiency is associated with abnormal oxidative phosphorylation in mitochondria, disturbing the energy production of the muscle (Nakahara et al. 1998; Schaefer et al. 2004; Paiva et al. 2005). Finally, prenylated protein abnormalities cause imbalances in intracellular signalling cascades, inducing apoptosis in myocytes (Sacher et al. 2005; Johnson et al. 2004; Salarieh et al. 2004). Since all of these abnormalities may involve modified intracellular Ca^{2+} signalling (Inoue et al. 2003; Sacher et al. 2005; Sirvent et al. 2005, 2012; Knoblauch et al. 2013), changes in Ca^{2+} homeostasis seem to be essential for understanding the statin-induced myopathy.

A systematic review concluded a few years ago that there were insufficient evidence to prove the etiologic role of coenzyme Q_{10} deficiency in statin-induced myopathy, and the effect of coenzyme Q_{10} supplementation on myopathic symptoms were contradictory (Marcoff and Thompson 2007). Also, the European Food Safety Authority found no proven beneficial effects of coenzyme Q_{10} supplementation in any of the areas claimed by the manufacturers (EFSA Panel on Dietetic Products, Nutrition and Allergies 2010). The clinical effectiveness of coenzyme Q_{10} supplementation is still controversial, with recently published studies reporting either protective effects (Littlefield et al. 2014; Skarlovnik et al. 2014) or lack of effects (Bookstaver et al. 2012; Banach et al. 2015; Taylor et al. 2015) of coenzyme Q_{10} on statin-induced adverse effects.

In our experiments, we administered fluvastatin chronically, for 4 weeks, to rats, and investigated the modifications of the Ca^{2+} homeostasis and the strength of their muscles. In order to examine the possible differences between the effect of chronic statin treatment of normocholesterolaemic rats and of chronic statin treatment of hypercholaestherolaemic rats, we used an established animal model published earlier (Füzi et al. 2012; Padra et al. 2014). Since statins block the mevalonate pathway, the endogenous coenzyme Q_{10} synthesis is also affected, and the reduced coenzyme Q_{10} level is hypothesized to be the reason for muscle pathologies, we also investigated the possible beneficial effects of administering coenzyme Q_{10} with the diets.

Methods

Animal models

Animals were housed in accordance with the guidelines and the approved protocol of the Animal Care Committee of the University of Debrecen. The animal model used was described previously (Füzi et al. 2012). In brief, female Fischer rats were fed with different pre-mixed chows from Charles River Laboratories for at least 28 days, and were allowed to consume the food and tap water ad libitum. The control (normocholesterolaemic; NC) group was fed with standard rodent chow. For the statin (NC+S) group this standard rodent chow was mixed with 6.4 mg/kg/day fluvastatin. The group with high blood cholesterol (hypercholesterolaemic; HC) was fed with high, 5 g/kg/day cholesterol containing chow, in addition with 1 g/kg/day cholic acid, which facilitates the absorption of cholesterol in the rat small intestine, and 1 g/kg/day thiouracil, which provided us an additional rise in the blood cholesterol level. The hypercholesterolaemic and statin treated (HC+S) group was kept on high cholesterol and fluvastatin containing diet at the above mentioned concentrations. We set up a second experiment to study the effects of coenzyme Q_{10} in which all the diets mentioned above contained coenzyme Q_{10} in dose 10 mg/kg/day. Bodyweights of the animals were measured daily as well as their daily food intake.

Animals were anaesthetized and sacrificed following a protocol approved by the Animal Care Committee of the University of Debrecen. After pentobarbital anaesthesia (27 mg/kg), the *m. flexor digitorum brevis* (FDB) from the

fore limb, and the *m. extensor digitorum longus* (EDL) and *m. soleus* (Sol) from the hind limb were dissected.

Detection of calcium release events

After enzymatic dissociation, FDB fibres were permeabilized using 0.01 % saponin for a few seconds. Spontaneous calcium release events were visualised by 50 μM Fluo-3 using a confocal laser scanning microscope (Zeiss LSM 510 META, Oberkochen, Germany) at room temperature (as described earlier by Lukacs et al. 2008).

Images containing spontaneous calcium release events were analysed using an automatic event detection program (Szentesi et al. 2004; Szabo et al. 2010), which calculated the amplitude ($\Delta F/F_0$), full width at half maximum (FWHM), rise time and duration of the identified events.

Preparation of RyRs

Heavy sarcoplasmic reticulum (HSR) vesicles were isolated from rat skeletal muscle and were used for ryanodine binding experiments as described earlier (Szegedi et al. 1999; Csernoch et al. 1999). In brief, skeletal muscles were removed from the front and hind limbs of the rats. The muscles were cut into small pieces, quickly frozen using liquid nitrogen, and stored at −70 °C until further use. Vesicles were obtained by first homogenizing the tissue then removing the unsolubilized particles in a clinical centrifuge. Crude membrane fraction was collected from the supernatant by centrifugation at 40,000×*g* (30 min). The actomyosin content of the pellet was then dissolved in 600 mM KCl and the crude microsome fraction was collected by centrifugation at 109,000×*g* (30 min). The microsome was loaded onto a 20–45 % linear sucrose gradient and spun for 16 h at 90,000×*g* (4 °C) in a swingout (SW-27) Beckman rotor (Beckman-Coulter, Fullerton, CA, USA). The protein-ring corresponding to the HSR fraction was extracted from the 36–38 % region. Vesicles were collected at 124,000×*g* for 60 min then resuspended in 92.5 mM KCl and 18.5 mM K-MOPS at pH 7.0 for vesicular measurements. Samples were stored at −70 °C until further use.

Ryanodine binding assay

The ryanodine binding was described previously (Sárközi et al. 2005). In brief, ryanodine binding assay was carried out using [^{3}H]ryanodine in an incubation medium of 1 M NaCl, 25 mM Na-PIPES at pH 7.1, 1 mM Pefabloc (Fluka, Buchs, Switzerland), 300 μM $CaCl_2$, and 205 μM EGTA. 50 ml aliquots, containing 25 mg protein were incubated at 37 °C for 2 h, with the various concentrations of the radioligand (Herrmann-Frank et al. 1996). The reaction was terminated by filtering the samples immediately on a Bio-Dot 96 well filter apparatus (Bio-RAD Lab., Hercules, CA, USA) using Millipore-50 filter paper (Millipore, Billerica, MA, USA). The dots were then rinsed with equal aliquots of washing medium without ryanodine (hot and cold), that were otherwise identical to the incubation medium. Filter papers were cut into appropriate pieces and their radioactivity was determined using a liquid scintillation counter (Packard, Meriden, CT, USA). Non-specific binding was determined in the presence of 50-100 μM ryanodine, added to the incubation mixture before the radioligand. Fluvastatin was found not to affect the non-specific binding. Binding data were fitted using the Hill equation:

$$\frac{B}{B_{max}} = \frac{X^n}{EC_{50}^n + X^n} \quad (1)$$

where B/B_{max} is the relative concentration of the bound form, EC_{50} is the half effective concentration, while X is the actual concentration of ryanodine and n is the Hill coefficient. The latter was constrained to 1 (making it equivalent to the Michaelis–Menten equation), because it is known that the RyR has a single binding site for ryanodine that is active in the concentration region used in our experiments, i.e. there was no cooperativity. Experiments were carried out in triplets and the averaged data were used in the calculations.

Measurement of muscle force

Muscle contractions were measured as described in our previous reports (Oddoux et al. 2009; Füzi et al. 2012). In brief, fast and slow twitch muscles, EDL and Sol, were removed and placed horizontally in an experimental chamber continuously superfused (10 ml/min) with Krebs' solution (containing in mM: NaCl 135, KCl 5, $CaCl_2$ 2.5, $MgSO_4$ 1, Hepes 10, glucose 10, $NaHCO_3$ 10; pH 7.2; room temperature) equilibrated with 95 % O_2 plus 5 % CO_2. One end of the muscle was attached to a rod while the other to a capacitive mechanoelectric force transducer. Two platinum electrodes placed adjacent to the muscle were used to deliver short, supramaximal pulses of 2 ms in duration to elicit single twitches. Force responses were digitized at 2 kHz by using Digidata 1200 A/D card and stored with Axotape software (Axon Instruments, Foster City, CA, USA). Muscles were then stretched by adjusting the position of the transducer to a length that produced the maximal force response and allowed to equilibrate for 60 min.

Single pulses 2 s apart were used to elicit single twitches. At least 10 twitches were measured under these conditions from every muscle. The individual force transients within such a train varied by less than 3 % in amplitude, thus the mean of the amplitude of all transients was

szentesi.peter_292_24

used to characterize the given muscle. To elicit a tetanus, single pulses were applied with a frequency of 200 Hz for 200 ms (EDL) or 100 Hz for 300 ms (Sol). Duration of individual twitches and tetani were determined by calculating the time between the onset of the transient and the relaxation to 90 % of maximal force.

Chemicals and statistical analysis

Fluo-3 was purchased from Molecular Probes (Eugene, OR, USA). [^{3}H]ryanodine was from Dupont (Boston, MA, USA) and all other chemicals were from Sigma (Sigma, St. Louis, MO, USA).

Averages—data unless otherwise stated were pooled over the fibres from animals within the same group—are presented as mean ± standard error of the mean or mean and 95 % confidence interval in case of relative results. For parameters of individual sparks n is the number of sparks, otherwise it indicates the number of fibres or muscles (whichever is relevant for the given experiment) isolated from the animals within that group. Significance of the differences between control and treated animals was assessed using parametric or non-parametric one way analysis of variance (ANOVA) and appropriate post hoc tests to discover pairwise differences. Differences were regarded significant at $p < 0.05$. Reported significance values are corrected for the multiple comparisons.

Results

We have reported recently that while hypercholesterolaemia did not impact muscle function, statin treatment significantly decreased muscle force (Füzi et al. 2012). Since the statin-induced muscle weakness was accompanied by elevated intracellular Ca^{2+} concentration (Füzi et al. 2012) and acute application of simvastatin was reported to alter calcium sparks (Sirvent et al. 2005), we aimed to investigate the effect of chronic fluvastatin treatment on spontaneous Ca^{2+} release events.

Fluvastatin increases the frequency of calcium sparks with minor alterations in individual spark parameters

Line scan images of isolated and permeabilized FDB fibres revealed spontaneous Ca^{2+} release events (sparks) both from normocholesterolaemic (NC) and from fluvastatin treated (NC+S) rats (Fig. 1a–d). Frequency of the sparks on FDB fibres isolated from NC+S animals was significantly higher than that isolated from NC animals (2.24 ± 0.2 Hz/sarcomere and 1.59 ± 0.1 Hz/sarcomere, n = 17 and 21, respectively, p = 0.033, Fig. 3a). While

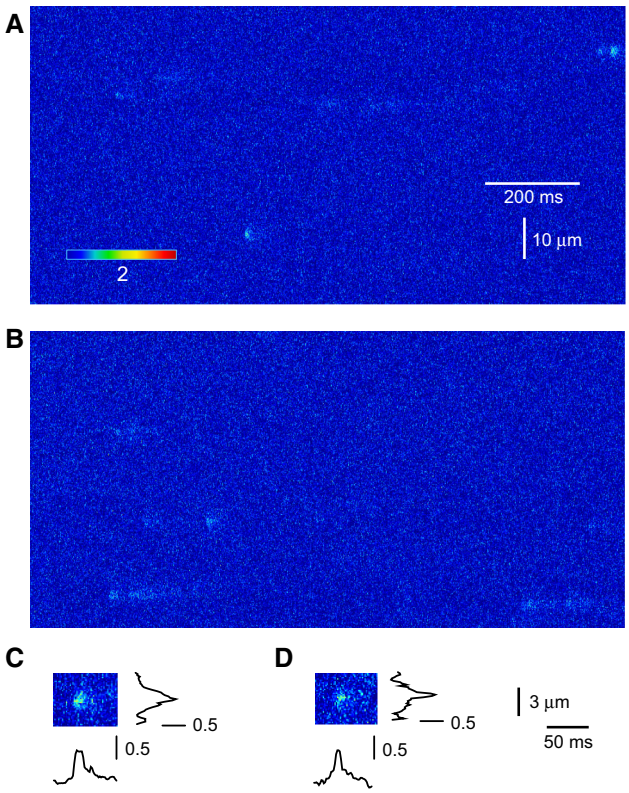


Fig. 1 Spontaneous Ca^{2+} release events in FDB fibres from normocholesterolaemic (NC) and statin treated (NC+S) animals. **a**, **b** Line-scan images from fibres of FDB muscles from control (**a**) and from statin treated (**b**) rats. Enzymatically isolated fibres were permeabilized with a brief exposure to 0.01 % saponin and loaded with Fluo-3. **c**, **d** Representative sparks with their spatial profiles and time courses detected in control (**c**) and in statin treated (**d**) rats. Spatial and temporal profiles were calculated from the average of five consecutive rows or columns at the maximum of the event. Acquisition parameters: 1024 × 512 pixel, 1.53 ms/line, 0.14 µm/pixel; temperature 22 °C. (Color figure online)

the major characteristics, such as amplitude, FWHM, and rise time of the individual sparks, did not differ significantly (Fig. 4a–c), a slight, but significant difference in duration was observed. Namely, the sparks from NC+S animals were longer than those from NC animals (39.3 ± 0.3 and 37.8 ± 0.4 ms, n = 3962 and 1605, respectively, p = 0.002, Fig. 4d).

Hypercholesterolaemia affects the major characteristics of the individual sparks, but not their frequency

The most common indication for prescribing statins is high cholesterol level, therefore, the highest relevance of studying the possible adverse effects of statins is on a hypercholesterolaemic (HC) population. To do so, the first question to answer was whether or not hypercholesterolaemia in itself would influence the spark parameters as

compared to those measured on muscles from normocholesterolaemic rats.

Frequency of the sparks on FDB fibres isolated from hypercholesterolaemic animals did not differ significantly from that isolated from NC animals (1.55 ± 0.17 Hz/sarcomere and 1.59 ± 0.1 Hz/sarcomere, n = 21 and 21, respectively, p = 0.871, Fig. 3a). The individual sparks from HC fibres and the sparks from NC fibres were slightly but significantly different in all parameters tested, namely in amplitude (0.31 ± 0.002 and 0.34 ± 0.003, n = 2239 and 1667, respectively, $p < 0.001$, Fig. 4a), in FWHM (1.25 ± 0.02 and 1.33 ± 0.02 μm, respectively, p = 0.002, Fig. 4b), in rise time (17.5 ± 0.3 and 15.7 ± 0.3 ms, respectively, $p < 0.001$, Fig. 4c), and in duration (41.1 ± 0.4 and 37.8 ± 0.4 ms, respectively, $p < 0.001$, Fig. 4d). Overall, the sparks from HC animals were somewhat smaller and slower but occurred with the same frequency as in NC rats.

Fluvastatin prevents the effects of hypercholesterolaemia on calcium sparks

Line scan images showed sparks on FDB fibres isolated both from HC and from fluvastatin treated hypercholesterolaemic (HC+S) rats (Fig. 2a–d). Frequency of the sparks on FDB fibres isolated from HC+S animals was significantly higher than that isolated from HC animals (2.38 ± 0.26 Hz/sarcomere and 1.55 ± 0.17 Hz/sarcomere, n = 18 and 21, respectively, p = 0.006, Fig. 3a). The individual sparks from HC fibres and the sparks from HC+S fibres were significantly different in amplitude (0.31 ± 0.002 and 0.35 ± 0.002, respectively, $p < 0.001$, Fig. 4a), in FWHM (1.25 ± 0.02 and 1.36 ± 0.02 μm, respectively, $p < 0.001$, Fig. 4b), in rise time (17.5 ± 0.3 and 16.0 ± 0.2 ms, respectively, $p < 0.001$, Fig. 4c), and in duration (41.1 ± 0.4 and 39.5 ± 0.3 ms, respectively, p = 0.003, Fig. 4d). Overall, sparks from fluvastatin treated hypercholesterolaemic animals were greater in amplitude, larger in spatial spread and shorter in duration than those from untreated HC animals. The sparks from HC+S fibres, however, did not differ significantly from the sparks detected on fibres from NC+S rats, indicating that fluvastatin treatment shifted the hypercholesterolaemia-associated parameters back to the control range (Fig. 4a–d).

Fluvastatin treatment does not alter the ryanodine binding to heavy SR vesicles

The finding that the frequency of sparks is significantly higher in fibres isolated from fluvastatin treated animals (either NC+S compared to NC, or HC+S compared to HC) might be explained by a direct, lasting effect of chronic application of fluvastatin altering the activity of the ryanodine receptors. To determine whether or not the presence of fluvastatin in the diet could have directly influenced the activity of the ryanodine receptors, we performed [^{3}H]ryanodine binding assays. It was found that the relative activity of the ryanodine receptors isolated from the skeletal muscle of both groups showed no difference at any [^{3}H]ryanodine concentration (Fig. 5). This was quantified by fitting the Hill (i.e. Michaelis–Menten) equation (Eq. 1) to the data points, which indicated that there was no significant difference in the EC_{50} values for ryanodine binding to the RyRs in SR vesicles isolated from NC and NC+S groups of animals (4.5 ± 0.8 and 4.0 ± 0.6 nM, respectively, p = 0.614).

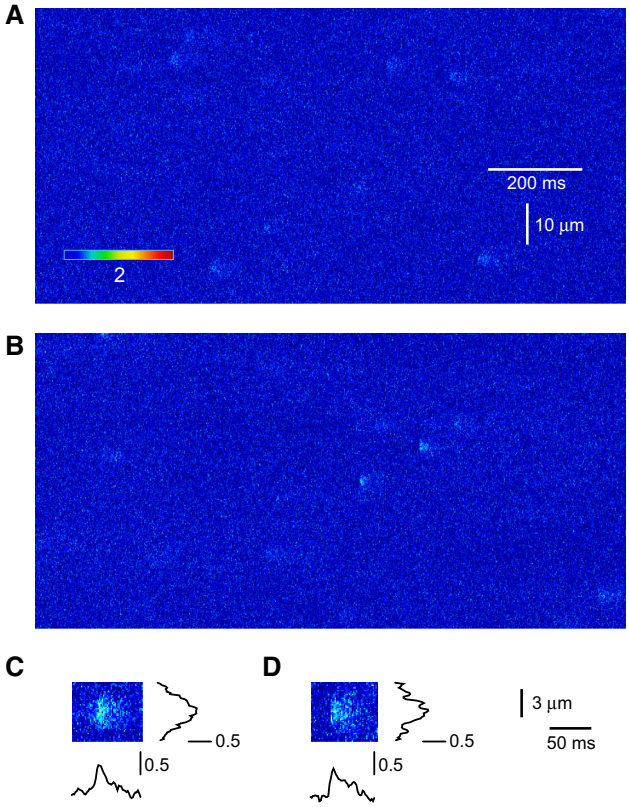


Fig. 2 Spontaneous Ca^{2+} release events in FDB fibres from hypercholesterolaemic (HC) and statin treated (HC+S) animals. **a**, **b** Line-scan images from fibres of FDB muscles from hypercholesterolaemic (**a**) and from hypercholesterolaemic and statin treated (**b**) rats. **c**, **d** Representative sparks with their spatial profiles and time courses detected in hypercholesterolaemic (**c**) and in hypercholesterolaemic and statin treated (**d**) rats. Acquisition parameters: 1024 × 512 pixel, 1.53 ms/line, 0.14 μm/pixel; temperature 22 °C. (Color figure online)

Coenzyme Q_{10} supplementation does not alter the strength of the muscle

Reduced levels of coenzyme Q_{10}, an important factor in mitochondrial energy production may contribute to the

szentesi.peter_292_24

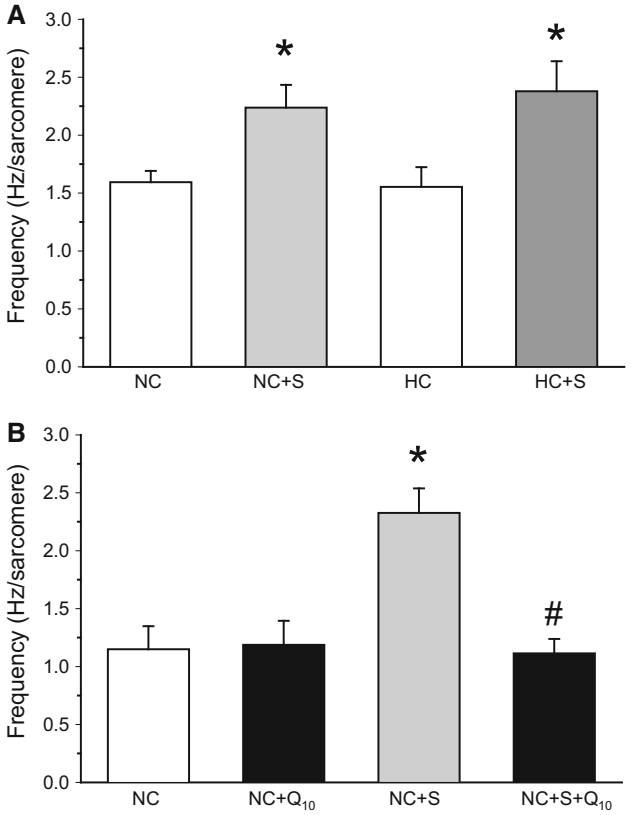


Fig. 3 Frequency of Ca^{2+} sparks. **a** Frequency of Ca^{2+} sparks on FDB fibres from NC, NC+S, HC and HC+S rats. **b** Frequency of Ca^{2+} sparks on fibres from NC, NC+Q_{10}, NC+S and NC+S+Q_{10} rats. *Asterisk* shows significant difference from fibres without statin treatment. *Hash* shows significant difference from fibres without Q_{10} treatment. Note that **a** and **b** represent different batches of experimental animals

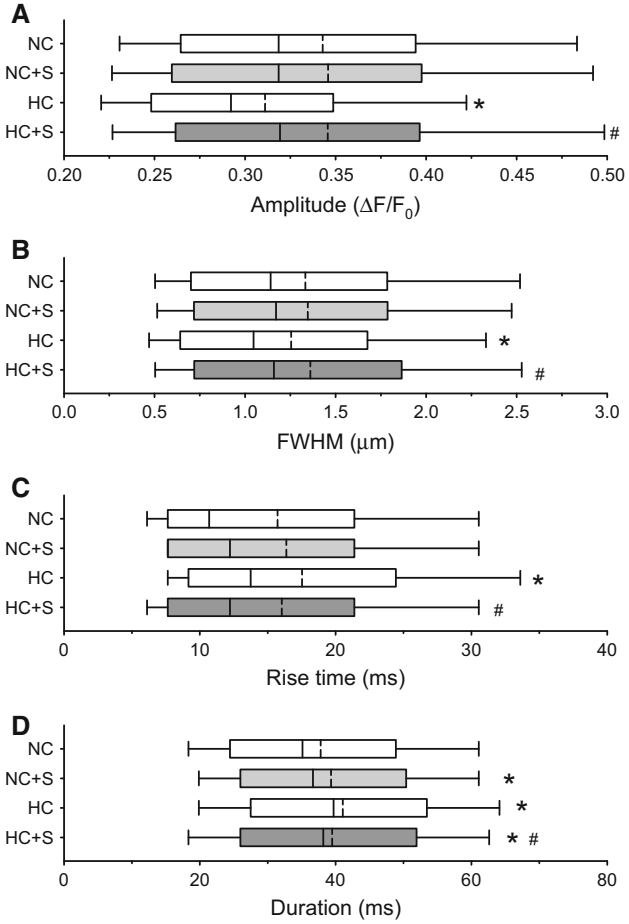


Fig. 4 Parameters of calcium release events. Amplitude (**a**), FWHM (**b**), rise time (**c**), and duration (**d**) of calcium release events from normocholesterolaemic (NC, *white bars*), from statin treated (NC+S, *grey bars*), from hypercholesterolaemic (HC, *white bars*), and from hypercholesterolaemic and statin treated animals (HC+S, *dark grey bars*). Events were identified in the line-scan images with an automated detection routine based on wavelet-transformation (see "Methods"). Values of the amplitudes (**a**) were binned and plotted as relative frequencies to present their distributions. FWHM (**b**), rise time (**c**), and duration (**d**) are presented as horizontal box plots. These plots show the mean (*dashed line*), the median (*solid line*), and the 1st and 3rd quartiles as *horizontal boxes* with *error bars* representing the 5th and 95th percentiles. Events with amplitudes smaller than 0.1 $\Delta F/F_0$ or with FWHM smaller than 0.3 μm were not included into the analysis. *Asterisk* shows significant difference between normocholesterolaemic and hypercholesterolaemic animals. *Hash* shows significant difference from fibres without statin treatment

development of statin-induced myopathy. In order to determine whether or not administration of coenzyme Q_{10} might be a powerful tool to prevent statin-induced muscle pathologies, we first investigated whether or not coenzyme Q_{10} supplementation had any effect on muscle strength.

No difference was found in the mean amplitude of the single twitches (Fig. 6a, b, e, f) or of the tetani (Fig. 6c–f) between the coenzyme Q_{10} supplemented (NC+Q_{10}) and the NC groups in either EDL (twitch: 246.4 ± 34.4 and 227.8 ± 17.7 mN, n = 8 and 14, respectively, p = 0.598; tetanus: 492.0 ± 40.4 and 471.1 ± 47.7 mN, n = 8 and 19, respectively, p = 0.793) or Sol (twitch: 108.5 ± 16.6 and 104.6 ± 5.5 mN, n = 9 and 17, respectively, p = 0.785; tetanus: 436.8 ± 86.4 and 436.0 ± 28.4 mN, n = 8 and 19, respectively, p = 0.991) muscles isolated from NC+Q_{10} and NC animals (5 and 10, respectively). There were no differences found in the twitch/tetanus ratio between the NC+Q_{10} and the NC muscles (data not shown).

We also examined the effect of coenzyme Q_{10} supplementation on the amplitude of twitches and tetani of muscles dissected from hypercholesterolaemic animals with or without fluvastatin treatment (Fig. 7). We found no significant change ($0.146 < p < 0.424$) between the HC and HC+Q_{10} groups (6 and 14 EDL muscles, 6 and 14 Sol muscles, from 3 and 7 animals, respectively) or the HC+S and the HC+S+Q_{10} groups (8 and 12 EDL muscles, 7 and

szentesi.peter_292_24

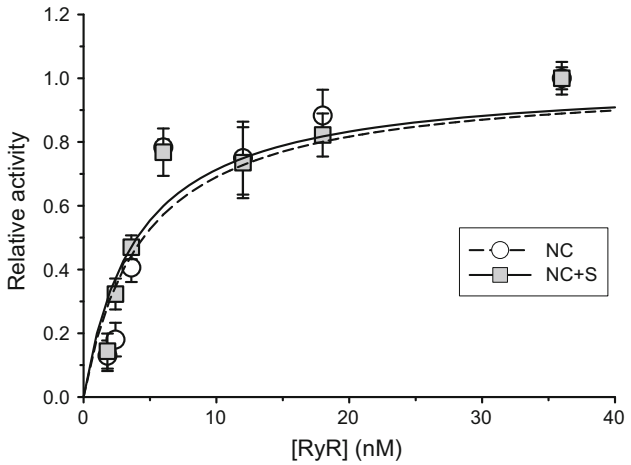


Fig. 5 Effects of chronic fluvastatin treatment on ryanodine binding to heavy SR vesicles. Ryanodine binding determined on muscle samples from control (NC, *open circle*) and statin treated (NC+S, *shaded square*) animals at different [^{3}H]ryanodine concentrations. The *solid lines* show the best fit of Eq. 1 to the data points. Assuming a single binding site (n = 1) the Hill fit resulted in EC_{50} = 4.49 ± 1.17 nM in control, whereas EC_{50} = 4.02 ± 0.81 nM in the presence of the drug in the diet. B_{max} was fixed as 1. The *lines* show the best fit of Eq. 1 to the data points (NC, *dashed line*; NC+S *solid line*)

12 Sol muscles, from 5 and 7 animals, respectively). No significant alteration of the temporal parameters (duration and time to peak) of the contractions was observed in any of the group pairs in the study (data not shown).

Coenzyme Q_{10} supplementation alters the amplitude of sparks in fibres isolated from normocholesterolaemic rats

Having established that coenzyme Q_{10} on its own has no effect on the strength of the muscles, the spontaneous Ca^{2+} release events on muscle fibres isolated from coenzyme Q_{10} supplemented rats were studied.

No difference was found between the frequency of the sparks on FDB fibres isolated from NC animals and the frequency of the sparks on fibres isolated from NC+Q_{10} animals (1.15 ± 0.2 Hz/sarcomere and 1.19 ± 0.21 Hz/sarcomere, n = 11 and 11, respectively, p = 0.989, Fig. 3b). No difference was found between the major characteristics of the individual sparks, either, except for a decrease in the amplitude. The amplitude of the sparks detected on FDB fibres isolated from NC+Q_{10} rats was 90.8 % (89.0–92.6 %, p < 0.001) of the amplitude of the sparks from NC rats (Fig. 8a), the rise time from NC+Q_{10} rats was 96.9 % (93.6–100.2 %, p = 0.1412, Fig. 8b), the FWHM was 100.3 % (96.4–104.2 %, p = 0.3202, Fig. 8c), and the duration was 100.3 % (97.8–102.7 %, p = 0.3049) of that from NC rats (Fig. 8d).

Coenzyme Q_{10} supplementation prevents the effect of fluvastatin on spark frequency

Once it had become clear that coenzyme Q_{10} by itself has no major effect on the parameters of sparks, the question arose, whether or not, and to what extent, the administration of coenzyme Q_{10} is able to prevent the effect of fluvastatin treatment on the frequency of sparks.

Frequency of the sparks on the FDB fibres isolated from coenzyme Q_{10} supplemented and fluvastatin treated (NC+S+Q_{10}) animals was significantly lower than that isolated from NC+S animals (1.11 ± 0.12 Hz/sarcomere and 2.33 ± 0.21 Hz/sarcomere, n = 12 and 15, respectively, p = 0.001, Fig. 3b), indicating that the frequency of sparks in muscles isolated from NC+S+Q_{10} animals decreased to the same range as in the NC animals. In statin treated animals coenzyme Q_{10} affected the sparks in the same way as in control animals, i.e. the amplitude was slightly decreased while all the other parameters remained unchanged (Fig. 8 grey bars).

Discussion

We shoved that a high-cholesterol diet that raises blood cholesterol level significantly (Füzi et al. 2012) does not alter the frequency of spontaneous calcium release events, but it makes the individual calcium sparks smaller and slower. Elevated blood cholesterol levels can lead to increased cholesterol content of cellular membranes (Somodi et al. 2013) and a previous study using artificially cholesterol-depleted membranes of cardiac and smooth muscle cells (Löhn et al. 2000) demonstrated that the membrane cholesterol level could affect the parameters of calcium sparks. The changes in the spark parameters seen in our experiments are, therefore, most probably attributable to the altered membrane fluidity levels due to the increased cholesterol level in rats on high-cholesterol diet.

It should, however, be noted at this point that in our experiments a short treatment with saponin was used to permeabilize the surface membrane of the isolated muscle fibers. Since saponin is known to interact with the cholesterol of the lipid bilayers (Glauert et al. 1962) to make them permeabilized, it is conceivable that the effect of saponin was slightly different, in this respect, for the animals with different blood cholesterol, as hypercholesterolaemic rats could have increased cholesterol content in their surface membrane. Albeit we believe that this effect was negligible, our conclusions regarding the effect of hypercholesterolaemia on spark parameters take this aspect into account. Nevertheless, as mentioned above, our results comply with those seen on heart and smooth muscle cells, confirming that the saponin treatment, on its own, had little

szentesi.peter_292_24

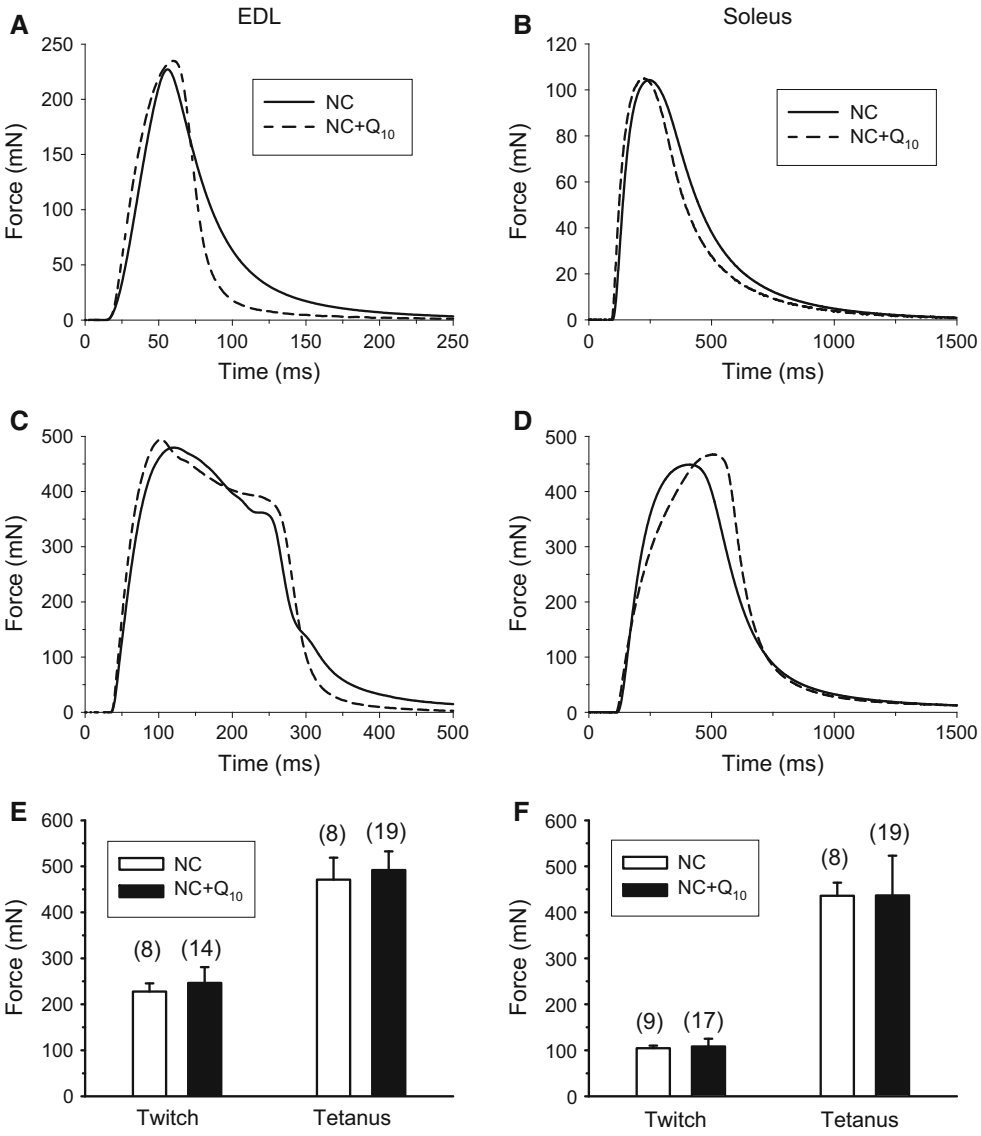


Fig. 6 Force transients in isolated muscles of normocholesterolaemic and coenzyme Q_{10} treated rats. Single twitches elicited by short (2 ms), supramaximal stimulation on EDL (**a**) and on Sol (**b**) from control (*solid line*) and from coenzyme Q_{10} treated (*dashed line*) rats. Tetani elicited by a train of supramaximal stimulation at 200 Hz for 200 ms on EDL (**c**) and at 100 Hz for 300 ms on Sol (**d**) from control (*solid line*) and from coenzyme Q_{10} treated (*dashed line*) rats. Mean amplitude of the twitches (**e**) and of the tetani (**f**). Maximum of the force transients (usually 10) were averaged on each individual record representing an individual muscle. Number of muscles studied in each group is given in parentheses. Measurements were done at 23 °C

if any effect on the parameters of the individual calcium sparks.

One of the major results of this study is that fluvastatin treatment increases the frequency of the spontaneous calcium release events, in muscles isolated both from normocholesterolaemic and from hypercholesterolaemic rats, but does not influence the main characteristics of the individual sparks, except for a minor change in the duration. An involvement of intracellular calcium handling has long been suspected in the pathomechanism of statin-associated myopathy. Simvastatin has been shown to trigger intracellular Ca^{2+} transients in skeletal muscle cells from healthy humans (Sacher et al. 2005), and to increase Ca^{2+} leak from the SR of muscle fibres isolated from healthy or ryanodine receptor mutant mice (Knoblauch et al., 2013). Acute application of simvastatin in vitro has been demonstrated to cause dysfunction of calcium homeostasis, including increased Ca^{2+} spark amplitude, in healthy human and rat muscle samples (Sacher et al. 2005; Sirvent et al. 2005). In our experiments, on the other hand, long-term fluvastatin therapy did not significantly influence the amplitude of the sparks. The discrepancy might very well be explained by the different application of the drug (acute application in vitro versus four-week-long administration in vivo).

Although it is possible that the effects of statins on the amplitude of calcium sparks depend on the duration and intensity of the treatment, it does not exclusively explain why we have found increased spark frequency in the fluvastatin treated group. We speculate that the explanation rather lies in the species differences, since—in accordance with our results—a recent investigation in a

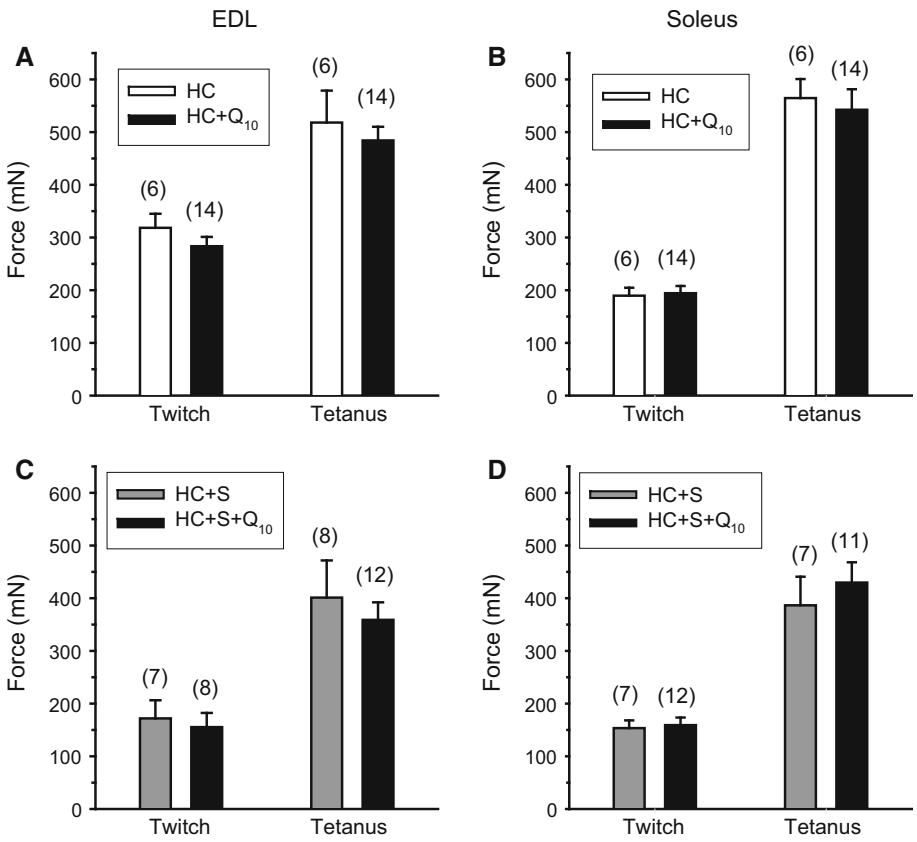


Fig. 7 Maximal force in isolated muscles of hypercholesterolaemic rats treated with fluvastatin and/or coenzyme Q_{10}. Mean amplitude of twitches and tetani on EDL (**a**, **c**) and Sol (**b**, **d**). Maximum of the force transients (usually 10; as presented in Fig. 6) were averaged on each individual record representing an individual muscle. Number of muscles studied in each group is given in parentheses. Measurements were done at 23 °C

similar rat model resulted in increased frequency and duration of calcium sparks following statin therapy (Lotteau et al., 2015), while statin-treated patients with muscle symptoms showed decreased frequency of calcium sparks (Sirvent et al. 2012). Interestingly, statin-treated patients who did not express muscle symptoms did not show altered spark frequency (Sirvent et al. 2012), suggesting that calcium homeostasis does relate to statin-induced myopathy. It is also worth noting that the increased spark frequency was characteristic of all treatment group pairs in our experiments where the only difference was the addition of fluvastatin (except for pairs containing coenzyme Q_{10}, see below) across multiple repeated experiments regardless whether the data were pooled for analysis or individual repeats were considered. Therefore, in our experimental model this change was the sole highly specific major change resulting from the addition of fluvastatin to the diet. As ryanodine binds to RyRs in a use-dependent and irreversible manner, quantity of ryanodine bound to the receptor in a unit time is an indirect measure of average ryanodine receptor open probability (Lanner et al. 2012), so we applied this method the describe the changes in RyR activity in the presence of fluvastatin in the diet. The lack of difference between the binding of ryanodine to RyRs isolated from control and fluvastatin-treated rats indicate that the higher spark frequency seen in the fluvastatin-treated group is not due to a long-term modification of the RyRs. Other proteins involved in the excitation–contraction coupling may, however, be involved in these changes since they had been removed during the isolation of the heavy SR vesicles containing RyRs. The investigation of those effects is to be carried out in a later study involving in vivo and in vitro experiments.

It should be noted here that we have previously demonstrated that in our animal model the addition of fluvastatin to rats fed with high-cholesterol diet reduces the blood cholesterol level to that of control rats (Füzi et al. 2012).Therefore, the difference between the parameters of individual sparks in the HC and HC+S groups is probably not a direct effect of fluvastatin itself on calcium sparks, rather, the result of the reduction in the cholesterol levels, since HC+S sparks were similar to those found under control conditions.

We also demonstrated that the most definite effect of coenzyme Q_{10} supplementation was to significantly reduce the frequency of the spontaneous calcium release events in muscles from fluvastatin-treated rats. This indicates that coenzyme Q_{10} supplementation prevented the spark frequency increasing effect of fluvastatin without having a

szentesi.peter_292_24

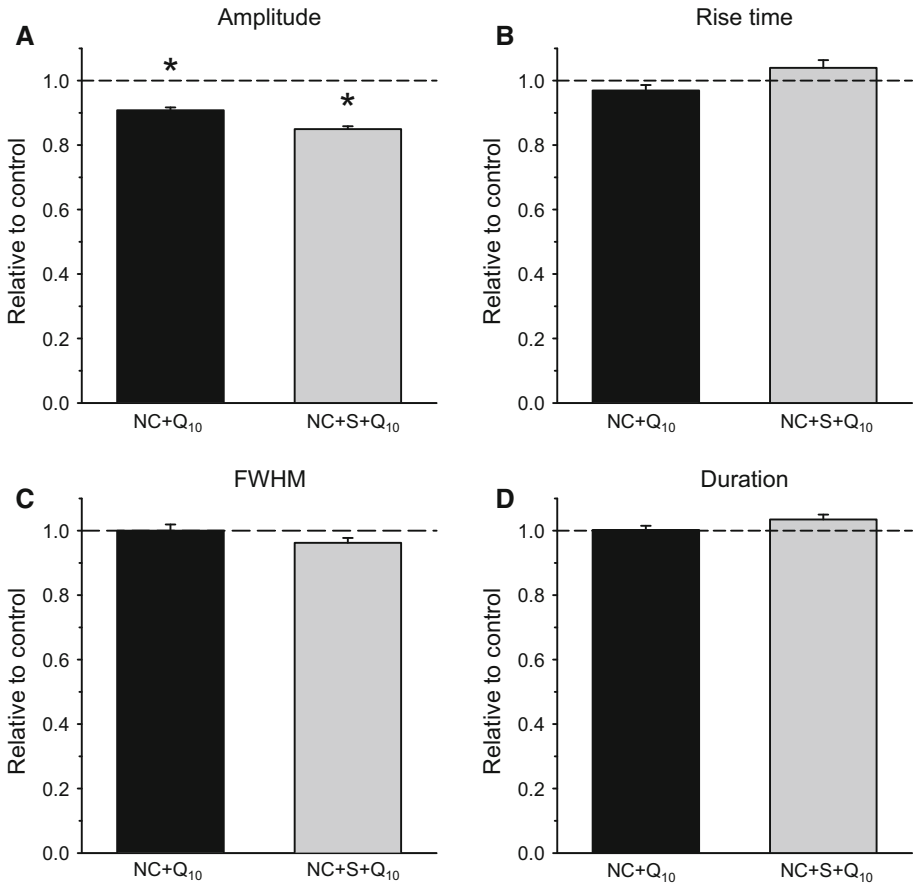


Fig. 8 Relative parameters of calcium release events in coenzyme Q_{10} treated animals. Amplitude (**a**), rise time (**b**), FWHM (**c**), and duration (**d**) of calcium release events from NC+Q_{10} (*black bars*), and from NC+S+Q_{10} (*grey bars*) animals. Values of the parameters were normalized to the average of the given parameter in the corresponding group without Q_{10} treatment. The *dashed line* indicates the relative value of the parameter in the corresponding reference group without coenzyme Q_{10} treatment. *Asterisk* shows significant difference from fibres without coenzyme Q_{10} treatment

major effect on the amount of calcium released during individual sparks. Assuming that the alterations in calcium homeostasis, more specifically the changes in calcium spark frequency and the statin-induced myopathy are related, our results further indicate that coenzyme Q_{10} supplementation might reduce the risk of the development of muscle pathologies in patients taking statins, especially fluvastatin, by preventing or reverting the changes caused by the cholesterol-lowering drug. Although the clinical effectiveness of coenzyme Q_{10} supplementation on statin-induced myopathy is controversial, our results opt for the view that coenzyme Q_{10} is protective against statin-induced adverse effects (Littlefield et al. 2014; Skarlovnik et al. 2014).

Furthermore, since the elevation of the level of reactive oxygen species (ROS) has been demonstrated to increase the frequency of calcium sparks in permeabilized skeletal muscle cells (Isaeva et al. 2005) and coenzyme Q_{10} supplementation has been reported to decrease ROS levels in the skeletal muscle of rats (Kon et al. 2007), our findings also suggest the role of ROS in the pathogenesis of statin induced myopathy. It has to be mentioned, however, that we did not find coenzyme Q_{10} supplementation being effective on the macroscopically measurable muscle functions in NC, HC or HC+S rats.

In conclusion, we have found that fluvastatin, independently from the cholesterol level in the diet, consistently and specifically increased the frequency of calcium sparks in skeletal muscle cells, an effect which can be prevented by the addition of coenzyme Q_{10} to the diet. These results reinforce theories indicating the role of calcium handling in the pathophysiology of statin-induced myopathy and also provide a possible pathway for the protective effect of coenzyme Q_{10} in patients symptomatic of this condition.

Acknowledgments This work was supported by grants from the Hungarian Scientific Research Found (OTKA K 81923), from the Hungarian Ministry of Human Resources (TÁMOP-4.2.1/B-09/1/KONV-2010-0007, TÁMOP-4.2.2/B-10/1-2010-0024, and TÁMOP-4.2.2.A-11/1/KONV-2012-0025). This research was supported by the European Union and the State of Hungary, co-financed by the European Social Fund in the framework of TÁMOP-4.2.4.A/2-11/1-2012-0001 'National Excellence Program' (DB, VJ).

References

Antons KA, Williams CD, Baker SK, Phillips PS (2006) Clinical perspectives of statin-induced rhabdomyolysis. Am J Med 119:400–409

Banach M, Serban C, Sahebkar A, Ursoniu S, Rysz J, Muntner P, Toth PP, Jones SR, Rizzo M, Glasser SP, Lip GY, Dragan S, Mikhailidis DP (2015) Effects of coenzyme Q_{10} on statin-

induced myopathy: a meta-analysis of randomized controlled trials. Mayo Clin Proc 90(1):24–34

Bookstaver DA, Burkhalter NA, Hatzigeorgiou C (2012) Effect of coenzyme Q_{10} supplementation on statin-induced myalgias. Am J Cardiol 110(4):526–529

Bruckert E, Hayem G, Dejager S, Yau C, Bégaud B (2005) Mild to moderate muscular symptoms with high-dosage statin therapy in hyperlipidemic patients—the PRIMO study. Cardiovasc Drugs Ther 19(6):403–414

Csernoch L, Szentesi P, Sárközi S, Szegedi C, Jóna I, Kovács L (1999) Effects of tetracaine on sarcoplasmic calcium release in mammalian skeletal muscle fibres. J Physiol 515(3):843–857

Daugird AJ, Crowell K, Saseen J (2003) Clinical inquiries. Do statins cause myopathy? J Fam Pract 52:973–977

EFSA Panel on Dietetic Products, Nutrition and Allergies (2010) Scientific Opinion on the substantiation of health claims related to coenzyme Q_{10} and contribution to normal energy-yielding metabolism (ID 1508, 1512, 1720, 1912, 4668), maintenance of normal blood pressure (ID 1509, 1721, 1911), protection of DNA, proteins and lipids from oxidative damage (ID 1510), contribution to normal cognitive function (ID 1511), maintenance of normal blood cholesterol concentrations (ID 1721) and increase in endurance capacity and/or endurance performance (ID 1913) pursuant to Article 13(1) of Regulation (EC) No 1924/2006. EFSA J 8(10):1793

Evans CD, Eurich DT, Lamb DA, Taylor JG, Jorgenson DJ, Semchuk WM, Mansell KD, Blackburn DF (2009) Retrospective observational assessment of statin adherence among subjects patronizing different types of community pharmacies in Canada. J Manag Care Pharm 15(6):476–484

Fernandez G, Spatz ES, Jablecki C, Phillips PS (2011) Statin myopathy: a common dilemma not reflected in clinical trials. Clevel Clin J Med 78(6):393–403

Füzi M, Palicz Z, Vincze J, Cseri J, Szombathy Z, Kovács I, Oláh A, Szentesi P, Kertai P, Paragh G, Csernoch L (2012) Fluvastatin-induced alterations of skeletal muscle function in hypercholesterolaemic rats. J Muscle Res Cell Motil 32(6):391–401

Gerber BL (2013) In vivo evaluation of atherosclerotic plaque inflammation and of anti-inflammatory effects of statins by 18F-fluorodeoxyglucose positron emission tomography. J Am Coll Cardiol 62(10):918–920

Glauert AM, Dingle JT, Lucy JA (1962) Action of saponin on biological cell membranes. Nature 196:953–955

Guarini G, Marzilli M (2013) Defining the role of high-dose statins in PCI. Am J Cardiovasc Drugs 3:189–197

Herrmann-Frank A, Richter M, Sarközi S, Mohr U, Lehmann-Horn F (1996) 4-Chloro-m-cresol, a potent and specific activator of the skeletal muscle ryanodine receptor. Biochim Biophys Acta 1289(1):31–40

Inoue R, Tanabe M, Kono K, Maruyama K, Ikemoto T, Endo M (2003) Ca^{2+}-releasing effect of cerivastatin on the sarcoplasmic reticulum of mouse and rat skeletal muscle fibers. J Pharmacol Sci 93(3):279–288

Isaeva EV, Shkryl VM, Shirokova N (2005) Mitochondrial redox state and Ca^{2+} sparks in permeabilized mammalian skeletal muscle. J Physiol 565(Pt 3):855–872

Jackevicius CA, Mamdani M, Tu JV (2002) Adherence with statin therapy in elderly patients with and without acute coronary syndromes. JAMA 288(4):462–467

Johnson TE, Zhang X, Bleicher KB, Dysart G, Loughlin AF, Schaefer WH, Umbenhauer DR (2004) Statins induce apoptosis in rat and human myotube cultures by inhibiting protein geranylgeranylation but not ubiquinone. Toxicol Appl Pharmacol 200(3):237–250

Knoblauch M, Dagnino-Acosta A, Hamilton SL (2013) Mice with RyR1 mutation (Y524S) undergo hypermetabolic response to simvastatin. Skelet Muscle 3(1):22

Kon M, Kimura F, Akimoto T, Tanabe K, Murase Y, Ikemune S, Kono I (2007) Effect of Coenzyme Q_{10} supplementation on exercise-induced muscular injury of rats. Exerc Immunol Rev 13:76–88

Lanner JT, Georgiou DK, Dagnino-Acosta A, Ainbinder A, Cheng Q, Joshi AD, Chen Z, Yarotskyy V, Oakes JM, Lee CS, Monroe TO, Santillan A, Dong K, Goodyear L, Ismailov II, Rodney GG, Dirksen RT, Hamilton SL (2012) AICAR prevents heat-induced sudden death in RyR1 mutant mice independent of AMPK activation. Nat Med 18(2):244–251

Littlefield N, Beckstrand RL, Luthy KE (2014) Statins' effect on plasma levels of coenzyme Q_{10} and improvement in myopathy with supplementation. J Am Assoc Nurse Pract 26(2):85–90

Löhn M, Fürstenau M, Sagach V, Elger M, Schulze W, Luft FC, Haller H, Gollasch M (2000) Ignition of calcium sparks in arterial and cardiac muscle through caveolae. Circ Res 87(11):1034–1039

Lotteau S, MacDougall D, Steele D, Calaghan S (2015) Statin induced myopathy: a role for mitochondrial Ca2D and no in enhanced sarcoplasmic reticulum Ca^{2+} Leak. Biophys J 108(2):567a

Lukács B, Sztretye M, Almássy J, Sárközi S, Dienes B, Mabrouk K, Simut C, Szabó L, Szentesi P, De Waard M, Ronjat M, Jóna I, Csernoch L (2008) Charged surface area of maurocalcine determines its interaction with the skeletal ryanodine receptor. Biophys J 95(7):3497–3509

Marcoff L, Thompson PD (2007) The role of coenzyme Q_{10} in statin-associated myopathy: a systematic review. J Am Coll Cardiol 49(23):2231–2237

Mihaylova B, Emberson J, Blackwell L, Keech A, Simes J, Barnes EH, Voysey M, Gray A, Collins R, Baigent C (2012) The effects of lowering LDL cholesterol with statin therapy in people at low risk of vascular disease: meta-analysis of individual data from 27 randomised trials. Lancet 380(9841):581–590

Nakahara K, Kuriyama M, Sonoda Y, Yoshidome H, Nakagawa H, Fujiyama J, Higuchi I, Osame M (1998) Myopathy induced by HMG-CoA reductase inhibitors in rabbits: a pathological, electrophysiological, and biochemical study. Toxicol Appl Pharmacol 152(1):99–106

Oddoux S, Brocard J, Schweitzer A, Szentesi P, Giannesini B, Brocard J, Fauré J, Pernet-Gallay K, Bendahan D, Lunardi J, Csernoch L, Marty I (2009) Triadin deletion induces impaired skeletal muscle function. J Biol Chem 284(50):34918–34929

Padra JT, Seres I, Oláh A, Fenyvesi F, Paragh G, Paragh G, Csernoch L, Fóris G, Kertai P (2014) A comparative study on dyslipidaemia inducing diets in various rat strains. Acta Physiol Hung 101(2):250–258

Päivä H, Thelen KM, Van Coster R, Smet J, De Paepe B, Mattila KM, Laakso J, Lehtimäki T, von Bergmann K, Lütjohann D, Laaksonen R (2005) High-dose statins and skeletal muscle metabolism in humans: a randomized, controlled trial. Clin Pharmacol Ther 78(1):60–68

Sacher J, Weigl L, Werner M, Szegedi C, Hohenegger M (2005) Delineation of myotoxicity induced by 3-hydroxy-3-methylglutaryl CoA reductase inhibitors in human skeletal muscle cells. J Pharmacol Exp Ther 314(3):1032–1041

Salarieh A, Soler AP, Axiotis CA (2004) Overexpression of neural cell adhesion molecule in regenerative muscle fibers in 3-hydroxy-3-methylglutaryl coenzyme: a reductase inhibitor-induced rhabdomyolysis. Appl Immunohistochem Mol Morphol 12(3):234–239

Sárközi S, Szegedi C, Lukács B, Ronjat M, Jóna I (2005) Effect of gadolinium on the ryanodine receptor/sarcoplasmic reticulum calcium release channel of skeletal muscle. FEBS J 272(2):464–471

Schaefer WH, Lawrence JW, Loughlin AF, Stoffregen DA, Mixson LA, Dean DC, Raab CE, Yu NX, Lankas GR, Frederick CB

szentesi.peter_292_24

(2004) Evaluation of ubiquinone concentration and mitochondrial function relative to cerivastatin-induced skeletal myopathy in rats. Toxicol Appl Pharmacol 194(1):10–23

Sirvent P, Mercier J, Vassort G, Lacampagne A (2005) Simvastatin triggers mitochondria-induced Ca2 + signaling alteration in skeletal muscle. Biochem. Biophys. Res. Commun. 329(3):1067–1075

Sirvent P, Fabre O, Bordenave S, Hillaire-Buys D, Raynaud De Mauverger E, Lacampagne A, Mercier J (2012) Muscle mitochondrial metabolism and calcium signaling impairment in patients treated with statins. Toxicol Appl Pharmacol 259(2):263–268

Skarlovnik A, Janić M, Lunder M, Turk M, Šabovič M (2014) Coenzyme Q_{10} supplementation decreases statin-related mild-to-moderate muscle symptoms: a randomized clinical study. Med Sci Monit 20:2183–2188

Somodi S, Balajthy A, Szilágyi O, Pethő Z, Harangi M, Paragh G, Panyi G, Hajdu P (2013) Analysis of the K+ current in human CD4+ T lymphocytes in hypercholesterolemic state. Cell Immunol 281(1):20–26

Szabó LZ, Vincze J, Csernoch L, Szentesi P (2010) Improved spark and ember detection using stationary wavelet transforms. J Theor Biol 264(4):1279–1292

Szegedi C, Sárközi S, Herzog A, Jóna I, Varsányi M (1999) Calsequestrin: more than 'only' a luminal Ca^{2+} buffer inside the sarcoplasmic reticulum. Biochem J 337(1):19–22

Szentesi P, Szappanos H, Szegedi C, Gönczi M, Jóna I, Cseri J, Kovács L, Csernoch L (2004) Altered elementary calcium release events and enhanced calcium release by thymol in rat skeletal muscle. Biophys J 86(3):1436–1453

Taylor F, Huffman MD, Macedo AF, Moore TH, Burke M, Davey Smith G, Ward K, Ebrahim S (2013) Statins for the primary prevention of cardiovascular disease. Cochrane Database Syst Rev 1:CD004816. doi:10.1002/14651858.CD004816.pub5

Taylor BA, Lorson L, White CM, Thompson PD (2015) A randomized trial of coenzyme Q_{10} in patients with confirmed Statin Myopathy. Atherosclerosis. 238(2):329–335

Tomlinson SS, Mangione KK (2005) Potential adverse effects of statins on muscle. Phys Ther 85:459–465

Waclawik AJ, Lindal S, Engel AG (1993) Experimental lovastatin myopathy. J Neuropathol Exp Neurol 52(5):542–549